Transactions of the ASME®

Technical Editor
H. D. NELSON (2001)

Associate Technical Editors
Advanced Energy Systems
M. J. MORAN (1999)
Gas Turbine (Review Chair)
D. WISLER (2001)
Gas Turbine
D. COOKE (1999)
M. MIGNOLET (2002)
J. PETERS (1999)
Internal Combustion Engines
D. ASSANIS (1999)
Nuclear
R. DUFFEY (2001)
Power
D. LOU

BOARD ON COMMUNICATIONS
Chairman and Vice President
R. K. SHAH

OFFICERS OF THE ASME
President, W. M. PHILLIPS
Executive Director, D. L. BELDEN
Treasurer, J. A. MASON

PUBLISHING STAFF
Managing Director, Engineering
CHARLES W. BEARDSLEY
Director, Technical Publishing
PHILIP DI VIETRO
Managing Editor, Technical Publishing
CYNTHIA B. CLARK
Managing Editor, Transactions
CORNELIA MONAHAN
Production Coordinator
COLIN MCATEER
Production Assistant
MARISOL ANDINO

Transactions of the ASME, Journal of Engineering for Gas Turbines and Power (ISSN 0742-4795) is published quarterly (Jan., April, July, Oct.) for $205.00 per year by The American Society of Mechanical Engineers, Three Park Avenue, New York, NY 10016. Periodicals postage paid at New York, NY and additional mailing offices. POSTMASTER: Send address changes to Transactions of the ASME, Journal of Engineering for Gas Turbines and Power, c/o THE AMERICAN SOCIETY OF MECHANICAL ENGINEERS, 22 Law Drive, Box 2300, Fairfield, NJ 07007-2300.
CHANGES OF ADDRESS must be received at Society headquarters seven weeks before they are to be effective. Please send old label and new address.
PRICES: To members, $40.00, annually: to nonmembers, $205.00. Add $40.00 for postage to countries outside the United States and Canada.
STATEMENT from By-Laws. The Society shall not be responsible for statements or opinions advanced in papers or . . . printed in its publications (B7.1, par. 3).

INDEXED by Applied Mechanics Reviews and Engineering Information, Inc. Canadian Goods & Services Tax Registration #126148048

Journal of Engineering for Gas Turbines and Power

Published Quarterly by The American Society of Mechanical Engineers

VOLUME 121 • NUMBER 1 • JANUARY 1999

TECHNICAL PAPERS

Gas Turbines: Aircraft

1 Preliminary Design of Low Cost Propulsion Systems Using Next Generation Cost Modeling Techniques
J. L. Younghans, R. M. Donaldson, D. R. Wallace, L. L. Long, and R. B. Stewart

6 Gas Turbine Cycle Design Methodology: A Comparison of Parameter Variation With Numerical Optimization
J. Kurzke

Gas Turbines: Ceramics

12 Development of a Combustor Liner Composed of Ceramic Matrix Composite (CMC)
K. Nishio, K.-I. Igashira, K. Take, and T. Suemitsu

18 Elevated-Temperature "Ultra" Fast Fracture Strength of Advanced Ceramics: An Approach to Elevated-Temperature "Inert" Strength
S. R. Choi and J. P. Gyekenyesi

Gas Turbines: Coal, Biomass, and Alternative Fuels

25 Cycle Analyses of 5 and 20 MWe Biomass Gasifier-Based Electric Power Stations in Hawaii
D. M. Ishimura, C. M. Kinoshita, S. M. Masutani, and S. Q. Turn

31 A Numerical Analysis of the Emissions Characteristics of Biodiesel Blended Fuels
C. Y. Choi and R. D. Reitz

38 Final Report on the Development of a Hydrogen-Fueled Combustion Turbine Cycle for Power Generation
R. L. Bannister, R. A. Newby, and W. C. Yang

46 Effect of Air Extraction for Cooling and/or Gasification on Combustor Flow Uniformity
T. Wang, J. S. Kapat, W. R. Ryan, I. S. Diakunchak, and R. L. Bannister

55 Co-Pyrolysis of Coal/Biomass and Coal/Sewage Sludge Mixtures
C. Storm, H. Rüdiger, H. Spliethoff, and K. R. G. Hein

64 A Small Scale Biomass Fueled Gas Turbine Engine
J. D. Craig and C. R. Purvis

Gas Turbines: Combustion and Fuels

68 An Investigation of the Formation and Venting of Flammable Mixtures Formed Within Liquid Fuel Vessels
R. Bunama, G. A. Karim, and C. Y. Zhang

74 The Effect of Time of Exposure to Elevated Temperatures on the Flammability Limits of Some Common Gaseous Fuels in Air
I. Wierzba and B. B. Ale

80 The Development of a Computer Code for the Estimation of Combustor Exhaust Temperature Using Simple Gas Analysis Measurements
R. J. Bideau

89 CFD Modeling of a Gas Turbine Combustor From Compressor Exit to Turbine Inlet
D. S. Crocker, D. Nickolaus, and C. E. Smith

Gas Turbines: Controls and Diagnostics

96 Distributed Flight Control and Propulsion Control Implementation Issues and Lessons Learned
W. R. Schley

102 Distributed Control System for Turbine Engines
P. L. Shaffer

(Contents continued on outside back cover)

This journal is printed on acid-free paper, which exceeds the ANSI Z39.48-1992 specification for permanence of paper and library materials. ♾ ™

♻ 85% recycled content, including 10% post-consumer fibers.

(Contents continued)

Gas Turbines: Cycle Innovations

108 Conceptual Design of the Cooling System for 1700°C-Class, Hydrogen-Fueled Combustion Gas Turbines
N. Kizuka, K. Sagae, S. Anzai, S. Marushima, T. Ikeguchi, and K. Kawaike

116 Zero-Emission MATIANT Cycle
P. Mathieu and R. Nihart

Gas Turbines: Heat Transfer

121 A Numerical Investigation of the Cooling Effect of Compressed Natural Gas Throttling on Engine Delivery Ratio
Y. Yacoub, L. Marbun, and R. Bata

Gas Turbines: Manufacturing, Materials, and Metallurgy

129 Application of Stress Relaxation Testing in Metallurgical Life Assessment Evaluations of GTD111 Alloy Turbine Buckets
J. A. Daleo, K. A. Ellison, and D. A. Woodford

138 Improved Performance Rhenium Containing Single Crystal Alloy Turbine Blades Utilizing PPM Levels of the Highly Reactive Elements Lanthanum and Yttrium
D. A. Ford, K. P. L. Fullagar, H. K. Bhangu, M. C. Thomas, P. S. Burkholder, P. S. Korinko, K. Harris, and J. B. Wahl

Gas Turbines: Structures and Dynamics

144 A Quasi-Two-Dimensional Method for the Rotordynamic Analysis of Centered Labyrinth Liquid Seals
M. Arghir and J. Frêne

153 Experimental Rotordynamic Coefficient Results for (a) a Labyrinth Seal With and Without Shunt Injection and (b) a Honeycomb Seal
E. A. Soto and D. W. Childs

160 A Test Facility for the Measurement of Torques at the Shaft to Seal Interface in Brush Seals
P. E. Wood and T. V. Jones

Gas Turbines: Turbomachinery

167 High Temperature Proximity Measurement in Aero and Industrial Turbomachinery
A. G. Sheard, S. G. O'Donnell, and J. F. Stringfellow

ANNOUNCEMENTS

30 Change of Address Form for the Journal of Engineering for Gas Turbines and Power

120 800-THE-ASME

128 infocentral@asme.org

Inside Back Cover Information for Authors

J. L. Younghans

R. M. Donaldson

D. R. Wallace

L. L. Long

R. B. Stewart

GE Aircraft Engines,
1 Neumann Way - MD G31,
Cincinnati, Ohio 45233

Preliminary Design of Low Cost Propulsion Systems Using Next Generation Cost Modeling Techniques

Introduction

At GE Aircraft Engines (GEAE), during the preliminary design process for aircraft propulsion systems, the designer has always been concerned about the cost implications of engine architecture and material requirements, which are driven by design specified engine thermodynamic operating conditions. The concern was not only about initial acquisition economics, but about maintenance costs associated with the propulsion life cycle as well as the development costs associated with design and certification of the power plant. The difficulty has been that there was no rapid, accurate cost estimating process to allow the designers ready access to the cost implications of design choices. High cycle pressure ratios and bypass ratios were thermodynamically attractive in reducing SFC. Technology, whether in the form of complex aerodynamic blade shapes to increase efficiency or higher temperature materials to reduce undesirable effects of cooling flows on SFC, was considered without in depth quantitative cost impacts of these design choices.

Unprecedented levels of airline financial losses in the early 1990s provided a clear focus, for both current and future products, indicating cost is a key discriminator. Airline customers demanded engines that are affordable both to buy and to own. Clearly a need had been established to quickly and accurately understand the cost and life implications of preliminary design choices.

Examination of cost models, both inside and outside the company, failed to locate a generic model which satisfied GEAE business needs; i.e., one that

- costed parts based on physical attributes and compared them to production parts in a cost data base
- utilized current production costs for parts and was tied to a system that was periodically updated
- costed development and certification programs associated with engine design choices
- reflected the impact of thermodynamic design choices on maintenance cost associated with long term product utilization

The technical challenge had been established and GEAE launched an initiative in the early 1990s to produce such a code. This paper presents trade studies considering engine cycle trades with cost as a key discriminator.

Contributed by the International Gas Turbine Institute and presented at the International Gas Turbine and Aeroengine Congress and Exhibition, Stockholm, Sweden, June 2–5, 1998. Manuscript received by the ASME Headquarters April 1, 1998. Paper No. 98-GT-182. Associate Technical Editor: R. Kielb.

Integrated Preliminary Design System

To function in a manner which provides rapid response and system optimization, a preliminary design tool set, capable of being integrated, is required. The specific needs are linkable models that define

- parametric engine cycle performance
- parametric engine weight
- engine cost
- A/C mission analysis

Ideally these programs would be linked and on-line user specified inputs would generate real time system impacts and interdependencies. At a minimum, the programs must provide input to each other with minimal user intervention. Emission and noise considerations must also be assessed in any actual product study. For the purpose of brevity and relative simplicity the emission and acoustic effects are not considered for the study presented here.

The preliminary design system currently in use at GEAE has the above linkable tool set inputs and was utilized to present the results contained in this paper.

Cost Modeling

The following three basic approaches are used in cost modeling: parametric, bottom-up, and comparative.

Parametric Techniques. These techniques use statistical relationships derived from general historical data. Parametrics are a function of one or more cost or noncost related parameters (i.e., weight, size), simplistic, and part specific. Parametrics are generally valid within a narrow technology band; however, for use on emerging technologies, these relationships typically become unreliable.

Bottom-Up Techniques. These techniques estimate costs operation by operation and are based on related parameters. Bottoms-up techniques require applicable historical data and are very time intensive.

Comparative Techniques. These techniques estimate the cost of a new part by adjusting the cost of existing parts to account for the differences in size, materials, configuration, and features. Because comparative costs are rolled up from the part level, they are comparable in accuracy to bottoms up techniques, but are much simpler.

The COMPEAT$™ Cost Model uses the comparative approach automating current manual cost estimating methods. The model takes advantage of advances in software technologies

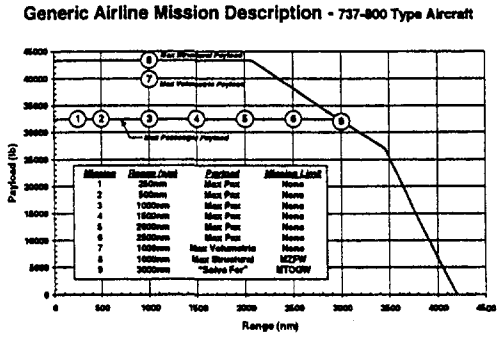

Fig. 1 Mission description

integrating engineering information systems and historical databases, from which comparative data is used as a basis of cost estimating. The COMPEAT^{TM} Cost Model comparative process provides bottom up accuracy with parametric simplicity.

Application of Surplus Value to Engine Optimization

In the following sections, the surplus value concept and its application to optimization of a medium range commercial aircraft engine will be described. How the maximum surplus value engine differs from the minimum fuel burn engine and the minimum direct operating cost engine will also be discussed.

Surplus Value Concept. The concept of surplus value was documented by Collopy in 1997 [1]. In simple terms, the surplus value of a commercial aircraft is the difference between the present value of the profit stream generated by the aircraft and the cost of manufacturing the aircraft and engines. Therefore, the surplus value represents the total profit potential of the aircraft, which is divided among the airline, airframe manufacturer, and engine manufacturer through the action of a competitive market.

Collopy further demonstrated that in a rational market where profit potential is the airlines' only aircraft selection criteria, two or more competing aircraft can share in the market on a sustained basis only when the sale prices of the aircraft are adjusted such that the net profit available to the airline (i.e., the difference between the present value of the revenue stream generated by the aircraft and the purchase price of the aircraft) is the same for all competing aircraft. Therefore, the airlines get the same surplus value from any of the competing aircraft in this scenario, and the airframe and engine manufacturers divide the difference between the total surplus value and the airlines' share. Hence, the manufacturers of the aircraft and engine combination with the highest total surplus value receive a larger profit than their competitors. By similar reasoning, it follows that when two or more engines compete on the same aircraft, the manufacturer whose engine provides the highest surplus value on the aircraft will receive a larger profit than his competitors. Therefore, it is in the best interests of the engine manufacturers, airframe manufacturers, airlines, and ultimately consumers, to optimize engine designs to achieve maximum aircraft surplus value.

Application of the Surplus Value Concept. To demonstrate the utility of the surplus value method in engine optimization, a typical domestic 160 passenger narrow-body aircraft (fixed not rubber), with a design range of approximately 3000 nm (range capability with max passenger loading) was considered. The aircraft was assumed to be unconstrained by installation issues that would have an adverse effect on engine to wing installation weight or drag. Also, the aircraft was not limited by fuel capacity for any of the engines studied. These were all done to ensure that aircraft specific items would not alter the general engine parameter trends that were being studied in this paper. Also, it is typical of a new aircraft/engine combination.

The Engine Synthesis Program (ESP) and the COMPEAT^{TM} Cost Model were used to evaluate the performance, weight, and cost of a parametric set of engines designed to the same high pressure turbine rotor inlet temperature limit, 2800°F, and the same takeoff and top of climb thrust levels. All of the engines were two spool turbofans of the following same basic architecture:

- single stage, solid metal, wide chord fan
- three to four stage booster
- seven to nine stage high pressure compressor
- dual annular combustor
- two stage high pressure turbine
- four to seven stage low pressure turbine
- separate flow nacelle

The mission and economic analyses for each of these engines were performed using the methodology described in the following sections.

Mission Mix Scenario. The mission mix scenario was created to model typical domestic aircraft operation. As shown in Fig. 1, nine missions were spread throughout the range/payload envelope.

A distribution of ranges and payloads was then determined from typical operating conditions, which when combined with the missions, yielded the breakdown shown in Fig. 2.

The first six missions are typical of "nonlimited" operations. This means each engine is carrying the same payload (average load of 65 percent pax and 35 percent cargo). The seventh mission is flown with maximum volumetric payload. Again, each engine carries the same payload, but the total payload is higher than that in missions 1–6 (payload is max passengers and max cargo using a typical cargo density). The eighth mission is flown with max structural payload. In this case, since aircraft are certified to a MZFW (max zero fuel weight), the engine weight affects the ability to carry payload. Hence, the heavier the engine, the less cargo that can be carried (each engine carries max passenger load but varying cargo loads). The ninth and final mission in the mix consists of a typical MTOGW (max takeoff gross weight) limited mission. A 3000 nm mission was chosen to allow for approximately a max passenger loading; however, each engine will carry a different payload in this case. The average range of the nine missions studied was $\approx$1300 nm, which is typical of aircraft in this market category.

Mission Analysis Methodology. The study aircraft was flown with each of the study engines for all of the nine missions described in the mission mix. The missions were executed using typical mission rules and reserves. A particular study engine configuration affects aircraft mission performance through engine SFC, nacelle drag, and engine weight. For the purposes of

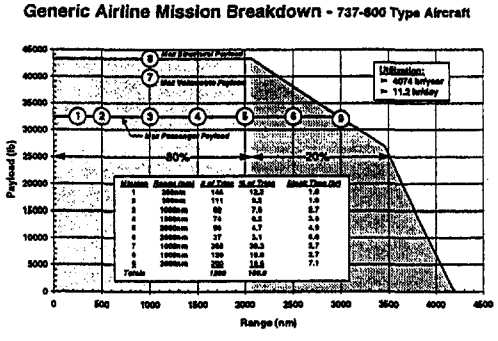

Fig. 2 Mission breakdown

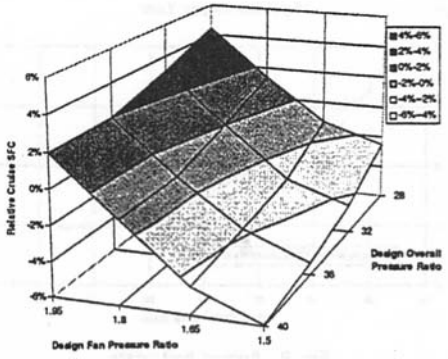

Fig. 3 Effect of fan pressure ratio and overall pressure ratio on cruise SFC

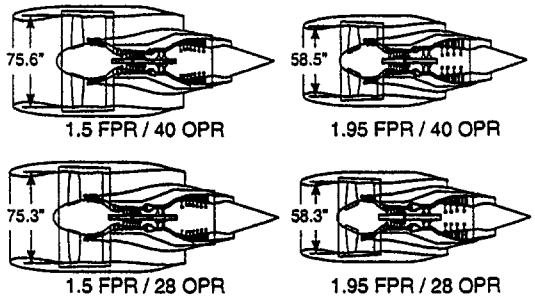

Fig. 5 Effect of engine cycle on size at constant takeoff and top of climb thrust

this study, engine SFC, relative to a given reference engine installation, is reflected in a change to aircraft specific range characteristics. A change in nacelle drag, due to fan diameter (i.e., low FPR = high fan diameter), is also reflected by a change in aircraft specific range characteristics. Propulsion system weight is reflected in aircraft empty weight. Since the study aircraft is a domestic 160 passenger aircraft (i.e., twin-engined) a particular engine's weight, relative to the reference engine, changes the empty weight by a factor of two on engine weight with an additional weight term added to reflect the structure required to mate those engines with the airframe. Each of the missions in the mission mix contributes to operating cost through fuel burn (i.e., a function of weight, drag, and SFC). In addition, operating cost is dependent on the mission results since engine flight hours affect maintenance costs. The major contributor to the overall profitability of the aircraft is revenue, which comes from payload capability in the form of passengers and/or cargo. Therefore, the profitability figures of merit (that vary with each study engine) are fuel burn, flight time, and payload.

Economic Analysis Methodology. In order to analyze the engines in terms of actual airline usage scenarios, an economic analysis has been performed based on the mission analysis results. As described earlier, the surplus value concept is a method which quantifies and ranks the appropriate items to be compared. A modification of this method has been used. This has been done in the interest of better showing the study engine trends as applied to the profit potential of the overall system. The simplification entails utilizing a markup of engine manufacturing cost to determine an engine price, and similarly utilizing the aircraft price, rather than aircraft cost. Inserting these assumptions into the surplus value calculation results in a typical NPV (net present value) analysis. No attempts have been made to study the distribution of the profit between engine manufacturer, airframe manufacturer, and airline. Rather, the study defines the relative profit available assuming the airframe and engine manufacturer have obtained a fixed profit through the markup of cost to price. The study engine trends developed with this simplified method are the same as would be seen with the surplus value method, only the magnitude of the results differ.

The methodology used in performing the economic analysis is a combination of standard DOC (Direct Operating Cost) techniques, coupled with a revenue stream and ultimately results in the NPV analysis. Total DOC+I (direct operating cost + interest) results are made up of flight crew, cabin crew, fuel burn, engine maintenance, airframe maintenance, insurance, landing fees, airframe and engine depreciation, and airframe and engine interest. The "cost" items from the nine missions, coupled with the mission weightings, are totaled to create a yearly "expense". The payload data from each of the nine missions is then divided into passenger and cargo revenue, based on the relevant distributions for each mission. When combined with the mission weightings, a yearly "revenue" is created. Combining the revenues, expense and tax information yields a yearly financial picture. Evaluating these items over a typical service life provides a cash flow stream that, when compared against the initial investment, allows an NPV calculation to be made. The NPV has been determined using a fixed discount rate. The NPV becomes the economic figure of merit used to determine the overall economic "winner" among the study engines. This approach allows the study engines to be ranked by potential economic benefit available to a typical airline customer.

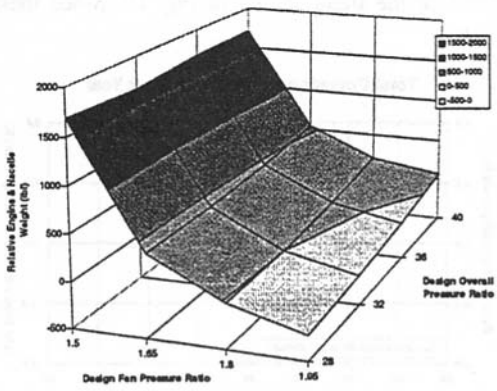

Fig. 4 Effect of fan pressure ratio and overall pressure ratio on engine weight

Engine Cycle Trade Study

The basic cycle parameters, fan pressure ratio (FPR), and overall pressure ratio (OPR), are of primary importance in the design of a new turbofan engine. These parameters, which are set very early in the design process, have a major impact on the engine weight, cost, and fuel consumption. To demonstrate

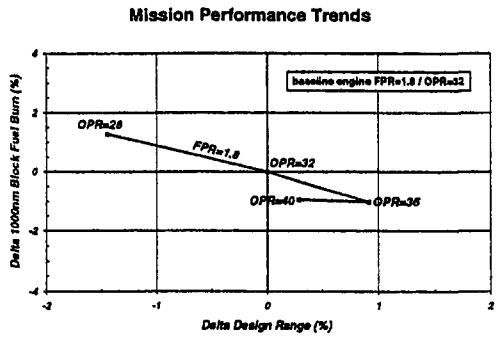

Fig. 6 Mission performance trends

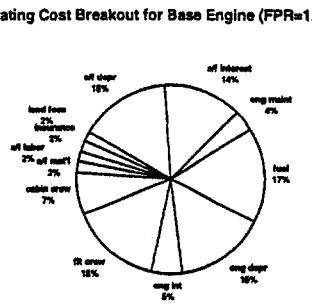

Fig. 7 Operating cost breakout

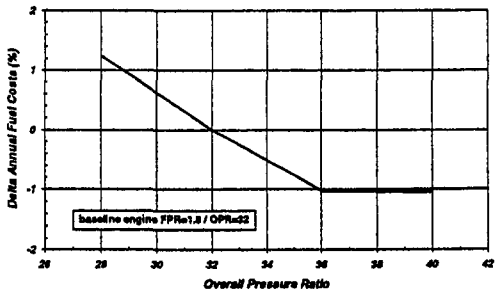

Fig. 9 Annual fuel costs

the surplus value method of optimizing these parameters, we examined the design space defined by a fan pressure ratio range of 1.5 to 1.95 and an overall pressure ratio range of 28 to 40. The results, discussed in the following sections, utilize FPR = 1.8 and OPR = 32 as a baseline.

Engine Characteristics. The specific fuel consumption and engine weight and trends are shown in Fig. 3 and Fig. 4 respectively. As fan pressure ratio is reduced, the bypass ratio and the propulsive efficiency both increase. This results in a significant improvement in specific fuel consumption. However, this also results in a weight increase because fan airflow, and hence diameter, must increase to maintain constant thrust. This effect is illustrated in Fig. 5, where the ESP-generated flowpath drawings are shown for the four corners of the design space. It should be noted that the weight increases rapidly between 1.65 and 1.5 fan pressure ratio because only solid metal fan blades have been chosen for this study. If the lower fan pressure ratio range looked favorable for this application, a weight reduction technology, such as a composite fan blade, could be used to mitigate the weight increase.

Engine specific fuel consumption, weight and cost are influenced by both overall pressure ratio as well. As overall pressure ratio is increased in the range of interest, the thermal efficiency of the cycle increases and the specific fuel consumption decreases. At the same time, the specific power of the core tends to decrease, so the core must be slightly larger to produce the same fan power.

Mission Analysis Results. For the purposes of simplification, the FPR = 1.80 engines have been selected to show the cost and revenue trends with varying OPR. This intermediate FPR was selected as a balance between mission performance and acoustic requirements. Figure 6 depicts mission performance as a function of engine OPR. Delta design range is an indication of MTOGW limited payload capability (mission 9) while 1000 nm delta fuel burn is a reflection of operating cost due to mission weighted fuel burn (missions 1–7). Here it can be seen that, on the study aircraft with the assumed study engine configuration, the high OPR engines offer better design range and fuel burn until that point at which the weight attendant with core size and stage count offsets that improvement in SFC associated with better thermal efficiency. Short haul aircraft are more sensitive to engine weight than SFC due to lower fuel fractions. The aircraft operating costs are based on the integration of fuel burns across the mission mix rather than 1000 nm fuel burn only.

Economic Results. Figure 7 shows the breakdown of individual cost items within the Total DOC+I (total op cost) term for the baseline engine over a one year operation. It must be noted that the engine affects only 35–40 percent of the total aircraft operational cost. Range of variation due to cycle impacts must be significantly less than 35 percent.

Figure 8 shows the relative manufacturing costs for varying OPR. The manufacturing cost trends are similar to the weight trends; larger engines tend to be both heavier and more expensive. However, the cost trends are not as smooth because they are more strongly influenced by discrete changes in materials and numbers of turbomachinery stages. The higher pressure compressor also requires more stages to produce the higher overall pressure ratio. These effects drive both weight and cost up. In addition, as overall pressure ratio rises, more costly materials are required in the compressor and turbines to withstand the resulting temperature increases.

Figure 9 shows the change in annual fuel costs for varying OPR at a constant FPR = 1.80. Essentially, this chart is a reflection of the block fuel burn results shown earlier, although the annual fuel costs are the result of the integration of fuel costs on all nine missions as they are weighted for one year's use.

Figure 10 shows aircraft total operating cost for one year's operation on a relative basis. As was mentioned earlier, engine related items account for about 35 percent of the total operating cost of the aircraft, of which fuel costs are but one contributor. The other engine related cost items, namely engine maintenance, depreciation, and interest, when combined with fuel costs, produce the trend shown in Fig. 10. Since these three

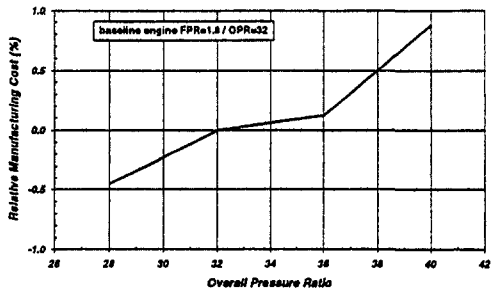

Fig. 8 Effect of overall pressure ratio on manufacturing cost

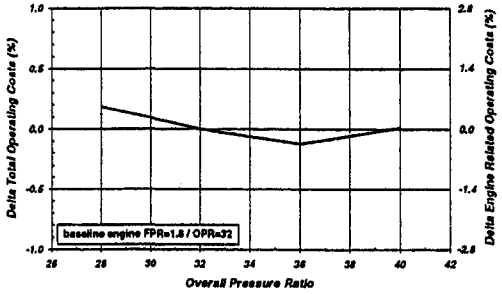

Fig. 10 Annual operating costs

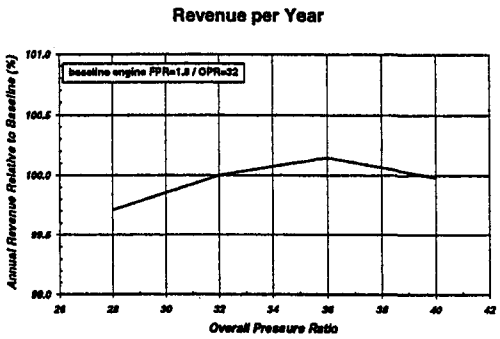

Fig. 11 Annual revenue

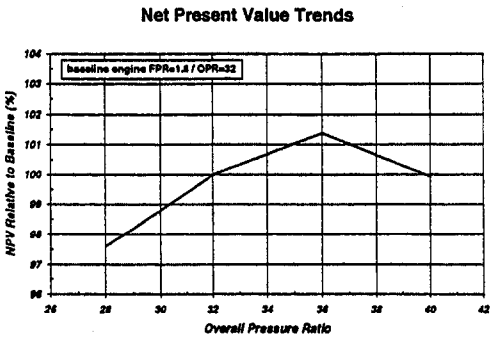

Fig. 12 Net present value trends

items are strong functions of manufacturing cost, the higher OPR engines, with the attendant higher manufacturing costs, are more expensive to operate on a relative basis. The combination of fuel costs, shown in Fig. 9, and manufacturing costs result in an optimal OPR = 36 engine from a total operating cost standpoint.

Figure 11 shows the annual total revenue for varying OPR engines at constant FPR = 1.80. Recall that for missions 1–7, payload (and thus revenue) are the same for all study engines. For mission 8, high engine weight results in lower revenue. For mission 9, payload is a function of engine weight, drag and SFC integrated over the mission. As a result, in Fig. 11, OPR = 36 shows the maximum revenue generating capability.

The integrated effects of total operating cost, acquisition cost, and revenue can be represented by a net present value (NPV) calculation over a fixed period of time. This calculation, for a period of 15 years, is shown in Fig. 12. It should be noted that all of the study engines are a good investment by the standards of the NPV calculation since absolute values are positive. Delta NPV is shown in order to highlight the trends. The combination of low operating costs, moderate acquisition cost, and high revenue result in the OPR = 36 engine having the highest profit potential for the airline.

Summary

A variation of the surplus value method was used to define the optimum engine cycle for a typical 160 passenger narrow-body aircraft. The results indicate that more traditional optimization parameters, such as fuel burn, fail to produce the best engine from an economic perspective, because they focus only on costs without regard to revenue generation potential.

Relative to the specific optimum cycle obtained, it must be remembered that this study has been performed on a 160 passenger narrow-body aircraft, operating over a typical domestic operation. The conclusions on engine FPR, OPR, cost, etc., are not applicable to all aircraft types and operational environments. Due to the short stage lengths that this type of aircraft sees in operation, the importance of SFC and, therefore, fuel burn are not as strong as would be seen in longer range operations. As a result, the impact of items such as maintenance cost and engine cost become much more important on a relative basis, than would be seen on a long range, wide-body application. Each aircraft and engine application should be studied in order to determine the proper relationship between engine parameters. Acoustic and emission requirements could also significantly alter the design choice.

It has also been shown that the basic thermodynamic cycle can have a significant impact on the economic viability of the engine. Although the data to prove it was not shown in this paper, the same is true of the basic engine architecture (i.e., the general engine layout, number of spools, and number and type of stages). Since both the cycle and the engine architecture are set very early in the engine design, an advanced, integrated set of design and analysis tools is required to perform the full engine economic analysis before significant engine design work is completed. The tools must be simple enough to allow rapid design iterations on the cycle and architecture, while having enough fidelity to obviate the need for significant cycle or architecture changes later in the design process.

References

1 Collopy, P. D., 1997, "Surplus Value in Propulsion System Design Optimization," AIAA 97-3159, presented at the AIAA Joint Propulsion Conference, July 6, 1997.

Gas Turbine Cycle Design Methodology: A Comparison of Parameter Variation With Numerical Optimization

J. Kurzke
DASA-MTU München GmbH,
Engine Performance Department TPSZ,
Dachauer Str. 665,
München, 80995
Germany

In gas turbine performance simulations often the following question arises: what is the best thermodynamic cycle design point? This is an optimization task which can be attacked in two ways. One can do a series of parameter variations and pick from the resulting graphs the best solution or one can employ numerical optimization algorithms that produce a single cycle that fulfills all constraints. The conventional parameter study builds strongly on the engineering judgement and gives useful information over a range of parameter selections. However, when values for more than a few variables have to be determined while several constraints are existing, then numerical optimization routines can help to find the mathematical optimum faster and more accurately. Sometimes even an outstanding solution is found which was overlooked while doing a preliminary parameter study. For any simulation task a sophisticated graphical user interface is of great benefit. This is especially true for automated numerical optimizations. It is quite helpful to see on the screen of a PC how the variables are changing and which constraints are limiting the design. A quick and clear graphical representation of trade studies is also of great advantage. The paper describes how numerical optimization and parameter studies are implemented in a Windows-based PC program. As an example, the cycle selection of a derivative turbofan engine with a given core shows the merits of numerical optimization. The parameter variation is best suited for presenting the sensitivity of the result in the neighborhood of the optimum cycle design point.

1 Introduction

The traditional way to select the thermodynamic cycle of a new gas turbine employs extensive parameter variations. For a complex engine with many design variables this is a time-consuming task. One looks for the optimum solution in a certain respect.

Instead of screening a wide range for the design variables with systematic parameter variations it is also possible to do an automatic search for the optimum engine design with the help of numerical optimization routines. This can be done for example with the Windows-based gas turbine performance program GasTurb developed by the author.

Certainly it is not sufficient, to get a single cycle as the best solution from the computer program for two main reasons.

Firstly, the numerical optimization algorithm will find the optimum of the mathematical model only as opposed to the "true" optimum. An exotic cycle as result of an optimization run is mostly a hint to a deficiency of the model. In such a case most probably a design constraint has been overlooked when defining the problem.

Secondly, it is always of interest to know about the neighborhood of the optimum solution. From a parameter study limited to the region of interest it becomes obvious which design variables and constraints have the biggest impact on the result.

One of the advantages of numerical optimization is, that the region where parameter studies should be performed is narrowed down significantly.

Contributed by the International Gas Turbine Institute and presented at the International Gas Turbine and Aeroengine Congress and Exhibition, Stockholm, Sweden, June 2–5, 1998. Manuscript received by the ASME Headquarters April 1, 1998. Paper No. 98-GT-343. Associate Technical Editor: R. Kielb.

2 Parameter Studies

The results of parameter studies are normally presented as graphics. In a single graph one can show for given ranges of two parameters the results for several dependant quantities. In a cycle study for a single spool turbojet engine, for example, with compressor pressure ratio and burner exit temperature as design parameters, one can plot the specific fuel consumption over specific thrust. In the resulting carpet one can additionally show lines for other calculated parameters as for example the turbine pressure ratio and the turbine exit temperature, see Fig. 1.

Let us assume, for example, that the design aim is a low cost turbojet with a single stage turbine and an uncooled turbine exit casing. The feasible region of design parameter combinations can be marked easily in the carpet since it is limited by the following constraints:

turbine pressure ratio	< 3.5	single stage turbine
turbine exit temperature	< 1200K	uncooled turbine exit casing

From Fig. 1 one can read that with these constraints the cycle with the highest specific thrust has a burner exit temperature of 1600K and a compressor pressure ratio of around 16.5.

However, most gas turbine cycles are much more complex than the turbojet example discussed above. A two-spool turbofan has the following five cycle design variables: low spool pressure ratio; high spool pressure ratio; burner exit temperature; bypass ratio; and fan pressure ratio. There will also be more constraints than with the turbojet example, as follows:

lp turbine inlet temp.	$<$	limit uncooled lp turbine
compressor exit temp.	$<$	limit material of compr. disk

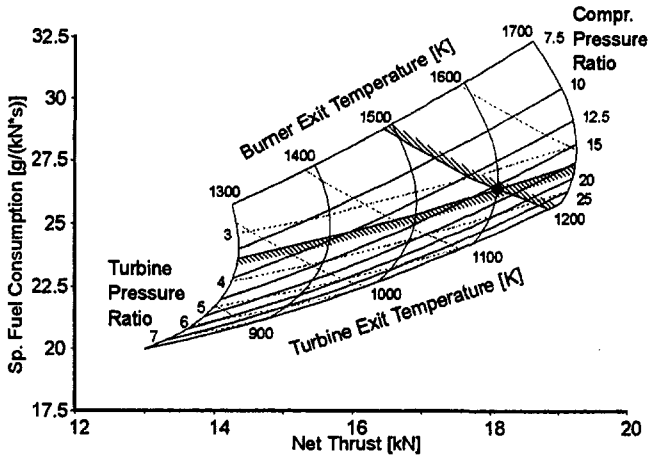

Fig. 1 Result of a parameter study

fan pressure ratio < limit
single stage fan

hp turbine press. ratio < limit
single stage turbine

In a more detailed study there will be even more design variables as for example the stage numbers for the high and the low pressure turbine. It is obvious that with a parameter study it will be very difficult and time consuming to find the optimum values for the design variables.

3 Numerical Optimization

By the way, how is the optimum defined in a mathematical sense? In a parameter study that question must not be answered a priori. In a numerical optimization, however, a figure of merit must be clearly defined before the calculation can commence. The figure of merit might be the specific fuel consumption of a turbofan at cruise which is to be minimized. For a fighter engine it might be that the specific thrust shall be maximized. One can also think of a weighted combination of these parameters.

When values for more than a few variables have to be determined while several constraints are existing, then numerical optimization routines can help to find the mathematical optimum (i.e., the minimum and maximum, respectively, of the figure of merit) faster and more accurately. As shown above with the turbojet example, in a parameter study with only two variables it is easy to find an optimum solution. If there are three variables the situation is not so clear. With more than three variables the picture may get obscure. In complex studies the true optimum may never be found with the conventional parameter study.

There are many numerical optimization algorithms known from literature. They can be divided basically into the following two major groups: methods that use gradient information and others. In the program GasTurb there is one method from each group implemented. A short explanation how these algorithms work is given in the following chapters.

3.1 Gradient Method. The following is a good example for the optimization task. A mountaineer shall climb the highest peak in a certain region. He has no map and the weather is foggy. His only tool is an altimeter. What is he going to do? He will certainly check his surroundings first and then go in the direction of the steepest ascent. In the end he will come to the top of a mountain. This is a place where each step leads downwards.

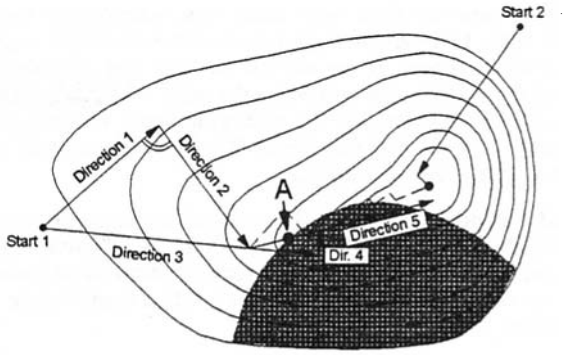

Fig. 2 Optimization strategy

The steepest ascent may, however, lead toward a border (which is either the lower or upper limit of a design variable) of the region. Then our mountaineer will walk along the border until he reaches the place where each step leads downwards or out of the allowed region.

Is that the end of the story? Not necessarily. There might be several summits within the region. Our mountaineer may have found the highest peak by chance, but he cannot be sure of that. He has to check other parts of the region. In mathematical terms there might be "local" optimums besides the "global" optimum.

Up to now we have not spoken of constraints. They are like fences. A part of the region is forbidden to our mountaineer. His task is made more difficult because on his way to the summit he may have to walk downwards for a while to avoid a forbidden region. The fences (the constraints) often exclude the summit (where each step leads downwards) as an acceptable solution. They create local optima that would not exist without fences. Constraints make the task of optimization difficult.

Let us turn to the mathematical algorithm now. The mountaineer who first makes test steps in several directions uses the "gradient strategy" as a search method. With the test steps he is looking for the partial derivatives $\partial Z/\partial V_i$. For each optimization variable he must do one test step before he can start his way in the "right" direction.

After the first step uphill the local gradients will be different. The test steps could now be repeated to find the new direction. Test steps take time, however, and it is therefore better to go on in the same direction as long as the altitude increases. Reaching a fence (violating a constraint) could be another reason for stopping the climb. Only then will new gradients be sought. The new direction will eventually take you along a fence.

The gradient search algorithm implemented in GasTurb was derived from [2]. The principle is the following (see Fig. 2). We begin at the point marked "Start 1", looking for the direction of the steepest gradient ("Direction 1"). Following this direction we walk to the highest point. Then we change the direction by 90 deg (orthogonal). This can be done without evaluating the local gradient. We again go for the highest point here. To define the third direction we use the experience from the first two directions. We connect the point "Start 1" with the optimum point found along "Direction 2". We follow this direction again as long as altitude increases.

This procedure can be applied repeatedly until the search steps or the changes in the "figure of merit" become very small. There is also a maximum limit for the number of optimization steps. In the example of the figure the optimum is found along search direction 6 (not marked in the figure, perpendicular to direction 5).

The dashed line in the figure shows how optimization would go on, if only local gradient information is used. With this simple strategy, the search direction would change very often.

Up to now we have only dealt with optimization without constraints. In the figure there is a shaded zone which suggests a forbidden region. If we use the strategy just described the search for the optimum will end at the point "A" along "Direction 5". We cannot find the global optimum if we begin at "Start 1". If we begin at "Start 2", however, we will be at the top of the hill very quickly.

3.2 Random Search. The second optimization strategy offered by GasTurb is based on [3]. In an adaptive random search, random numbers are used for the optimization variables that are concentrated around the best solution found before. The algorithm is

$$V_i = V_i^* + \frac{R_i}{k_R}(2\Theta - 1)^{k_v}$$

with

V_i = new value for optimization variable
V_i^* = value of V_i producing the best figure of merit
R_i = search region for variable V_i
k_R = range reduction coefficient (positive integer)
k_v = distribution coefficient (positive odd integer)
Θ = random number between zero and one

To start an adaptive random search one should have a variable combination which fulfills all of the constraints. At the start of the search k_R is 10 and k_v is 1. In one search run, the program tries (40 times the number of Optimization Variables) random engine cycles. When all cycles have been calculated, then k_R will be duplicated and k_v will be increased by 2. The search region will get smaller. Another (40 times the number of Optimization Variables) cycles will be calculated and then k_R will be duplicated again and k_v will be further increased by 2. This procedure will be repeated until all cycles for $k_R = 80$ have been tried. Cycles that do not fulfill the constraints will be ignored.

4 Cycle Selection for a Derivative Turbofan

A very common design task is to adapt an existing engine for a new application. It is quite obvious that in this case there are more constraints than during the design of a brand new engine. In this chapter at first the basic engine will be described and then the design variables, the constraints and the figure of merit for the numerical optimization of a derivative engine.

4.1 Description of the Basic Engine. Let us assume that we can start from an existing unmixed flow turbofan engine for a business jet. This type of engine has a rather low overall pressure ratio and a moderate burner exit temperature compared to the big turbofan engines used on commercial airliners. The main cycle parameters are shown in the table below.

Table 1 Main cycle parameters of the basic engine

Flight Condition	11 km / Mach 0.8 Max Climb installed
Thrust	3.64 kN
SFC	19.7 g/kN*s
Bypass Ratio	4.5
Burner Exit Temperature	1350 K
Overall Pressure Ratio	17.82
Core Pressure Ratio	12
ISA Corrected Mass Flow	60 kg/s

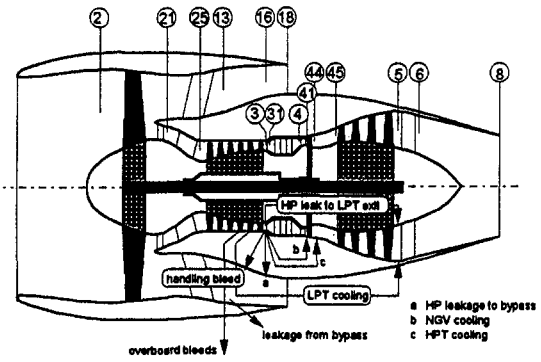

Fig. 3 Configuration of the basic engine

4.2 Design Variables, Constraints and Figure of Merit.

Design Variables. Besides the pressure ratios of the new booster and the fan there will be the bypass ratio and the burner exit temperature among the design variables of the growth engine. A new low pressure turbine will be required while the gas generator remains unchanged. The configuration of the growth engine will be as shown in Fig. 4.

The core compressor of the new engine must not necessarily be operated at the same operating point as in the basic engine. In fact that might even be impossible because doing that would require an increase in the mechanical spool speed beyond the limits of the original design. Thus, we get as two further design variables for the derivative engine the core compressor mass flow and its pressure ratio.

It is standard practice not to read a compressor map with given mass flow and pressure ratio, but with given corrected speed and a value for an auxiliary coordinate (here called beta) (see, for example, [4]). In the list of the design variables we get instead of the compressor mass flow and its pressure ratio the two equivalent variables corrected speed and map coordinate beta.

Altogether there are six design variables for the derivative engine.

Constraints. There are several constraints for the new engine design to be observed. The common core with the basic engine requires that both high pressure turbines have practically the same flow capacity. We want the Mach number at the core exit also to be nearly the same and that has the consequence, that the flow capacity of the low pressure turbine must also be very similar between both engines. As a consequence there will be practically no difference between both engines with respect to the high pressure turbine pressure ratio.

A further constraint is, that the low pressure turbine inlet temperature T_{45} must be below say 1150K which allows to

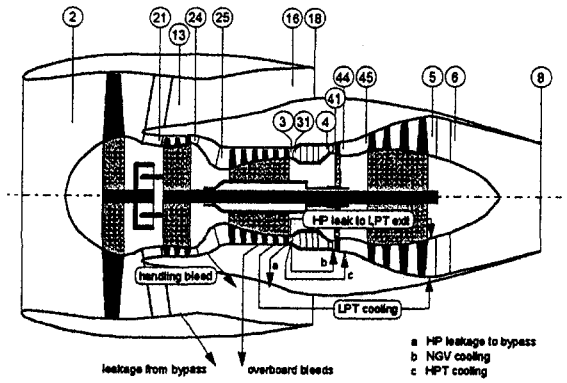

Fig. 4 Configuration of the growth engine

design an uncooled low pressure turbine from inexpensive materials.

The core compressor will eventually cause several constraints for the design. There might be a temperature limit when the last stage is made from titanium, for example. Also, a mechanical speed limit may exist. And last but not least the minimum surge margin requirements must be met.

Another constraint may come from the nacelle in which the engine has to be installed. This will limit the fan diameter of the growth engine.

In our example the task is, to increase the Max Climb thrust by 25 percent. Engine designs with less thrust than required will not be acceptable, and, therefore, the thrust is a design constraint for the growth engine. In summary, the design constraints for the derivative engine are:

$$\text{hp turbine flow capacity} = \text{reference value} \pm 5 \text{ percent}$$

$$\text{lp turbine flow capacity} = \text{reference value} \pm 5 \text{ percent}$$

$$\text{lp turbine inlet temp } T_{45} < 1150\text{K}$$

$$\text{compressor exit temp } T_3 < 750\text{K}$$

$$\text{core spool speed} < \text{reference} + 5 \text{ percent}$$

$$\text{fan tip diameter} < 0.75\text{m}$$

$$\text{Max Climb thrust} > 4.5 \text{ kN}$$

Figure of Merit. The specific fuel consumption (SFC) for Max Climb rating is the figure of merit which is to be minimized. This will automatically result in a low fuel consumption for cruise.

4.3 Mathematical Model of the Engine. A mathematical model of the growth engine requires a mixture of design and off-design calculations. The components on the low pressure spool will be newly designed while the core components will be operated at some off-design condition compared to the design point of the basic engine.

We select as the cycle design point for the growth engine the Max Climb rating at altitude. For this flight conditions the optimum values for the design variables will be found.

The mathematical model of the engine must take into account, that the design point efficiencies of the fan, the booster and the low pressure turbine will change with the aerodynamic loading. For axial compressors an appropriate correlation has been published by Glassman [5] and for the low pressure turbine one can use a simplified version of the preliminary turbine design routine from Warner [6].

The efficiency and the surge margin of the core compressor will be read from the map dependent from the values for the design variables core compressor corrected speed and map coordinate beta.

Note that the temperature limits for T_3 and T_{45} in the list of constraints are not applicable to the Max Climb rating, but for the flight case with the highest temperatures encountered in the flight envelope. That means, that the numerical model of the engine must be capable to simulate both the Max Climb flight case at altitude (as a cycle design point) and the Take Off rating for the "hot day" (ISA + 15K) at sea level, Mach 0.2 (as an off-design condition).

5 Optimizing the Growth Engine

5.1 Ranges for the Design Variables. Another argument for setting the range of a design variable is that either the lower or the upper limit represents a true limit for the engine design. In our example, this is the case for the pressure ratio of the single stage fan which is introduced with an upper limit of 1.9. In the table below the ranges for all six design variables are given.

Table 2 Ranges for the design variables

	min value	max value
fan P/P	1.1	1.9
booster P/P	1.4	2.3
bypass ratio	4	6
burner exit temp	1300 K	1600 K
relative core compr. corr. speed	0.9	1.02
core compr. map coord. beta	0.3	0.8

Before the numerical optimization algorithm can start, we need to define a range for the design variables. On one side this range should be as narrow as possible because then the search for the optimum will take less effort. However, when the range is too narrow, then the true optimum might be excluded from the search unintentionally.

5.2 Starting Point. Many numerical optimization algorithms require that a set of design variables that fulfills all constraints must be known before the calculation can commence. The cycle of the basic engine is within the ranges of all design variables, however, obviously it does not fulfill the minimum thrust constraint.

How can we get a valid cycle to start with? One possible approach would be, to do a rough parameter study which has only the aim to find a feasible solution, but not the best solution for the problem. However, this parameter study takes more effort than necessary. We can redefine the figure of merit for the moment and do a slave optimization with the aim of maximizing the Max Climb thrust. The minimum thrust constraint is dropped for that preliminary exercise which makes the cycle of the basic engine valid as a start point.

While the slave optimization is running, one can observe on the computer screen the progress. As soon as a cycle is found which has more Max Climb thrust than required (and fulfills all constraints) we can stop. Now we redefine the figure of merit as specific fuel consumption and introduce the minimum thrust constraint. The final optimization can commence now.

5.3 Graphical User Interface. Figure 5 shows the optimization window of GasTurb for the example of this paper with six horizontal gauges for the design variables on the left and seven gauges for the constraints in the upper right part. The gauges are continuously updated while the optimization is running. In the lower part of the screen the figure of merit is shown

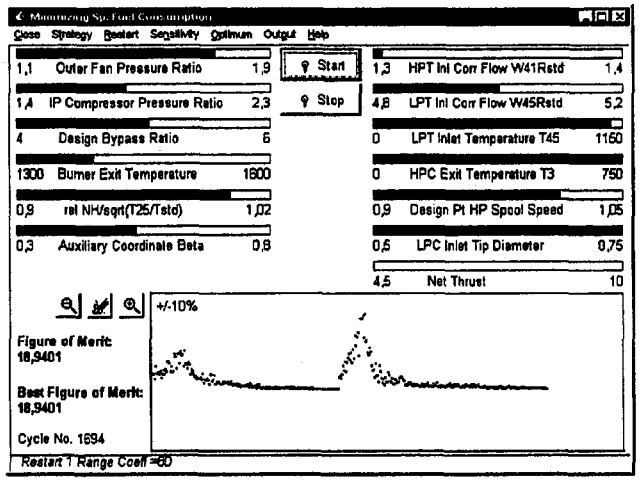

Fig. 5 Graphical user interface of Gas Turb

Table 3 Cycle parameter summary

	Basic Engine		Growth Engine	
	Max Climb	Hot Day Take Off	Max Climb	Hot Day Take Off
Thrust [kN]	3.61	13.10	4.50	16.94
SFC [g/(kN*s)]	19.86	14.23	18.93	13.33
Bypass Ratio	4.5	4.65	5.06	5.23
Fan P13/P2	1.775	1.62	1.73	1.60
Ideal Jet Vel. Ratio	0.761	0.886	0.726	0.839
Booster P24/P2	1.5	1.33	1.80	1.61
HPC P3/P25	12	11.36	12.3	11.67
T4 [K]	1350	1479	1393	1530
W41Rstd	1,35	1,35	1,31	1,31
W45Rstd	4,98	4,96	5,01	5,00
T3[K]	610	708	649	750
T45 [K]	973	1076	1000	1108

both as numbers and as graphic with a dot for every valid solution.

One can immediately see from the gauges when a variable or a constraint is driven toward a range boundary respectively limit. When the range boundary of a design variable happens to be not a true limit for the engine design then one can stop the calculation and redefine the range for the corresponding design variable.

In practice it happens quite often, that during the first attempts the optimization problem is not formulated correctly. In such a case the numerical algorithm drives the mathematical model in a direction which is obviously nonsense because a constraint was forgotten, for example. Therefore, an easy to survey graphical user interface is very helpful for avoiding a waste of computing time.

The optimization can be stopped at any time, which allows to check the best solution found in more detail than possible from the values for design variable and constraints alone. For both the engine design point (Max Climb at altitude) and the off-design condition (SL Take Off ISA + 15K Mach 0.2) there are all details accessible. This includes even graphs with the

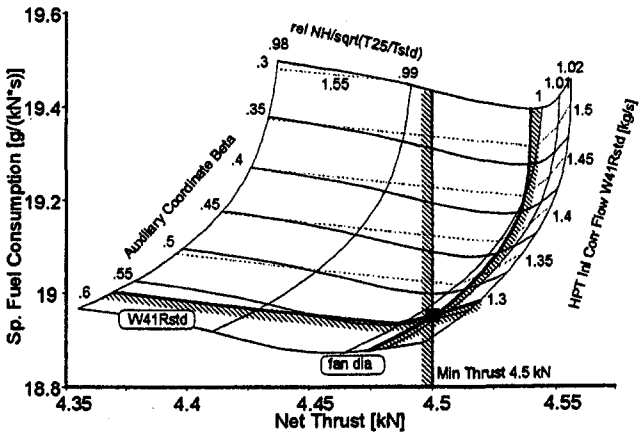

Fig. 7 Sensitivity for HPC map operating point

low pressure turbine design and the operating points in the component maps at off-design.

5.4 Local and Global Optima. As explained in the chapter about the gradient search strategy with numerical optimization there is always the danger that the algorithm finds only a local optimum but not the global optimum within the parameter range. When there are several local optima within the feasible region, then it depends on the starting point of the algorithm which local optimum will be found. Therefore, one should repeat the optimization run several times and pick from all local optima the best one.

One can find easily a new starting point for the optimization by redefining the search direction. Instead of minimizing the specific fuel consumption one looks during a restart run for the cycle with the maximum SFC. The random adaptive search will lead for each restart run to a different starting point even when it commences several times from the same optimum.

In Fig. 5 one can see from the graphics for the figure of merit, that twice a restart has happened. This was caused by the algorithm called "endless random search" which restarts automatically after the algorithm has homed into an optimum. The best solution found will be stored in memory and can be restored as soon as the calculation is stopped.

Some important data for our growth engine example is summarized and compared to the basic cycle in Table 3 below.

6 Discussion of the Results

The optimum growth engine is influenced by three of the design constraints. It has a fan diameter of 0.75 m, i.e., it uses

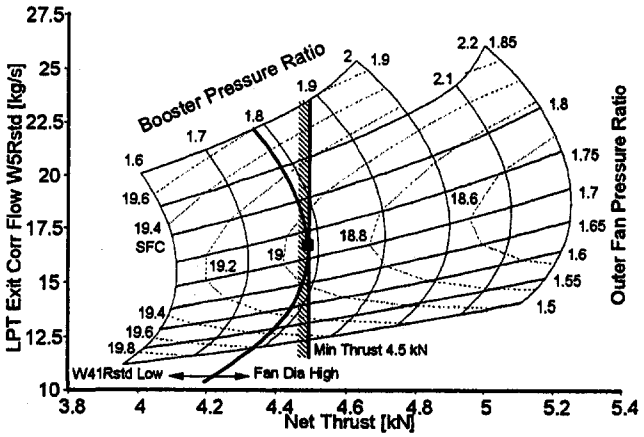

Fig. 6 Sensitivity for booster and outer fan pressure ratio

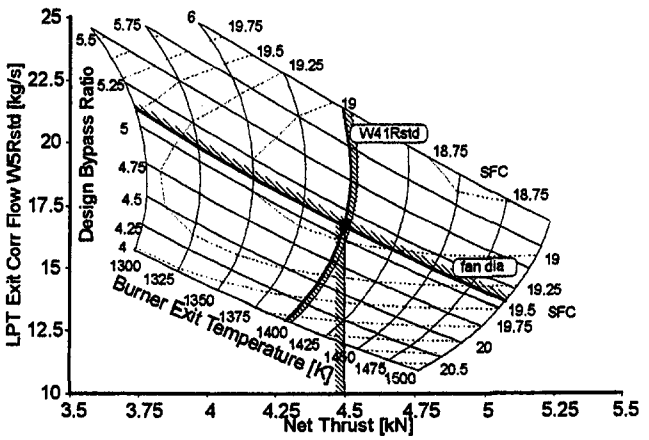

Fig. 8 Sensitivity for bypass ratio and burner exit temperature

the largest fan which was allowed in this exercise. The second constraint which had an impact on the design of the growth engine is the compressor exit temperature which was limited to 750 K for the hot day take off case. The third constraint was the minimum high pressure turbine flow capacity W41Rstd.

All design variables did remain within the predefined range during the optimization. The thrust increase for Max Climb rating at altitude is 25 percent and at Take Off even 29 percent. Note that both engines run during Take Off speed with 7 percent more mechanical high pressure spool speed than at Max Climb in this example. The specific fuel consumption at altitude is nearly 5 percent better for the growth engine.

In the table there is also a row for the ideal jet velocity ratio. From theoretical considerations one can derive, that this ratio should be equal to the product of fan and low pressure turbine efficiency when an unmixed flow turbofan is to be optimized for SFC. Note that the numerical optimization algorithm has automatically found a cycle for which the jet velocity ratio is near to its theoretically best value.

It is quite useful to do a parameter variation in the neighborhood of the optimum solution. This gives an insight to the sensitivity of the result. Figure 6 shows the influence of "outer fan pressure ratio" and "booster pressure ratio" on thrust and specific fuel consumption. Note that the parameter on the vertical axis was mainly selected because it spreads the carpet nicely. The corrected flow at the low pressure turbine exit is not a very important engine design parameter.

Actually, the limiting line for the fan diameter (0.75 m) is identical to the line for the minimum high pressure turbine flow capacity. To the left of the line for booster pressure ratio $\approx$ 1.79 the lower limit for the high pressure turbine flow capacity is violated and to the right of this line the fan diameter is too big. In this graph only one point is a valid solution: the square which fulfills the thrust requirement. One can see, that the optimum solution is pretty much boxed in by the design constraints.

In Fig. 7 two more design variables were systematically varied around the optimum solution. Again the square marks the only point which fulfills all constraints.

Figure 8 deals with the operating point of the high pressure compressor. High values for the auxiliary coordinate beta go with a low surge margin. The square marks the point with lowest SFC in the region of feasible designs.

7 Summary

With a conventional parameter study it is very difficult to find the optimum solution for a problem as soon as four or more design variables and several constraints are involved. With the help of numerical optimization algorithms one can easily find the mathematical correct solution to the problem. Extensive parameter studies around the solution will help to understand why this combination of design variables is the best choice and how sensitive the figure of merit is to small deviations from the optimum.

As an example, the cycle selection of a derivative turbofan engine with a given core shows the merits of numerical optimization. The parameter variation is best suited for presenting the sensitivity of the result in the neighborhood of the optimum cycle design point. Sometimes this leads to a redefinition of the figure of merit or the constraints imposed on the solution. In rare cases even an outstanding solution is found which was overlooked while doing a preliminary parameter study.

8 References

1 Kurzke J., 1998, "Manual GasTurb 8.0 for Windows—A Program to Calculate Design and Off-Design Performance of Gas Turbines," available from the author.

2 Jacob, H. G., 1982, "Rechnergestützte Optimierung statischer und dynamischer Systeme," Fachberichte Messen—Steuern—Regeln, Springer-Verlag KG, Berlin.

3 Kelahan, R. C., Gaddy, J. L., 1978, "Application of the Adaptive Random Search to Discrete and Mixed Integer Optimization," *International Journal for Numerical Methods in Engineering,* Vol. 12, pp. 289–298.

4 Kurzke, J., 1996, "How to Get Component Maps for Aircraft Gas Turbine Performance Calculations," ASME Paper 96-GT-164.

5 Glassman, A. J., 1992, "Users Manual for Updated Computer Code for Axial-Flow Compressor Conceptual Design," NASA Contractor Report 189171.

6 Stewart, W. L., 1961, "A Study of Axial-Flow Turbine Efficiency Characteristics in Terms of Velocity Diagram Parameters," ASME Paper 61-WA-37.

7 Cohen, H., Rogers, G. F. C., Saravanamuttoo, H. I. H., 1996, "Gas Turbine Theory," 4th ed., Addison-Wesley Longman, London, United Kingdom.

Development of a Combustor Liner Composed of Ceramic Matrix Composite (CMC)

K. Nishio

K.-I. Igashira

K. Take

Research Institute of Advanced Material Gas-Generator, Tokyo, Japan

T. Suemitsu

Material Research Department of Akashi Technical Institute, Kawasaki Heavy Industries Limited, Hyogo, Japan

The Research Institute of Advanced Materials Gas-Generator (AMG), which is a joint effort by the Japan Key Technology Center and 14 firms in Japan, has, since fiscal year 1992, been conducting technological studies on an innovative gas generator that will use 20 percent less fuel, weigh 50 percent less, and emit 70 percent less NOx than the conventional gas generator through the use of advanced materials. Within this project, there is an R&D program for applying ceramic matrix composite (CMC) liners to the combustor, which is a major component of the gas generator. In the course of R&D, continuous SiC fiber-reinforced SiC composite (SiC^F/SiC) was selected as the most suitable CMC for the combustor liner because of its thermal stability and formability. An evaluation of the applicability of the SiC^F/SiC composite to the combustor liner on the basis of an evaluation of its mechanical properties and stress analysis of a SiC^F/SiC combustor liner was carried out, and trial SiC^F/SiC combustor liners, the largest of which was 500-mm in diameter, were fabricated by the filament winding and PIP (polymer impregnation and pyrolysis) method. Using a SiC^F/SiC liner built to the actual dimensions, a noncooling combustion test was carried out and even when the gas temperature was raised to 1873K at outlet of the liner, no damage was observed after the test. Through our studies we have confirmed the applicability of the selected SiC^F/SiC composite as a combustor liner. In this paper, we describe the present state of the R&D of a CMC combustor liner.

Introduction

In the process of developing more efficient industrial gas turbines and turbine engines for airplanes to travel at supersonic speeds, much effort has been directed at raising the combustor outlet (turbine inlet) temperature, as is shown in the chart of the increase in gas turbine inlet temperature in Fig. 1 [1]. This has created the need to develop new materials that can withstand these ultra-high temperatures. In response to that need, as is shown in Fig. 2, such new metallic materials as DS (directionally solidified) superalloys and SC (single crystal) superalloys have already reached the stage of practical application and the development of intermetallic compounds, oxide dispersed superalloys, and other metallic materials is under way [2]. In response to the drive to achieve combustion at temperatures that exceed the limits of durability of metallic materials, CMC materials that can be applied as materials with greater heat resistance than metallic materials are being developed.

The Research Institute of AMG is conducting research and development to apply these composite materials as parts for gas generators that operate at ultra-high temperatures. The research period is nine years and one month, from March 1993 to March 2002, as shown in Fig. 3. The total research budget amounts to 10 billion yen (about $100 million). The fourteen participating domestic companies are three gas turbine manufactures, five materials companies, four mechanical components manufactures, and two control systems companies [3].

In the AMG program, we are engaged in the R&D of application technology and processing technology for CMC parts with the aim of applying CMC materials to gas generator static parts.

In this paper, we describe the results of our evaluation of CMC's applicability as a combustor liner based on an analysis of thermal stress and evaluation of a CMC liner model, and an evaluation of an actual CMC liner assembled in a combustor and subjected to a combustion test.

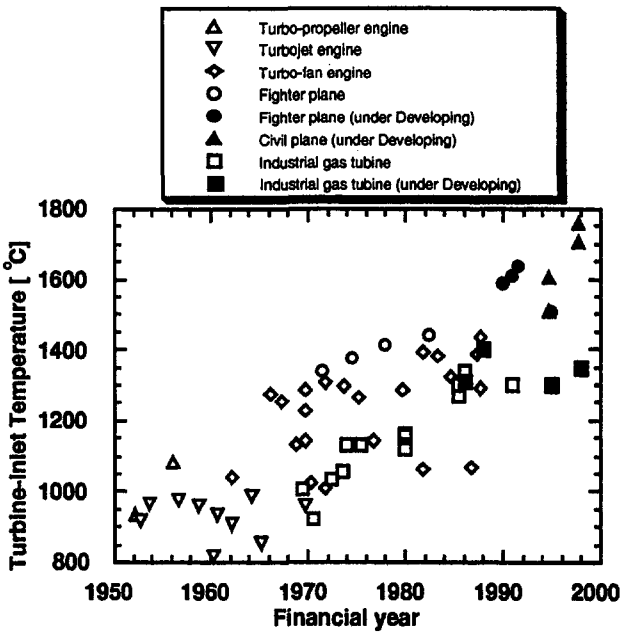

Fig. 1 Turbine inlet temperature in gas turbines

Concept of Advanced Materials Application to the AMG Combustor

In the AMG combustor, the plan is to apply CMC to the combustor liner and TiAl to the combustion gas swirl introduction swirler. Silicon carbide fiber-reinforced silicon carbide (SiC^F/SiC), which features superb resistance to high tempera-

Contributed by the International Gas Turbine Institute and presented at the International Gas Turbine and Aeroengine Congress and Exhibition, Stockholm, Sweden, June 2–5, 1998. Manuscript received by the ASME Headquarters April 1, 1998. Paper No. 98-GT-104. Associate Technical Editor: R. Kielb.

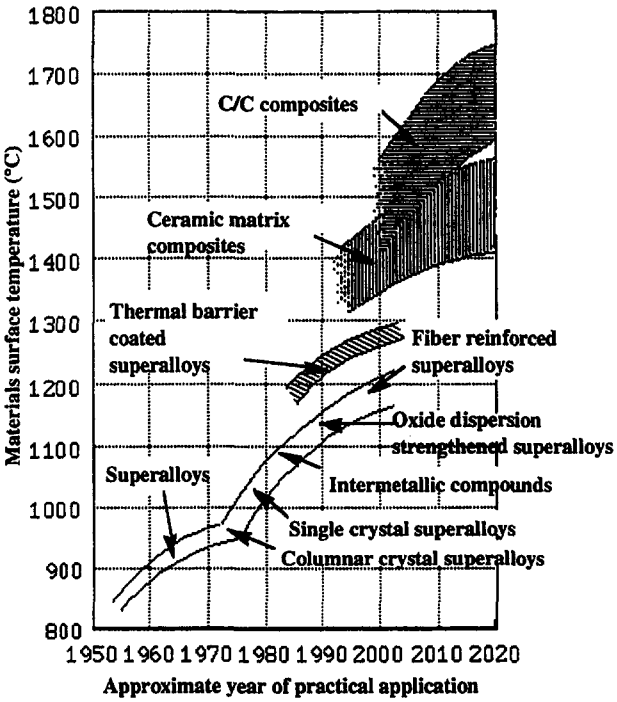

Fig. 2 Development trends of heat-resistant materials

tures and oxidation, was selected as the candidate CMC material for the AMG combustor liner. The conceptual configuration of the combustor is shown in Fig. 4.

To produce the combustor liner we selected the filament winding (FW) method, which makes it easy to adjust the fiber orientation angle and makes it easy to form a near net shape over a wide range, from small to large parts, by replacing the mold.

Material Characteristics of CMC [4]

As the test piece for evaluating the material characteristics of the CMC combustor liner, a fiber-oriented pre-preg sheet was laminated by deflecting at a specified angle and this fiber-laminated material was composited by the polymer impregnation and pyrolysis (PIP) method to obtain a sheet of CMC, from which the test piece was taken. The fiber used was Si-Ti-C-O fiber (Tyranno Lox M-S5 from Ube Industries Ltd.). The fiber has a carbon surface layer that becomes the fiber/matrix interface layer during compositing. Polycarbosilane (PCS) was used as the matrix precursor polymer. A tensile strength test at room temperature was used as the characteristics evaluation test and the relationship between tensile characteristics and fiber orientation angle was found. The fiber orientation angle of the test piece was set at seven values, in the range of 0° to ±82.5°, which included ±22.5°, which is equivalent to the combustor liner forming angle. The relationship between tensile strength

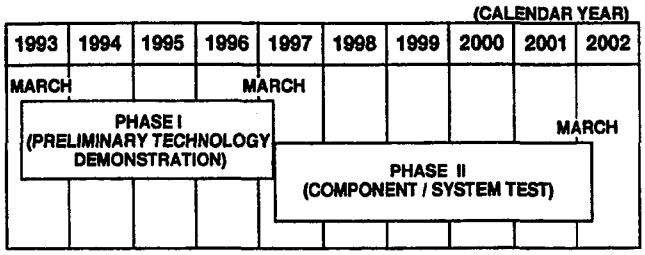

Fig. 3 AMG research and development schedule

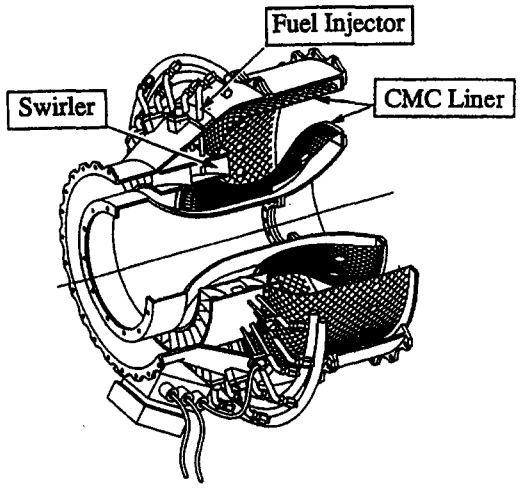

Fig. 4 Conceptual configuration of the AMG combustor

and fiber orientation angle is shown in Fig. 5. Tensile strength decreased as the orientation angle increased and tensile strength approached zero when the fiber orientation angle exceeded 75 deg. Regarding the material strength of the combustor liner, the tensile strength at an angle (about 20 deg) equivalent to the fiber orientation angle of the combustor liner is believed to be about 250 MPa. When we subjected the experimental material to a separate frexural strength test we found virtually no difference in strength between RT (room temperature) and 1473K. Based on this, we concluded that the results at RT discussed in this paper also apply at 1473K, which is in the liner's operating temperature range.

Thermal Stress Analyses in CMC Combustor Liner

The thermal stress generated when a combustor fitted with a CMC combustor liner is operated was estimated by numerical analysis using representative characteristic values of the trial-produced composite materials, aiming at clarifying the question of strength in the application of the composite material in a combustor liner.

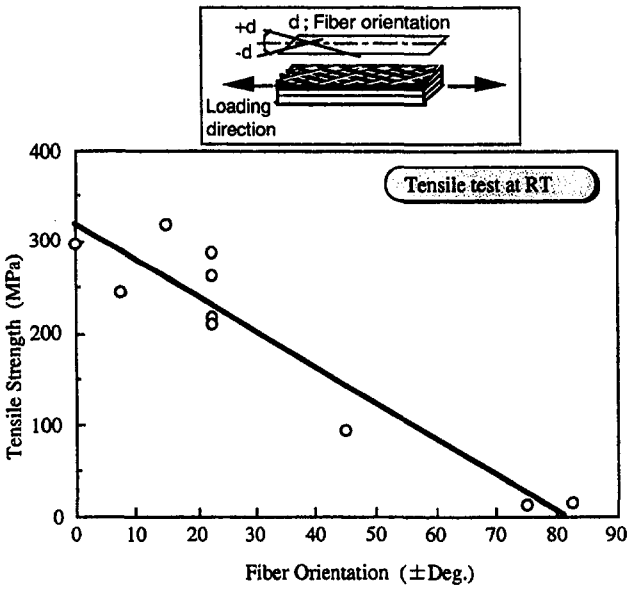

Fig. 5 Relationship between tensile strength and fiber orientation of trial-produced composite material

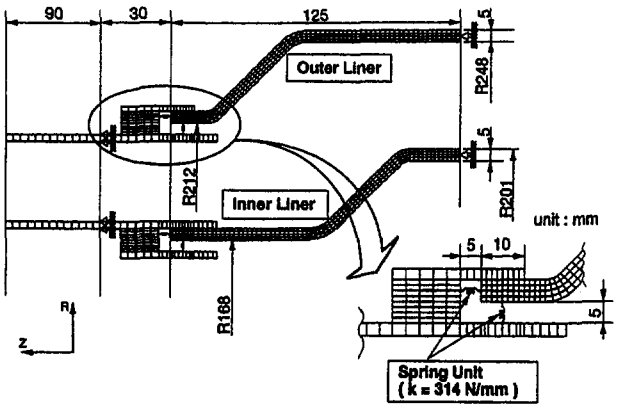

Fig. 6 Thermal stress analysis model of CMC combustor liner

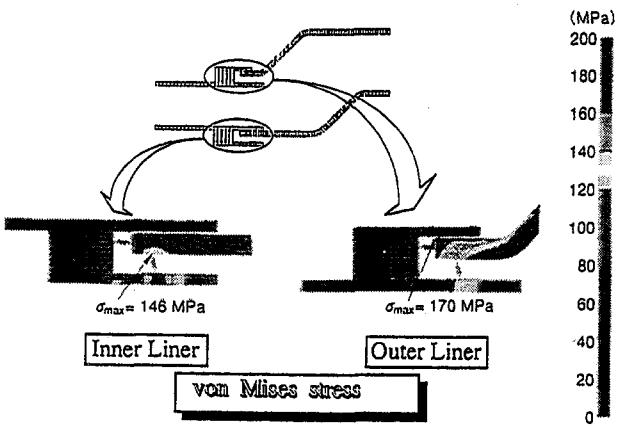

Fig. 7 Results of steady state thermal stress analysis of CMC liner for AMG combustor

The thermal stress analysis model and analysis method were studied in accordance with the basic design specifications of the CMC combustor liner. As the combustor liner, to be the subject of analysis, a model was created using axis symmetric solid elements. For the tie-in part between the liner and the swirler, a spring-type fitting structure was used with the aim of relieving the thermal stress arising from the difference in the thermal expansion rates of SiC^F/SiC and TiAl, and a model was produced using linear spring elements. The model used for analysis is shown in Fig. 6.

The temperature distribution in the liner's axial direction and the liner's thickness direction was found by means of heat transfer analysis using heat boundary conditions that were estimated based on the results of combustion tests of a metal liner. The swirler temperature was assumed to be constant at 973K.

The analysis of heat transfer thermal stress was made using ABAQUS analysis software, based on the material data obtained from the characteristics test of the trial produced materials. The material characteristics data used for the analysis are shown in Table 1.

1 Results of Thermal Stress Analysis at Steady-State Conditions and Discussion [4]. The results of thermal stress analysis at steady-state conditions of the CMC liner are shown in Fig. 7. The maximum thermal stress occurred on the liner side in the vicinity of the liner and swirler tie-in part. The peak thermal stress did not exceed the 200 MPa set as a preliminary criterion for the application of SiC^F/SiC and was not considered excessive stress when compared with the tensile strength (about 250 MPa) obtained through the characteristics evaluation of the trial-produced composite material. The value of the maximum thermal stress was 170 MPa for the outer liner and 146 MPa for the inner liner at the respective material temperatures of approximately 1350K and 1300K. The maximum main stress direction was in the circumferential direction and the liner's thermal stress was believed to be mainly hoop stress. Therefore, applying SiC^F/SiC in the combustor liner should present no problem.

In this analysis, a spring constant equivalent to that of a practical material was used and it would be possible to reduce thermal stress caused by replacing the spring with one with a lower spring constant.

Through thermal stress analysis during steady combustion of a model in which the material was applied as the combustor liner, the thermal stress generated was found to be less than the material strength. These results suggest the suitability of using SiC^F/SiC as the combustor liner.

Table 1 Material characteristics data used for analysis

Materials		SiC^F/SiC			TiAl	
Properties	Units	Temperature	Orientation: In Plane	Orientation: Through the thickness	Temperature	
Tensile Young's Modulus	GPa	1273K	100	50	973K	150
Tensile Poisson's Ratio	—	1273K	0.16	—	973K	0.3
Thermal Expansion Coefficient	$\times 10^{-6}$/K	1273K	4.3	6.9	973K	11.5
		1573K	4.2	5.0		
Thermal Conductivity	W/mK	1273K	—	1.59		—
		1573K	—	2.34		
Specific Heat	J/kgK	1273K	1.47			—
		1573K	1.62			
Application Parts		Combustor Liner			Swirler	

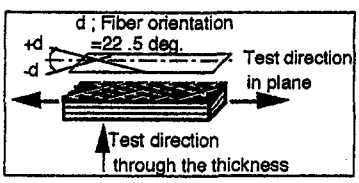

2 Results of Thermal Stress Analysis at Transient Conditions and Discussion. As thermal stress analysis while simulating the combustor in operation, we analyzed heat transfer thermal stress under transient conditions when the combustion state shifted from idle combustion to design point combustion and from design point combustion to idle combustion. For the analysis, the heat boundary conditions were varied in stages by assuming that the shift in combustion state between idle combustion and design point combustion would be immediate.

The results of analyzing heat transfer and thermal stress were collated by focusing on the center point of the region where the

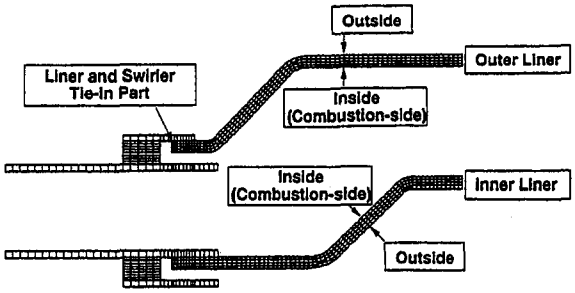

Fig. 8 Focal points of temperature and stress

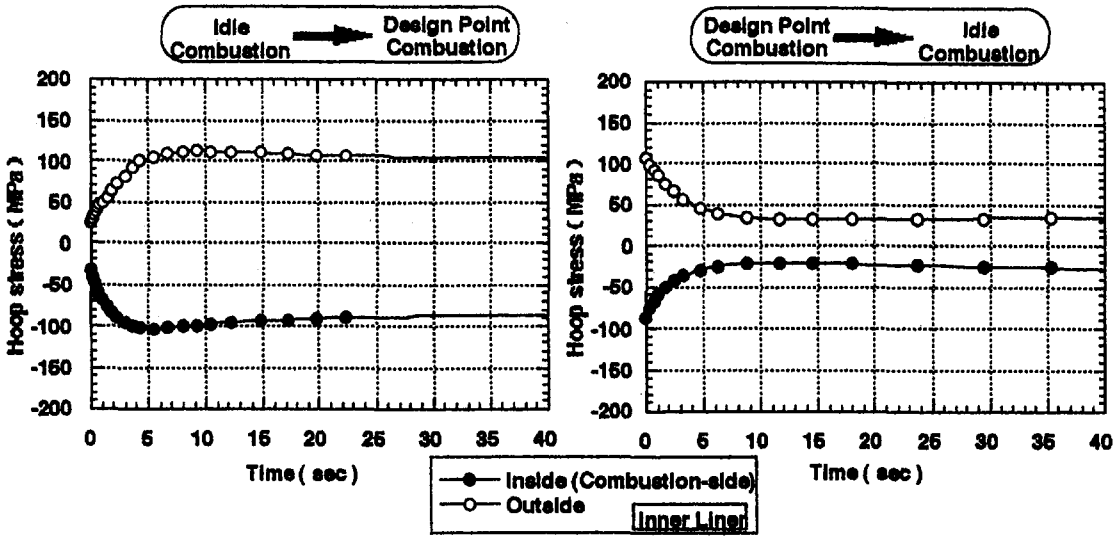

Fig. 9 Results of transient thermal stress analysis of CMC liner for AMG combustor

combustion gas temperature is assumed to reach the highest point and the tie-in point between the liner and the swirler. The location of these focal points are shown in Fig. 8. The heat transfer analysis confirmed that the liner temperature reached the highest level at the focal point (the center of the region where the combustion gas temperature reaches the highest level).

The analysis of thermal stress under transient conditions as the combustion state varied between idle combustion and design point combustion revealed that, due to the difference in the change of temperature between the liner surface and the inside of the liner's wall, the peak thermal stress appears several seconds after the combustion state shifts in the combustion side of both the inner and outer liner. The peak thermal stress did not exceed the maximum thermal stress in the steady-state analysis. Therefore, applying SiC^F/SiC in the combustor liner should present no problem. Changes in thermal stress over the passage of time at the focal point of the inner liner is shown in Fig. 9 as examples of the analysis of thermal stress under transient conditions.

Evaluation of CMC Combustor Liner in Combustion Test

1 Method for Producing the Liner. The liner was produced by filament winding molding and the polymer impregnation and pyrolysis (PIP) method using a low-oxygen silicon carbide fiber (product name: Tyranno LoxE) from Ube Industries Ltd. as the reinforcement fiber and polycarbosilane (product name: Nipushi) from Nippon Carbon Co. Ltd. as the matrix precursor polymer. The fiber orientation of the liner was about ±20 deg as shown in Fig. 10. Neither a fiber coating nor seal coat for oxidation resistance was applied to the prototype liner. We are currently testing a fiber coating and seal coat applied using a process developed by Kawasaki Heavy Industries Ltd. for durability and other properties.

2 Method for Evaluating the Combustion Test. To evaluate the applicability of the prototype combustor liner made of composite material, we produced a CMC combustor liner, subjected it to a combustion test, and looked for changes in its basic characteristics after the combustion test by observing external appearance and measuring the dimensions and weight of the prototype composite liner before and after the test. Restrictions on liner shape and dimensions made it impossible for us to use NDE such as X-ray CT scanning. Neither a strength test nor structure examination, in which the liner needs to be cut to take samples, was conducted because a combustion test was to be performed following the damage assessment.

The prototype liner made of composite material was assembled to the combustor body and a combustion test was conducted. A diagram and view of the assembled combustor are shown in Fig. 11 and Fig. 12. The combustion test consisted

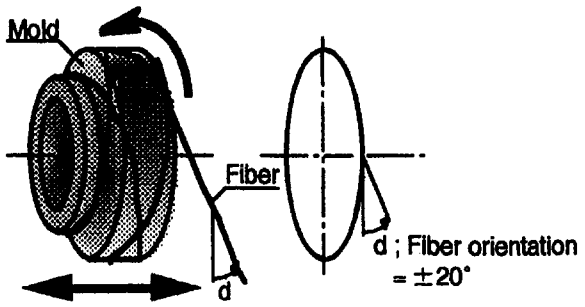

Fig. 10 Fiber orientation of CMC liner for AMG combustor

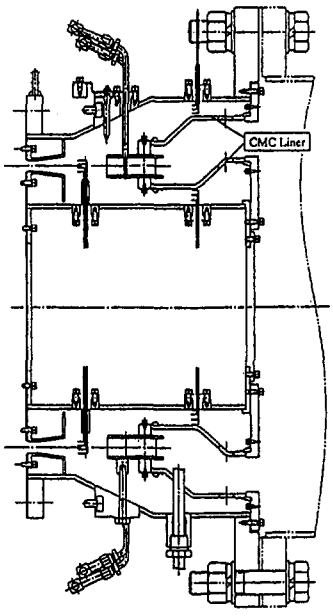

Fig. 11 Schematic view of combustion test equipment

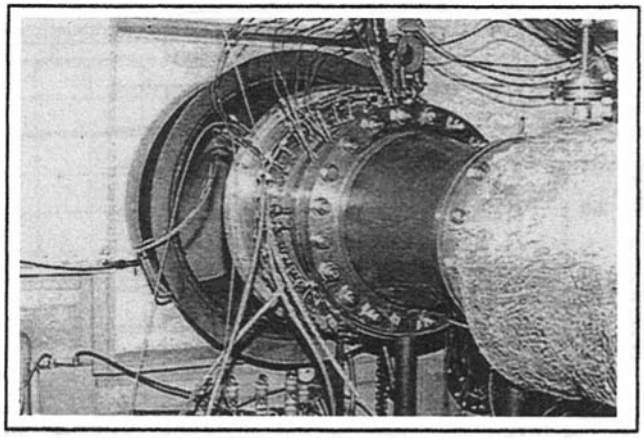

Fig. 12 External view of combustion test equipment

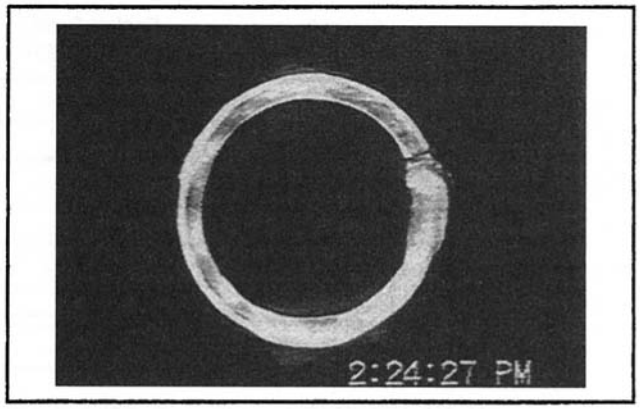

Fig. 14 State of combustion viewed from behind the combustor outer

of methane combustion under such combustion conditions that the combustor outlet gas temperature would reach the AMG target temperature of 1873K. The test conditions are shown in Fig. 13.

Combustion was repeated at ten-minutes intervals because the fuel cylinder had to be replaced after each combustion. The cycle of combustion and pause was repeated 18 times and the high-temperature retention time was about three hours. The state of combustion viewed from behind the combustor outlet is shown in Fig. 14. The temperature of the liner during the combustion test was measured with a thermocouple fitted near the dilution hole on the inner surface (combustion gas side) of the outer liner.

3 Results of Combustion Test and Discussion. Upon completion of the test, the external appearance was observed and the liner's dimensions and weight were measured to analyze changes from the pre-test condition.

The changes in external appearance are shown in Fig. 15. The inspection of external appearance revealed that no abnormalities like cracking or lamination had occurred but the surface on the combustion gas side had turned blue due to the formation of an oxide layer.

Regarding dimensions, we measured the liner's inlet and outlet diameter, thickness, and overall length at eight points in the circumferential direction and compared the values before and after the test. The changes in dimensions are shown in Fig. 16. A fairly large degree of change was seen at each measuring point. However, we believe this was due to undulations caused by the reinforcement fiber flux appearing on the surface, producing changes in the circumferential direction. The measuring points in the circumferential direction were not especially uniform before and after the test and the effect of the undulations in the surface must be taken into account regarding the changes in dimensions.

Due to those undulations, the measuring precision is believed to be ±1 mm and the measuring precision in comparing the dimensions before and after the test is believed to be about double that figure, ±2 mm. When the results of measuring the dimensions are compared by taking into account measuring precision, the amount of change before and after the test falls within the measurement tolerance range, so it can be said that there was no deformation during the combustion test.

The changes in weight are shown in Fig. 17. Although there was a slight (10 g) change in weight, we believe the true weight changed very little during the combustion test, after taking into account the change in weight caused by coating of the thermopaint and the change in weight due to the sample being weighed when in a dry state. Apart from the combustion test, a hot-rig test simulating a combustion test was conducted using a cylindrical model test piece to perform microstructural and powder X-ray analyses. In the test, no SiO2 was detected. From this result, we concluded that there was no increase in weight due to SiC oxidation in the short-time combustion test.

In the combustion test, although the combustion period was brief, the SiC^F/SiC liner suffered no changes in characteristics during combustion using gas fuel. Therefore, we believe the applicability of SiC^F/SiC in the combustor liner was confirmed. This was a first phase, short-time combustion test using methane conducted to gauge the performance of the prototype combustor. Preparations are being made for second-phase combustion tests using kerosene.

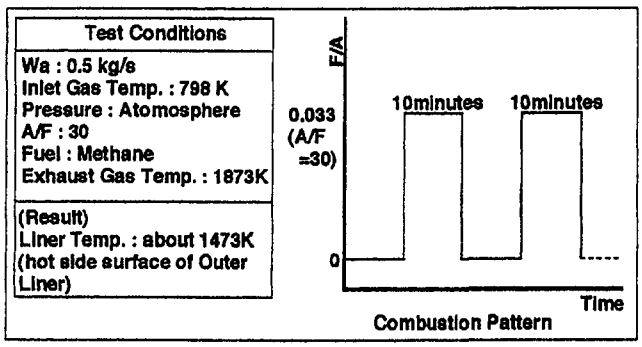

Fig. 13 Combustion test conditions

Conclusions

To evaluate the applicability of CMC in the combustor liner, we evaluated the material characteristics of SiC^F/SiC as a candidate CMC material of the combustor liner, we estimated the amount of stress generated in a model SiC^F/SiC combustor liner by analyzing thermal stress during combustion and we subjected an actual SiC^F/SiC combustor liner to a combustion test. The followings is a summary of the results.

1 In the evaluation of the material characteristics of the CMC combustor liner, the tensile strength of the trial-produced SiC^F/SiC for the combustor liner declined as the fiber orientation angle increased. At the fiber orientation angle for liner formation, it had a tensile strength of about 250 MPa at RT. Based on other test results, we concluded that the results at RT also apply at the liner's operating temperature range.

2 In the analysis of heat transfer thermal stress under steady-state conditions, the thermal stress generated during steady combustion of the SiC^F/SiC combustor liner generated a maximum hoop stress in the vicinity of the swirler tie-in part. The peak thermal stress did not exceed the material's strength and did

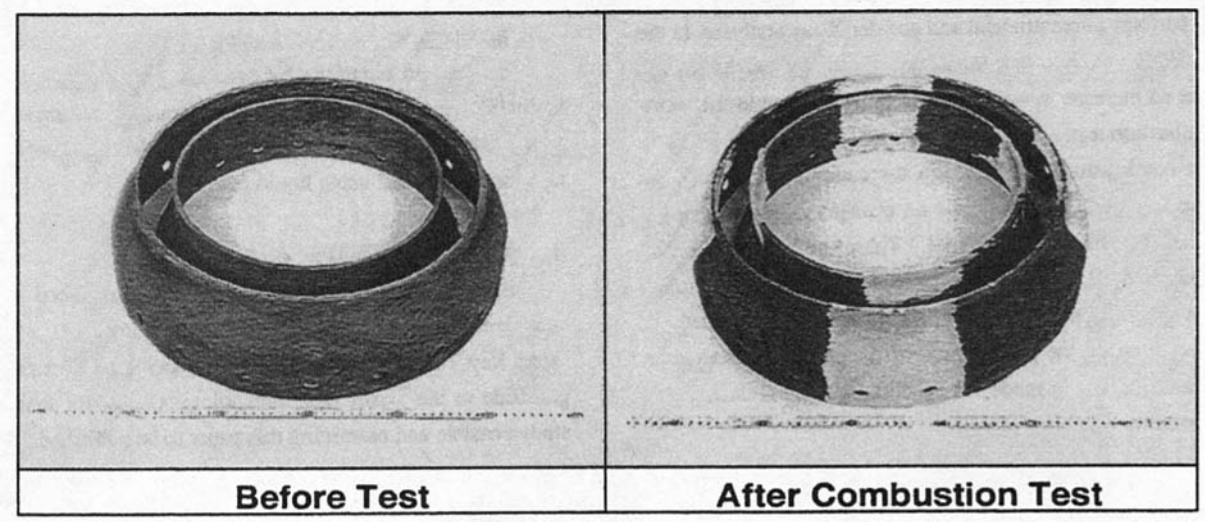

Fig. 15 Results of combustion test (external appearance)

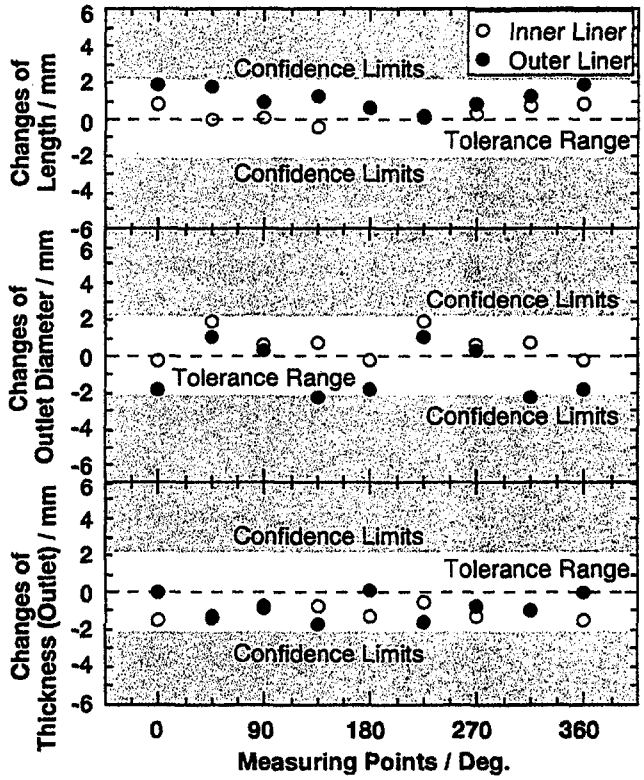

Fig. 16 Results of combustion test (measurement of dimensions)

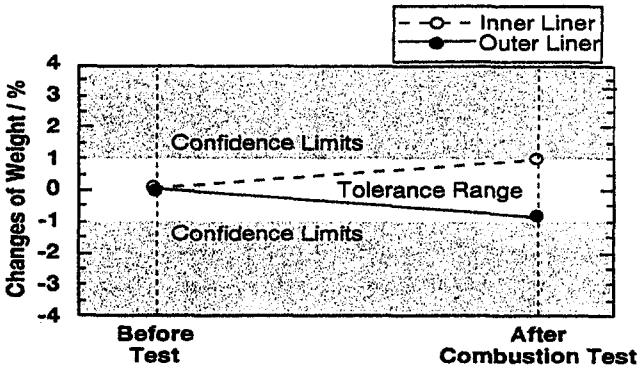

Fig. 17 Results of combustion test (measurement of weight)

not exceed the stress set as a preliminary criterion for application. The value was 170 MPa on the outer liner and 146 MPa on the inner liner.

3 In the analysis of heat transfer thermal stress under transient conditions, the peak thermal stress in the SiC^F/SiC composite material generated during the transition between idle combustion and design point combustion did not exceed the maximum thermal stress in the steady-state analysis.

4 In the combustion test lasting for about three hours with the combustor outlet gas temperature at 1873K, the SiC^F/SiC composite material liner suffered no changes in characteristics.

Based on these results, we have confirmed the applicability of SiC^F/SiC composite material to the combustor liner for the AMG project.

In the future, we intend to develop a CMC combustor liner with superior strength reliability by evaluating the durability of SiC^F/SiC, improving the process to increase strength, and improving the structure to reduce thermal stress, and to subject the prototype liner to a combustion test using liquid fuel.

Acknowledgments

This study is being carried out under the Advanced Materials Gas-Generator R&D program with a joint investment from the Japan Key Technology Center. The authors wish to express their gratitude to the Japan Key Technology Center for making this study possible and permitting this paper to be published.

References

1 Yoshida, T., 1993, "The Progress and Future of Cooling Technology of High Temperature Gas Turbines," *Journal of the Japan Gas Turbine Society,* Vol. 20, No. 80, p. 4.

2 Petrasek, D. W., McDaniels, D. L., Westfall, L. J., and Stephens, J. R., 1986, "Fiber-Reinforced Superalloy Composites Provide an Added Performance Edge," *Metal Progress,* Vol. 130, No. 2, p. 27.

3 Hiromatsu, M., Yamamura, T., Chikata, T., Sekido, T., Ohama, S., Miyagawa, H., Murakami, I., and Seki, S., 1995, "Research and Development Status of Advanced Material Gas-Generator (AMG) Project," ASME95-GT-287.

4 Nishio, K., Igashira, K., Take, K., Suemitsu, T., 1997, "Development of Combustor Liner Composed of Ceramic Matrix Composite (CMC)," *Journal of the Japan Gas Turbine Society,* Vol. 25. No. 98, p. 94.

Elevated-Temperature "Ultra" Fast Fracture Strength of Advanced Ceramics: An Approach to Elevated-Temperature "Inert" Strength

S. R. Choi

Cleveland State University
Cleveland, OH 44115
and
Senior Resident Research Scientist
NASA Lewis Research Center
21000 Brookpart Road, MS 24-1,
Cleveland, OH 44135

J. P. Gyekenyesi

NASA Lewis Research Center,
21000 Brookpart Road, MS 24-1,
Cleveland, OH 44135

The determination of "ultra" fast fracture strengths of five silicon nitride ceramics at elevated temperatures has been made by using constant stress-rate ("dynamic fatigue") testing with a series of "ultra" fast test rates. The test materials included four monolithic and one SiC whisker-reinforced composite silicon nitrides. Of the five test materials, four silicon nitrides exhibited the elevated-temperature strengths that approached their respective room-temperature strengths at an "ultra" fast test rate of 3.3 × 10⁴ MPa/s. This implies that slow crack growth responsible for elevated-temperature failure can be eliminated or minimized by using the "ultra" fast test rate. These ongoing experimental results have shed light on laying a theoretical and practical foundation on the concept and definition of elevated-temperature "inert" strength behavior of advanced ceramics.

Introduction

The inert strength of a brittle material at ambient temperature is typically regarded as free of the effects of slow crack growth (or delayed failure or subcritical crack growth) due to stress corrosion. Hence, the inert strength of a ceramic material or glass is considered as the maximum attainable or ultimate strength for a given flaw configuration. The inert strength at ambient temperature can be determined either by eliminating active species, especially moisture, with an appropriate inert medium (liquid nitrogen, dry nitrogen gas, or oil), or by using very high test rates. The use of very high test rates can minimize or eliminate the time for slow crack growth by inducing failure at a rate faster than the rate of stress corrosion at the crack tip.

However, at elevated temperatures, the concept or definition of "inert" strength is not explicit, since temperature itself acts as an environment, resulting in strength degradation through slow crack growth and/or creep. The mechanism that has been attributed to the slow crack growth of advanced ceramics at elevated temperatures is grain boundary sliding controlled by the viscous flow of the intergranular phase, and is known to be rate-dependent [1–10]. Therefore, the only conceivable way to determine the "inert" strength at a given temperature is to utilize very fast test rates that minimize the time for or eliminate slow crack growth. Few experimental studies have been made regarding the measurements of elevated-temperature, "inert" (or "ultra" fast fracture) strength of advanced ceramics. This is in part due to the fact that conventional testing machines are incapable of very high-rate testing, coupled with inadequate data acquisition system as well as safety concerns. Commonly, a maximum test rate of about 0.5 mm/min or 5 mm/min has been used to determine elevated-temperature strength of ceramic materials [1, 4, 8, 9, 11–19]. The strength determined at this test rate has been called "fast" fracture strength, implying that the obtained strength is presumably a maximum attainable or ultimate strength of the material at the temperature.

The experimental study to better understand "inert" or "ultra" fast fracture strength behavior of advanced ceramics at elevated temperatures is in progress at the NASA Lewis Research Center using digitally controlled test frames. A total of twelve advanced ceramics, one alumina, ten silicon nitrides, and one silicon carbide, have been tested to date using constant stress-rate ("dynamic fatigue") testing in flexure with a series of very high stress rates up to 3.3 × 10⁴ MPa/s. The test temperatures ranged from 700 to 1371°C in air, depending on material. Of the seven advanced ceramics previously tested [20, 21], one alumina and three silicon nitrides exhibited elevated-temperature strengths that approached their room-temperature inert strengths at "ultra" fast stress rates of 3.3 × 10³ to 3.3 × 10⁴ MPa/s. By contrast, one carbide and two other silicon nitrides exhibited elevated-temperature strengths 20 and 10 percent lower than their respective room-temperature counterparts. This paper, as an extension of the previous studies, summarizes the recent experimental results on "ultra" fast fracture strength behavior of five silicon nitride ceramics at elevated temperatures. The elevated-temperature strengths of each material were determined in a range of stress rates from 3.3 × 10⁻² to 3.3 × 10⁴ MPa/s in flexure. The measured strength data were analyzed with the analytical relations of fracture strength and critical crack size versus stress rate, in conjunction with the "critical" stress rate above which a strength convergence may take place.

Theoretical Background

The relationship between fracture stress and stress rate in constant stress-rate testing will be presented in this section with a special emphasis on the very high stress-rate regime. For most glass and advanced ceramics, the slow crack growth (SCG) rate, either by stress corrosion at ambient temperature or by grain boundary sliding at elevated temperatures, can be expressed by the following empirical power-law relation [2, 8, 22]

$$v = \frac{da}{dt} = A\left[\frac{K_I}{K_{IC}}\right]^n \tag{1}$$

where v, a, and t are crack velocity, crack size and time, respec-

Contributed by the International Gas Turbine Institute and presented at the International Gas Turbine and Aeroengine Congress and Exhibition, Stockholm, Sweden, June 2–5, 1998. Manuscript received by the ASME Headquarters April 1, 1998. Paper No. 98-GT-479. Associate Technical Editor: R. Kielb.

tively. A and n are the material/environment dependent SCG parameters, and K_I and K_{IC} are, respectively, the applied stress intensity factor and the critical stress intensity factor of the material under Mode I loading. For constant stress-rate testing which employs a series of constant loading or stress rates ($\dot{\sigma}$), the corresponding fracture strength (σ_f) as a function of stress rate for the case of a weak threshold stress intensity for SCG can be approximated for $n \geq 5$ as follows [23]:

$$\sigma_f = [B(n+1)S_i^{n-2}\dot{\sigma}]^{1/(n+1)} = D[\dot{\sigma}]^{1/(n+1)} \quad (2)$$

where

$$B = \frac{2K_{IC}^2}{AY^2(n-2)} \quad (3)$$

S_i is the inert strength, Y is the crack geometry factor in the relation $K_I = Y\sigma_a a^{1/2}$ with σ_a being the remote applied stress, and $D = [B(n+1)S_i^{n-2}]^{1/(n+1)}$. The SCG parameters n and D can be determined from the slope and intercept, respectively, of a best-fit linear regression analysis of log σ_f plotted as a function of log $\dot{\sigma}$ based on Eq. (2). Because of simplicity in both testing and parameter estimation, a new ASTM standard C1368 has been developed for the determination of SCG parameters of advanced ceramics using constant stress-rate testing in flexure at ambient temperature [24].

Since the slow crack growth can be minimized or eliminated at sufficiently high stress rates, the corresponding strength at this region is expected to converge to a certain specific value, possibly close to an inert strength of the material. The functional form of Eq. (2), which does not indicate such an upper limit in fracture strength at sufficiently high stress rates, is contradictory to actual material behavior as well as to the exact solutions derived from Eq. (1). In a previous study [21], the relationship between strength and stress rate was numerically obtained particularly at very high stress-rate regime in order to determine a critical stress rate above which a strength convergence exists. The resulting numerical solution of normalized strength (log σ_f^*) as a function of normalized stress rate (log $\dot{\sigma}^*$) at different values of n is presented in Fig. 1 [21]. The normalized critical crack size at failure as a function of normalized stress rate can also be obtained based on the same numerical scheme that was used for the strength-stress rate analysis. The normalized variables used in the numerical solution were as follows:

$$J = \frac{A}{a_{fi}}t; \quad \sigma^* = \frac{\sigma_a}{S_i}; \quad C^* = \frac{a}{a_{fi}}; \quad \dot{\sigma}^* = \frac{\sigma^*}{J} \quad (4)$$

where J, σ^*, C^*, and $\dot{\sigma}^*$ are, respectively, normalized time, normalized applied stress, normalized crack size and normalized stress rate. a_{fi} is the critical crack size in an inert environment or the initial crack size. Using these normalized variables, the power-law SCG rate (Eq. (1)) becomes

$$\frac{dC^*}{dJ} = [K^*]^n = [\dot{\sigma}^* J (C^*)^{1/2}]^n \quad (5)$$

where K^* is normalized stress intensity factor, $K^* = K_I/K_{IC}$. A solution of the differential equation of Eq. (5) in terms of normalized critical crack size versus normalized stress rate was obtained by numerical integration with required initial and instability conditions [21]. The resulting plot is shown in Fig. 2. It is evident from Figs. 1 and 2 that with increasing stress rate both strength and critical crack size at failure converge to, respectively, the inert strength ($\sigma_f^* = 1$) and the initial crack size ($C_f^* = 1$), regardless of n. The corresponding stress rate is defined as normalized critical stress rate ($\dot{\sigma}_{cr}^*$), where $\sigma_f^* = 1$ and $C_f^* = 1$, and can be approximated from Figs. 1 and 2 as follows:

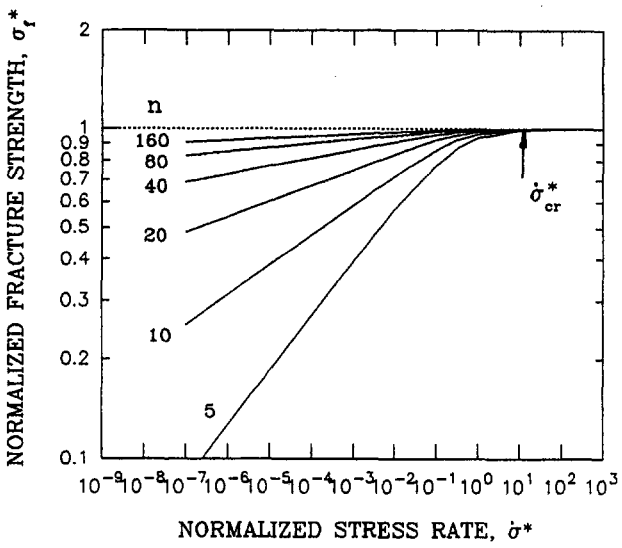

Fig. 1 Numerical solution of normalized strength (log σ_f^*) as a function of normalized stress rate (log $\dot{\sigma}^*$) [21]. σ_{cr}^* denotes the normalized critical stress rate.

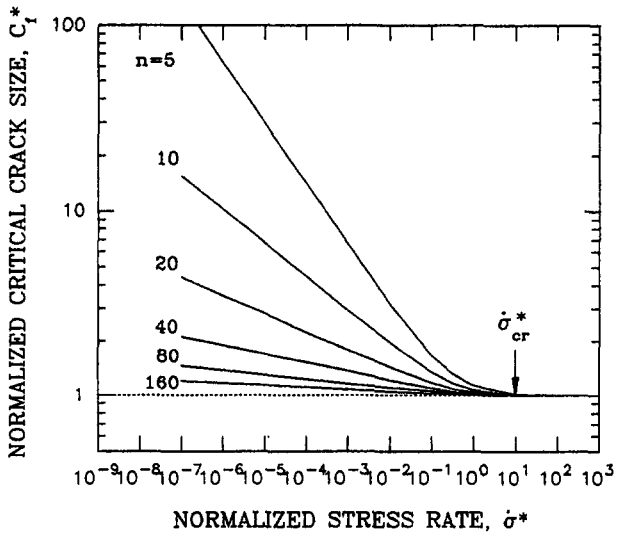

Fig. 2 Numerical solution of normalized critical crack size (log C_f^*) as a function of normalized stress rate (log $\dot{\sigma}^*$). σ_{cr}^* denotes the normalized critical stress rate.

$$\dot{\sigma}_{cr}^* \approx 10^1 \quad (6)$$

From Eqs. (2) through (6) the non-normalized critical stress rate becomes (also from [21])

$$\dot{\sigma}_{cr} \approx \frac{20S_i^3}{B(n-2)} \quad (7)$$

If S_i, B, and n are known, the critical stress rate can be calculated from Eq. (7). Above this critical stress rate, slow crack growth is minimized or eliminated by the extremely short failure (or test) time. Based on Figs. 1 and 2 it is apparent that constant stress-rate testing with a series of very high ("ultra" fast) test rates, including the critical stress rate, is required to reach the strength convergence and to measure the possible elevated-temperature, "inert" strength of the material.

Experimental Procedure

Constant stress-rate ("dynamic fatigue") testing for five silicon nitride ceramics was performed in four-point flexure at

Table 1 Room-temperature density, Young's modulus, fracture toughness, hardness, and strength of A2Y6, AS440, NT154, SiC whisker (20 vol %)-reinforced composite ("Kryptonite"), and AS800 silicon nitrides

Material	Density (g/cm^3)[a]	Young's Modulus, E (GPa)[b]	Fracture Toughness, K_{IC} ($MPa\sqrt{m}$)[c]	Hardness, H (GPa)[d]	Strength, σ_f (MPa)[e]
A2Y6 Si_3N_4	3.21	300(3)*	7.32(0.25)*	13.9(0.2)*	701(89)*
AS440 Si_3N_4	3.21	305(1)	7.30(0.30)	13.9(0.5)	773(119)
NT154 Si_3N_4	3.18	310(1)	5.51(0.17)	15.5(0.1)	793(56)
SiC_w/Si_3N_4	3.23	313(3)	6.63(0.18)	17.4(0.1)	667(27)
AS800 Si_3N_4	3.27	308(1)	7.24(0.23)	14.3(0.8)	778(39)

Notes:

a. By the specimen mass/volume method; b. By the impulse excitation technique (ASTM C 1259) [25]; c. By the single edge precracked beam (SEPB) method (with typically 5 specimens) [26]; d. By the Vickers indentation (ASTM C 1327) [27]; e. By four-point flexure tests (10/22 mm spans). * The parenthesis represents ± 1.0 standard deviation.

elevated temperatures in air. The materials consisted of hot-pressed A2Y6 silicon nitride (GTE, vintage 1984), sintered AS440 silicon nitride (AlliedSignal, vintage 1990), hot-pressed NT154 silicon nitride (Norton, vintage 1991), 20 vol % SiC whisker-reinforced composite silicon nitride (designated as "Kryptonite"™, Japan Metals & Chemicals Co. Ltd., Japan), and sintered AS800 silicon nitride (AlliedSignal, vintage 1994). The basic physical and mechanical properties such as density, Young's modulus, fracture toughness, hardness and strength of each material at room temperature were determined and are shown in Table 1.

The nominal dimensions of all the flexural beam specimens were 3 mm by 4 mm by 23–25 mm, respectively, in height, width, and length. All the test specimens were annealed for 2 h at 1200°C in air, prior to testing, to eliminate any residual stresses associated with machining. Each specimen was tested with SiC fixtures with 10 mm inner and 22 mm outer spans after equilibration at the test temperature for about 20 min. The AS440 silicon nitride was tested at 1100°C in air, and the remaining four silicon nitrides tested at 1200°C in air. The electromechanical test frame (Model 8562, Instron) was utilized up to stress rates of 3.3×10^3 MPa/s. However, the electromechanical test frame was unable to load at stress rates greater than 3.3×10^3 MPa/s so that the hydraulic test frame (Model 8501, Instron), which exhibited better high rate, load-controlled than the electromechanical frame, was exclusively used for testing at the highest stress rate of 3.3×10^4 MPa/s. Typically, four stress rates ranging from 3.3×10^{-2} to 3.3×10^4 MPa/s were used for each material, with a total of five specimens at each stress rate. The output-wave forms for stress rates greater than 3.3×10^3 MPa/s were recorded and checked with a digital storage oscilloscope. The room-temperature strength of each material was also determined at 33 MPa/s in ambient air using the same fixture that was used for the elevated-temperature testing. Typically, a total of five to ten specimens were used for each material at room-temperature testing. Note that room-temperature strength of most silicon nitrides is insensitive to test rate in ambient air, due to their significant SCG resistance with SCG parameter $n \geq 100$.

Results and Discussion

The results of constant stress-rate testing for the five silicon nitrides, four monolithics, and one composite, are summarized in Fig. 3, where log σ_f (fracture strength) was plotted as a function of log $\dot{\sigma}$ (stress rate) based on Eq. (2). The room-temperature strength for each material with ±1.0 standard deviation was also plotted for comparison. The four materials except AS800 exhibited an increase in strength with increasing stress rate, which represents susceptibility to slow crack growth. The value of n for each material was determined by a linear regression analysis using the mean strength data, based on Eq. (2) together with the data presented in the figure. The resulting SCG parameter n was $n = 22.7 \pm 4.0$, 24.6 ± 1.3, 45.8 ± 6.0, and 37.5 ± 4.0, respectively, for A2Y6, AS440, NT154, and the composite ("Kryptonite"). It is important to note that all four silicon nitrides exhibited strengths at an "ultra" fast stress rate of 3.3×10^4 MPa/s that approximated (within 5 percent) their room-temperature strengths. By contrast, AS800 exhibited a significant resistance to SCG with a very high SCG parameter $n = 154 \pm 77$. Furthermore, the corresponding "ultra" fast strength of AS800 did not approach the room-temperature counterpart.

To better represent strength degradation as well as strength approach behavior in more details, the elevated temperature strengths of each material were normalized with respect to the corresponding room-temperature strength, to give the "reduced" strength, σ_r^*. The "reduced" strength was defined as follows [21]:

$$\sigma_r^* = \frac{\sigma_{f/HT}}{\sigma_{f/RT}} \tag{8}$$

where $\sigma_{f/HT}$ and $\sigma_{f/RT}$ are elevated and room-temperature strengths, respectively. The resulting plots of "reduced" strength as a function of stress rate are depicted in Fig. 4. The maximum "reduced" strengths of A2Y6, AS440, NT154, the composite ("Kryptonite") and AS800 silicon nitrides at 3.3×10^4 MPa/s were $\sigma_r^* = 0.97$, 0.98, 1.05, 0.96, and 0.86, respectively. The results in Fig. 4 also indicates that the strength increase from the conventional test rate (of the order of 3×10^1 MPa/s or 0.5 mm/min) to the "ultra" fast stress rate of 3.3×10^4 MPa/s was appreciable: σ_r^* increased from 0.67 to 0.97 (45 percent increase) for A2Y6, 0.74 to 0.98 (32 percent increase) for AS440, 0.92 to 1.05 (14 percent increase) for NT154, and from 0.79 to 0.96 (22 percent increase) for the composite, respectively. However, no strength increase was observed for AS800, due to its very high SCG parameter $n = 154$ (i.e., no slow crack growth).

The critical stress rate was determined from Eq. (7) with the evaluated SCG parameters n and D (hence, B) and the room-temperature strength (S_i) of each material. The resulting critical stress rate was $\dot{\sigma}_{cr} = 7 \times 10^6$, 1×10^6, 1×10^5 MPa/s, 1×10^6, and 4×10^{14} MPa/s, respectively, for A2Y6, AS440,

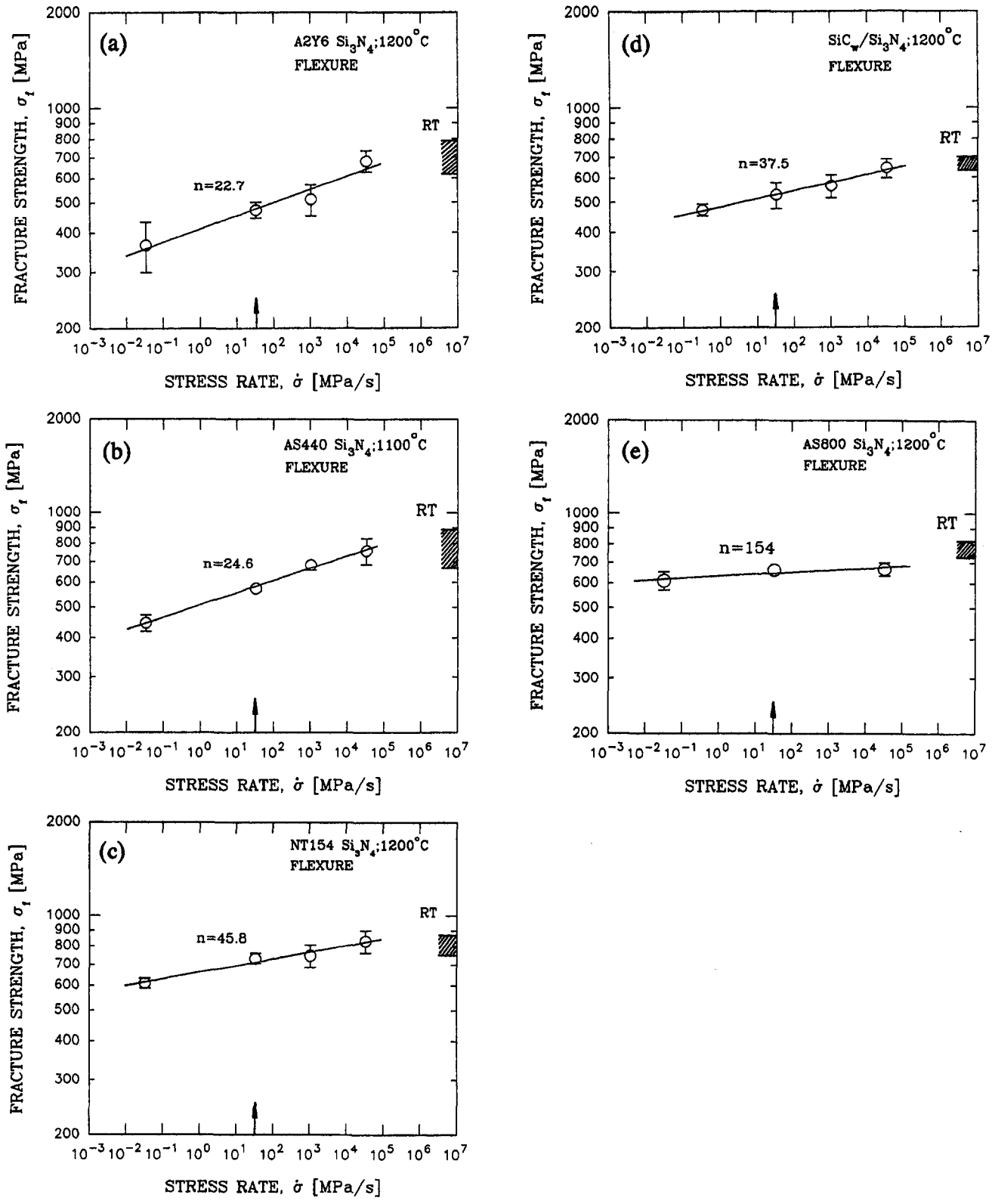

Fig. 3 Elevated-temperature, constant stress-rate flexural testing results for A2Y6 (*a*), AS440 (*b*), NT154 (*c*) monolithic, 20 vol % SiC whisker-reinforced composite ("Kryptonite") (*d*), and AS800 monolithic (*e*) silicon nitrides at elevated temperatures in air. The solid lines represent the best-fit lines based on Eq. (2). The error bars represent ±1.0 standard deviation. The room-temperature inert strength with ±1.0 standard deviation ("RT") was included for comparison. The arrow in the "stress rate" axis indicates the conventional test rate (of the order of 3×10^1 MPa/s or 0.5 mm/min).

NT154, "Kryptonite," and AS800. This is an order of magnitude greater than that estimated from the actual data shown in Fig. 3 or Fig. 4. However, if the normalized critical stress rate is taken as $\dot{\sigma}^*_{cr} = 10^0$ instead of $\dot{\sigma}^*_{cr} = 10^1$ in Eq. (6), based on Fig. 1 for $n \geq 20$, the calculated and estimated values are in good agreement, implying a reasonable prediction by Eq. (7). The extreme value of $\dot{\sigma}_{cr}$ ($=10^{14}$ MPa/s) exhibited by AS800 was attributed to the very high SCG parameter n.

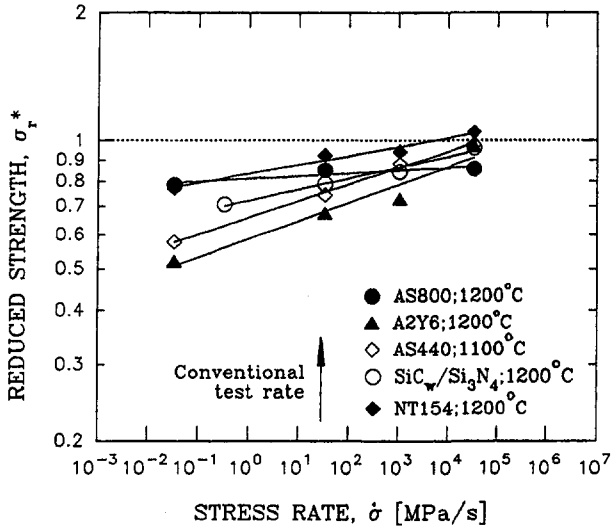

Fig. 4 A summary of "reduced" strength as a function of stress rate for five silicon nitrides (A2Y6, AS440, NT154, "Kryptonite," and AS800) from this study

Figure 5 shows a summary of the "reduced" strength as a function of stress rate determined previously for the seven advanced ceramics, one alumina, five silicon nitrides, and one silicon carbide [20, 21]. The 96 wt % alumina and the three silicon nitrides (GN10 monolithic, GN10 SiC whisker (30 vol %) reinforced composite, and NCX34 monolithic) exhibited the elevated-temperature strengths approximately close to the corresponding room-temperature counterparts. The "reduced" strengths at stress rates $\geq 10^3$ MPa/s were $\sigma_r^* = 0.95, 0.96, 1.00, 0.99$, respectively, for 96 wt% alumina, GN10, GN10 composite and NCX34 silicon nitrides. By contrast, the maximum "reduced" strengths obtained at 3.3×10^4 MPa/s for SN252 and NC132 silicon nitrides and NC203 silicon carbide were $\sigma_r^* = 0.89, 0.90$, and 0.80, respectively. However, the strength increase from the conventional test rate to the "ultra" fast stress rate (3.3×10^4 MPa/s) was remarkable for these materials, similar to the A2Y6, AS440, NT154, and the composite silicon nitrides observed in this study (see Fig. 4): the percentage of increase was 27, 41, and 18 percent, respectively, for SN252, NC132, and NC203.

All of the experimental results for the four silicon nitrides ceramics (except AS800) in this study as well as for seven other ceramics previously studied [20, 21] show that, notwithstanding possible changes in flaw populations at elevated temperatures, the strength at 3.3×10^4 MPa/s approached a specific value close to the room-temperature strength or reached a higher value than that measured at the conventional test rate of the order of 3×10^1 MPa/s. Elevated-temperature SCG as well as creep is known to be a rate-dependent process occurring by viscous flow of the grain boundary phase [1–10]. If an extremely high-test rate is used, creep and/or possibly oxidation could be minimized due to the extremely short test time (10–20 ms), thereby resulting in SCG as a unique failure mechanism. The fact that the elevated-temperature strengths of at least eight materials tested at 3.3×10^4 MPa/s approached the room-temperature counterparts indicates not only that SCG was minimized but also that grain softening, which can also control strength, was insignificant.

This ongoing study on elevated-temperature, "ultra" fast fracture strength of advanced ceramics repeatedly casts some insight into fracture toughness behavior of the materials at elevated temperatures. As stated in the previous study [21], elevated-temperature fracture toughness, like strength, is regarded to be controlled by flow characteristics of the grain boundary phases, so that it is rate dependent. Therefore, if rate dependency is eliminated using a very high test rate and if the grains remain rigid, the fracture toughness may not be so dependent on temperature, as postulated for the "ultra" fast fracture strength behavior. In fact, for many silicon nitride and silicon carbide ceramics, their values of fracture toughness exhibit no significant variation from room temperature to 1200 or 1300°C [21]. The same speculation may be applicable to an elevated-temperature Young's modulus of advanced ceramics.

Based on the experimental data to date as well as the numerical solution, it can be stated that the elevated-temperature "inert" strength of an advanced ceramic material can be "defined," although tentative, as a strength whereby no slow crack growth occurs at the temperature. In addition, the elevated-temperature "inert" strength of a material would be close to its room-temperature counterpart, and may be obtained using a series of "ultra" fast stress rates $\geq 10^4$ MPa/s. This can be better verified if test frames are able to run at test rates faster than the critical stress rates, 10^5–10^7 MPa/s, particularly for the materials that showed some strength degradation (10–20 percent) at 3.3×10^4 MPa/s. The current, digitally controlled test frames, however, were unable to achieve stress rates faster than 3.3×10^4 MPa/s [21]. It is also believed that more than one test temperature, probably ranging from 1100 to 1400°C, depending on material, are required for laying a better foundation on the concept and/or definition of elevated-temperature "inert" strength of a material.

Typical examples of strength degradation with respect to test temperature is shown in Fig. 6, where the "reduced" strength of the NT154 silicon nitrides was plotted for two different test rates of the orders of 10^1 MPa/s (conventional) and 10^4 MPa/s ("ultra" fast). The "ultra" fast strength of NT154 was obtained additionally at 1371°C, with a total of five specimens. The figure also includes the "reduced" strength data of 96 wt% alumina for a wide range of stress rates, reconstructed from the previously published data [21]. A remarkable difference in strength degradation between the "ultra" fast and the conventional test rates is evident. The NT154 silicon nitride exhibited almost no strength degradation up to 1371°C at the "ultra" fast stress rate of 3×10^4 MPa/s; whereas, a significant strength degradation occurred if the conventional test rate of 3×10^1 MPa/s was used. The similar behavior was true for the 96 wt % alumina, as seen in the figure. Therefore, entirely different information on strength degradation behavior could be obtained

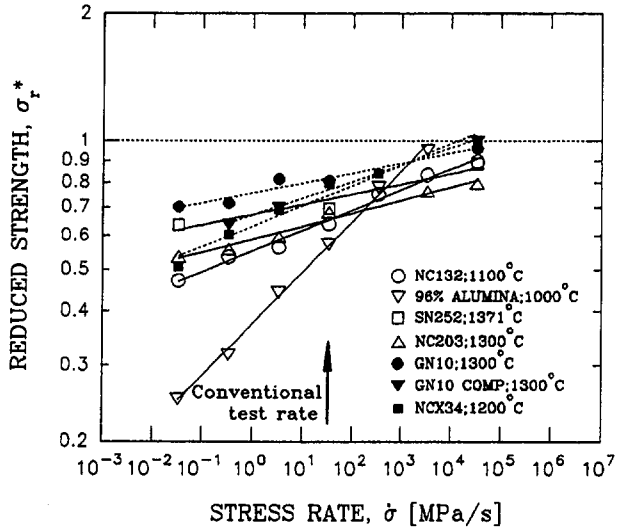

Fig. 5 A summary of "reduced" strength as a function of stress rate for seven advanced ceramics determined from the previous studies: GN10, NCX34, and GN10 composite (30 vol % SiC whisker-reinforced) silicon nitrides [20]; alumina, NC132 and SN252 silicon nitrides and NC203 silicon carbide [21].

if one adopts different stress rates. At least two (highest and lowest) or three stress rates (highest, intermediate, and lowest), depending on the degree of SCG susceptibility of a material, are recommended to completely characterize elevated-temperature strength behavior of the material, as suggested previously [20, 21].

The SCG parameter A in Eq. (1) is usually calculated from Eqs. (2) and (3) as follows:

$$A = \frac{2K_{IC}^2 S_i^{n-2}(n+1)}{D^{n+1}Y^2(n-2)} \tag{9}$$

This equation indicates that the SCG parameter A is a strong function of "inert" strength for a given material/load/environment system. Because of the functional form of Eq. (9), a significant difference in A can be made if one uses S_i from the conventional "fast" fracture strength data rather than from the "ultra" fast (or room temperature) strength data. Figure 7 shows the results of such a difference in crack velocity (Eq. (1)) between the two different "inert" strengths ("fast" fracture and "ultra" fast) for the A2Y6 monolithic and the composite ("Kryptonite") silicon nitrides at 1200°C. As seen in the figure, the lifetime parameter (A) using the strength determined at the "ultra" fast test rate is almost three order of magnitude greater than that using the conventional "fast" fracture strength at 3×10^1 MPa/s. This demonstrates a significant influence of elevated-temperature "inert" strength on the determination of life prediction parameter. The use of the conventional "inert" strength could result in unrealistically conservative life/reliability estimates.

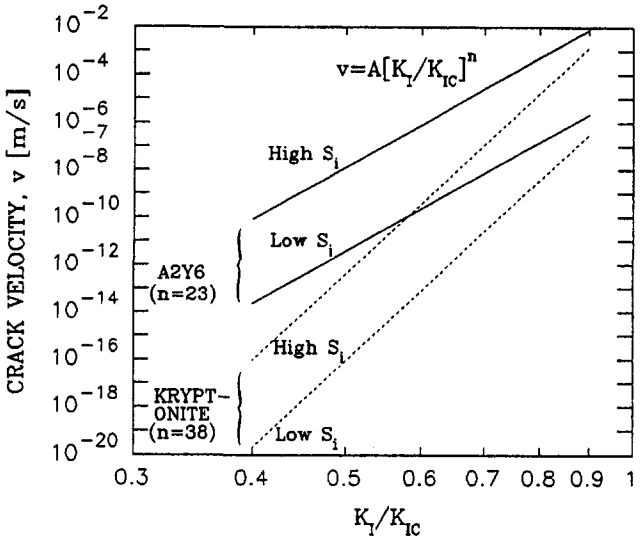

Fig. 7 Slow crack growth rate curves (Eq. (1)) using the two different "inert" strength values determined at "ultra" fast test rate of 3.3×10^4 MPa/s ("High S_i") and at conventional "fast" test rate of 3×10^1 MPa/s ("Low S_i") for A2Y6 monolithic and "Kryptonite" composite silicon nitrides at 1200°C.

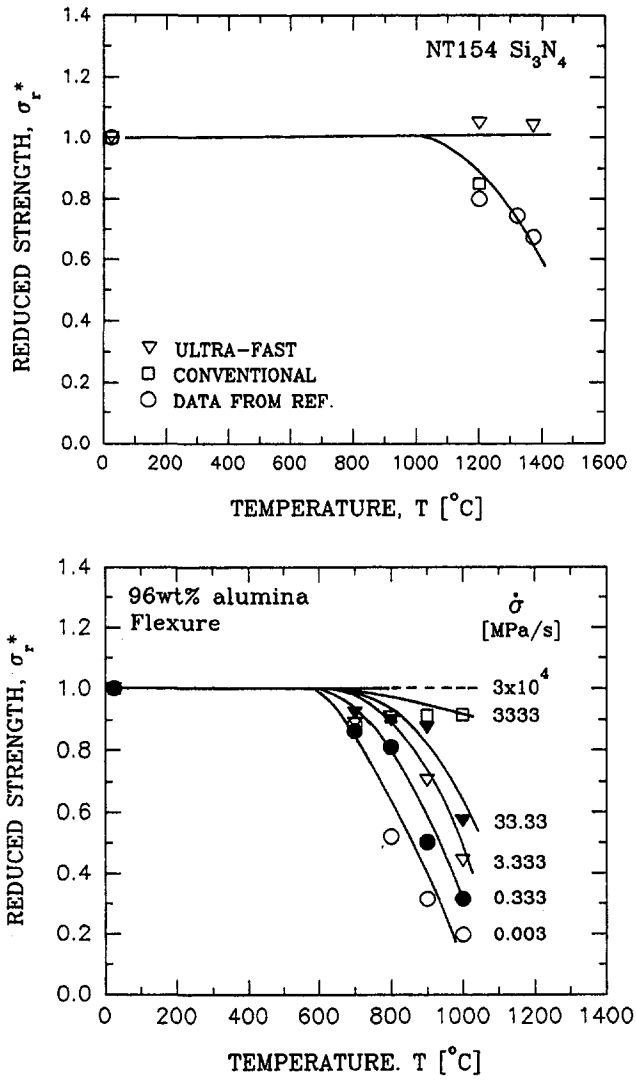

Fig. 6 Typical examples of "reduced" strength of NT154 silicon nitride and 96 wt % alumina [21] as a function of temperature, obtained at different test rates including "ultra" fast test rate (3.3×10^4 MPa/s) and at conventional "fast" test rate (of the order of 3×10^1 MPa/s). The conventional "fast" fracture strength data for NT154 were quoted from [28].

Conclusions

The elevated-temperature strengths of A2Y6, AS440 and NT154 monolithic and 20 vol % SiC whisker-reinforced composite silicon nitrides approached approximately (within 5 percent) the room-temperature strengths at an "ultra" fast stress rate of 3.3×10^4 MPa/s. One exception to this was AS800 silicon nitride that exhibited a significant resistance to slow crack growth. The overall behavior for the four silicon nitride ceramics (except AS800) is consistent with that of the three different silicon nitrides and one alumina obtained previously [20, 21]. Based on the experimental data to date as well as the analytical approach, it can be tentatively stated that elevated-temperature "inert" strength can be defined as a strength with no slow crack growth and can be estimated with "ultra" fast stress rates $\geq 3 \times 10^4$ MPa/s. In order to lay firmer foundation of the concept and definition of elevated-temperature "inert" strength, however, a series of "ultra" high test rates including the critical stress rate, 10^5 to 10^7 MPa/s, would be required. Because of slow crack growth, at least two or three stress rates are recommended to characterize the complete, elevated-temperature strength behavior of a given material. The importance of appropriate use of elevated-temperature "inert" strength should be considered in life prediction estimation/reliability of advanced ceramics.

Acknowledgments

The authors are grateful to R. Pawlik for the experimental work during the course of this research. This work was sponsored in part by the Advanced Automotive Materials Technologies Project, US Department of Energy, under contract DE-AC05-96OR22464 with Lockheed Martin Energy Research Corporation.

References

1 Lange, F. F., 1974, "High-Temperature Strength Behavior of Hot-Pressed Si_3N_4: Evidence for Subcritical Crack Growth," *J. Am. Ceram. Soc.,* Vol. 57, pp. 84–87.

2 Evans, A. G., and Wiederhorn, S. M., 1974, "Crack Propagation and Failure Prediction in Silicon Nitride at Elevated Temperatures," *J. Mater. Sci.,* Vol. 9, pp. 270–278.

3 Kossowsky, R., Miller, D. G., and Diaz, E. S., 1975, "Tensile and Creep Strengths of Hot-Pressed Si_3N_4," *J. Mater. Sci.,* Vol. 10, pp. 983–997.

4 Weston, J. E., and Pratt, P. L., 1978, "Crystallization of Grain Boundary Phases in Hot-Pressed Silicon Nitride Materials," *J. Mater. Sci.,* Vol. 13, pp. 2147–2156.

5 Tighe, N. J., 1978, "The Structure of Slow Crack Growth Interfaces in Silicon Nitride," *J. Mater. Sci.,* Vol. 13, pp. 1455–1463.

6 McHenry, K. D., and Tressler, R. E., 1980, "Fracture Toughness and High-Temperature Slow Crack Growth in SiC," *J. Am. Ceram. Soc.,* Vol. 63, pp. 152–156.

7 Tsai, R. L., and Raj, R., 1980, "The Role of Grain-Boundary Sliding in Fracture of Hot-Pressed Si_3N_4 at High Temperatures," *J. Am. Ceram. Soc.,* Vol. 63, pp. 513–517.

8 Jakus, K., Service, T., and Ritter, J. E., 1980, "High-Temperature Fatigue Behavior of Polycrystalline Alumina," *J. Am. Ceram. Soc.,* Vol. 63, pp. 4–7.

9 Govila, R. K., 1990, "Strength of Slip-Cast, Sintered Silicon Nitride," *J. Am. Ceram. Soc.,* Vol. 73, pp. 1744–1751.

10 Quinn, G. D., 1990, "Fracture Mechanism Maps for Advanced Structural Ceramics Part I: Methodology and Hot-Pressed Silicon Nitride Results," MTL TR 90-6, U.S. Army Materials Technology Laboratory, Watertown, MA.

11 Evans, A. G., and Lange, F. F., 1975, "Crack Propagation and Fracture in Silicon Carbide," *J. Mater. Sci.,* Vol. 10, pp. 1659–1664.

12 Miller, D. G., Anderson, C. A., Singhal, S. C., Lange, F. F., Diaz, E. S., and Kossowsky, R., 1976, "Brittle Materials Design, High Temperature Gas Turbine Material Technology," AMMRC CTR 76-32, Army Materials and Mechanics Research Center, Watertown, MA.

13 Govila, R. K., 1980, "Ceramic Life Prediction Parameters," AMMRC TR 80-18, Army Materials and Mechanics Research Center, Watertown, MA.

14 Khandelwal, P. K., Chang, J., and Heitman, P. W., 1986, "Slow Crack Growth in Silicon Nitride," in *Fracture Mechanics of Ceramics,* Vol. 8, R. C. Bradt, et al., eds., Plenum Press, New York, pp. 351–362.

15 Rawlins, M. H., Nolan, T. A., Allard, L. F., and Tennery, V. J., 1989, "Dynamic and Static Fatigue of Sintered Silicon Nitride: II, Microstructure and Failure Analysis," *J. Am. Ceram. Soc.,* Vol. 72, pp. 1338–1342.

16 Braue, W., Goring, J., and Ziegler, G., 1989, "Correlation of Slow Crack Growth and Microstructure in HIP-SiC," in *Ceramic Materials & Components for Engines,* V. J. Tennery, ed., The American Ceramic Society, Westerville, OH, pp. 817–830.

17 Tajima, Y., Urashima, K., Watanabe, M., and Matsuo, Y., 1989, "Static, Cyclic and Dynamic Fatigue Behavior of Silicon Nitride," in *Ceramic Materials & Components for Engines,* V. J. Tennery, ed., The American Ceramic Society, Westerville, OH, pp. 719–728.

18 Hecht, N. L., McCullum, D. E., and Graves, G. A., 1989, "Investigation of Selected Si_3N_4 and SiC Ceramics," in *Ceramic Materials & Components for Engines,* V. J. Tennery, ed., The American Ceramic Society, Westerville, OH, pp. 806–816.

19 Hecht, N. L., 1993, *Ceramic Technology Project, Semiannual Progress Report for October 1992 Through March 1993,* ORNL/TM-12428, Oak Ridge National Laboratory, Oak Ridge, TN, pp. 329–342.

20 Choi, S. R., and Salem, J. A., 1996, "'Inert" Strength of Silicon Nitride Ceramics at Elevated Temperatures," *Ceram. Eng. Sci. Proc.,* Vol. 17, pp. 454–461.

21 Choi, S. R., and Salem, J. A., 1998, "Ultra-Fast Fracture Strength of Advanced Ceramics at Elevated Temperatures," *Mat. Sci. Eng.,* Vol. A242, pp. 129–136.

22 Wiederhorn, S. M., 1978, "Subcritical Crack Growth in Ceramics," in *Fracture Mechanics of Ceramics,* Vol. 2, R. C. Bradt, et al., eds., Plenum Publishing Co., New York, pp. 613–646.

23 Ritter, J. E., 1978, "Engineering Design and Fatigue Failure of Brittle Materials," in *Fracture Mechanics of Ceramics,* Vol. 4, R. C. Bradt, et al., eds., Plenum Publishing Co., New York, pp. 667–686.

24 ASTM C 1368, 1998, "Test Method for Determination of Slow Crack Growth Parameters of Advanced Ceramics by Constant Stress-Rate Flexural Testing at Ambient Temperature," *Annual Book of ASTM Standards,* Vol. 15.01, American Society for Testing and Materials, Philadelphia, PA.

25 ASTM C 1259, 1997, "Standard Test Method for Dynamic Young's Modulus, Shear Modulus, and Poisson's Ratio for Advanced Ceramics by Impulse Excitation of Vibration," *Annual Book of ASTM Standards,* Vol. 15.01, American Society for Testing and Materials, Philadelphia, PA.

26 ASTM PS070, 1998, "Provisional Test Method for Determination of Fracture Toughness of Advanced Ceramics at Ambient Temperature," *Annual Book of ASTM Standards,* Vol. 15.01, American Society for Testing and Materials, Philadelphia, PA.

27 ASTM C 1327, 1997, "Standard Test Method for Vickers Indentation Hardness of Advanced Ceramics," *Annual Book of ASTM Standards,* Vol. 15.01, American Society for Testing and Materials, Philadelphia, PA.

28 Morey, R. E., and Lucas, G. A., 1980, 18th Bimonthly Report, ATTAP, 7-8/1990, NASA Lewis Research Center, Cleveland, OH.

D. M. Ishimura

C. M. Kinoshita

S. M. Masutani

S. Q. Turn

Hawaii Natural Energy Institute,
University of Hawaii at Manoa,
2540 Dole Street,
Honolulu, HI 96822

Cycle Analyses of 5 and 20 MWe Biomass Gasifier-Based Electric Power Stations in Hawaii

Thermodynamic cycle analyses of biomass gasifier-based electric power stations at two scales, nominally 5 and 20 MWe (net electric power output), were performed to assess process performance and viability. Various configurations (Rankine, simple, steam-injected gas turbine, and combined cycles) of a 5 MW stand-alone power station were modeled and a 20 MW biomass-based integrated gasifier combined-cycle cogeneration facility at a sugar factory was simulated. Information gained from these analyses will be applied to determine whether biomass gasification-based electricity production is practicable in Hawaii and other sugar producing locales.

Introduction

Imported fossil fuels account for nearly 95 percent of the energy consumed in the State of Hawaii. Electricity prices in Hawaii are the third highest in the U.S., and utility gas and gasoline prices are the highest in the nation. Moreover, oil price shocks, such as the crisis experienced in the early 1970s, pose a major threat to local industry and the economy. Diversification of the energy mix by incorporating renewable resources can promote economic stability by reducing the reliance on fossil fuels.

The utilization of biomass resources to produce electricity and transportation fuels has other far reaching benefits. Producing fast-growing energy crops for dedicated biomass-to-energy conversion can expand markets for agribusiness, and growing and consuming biomass on a sustained basis does not contribute to the greenhouse effect because net CO_2 emissions are nil (over the life cycle). Biomass residues are the least costly and most readily accessible type of biomass available. The use of agricultural residues and wastes, such as sugar cane bagasse, for energy conversion can reduce land disposal problems and emissions associated with open-field burning. The processing of sugar cane results in a feedstock ideally suited for thermal energy conversion processes (since alkali content, moisture, and particle size are reduced in the milling process).

Biomass gasification, the thermochemical conversion of a solid fuel into a fuel gas, has the potential to offer clean, economically competitive power when coupled to advanced fuel-based power generation systems. To investigate this potential, two case studies for biomass-to-electricity conversion were identified and thermodynamic analyses of biomass gasifier-based electric power stations were conducted. Power systems at two scales, nominally 5 and 20 MWe (net electric power output), located at Hawaiian sugar cane factories, were modeled using the ASPEN PLUS™ Process Simulation software package to determine performance and process information. Information from these analyses can be used to evaluate the potential for commercial applications of biomass gasifier-based power generation in local and global markets.

Overview of Power Stations and Analysis Results

The two scales of power stations analyzed in the present investigation have been targeted for near-term commercialization. The Hawaiian Commercial and Sugar Company Paia (HC&S-Paia) sugar factory on the island of Maui and the Gay and Robinson Company sugar factory at Olokele (Olokele/G&R) on the island of Kauai were chosen to model the 5 and 20 MWe power plants, respectively. Technical issues, such as suitability and availability of feedstock and compatibility with host operation, were factors in power-station site selection. Economic issues unique to each site were also considered. For example, the HC&S-Paia factory is the site of a demonstration scale, 90 bone-dry tonne per day (TPD) biomass gasification facility (Kinoshita et al., 1996).

Integrating a power station with the HC&S-Paia sugar factory may not be justified given the lack of economies of scale inherent to small (~5 MWe) power plants. A more likely scenario for a power plant of that scale is a separate facility which generates only electric power for export, without returning steam or other forms of process energy to the host facility. The factory might, however, be required to supply steam to the power station. By contrast, a 20 MWe power station fully integrated with the sugar factory would be advantageous owing to the large demand for biomass feedstock and support services and economies of scale inherent to larger power stations. This type of power station would provide steam to the factory for sugar cane processing and in-house mechanical power requirements.

Operating parameters of specific power-system components and processes served as the basis for plant configuration. Standard unit operation models available from ASPEN PLUS™ were used to simulate plant components, including the gasifier, gas turbine, and steam turbine, and input data, such as mass flow, pressure, temperature, and turbine efficiencies, were specified for these components. Although extensive optimization was beyond the scope of the present investigation, sensitivity analyses were performed and different configurations and state points were examined.

5 MWe Power Station—HC&S-Paia Sugar Factory

Overview. The 5 MWe stand-alone power station at HC&S-Paia was modeled as a biomass-based integrated gasifier combined-cycle (BIGCC) power plant as shown in Fig. 1. Approximately 90 TPD of run-of-the-mill bagasse at 45 percent moisture content is supplied by the factory. Flue gas exiting a heat-recovery steam generator (HRSG) is used in a rotary drum dryer to reduce bagasse moisture content to 20 percent. Flue gas drying of bagasse has been used by the cane sugar industry for nearly twenty years (Kinoshita, 1991a). Bagasse, having a higher heating value (HHV) of 18.9 MJ kg^{-1} (dry basis), is

Contributed by the International Gas Turbine Institute for publication in the JOURNAL OF ENGINEERING FOR GAS TURBINES AND POWER. Manuscript received on October 6, 1997; revision received on September 28, 1998. Technical Editor: H. Nelson.

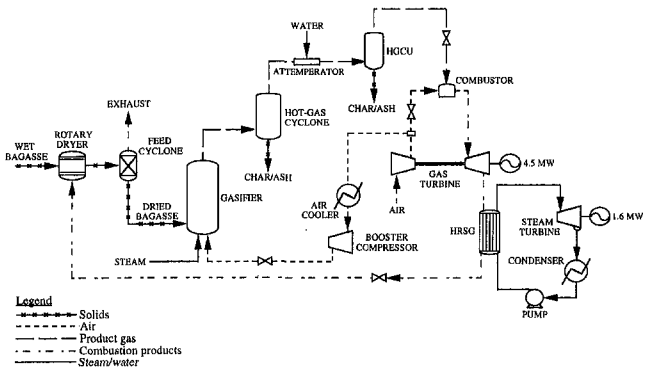

Fig. 1 Process flow diagram of 5 MWe Base Case BIGCC power station at HC&S-Paia

separated from the flue gas in a cyclone before being transported to a lockhopper feed system.

The gasifier is a 10:1 scale-up of the Renugas® Process Development Unit (PDU) developed by the Institute of Gas Technology (IGT). Gasifier operating conditions (including the equivalence ratio and the steam:biomass ratio) and product gas composition, yield, and temperature are based on IGT extrapolations of the PDU operating at anticipated commercial conditions as summarized in Table 1 (Institute of Gas Technology, 1996). Gasification air is supplied by a booster compressor that pressurizes a portion of the air exiting the gas turbine compressor. Steam at 23 bar and 235°C is provided by the sugar factory for gasification. In the present analysis, the hot-gas cyclone and hot-gas cleanup unit (HGCU) removes 95 percent and 5 percent, respectively, of the char produced during gasification. Experimental data suggest that tars and oils account for about 1 percent of the mass and add roughly 10 percent to the heating value of gasified bagasse (dry basis) generated by a pressurized, fluidized bed gasifier. Tars and oils were neglected in the analyses to simplify modeling and to be conservative in estimating the heating value of the gasifier product gas. It was assumed that temperature and pressure drops across the hot-gas cyclone are, respectively, 11°C and 0.7 bar and across the HGCU are 17°C and 2.8 bar.

Attemperation of the product gas exiting the hot-gas cyclone is accomplished by a direct water quench to cool the gas below 538°C; this is done to facilitate condensation of alkali vapors onto char particles (Craig and Mann, 1996) and to satisfy temperature constraints of key downstream components. Char and alkali compounds are removed from the gas stream by the HGCU to ensure that levels are within gas turbine specifications. Combustor and gas turbine working surfaces are subject to corrosion induced by alkali vapors. Experimental results (Westinghouse Electric Corporation, 1995; Turn et al., 1996) indicate that alkali gettering systems may be needed to effect adequate removal.

Complete combustion of product gas is assumed to occur in the gas turbine combustor. Excess air for combustion was determined by targeting an assumed turbine inlet temperature (979°C) inferred from published specifications for an Allison Engine Company 501-KB7 gas turbine (Gas Turbine World 1996 Handbook, 1996). Pressure ratio and mass flow are also comparable to manufacturer specifications. Gas turbine compressor stage intercooling was assumed; however, detailed modeling of turbine expander stage cooling by air extraction was not performed. Gasifier air compressor isentropic efficiency and gas turbine-generator unit efficiency were both assumed to be 85 percent. (Turbine-generator unit efficiency accounts for irreversibilities within the turbine as well as losses associated with mechanical-to-electrical energy conversion.) Gas turbine exhaust provides the thermal energy for steam production in the HRSG. The amount of steam produced in the HRSG was constrained by the minimum temperature of the dryer exhaust gas; i.e., available thermal energy for steam production was limited such that the dryer exit gas (at 93°C) remained sufficiently above the dew point. Steam having 56°C of superheat is expanded through a full-condensing steam turbine-generator having a unit efficiency of 80 percent.

Five percent of the gross electrical output of the steam turbine is assumed to be consumed by pumps and related motors of the steam bottoming cycle. Motors, fans, pumps, and miscellaneous equipment installed at the plant, including feedstock preparation and handling equipment and inert gas supply components, were assumed to consume 70 percent of the nameplate power requirements.

Results. Process conditions and performance information for the Base Case 5 MWe BIGCC power station are summarized in Table 2. Expansion of 19 kg s^{-1} of combustion products at 946°C through a gas turbine-generator operating at a pressure ratio of 13.1 produces 4.5 MW of net power. Gas turbine exhaust at 471°C generates roughly 8,300 kg h^{-1} of steam in the HRSG. About 1.5 MW of net power is produced as the steam expands through the full-condensing steam turbine-generator to an exit pressure of 0.14 bar. The net power output (gas and steam-generator net power outputs, less gasifier air compressor and plant ancillary power requirements) of the Paia BIGCC power station is 5.5 MW, with a plant efficiency of 27.6 percent (13,065 kJ kWh^{-1}). Plant efficiency is defined as the net electric power output divided by the bagasse energy content (HHV basis).

Operating and performance data for the various configurations investigated in the present analysis are summarized in Table 3. Projected output and performance of a BIGCC power station at HC&S-Paia are significantly higher than those of a conventional steam Rankine cycle and a simple-cycle, gasification-based power station. If bagasse were burned directly in a boiler similar to that presently installed at HC&S-Paia (65 percent boiler efficiency) and the steam produced by this boiler were expanded in a full-condensing steam turbine-generator (80 percent unit efficiency), about 3 MW of net power would be generated at a plant efficiency of 15.3 percent.

The simple-cycle configuration consists of the gasification system coupled to a gas turbine generator. Gas turbine exhaust, diluted with ambient air prior to entering the bagasse dryer to prevent fires, is used to reduce bagasse moisture content. Net power output and plant efficiency are calculated to be 3.9 MW and 19.8 percent, respectively. Justification of the additional capital expenditure for a steam bottoming cycle of the BIGCC ultimately will be determined by economic considerations.

Table 1 Projected operating conditions and product gas composition and yield for commercial air-blown, pressurized, fluidized-bed gasifier

Pressure, bar	23.4
Temperature, °C	854
Bagasse feed rate to gasifier @ 20% m.c., kg h^{-1} (wet)	4,725 (HC&S-Paia) 21,262 (Olokele/G&R)
Steam, kg/kg feed (wet)	0.15
Air, kg/kg feed (wet)	1.23
Product gas composition, vol%	
H_2	7.3
O_2	0.05
N_2	37.2
CO	10.6
CH_4	7.0
CO_2	14.6
H_2O	23.0
C_2H_4	0.11
C_2H_6	0.08
C_6H_6	0.14
Gas yield, m^3 kg^{-1} feed (wet)	2.1
Gas heating value, MJ m^{-3}	5.1

Table 2 Process conditions and performance data for Base Case HC&S-Paia and Olokele/G&R power stations

	HC&S-Paia	Olokele/G&R
Gasifier Inputs		
Bagasse to gasifier (20% m.c.), kg h^{-1}	4,725	21,262
Air flow rate, kg h^{-1}	5,812	26,152
Steam flow rate, kg h^{-1}	709	3,189
Fuel Gas (post attemperation)		
Fuel gas flow rate, kg h^{-1}	12,014	47,227
Temperature, °C	530	530
HHV, MJ m^{-3}	4.2	5.1
Gas and Steam Turbine Data		
Gas turbine inlet pressure, bar	13.6	13.6
Gas turbine pressure ratio	13.1	13.1
Mass flow through gas turbine, kg s^{-1}	19	87
Gas turbine inlet temperature, °C	946	946
Gas turbine outlet temperature, °C	471	468
Gas turbine-generator unit efficiency, %	85	85
HRSG-generated steam, kg h^{-1}	8,303	42,799
Auxiliary boiler steam, kg h^{-1}	—	10,286
Process steam to factory, kg h^{-1}	—	49,895
Steam turbine inlet pressure, bar	27.6	41.4
Steam turbine inlet temperature, °C	285	316
Steam turbine exit pressure, bar	0.14	2.1
Steam turbine-generator unit efficiency, %	80	80
Plant Performance Summary		
Bagasse energy input, GJ h^{-1} (HHV basis)	71.3	321
Auxiliary energy input, GJ h^{-1} (HHV basis)	—	36.1
Net gas turbine power output, MW	4.485	18.858
Net steam turbine power output, MW	1.531	4.295
Booster compressor power, MW	0.106	0.475
Plant parasitic load, MW	0.451	0.902
Net plant power, MW	5.459	21.776
Plant efficiency, %	27.6	22.0*
Plant heat rate, kJ kWh^{-1}	13,065	16,396*

* energy in process steam exported to sugar factory not included.

Various configurations of the combined-cycle power station were investigated to determine the effects of alternative modes of HRSG-generated steam utilization, product gas attemperation, and bagasse drying on plant performance. Performance data for these configurations are summarized in Table 3. Integrating the gasification system with a steam-injected gas turbine (STIG) offers the benefit of more complete heat recovery than the simple cycle, at potentially lower cost than the Base Case BIGCC because a steam turbine bottoming cycle is not needed. In the STIG-based configuration investigated in the present analysis, steam (28 bar/404°C) generated in a HRSG is injected into the gas turbine combustor until the assumed minimum allowable heating value of the gas, 3.9 MJ m^{-3}, is attained (Larson and Williams, 1990). Excess air is added to the combustor to achieve an exit temperature of 1,093°C and HRSG steam is injected downstream of the combustor to achieve the design turbine inlet temperature (973°C) for an Allison 501-KH STIG. A net power output of 5.2 MW and a plant efficiency of 26.4 percent were calculated for this cycle.

Other variants of the BIGCC power plant analyzed include Case CC1 (feedwater heat exchanger replaces direct water injection to attemperate product gas), Case CC2 (slip stream of product gas is used to fuel bagasse dryer burner), and Case CC3 (propane is used to fuel bagasse dryer burner). Analysis results are summarized in Table 3. Attemperating product gas with a direct water quench is an attractive option because it is simple and inexpensive, however, diluting the low-energy-content product gas with water can negatively impact gas turbine combustor performance. Cooling the gas by preheating feedwater going to the HRSG (Case CC1) in a heat exchanger results in a 0.1 percentage point increase in plant efficiency compared to the Base Case. The greater volumes of product gas that may be required in the gas turbine due to the low energy density of gasified biomass, compared to fuels such as natural gas, can pose a problem for commercial turbines required to operate at near choking conditions. Diverting a portion of the product gas to a bagasse dryer burner (Case CC2) to reduce mass flow through the gas turbine may be a viable option for the BIGCC. Net plant output and plant efficiency for this configuration were calculated to be 5 MW and 22.6 percent, respectively. Fueling the bagasse dryer burner with propane (Case CC3) was investigated due to uncertainties associated with the ability of the existing rotary dryer combustor at Paia to burn low-Btu product gas. Utilization of a propane-fired dryer burner reduces plant efficiency to 24.4 percent. Hence plant efficiency is lowered appreciably when HRSG waste heat is not recovered by drying bagasse.

Critical performance information for several key system components were not available, necessitating the use of assumed parameters. Analyses were performed to determine the sensitivity of plant performance on assumptions for gas turbine inlet temperature and HGCU inlet temperature. In addition, gains or penalties associated with variations of HRSG steam conditions were quantified. Net plant power and plant efficiency are plotted as functions of gas turbine inlet temperature in Fig. 2. Increasing gas turbine inlet tem-

Table 3 Plant performance summary—alternative configurations for HC&S-Paia 5 MWe power station

Configuration case	BIGCC Base	Rankine	Simple	STIG	BIGCC CC1	BIGCC CC2	BIGCC CC3
Gas turbine inlet pressure, bar	13.6	—	13.6	13.6	13.6	13.6	13.6
Gas turbine inlet temperature, °C	946	—	946	946	946	946	946
Gas turbine pressure ratio	13.1	—	13.1	13.1	13.1	13.1	13.1
HRSG/boiler steam pressure, bar	27.6	30.3	—	27.6	27.6	27.6	27.6
HRSG/boiler steam temperature, °C	285	404	—	404	285	285	285
Steam turbine exit pressure, bar	0.14	0.14	—	—	0.14	0.14	0.14
Gas turbine power, MW	4.49	—	4.49	5.78	4.19	3.72	4.49
Steam turbine power, MW	1.53	3.03	—	—	1.85	1.31	1.53
Gross plant power, MW	6.02	3.03	4.49	5.78	6.04	5.03	6.02
Gasifier compressor power, MW	0.11	—	0.11	0.11	0.11	0.11	0.11
Plant auxiliaries, MW	0.45	0	0.45	0.45	0.45	0.45	0.45
Net plant power, MW	5.46	3.03	3.93	5.22	5.48	4.47	5.46
Bagasse energy, GJ h^{-1}	71.32	71.32	71.32	71.32	71.32	71.32	71.32
Aux. fuel energy, GJ h^{-1}	—	—	—	—	—	—	9.18
Plant efficiency, %	27.6	15.3	19.8	26.4	27.7	22.6	24.4
Plant heat rate, kJ kWh^{-1}	13,065	23,536	18,157	13,666	13,013	15,948	14,744

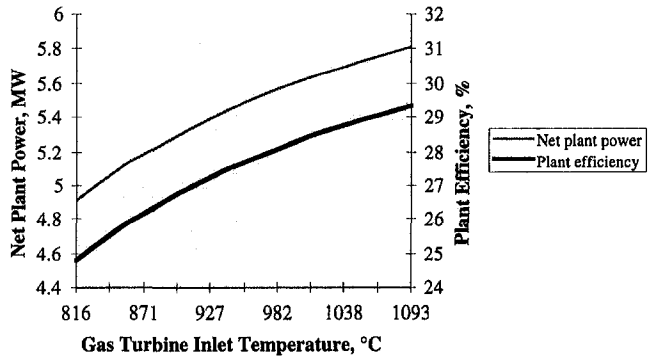

Fig. 2 Net plant power and plant efficiency as functions of gas turbine inlet temperature

perature by 111°C raises plant efficiency to 29.0 percent, while decreasing by 111°C lowers plant efficiency to 25.3 percent. Plant efficiency changes by less than 1 percentage point when HGCU inlet temperature varies by ±83°C from the 530°C assumed in this study. Sufficient alkali removal, as opposed to optimal plant performance, will likely establish HGCU inlet temperature. If HRSG steam conditions were changed from 28 bar/285°C to match those for the existing HC&S-Paia boiler (30 bar/404°C), a 0.4 percentage point increase in plant efficiency over the Base Case would result.

Larger BIGCC systems are projected to have significantly higher efficiencies than those calculated for the 5 MWe power station simulated in the present analysis. For example, a study by Craig and Mann (1996) predicted a net plant output of 56 MW and a plant efficiency of 36 percent for a BIGCC utilizing a 680 TPD pressurized wood-fired gasifier coupled to a GE LM-5000PC aeroderivative gas turbine and a steam turbine bottoming cycle operating with input steam at 53 bar/394°C. A 1470 TPD BIGCC plant consisting of a GE MS-6101FA advanced utility gas turbine and a steam turbine bottoming cycle (101 bar/538°C steam) would generate 132 MW of net power at a plant efficiency of 40 percent.

20 MWe Cogeneration Station—Olokele/G&R Sugar Factory

Overview. The process flow diagram of the BIGCC cogeneration power station at the Olokele/G&R sugar factory is presented in Fig. 3. The power station receives about 400 TPD bagasse from the sugar factory at a moisture content of 48 percent. Flue gas drying in a rotary drum dryer reduces bagasse moisture content to 20 percent. The gasifier is a four to five-fold scale-up of the Paia 5 MWe power station gasifier; gasifier operating conditions, fuel gas properties, and pressure and temperature drops across the hot-gas cyclone and HGCU are identical to the Paia case. Gasification air is supplied by a booster compressor that pressurizes a portion of the air exiting the gas turbine compressor. Approximately 3200 kg h^{-1} of steam from the HRSG is directed to the gasifier.

The temperature of the product gas is reduced by preheating the feedwater going to the HRSG. Products of the complete combustion of gasified biomass expand through a gas turbine-generator to produce electricity. The efficiency of the gas turbine-generator unit was assumed to be 85 percent. Steam generated in the HRSG at 41 bar and 316°C proceeds to a double-extraction/condensing turbine-generator unit. The first extraction, at 14 bar, feeds back-pressure mechanical drives that power factory equipment, and the second extraction recombines with steam exiting the mechanical drives, at 2 bar, to supply the sugar factory with process steam. The steam turbine-generator unit efficiency and the mechanical drive isentropic efficiency were 80 percent and 65 percent, respectively. Electricity generated by the steam turbine-generator is also available for export.

Simulations indicated that the amount of steam produced in the HRSG is insufficient to meet the requirements of the sugar factory, therefore, an auxiliary boiler fired with No. 2 fuel (diesel) oil was incorporated into the model. The boiler, with an assumed efficiency of 85 percent, supplies steam at conditions identical to the HRSG to meet the 49,900 kg h^{-1} process steam demand. Use of this steam to process 117 tonne cane per hour (tch) translates to 42 percent steam on cane, which falls within the range of ~30–50 percent that applies to the Hawaiian sugar industry (Kinoshita, 1991b).

The same percentage of steam turbine-generated electric power assumed for the HC&S-Paia power station is required to drive the Olokele/G&R steam cycle ancillary equipment. Plant parasitic load is assumed to be twice that of the Paia plant, which implies parasitic load scales as the square root of nominal power output.

Results. Process information and performance data for the 20 MWe Olokele/G&R cogeneration power station are summarized in Table 2. Gas turbine net power output is 18.9 MW. Thermal energy provided by 87 kg s^{-1} of combustion products generates approximately 42,800 kg h^{-1} of steam at 41 bar/316°C in the HRSG, 7 percent of which is sent to the gasifier. An auxiliary diesel-fired boiler generates 10,290 kg h^{-1} of steam to meet the 49,900 kg h^{-1} process steam demand of the sugar factory. Combusting product gas to generate steam in the existing bagasse boiler at Olokele/G&R is an alternative to burning diesel fuel in an auxiliary boiler, however, the cost to modify the burners in the existing boiler-furnace may be significant. The steam turbine-generator produces 4.3 MW of net power. About 1.6 MW of motive power is generated by expanding 27,200 kg h^{-1} of steam at 14 bar in a mechanical drive. Excess steam flows through the condensing stage of the steam turbine (no excess steam was assumed in the present analysis). Make-up water compensates for gasification steam and losses such as boiler blowdown. Plant net power output is 22 MW and plant efficiency (net electrical output divided by gross fuel energy input) is 22 percent (16,396 kJ kWh^{-1}). It should be noted that plant efficiency is lower than that of the 5 MWe HC&S-Paia power station because energy used by the Olokele/G&R factory is not included in the calculated plant efficiency. By comparison, a stand-alone power station at Olokele/G&R, which does not supply any process steam to the sugar factory, would generate approximately 25.4 MW of net power at a plant efficiency of 28.5 percent.

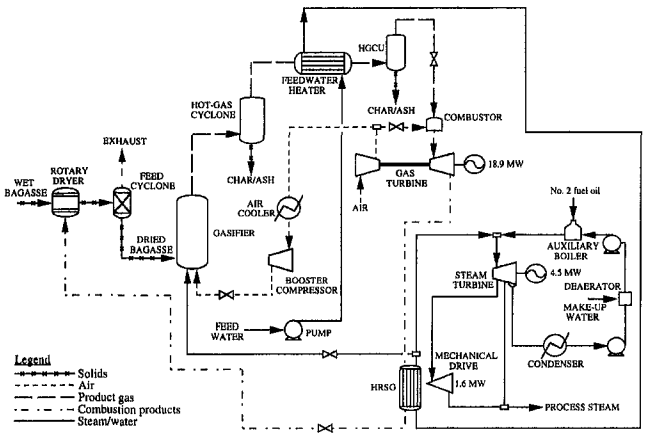

Fig. 3 Process flow diagram of 20 MWe BIGCC cogeneration power station at Olokele/G&R

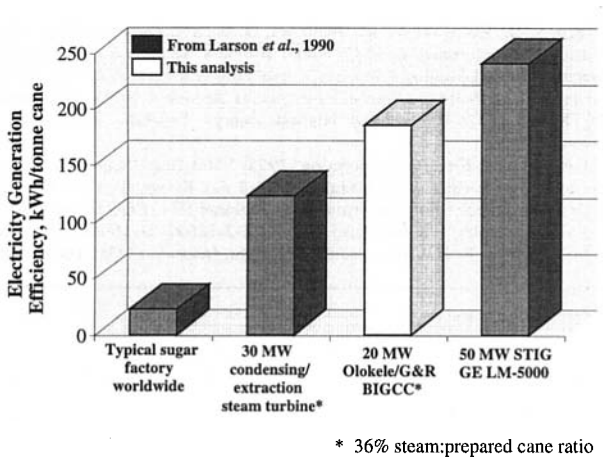

Fig. 4 Comparison of electricity generating efficiency for conventional and gasification-based cogeneration systems

As stated previously, only about 80 percent of the sugar factory process steam requirement is met with bagasse under the assumed operating conditions. This can be increased to about 85 percent if the gas turbine inlet temperature increased by 111°C. The following options to achieve full power station/sugar factory integration could be implemented: (1) utilize an auxiliary boiler to generate additional steam (scenario modeled in present analysis); (2) operate the power station at conditions more favorable for steam production; or (3) improve factory steam utilization. Utilizing a gas turbine with significantly higher inlet temperature than that assumed in the present analysis, which operates at a lower, or derated, pressure ratio, would increase steam generation in the HRSG. In addition, employing HRSG steam conditions that favor steam production, as opposed to power generation in the steam turbine generator, would further improve the prospects for a self-sufficient and fully integrated BIGCC cogeneration plant at Olokele/G&R. An auxiliary boiler system would not be needed at Olokele if factory operations improved such that processing required only 33 percent to 36 percent steam:cane ratio. Such improvements may involve recovery of heat from juice evaporator condensates, reducing dilution of mixed or clarified cane juice or syrup, optimizing sugar syrup brix, and reducing recirculation of process streams in the sugar factory.

Exportable electricity potential of conventional and gasification-based cogeneration systems are shown in Fig. 4. Larson et al. (1990) state that sugar cogeneration plants worldwide typically produce about 22 kW per tonne cane per hour (kW tch^{-1}). In the mid-1980s, sugar factories in Hawaii typically generated about 67 kW tch^{-1} and in some instances exceeded 112 kW tch^{-1} (Kinoshita, 1991b). Based on calculations performed for the 20 MWe plant in the present analysis, efficient use of steam in the sugar factory to operate at 36 percent steam:cane ratio could yield over 185 kW tch^{-1}. The study by Larson et al. (1990) reports that a modern 27 MWe condensing/extraction steam turbine system operating with 60 bar/480°C steam at a 36 percent steam:cane ratio can generate approximately 120 kW tch^{-1} and a larger capacity gasifier-based STIG cogeneration plant producing 53 MWe with a GE LM-5000 gas turbine operating at the same steam:cane ratio can expect to generate approximately 240 kW tch^{-1} (extrapolated data).

Summary and Conclusions

Process and performance information of biomass gasifier-based power stations sited at two Hawaiian sugar factories were simulated using the ASPEN PLUS™ Process Simulation software. Conventional steam cycle, simple gas turbine cycle, steam-injected gas turbine cycle, and various configurations of combined-cycle systems were considered in modeling a 5 MWe power station at the HC&S-Paia sugar factory. A 20 MWe combined-cycle cogeneration power plant was evaluated for the Olokele/G&R sugar factory.

A stand-alone BIGCC power station supplied by 90 TPD of bagasse from the HC&S-Paia sugar factory is expected to be capable of exporting 5.5 MW of net power at a plant thermal efficiency of 27.6 percent. Plant performance of a STIG-based system is slightly inferior to the BIGCC system, but should require less capital investment. Although a simple cycle power station would require substantially less capital investment, exportable power and plant efficiency from such a plant is significantly lower. Additionally, results indicate that the performance of gasification-based power plants is much higher than that of conventional steam Rankine power plants.

An integrated 20 MWe BIGCC cogeneration power station at Olokele/G&R would require about 400 TPD of bagasse to export 22 MW of net power at a plant efficiency of 22 percent. An auxiliary boiler system may be needed to meet the process steam demand of the sugar factory. For the conditions assumed in the present analysis, a sugar factory operating at 117 tch must reduce its steam:cane ratio to less than 36 percent to become self-sufficient and fully integrated with the BIGCC power station.

Analysis results indicate that attemperating the product gas upstream of the HGCU by preheating feedwater directed to the HRSG, as opposed to injecting water directly into the product gas stream, results in an insignificant increase in plant efficiency. However, plant performance is significantly derated if HRSG exhaust gas is not used to dry bagasse. Combusting a slip stream of product gas or propane in a dryer burner lowers plant efficiency. Sensitivity analyses indicate that increasing gas turbine inlet temperature by 111°C increases plant efficiency by 1.4 percentage points and deviation of HGCU inlet temperature by ±83°C affects plant performance by less than 1 percentage point. Additionally, higher HRSG steam pressure can increase plant efficiency.

Results of the ASPEN simulations of 5 and 20 MWe power stations sited at selected Hawaiian sugar factories indicate that BIGCC technologies offer the potential for significant improvements in power generating performance. The following processes can be pursued to improve plant performance: (1) operate at higher gas turbine inlet temperature; (2) operate at higher HGCU inlet temperature; (3) generate steam at higher HRSG pressure; and (4) recover waste heat via booster compressor precooling and gas turbine intercooling. Implementation of steam bottoming cycles, feedwater heating systems, higher pressure HRSGs, gas turbine heat recovery schemes, and sugar factory steam utilization improvements will likely be determined by a combination of capital cost considerations and technical factors.

Acknowledgments

The authors wish to thank the Pacific International Center for High Technology Research and the State of Hawaii's Department of Business, Economic Development and Tourism for funding this project and for their continued support of our biomass energy program.

References

Craig, K. R., and Mann, M. K., 1996, "Cost and Performance Analysis of Biomass-Based Integrated Gasification Combined-Cycle (BIGCC) Power Systems," NREL/TP-430-21657, National Renewable Energy Laboratory, Golden, CO.

Gas Turbine World 1996 Handbook, 1996, Vol. 17, Pequot Publishing, Inc., Fairfield, CT.

Institute of Gas Technology, 1996, projected data for PDU operated under conditions of commercial-scale gasifier, submitted to Westinghouse Electric Corporation.

Kinoshita, C. M., 1991a, "Flue Gas Drying of Bagasse," *ASAE Applied Engineering in Agriculture,* Vol. 7, No. 6, pp. 729–734.

Kinoshita, C. M., 1991b, "Potential for Cane Energy," *Proceedings of the International Conference on Energy from Sugarcane,* pp. 41–65.

Kinoshita, C. M., Turn, S. Q., Overend, R. P., and Bain, R. L., 1996, "Power Generation Potential of Biomass Gasification Systems," *Proceedings of the 1996 American Power Conference,* April 11–19, Chicago, IL.

Larson, E. D., and Williams, R. H., 1990, "Biomass-Fired Steam Injected Gas Turbine Cogeneration," *Biologue,* pp. 12–19.

Turn, S. Q., Kinoshita, C. M., Ishimura, D. M., and Zhou, J., 1997, "Gasification Characteristics of High Alkali Biomass Subjected to Mechanical Dewatering and Leaching Processes," *Leaching of Alkalis in Biomass Using Banagrass as a Prototype Herbaceous Species, Section 3,* NREL Subcontract No. XCF-5-14326-01, Hawaii Natural Energy Institute, University of Hawaii.

Westinghouse Electric Corporation, 1995, "Hot Gas Cleanup for Operation of a Gas Turbine with a Fluidized Bed Air Blown Biomass Gasifier, Filter Performance Short Duration Tests, Volume III—PDU Operation and Analytical Results," Subcontract No. XAZ-3-12092-01-106794, prepared by M. Onischak, R. H. Carty, and R. A. Knight, Institute of Gas Technology.

A Numerical Analysis of the Emissions Characteristics of Biodiesel Blended Fuels

C. Y. Choi

R. D. Reitz

Engine Research Center,
1500 Engineering Drive,
University of Wisconsin-Madison,
Madison, MI 53706

Computer simulations were conducted to study the combined effects of methyl soyate (biodiesel) blends with no. 2 diesel fuel on diesel engine (D.I.) performance. Diesel engine emissions and heat release rates were some of the parameters studied.

The results from the computer simulations were compared against previously published results (Choi et al., 1997) from engine tests conducted on a single cylinder version of the Caterpillar 3400 series heavy duty diesel engine. The experiments and simulations were performed over a range of injection timings allowing particulate versus NO_x trade-off curves to be generated. Phillips 66 certified no. 2 diesel fuel was used as the baseline; mixtures of 20 percent and 40 percent by volume of methyl soyate with the baseline no. 2 diesel fuel were used as the biodiesel blends.

The multidimensional KIVA-II code (ERC version 2.4) was used to better understand the factors controlling the formation of NO_x and soot. KIVA-II modeled the high load, single injection combustion of the baseline #2 diesel fuel and the biodiesel blends. The code was changed to account for different fuel effects and the computational results were then compared against the experimental data. It is concluded that the increased NO_x observed with the use of biodiesel fuels (in spite of their lower heats of combustion) is due to increased local temperatures as a result of enhanced fuel/air mixing and increased spray penetration. The increased spray penetration results from the higher fuel viscosity of the biodiesel blended fuels which leads to reduced injection durations.

Introduction

In past studies, vegetable-oil-based fuels have been shown to be good alternatives to fossil fuels for diesel engines. This renewable source of fuel may also help in reducing the net production of CO_2 from combustion sources and our dependence on foreign oil. The methyl esters of vegetable oils (biodiesel), which are produced by combining methanol with the vegetable oil, are of particular interest; these fuels tend to burn cleaner, perform comparably to conventional diesel fuel, and combust similarly to diesel fuel (Scholl and Sorenson, 1993).

The reaction between an acid and an alcohol results in an ester which, in general, is insoluble in water and has a higher boiling point than hydrocarbons of similar molecular weight. The monoester of vegetable oils is produced by combining a vegetable oil with alcohol; in particular, the more popular methyl ester of soybean oil, also commonly known as biodiesel, is made by combining soybean oil with methanol (Scholl and Sorenson, 1993; Zhang and Van Gerpen, 1996).

Computationally, modeling these types of fuels and blends thereof represents quite a challenge. In the current study, the KIVA-II engine code is used to model the experimental engine cases. Significant fuel parameters are addressed and modified to match the experimental fuels. Comparisons and studies of the predicted and measured pressure, heat release rate, and emissions are conducted, and the results are used to provide explanations of the measured trends.

Experimental Test Conditions and Experimental Results

All engine experiments were performed on a fully instrumented, single cylinder, Caterpillar 3400 series heavy duty diesel engine. This engine can produce 54 kW at 2100 revolutions per minute. Intercooled turbocharging is simulated by controlling the intake air temperature and pressure, and regulating the back pressure in the exhaust surge tank. Additionally, the combustion chamber was designed to be a quiescent, low-swirl/low-turbulence chamber.

Various injection schemes were studied through the use of an electronically controlled, common rail injection system. This system is capable of injection pressures up to 120 MPa and a maximum of four injections per combustion event (Miyaki et al., 1991). Additionally, the injection timing and duration can be varied per the user's specifications.

Cylinder pressures were recorded (at $\frac{1}{2}$ crank angle degree increments) and 20 cycle ensemble averaged on a 486DS-based data acquisition system. Rate of fuel injection was determined through the use of a Bosch rate of injection meter. Fuel rate-of-injection profiles were recorded on BCAP version 4.0, a PC based program manufactured by DSP Technology Inc.

Measured cylinder pressure and other operating parameters were used to compute the apparent heat release rate. The heat release program which is based on the first law of thermodynamics was developed by Borman and Krieger (1966). Tree (1992) then modified the original program to include the Woschni (1967) heat transfer correlation.

Additional details of the engine test conditions, fuel properties, fuel blends, and engine experimental results can be found in reference Choi et al. (1997).

Computational Test Conditions

The computer model used is based on the KIVA-II code (Amsden et al., 1989). KIVA-II is a computational fluid dynamics code that is capable of modeling multiphase reacting flows. The code has been modified to more accurately model diesel engine combustion; these modifications are shown in Table 1 (references are in parentheses). More detailed descriptions of

Contributed by the Internal Combustion Engine Division for publication in the JOURNAL OF ENGINEERING FOR GAS TURBINES AND POWER. Manuscript received on January 3, 1998; revision received on June 25, 1998. Associate Technical Editor: D. Assanis.

Table 1 KIVA-II models

Physical Phenomena	Model (reference)
Turbulence	Modified RNG k-e (Han and Reitz, 1996)
Wall Heat Transfer	Model of Han and Reitz (1996)
Spray Breakup	KH-RT Break-up Length Model (Ricart et al., 1997)
Spray Drag	Dynamic Drag Model (Liu et al., 1993)
Spray Ignition	Shell Model (Kong and Reitz, 1993)
Combustion	Princeton Combustion Model (Kong et al. 1995)
NO_x Formation	Extended Zel'dovich Mechanism (Han et al., 1996)
Soot Formation	Hiroyasu Model (Han et al., 1996)
Soot Oxidation	Magnussen and Hjertager-modified (Hampson, 1996)

the KIVA-II code used in this study can be found in papers by Kong and Reitz (1993) and Han et al. (1996).

Normally, tetradecane is the reference fuel used for diesel combustion simulations. To account for the different fuel characteristics in the two biodiesel blends and baseline fuel used in the experiments, viscosity effects and fuel molecular structures were changed to represent the respective fuels modeled. Table 2 shows the cases modeled.

Computational Results

In this study, the computational results are compared against the results obtained from the Caterpillar diesel engine experiments. The engine's combustion chamber geometry and six hole fuel injector assembly is symmetric about the center axis. Therefore, the computational domain represents one-sixth of the combustion chamber for computational efficiency. There are 20 cells in the radial direction, 30 cells in the azimuthal direction, and 30 cells in the axial direction, with 5 cells in the squish region at top dead center. A similar mesh resolution was found to give adequately grid-independent results by Han and Reitz (1995).

Shell Ignition Model. In diesel combustion, ignition delay is an important variable that influences hydrocarbon and NO_x emissions. The injected fuel undergoes several physical and chemical processes during the ignition delay period. These processes include atomization, evaporation, mixing, and preliminary chemical reaction. Halstead et al. (1997) developed the multistep "Shell" ignition model which models the autoignition of hydrocarbon fuels at high pressures and temperatures. Kong and Reitz (1993) and Theobald and Cheng (1987) have implemented the Shell model in diesel combustion. The following expressions describe the species and reactions used in the Shell kinetic model:

$$RH + O_2 \rightarrow 2R^* \quad Kq \tag{1}$$

$$R^* \rightarrow R^* + P + \text{Heat} \quad Kp \tag{2}$$

$$R^* \rightarrow R^* + B \quad f_1 Kp \tag{3}$$

$$R^* \rightarrow R^* + Q \quad f_4 Kp \tag{4}$$

$$R^* + Q \rightarrow R^* + B \quad f_2 Kp \tag{5}$$

$$B \rightarrow 2R^* \quad Kb \tag{6}$$

$$R^* \rightarrow \text{termination} \quad f_3 Kp \tag{7}$$

$$2R^* \rightarrow \text{termination} \quad Kt \tag{8}$$

RH = hydrocarbon fuel

R^* = radical formed from fuel

B = branching agent

Q = labile intermediate species

P = oxidized products

Kp, Kq, f_1, f_2, etc.

= expressions given by Halstead et al. (1977)

The reaction rate of reaction (4) is crucial to the ignition process and found to control the chemical ignition delay (Kong and Reitz, 1993). $f_4 Kp$ is the formation rate of Q, where f_4 is defined as follows:

$$f_4 = Af_4 \exp(-Ef_4/RT)[O_2]^{x4}[RH]^{y4}, \tag{9}$$

where

$$Ef_4 = 3.0e4,\ x4 = -1, \text{ and } y4 = 0.35.$$

To account for residual gas effects, the pre-exponential ignition model constant, Af_4, was adjusted to be dependent on computed cylinder gas temperature at intake valve closure, T_{IVC} (Xin et al., 1997).

$$Af_4 = (160.5 - 0.424T_{IVC}) \times 10^4 \tag{10}$$

As the amount of residual gas increases, the initial gas temperature increases and slower reaction rates are observed, which is expected due to the reduction in the concentration of the reactants.

Several empirical correlation constants are used in the various submodels, but the ignition model constant, Af_4, was of particular interest in this study. Af_4 was calibrated to match ignition delay data for the three different fuel blends, but held constant for each fuel at different fuel injection timings (SOI). Figure 1 shows the resulting dependence of Af_4 on fuel type. As shown, when biodiesel was added to the baseline fuel, a corresponding near linear increase in Af_4 was required to match the ignition delay timings. The linear regressions for Af_4 as a function of biodiesel concentration is shown in the legend of Fig. 1.

Table 2 Modeled cases

Fuel Blend	Engine Operating Conditions	Fuel SOI (CA ATDC)	Mass Percent Oxygen	Viscosity at 40 °C, cS	Cetane Number
Baseline #2 Diesel Fuel	1600 rev/min, 75% load (reference to #2 DF), single injection	-7, -4, -1, 2, 5	0 %	2.64	46.3
20% Biodiesel Blend	1600 rev/min, 75% load (reference to #2 DF), single injection	-7.2, -4.2, -1.2, 1.8, 4.8	2.4%	2.82	46.3
40% Biodiesel Blend	1600 rev/min, 75% load (reference to #2 DF), single injection	-7.6, -4.6, -1.6, 1.4, 4.4	4.8%	3.04	47.1

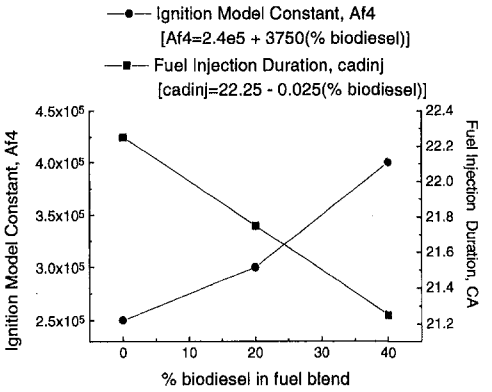

Fig. 1 Af4 and fuel injection duration dependence on fuel type

To account for fuel cetane number, the activation energy of reaction (4), Ef_4, was multiplied by a factor $71.3/(CN + 25)$ (Ayoub, 1995). With the baseline #2 *DF* cetane number of 46.3, the factor is unity. Using Ayoub's modification factor (Eq. 10), the Af_4 data (Fig. 1), the Ef_4 factor, and the baseline fuel as a reference point, an effective cetane number for the biodiesel blended fuels was calculated to be 50 and 56 for the 20 percent and 40 percent biodiesel blends, respectively, which is higher than the measured cetane numbers for the biodiesel blends. This is consistent with Siebers' (1985) observation that both degummed sunflower oil and sunflower oil monoester would ignite like a fuel with a higher cetane number than that assigned to the sunflower oil fuels.

NO_x and Soot Models. Multidimensional soot and NO_x emissions models have been implemented in the KIVA-II code to better model actual diesel engine combustion. Patterson et al. (1994) implemented an Extended Zel'dovich NO model and the Hiroyasu soot formation model. NO predicted by the Zel'dovich model was converted to NO_x by multiplying a factor 1.533 (the ratio of molecular weights of NO_2 to NO).

Hiroyasu (1976) determines the rate of soot mass formation by using a single species, two equation model. The Hiroyasu soot mass formation model is given as follows.

$$\dot{M}_{sf} = K_f M_{fv} \tag{11}$$

$$K_f = A_{sf} P^{0.5} \exp(-E_{sf}/RT), \tag{12}$$

where

$\dot{M}_{sf}$ = soot mass formation rate
M_{fv} = fuel vapor mass
A_{sf} = soot formation constant
E_{sf} = soot formation activation energy
R = universal gas constant
T = absolute temperature
P = pressure

Hampson (1996) implemented the Magnussen and Hjertager-modified soot oxidation model. This soot oxidation model considers oxidation by oxygen and turbulent mixing. Magnussen and Hjertager (1976) suggested that soot oxidation rates may also be controlled by mixing as opposed to kinetics alone. In the Magnussen and Hjertager model, the soot mass oxidation rate is given as follows:

$$\dot{M}_{SO} = \left(\alpha A \frac{\epsilon}{\kappa}\right) M_S \tag{13}$$

$$\alpha = \min\left\{1, \left(\frac{M_{O2}}{M_S \phi_S + M_f \phi_f}\right)\right\}, \tag{14}$$

where

$\dot{M}_{SO}$ = soot mass oxidation rate
A = tunable constant
κ = turbulent kinetic energy
ϵ = rate of dissipation of k
M_s = soot mass
M_{O2} = available oxygen
M_f = fuel mass
ϕ_s = stoichiometric oxygen requirement to burn 1 g soot
ϕ_f = stoichiometric oxygen requirement to burn 1 g fuel

When plenty of oxygen, M_{O2}, is available, $\alpha = 1$, but when the available oxygen is less than the oxygen required to oxidize all the fuel and soot in the cell, α is less than unity, as shown in Eq. 14 (Hampson, 1996).

The NO_x and soot trends were seen to be predicted well when the computed and measured cylinder pressure traces were in good agreement. Detailed descriptions of these emissions models can be found in references by Patterson et al. (1994), Magnussen and Hjertager (1976), and Hampson (1996).

Cylinder Pressure. Figure 2 shows good agreement between computed and measured cylinder pressures as the fuel type is varied. Not only are the start of combustion timings accurate but the general shape of the predicted pressure curve and the magnitude of the peak pressure is seen to be in excellent agreement with the measured data. Although only a fuel injection timing of SOI-7 CA ATDC is shown, very good agreement was also observed for the other fuel injection timing cases. The greatest discrepancy between the KIVA predicted and measured pressure occurred at an SOI timing of 5 CA ATDC with the baseline fuel case where KIVA predicted ignition somewhat later in the engine cycle as compared to the measured data (not shown). Discrepancies at very retarded timings have also been noted by Xin et al. (1997) and may be due to incomplete combustion in the predictions. Work is in progress on improved models for these cases.

For both the biodiesel blend cases, a shorter fuel injection duration was required in order to match combustion data later in the combustion cycle. In the experiments, the fuel injection duration was measured using a Bosch rate-of-injection meter. The average fuel injection duration from the measurement was 21 ± 1.25 CA. In the computations, this injection duration was adjusted, within the experimental error, to best match the measured pressure trace late in the engine cycle. These changes could be due to fuel viscosity effects since the viscosity of the biodiesel blends varies with the blend amount, as shown in Table 2. The dependence of fuel injection duration on biodiesel concentration is shown in Fig. 1.

The biodiesel blended fuels have higher densities than the baseline no. 2 *DF* with densities increasing as the biodiesel concentration increases. The denser fuel would require a shorter fuel injection duration, i.e., shorter time is required to inject the same amount of fuel mass with a denser fuel. However, the differences in densities are small; the 40 percent biodiesel blend fuel has the highest density at 0.8632 g/cm^3, which is 1.8 percent larger than the baseline fuel density of 0.8479 g/cm^3. This difference in density is not sufficient to explain the shorter fuel injection durations for the biodiesel blended fuels. Hence, the fuel injection durations used in the model for the different fuel cases suggest higher injection velocities and thus faster fuel penetration for the biodiesel blend cases.

Chang et al. (1997) studied the effects of fuel viscosity on spray tip penetration. They observed faster penetration with higher viscosity fuels than the lower viscosity fuels when a rounded inlet nozzle was used. Although the nozzle used in the current experiment was not explicitly machined for roundness at the nozzle inlet, its measured discharge coefficient is about 0.72, indicating that some inlet rounding is present. This fact may be able to explain the faster injection (shorter duration) in the present study with the higher viscosity, biodiesel blended fuels versus the baseline no. 2 diesel fuel.

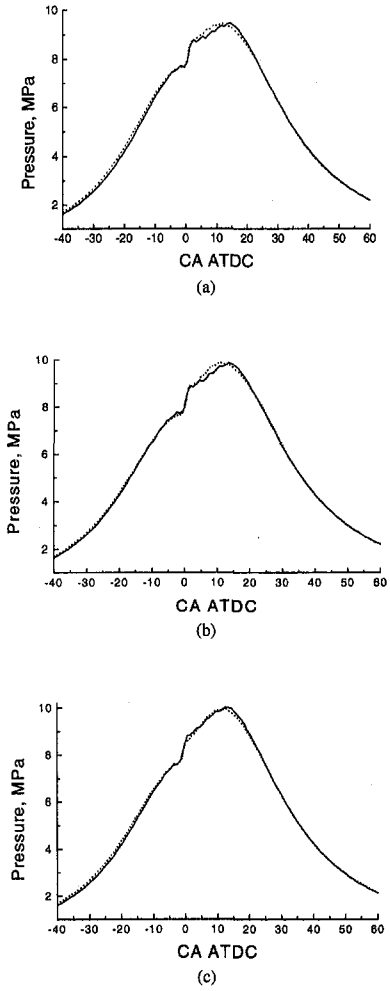

Fig. 2 Predicted (dotted lines) and measured (solid lines) pressure traces for SOI ~ −7 CA ATDC

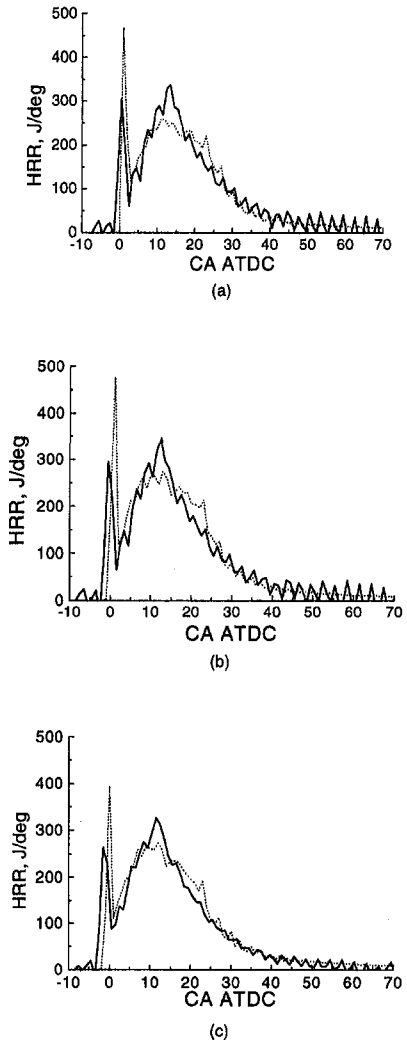

Fig. 3 Predicted (dotted lines) and measured (solid lines) heat release rates for SOI ~ −7 CA ATDC

Heat Release Rates. Figure 3 shows the corresponding comparisons of the measured and KIVA predicted heat release rates for the three different fuel cases at an SOI timing of −7 CA ATDC. Again, overall good agreement is observed between the predicted and measured results. The predicted premixed burn magnitude and duration are also seen to be in excellent agreement.

Emissions. Predicted and measured total in-cylinder soot versus NO_x trade-off curves for the three different cases of Fig. 2 are shown in Figs. 4, 5, and 6.

For the baseline case, the NO_x emissions trends are predicted well when compared to the measured NO_x results. However, soot is underpredicted for the later SOI timings; this discrepancy is likely to be related to the predicted incomplete combustion of the present combustion model. For the biodiesel blend cases, predicted NO_x again matches well against measured data.

For the 20 percent biodiesel blend case, the big reduction in soot magnitude seen in the experiments relative to the baseline is predicted. The soot was once again underpredicted for the later SOI timings, but the model was able to predict the correct emissions trends at advanced timings. However, for the most advanced 40 percent biodiesel blend case, there is a larger discrepancy between the predicted case versus the measured case.

In the Magnussen and Hjertager soot oxidation model, the total amount of available oxygen from the intake air and the fuel (in the case of oxygenated fuels) is available for fuel and soot oxidation (Eq. 14). Thus, the soot oxidation model used in this study does account for the oxygen contribution in the modeled oxygenated biodiesel blended fuels. However, the Hiroyasu soot formation model is somewhat insensitive to the type of fuel being modeled; therefore, further investigation in the soot predictions is required to better understand whether or not the oxygenated fuel blends greatly effect the formation of soot.

Note that only the dry soot fraction of the particulate matter is predicted in the computations. As a result, the predicted results are compared against experimental data where only the solid fraction is reported, i.e., the soluble organic fraction is not included in the reported experimental data.

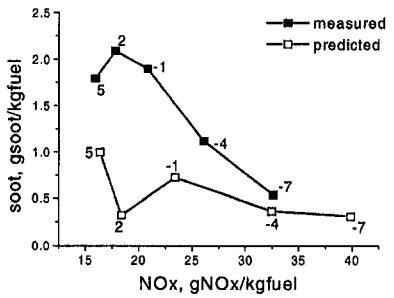

Fig. 4 Baseline case—measured and predicted soot versus NO_x trade-off curves

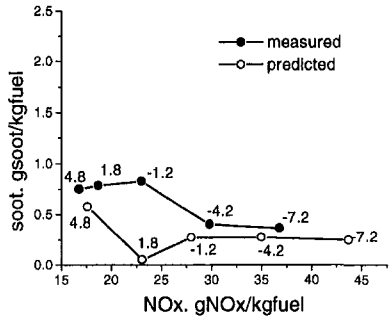

Fig. 5 20 percent biodiesel blend case—measured and predicted soot versus NO_x trade-off curves

Soot and NO_x Contours. In order to help explain the NO_x and soot emission results, the detailed in-cylinder distributions were examined. Figure 7 displays predicted contours of soot concentration in the cylinder for a nominal SOI timing of −7 CA ATDC for the baseline and 20 percent biodiesel blend cases. The greatest differences in soot contours are seen later in the combustion cycle, e.g., beginning at about 63 CA ATDC which is the case shown in Fig. 7. The contours are shown in the plane of one of the six spray plumes, and the injector is located at the top left of each frame. The spray (not shown) is directed downward into the piston bowl in the test engine.

The size of the high soot concentration containing region is larger with the 20 percent biodiesel blend case; however, higher local concentrations of soot are observed with the baseline case which are expected since the predicted engine-out soot concentrations were highest for the baseline case. These higher soot concentrations are addressed later when fuel concentrations are studied.

The measured peak bulk cylinder temperatures were lower for the biodiesel blend cases versus the baseline case for SOI timings of −4, −1, 2, and 5 CA ATDC (Choi et al., 1997); at an SOI timing of −7, the peak bulk cylinder temperatures were comparable between the three fuel blends. However, the engine NO_x emissions were higher for the biodiesel blend cases as compared to the baseline case for all fuel injection timings. Therefore, it appeared that the biodiesel blended fuel NO_x results contradicted the common thinking that NO_x emissions correlate with peak combustion temperatures (Choi et al., 1997). To better understand the predicted and measured NO_x emissions results, contours of NO_x concentration for an SOI timing of −4 CA ATDC were also studied.

The formation of NO_x was found to be almost frozen at its peak concentration by 36 CA ATDC. However, significant differences in the in-cylinder NO_x contours appear at 36 CA ATDC. As shown in Fig. 8, larger areas of high NO_x concentration are observed with biodiesel blend cases as compared to the baseline where peak NO_x magnitudes are lower. The predicted

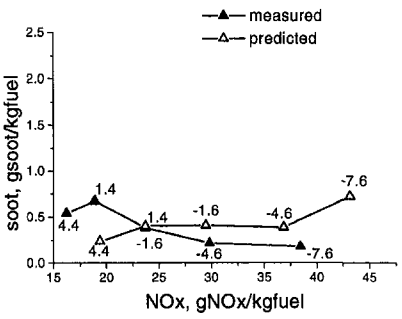

Fig. 6 40 percent biodiesel blend case—measured and predicted soot versus NO_x trade-off curves

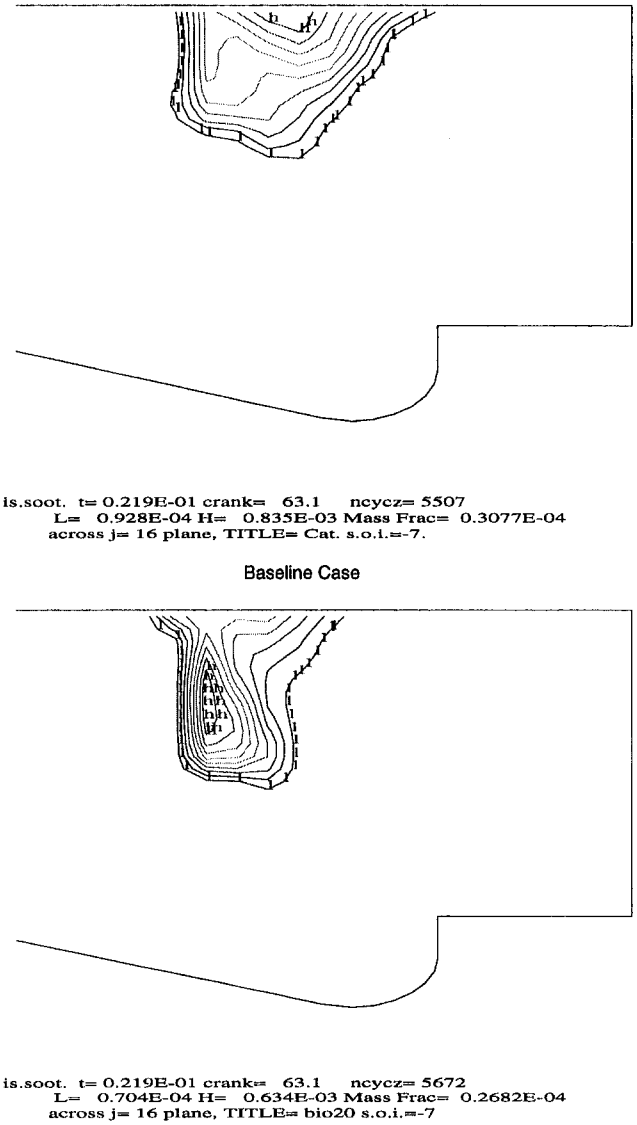

Fig. 7 Soot contours for SOI-7 CA ATDC at engine timing 63 CA ATDC

NO_x contours suggest that higher local temperatures are encountered in the biodiesel blend cases.

Figure 9 shows the in-cylinder histories of the amount of the charge that is at a temperature greater than 2600 K. As can be seen, the amount of high temperature gas increases with increasing biodiesel concentration with the largest amount of high temperature gas with the 40 percent biodiesel concentration. The results shown in Fig. 9 are consistent with the results seen in the NO_x contour plots.

Temporal Fuel Distribution. Large differences in fuel vapor penetration for the three different fuel blends begin to appear at around 12.5 CA ATDC, as shown in Fig. 10. Greater vapor penetration is observed with the biodiesel blends. Due to the shorter injection duration, the biodiesel cases inject the same amount of fuel more quickly than the baseline case. The higher concentrations of soot observed in Fig. 7 for the baseline case may thus be due to the slower fuel injection, i.e., fuel is being injected later in the cycle and is having the same effect as injecting fuel at a more retarded timing, thus increasing the engine-out soot emissions. The greater fuel penetration for the biodiesel blend cases may also help explain the increase in NO_x observed in both the experimental and predicted results for the biodiesel blend cases.

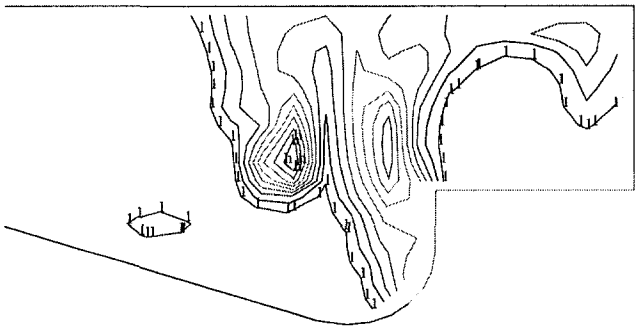

is...no. t= 0.191E-01 crank= 36.1 ncycz= 5873
L= 0.394E-03 H= 0.355E-02 Mass Frac= 0.6508E-03
across j= 16 plane, TITLE= Cat. s.o.i.=-4.

Baseline Case

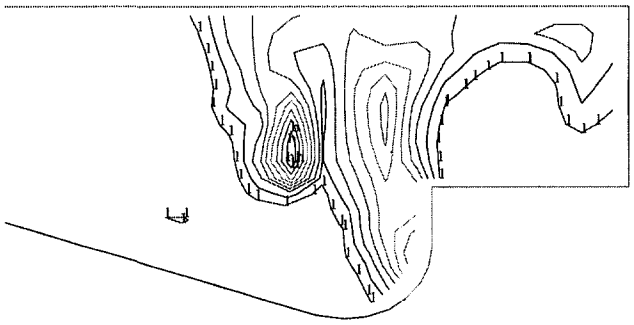

is...no. t= 0.191E-01 crank= 36.1 ncycz= 5562
L= 0.432E-03 H= 0.388E-02 Mass Frac= 0.7054E-03
across j= 16 plane, TITLE= bio20 s.o.i.=-4

20% Biodiesel Blend Case

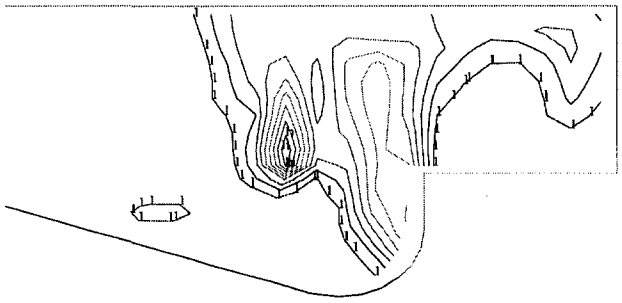

is...no. t= 0.191E-01 crank= 36.1 ncycz= 6028
L= 0.482E-03 H= 0.433E-02 Mass Frac= 0.7497E-03
across j= 16 plane, TITLE= bio40 s.o.i.=-4

40% Biodiesel Blend Case

Fig. 8 NO_x contours of the various fuel blends for SOI-4 CA ATDC at an engine timing of 36 CA ATDC

Chikahisa et al. (1995) found that longer penetration of fuel sprays (in terms of distance) relative to the nozzle diameter was a major cause of increases in NO emissions from engines using high pressure fuel injections. They observed that as the penetration length increased, the air and fuel spray mixed more slowly near the spray tip due to slower velocities resulting in more time for NO reaction and longer mixing time scales, thus increasing NO formation. As shown in Fig. 8, the locations of high NO concentrations and high temperatures are near the periphery of the fuel spray where the spray velocities are rela-

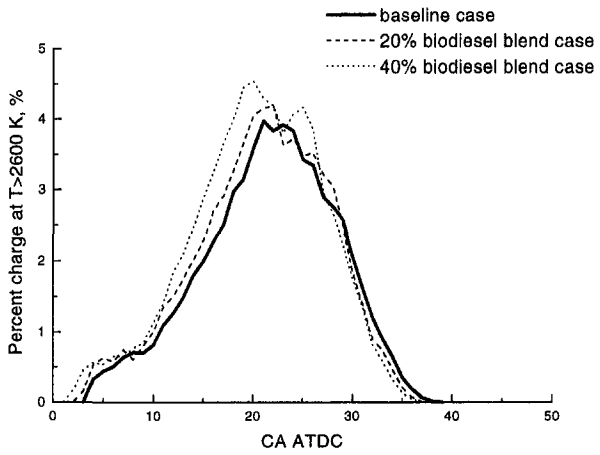

Fig. 9 Temporal history of the amount of charge in-cylinder at temperatures greater than 2600 K, SOI-4 CA ATDC

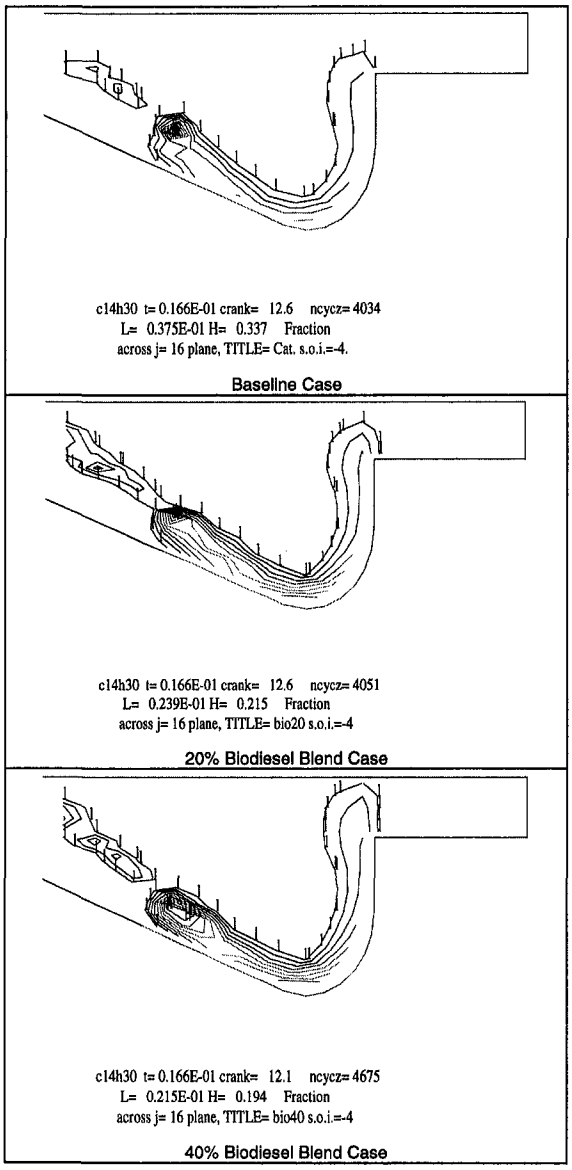

c14h30 t= 0.166E-01 crank= 12.6 ncycz= 4034
L= 0.375E-01 H= 0.337 Fraction
across j= 16 plane, TITLE= Cat. s.o.i.=-4.

Baseline Case

c14h30 t= 0.166E-01 crank= 12.6 ncycz= 4051
L= 0.239E-01 H= 0.215 Fraction
across j= 16 plane, TITLE= bio20 s.o.i.=-4

20% Biodiesel Blend Case

c14h30 t= 0.166E-01 crank= 12.1 ncycz= 4675
L= 0.215E-01 H= 0.194 Fraction
across j= 16 plane, TITLE= bio40 s.o.i.=-4

40% Biodiesel Blend Case

Fig. 10 Fuel distribution for the various fuel cases (SOI-4 CA ATDC at an Engine Timing ~12.5 CA ATDC)

tively slow and mixing time scales are large. Additionally, the higher viscosity in the biodiesel blends and greater turbulent momentum which is evident from the longer fuel penetration may have helped promote greater fuel and air mixing. Therefore, it appears the effects from both the increased fuel penetration and higher viscosity were accounted in the KIVA simulation and may help explain the difference in NO_x results for the three fuels.

Summary

Computer simulations were conducted to better understand the controlling factors in NO_x and soot formation when a mixture of 20 percent and 40 percent by volume in no. 2 diesel fuel was used. The modified multidimensional KIVA-II code modeled the high load, single injection case and its predicted results were compared against those measured. The modeled results are summarized as follows.

- Due to increased fuel viscosity, for the biodiesel blend cases, a shorter fuel injection duration was required to match combustion data later in the combustion cycle.
- Very good agreement was seen between the predicted and measured pressure traces and heat release for all fuel injection timings.
- In general, NO_x predictions matched well against measured data for all three fuel cases. Soot was underpredicted at the more retarded SOI timings; this could be related to the predicted incomplete combustion of the present combustion model at retarded timings. Additionally, ongoing research on the soot models is currently underway to better represent in-cylinder soot formation.
- Although the measured peak bulk cylinder temperatures were lower for the biodiesel blend cases, the amount of charge at high temperatures increased as the concentration of biodiesel increased. The predicted results help to explain the anomalous increase in measured NO_x emissions for biodiesel blend cases which have lower heats of combustion than the baseline fuel.
- Overall, high engine-out concentrations of soot were observed with the baseline case, in agreement with the experiments. This is primarily due to the lack of the presence of oxygenate in the baseline fuel. The higher soot encountered with the no. 2 DF may also be due to the slower fuel injection where, in effect, fuel is being injected at a more retarded timing, thus, increasing the soot emissions.
- Greater fuel penetration was observed with the biodiesel blend fuels due to the shorter fuel injection duration. It appeared that fuel/air mixing was enhanced with the longer fuel penetration by the greater fuel momentum, larger viscous effects, and larger mixing time scales on the periphery of the fuel spray, thus, increasing NO formation for the biodiesel blend cases.

Acknowledgments

This work was supported at the University of Wisconsin-Madison by the National Biodiesel Board and Sandia National Laboratories. Additional support was provided by the Army Research Office. The authors would like to thank Glenn Bower, Andrei Kazakov, Ali Uludogan and other individuals at the Engine Research Center who assisted in the current research.

References

Amsden, A. A., O'Rourke, P. J., and Butler, T. D., 1989, *KIVA-II,* a computer program for chemically reactive flows with sprays, Los Alamos National Labs., LA-11560-MS.

Ayoub, N., 1995, "Modeling Multicomponent Fuel Sprays in Engines With Application to Diesel Cold-Starting," Ph.D. thesis, Mechanical Engineering Department, University of Wisconsin-Madison, Madison, WI.

Chang, C., and Farrell, P., 1997, "A Study on the Effects of Fuel Viscosity and Nozzle Geometry on High Injection Pressure Diesel Spray Characteristics," SAE Technical Paper 970353.

Chikahisa, T., Konno, M., and Murayama, T., 1995, "Analysis of NO Formation Characteristics and Control Concepts in Diesel Engines from NO Reaction-Kinetic Considerations," SAE Technical Paper 950215.

Choi, C., Bower, G., and Reitz, R., 1997, "Effects of Biodiesel Blended Fuels and Multiple Injection on D.I. Diesel Engine Emissions," SAE Technical Paper 970218.

Halstead, M., Kirsh, L., and Quinn, D., 1977, "The Autoignition of Hydrocarbon Fuels at High Temperatures and Pressures—Fitting of a Mathematical Model," *Combust. Flame,* Vol. 30, pp. 45–60.

Hampson, G., 1996, "A Theoretical and Experimental Study of Emissions Modeling for Diesel Engines with Comparisons to In-Cylinder Imaging," Ph.D thesis, Mechanical Engineering Department, University of Wisconsin-Madison, Madison, WI.

Han, Z., and Reitz, R., 1996, "A Temperature Wall Function Formulation for Variable-Density Turbulence Flows with Application to Engine Convective Heat Transfer Modeling," *International Journal of Heat and Mass Transfer.*

Han, Z., and Reitz, R., 1995, "Turbulence Modeling of Internal Combustion Engines Using RNG k-ϵ Models," *Comb. Sci. Tech.,* Vol. 106, pp. 4–6, 267.

Han, Z., Uludogan, A., Hampson, G., and Reitz, R., 1996, "Mechanism of Soot and NOx Emissions Reduction Using Multiple-Injection in a Diesel Engine," SAE Technical Paper 960633.

Hiroyasu, H., and Kadota, T., 1976, "Models for Combustion and Formation of Nitric Oxide and Soot in DI Diesel Engines," SAE Paper 760129.

Kong, S., and Reitz, R., 1993, "Multidimensional Modeling of Diesel Ignition and Combustion Using a Multistep Kinetics Model," ASME JOURNAL OF ENGINEERING FOR GAS TURBINES AND POWER, Vol. 115, No. 4, pp. 781–789.

Kong, S., Han, Z., and Reitz, R., 1995, "The Development and Application of a Diesel Ignition and Combustion Model for Multidimensional Engine Simulations," SAE Technical Paper 950278.

Krieger, R. B., and Borman, G. L., 1966, "The Computation of Apparent Heat Release for Internal Combustion Engines," ASME Paper 99-WA/DGP-4.

Liu, A., Mather, D., and Reitz, R., 1993, "Modeling the Effects of Drop Drag and Breakup on Fuel Sprays," SAE Technical Paper 930072.

Magnussen, B. F., and Hjertager, B. H., 1976, "On Mathematical Modelling of Turbulent Combustion with Special Emphasis on Soot Formation and Combustion," *16th Symposium (International) on Combustion,* Combustion Institute, pp. 719–729.

Miyaki, M., Fujisawa, H., and Yamamoto, Y., 1991, "Development of New Electronically Controlled Fuel Injection System ECD-U2 For Diesel Engines," SAE 910252.

Ricart, L. M., Xin, J., Bower, G. R., and Reitz, R. D., 1997, "In-Cylinder Measurement and Modeling of Liquid Fuel Spray Penetration in a Heavy-Duty Diesel Engine," SAE Technical Paper 971591.

Siebers, D., 1985, "Ignition Delay Characteristics of Alternative Diesel Fuels: Implications on Cetane Number," SAE Technical Paper 852102.

Scholl, K. W., and Sorenson, S. C., 1993, "Combustion of Soybean Oil Methyl Ester in a Direct Injection Diesel Engine," SAE Technical Paper 930934.

Tree, D. R., 1992, "A Study on the Effects of Aromatics on Exhaust Particulates and Soot in a Direct Injection Diesel Engine," Ph.D. thesis, Mechanical Engineering Department, University of Wisconsin-Madison, Madison, WI.

Theobold, M., and Cheng, W., 1987, "A Numerical Study of Diesel Ignition," ASME Paper 87-FE-2.

Woschni, G., 1967, "A Universally Applicable Equation for the Instantaneous Heat Transfer Coefficient in the Internal Combustion Engine," SAE 670937.

Xin, J., Montgomery, D., Han, Z., and Reitz, R., 1997, "Multidimensional Modeling of Combustion for a Six-Mode Emissions Test Cycle of a DI Diesel Engine," Journal of Engineering for Gas Turbines and Power, in press.

Zhang, Y., and Van Gerpen, J. H., 1996, "Combustion Analysis of Esters of Soybean Oil in a Diesel Engine," SAE Technical Paper 960765.

Final Report on the Development of a Hydrogen-Fueled Combustion Turbine Cycle for Power Generation

R. L. Bannister
Westinghouse Power Generation,
4400 Alafaya Trail,
Orlando, FL 32826-2399

R. A. Newby

W. C. Yang

Westinghouse Power Generation,
Science and Technology Center,
Pittsburgh, PA 15235

Through its New Energy and Industrial Technology Development Organization (NEDO) the Japanese government is sponsoring the World Energy Network (WE-NET) Program. WE-NET is a 28-year global effort to define and implement technologies needed for hydrogen-based energy systems. A critical part of this effort is the development of a hydrogen-fueled combustion turbine system to efficiently convert the chemical energy stored in hydrogen to electricity when hydrogen is combusted with pure oxygen. A Rankine cycle, with reheat and recuperation, was selected by Westinghouse as the general reference system. Variations of this cycle have been examined to identify a reference system having maximum development feasibility, while meeting the requirement of a minimum of 70.9 percent low heating value (LHV) efficiency. The strategy applied by Westinghouse was to assess both a near-term and long-term Reference Plant. The near-term plant requires moderate development based on extrapolation of current steam and combustion turbine technology. In contrast, the long-term plant requires more extensive development for an additional high pressure reheat turbine, and is more complex than the near-term plant with closed-loop steam cooling and extractive feedwater heating. Trade-offs between efficiency benefits and development challenges of the near-term and long-term reference plant are identified. Results of this study can be applied to guide the future development activities of hydrogen-fueled combustion turbine systems.

Introduction

The development of a comprehensive global energy system based on renewable and/or nuclear energy using hydrogen as a storage and transportation medium is a necessary step towards realization of a pollution-free civilization. In 1992, the Japanese government, through its New Energy and Industrial Technology Development Organization (NEDO) created the World Energy Network (WE-NET) Program, a 28-year effort from 1993 to 2020, directed at research and development of the technologies needed to develop a hydrogen-based energy conversion system (MITI, 1993). Part of this effort is directed toward research and development of a hydrogen-fueled combustion turbine system (NEDO, 1994) which can efficiently convert the chemical energy stored in hydrogen to electricity via a heat engine in which the hydrogen is combusted with pure oxygen.

Westinghouse has worked to develop a hydrogen-fueled combustion turbine system designed to meet the goals set by the WE-NET Program (Bannister et al., 1996). These goals include greater than 70.9 percent low heating value (LHV)[1] thermal efficiency, a reliability-availability-maintainability (RAM) equivalent to current base-loaded natural gas-fired combined cycles, and elimination of CO_2, NO_x, and SO_x during power generation. Other turbine manufacturers developing hydrogen-fueled power generation cycles under the WE-NET program are Toshiba and Mitsubishi Heavy Industries (NEDO, 1996).

This paper reports on the third and final year of progress by the Westinghouse team on the study for an optimum hydrogen-fueled combustion turbine system. In the previous two years, alternative turbine systems were evaluated (Bannister et al., 1997). The Rankine cycle with regeneration and reheat was identified as the best system. Activities completed during the third year include the selection of a Reference System, and the conceptual design of the reference plant. A Rankine cycle with reheat and recuperation was selected as the general reference system. Variations of this cycle were examined to identify a Reference System having maximum development feasibility while meeting the requirement of a minimum of 70.9 percent efficiency. The reference system selected has multiple reheat stages and a recuperator, or heat recovery steam generator (HRSG) that operates at atmospheric pressure, followed by a low pressure (LP) steam turbine. This reference system confines developmental components to the high pressure (HP) and intermediate pressure (IP) combustors and turbines, and provides a relatively simple power plant configuration.

Basic technologies and concepts to support the hydrogen-fueled combustion turbine are to be first demonstrated in a pilot plant in the 50–60 MW size range which will have greater than 64.9 percent thermal efficiency. This is to be followed by the full-scale 500 MW demonstration plant startup in 2020. The demonstration plant will meet all the above mentioned requirements for the WE-NET Program. The full-scale demonstration will be at a new Japanese power plant to be located seaside.

It should be noted that WE-NET intends to construct a total hydrogen energy system. From production using renewable energy such as hydraulic power and solar energy, to transportation to high demand areas via ship by converting hydrogen into other transportable energy mediums, including chemical mediums such as methanol, ammonia, etc., to utilization. Pure hydrogen is a clean fuel; however, it is expensive to make. Within the WE-NET program, hydrogen production technology, using renewable energy research, has been conducted by others on water electrolysis, photoelectrochemical (conversion of water

Contributed by the International Gas Turbine Institute and presented at the International Gas Turbine and Aeroengine Congress and Exhibition, Stockholm, Sweden, June 2–5, 1998. Manuscript received by the ASME Headquarters April 1, 1998. Paper No. 98-GT-21. Associate Technical Editor: R. Kielb.

[1] All efficiency values in this paper will be LHV.

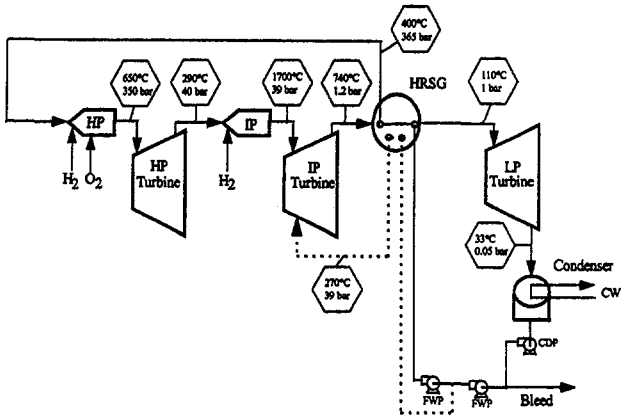

Fig. 1 Near-term plant cycle

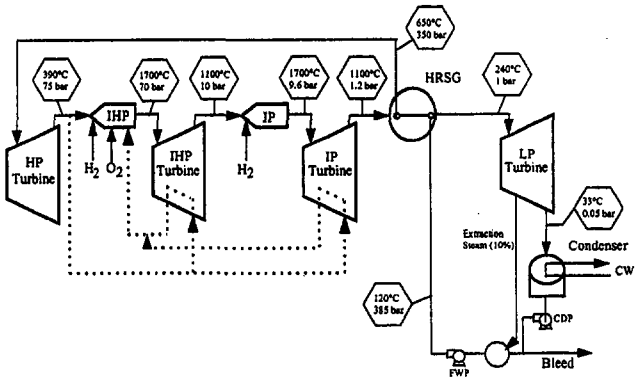

Fig. 2 Long-term plant cycle

directly into hydrogen), and the thermochemical (production of carbon-free hydrogen utilizing nuclear heat) conversion methods. Solid polymer electrolyte water electrolysis has been selected as the hydrogen production method for the WE-NET Program (NEDO, 1995), in part, because of its high energy conversion efficiency (90 percent is the development target).

Conceptual Design Assumptions

The strategy formulated for the selection of the reference plants concluded that the number of developmental components and complexity of the plant should be minimized. Both near-term plants and long-term plants should be evaluated. The designation near-term implies that the technology applied is an adaptation of current technology requiring only moderate development effort, while long-term implies that the technology applied is a major advance in technology requiring extensive development effort.

Westinghouse has assessed both a near-term reference plant and a long-term reference plant. The near-term plant requires moderate development based on extrapolation of current steam turbine technology for the HP turbine (650°C inlet temperature), and extrapolation of current combustion turbine technology for the IP turbine (1700°C inlet temperature). In contrast, the long-term plant requires more extensive development for an additional intermediate high pressure (IHP) reheat turbine (1700°C inlet temperature), and is more complex than the near-term plant, with closed-loop steam cooling (Little et al., 1993) of the IHP and IP turbines, and extractive feedwater heating. A single reheat stage is used in the near-term plant and two reheats in the long-term plant. The HRSG operates at atmospheric pressure, producing supercritical steam.

The trade-offs between the efficiency benefits and the development challenges of the near-term and long-term reference Plants were identified. The near-term plant achieves 65.2 percent net plant efficiency, and the long-term plants achieve 71.4 percent net plant efficiency. Even though the near-term plant does not achieve the goal of 70.9 percent net plant efficiency, its relative simplicity and low cost make it attractive as a next step.

Process flow diagrams for the near-term and long-term plants are shown in Figs. 1 and 2. Representative temperatures and pressures are listed at various locations on the flow diagrams. In the near-term plant, Fig. 1, hydrogen and excess oxygen are combined in the HP combustor and are mixed with recycle steam to produce a 650°C combustion product at a nominal pressure of 350 bar. This is expanded through the uncooled HP turbine, producing an exhaust stream having nominal conditions of 540°C and 40 bar. This exhaust stream, containing excess oxygen, is combined with stoichiometric hydrogen to generate the IP combustion products at a temperature of 1700°C. The IP turbine expands this combustion stream to exhaust conditions of about 740°C and 1.15 bar. The IP turbine exhaust stream is cooled in the HRSG down to about 110°C before being expanded through the LP turbine to about 33°C and the condenser pressure. A bleed stream of water is taken from the water condensate. Feedwater pumps provide high-pressure water for the HRSG to produce high-pressure steam for recycle, and intermediate-pressure water for the HRSG to produce intermediate-pressure steam for open-loop cooling of the IP turbine.

Figure 2 shows the long-term reference plant process diagram. The differences between the long-term plant and near-term plant diagrams are primarily related to the insertion of an additional turbine stage, the IHP turbine, and the use of extractive feedwater heating. The long-term plant HP turbine expands recycle steam at 650°C and 350 bar. The HP turbine exhaust stream has nominal conditions of 387°C and 75 bar. A portion of the HP exhaust stream is used for closed-loop cooling of the IHP turbine and the IP turbine. The remainder of the HP exhaust stream is combined with hydrogen fuel, excess oxygen, and the exiting IHP and IP turbine closed-loop cooling streams. The IHP combustion produces a 1700°C, 70 bar stream to be expanded in the IHP turbine. The IHP turbine exhaust stream is about 1100°C and 10 bar pressure. The IHP exhaust stream is combined with stoichiometric hydrogen to generate IP combustion products at 1700°C and 9.6 bar for expansion in the IP turbine. The IP turbine exhaust is about 1100°C and 1.2 bar pressure. Both the IHP turbine and the IP turbine produce very high temperature exhaust streams requiring high temperature piping designs. The IP expansion stream is cooled in the HRSG to about 240°C before expansion in the LP turbine. Steam is extracted from the IP turbine for feedwater heating. In contrast to the near-term plant, the long-term plant HRSG produces recycle steam at a single pressure level to expand in the HP turbine.

The HP turbine in both the near-term and long-term plants is close to, or within the range of current steam turbine technology (Bannister and Silvestri, 1989; Bannister et al., 1987). In contrast, the long-term plant IHP turbine is a large technology step above both current steam turbine practice and advanced combustion turbine developments. The IP turbine has conditions close to the conditions of advanced combustion turbines being developed for natural gas fuels (Bannister et al., 1994).

The conceptual design of the reference plant was developed by using several design tools and sources of engineering experience. A commercial process simulator (ASPEN PLUS™) was applied to develop the reference plant process flow diagrams and thermal performance estimates. Westinghouse proprietary design codes were used to design and size turbines, combustors, and the HRSG. Advanced combustion turbine engineering experience resulting from current development programs in the United States (Diakunchak et al., 1996; Amos et al., 1997) and advanced steam turbine engineering experience resulting from past studies and testing at Westinghouse (Silvestri et al., 1992)

Table 1 Estimated component performance factors and reference plant conditions

PLANT	
capacity, MWe:	500
site type:	greenfield, sea-side
ambient air temperature (°C):	15
ambient pressure, bar:	1.01325
relative humidity (%):	60
cooling sea water temperature (°C):	21
hydrogen and oxygen supply temperature (°C):	15
hydrogen and oxygen supply pressure:	as required
hydrogen purity, %:	100
oxygen purity, %:	100
hydrogen HHV, kJ/kg:	141742
CONDENSER	
type:	vacuum
shell pressure (bar):	0.0508
PUMPS	
adiabatic efficiency (%):	85
motor efficiency (%):	98
mechanical efficiency (%):	98
HRSG	
tube-side pressure drop (%):	3
shell-side pressure drop (%):	3
heat loss (% of heat transferred):	0.2
COMBUSTORS	
pressure drop (%):	3
combustion efficiency (%):	99.9
heat loss (% of heat input):	0.1
TURBINES	
rotation speed (rpm):	3600
bearing losses (% of shaft power):	0.6
adiabatic efficiency (%; HP, IHP, IP, LP):	93, 93, 93, 93
exhaust losses	neglect for HP turbine
steam leaks (% of inlet flow):	2
shaft leakages:	neglect
windage and pumping for steam leaks:	neglect
steam cooling (% of inlet flow for IHP, IP):	15, 15
coolant pressure drop (%):	10
LP turbine maximum moisture content (%):	15
LP turbine minimum inlet temperature (°C):	110
OTHERS	
steam piping pressure drop (%):	3
generator efficiency (%):	99.2
house load (% of plant shaft power):	1.5 (near-term); 1.0 (long-term)

were used to extrapolate current technology to the demands of the reference plant.

The conceptual design procedure for the reference plant was iterative. The selected reference plant configuration and an initial list of estimated component performance factors were applied to generate the initial process flow diagram and materials and energy balances. This initial set of data was used to conceptually design and size the major equipment in the Reference Plant power island. This was followed by generating an initial plant layout configuration. The initial equipment designs and plant layout provided the basis to make better estimates of the set of component performance factors which were again applied with the system model to generate a second, improved process flow diagram and materials and energy balances. This iteration has been repeated several times, with additional modifications to improve the reference plant feasibility and performance made, as needed. The final form of the plant was used as the basis to estimate the major equipment capital cost, to identify the component development needs, and to formulate the pilot plant plan.

Table 1 provides a summary of the essential technical assumptions for the component performance factors, and the reference plant requirements and boundary conditions. The scope of the reference plant conceptual design is limited to the power block. The following are some of the key assumptions in Table 1:

- 100 percent pure hydrogen and oxygen were assumed to be provided—contaminants might be present that must be considered in the design.
- The HP turbine efficiency was assumed at a representative value for HP steam turbines (93 percent) even with the relatively small size of the HP turbine blades. (The 93 percent efficiency is a projection of future capabilities that may be possible with improved airfoil design.)
- The conceptual near-term IP turbine design has an adiabatic efficiency of 86 percent. To achieve the targeted overall plant thermal performance an IP turbine efficiency of 93 percent is required.
- The HP turbine is uncooled. The conceptual design of the IP turbine in the near-term plant uses open-loop steam cooling, estimated at 33 percent of the turbine inlet flow. For the near-term IP turbine, plant thermal efficiency was also calculated using open-loop steam cooling with 15 percent of the turbine inlet flow. The IHP and IP turbines in the long-term plant uses closed-loop steam cooling, estimated at 15 percent of the turbine inlet flow.
- The generator efficiency is assumed to be 99.2 percent. This value is about 0.2 percent greater than current generator technology, representing the efficiency goal of the next generation of Westinghouse generators. (Superconductivity technology was not considered in the next generation of Westinghouse generators.)

Conceptual Design Details

The focus of the reference plant conceptual design is the near-term plant, although the long-term plant performance and development needs were also assessed. Conceptual designs and specifications have been completed for the major near-term plant components (HP and IP combustors and turbines, LP turbine, HRSG, condenser, water pumps, and generator). The near-term plant HP and IP combustor and turbine conceptual designs are based on modifications to existing steam turbine and combustion turbine design configurations.

The long-term IHP turbine will be a major extrapolation of steam turbine and combustion turbine technology with extensive closed-loop cooling of flow path elements required. The other nondevelopmental components of the long-term plant will have conceptual designs and specifications very similar to those in the near-term plant, except that the IHP and IP stages connecting piping will potentially be very hot in the long-term plant and will require special consideration.

The near-term HP turbine combustors have been designed to premix excess oxygen with recycle steam, generating a low-value oxidizing gas for combustion of hydrogen. The combustors proposed apply principles similar to combustors developed for low-heating value fuels (Garland and Pillsbury, 1992). The combustor should have no ignition difficulties at the oxygen-steam-hydrogen ratios used. The cooling of the combustor is by steam impingement and film cooling techniques. In the conceptual designs, the combustor design velocity, residence time and intensity have been selected from prior experience.

The HP combustors would be placed external, but closely coupled to the HP turbine expanders. The excess oxygen and recycle steam are premixed in an inlet chamber. The low-value oxidant flows (composed of 10 percent oxygen and 90 percent steam) through an axially located tube, and an annular tube carries hydrogen. Both oxygen/steam and hydrogen flow through swirlers, producing an intensely back-mixing zone for the primary combustion. The mixed temperature of the primary zone combustion products is about 1600°C. Cooling steam also passes through the combustor liner, keeping the liner at an acceptable temperature. Additional dilution steam passes

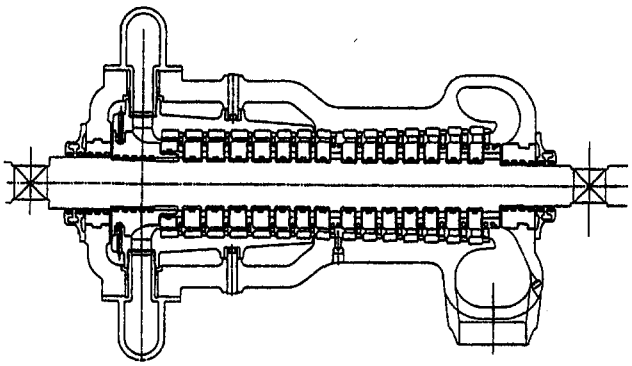

Fig. 3 Near-term HP turbine cross-section

through swirlers surrounding the primary zone outlet, and into a highly mixed quench zone where the temperature is dropped to the desired outlet temperature of 650°C.

The IP combustors are located internal to the turbine casing. They apply the same combustion concept as used for the HP combustors. Excess oxygen remains in the HP turbine exhaust stream and reacts stoichiometrically with the hydrogen fuel in the primary zone. Cooling steam that has flowed through the IP turbine to cool the turbine components helps to cool the liners. In the high intensity, secondary mixing zone, the combustion products are cooled by dilution to 1700°C by the combustor liner cooling steam. The combustor liners and transitions would be made from high-alloy steels with TBCs, or would be of ceramic construction.

The HP combustion product stream enters the HP turbine at 650°C and 350 bar. This stream of thermal energy is converted to torque through the combination of rotating and stationary blades. The steam expands through the HP blade path, exiting at the HP exhaust. Torque created by the steam is transferred along the rotor to the generator end. The HP turbine cross-sectional drawing is shown in Fig. 3, listing some major HP turbine dimensions. It shows the closely integrated, external HP combustors as well as the HP turbine flow path and exit nozzles. Table 2 lists some design characteristics for the HP turbine.

The HP casing consists of an outer cylinder and an inner cylinder. The outer cylinder is suspended on two support paws at each end. The support paws rest on pedestals that transfer the turbine weight to the building foundation. Large studs through the support paws keep the turbine from lifting off the pedestals, but allow longitudinal and transverse movement for thermal expansion.

The inner cylinder is located and supported by the outer cylinder. The inner cylinder provides passageways for steam to enter the HP blade path. It supports part of the HP stationary blades, while isolating the outer cylinder from the high inlet pressure and temperature.

Table 2 Near-term HP turbine design characteristics

Cooling Needs	None
Inlet temperature (°C)	650
Exhaust temperature (°C)	288
Inlet pressure (bar)	350
Expansion ratio	8.75
Gas flow (kg/s)	150
Number of stages	15
Number of cooled stages	0
Blade heights (first-stage/last stage) (cm)	2.3/6.4
Turbine casing diameter (m)	1.7
Length of flow passage (cm)	270
Total turbine length (m)	4.9

Table 3 Near-term IP turbine conceptual characteristics

Cooling Needs	Open-loop steam
Inlet temperature (°C)	1700
Exhaust temperature (°C)	740
Inlet pressure (bar)	38.8
Expansion ratio	33.7
Gas flow (kg/s)	154
Number of stages	6
Number of cooled rows	11
Blade heights (first-stage/last stage) (cm)	7.4/36.4
Turbine casing diameter (inlet/exhaust) (m)	2.3/3.7
Length of flow passage (cm)	200
Total turbine length (m)	5.6

The rotor is a no-bore design. It is fully integral with the dummy and gland rings, which separate pressure zones along the rotor. Blade attachments are machined into the rotor. Design evaluations included low-cycle and high-cycle fatigue stress, and tangential stress. Low-cycle fatigue stress is created from start-up, load changes and shutdowns. High-cycle fatigue is due to gravity bending, partial admission steam loads, and bearing misalignments. The tangential stress is created from centrifugal forces from the bending and the main body of the rotor. Creep due to large duration in high temperature aggravates tangential stress.

The main design features of the IP turbine are simple open-loop steam cooling, optimized stage loading, low stresses, internal blade ring cylinders for reduced maintenance and control of clearances, and use of existing combustion turbine technology (Southall and McQuiggan, 1995).

Westinghouse applied a highly interactive computer based turbine design system to do the conceptual design of the IP turbine (Little and Cobley, 1996). This design system enabled the engineer to optimize the aerodynamic and heat transfer design of turbine blading. Further iteration with other linked subsystems (through central blade files for data storage) allows rapid aeromechanical optimization of the component.

To optimize the airfoil loading, in a detailed design, accurate modeling of the boundary layer is required in the quasi-three-dimensional and fully three-dimensional design analysis. Boundary layer codes have been developed using appropriate cascades and engine representative rig tests. Laminar and turbulent boundary layer growth can be predicted, along with improved modeling of effects of free-stream turbulence, prediction of onset and length of transition, separation, etc., enabling the engineer to refine the airfoil lift distribution developed in the blade-to-blade program.

Within the detailed design iteration, fully three-dimensional viscous blade-to-blade calculations are performed to assess the development of the secondary flow and the airfoil surface static pressures, exit swirl angle, and loss. While three-dimensional calculations remain a developing technology, the database of experimental information has facilitated the code development.

Table 3 lists the IP turbine conceptual design characteristics, and Table 4 lists the IP turbine blade and vane parameters. Figure 4 shows the IP turbine cross section.

The selected reference cooling schemes encompass the full range of cooling requirements for the IP turbine components. All the cooling schemes employ open-loop steam cooling. As is typical of high temperature combustion turbines, the component cooling requirements can be dictated by surface oxidation concerns, metal creep, or low-cycle fatigue. In this study, only oxidation and creep were considered, because low-cycle fatigue requirements generally result from the in-depth design phase. The maximum surface temperature assumed for oxidation limited components was 955°C.

It was assumed that a layer of thermal barrier coating (TBC) applied by the electron beam physical vapor deposition process

Table 4 Near-term IP turbine blade and vane parameters*

	ROW 1		ROW 2		ROW 3		ROW 4		ROW 5		ROW 6	
	Vane	Blade	Vane	Blade	Vane	Blade	Vane	Blade	Vane	Blade	Vane	Blade
Number of airfoils	40	69	40	45	40	49	36	45	32	45	50	49
True chord at mid-span	10.7	6.0	9.8	10.4	11.4	10.5	15.6	14.5	18.6	19.7	18.4	20.1
Blade height	6.5	7.4	8.8	10.3	11.5	13.4	15.3	20.4	26.4	32.0	35.0	36.4

*All dimensions are in cm.

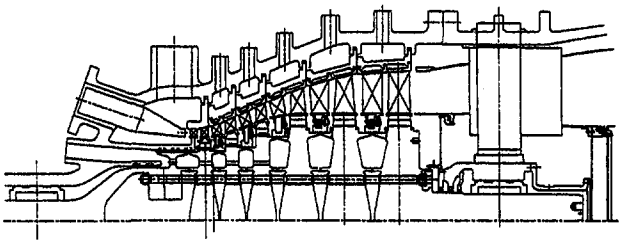

Fig. 4 Near-term IP turbine cross section

Table 5 HRSG conceptual characteristics

Flue Side	
Inlet gas	steam with trace oxygen and noncondensibles
Inlet gas flow (kg/sec)	177
Inlet gas temperature (°C)	740
Inlet gas pressure (bar)	1.15
Outlet temperature (°C)	110
Pressure drop (bar)	0.09
Tube Side	
Inlet fluid	0.15 μS cation conductivity water
Inlet temperature (°C)	33
IP inlet pressure (bar)	40
Inlet flow (kg/sec)	121
HP inlet pressure (bar)	385
HP outlet flow (kg/sec)	98
IP outlet temperature (°C)	269
HP outlet temperature (°C)	397
HRSG Dimensions	
HRSG length (m)	24
HRSG width (m)	12
HRSG height (m)	14

would be applied to all cooled components. Although the benefits of TBC are substantial, it is possible that subsequent in-depth design and economic considerations would result in a change in the type of TBC coating or the omission of TBC from some components.

Table 5 lists the operation HRSG design parameters and some of its design characteristics. The design philosophy for the steam generator selection incorporates design simplification to minimize design and operating costs over the life cycle of the plant. The major design parameters required for the steam generator use are delineated. Water treatment programs are driven by corrosion, scale, and foaming characteristics of the water in the cycle. Boiler blowdown and the requisite makeup is required in many cases to keep contaminants below threshold values. Design features that can eliminate or minimize the impact of these items on performance will contribute to a reduction in the cost of electricity. These design features were incorporated into

Table 6 Reference plant thermal performance

	Long-Term Plant	Near-Term Plant
HP Turbine, MWe	42.3	81.6
IHP Turbine, MWe	189.9	---
IP Turbine, MWe	215.4	362.5
LP Turbine, MWe	67.9	74.1
Gross Power, MWe	515.5	518.2
Gross Efficiency, %	73.5	67.6
Generator Losses, MWe	4.1	4.1
Pumping Power, MWe	6.2	6.5
BOP Losses, MWe	5.2	7.8
Net Power, MWe	500.0	500.0
Net Efficiency, %	71.4	65.2

the steam generator. The once-through steam generator configuration was selected as the optimum system to fulfill these design requirements.

The HRSG incorporates the simplest design possible to recover exhaust heat in the cycle. No drums, level controls, downcomers, or steam separation equipment is required. Thin wall, high-nickel, stainless-steel tubes with stainless-steel fins metallurgically bonded to the tubes are arranged in modules prefabricated in the shop. The HRSG weighs much less than a typical drum heat recovery steam generator. The modular arrangement allows for a great degree of configuration flexibility, whether horizontal or vertical exhaust gas flow. The lightweight and low volume nature of the design reduces erection time and simplifies commissioning.

The LP turbine represents entirely commercial technology. Two parallel, split-flow units of this type are used. The rotating blade lengths in each unit are (1) first row (28.2 cm), (2) second row (46.2 cm), and (3) last row (90.2 cm).

Several other major components in the near-term plant are representative of commercial technology, but are specially adapted to the requirements of the plant:

— **Generator:** Hydrogen-cooled generator (60 Hz, 3600 rpm, 560 MVA, 0.9 power factor, 13.8 kV).
— **Condenser:** Special features added for sea-water leak minimization and water contaminant removal.
— **Water Pumps.**

In the future, the hydrogen coolant in the generator might be integrated into the power cycle to return the generator heat losses to the IP turbine as preheated hydrogen fuel.

Plant Efficiency

Plant heat and materials balances and cycle calculations were generated for the reference plant at its rated load of 500 MWe using the component performance assumptions described. Various other parameters were also considered. No hydrogen or oxygen preheat is used in the plants, and extractive feedwater heating is used in the long-term plant, but not in the near-term plant, providing a simple, compact plant configuration.

Table 6 lists the reference plant performance and power generation breakdown for the long-term and the near-term plants.

The table lists the gross power output of each turbine, the power losses, the net power generated and the plant net efficiency.

Estimates of the generation efficiency of the near-term plant at part-load conditions are as follows:

— 75 percent load, 62.1
— 50 percent load, 59.6
— 25 percent load, 58.5

Several options are available for load reduction in the near-term plant, (e.g., reducing flow, modifying inlet temperatures, bypass of a turbine, etc.), but a complete evaluation of these options was not performed.

Environmental Performance

The reference plant environmental performance is expected to be superior to that of other power generation concepts using other fuels, by having very low NOx, sulfur oxide, particulate, toxic species, and green-house gas emissions. The generation of solid waste and liquid/sludge wastes would also be negligible. The only significant emissions could result from fuel or oxygen contaminants, or from noise.

Impurities may be introduced with the oxygen supply, with the fuel hydrogen supply, through the condenser from the sea water coolant, or internally by corrosion of materials in the flow path. The oxygen generated by air separation will generally contain as much as 0.1 percent argon (by volume), and traces of nitrogen, depending on the design and operation of the air separation system. The air supply that is drawn from for air separation may also contain various contaminants, and any component in the air supply that is heavy relative to oxygen will tend to remain with the oxygen.

Hydrogen can be produced by many methods, (as previously mentioned, solid polymer electrolyte water electrolysis has been selected as the NEDO hydrogen production method). Contaminant levels in the hydrogen will depend on the nature of the specific producer's electrolysis system, as well as the nature of the hydrogen transport equipment. Typically, contaminants expected in the electrolysis hydrogen might have levels as high as 0.1 percent oxygen, 0.14 percent nitrogen, 50 ppm methane, and traces of mercury. Thus, there is the potential for very small emissions of NOx, CO_2, particulate, SO_2 and some trace elements from the plant.

Plant safety can be achieved with current technology in the reference plant. Based on industrial and defense experience with hydrogen, it is expected that the handling and safety requirements will be comparable in scope and cost to those of similarly flammable (e.g., methane and gasoline). The plant safety systems required for the hydrogen/oxygen environment in the reference plant will differ from those in a conventional combustion turbine combined-cycle power plant, but the safety technology is available, economical and reliable.

Contaminant Control

Impurities that may enter the reference plant at various locations are also of concern from their impact on the plant reliability, availability, and maintenance. Salts would be the most severe contaminants with respect to corrosion potential. (Salts would be likely to be introduced into the recycle water system through the sea water-cooled condenser). Once salts enter the system, corrosion products could exist in the turbine exhausts in particulate, liquid, or gaseous forms. The turbine exhausts in particulate, liquid, or gaseous forms. The turbine exhaust might also contain either excess hydrogen or excess oxygen, and traces of unburned hydrocarbons, NO_x, CO_2, and CO resulting from hydrogen fuel and oxygen contaminants.

The control of contaminants can best be undertaken at the condenser. Here, noncondensible gases and vapors can be separated and compressed for either recycled or disposed. An ion exchange, deep bed polisher can be used to efficiently remove ions from the recycle water. This is commercial technology. The power consumption for the polisher is associated only with the additional feed water pressure drop. (Estimated from commercial practice to be about 3 bars, the pressure drop will have a negligible impact on the net plant efficiency.) Power consumption for the regeneration of the ion exchange media (probably done off-site) would be treated as an operating cost for the system.

The practice of the water/steam chemistry technology would be focused primarily on the maintenance of the integrity and performance of cycle components. The optimum power plant water chemistry treatment program would minimize the losses associated with corrosion damage at the lowest possible cost. Corrosion of wetted piping, valve, turbine and appurtenances would always be present.

The supercritical operating regime of the water/steam requires the use of ultrapure water. The suggested optimum water/steam chemistry program for the hydrogen turbine cycle would be developed around two primary areas. The first, dealing with materials, requires the use of austenitic alloy steels in piping, fittings and wetted components. The second, relies upon a water treatment program commonly referred to as oxygenated feedwater chemistry. This coordinated preventative approach would simplify the water treatment program.

Since the condenser water is a major source of ingress contamination, the use of double walled titanium tube sheets is suggested to minimize the probability of leaks. If double-walled tube sheets are not acceptable due to performance degradation, then segregated hotwells with specific conductivity cells in each region are specified to provide early warning of contamination.

Oxygenated feedwater chemistry is the preferred water chemistry program because of the use of oxygen in the cycle. Only very low levels of contaminants are allowed. (Only 0.1 μSiemens cation conductivity in the condensate is allowed.) The program requires minimal chemical feed, only oxygen and oxygen scavenger are required. A slight excess of oxygen in the combustion process is recommended from the water/steam chemistry perspective. This would assist in the maintenance of the 50 ppb oxygen levels required in the feedwater, and reduce the potential hydrogen embrittlement problems that may arise.

A condensate polisher would be added to maintain water purity. It would provide a second line of defense in the event of a condenser leak. The full-flow condensate polisher would protect the boiler against contamination. Resin traps in the polisher are recommended to prevent resin contamination. A foolproof regeneration scheme is required. A three bed polisher with separate cation/anion beds reduces the possibility of acid/caustic contamination.

Discussion

The near-term plant HP turbine development centers on the combustor (combustion phenomena and design features) and materials selection. The near-term HP turbine design needs to be an adaptation of conventional HP steam turbine designs, and component cooling needs will be very limited. The IP turbine development needs would center on the combustor and materials development. In the IP turbine the component cooling needs are extensive (airfoils, cylinder, blade rings, rotor bearings) and the cooling design follows from closed-loop steam cooling features currently under development for advanced combustion turbines operating under similar temperature and pressure conditions.

HP and IP combustion development should focus on the nature of the hydrogen combustion products and the control of its chemistry, as well as the combustor operability: flame stability, ignition, flame detection, and combustion induced oscillations. Combustor liner and transition cooling would also be part of the combustor development testing using available techniques.

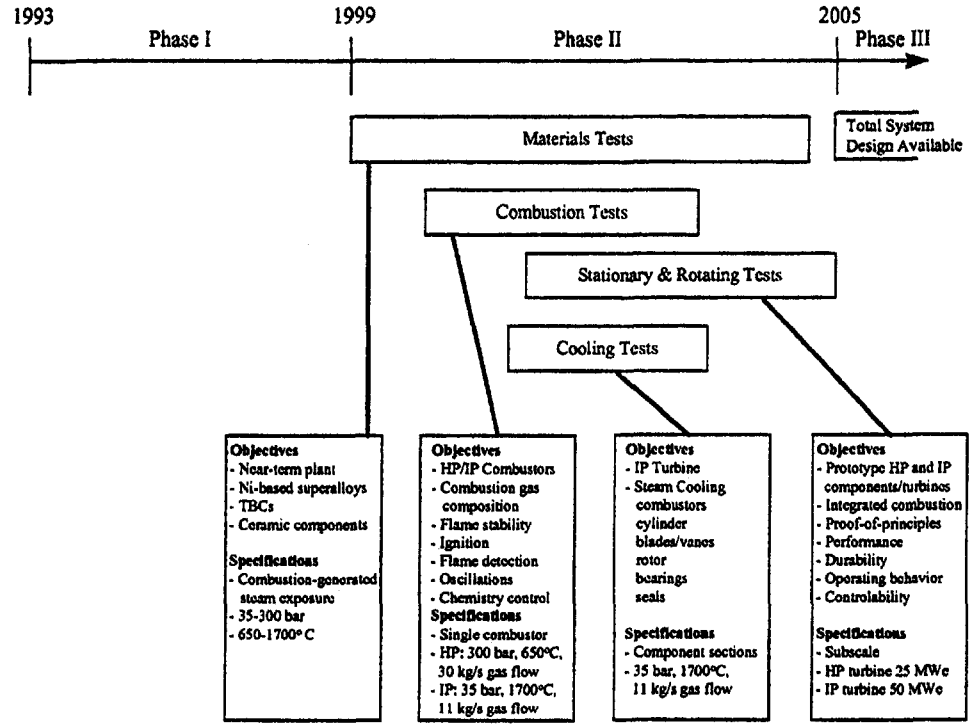

Fig. 5 Development plant

Materials testing should focus on the durability of candidate materials during exposure to the hydrogen combustion products at simulated commercial operating duty conditions (hydrogen embrittlement, oxidation, stress corrosion cracking, corrosion deposits, creep rupture). The development of appropriate corrosion coatings and TBCs, and their associated bond coating, should be a major part of the materials program. The initial testing would consider advanced combustion turbine Ni-based superalloys (single crystal and directionally solidified), and advanced combustion turbine TBCs (e.g., yttria-stabilized zirconia, alumina, TiN). The materials testing associated with the IP turbine should also consider the limited use of ceramic components (ring segments, combustor liners and transitions, vane and blade leading edges), and would consider the stability of candidate ceramic materials and alternative ceramic forms in simulated combustion-steam environments (e.g., zirconia in composite forms, tile forms, and fibrous insulating forms).

Verification tests would be performed at sub-scales sufficient to generate data that can be interpreted for operating conditions. Tests would address the HP and IP combustors, and the IP turbine cooling features (combustor and transition, cylinder, blades and vanes, rotor, bearing, and seals) with the components made from optimum materials and TBCs. Rotating tests of the turbines, with integrated hydrogen combustion, would ultimately be required to demonstrate the operability and performance of the nonintegrated components and to develop confidence for the technology in industry.

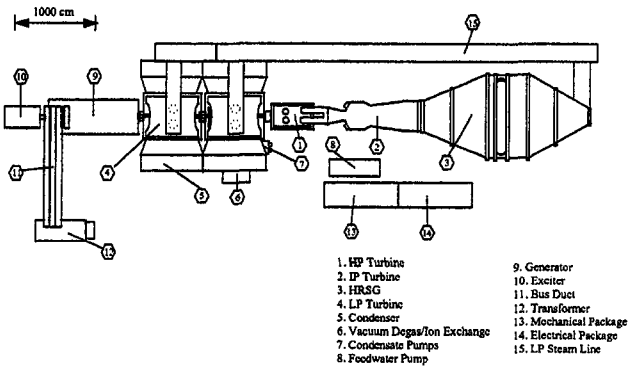

Fig. 6 Near-term reference plant layout

Engineering studies of many plant components and features should continue in parallel with development testing in Phase II. The engineering studies should address areas such as

- throat and pipe airborne noise and vibration,
- high temperature, anti-seize coatings,
- face seals and radial seals,
- high temperature thrust bearings,
- coating process development,
- valves,
- concentric shafts to insulate bearings, and
- plant control (start-up, load follow, trip, and combustion stoichiometry).

In addition, parallel engineering studies should update the reference plant design as new development test data becomes available, and the optimum integration of the reference plant components should continue to be refined.

Figure 5 depicts the major development phases, and development programs on a time-line for the NEDO program. Each development project block in Phase II lists the objectives and features of the testing, as well as listing facility specifications and estimated costs.

Conclusions

The development of a hydrogen fired power plant with an efficiency of 70.9 percent can be accomplished. Conceptual reference plant layouts of the near-term plant have been prepared based on the conceptual equipment sizing described. Figure 6 shows the near-term plant power island layout. The major power island components have been roughly sized and are depicted in the drawing. The HP turbine, IP turbine, LP turbine and generator are arranged on a single shaft. The HRSG is depicted as a conventional HRSG design, although other tube-

in-shell designs might be more appropriate for this application. The location of the vacuum degas and ion exchange polisher is also shown. The overall 500 MWe plant is compact and simple in configuration, and only the HP and IP turbine/combustor components require development.

The component development phase of this 28-year program is scheduled to start in 1999. Suggested objectives for Phase II (1999–2005) include the following:

— focus efforts on the near-term plant conditions
— perform initially sub-scale testing that simulates key components of the HP and IP combustors and turbines
— operate the tests to generate critical design data that provide proof of principles for the components

Acknowledgments

The studies described in this paper were performed under a contract from the Japanese New Energy and Industrial Technology Development Organization (NEDO). The program was administered through the Central Research Institute of Electric Power Industry (CRIEPI) as a part of the International Clean Energy Network Using Hydrogen Conversion (WE-NET) Program.

Numerous Westinghouse personnel have participated in this program. Over the contract's three-year life, the authors are indebted to Ryuhei Kondo, from our Tokyo office, who interacted with NEDO and CRIEPI on our behalf. Additional support in Japan was provided by George Mulligan and Hector Ponce. Contract administrative support was provided by Lloyd Dean in Orlando, FL. In the final year of the program, the authors also acknowledge the technical support provided by Mark Suchor (steam turbines), David Little (gas turbines), Edward North (turbine cooling), John Brushwood (balance-of-plant equipment, and steam chemistry), and others within power generation.

References

Amos, D. J., Diakunchak, I. S., McQuiggan, G., Southall, L. R., and Wagner, G. P., 1997, "Update on Westinghouse's Advanced Turbine Systems Program," ASME Paper 97-GT-369.

Bannister, R. L., Newby, R. A., and Yang, W. C., 1997, "Development of a Hydrogen-Fueled Combustion Turbine Cycle for Power Generation," ASME Paper 97-GT-14.

Bannister, R. L., Huber, D. J., Newby, R. A., and Paffenbarger, J. A., 1996, "Hydrogen-Fueled Combustion Turbine Cycles," ASME Paper 96-GT-247.

Bannister, R. L., Cheruvu, N. S., Little, D. A., and McQuiggan, G., 1994, "Turbines for the Turn of the Century," *Mechanical Engineering,* Vol. 116, No. 6, pp. 68–75.

Bannister, R. L., Silvestri, G. J., Hizume, A. and Fujikawa, T., 1987, "High-Temperature Supercritical Steam Turbines," *Mechanical Engineering,* Vol. 109, No. 2, pp. 60–65.

Bannister, R. L., and Silvestri, G. J., 1989, "The Evolution of Central Station Steam Turbines," *Mechanical Engineering,* Vol. 111, No. 2, pp. 70–78.

Diakunchak, I. S., Bannister, R. L., Huber, D. J., and Roan, F., 1996, "Technology Development Programs for the Advanced Turbine Systems Engine," ASME Paper 96-GT-5.

Garland, R. V., and Pillsbury, P. N., 1992, "Status of Topping Combustor Development for Second-Generation Fluidized Bed Combined Cycles," ASME JOURNAL OF ENGINEERING FOR GAS TURBINES AND POWER, Vol. 114, pp. 126–131.

Little, D. A., and Cobley, K., 1996, "Application of Aeroengine Aerodynamic Design Codes to Industrial Gas Turbine Design," ASME Paper 96-GT-280.

Little, D. A., Bannister, R. L., and Wiant, B. C., 1993, "Development of Advanced Turbine Systems," Proceedings, ASME Cogen Turbo Power '93, ASME, New York, pp. 271–280.

MITI, 1993, "Comprehensive Approach to the New Sunshine Program which supports the 21st Century," *Sunshine Journal,* No. 4, Agency of Industrial Science and Technology in Ministry of International Trade and Industry (MITI), pp. 1–6.

NEDO, 1994, International Clean Energy Network Using Hydrogen Conversion (WE-NET), 1993 annual summary report on results, New Energy and Industrial Technology Development Organization (NEDO).

NEDO, 1995, International Clean Energy Network Using Hydrogen Conversion (WE-NET), 1994 annual summary on results, New Energy and Industrial Technology Development Organization (NEDO).

NEDO, 1996, "Subtask 8 Development of Hydrogen-Combustion Turbine, Study for an Optimum System for Hydrogen-Combustion Turbine," 1995 annual technical results report, New Energy and Industrial Technology Development Organization (NEDO).

Silvestri, G. J., Bannister, R. L., Fujikawa, T., and Hizume, A., 1992, "Optimization of Advanced Steam Condition Power Plants," ASME JOURNAL OF ENGINEERING FOR GAS TURBINES AND POWER, Vol. 114, pp. 612–620.

Effect of Air Extraction for Cooling and/or Gasification on Combustor Flow Uniformity

T. Wang

J. S. Kapat[1]

Gas Turbine Research Laboratory,
Department of Mechanical Engineering,
Fluor Daniel Building 239,
Clemson University,
Clemson, SC 29634-0921

W. R. Ryan

I. S. Diakunchak

R. L. Bannister

Power Generation Business Unit,
Siemens Westinghouse Power Corporation,
Orlando, FL

Reducing emissions is an important issue facing gas turbine manufacturers. Almost all of the previous and current research and development for reducing emissions has focused, however, on flow, heat transfer, and combustion behavior in the combustors or on the uniformity of fuel injection without placing strong emphasis on the flow uniformity entering the combustors. In response to the incomplete understanding of the combustor's inlet air flow field, experiments were conducted in a 48 percent scale, 360 deg model of the diffuser-combustor section of an industrial gas turbine. In addition, the effect of air extraction for cooling or gasification on the flow distributions at the combustors' inlets was also investigated. The following three different air extraction rates were studied: 0 percent (baseline), 5 percent (airfoil cooling), and 20 percent (for coal gasification). The flow uniformity was investigated for the following two aspects: (a) global uniformity, which compared the mass flow rates of combustors at different locations relative to the extraction port, and (b) local uniformity, which examined the circumferential flow distribution into each combustor. The results indicate that even for the baseline case with no air extraction there was an inherent local flow nonuniformity of 10 ~ 20 percent at the inlet of each combustor due to the complex flow field in the dump diffuser and the blockage effect of the cross-flame tube. More flow was seen in the portion further away from the gas turbine center axis. The effect of 5 percent air extraction was small. Twenty percent air extraction introduced approximately 35 percent global flow asymmetry diametrically across the dump diffuser. The effect of air extraction on the combustor's local flow uniformity varied with the distances between the extraction port and each individual combustor. Longer top hats were installed with the initial intention of increasing flow mixing prior to entering the combustor. However, the results indicated that longer top hats do not improve the flow uniformity; sometimes, adverse effects can be seen. Although a specific geometry was selected for this study, the results provide sufficient generality to benefit other industrial gas turbines.

Introduction

Reducing emissions is an important issue facing gas turbine manufacturers. However, almost all of the previous and current research and development for reducing emissions has focused on the flow, heat transfer, and combustion behavior in the combustors or on the uniformity of fuel injection without placing strong emphasis on the flow uniformity entering the combustors. Combustion research has been frequently conducted using uniform flow as the inlet condition in laboratories. Therefore, the factor of nonuniform combustor inlet flow distribution has not been intensively investigated. The extent of flow uniformity at the inlet to the combustors has been identified as an important factor which significantly affects the emission (Lyons, 1981). The cause of the nonuniform combustor inlet flow of many gas turbines can be traced to the complex flow field inside the dump diffuser.

The heavy-frame industrial gas turbines designed by several major manufacturers typically use a two-part diffuser-combustion section to decelerate air exiting the compressor. First, air from the compressor flows through an annular pre-diffuser and recovers some of its kinetic energy before being discharged into a comparatively large chamber called the dump diffuser or the dump chamber. The diffuser-combustor section has two major functions (i) to decelerate the high velocity air coming from the compressor in order to provide an adequate air velocity for the combustion process (Wilson, 1984) and (ii) to distribute air uniformly to the combustors to reduce the nonhomogeneity of the combustion process, and, therefore, reduce the level of the exhaust emissions. For aircraft engines and small industrial gas turbines, the diffuser-combustor section adopts an in-line design where air from the dump chamber flows around the dome of an annular combustor (e.g., Fishenden and Stevens, 1977; Stevens et al., 1978; Carrotte et al., 1993). As a result of the in-line geometry, air is distributed relatively uniformly to the combustor. However, overall machine length impacts the turbine package size and rotor dynamics, and, thus, is an important design issue in heavy-frame industrial gas turbines. To minimize machine length, reverse-flow diffusers with can-annular combustors are generally used. In reverse-flow diffusers, air from the annular pre-diffuser turns approximately 150 deg before entering the combustors and must maneuver around the combustor and the transitional piece. As a result, the flow characteristics of these diffusers are entirely different from those of in-line diffusers.

Relatively few experimental studies have been performed on dump diffusers with flow reversal. In an earlier study, the authors experimentally investigated, in the same facility as used in this study, detailed three-dimensional flow characteristics and aerodynamic performance in the diffuser-combustor section (Kapat et al., 1996). They discovered that most flow tended to move toward the outer part (away from the gas turbine center axis) of the dump diffuser. As a consequence, more flow entered

[1] J. Kapat is currently at the University of Central Florida.

Contributed by the International Gas Turbine Institute and presented at the International Gas Turbine and Aeroengine Congress and Exhibition, Stockholm, Sweden, June 2–5, 1998. Manuscript received by the ASME Headquarters April 1, 1998. Paper No. 98-GT-102. Associate Technical Editor: R. Kielb.

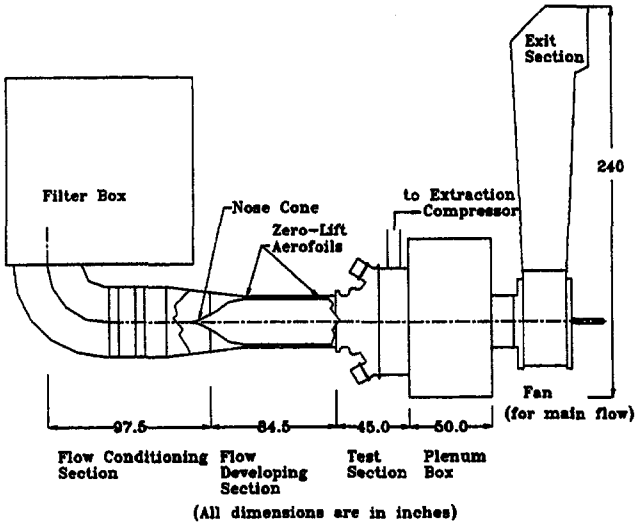

Fig. 1 Layout of test facility

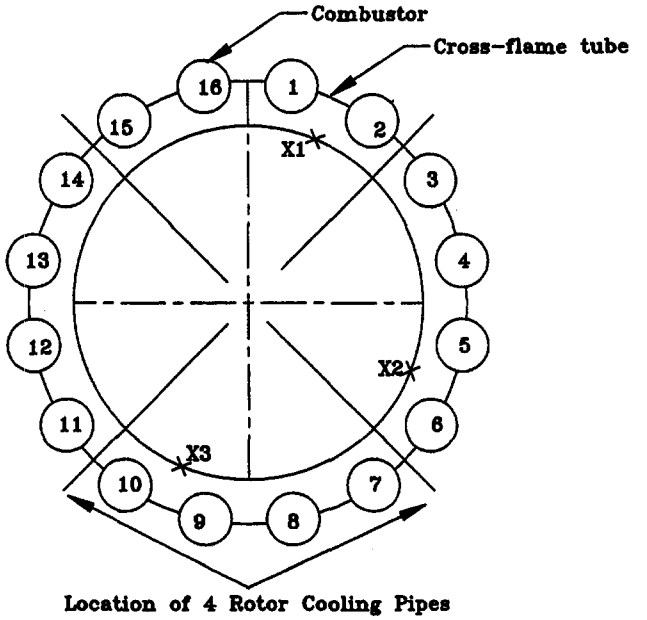

Fig. 3 Circumferential layout of air extraction locations X1, X2, and X2. Each circle represents the inlet cross section of a combustor and is shown in detail in Fig. 6

the combustor from the outer portion (away from the gas turbine center axis) of each combustor. A concurrent CFD study conducted by Zhou et al. (1996) provided a more detailed flow pattern, which helped to improve the understanding of the extremely complex three-dimensional flow interactions between the dump diffuser and the combustor inlet flow characteristics. The experimental results, although not as detailed as the CFD results, were necessary for verifying and interpreting the CFD results. The nonuniform flow distribution, discovered by both experimental and computational studies, prevailed in all the combustors. In this study, this is identified as the "local nonuniformity" since it considers nonuniformity in the local flow field entering each individual combustor rather than the bulk distribution of mass flow to all of the combustors.

As air extractions are needed for cooling and/or for integrated gasification of combined cycle (IGCC), the flow characteristics become more complex and nonaxisymmetric. Kapat et al. (1994) have reported the effect of air extraction on diffuser performance for another manufacturer's industrial gas turbines. They reported that use of a single port for extracting air adversely affects the cooling of the transition pieces of the gas turbine. It was discovered that some cooling air is sucked outward from the transition piece cooling holes by the extraction force instead of impinging on the transition pieces as originally

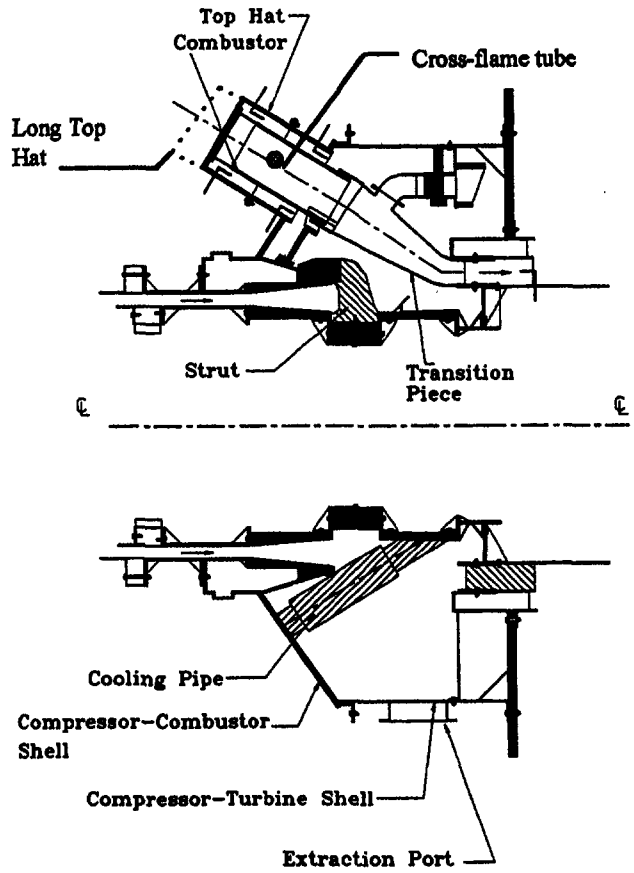

Fig. 2 Sub-scale test model

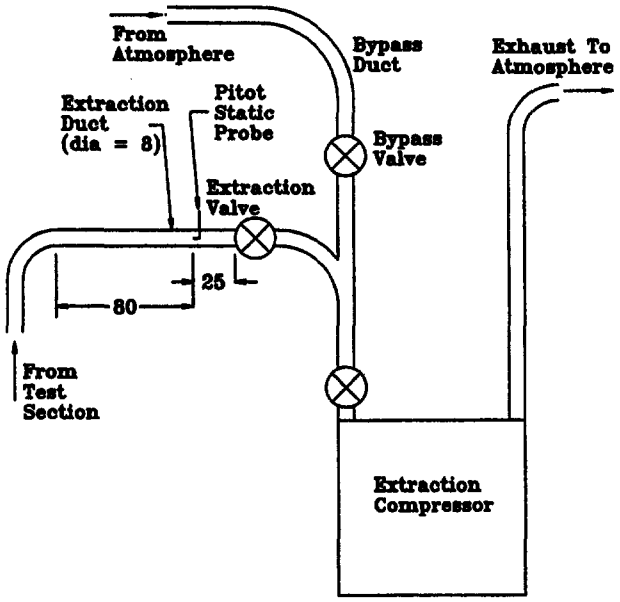

Fig. 4 Bypass duct for controlling the air extraction rate

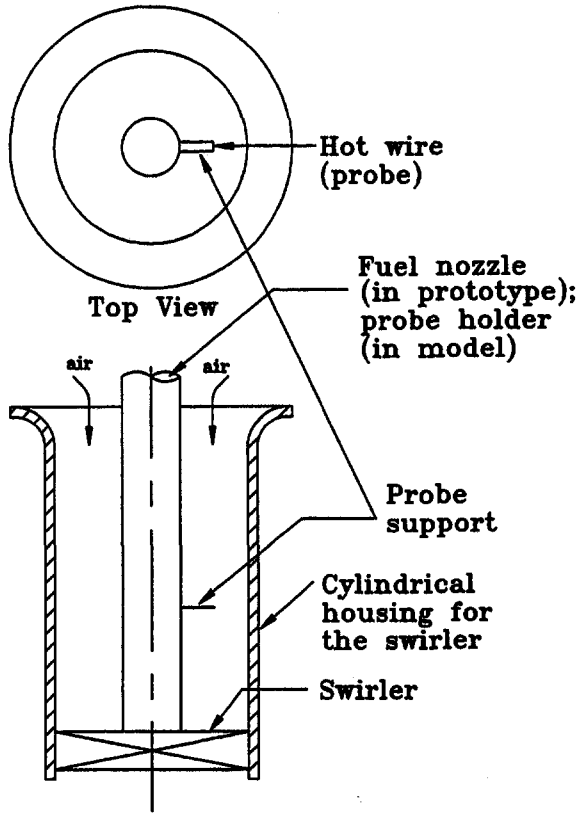

Fig. 5 Instrumentation of hot-wire sensor in the fuel nozzle-swirler assembly

designed. Later, Kapat et al. (1997) conducted experiments in the same facility used in this study and discovered that there was approximately a 35 percent mass flow nonuniformity occurring between the combustor located near the extraction port and away from it. This nonuniformity of overall air flow between combustors produced by single-port air extraction is identified as "global nonuniformity" in this paper.

Evidence both from the inherent local nonuniformity due to the design of the existing diffuser-combustor configuration and global nonuniformity generated by air extraction motivated the present study to investigate the local flow distribution at the combustors' inlets.

The following three different conditions were studied: 0 percent (baseline), 5 percent (for airfoil cooling), and 20 percent (for coal gasification). The air extractions were made at the dump diffuser outer wall (sometimes referred to as the combustor shell). The flow uniformity was investigated for the following two aspects: (a) global uniformity that compared the mass flow rates of combustors at different locations relative to the extraction port, and (b) local uniformity that examined the circumferential flow distribution of each combustor including the local flow distribution surrounding each of the swirlers at the combustor inlet.

Although a specific geometry was selected for the present study, the results should provide sufficient generality for improving understanding of the complex flow behaviors in the reverse-flow-type diffuser-combustor sections of industrial gas turbines with/without air extraction.

Experimental Program

Test Facility. The desired air flow through the test model was provided by an open-circuit, suction-type wind tunnel. The overall layout is shown in Fig. 1. Air from the test section went into a plenum box that was maintained at $-40''$ H_2O gage pressure by a suction fan rated at 15.6 m^3/s (33,000 cfm) at 9.65 kPa (1.4 psi) and driven by a 220 hp motor. The plenum box isolated the test section from vibrations or oscillations of the fan and provided the necessary work space for installing a probe traversing system and changing the instrumentation. A detailed description of the experimental facility is provided in Kapat et al. (1996a).

Test Section. Figure 2 shows a sectional view of the test section. A 48 percent sub-scale, 360 deg model of the diffuser-combustor section of a developmental heavy-frame gas turbine was constructed. The selection of a 360 deg model was necessary to investigate the effect of asymmetric air extraction (for cooling or IGCC) on the flow patterns in this study.

Before entering the model, the flow traveled through a straight annular section used to condition the flow. At the end of the developing section, the flow entered the annular prediffuser where it decelerated before being discharged into the dump diffuser.

After entering the dump diffuser, the air turned approximately 150 deg, maneuvered around the transition pieces and combustors, and entered the annular passage between the combustor and the top hat (Fig. 2). The annular passage in the top hat helped to distribute the flow before it turned approximately 180 deg and entered the combustor. After passing through the combustor and the transition piece, the flow was exhausted into a plenum.

The dump diffuser in this test model contained all the components in the actual engine including the cooling pipes and support struts. The annular passages in the top hats around the combustors contained the combustor cross-flame tubes with their complex angles to the flow maintained. In the actual engine, cross-flame tubes are used to sequentially ignite the combustors by circumferentially conducting flame through the tubes. The transition pieces were vacuum-formed to match the outer contours of the actual engine transition pieces. Cooling holes were drilled in the transition pieces such that the fraction of cooling air flow entering the transition piece lining was identical to that expected in the actual engine. Geometric similarity between the prototype and the model was maintained everywhere. One of the combustors was a true scaled model fabricated with all the swirlers and fuel injectors in place. The other fifteen mock combustors were fabricated with a circular orifice being placed at the combustor inlet. The diameter of the orifice for each combustor was calibrated to render the same drag

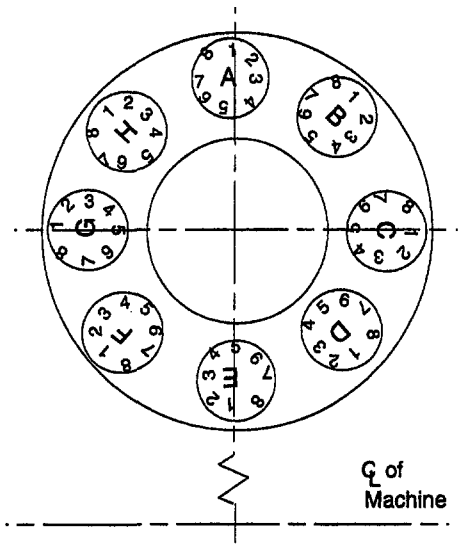

Fig. 6 End view of combustor inlet showing hot-wire measurement locations at inlet of each of the eight swirlers

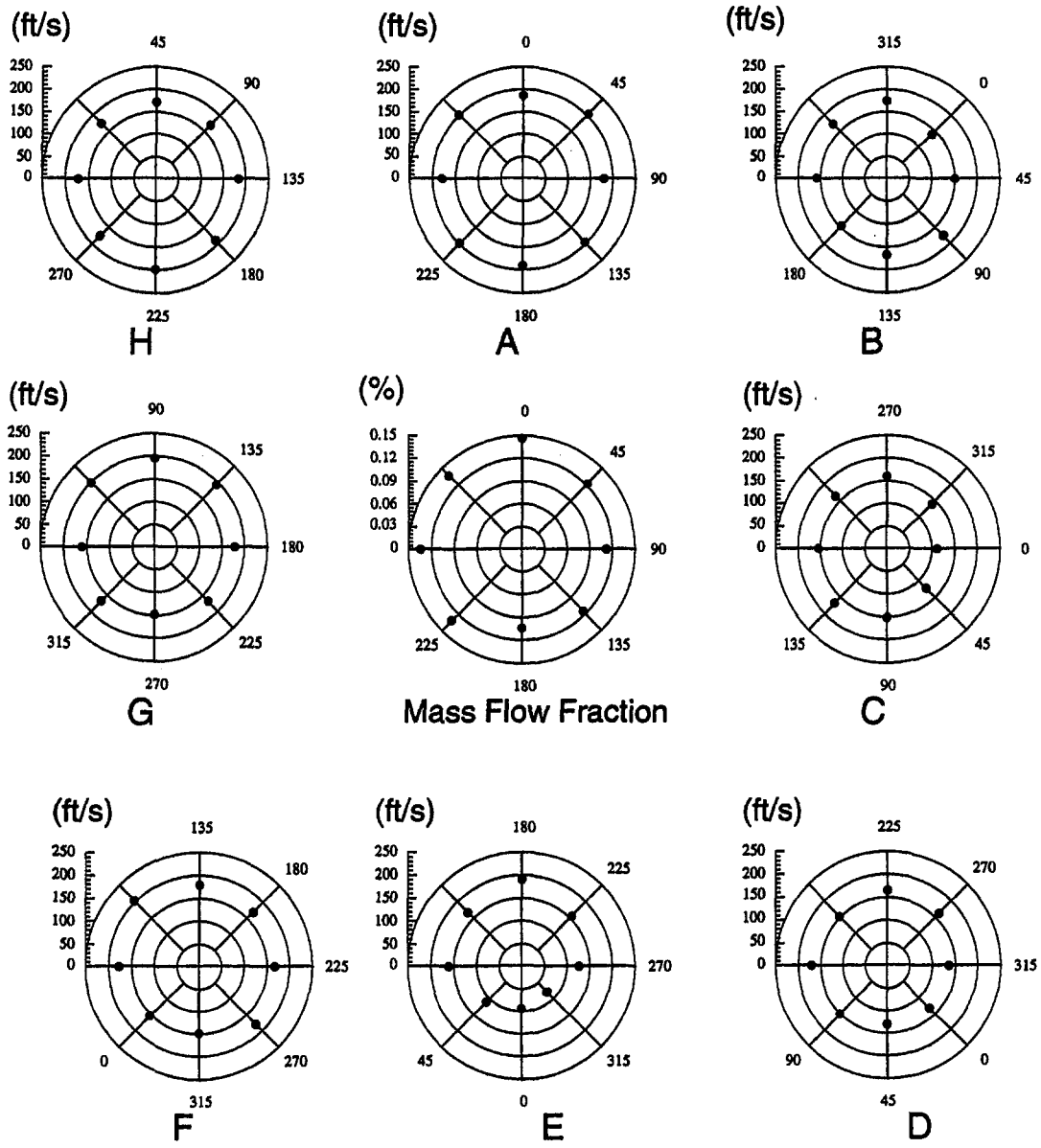

Fig. 7 Local and overall combustor inlet flow distribution of case S012 (short hat, no extraction, test 1 at combustor 2)

coefficient as the "true scaled" model at various flow speeds. Detailed information on the test section and calibration of the combustor pressure loss coefficient is described in Kapat et al. (1996).

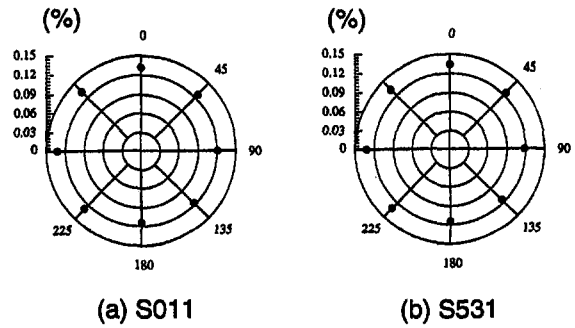

Fig. 8 Overall combustor inlet flow distribution for cases S011 and S531

Top Hat Length. To investigate if more room in the top hat area can promote better flow mixing, longer top hats with twice the mixing space of the existing design were installed for a portion of the experiment. The mixing space is the space between the end of the top hat and the inlet of the combustor.

Air Extraction. The extraction ports were located on the outer casing around the dump diffuser as indicated in Figs. 1 and 2. Three different extraction ports (X1, X2, and X3) situated 90 deg apart circumferentially were built into the test section (see Fig. 3). Only one of these ports was used at a time for extraction. By extracting air at different circumferential locations while taking measurements at the same locations, circumferential variation of the effects of extraction was studied with minimal instrumented sites.

The extraction duct was equipped with a pitot-static probe that was used to monitor the air flow rate through the extraction duct. The desired flow rate through the extraction duct was achieved using both the extraction and the bypass ducts (Fig. 4). Small adjustments in the flow rate were performed by adjusting the extraction valve. However, for large variations the

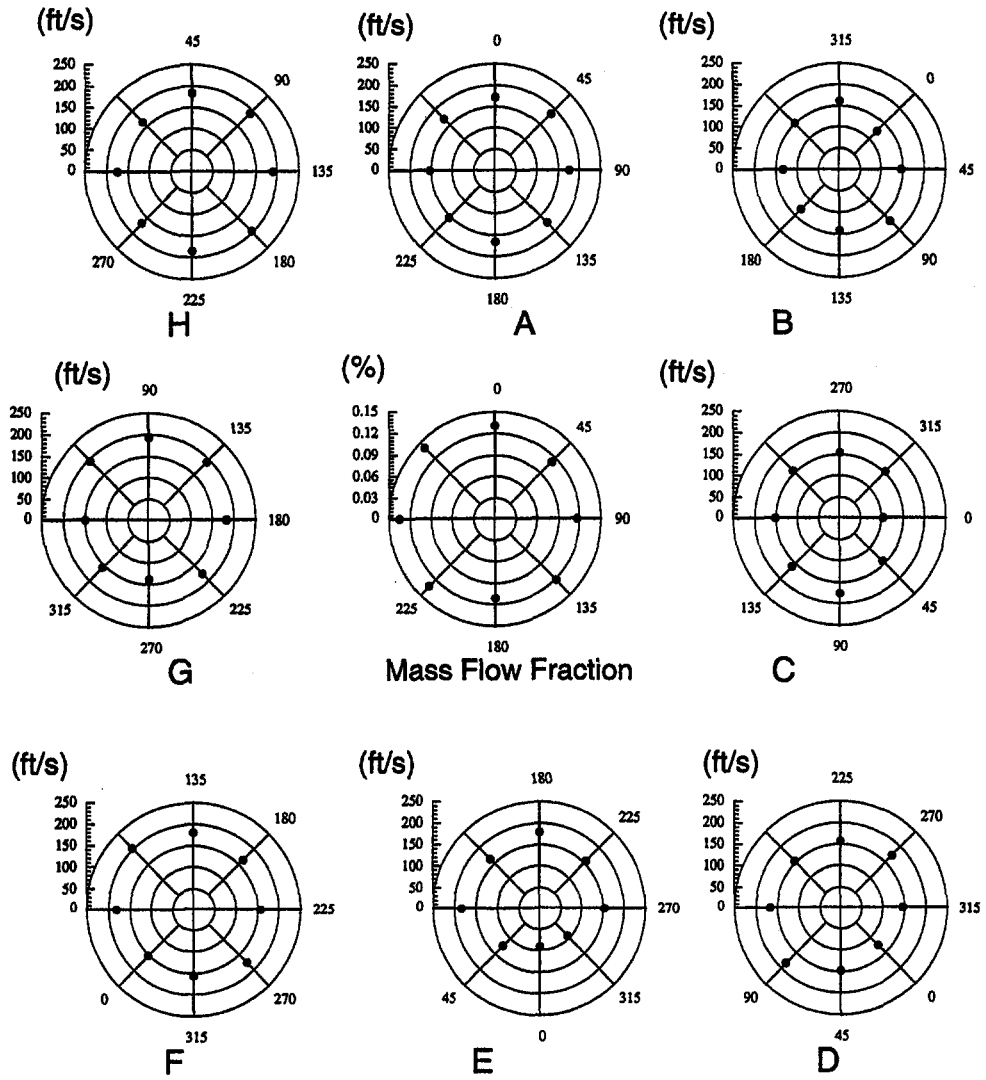

Fig. 9 Local and overall combustor inlet flow for case S512 (short hat, 5 percent extraction, test 1 at combustor 2)

bypass valve was used to maintain the total flow rate through the extraction compressor within the operating range. The extraction compressor is comprised of six stages and was rated at 2.36 m^3/s (5,000 cfm) at 0.34 bars (5 psia).

For different combination openings of the extraction and/or bypass valves, the pitot-static probe was traversed inside the duct, and velocity profiles were obtained. By integrating the profiles, the corresponding flow rates were calculated.

During the main experiments with 5 percent or 20 percent extraction, one of the three extraction ports X1, X2, and X3 was connected to the extraction duct. First, the main flow through the test section was adjusted with the extraction valve closed. Then, the extraction flow rate was obtained by adjusting the extraction and/or bypass valves. Since the adjustment of the extraction flow rate affected the main flow rate, the main flow needed adjustment again, and the process was repeated until both main and extraction flow rates were at the desired values. The process was repeated for each of the other two extraction ports.

Experimental Cases. Each experimental case was assigned a four digit number. The meaning of each digit is as follows:

First digit. "S" or "L" represents short or long top hats.

Second digit. "0, 5, or 2" represents zero, 5 percent, or 20 percent air extraction respectively.

Third digit. (i) for the baseline case, it represents the number of test runs, e.g., 1 is the first run and 2 is the repeated run; (ii) for the extraction cases, it represents the location of extraction ports X1, X2, or X3.

Fourth digit. The fourth digit represents the instrumented combustor 1 or 2 which is located away or near the rotor cooling pipe, respectively (see combustor 1 or 2 in Fig. 3). For example, S012 represents short top hat baseline case (0 percent air extraction) at first test run for combustor number 2 that is located adjacent to the rotor cooling pipe. S022 is the repetitive run of S012. L232 represents long top hat case with 20 percent air extraction applied at extraction port X3 for combustor 2. There were a total of 24 test cases conducted.

Instrumentation and Measurements. A custom-made tungsten hot wire, 2.5 μm in diameter, was used to measure the flow distribution at the combustor inlet. The measurements were performed in the only combustor that was a true scaled model of the prototype containing eight swirlers housed within eight circular ducts through which combustion air has to flow before mixing with the fuel. In the true scaled combustor model, fuel nozzle models were fabricated with plexiglas cylindrical rods, which were situated at the middle of the cylindrical duct. Only one of the eight fuel nozzles was instrumented with a hot wire

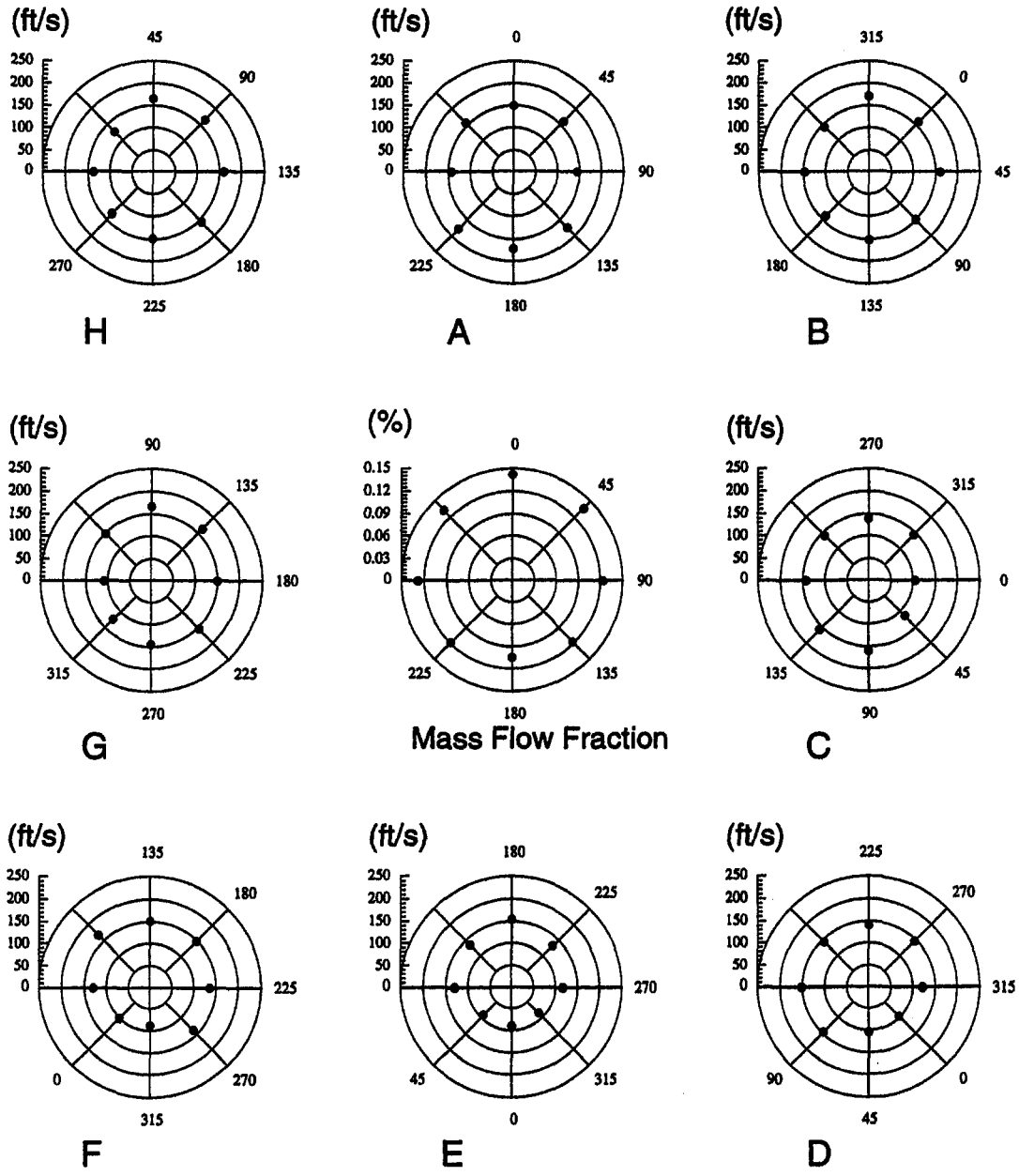

Fig. 10 Local and overall combustor inlet flow for case S212 (short hat, 20 percent extraction, test 1 at combustor 2)

sensor which was placed approximately 4 mm from the fuel nozzle surface and 5 mm upstream of the corresponding swirler as shown in Fig. 5. The fuel nozzle can be rotated around its own axis so the hot wires can measure at any circumferential angle. For each swirler location eight angular locations at a 45 deg interval (numbered 1 to 8 in Fig. 6), were measured. The hot-wire measurements were performed one at a time at each of the eight swirler ducts. Similar measurements were then made on the rest of the seven swirlers by rotating the fixture that held the eight fuel nozzles to the appropriate locations. Each test case was completed when 64 measurements were made. For

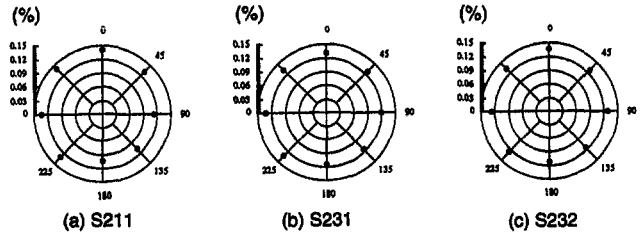

Fig. 11 Overall combustor inlet flow distribution for cases (*a*) S211, (*b*) S231, and (*c*) S232

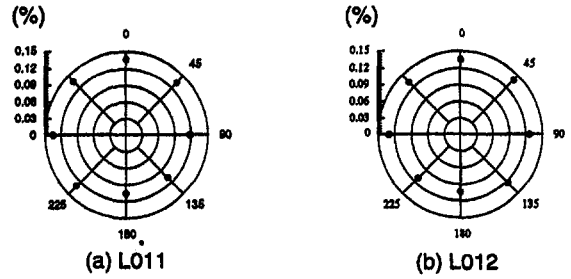

Fig. 12 Overall combustor inlet flow distribution for cases (*a*) L011 and (*b*) L012

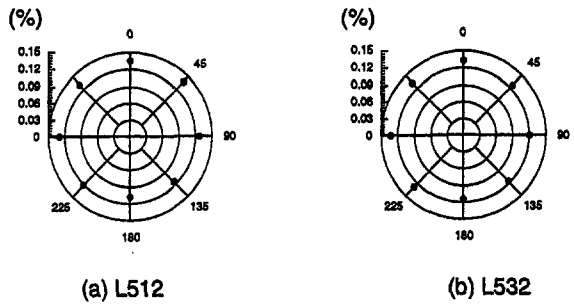

Fig. 13 Overall combustor inlet flow distribution for cases (*a*) L512 and (*b*) L532

the first case (S011), the measurements were repeated at two different sampling rates: 2000 Hz for three seconds and 200 hz for 30 seconds. The difference of the mean velocities between the two sets was less than 2 percent. For this reason, in the rest of the cases, measurements were taken at 200 Hz for 30 seconds.

A constant temperature hot-wire anemometer, IFA-100, made by TSI, Inc. was used. The hot-wire sensor was calibrated against a pitot-static tube in a separate calibration wind tunnel over similar ranges of air velocities. The temperature difference between the calibration and operating conditions was corrected during data reduction process.

The overall mass flow rate entering each swirler in Fig. 6 was calculated by integrating eight circumferential measurements and the overall mass flow rate of each combustor was calculated by adding the mass flow rate of each swirler. Figure 6 is drawn as the flow enters the paper. The top of Fig. 6 is away from the turbine axis.

Experimental Uncertainty. For each of the baseline cases, at least two replications were performed. The third replications were further performed for cases S011, S021, and L011. Uncertainty due to replications for different locations varied from 1.5 percent to 8 percent with the average at 3.5 percent.

Results and Discussion

Short Top Hat, No Air Extraction (Baseline Cases). The flow distribution results of S012 are shown in polar coordinates in Fig. 7 with an arrangement matching that of Fig. 6. The scale of each concentric circle is in velocity (ft/s) on the left-hand side of each polar diagram. Each polar diagram represents the local flow distribution around a swirler. Integra-

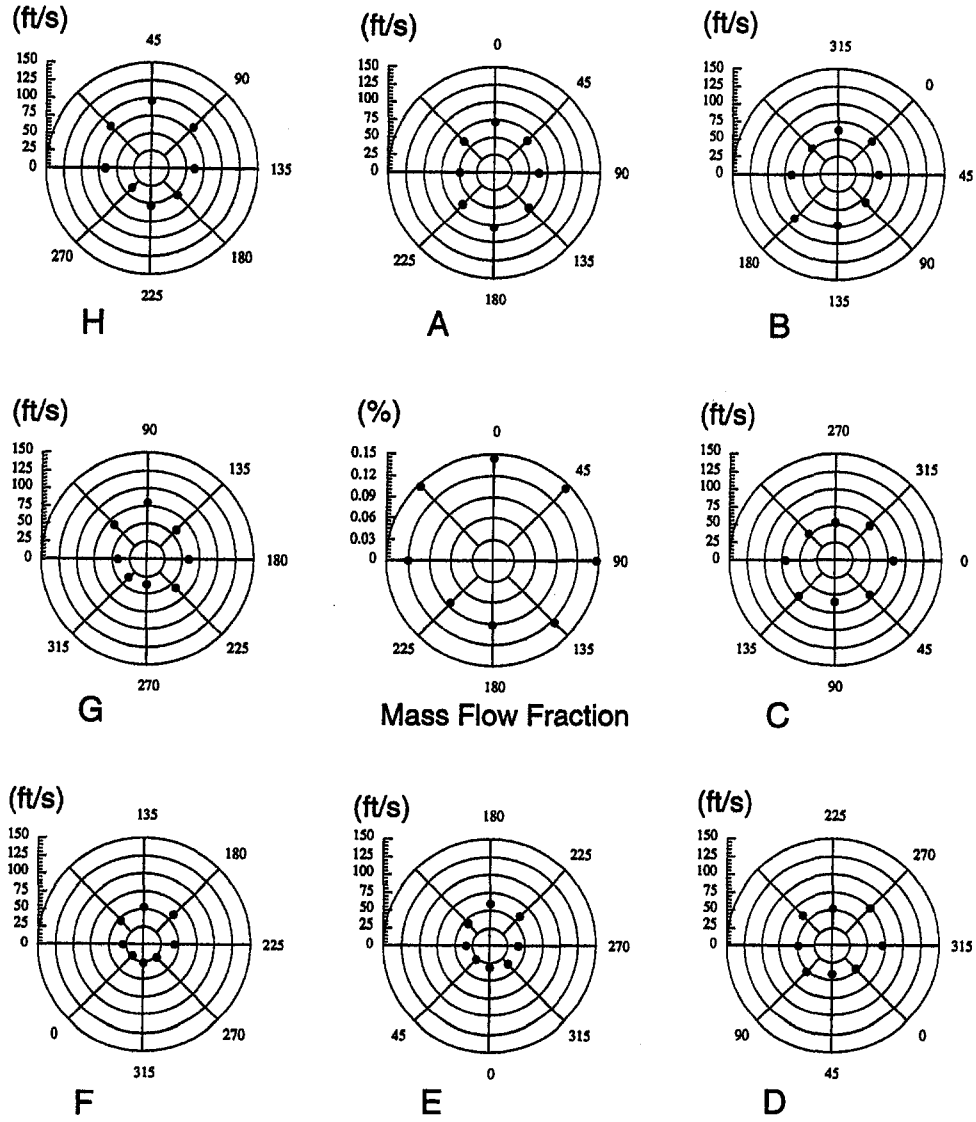

Fig. 14 Local and overall combustor inlet flow for case L212 (long hat, 20 percent extraction, test 1 at combustor 2

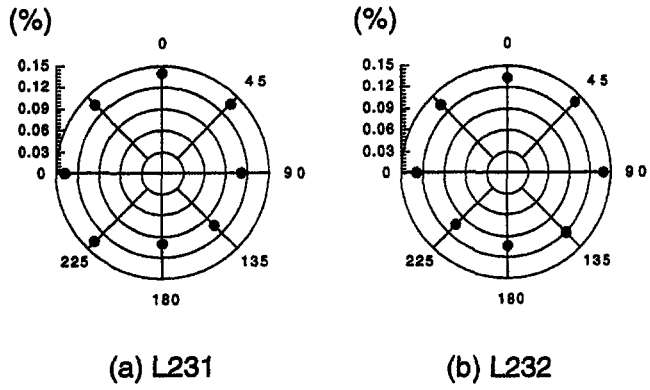

Fig. 15 Overall combustor inlet flow distribution for cases (*a*) L231 and (*b*) L232

tion of the mass flow rate of each swirler gave the total mass flow rate of that swirler and was represented as a single dot in the central polar diagram in terms of fraction of total mass flow rate of the combustor. The central polar diagram represents the overall mass flow distribution in the combustor. Since the density and representative area of each point are the same, the velocity is shown in the figures instead of mass flow rate.

It can be seen in Fig. 7 that swirlers A and H had better uniformity than other swirlers. Swirler E had the worst nonuniform distribution. Most swirlers had more flow in the inner portion; this was specifically true for swirlers C, D, and E. The overall distribution, shown in the central diagram, indicated that there were approximately 20 percent more flow in the region covered by swirlers G, H, A, and B (upper-left half circle from 225 deg to 45 deg) than the lower-right half circle covered by swirlers C, D, E, and F. This case (S012) was measured at combustor 2, which is closer to the rotor cooling pipe. The effect of rotor cooling pipe to flow distribution can be obtained by comparing the results with those of case S011. The results of S011 had a similar trend in local (not shown) and overall distributions (Fig. 8(*a*)) as S012 (see Fig. 7) but approximately one half less nonuniform in overall distributions than S012.

Short Top Hat, 5 Percent Air Extraction. The effect of 5 percent air extraction for case S512 was shown in Fig. 9. Comparison between Figs. 7 and 9 did not reveal much difference, except that swirlers A and B had approximately 3 percent less flow than the baseline case. This indicates that the effect of 5 percent air extraction on the combustor flow distribution is negligible. The similarity of the local distribution of corresponding swirlers between Fig. 7 and 9 also validated a good repeatability of the test results within a span of three months. Although the effect of 5 percent air extraction is not significant, other 5 percent air extraction cases, for example, case S531, with air being extracted at port X3 that was located diametrically from the combustor did show some variations on local flow distributions of swirlers D and E (not shown). This indicated that the air extraction could marginally affect the inner part of the combustor (i.e., swirlers D and E) diametrically across the dump diffuser. However, the overall combustor flow distribution of case S531 (Fig. 8(*b*)) is similar to case S512 (central diagram in Fig. 9).

Short Top Hat, 20 Percent Air Extraction. The effect of 20 percent air extraction was significant, which can be seen by comparing case S212 in Fig. 10 with the baseline case S012 in Fig. 7. Case S212 had air extraction employed at port X1 located close to combustor 2 near one of the rotor cooling pipes. The most obvious difference is that flow is significantly retarded in the outer portion (the quadrant 45 deg - 0 deg - 315 deg) of every swirler. For example, the velocities at 0 deg and 45 deg reduced from 135 ft/s at swirler D in Fig. 7 to approximately 100 ft/s in Fig. 10; similarly, at the same quadrant of swirler F, velocities were reduced from 145 ft/s in Fig. 9 to 95 ft/s in Fig. 10. Although the 20 percent air extraction significantly distorted the local distribution of each swirler, the nonuniformity of overall mass flow rate distribution (central diagram in Fig. 10) was about the same as that in the baseline case shown in Fig. 7.

The effect of the rotor cooling pipe can be seen by comparing the results of combustor 1 of case S211 (Fig. 11(*a*)) with those of case S212 (Fig. 10). The comparison indicated that the rotor cooling pipe had affected the local flow distribution of each swirler (not shown) but had negligible effect on the overall combustor flow distribution (Fig. 11(*a*)). Both cases (S211 and S212) had approximately 15 percent more flow in the upper-left half circle (including swirlers G, H, A, and B) than the lower half of the circle (including swirlers C–F).

The effect of the distance from the air extraction port can be seen by comparing cases S232 (Fig. 11(*c*)) and S212 (Fig. 10). When the air extraction was changed to port X3, the distortion of local flow distribution that appeared in case S212 (Fig. 10) could still be seen in the outer portion (the quadrant 45 deg – 0 deg – 315 deg) of every swirler in case S232 (not shown). The uniformity of the overall combustor mass distribution of case S232 (Fig. 11(*c*)) was, however, approximately within 8 percent between the upper-left and lower-right half circles; this was better than the 15 percent nonuniformity for case S212 (central diagram in Fig. 10). The improved flow uniformity in case S232 could be explained as follows: when the air was extracted diametrically across the dump diffuser, the flow moving toward outer part of the dump diffuser (away from the turbine axis) experienced an opposite force from the low pressure site near port X3; therefore, the flow on the upper half of the combustor reduced and overall flow distribution improved. The mass flow for the lower half of the combustor was also affected by the extraction; however, since the rotor cooling pipe had already exerted resistance to the flow moving toward the lower portion of the combustor, the effect from the suction became less.

The effect of rotor cooling pipe with air extraction diametrically across the dump diffuser can be seen from the comparison between case S231 and S232 (Fig. 11(*b*) and 11(*c*)). With air being extracted at port X3, the flow distribution of combustor 1 of case S231, which was away from the rotor cooling pipe, showed better local flow uniformity at each swirler (not shown) than for case S232 (not shown). This was expected and was consistent with the results of baseline cases, which showed that combustor 1 had more uniform local flow distribution than combustor 2. The overall distribution of case S231 became a little worse, however, with 10 percent more flow in the upper-left portion of the combustor 1 (Fig. 11(*b*)) compared to 8 percent of the combustor 2 in case S232 (Fig. 11(*c*)). A plausible explanation for this unexpected result could be that combustor 1 was away from the rotor cooling pipe, and the flow near the lower half of the combustor 1 was closer to port X3, so the suction force at X3 reduced flow more in the lower half of the circle. Nevertheless, a 2 percent difference was not that much, so this explanation should not be treated, however, as an absolute fact.

Long Top Hat, No Air Extraction. To improve the flow uniformity, longer top hats were installed based on the hypothesis that increasing the size of the end zone of the top hat may provide a longer time for better mixing. The results of overall combustor flow distribution for cases L012 and L011, using the long top hats without air extraction, are shown in Fig. 12. When they are compared with the corresponding short top hat cases of S012 (Fig. 7) and S011 (Fig. 8), there seems to be no significant changes even though the short top hats were replaced with the longer ones. Both L012 and L011 (Fig. 12) cases have

approximately 15 percent more flow in upper-left half circle (from 225 deg to 45 deg) than in the lower-right half circle.

Long Top Hat, 5 Percent Air Extraction. Long top hats somehow affect the local flow distributions for each swirler (not shown here) with 5 percent air extraction. As a consequence, the overall flow distributions for cases L512 and L532 (Fig. 13) also changed. In the short top hat cases of S531 (Fig. 8) and S512 (Fig. 9), 15 percent more flow enters the combustor in the upper-left half circle from 225 deg to 45 deg than in the lower half circle. The longer top hats shift the higher flow region to the upper half circle (from 270 deg to 90 deg). The flow uniformity is improved a bit, from 15 percent nonuniformity in case S512 (Fig. 9), to 10 percent in case L512 (Fig. 13), but maintains the same 15 percent nonuniformity between cases S531 (Fig. 8) and L532 (Fig. 13).

Long Top Hat, 20 Percent Air Extraction. The effect of long top hat on the local flow distribution at each swirler can be seen by comparing case S212 (Fig. 10) and case L212 (Fig. 14). No specific pattern is observed and no clear improvement of uniformity around each swirler is observed. By comparing the central diagrams in Fig. 10 and Fig. 14, the overall combustor flow distribution becomes less uniform in the long top hat case L212 than in the short top hat case S212. The S212 case has 15 percent more flow in the upper half circle (270 deg - 0 deg - 90 deg), whereas the L212 case has 25 percent more flow in the upper-right half circle (315 deg - 0 deg - 135 deg).

When air extraction was employed at port X3, the long top hats did not improve the flow uniformity, which can be seen by comparing case S232 and S231 (Fig. 11) with cases L232 and L231 (Fig. 15). Both S231 and L231 have about 9 percent nonuniformity. However, the long top hat makes flow less uniform in case L232 that has 16 percent more flow in the upper half circle (270 deg - 0 deg - 90 deg) than case S232 that has 8 percent more flow in the upper-left half circle (225 deg - 0 deg - 45 deg).

From all the long top hat cases presented above, increased top hat size does not improve the flow uniformity, and may even make flow become less uniform. Therefore, the employment of long top hats is not recommended.

Suggestions for Improvement

Since large top-hats did not improve airflow uniformity as was initially hypothesized, other possible means under consideration are listed as follows:

(a) *Uniform Resistance Method*—provide circumfrentially varying resistance in the top hat to counteract the effect of uniform flow resistance in the dump diffuser. The following three possible ways are suggested: (i) vary the width of the flow passage circumfrentially, (ii) add screen or honeycomb, (iii) add a long flow shield extending from the top hat radially into the dump diffuser.

(b) *Mixing Method*—install turbulators near the combustor inlet to promote mixing.

Conclusions

An experimental study was performed in a 48 percent scale, 360 deg model of the diffuser-combustor section of a developmental industrial gas turbine to investigate (a) the combustor inlet flow distribution in the reversed-flow type dump diffuser and (b) the effects of various air extractions for cooling (5 percent) and gasification (20 percent) on uniformity of the flow entering the combustors. The results indicated that even at the baseline case with no air extraction there was an inherent local flow nonuniformity of 10 $\sim$ 20 percent at the inlet of each combustor due to the complex flow field in the dump diffuser and the blockage effect of the cross-flame tube. The combustors near the rotor cooling pipes have less uniformity than those away from the cooling pipes. More flow was seen in the portion further away from the gas turbine center axis. The effect of 5 percent air extraction was small. Twenty percent air extraction introduced approximately 35 percent global flow asymmetry diametrically across the dump diffuser. The effect of air extractions on the local flow uniformity of the combustors varied with the distances between the extraction port and each individual combustor. The most obvious difference is that flow is significantly retarded in the outer portion (the quadrant 45 deg - 0 deg - 315 deg) of every swirler. Although the 20 percent air extraction significantly distorts the local distribution of each swirler, the nonuniformity of overall mass flow rate distribution is about the same as that in the baseline case. This nonuniformity could be alleviated by extracting the air necessary for gasification at more than one locations.

Longer top hats were installed with the initial intention to increase flow mixing. The results indicated that the longer top hats do not improve the flow uniformity. It was concluded that the degree of flow uniformity at the combustor's inlet was critical to the combustion uniformity and consequently emissions. It should be examined and improved for each gas turbine model. Although a specific geometry was selected in this study, the results provide sufficient generality to benefit other industrial gas turbines.

Acknowledgment

The authors wishes to thank Mr. Michael Thom for his help in constructing the experimental facility and the test model. This work was supported by the Morgantown Energy Technology Center of the U.S. Department of Energy through DOE/METC contract No. DE-AC21-93MC30247. The authors also wish to thank Dr. Richard A. Johnson at the Morgantown Energy Technology Center for his guidance in this program.

References

Kapat, J. S., Agrawal, A. K., and Yang, T. T., 1994, "Air Extraction in a Gas Turbine for Integrated Gasification Combined Cycle (IGCC): Experiments and Analysis," ASME Paper 94-GT-193.

Kapat, J. S., Wang, T., Ryan, W. R., Diakunchak, I. S., and Bannister, R. L., 1996, "Cold Flow Experiments in a Sub-Scale Model of the Diffuser Combustor Section of an Industrial Gas Turbine," ASME Paper 96-GT-518.

Kapat, J. S., Wang, T., Ryan, W. R., Diakunchak, I. S., and Bannister, R. L., 1997, "Experimental Studies of Air Extraction for Cooling and/or Gasification in Gas Turbine Applications," ASME JOURNAL OF ENGINEERING FOR GAS TURBINES AND POWER. Vol. 119, pp. 807–814.

Lefebvre, A. H., 1983, *Gas Turbine Combustion,* Hemisphere Pub. Corp., Washington, DC.

Lyons, V., 1981, "Effect of Fuel-Air-Ratio Nonuniformity on Emissions of Nitrogen Oxides," NASA TP 1798.

Welz, J. P., 1986, "An Algorithm for Using the Five-Hole Probe in the Non-Nulled Mode," AIAA/ASME 4th Fluid Mechanics, Plasma Dynamics and Lasers Conference, Atlanta, May 11–14, FED-Vol. 34, pp. 9–12.

Wilson, D. G., 1984, *The Design of High-Efficiency Turbomachinery and Gas Turbines,* MIT Press, Cambridge, MA.

Zhou, D., Wang, T., and Ryan, W. R., 1996, "Cold Flow Computations in a Sub-Scale Model of the Diffuser-Combustor Section of an Industrial Gas Turbine," ASME Paper 96-GT-513.

C. Storm
e-mail: storm@ivd.uni-stuttgart.de

H. Rüdiger

H. Spliethoff

K. R. G. Hein

Institut für Verfahrenstechnik und Dampfkesselwesen,
(Institute for Process Engineering and Power Plant Technology)
University of Stuttgart,
Pfaffenwaldring 23,
D-70569 Stuttgart,
Germany

Co-Pyrolysis of Coal/Biomass and Coal/Sewage Sludge Mixtures

Biomass and sewage sludge are attracting increasing interest in power plant technology as a source of carbon-dioxide-neutral fuels. A new way to reduce the consumption of fossil fuels could be the co-combustion or co-gasification of coal and biomass or coal and sewage sludge. In both cases, pyrolysis is the first step in the technical process. In order to obtain detailed information about the pyrolysis of coal/biomass and coal/sewage sludge mixtures as well as unblended fuels, the "Institut für Verfahrenstechnik und Dampfkesselwesen (IVD)" at the University of Stuttgart has carried out investigations using an electrically heated entrained flow reactor. The test runs provided information about fuel conversion efficiency, pyrolysis gas and tar yield, and composition of pyrolysis gas and tar. Besides gas and tar analysis investigations regarding the path of trace elements, like heavy metals, alkali, chlorine and nitrogen components, during the pyrolysis process varying different parameters have been carried out. The fuel nitrogen distribution between pyrolysis gas, tar, and char has been analyzed, as well as the ash composition, and, thus, the release of mineral components during pyrolysis.

Introduction

Various forms of biofuels, including biomass and sewage sludge, represent an interesting feedstock for combustion and gasification processes in power plant technology as a source of CO_2-neutral fuels. An estimation of available biomass for thermal use is given in [1]. Biomass has a potential of about 660 PJ (1 Petajoule = 10^{15} Joule). This is equivalent to about 5 percent of the annual primary energy consumption in Germany.

A refined purification of municipal (and industrial) waste water results in an increasing yield of sewage sludge. In 1991 about 2.5 Mt (dry matter) sewage sludge was produced in Germany [2] and about 19 Mt in the European Community [3]. Disposal of sewage sludge in Germany (1991) was carried out by [4] the following:

- dumping (56%)
- agricultural using (29%)
- incineration (15%)

Due to tightening restrictions regarding the disposal of sewage sludge, an increasing share of thermal use of sewage sludge is to be expected.

The application of gasification or pyrolysis processes in power plant technology using biofuel as feedstock could start with the co-feeding of a certain amount of biomass or sewage sludge together with the main fuel coal. To obtain information on the influence of biofuel on the pyrolysis process, pyrolysis of several fuel mixtures has been investigated.

One aim of the research was to determine the impact of biomass and sewage sludge as co-feedstocks in coal pyrolysis processes. IVD studied the pyrolysis of biomass together with a high volatile coal as main fuel. The experiments were carried out in a small-scale electrically heated entrained flow reactor.

The main parameters to be investigated were the wall temperature of the pyrolysis reactor (up to 1200°C) and the coal/biofuel ratio. It was expected that the high reactivity of the biomass would result in a higher yield of pyrolysis gas. An effect on the production of tar components was also expected. The test runs have provided information about fuel conversion efficiency, pyrolysis gas and tar yield, composition of pyrolysis gas and tar, and fuel nitrogen distribution between pyrolysis gas, tar, and char.

The same experiments have been carried out with a mixture of sewage sludge and high volatile coal.

Another part of the research was also to determine suitable pyrolysis char compositions for further use in different processes with simultaneous generation of a pyrolysis gas with a high NO_x reducing potential. Detailed results of the investigations using pyrolysis gas from coal [5], sewage sludge [6], or biomass [7] for NO_x reduction are published elsewhere. To get information about the path of different feedstock components during pyrolysis the quality and quantity of pyrolysis char depending on temperature has been analyzed [8].

Test Facility Description

The BTS (Brennstofftrennstufung/fuel splitting and reburning) test facility is a joint development by the Institut für Verfahrenstechnik und Dampfkesselwesen (IVD) and the Saarbergwerke AG, Saarbrücken, a German coal mining company and utility. The plant has been built to investigate possibility of simultaneously minimizing NO_x formation and reducing NO_x levels formed during the combustion of pulverized hard coal. The process separates coal into volatiles and residual char. These are burned in a fuel staged combustion with char as primary fuel and volatiles as reburn fuel. Results of these investigations are published for example in [9]. Pyrolysis gas from solid fuels can either be produced in an entrained flow pyrolysis reactor (50 kW_{th}) or in a fluidized bed reactor (50 kW_{th}). For investigations on NO_x reduction and reburn efficiency the generated pyrolysis gas is injected into the reduction zone of a pulverized fuel combustion reactor (50 kW_{th}) after the solid pyrolysis residuals are separated from the pyrolysis gas in a hot gas filtration unit.

The presented pyrolysis results have been gained from experiments at a bench scale entrained flow reactor (total height 2400 mm). The pyrolysis test facility consists of a fuel feeding unit, the pyrolysis reactor and a hot gas filtration. A flow schematic

Contributed by the International Gas Turbine Institute and presented at the International Gas Turbine and Aeroengine Congress and Exhibition, Stockholm, Sweden, June 2–5, 1998. Manuscript received by the ASME Headquarters April 1, 1998. Paper No. 98-GT-103. Associate Technical Editor: R. Kielb.

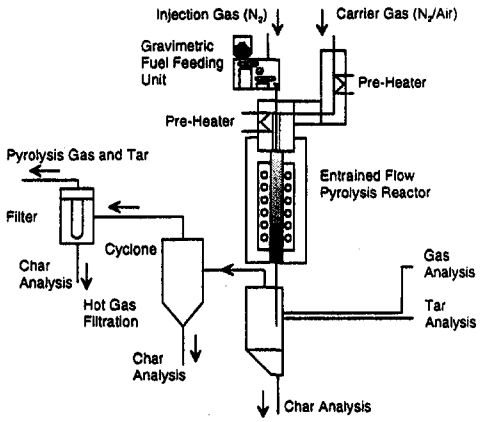

Fig. 1 Flow schematic of the entrained flow pyrolysis reactor at IVD

is shown in Fig. 1. The fuel, dosed by a gravimetric feeding unit with a capacity of 1 to 5 kg/h of fuel, enters the reactor through a water cooled burner where it is united with the carrier gas (nitrogen), which is preheated to reactor temperature (400°C to 1200°C). The reaction pipe (CrNi-steel) has a length of 2000 mm, an inner diameter of 94 mm and is electrically heated (30 kW_{el}) to a maximum reactor temperature of about 1200°C. The hot gas filtration unit consists of an ash hopper, a cyclone, and a ceramic candle filter. All pipes are heated up to 400°C to avoid tar condensing.

An important criterion in running a pyrolysis reactor is the residence time of the fuel in the reaction zone. Sinking velocities of different particles compared with the gas velocity of the laminar flow in the reaction tubes are determined according to [10]. The results show that coal and sewage sludge particles ($d_{50} \approx 40$ μm) follow the gas stream in good compliance, so the residence time can be determined by calculating the gas velocity at different operation conditions. Biomass particles have a shorter residence time because of their greater size; their sinking velocity is higher than that of coal particles. Table 1 shows the residence time of pulverized coal and the gas velocity depending on the reactor temperature. The inert gas volume was the same in all test runs, the total gas volume at operating conditions contained generated pyrolysis gas as well as the inert carrier gas.

A further criterion are the heating rates of fuel particles in the reactor. Figure 2 contains calculated particle temperatures for coal (particle diameter 100 μm) for different reaction temperatures (according to [11]). The model describes a single particle in a laminar flow, with no relative velocity against the carrier medium.

Figure 2 shows that the particles reach their final temperature after about 40 ms to 50 ms.

Sampling System Description. The pyrolysis gases CO, CO_2, H_2, C_mH_n, and O_2 were constantly connected on-line to the sampling system for all test runs. The sampling point was located at the end of the reaction tube. In addition to the analysis by the on-line sampling system, the gases were analyzed by a Unicam gas chromatographic analyzer for H_2 (TCD), C_1, C_2, C_3, and C_{5+} hydrocarbons (FID).

Table 1 Residence time of pulverized coal particles and gas velocity in the pyrolysis reactor at different reaction temperatures

reactor temperature [°C]	600	800	1000	1200
inert gas volumetric flow [m^3/h_{norm}]	4.0	4.0	4.0	4.0
total gas volumetric flow [m^3/h_{oper}]	13.4	16.7	20.8	24.6
gas velocity [m/s]	0.54	0.67	0.83	0.99
residence time [s]	3.7	3.0	2.4	2

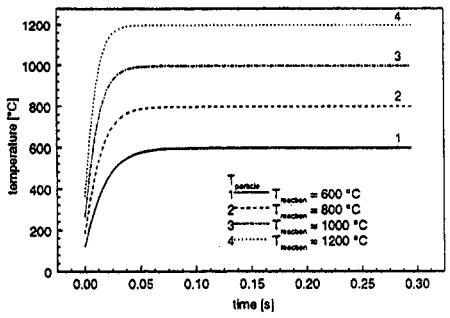

Fig. 2 Calculated particle temperatures [11]

To determine the different tar components in the pyrolysis gas, a tar sampling system has been installed. The sampling systems was situated after a short, heated and insulated stainless steel line, which was located at the gas sampling point. A flat filter (ceramic fiber paper) is used to condense heavy tars and tar aerosols. The filter is followed by an activated carbon cartridge. After the sampling, filter and activated carbon were weighed and dissolved in dichlormethane for gas chromatographic analysis (GC-MS).

The tar species are devided into two groups. The term heavy tars describes the sum of all species with a boiling point above about 200°C. These are all aromatic hydrocarbons with more than two benzene rings (naphthalene and above). The light tars are mainly benzene, toluene, and xylene. The boiling point of the compounds is below 200°C and the number of benzene rings does not exceed two.

The analyzed char samples are collected from the hot gas cleaning unit. The coarse particles come from the ash hopper, the fine char particles from the hot gas cyclone. For proximate and ultimate analyses the two samples have been mixed.

A detailed description of the test facility and the sampling system can be found in [8, 9, 12, 13].

Fundamentals

Pyrolysis (or devolatilization) is a thermal decomposition of organic matter in an inert atmosphere. The process has been well known in coal refinement (e.g., carbonization) for a long time. Pyrolysis is also the first step in combustion. The pyrolysis product composition depends on the following:

- process parameters (e.g., reaction pressure, temperature, heating rates)
- fuel parameters (e.g. moisture, particle size, fuel composition)

Main reactions. Homogeneous and heterogeneous reactions in the pyrolysis process cause a changing product composition, depending on the reaction temperature. The main reactions are

- methane gasification: $CH_4 + H_2O \Leftrightarrow CO + 3H_2$
- water gas reaction: $C + H_2O \Leftrightarrow CO + H_2$
- boudouard reaction: $C + CO_2 \Leftrightarrow 2CO$
- methane decomposition: $CH_4 \Leftrightarrow C + 2H_2$

The equations have their equilibrium on the right side with increasing temperatures. As shown, with higher temperatures more hydrogen and carbon monoxide are produced (Fig. 3).

Main Reaction Processes. In pyrolysis, the following main reaction processes are distinguishable [14]:

- Primary processes. Products are formed in the fuel (solid phase) at low temperatures (water, carbon oxides, aliphates, oxygen containing carbon hydrogens).

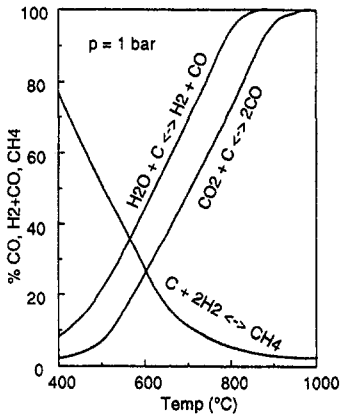

Fig. 3 Equilibrium of different gasification reactions depending on the reaction temperature

- Secondary processes. Products are formed in the gaseous phase out of primary products (especially by cracking).
- Tertiary processes. New products are created at high temperatures by cracking secondary products or by repolymerization to heavy aromatics (recombination).

Coal Pyrolysis. Coal pyrolysis has been already investigated intensively for a long period. Therefore, in this paper only a small part of essential results (regarding the co-pyrolysis with other fuels) are presented.

An essential reason for the different product yield in coal pyrolysis compared to biomass pyrolysis is the different molecular design of the fuels. Coal is formed by three-dimensional cross-linked macromolecules, in which smaller molecules are integrated.

Different energies of chemical bondings are responsible for the different product formation in pyrolysis, depending on the reaction temperature. Initially, aliphatic bonds are broken at lower temperatures; with increasing temperature, thermal decomposition of aromatic bonds starts.

Biomass Pyrolysis. The pyrolysis of biomass has several steps depending on the reaction temperature [15].

Between 100°C and approx. 400°C, the depolymerization of macromolecules starts, free and cellular water in the fuel is released. With higher temperatures hydrolysis reactions take place, molecules are cracked, and the quantity of pyrolysis products increases rapidly, the fuel weight loss can reach 70 percent.

At temperatures over 400°C, cracking of the pyrolysis products in the gaseous phase form new products. At the same time, other products are recreated in the solid phase or near the solid phase by recombination [14, 16].

The structure of biomass and the ultimate analysis explain the different behaviour in devolatilization, compared to coal. Biomass contains more linear and weaker connected macromolecules than the highly cross-linked coal with its aromatic components. Photosynthesis is the basic step in the formation of biomass. An endothermic reaction creates glucose from carbon dioxide and water. In a second step, the main components cellulose, hemi-cellulose and lignin are created.

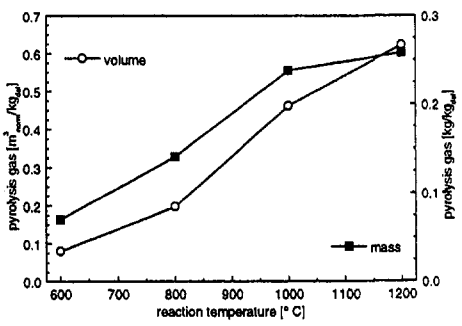

Fig. 4 Total gas generation in hard coal pyrolysis

Table 2 Analyses of feedstocks

Feedstock	Göttelborn hard coal	Swiss Combi sewage sludge	straw biomass
Proximate analyses [$\%_{dry}$]			
fixed C	57.0	2.6	16.4
volatile matter	33.9	51.0	77.7
ash	9.1	46.4	5.9
Ultimate analyses [$\%_{daf}$]			
C	81.4	52.1	50.5
H	5.6	7.7	4.8
N	1.5	6.7	0.8
S	1.0	2.1	0.1
Cl	*	0.05	0.8
O (diff.)	10.6	31.4	43.0
Moisture ** [g/kg]	5.3	2.3	7.4
Particle size			
d_{50} [μm]	58.8	28.6	
sieve [mm]			1.5
Ash [%]			
SiO_2	42.3	22.4	52.6
Al_2O_3	24.3	9.0	1.2
Fe_2O_3	11.3	24.6	1.2
CaO	6.5	12.5	6.5
MgO	4.1	2.8	3.0
K_2O	3.3	0.8	23.7
SO_3	6.6	2.6	1.1
Heavy metals [mg/kg_{dry}]			
Ba	1350	195	90
Pb	530	<20	45
Cd	0.5	2.9	3.0
Cr	308	330	58
Cu	360	485	85
Ni	290	76	45
Hg	<5	<5	<5
Zn	940	995	125

* not determined ** as received, feedstock has been dried for experiments

Sewage Sludge Pyrolysis. It is not easy to give a clear description of the composition of sewage sludge. Sewage sludge is formed by organic and inorganic matter. The organic matter contains proteins, carbohydrates and lipids. The distribution of organic matter is approximately [17]; 20–30 percent proteins, 10–30 percent lipids, and 10–15 percent carbohydrates.

Unlike coal, sewage sludge is composed by long-chained aliphatic hydrocarbons, which are not cross-linked in a three-dimensional model. Single molecules can reach large dimensions with a high molecular mass. The structure $C_{372}H_{710}O_{236}N_{61}S_3Cl_2P_6$ of the organic matter in sewage sludge is suggested in [18].

Feedstocks

Different fuels have been used in the pyrolysis test runs. Feedstock analyses are shown in Table 2.

Results of Pyrolysis Experiments With Unmixed Fuels

Coal Pyrolysis.

Gaseous Components. All pyrolysis experiments have been carried out with one hard coal (type: Göttelborn, high volatile matter, Saarland, Germany).

Figure 4 gives information about the total gas yield in coal pyrolysis. In the temperature range investigated, the gas yield increases with increasing reaction temperature. At high temper-

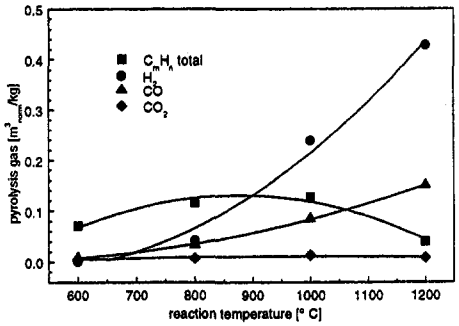

Fig. 5 Devolatilization of hard coal, gaseous components

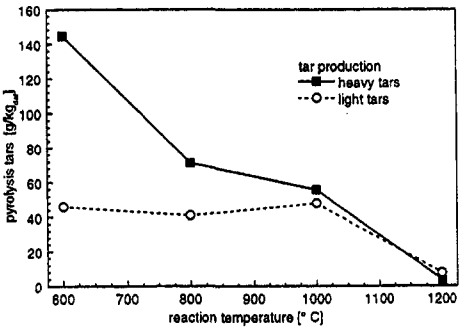

Fig. 6 Tar generation (heavy and light fraction) in coal pyrolysis

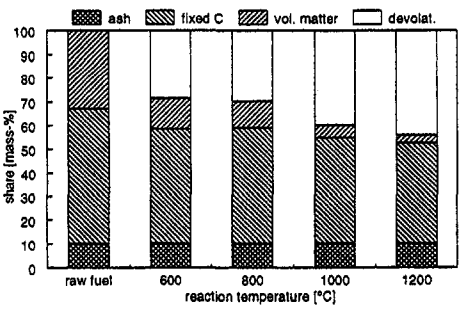

Fig. 7 Proximate analysis of coal (raw material and residual char), values related to ash content of raw fuel

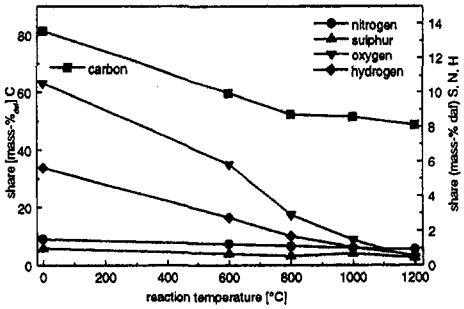

Fig. 8 Release of different elements in coal pyrolysis

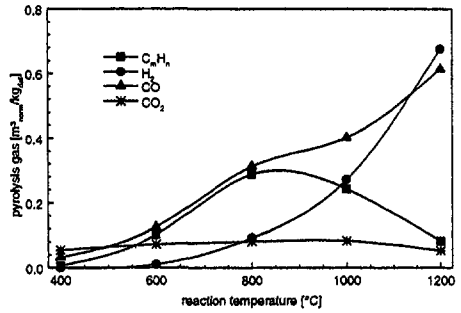

Fig. 9 Devolatilization of dried straw

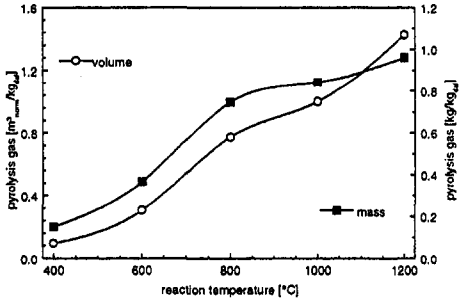

Fig. 10 Total gas generation

atures the mass curve flattens while there is an increasing volume curve. This is caused by an increasing share of light pyrolysis products at high temperatures. The gas production seems to reach a maximum in pyrolysis, if there is no gasification medium in the reaction zone.

The gaseous species are shown in Fig. 5. Hydrocarbons have a production maximum between 800°C and 1000°C. Hydrogen shows a strong increase at temperatures higher than 800°C. At 1200°C the hydrogen yield is about 0.43 m^3_{norm}/kg_{daf}, the share in the pyrolysis gas is nearly 70 percent. Carbon monoxide production also increases, together with the reaction temperature. The formation is caused by oxygen in the fuel (10.5%/kg_{daf}) and oxygen (0.05%/kg_{daf}) from air contained in the bulk material.

Tar Components. Figure 6 shows the production of heavy and light tar species, depending on the reaction temperature. Heavy tar components decrease strongly with increasing temperatures. The generation of light tars shows a flatter curve, which also decreases strongly at high pyrolysis temperatures.

Residual Char. Figure 7 shows the share of char components related to the share of ash in the raw material. In coal pyrolysis there is only a small decomposition of fixed C, but almost a total devolatilization of volatile matter at 1200°C reaction temperature.

Figure 8 contains the ultimate analyses of raw fuel and residual char related to the share in raw fuel. These values give information about the release of different elements in coal pyrolysis. All elements show an increasing release with increasing temperatures. The release of hydrogen and oxygen is more strongly influenced by the reaction temperature than that of nitrogen and sulfur. At 1200°C reaction temperature about 90 percent of hydrogen, 55 percent of sulfur, 41 percent of carbon and 38 percent of nitrogen are released.

Biomass Pyrolysis.

Gaseous Components. Figure 9 shows the yield of the main components of straw. Carbon monoxide and hydrogen are generated in a higher share with increasing reaction temperatures. Carbon monoxide production starts already at 400°C; hydrogen is significantly generated at temperatures higher than 800°C. Hydrocarbons are also produced at low temperatures and reach a maximum somewhat over 800°C. Carbon dioxide is not strongly influenced by the reaction temperature.

The overall production of gaseous pyrolysis products is described in Fig. 10. As shown, at temperatures over 800°C the gas mass increases only a little; gas production is complete at

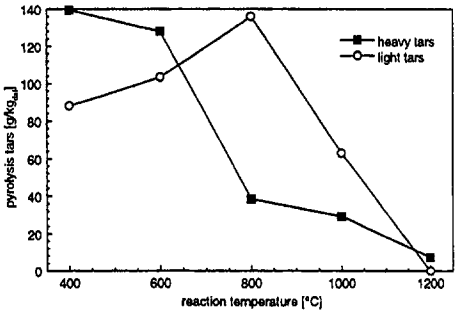

Fig. 11 Tar production during straw pyrolysis

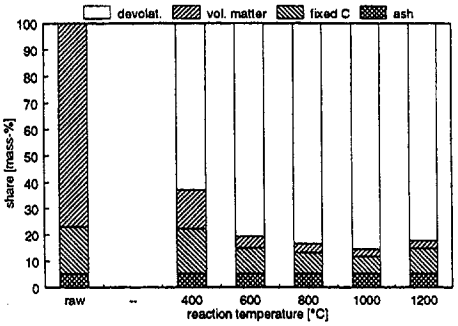

Fig. 12 Proximate analysis of straw (raw material and residual char), values related to ash content of raw fuel

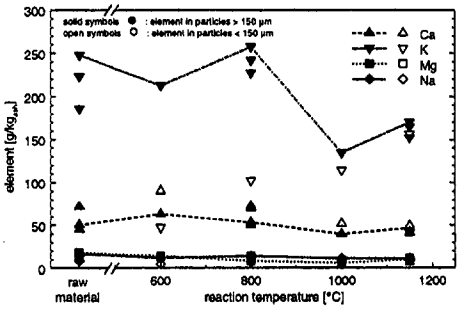

Fig. 13 Behaviour of mineral ash components in char during straw pyrolysis

about 1000°C reaction temperature. The gas volume increases strongly at high temperatures because of the change in the gas composition. Cracking reactions form lighter pyrolysis components. The yield of hydrogen in the pyrolysis gas increases rapidly at high reaction temperatures.

Tar Components. Figure 11 gives information about the tar production of straw. At low temperatures, more heavy components are produced. Light tars are formed by cracking out of heavy components with higher temperatures and reach a maximum between 800°C and 900°C. With further increasing temperatures, both tars, heavy and light, decrease rapidly.

Residual Char. Figure 12 shows the devolatilization and residual char of straw. Investigations were carried out in a thermobalance according to DIN 51718-DIN 51720. The results of the thermogravimetric measurements are related to the ash content of the raw fuel. Straw shows a high devolatilization at low temperatures.

The behavior of the main mineral ash components during the pyrolysis of straw, shown in Fig. 13, reveals in a decreasing share in the ash with increasing pyrolysis temperature. The char samples are devided into a coarse and a fine sample. The main

Table 3 Particle size and ash content of the different char samples

char sample	particle size	share of sample	ash content [% dry]				
	[µm]	[%]	raw	600°C	800°C	1000°C	1150°C
coarse straw	>150	77 - 88	5.5	27.1	29.1	30.2	29.4
fine straw	<150	12 - 23		41.5	40.4	40.7	33.6
coarse sew. sl.	>40	85	46.6	73.6	81.6	90.1	98.8
fine sew. sl.	<40	15		70.5	82.3	90.3	99.4

difference between those particles is the residence time in pyrolysis gas atmosphere and in the trace heated hot gas filtration unit. In contrast to the results of the sewage sludge pyrolysis the composition of the char from straw pyrolysis depends on the size of the char particles and thus on the residence time in pyrolysis gas atmosphere and in hot environment.

Table 3 shows the particle sizes and the ash contents of the analyzed samples. The higher share of ash in fine particles might come from ongoing devolatilization in the hot gas filtration unit. The share of calcium decreases in both straw char samples with decrease of the temperature. The higher calcium content in fine particles may come from reactions with some pyrolysis gas components, like recombination of carbonates. A major potassium release during straw pyrolysis takes place above 800°C. Particles with a longer residence time in pyrolysis gas atmosphere have less potassium and sodium in the ash due to further release and reactions with pyrolysis gas components, especially chlorine.

Figure 14 shows the release of chlorine, nitrogen, and sulfur during the straw pyrolysis. There is no distinct influence of the reaction temperature above 600°C for all three components. 25 percent of nitrogen and 55 percent of chlorine stay in solid pyrolysis residues.

Sewage Pyrolysis.

Gaseous Components. Total gas generation in sewage sludge pyrolysis is comparable to that of biomass pyrolysis. At high temperatures there is nearly total release of organic matter; therefore, mass release flattens at a high temperature while the volume release increases.

Figure 15 presents the gaseous compounds in sewage sludge pyrolysis. Hydrocarbons show a maximum between 800°C and 900°C. This is comparable to other fuels. As in biomass pyrolysis, the release of hydrogen starts at about 600°C and strongly increases at temperatures higher than 800°C because of cracking reactions. Carbon monoxide shows a strong increase with increasing reaction temperatures, too. Carbon dioxide seems to have a small production maximum between 800°C and 900°C.

Tar Components. As expected, tar production and distribution is influenced by the reaction temperatures. The tendency for tar formation is similar to those in biomass pyrolysis. Figure 16 shows the tar production in sewage sludge pyrolysis at different reaction temperatures as determined by weighting. Total tar

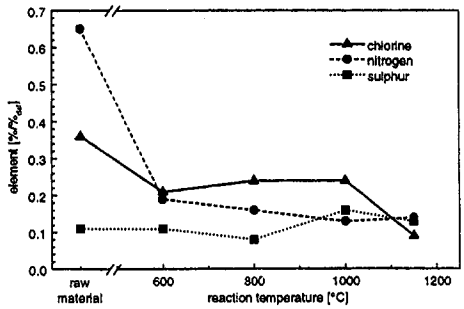

Fig. 14 Behaviour of Cl, N, and S in char during straw pyrolysis

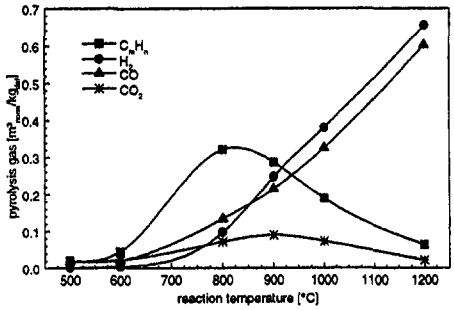

Fig. 15 Gaseous components in sewage sludge pyrolysis

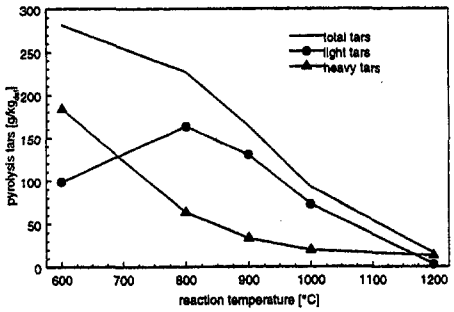

Fig. 16 Tar production in sewage sludge pyrolysis

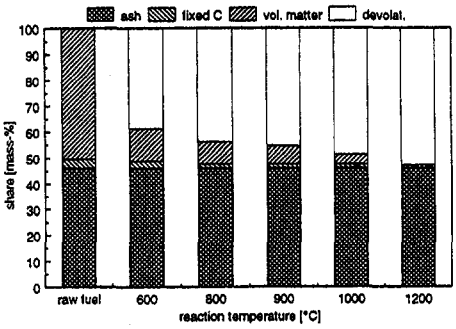

Fig. 17 Proximate analysis of sewage sludge (raw material and residual char), values related to ash content of raw fuel

release is about 280 $g/kg_{fuel,daf}$ at 600°C and about 10 g/kg at 1200°C. Light tar species show a production maximum between 800°C and 900°C. This is comparable to biomass and coal pyrolysis. Heavy tar components decrease with increasing reaction temperatures.

Residual Char. Sewage sludge shows a high devolatilization at low temperatures. At 400°C reaction temperature, about 80 percent of organic matter (volatiles and fixed C) is transformed into gas or tar products.

At 1200°C reaction temperature, there is nearly total release of organic compounds in sewage sludge pyrolysis. Figure 17 shows results of the proximate analysis related to the ash content of raw fuel.

In sewage sludge pyrolysis, there is no release of the main mineral ash components in the investigated range of temperature (Fig. 18). The differences between coarse and fine particles are listed in Table 3.

There is no distinct decrease of lead and manganese in the coarse nor in the fine particles during the pyrolysis of sewage sludge, shown in Fig. 19. The release of lead starts depending on the lead containing compounds in the ash above 1200°C in reducing atmosphere. Zinc decreases steadily with increasing

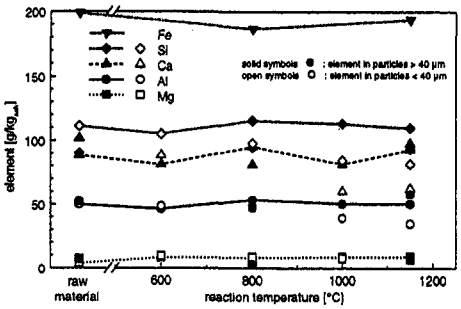

Fig. 18 Behaviour of mineral ash components in char during sewage sludge pyrolysis

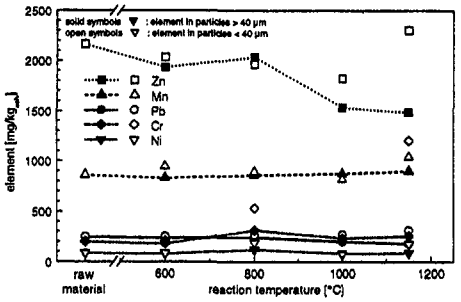

Fig. 19 Behaviour of heavy metals in char during sewage sludge pyrolysis

temperature. A slightly higher concentration in fine particles comes from condensation of heavy metals on the particles in the hot gas filtration unit, which is trace heated only to 400°C.

Results of Co-Pyrolysis Experiments

Co-pyrolysis test runs have been carried out with coal together with straw and sewage sludge, which are of interest for use in co-gasification. Studies have been focused on particular reactions which are caused by co-pyrolysis effects and not only by blending effects of the fuel mixtures. To obtain information on product generation, temperature was varied from 800°C to 1100°C (100 K steps) in experiments with sewage sludge, and from 800°C to 1000°C in test runs with straw.

Rules of Mixture.

$$c = (a100*a1 + b100*b1)/100$$

$$r = (m - c)/c,$$

where c = calculated result; $a100$ = measurement in unmixed pyrolysis of fuel a; $a1$ = share (percent) of fuel a in the mixture in co-pyrolysis; b = fuel b; r = related result; m = measurement.

Co-Pyrolysis of Coal and Straw.

Gaseous and Solid Pyrolysis Products. Figure 20 shows gaseous and solid pyrolysis products in the co-pyrolysis of straw and coal at 800°C.

Analysis results are related to calculations according to rule of mixture (left axis = r; 100 percent coal and 100 percent straw are equal 1). The expected values for mixed fuels should be 1, if there are no special effects caused by co-pyrolysis.

Figure 20 shows that all measured values (devolatilization = fuel input-char production) are in a range of about ±10 percent. This range describes the average deviation of mass balances in pyrolysis experiments. The result of residual char production and pyrolysis gas generation in co-pyrolysis test runs

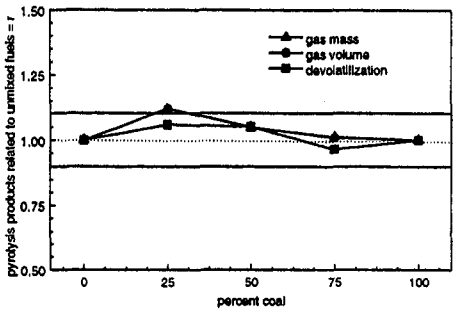

Fig. 20 Gaseous components and devolatilization in co-pyrolysis of coal and straw at 800°C reaction temperature

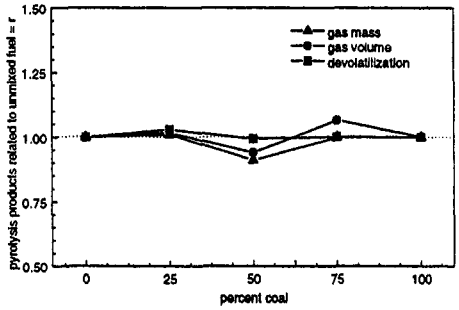

Fig. 21 Gaseous components and devolatilization in co-pyrolysis of coal and straw at 1000°C reaction temperature

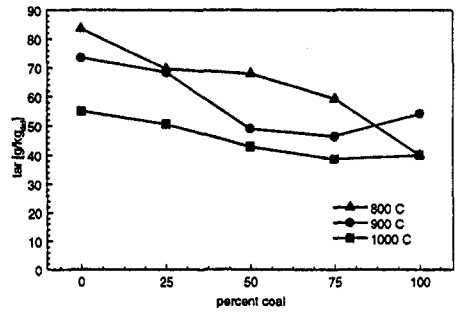

Fig. 22 Light tars in co-pyrolysis of coal and straw

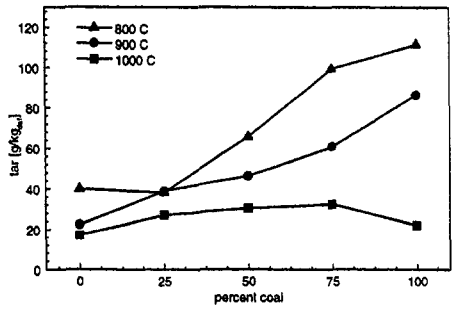

Fig. 23 Heavy tars in co-pyrolysis of coal and straw

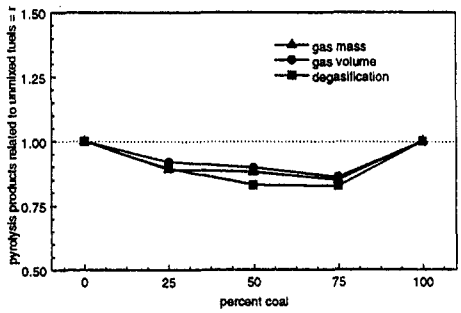

Fig. 24 Gaseous components and devolatilization in co-pyrolysis of coal and sewage sludge at 800°C reaction temperature

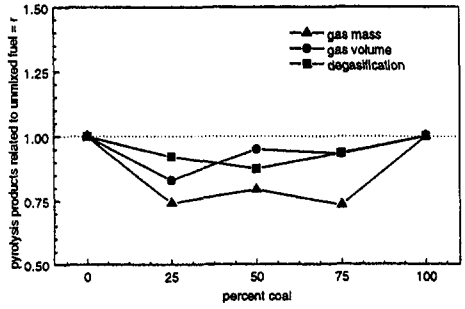

Fig. 25 Gaseous components and devolatilization in co-pyrolysis of coal and sewage sludge at 1100°C reaction temperature

with coal and straw shows that there are only effects caused by rules of mixtures.

In Fig. 21, results are presented for test runs at 1000°C. These figures show that devolatilization (and therefore char production) is not influenced by synergetic effects caused by co-pyrolysis. All analysis results are in a range of approx. ±10 percent around the value, which is given by the rules of mixture.

Tar Products. If no influence on pyrolysis gas generation and residual char production exists, no effect on tar production due to the mass balance should be expected. Figure 22 and Fig. 23 show the measured tar production in the co-pyrolysis of coal and straw. Quantitative tar measurements are not easy to make and imply a certain measurement deviation. All measured values are roughly on a line. If those values are connected with a linear regression, there are points over and under the regression line. Therefore, it is expected that the investigations on tar production in co-pyrolysis of coal and straw in the range of the tested parameters are not influenced by special effects caused by the fuel blending.

Co-Pyrolysis of Coal and Sewage Sludge.

Gaseous and Solid Pyrolysis Products. Unlike co-pyrolysis of coal and straw, test runs with fuel mixtures (coal and sewage sludge) show that a combined pyrolysis has an influence on product yield and product distribution. Figure 24 and Fig. 25 contain measurements of pyrolysis gas (mass and volume) and devolatilization (=fuel input-residual char). Again, all values are related to calculations according to the rules of mixture.

In all measurements, the devolatilization is smaller than 1, inducing a higher residual char than the calculation predicts. This effect weakens with increasing temperatures. In all cases, gas values (mass and volume) are also less than 1; this is caused by the influence of the fuel mixtures on pyrolysis. Related results of the mass of gas are usually smaller than results of gas volume.

It seems that, together with an increasing reaction temperature, the difference between gas mass and gas volume is increasing. This must be caused by a change in pyrolysis gas product distribution.

Tar Products. Tar measurements in co-pyrolysis test runs of coal/sewage sludge mixtures are shown in Fig. 26 and Fig. 27. It should be considered that quantitative tar measurements are not of the accuracy of gas or char measurements.

All tar values determined in co-pyrolysis of coal and sewage sludge are similar, thus precluding any definitive conclusions

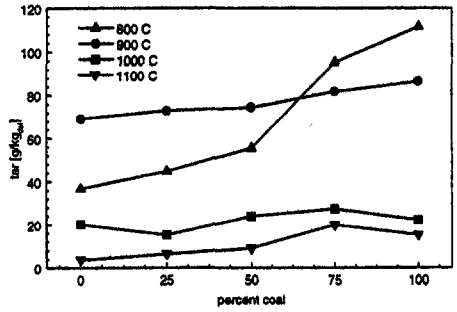

Fig. 26 Heavy tars in co-pyrolysis of coal and sewage sludge

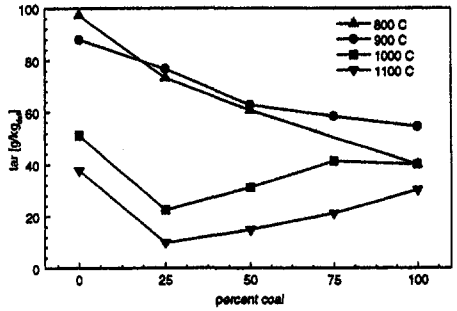

Fig. 27 Light tars in co-pyrolysis of coal and sewage sludge

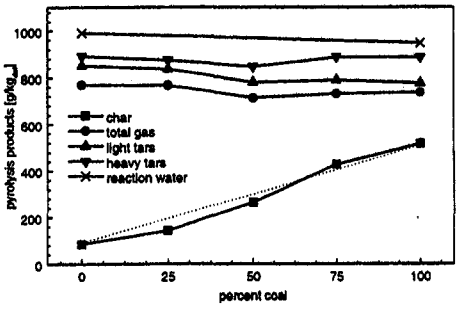

Fig. 28 Mass balance in co-pyrolysis of coal and straw

as to the effect of feedstock mixture. Figure 26 contains measurements of heavy tars. It seems that all setpoints are more or less on a line between the unmixed fuels. No strong influence of co-pyrolysis on heavy tar production appears to exist.

Figure 27 shows light tar measurements. The values measured at the setpoints do not greatly differ from a connecting line between the unmixed fuels. But if tar measurements of all test series are connected with a polynomial regression, it appears that light tar generation in mixed fuel test runs may be lower than expected. Thus, light tar generation could be influenced by co-pyrolysis of coal and sewage sludge. This could be possible because there exists an influence on gas generation in these test runs (shown in Figure 24 and Figure 25) and behaviour of light tars could be similar to that of the gaseous fraction.

Total Balance in Co-Pyrolysis. Figure 28 and Fig. 29 show summarized measurements of co-pyrolysis experiments (coal/straw and coal/sewage sludge) at 800°C. All measured values have a symbol. Reaction water determination was performed by means of oxygen balances only with unmixed fuels. The figures show that a satisfactory mass balance exists for all set points. Deviation in the mass balance in both figures is less than 10 percent. Figure 29 (co-pyrolysis of coal and sewage sludge) demonstrates the increasing yield of char in those test runs, that are influenced by the fuel mixtures, in contrast to Fig.

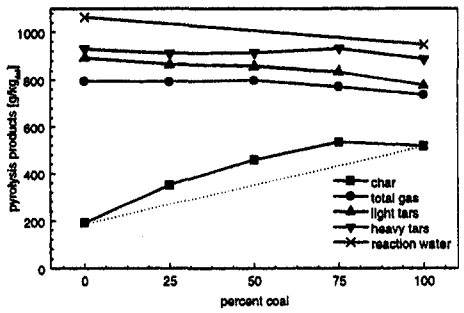

Fig. 29 Mass balance in co-pyrolysis of coal and sewage sludge

28 describing the co-pyrolysis of coal and straw. (Dotted lines are expected values.)

The following model could help to explain the measured effects. Both straw and sewage sludge are high volatile fuels. The high devolatilization rate even at low reaction temperatures is caused partly by the internal structure of biomass and sewage sludge (no highly cross-linked molecules). Therefore devolatilization of both fuels should not necessarily be influenced, if there is any other fuel in the reaction zone for co-pyrolysis. The start of straw pyrolysis is delayed compared to that of sewage sludge; this is due to the different particle size.

On the other hand, coal contains a lower amount of volatile matter and has a highly crosslinked structure. This is one reason for the general requirement of higher temperatures in coal pyrolysis.

It seems possible that coal pyrolysis is influenced by the reaction atmosphere, generated in co-pyrolysis. In the co-pyrolysis of coal and sewage sludge, the sludge degases much faster than coal because of the structure of sewage sludge and its small particle (sewage sludge $d_{50} = 40$ μm, hard coal $d_{50} \approx 60$ μm). The coal pyrolysis taking place afterwards in the reaction tube occurs in a different atmosphere, compared to the baseline tests.

In the co-pyrolysis of coal and straw, straw particles show delayed degasing compared to the coal particles. It was also noted that, during co-combustion tests, straw particles ignited after coal particles in the combustion chamber [1]. Therefore, the devolatilization of coal in pyrolysis test runs with biomass feedstock happened in an inert atmosphere and was not disturbed by gaseous products from the straw. The straw devolatilization that follows in the inert atmospheric thus formed does not seem to be strongly influenced by this.

To obtain more detailed information about the model described, it could be useful to carry out investigations in a reactor with staged fuel feeding. First experiments could be done by investigating co-pyrolysis with a view to the residence time of the mixed feedstocks, using a probe for profile measurements.

Conclusions

Increasing reaction temperatures result in a higher devolatilization for all fuels. Biomass shows a devolatilization of approx. 80 percent$_{dry}$ at 1200°C. Hard coal shows a weight loss of approximately 45–50 percent (dry) at the same temperature. Sewage sludge devolatilization is also approximately 50 percent (dry) at 1200°C; this is nearly a total release of organic matter because of the high ash content (approximately 50 percent (dry)) in sewage sludge.

Gaseous hydrocarbons have a production maximum at about 800°C reaction temperature for all feedstocks. Carbon monoxide and hydrogen are increasingly formed at high pyrolysis temperatures due to gasification reactions. Mineral elements are released during straw pyrolysis, but within the hot gas filtration unit further recombination reactions and condensation of elements on particles take place. There is no release of mineral

elements during sewage sludge pyrolysis and only a slight release of heavy metals at high pyrolysis temperatures.

The effect of co-pyrolysis depends on the feedstocks used in association with the particle size. Pyrolysis of coal and straw show no particular influence, as a result of fuel blending. This may be due to the delayed devolatilization of straw compared with coal. Co-pyrolysis of coal and sewage sludge has an influence on char, gas and tar production. The yield of char increases with mixed feedstocks. This effect weakens with increasing temperatures. Gaseous products are lower than predicted by the rules of mixture. Light tars also seem to be less. This behavior may be caused by rapid sewage sludge devolatilization in the entrained flow reactor, followed by the coal devolatilization, which is influenced by the reaction atmosphere thus created.

To obtain detailed information on effects of co-pyrolysis or co-gasification it seems necessary to focus research on devolatilization velocity of the baseline fuels and on the influence of reaction atmosphere on the unblended feedstocks.

Acknowledgment

The research is funded in part by the Commission of the European Community, APAS Research Programme (COAL-CT92-0001), Joule III Research Programme (JOR3-CT95-0057), and the Bundesministerium für Wirtschaft (Federal German Ministry of Economic Affairs).

References

1 Kicherer A., Gerhardt T., Spliethoff, H., and Hein, K. R. G., "Co-Combustion of Biomass/Sewage Sludge with Hard Coal in a Pulverized Fuel Semi-Industrial Test Rig," Final Report, in: Bemtgen, J. M., Hein, K. R. G., and Minchener, A. J., "Combined Combustion of Biomass/Sewage Sludge and Coals, EC-Research Programme," APAS-Contract COAL-CT92-0002, Institute for Process Engineering and Power Plant Technology, University of Stuttgart, 1995.

2 Lungwitz H., "Thermische Klärschlammbehandlung," Berichte der Abwassertechnischen Vereinigung (ATV) Nr. 42, St. Augustin, 1992.

3 Kaminsky W., "*Klärschlammpyrolyse: Vor dem großtechnischen Einsatz,*" Chemische Industrie Nr. 6, 1987.

4 Lindner K.-H., "Anforderung an die Klärschlammentsorgung," Berichte der Abwassertechnischen Vereinigung (ATV) Nr. 42, St. Augustin, 1992.

5 Greul, U., Magel, C., Moersch, O., Rüdiger, H., Storm, C., Schnell, U., Spliethoff, H., and Hein, K. R. G., "Einsatz von kohlestämmigem Pyrolysegas als Reduktionsbrennstoff," Final Report, Proj. No. 0326766A, German Federal Ministry of Education, Science, Research, and Technology BMBF, Bonn, 1996.

6 Rüdiger, H., Gerhardt, T., Spliethoff, H., and Hein, K. R. G., "Co-Combustion Concepts for Sewage Sludge in a Coal Fired Furnace Using Pulverized or Pre-Pyrolysed Feedstock," Finnish-Swedish Flame Days, Naantali, Finland, 1996.

7 Rüdiger, H., Kicherer, A., Greul, U., Spliethoff, H., and Hein, K. R. G., "Investigations in Combined Combustion of Biomass and Coal in Power Plant Technology," *Energy & Fuels,* Vol. 10, No. 3, pp. 789–796, 1996.

8 Storm, C., Spliethoff, H., and Hein, K. R. G., "Behaviour of Trace Elements During the Pyrolysis of Biomass and Sewage Sludge," 9th ICCS'97, Essen, Germany, *DGKM Tagungsbericht 9703,* Vol. II, Pp. 721–724, 1997.

9 Spliethoff, H., Rüdiger, H., Greul, U., Spliethoff, H., and Hein, K. R. G., Kombinierte Minderung der NO_x-Bildung und Reduzierung von gebildetem NO_x bei der Verbrennung von Steinkohle, Phase 3," Final Report, Proj. No. 0326535C, German Federal Ministry of Research, and Technology BMFT, Bonn, 1993.

10 Ruck B., "Influence of Tracer Particle Size on Flow Information in Laser Doppler Anemometry," (in German), Technisches Messen-tm, No. 7/8, 1990.

11 Smith, I. W., and Watts, A., "Heat Exchange Between a Particle an Its Surroundings: A Theoretical Study," Investigation Report, CSIRO, 1968.

12 Rüdiger H., "Pyrolysegas von festen biogenen und fossilen Brennstoffen zur Erzeugung eines Zusatzbrennstoffes für Feuerungsanlagen," Berichte aus der Energietechnik, Shaker Verlag, Aachen, 1997.

13 Rüdiger, H., Greul, U., Spliethoff, H., and Hein, K. R. G., "Co-Pyrolysis of Coal/Biomass and Coal/Sewage Sludge Mixtures in an Entrained Flow Reactor," Final Report, in: Bemtgen, J. M., Hein, K. R. G., and Minchener, A. J., "Co-Gasification of Coal/Biomass and Coal/Waste Mixtures," EC-Research Programme, APAS-Contract COAL-CT92-0001, Institute for Process Engineering and Power Plant Technology, University of Stuttgart, 1995.

14 Evans, R. J., Milne, T. A., "Molecular Characterization of the Pyrolysis of Biomass, 1: Fundamentals," *Energy & Fuels,* Vol. 1, No. 2, 1987.

15 Antal, M. J., "Biomass Pyrolysis: A Review of the Literature, Part 1 and 2," *Advances in Solar Energie,* American Solar Energy Society, New York, 1983.

16 Canel, M., and Wanzl W., "Pyrolysis of a Turkish Lignite at High Heating Rates," *Fuel,* Vol. 73, No. 1, 1994.

17 Sahm, H., *Klärschlamm als chemischer und biologischer Rohstoff,* GVC-Tagung, 1984.

18 Wandrasz, J., "Ausgewählte Probleme der Schlammverbrennung," in *Recycling von Klärschlamm 1,* EF-Verlag, Berlin, 1987.

A Small Scale Biomass Fueled Gas Turbine Engine

J. D. Craig
Cratech, Inc.,
P.O. Box 70,
Tahoka, TX 79373

C. R. Purvis
U.S. Environmental Protection Agency,
Air Pollution Prevention
and Control Division,
Research Triangle Park, NC 27711

A new generation of small scale (less than 20 MWe) biomass fueled, power plants are being developed based on a gas turbine (Brayton cycle) prime mover. These power plants are expected to increase the efficiency and lower the cost of generating power from fuels such as wood. The new power plants are also expected to economically utilize annual plant growth materials (such as rice hulls, cotton gin trash, nut shells, and various straws, grasses, and animal manures) that are not normally considered as fuel for power plants. This paper summarizes the new power generation concept with emphasis on the engineering challenges presented by the gas turbine component.

Biomass Power Plant Rationale

Many entities worldwide greatly desire improved and more economic methods for using and/or disposing of biomass in the course of generating electricity. At present, the amount of useable power being produced from biomass is very small relative to the biomass resources available for this use. If there is such a desire to employ biomass power and there are vast biomass resources for fueling biomass power plants, why do we not see rapid development of this industry? First, any proposed biomass power plant has to compete with other power supply options. In the majority of cases the only other option is power supplied by a fossil fueled power plant. Power supplied by a fossil fueled power plant can be very economical. It is economical because it is reliable, uses the latest in power plant technology (e.g., an efficient gas turbine engine combined with the steam cycle), can be installed relatively quickly, can be built on both a small and large scale, and is well known by the finance community. Fossil fuels are currently abundant and available at a reasonable price in many parts of the world. Second, biomass power plants rely on less efficient boiler/steam turbine technology, have a higher installed price per kWe, and draw on fuel supplies that are bulkier, less homogeneous, and more difficult to fire and handle than fossil fuels (especially relative to oil and natural gas which are not solids).

The major reasons for consideration of the biomass power option are as follows: (1) disposal of biomass waste combined with the production of electricity and heat, (2) power production from abundant indigenous biomass resources, (3) power for remote locations rich in biomass resources, and (4) it is a renewable energy option. This option has been chosen for many applications. In the U.S. there is an estimated 6000 MWe of wood-based generating capacity that is dispatchable (NEOS, 1992). The amount of power that could be generated from biomass resources is much greater, especially considering the worldwide market. But to effectively capture this underutilized renewable resource requires a new generation of biomass power plants.

This paper briefly describes development of a new generation biomass power plant with emphasis on the modifications required of the gas turbine generator component to accept hot low energy gas.

Technical Path for Producing Electricity From Biomass

There are numerous decisions to be made when choosing a path for producing electricity from biomass. The path Cratech has chosen is shown in the simplified block diagram of Fig. 1. The block diagram of Fig. 1 shows a pressurized air-blown fluid bed reactor with fuel injection from a biomass pressurization and metering unit. The air is supplied to the reactor from a booster compressor which in turn is fed from the turbine compressor final stage. The product gas is passed through a hot gas clean-up system followed by injection into the turbine combustor. Electricity is produced from the generator which is powered by the output shaft of the gas turbine. Also, shown is a heat recovery steam generator (HRSG) that can be added if desired. The gasification system of Fig. 1 has been tested with the results reported in (Craig 1996). Cratech is projecting to have an operating power plant as shown in Fig. 1 (excluding the HRSG) by the fourth quarter of 1998. Many hours of further testing will be required before the unit can be offered for sale. This path is a promising option for cost effective production of electricity from the largest variety of biomass materials. This system takes advantage of the higher practical thermodynamic efficiency of the Brayton cycle over the Rankin cycle.

Gumz (1950) is the earliest reference found describing the concept of combining a pressurized gasifier with a gas turbine engine, although Gumz himself references an earlier work proposing this concept. He also states that the combination could certainly benefit from future development of pressurized hot gas cleaning to avoid excessive turbine blade wear. Gumz was speaking of coal-fueled plants but the concept is similar when using biomass as fuel. Currently, similar concepts are being developed for using biomass as fuel in Hawaii (Wiant et al., 1997), Sweden (Skog, 1993), Finland (McKeough and Kurkela, 1993), Minnesota (DeLong et al., 1995), Europe (Maniatis and Ferrero, 1995), and other locations.

The Cratech system can operate at a maximum design pressure of 13.8 atm (1353 kPa), at a feed rate of 2 tonnes (2.2 tons) per hour of wood, and at a gasification temperature just below 730°C (1346°F). The gas is maintained at, or just below, this temperature to retain valuable sensible energy and prevent condensation of the tars. In this state, the solid particles are removed from the gas by a hot, dry gas cleaning system. The gas is then directed into the combustion chamber of a gas turbine engine. This path has the following notable benefits: it avoids ash softening temperatures before the ash is removed, thus avoiding ash slagging problems; it retains the sensible energy in the gas, which helps maintain overall system efficiency; wet scrubbers are not used, therefore, no wastewater will have to be treated; the tars will remain in a vapor state, avoiding tar sticking and corrosion problems; the chemical energy contained in the tar will be recovered as the hot vaporized tar is burned; and no catalyst or higher temperatures are needed for tar destruction before combustion.

Contributed by the International Gas Turbine Institute and presented at the International Gas Turbine and Aeroengine Congress and Exhibition, Stockholm, Sweden, June 2–5, 1998. Manuscript received by the ASME Headquarters April 1, 1998. Paper No. 98-GT-315. Associate Technical Editor: R. Kielb.

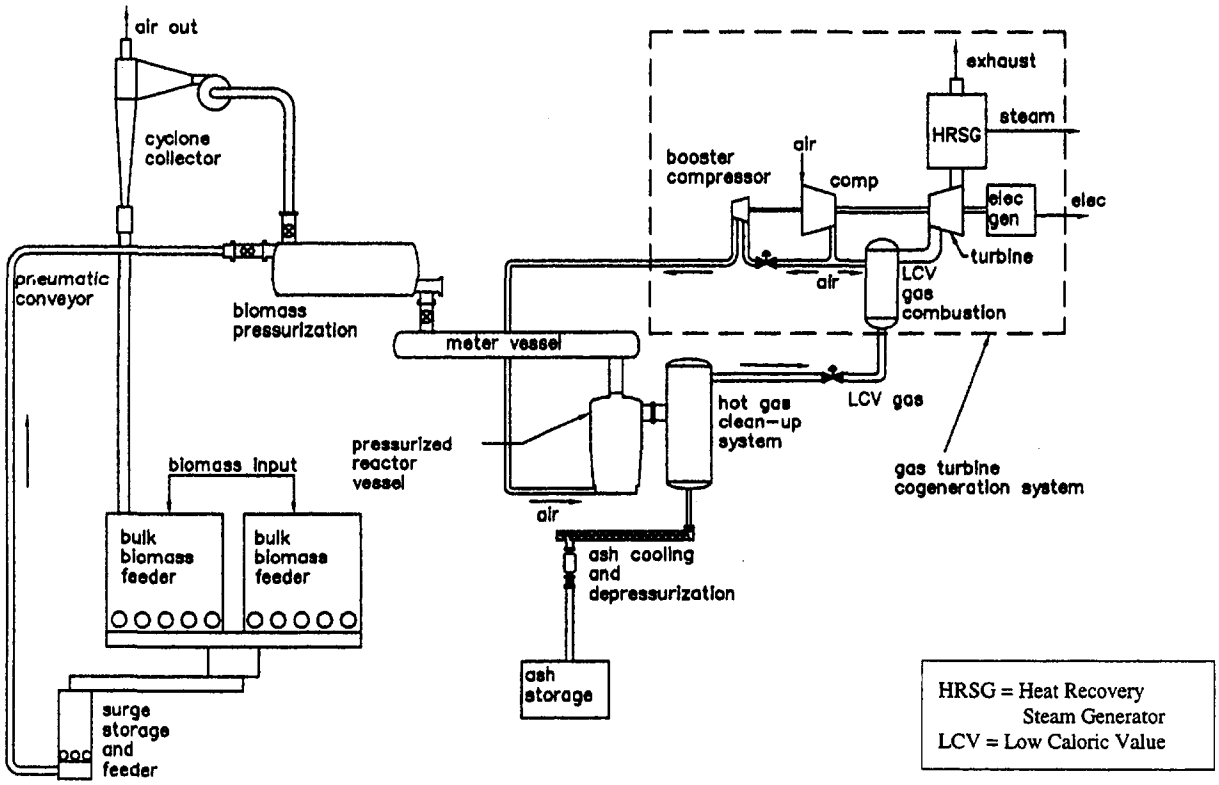

Fig. 1 Cratech's chosen path for producing electricity from biomass

Pressurized operation allows for higher heat rates per square area of the reactor, reduces the size of the hot gas clean-up system, and eliminates the need for compression of the gas prior to injection into the gas turbine. Direct, or air, gasification was chosen over indirect gasification to reduce the overall complexity of the system. Steam is not required for fluidization, and minimizing steam use cuts down on latent heat losses.

There are barriers to overcome with this path. Most prominent are feeding biomass into a pressure vessel, developing hot gas cleanup, low carbon conversion efficiency at low gasification temperatures, alkali vapors in the fuel gas, and fueling a gas turbine engine with a hot low energy gas. These barriers are worth overcoming to obtain the significant advantages cited above. This paper does not discuss Cratech's methods or efforts for overcoming all the barriers as it is focused on the gas turbine component of the power plant.

Table 1 LCV gas composition

Component	% mole fraction
H_2	10.4
CH_4	3.0
C_2H_4	1.0
C_2H_6	0.3
CO	17.0
CO_2	15.3
N_2	41.0
H_2O	12.0

Gas Turbine Engine Modifications

Low calorific value (LCV) gas will fuel the gas turbine. Table 1 contains the LCV gas composition and Table 2 contains the LCV gas characteristics as produced from cotton gin trash fuel. Figure 2 is a block schematic of the gas turbine and its fuel control scheme. Table 3 contains the corresponding mass flow rate at each station identified in Fig. 2.

The Cratech gasification system is capable of fueling a turbine of 1500 kWe output with a maximum pressure ratio of about 11.0; however, the initial gas turbine combustion test will be performed with a Solar Spartan turbine rated at 225 kWe with a pressure ratio of 4.0. This small gas turbine generator package will provide for economical fuel system and combustor modification, and subsequent testing.

An Engineering Challenge. One major challenge to overcome in making this type of power plant possible is designing a gas turbine fuel and combustion system that will accept and burn hot LCV gas. An EGT Typhoon gas turbine has been designed to operate on gas of 5 MJ/scm (134 Btu/scf) at a

Table 2 LCV gas characteristics

Molecular weight: 26.2
Gas temperature: 700°C (1292°F)
Chemical energy of gas: 5.18 MJ/scm (139 Btu/scf)
Sensible energy of gas: 1.05 MJ/scm (28 Btu/scf)
Solid particle concentration < 6 ppmw with max particle size of 3 μm
Tar content was not measured.

Table 3 Approximate relative mass flow rates at station points identified in Fig. 2

Station	Description	as a ratio of m_1
1	m_1= compressor inlet mass flow	m_1/m_1= 1
2	m_2= compressor discharge	m_2/m_1= 1
2g	m_{2g}= air supply to gasifier	m_{2g}/m_1= 0.10
2p	m_{2p}= fuel premix air	m_{2p}/m_1= min of 0.00, max of 0.14
3	m_3= air supply to combustor	m_3/m_1= min of 0.76, max of 0.90
4	m_4= produced fuel gas flow	m_4/m_1= 0.14
5	m_5= hot gas flow to turbine	m_5/m_1= 1.04
6	m_6= turbine outlet flow	m_6/m_1= 1.04

fuel injection temperature of 400°C (752°F) (Mina et al., 1994). Westinghouse is planning to fuel a 251B12 gas turbine with 5 MJ/scm (134 Btu/scf) LCV gas at an injection temperature of 550°C (1022°F) (Stambler, 1997). Cratech plans to fuel a modified Solar Spartan gas turbine with 5 MJ/scm (134 Btu/scf) LCV gas at a fuel injection temperature of 700°C (1292°F). This challenge consists of designing a suitable fuel delivery system and an LCV gas combustor.

LCV Gas Delivery and Injection System. The EGT and Westinghouse turbines receive biomass-derived LCV gas from gasification systems very similar to that shown in Fig. 1. However, the systems are apparently targeted for power plants in the 20 MWe and greater power range. Cratech is developing biomass power plants for the 20 MWe and less power range market. The larger systems may benefit from the increased complexity of employing a heat recovery steam generator to lower the LCV gas temperature and thus receive the benefits of lower temperature LCV gas fuel injection. The steam produced from hot gas cooling can be used effectively in a combined cycle application. But if this power concept is to be applied in smaller sizes (as low as 1 MWe) and in simple cycle operation, it would be desirable from a thermal efficiency standpoint to inject the LCV gas directly into the gas turbine combustor without LCV gas cooling.

Designing a fuel gas delivery and injection system that can handle the high temperature LCV gas is a major engineering challenge. Careful attention must be paid to selection of valves and materials that can handle the high temperatures and pressures. Valves V1 and V2 of Figure 2 have been selected and are included in the test program. Valve V1 is an on/off or blocking valve. This valve closes in the event of overspeed of the turbine shaft, over temperature of the turbine inlet gas, or emergency shutdown. Valve V2 is the fuel gas control valve and operates in relation to the turbine shaft speed. This valve will be required to operate at high temperatures while controlling the fuel flow required to maintain a constant shaft speed over the entire power range of the generator. Cratech will collect data on technical performance and cost effectiveness of the valves.

LCV Gas Combustion. Fueling gas turbine engines with LCV gas is not unprecedented. One of the most common applications in the past was use of off gases from a blast furnace to fuel gas turbines. Palmer (1976) discusses this application and the modifications required to successfully burn this gas in tur-

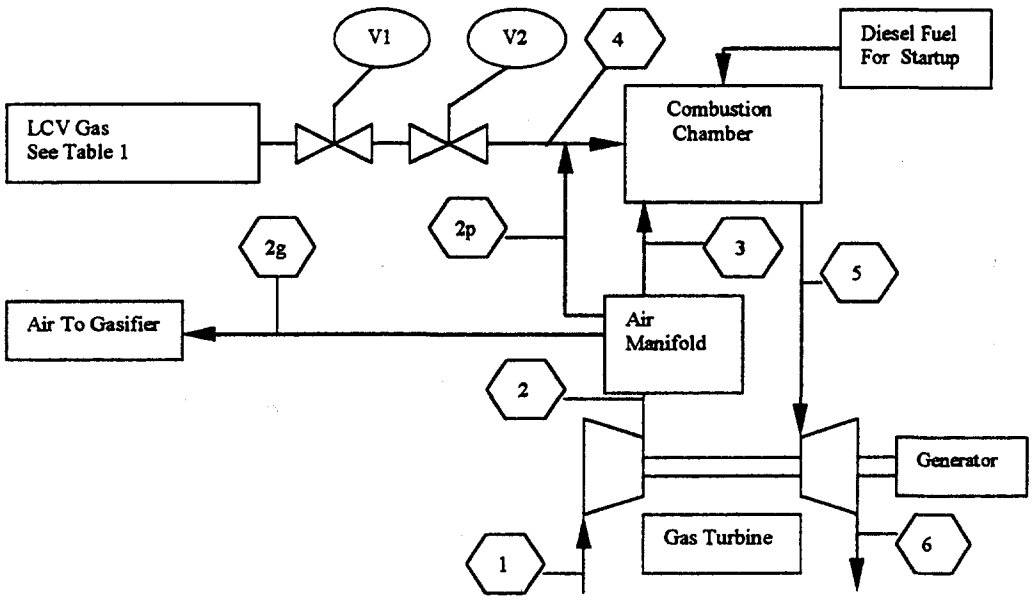

Fig. 2 Gas turbine fuel control scheme

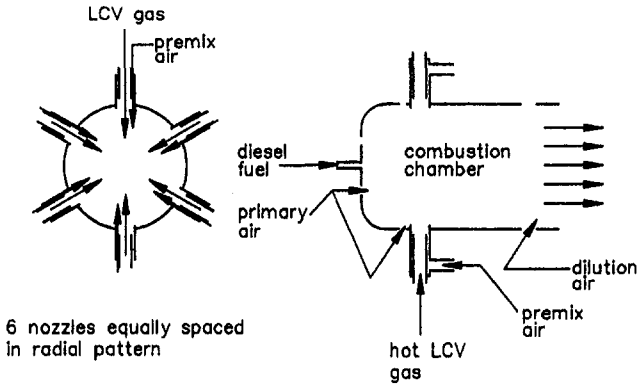

Fig. 3 Depiction of LCV gas fuel injector and combustor arrangement

bine engines. Beginning in the late 1970s, there has been a great deal of work on burning LCV coal gas in gas turbine engines. From this experience, gas turbine manufactures have confidence that biomass derived LCV gas can be successfully burned in gas turbine engines. EGT (Mina et al., 1994) and Westinghouse (Stambler, 1997) are examples of this confidence.

Most large industrial gas turbines have large combustion chambers with the volume necessary to support combustion of LCV gas once the fuel delivery and injection system has been modified. The Spartan is a much smaller turbine than any that has been fueled with biomass derived LCV gas to date; however, it will be possible to fuel this small turbine with an extensively modified combustion chamber. Figure 3 is a simplified depiction of the nozzle and combustor arrangement designed by Cratech for this turbine. Several parameters were considered when designing the turbine combustor for burning LCV gas. One of the most important parameters is the pressure drop across the combustor. The objective is to maintain and promote stable combustion with a combustor pressure drop of approximately 4 percent. With this arrangement, Cratech will learn how best to fuel small combustors with hot biomass derived LCV gas.

Diesel fuel will be used for startup in the conventional manner. The initial test runs will be conducted under no load conditions. LCV fuel gas will gradually be fed to the combustor, and the flow of diesel fuel will be gradually cut back. It is expected that the diesel fuel can be completely shut off and the turbine will operate totally on LCV gas. When stable combustion is occurring with 100 percent LCV gas under no load conditions, the process will be repeated under gradually increasing load conditions until the goal of 100 percent load with 100 percent LCV gas is reached. With a fuel delivery and combustion system properly operating, the next step would be a 100 h test run to check for any seriously detrimental effects from solid particles or possible alkali attack on the gas turbine blades. The gasification system has been designed so that alkalis remain in solid form and exit with the filter ash. The hot gas filtration system is expected to remove more than enough particulate matter to protect the turbine blades. Once the power plant demonstrates satisfactory operation for short periods of time, Cratech plans to relocate the plant to a commercial site for long term endurance and reliability testing.

The successful completion of such an ambitious gas turbine development program will bring the new generation of small scale biomass power plants much closer to technical, economic, and commercial reality.

Acknowledgments

The authors would like to acknowledge the following: the State of Texas; the State of Vermont; the Tennessee Valley Authority; the U.S. Department of Defense, Strategic Environmental Research and Development Program; the U.S. Department of Energy, Western Region Biomass Energy Program; and the U.S. Environmental Protection Agency, National Risk Management Research Laboratory.

References

Craig, J. D., 1996, *Development of a Small Scale Biomass-Fueled Integrated-Gasifier Gas Turbine Power Plant: Phase 1,* Western Regional Biomass Energy Program, Golden, CO.

DeLong, M. M., Oelke, E. A., Onischak, M., Schmid, M. R. and Wiant, B. C., 1995, "Sustainable Biomass Energy Production and Rural Economic Development Using Alfalfa Feedstock," Proceedings, Second Biomass Energy Conference of the Americas, National Renewable Energy Laboratory, Golden, CO.

Gumz, W., 1950, *Gas Producers and Blast Furnaces,* John Wiley and Sons, New York pp. 166–167.

McKeough, P., and Kurkela, E., 1993, "Biomass Gasification Activities in Finland," presented at the EPRI Strategic Benefits of Biomass and Waste Fuels Conference, March 30–April 1, 1993, Washington, DC.

Maniatis, Kyridkos, and Gian-Luca Ferrero, 1995 "The Thermie Targeted Projects on Biomass Gasification," Proceedings, Second Biomass Conference of the Americas, National Renewable Energy Laboratory, Golden, CO

Mina, Theo, Robinson, G. S., and Seamer, A., 1994, "Gas Turbine System Development to Meet the Requirements of a Dual Fuel Biomass/Diesel Oil Application," Proceedings, Sixth National Bioenergy Conference, Western Regional Biomass Energy Program, Golden, CO.

Preliminary Market Potential Analysis for a Biomass-Fueled Integrated Gasifier Gas Turbine, 1992, NEOS Corporation Western Regional Biomass Energy Program, Golden, CO.

Palmer, R. J., 1976, "*Modern Gas Turbines for Low BTU Gas Fuel Operation,*" ASME Paper 76-GT-117.

Skog, Eric, 1993, "Biomass Gasification Combined-Cycle Power Plant Demonstration in Varnamo, Sweden," presented at the EPRI Strategic Benefits of Biomass and Waste Fuels Conference, March 30–April 1, 1993, Washington, DC.

Stambler, I., 1997, "75 MW Biomass Gasification Plant Will Be Fueled by Alfalfa Farm Crops," *Gas Turbines World,* Vol. 27, No. 1, Pequot Publications, Inc. Fairfield, CT.

Wiant, B., Larkin, J., and Onischak, M., 1997, "Hawaiian Biomass Gasification Commercialization Program," Proceedings, Third Biomass Energy Conference of the Americas,

An Investigation of the Formation and Venting of Flammable Mixtures Formed Within Liquid Fuel Vessels

R. Bunama

G. A. Karim

C. Y. Zhang

Department of Mechanical Engineering,
University of Calgary,
Calgary, Alberta, T2N 1N4,
Canada

The paper describes results of a parametric study obtained while using an analytical model described earlier (Bunama and Karim, 1997b) investigating the combined effects of mass, energy, and momentum transfer with variable transport and thermodynamic properties on the formation of fuel vapor-air mixtures above a stagnant liquid fuel surface within the confines of a vertical cylindrical vessel. This was done mainly to examine the establishment of the formation of flammable mixtures and their changes in size and location with time within liquid fuel tanks that are partially empty. The effects of changes in the ambient and wall temperatures, presence of liquid on the walls and vessel geometry were considered. Moreover, the results of a corresponding experimental investigation are presented. Much of the data relates to the high volatility fuel n-pentane that represents the lighter fuel fractions in commercial fuels which through their early evaporation contribute much to the fire hazards in fuel tanks.

Introduction

The subject of ensuring the safety of fuel storage and handling facilities in gas turbine installations remains of paramount importance. Transient changes in key influencing parameters, such as temperature and fuel vapor concentration distributions that commonly occur as a matter of course in liquid fuel containers may increase the fire hazard. Moreover, the question of limiting the release of fuel vapor components into the immediate surroundings of fuel containers is equally of increasing significance and concern. Numerous interacting parameters that result from the transient changes in the local conditions or specific features of design, control the phenomena involved in a complex and often unknown manner. There is a need to understand better the nature of these processes and identify the potential and extent of fire hazards so as to develop effective guidelines for their control. Full scale testing of fuel tanks to assess their fire hazard or evaporative emissions, apart from being too expensive and time consuming is specific to a set of configurations. It would not account adequately for the contribution of numerous influencing factors to the associated transient phenomena involved. Obviously, comprehensive models that can describe reliably the events that take place within liquid fuel tanks can serve as a useful tool for dealing with the corresponding issues of fire hazards and safety.

Fire hazards within liquid fuel tanks that are partially empty relate closely to the transient processes of vaporization and convective mixing of the vapor produced off the liquid fuel surfaces with the overlaying atmosphere of air. Of particular concern is the possible formation of a flammable atmosphere within such containers for part of the time and the subsequent slow release of fuel vapor into the outside atmosphere when the tank is left either fully or partially open to the outside. There is a need to establish whether a flammable region will be formed within a tank and how it may develop in size and location with time. Moreover, how much time is subsequently needed to render the whole contents of the vessel too rich in fuel vapor to fail supporting a flame.

Contributed by the International Gas Turbine Institute and presented at the International Gas Turbine and Aeroengine Congress and Exhibition, Stockholm, Sweden, June 2–5, 1998. Manuscript received by the ASME Headquarters April 1, 1998. Paper No. 98-GT-178. Associate Technical Editor: R. Kielb.

Analytical studies of the transport processes involving the simultaneous presence of differences in temperature and variations in concentration in confined spaces in which a lighter gas is overlaying a heavy vapor tends to be few since they are computationally demanding (Cussler, 1992). Markham and Rosenberger (1980) used a two-dimensional model and considered the concentration and velocity profiles of liquid vapor of a molecular weight greater than air (Benzene). Their study was limited to a steady state, constant property and isothermal mass transfer.

Bunama and Karim (1997a) modeled the formation and mixing of liquid fuel vapor with the overlaying air within a vertical circular cylindrical tanks. The diffusive flow of air towards the interface from a higher concentration at the ambient produces a balancing outward convective flow of air and vapor away from the interface. This results in an enhanced diffusion and accelerated spread of the vapor.

The negative solutal buoyancy and cooling at the interface both tend to act as suppressants to the flow field, but convective transfer tends to have a noticeable role, especially at the early stages of the diffusion process when the space above the liquid surface is not yet saturated with the vapor. Moreover, a local positive thermal buoyancy occurring near the vessel walls such as due to a higher wall temperature relative to a cooler interface, enhances the mass transfer processes. In order to understand and describe such complex transient formation of fuel vapour-air mixtures typically within the confines of a cylindrical vessel, a comprehensive analytical model that includes the effects of convection, temperature gradients and variations in transport properties was described by Bunama and Karim (1997b).

The present contribution describes results of a parametric study obtained while using this analytical model, with the objective of investigating the combined effects of convection, energy transport, and variable properties on the formation of fuel vapor-air mixtures above a liquid fuel surface within the confines of a vertical cylindrical container. The effects of changes in ambient and wall temperatures, presence of liquid traces on the walls and vessel geometry on the transient formation of these mixtures can be made. In parallel with the analytical model the results of a corresponding experimental investigation is made. The relatively high volatility n-Pentane was chosen to represent the

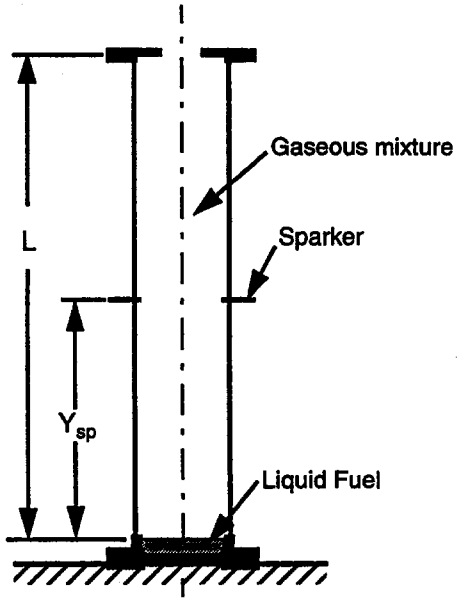

Fig. 1 Schematic representation of the cylindrical vessel arrangement considered in the experiments and modeling

lighter fuel fractions in commercial fuels that through their early evaporation contribute to much of the initial fire hazards within fuel tanks.

It was shown then that the employment of relatively simple transient mass transfer modeling approaches that are based on one-dimensional fixed property simulation produced results that were significantly different from those obtained when more comprehensive modeling approaches are employed. These involved three-dimensional axisymmetric simulation that accounts for changes in the local temperature and properties arising from the effects of continued fuel vaporization, heat transfer, and the resulting fuel vapor diffusion into the overlaying air. These later approaches were shown to produce results that tend to be in much better agreement with the limited experimental results available.

Another important related feature that has serious safety implication to fuel containers is the fact that when an ignition source is introduced into the space within a fuel tank and a fire flash develops, then the consumption by fire of much of the fuel vapor present would not ensure necessarily safety from subsequent flashes (Karim and Zhang, 1992). As long as some liquid fuel remains present somewhere within the tank that is in communication with the outside atmosphere, then given time, a flammable region will develop once more—albeit in the presence of some vitiated air. This can lead in the presence of an ignition source to yet another fire spread that consumes part of the fuel vapor developed. This repeated fire flashing resulting from the continued formation of flammable regions and their consumption by fire is much too complex to be simulated reliably analytically, and a resort to experimentation at present is needed for its examination.

Analytical Formulation

The system examined, as shown schematically in Fig. 1., is an open-topped vertical cylindrical vessel of radius (R). The lower part of the vessel contains a stagnant liquid fuel to a shallow depth at atmospheric pressure. The upper part of length (L) is assumed initially to contain air or air plus traces of the vapor at an initial uniform known concentration. The vessel side walls can be either dry or wetted uniformly to various extents with a liquid film. The transfer processes are initiated by assuming that surface of the stagnant liquid becomes exposed promptly to the air above it. With time, the evaporation processes proceed with the resulting vapor diffusing upwards towards the open top. Some air enters from the surrounding atmosphere and diffuses downwards towards the lower air concentration at the gas/liquid interface. Hence, a varying concentration gradient becomes established with time along the vessel axis. A steady-state condition may be eventually reached. The two parts are considered initially to be each at a uniform temperature that can be either equal or different from the surrounding ambient temperature. Also, the side walls of the vessel can be at a temperature either similar to that of the ambient or higher.

As some of the liquid evaporates, the supply of the latent heat of vaporization from the surface of the liquid cools down the interface that results in the establishment of temperature gradients within both the liquid and the overlying space in the vessel. These gradients of concentration and temperature control directly the transfer process and significantly affect the transport and thermodynamic properties of the mixture. Accordingly, the spatial and time variations of temperature and concentration profiles could be determined.

The governing equations for this axisymmetric two-dimensional system are the coupled unsteady momentum, species, and energy conservation equations for the gaseous phase. The thermodynamic and transport properties were taken to be variable and their equations were solved simultaneously along with the conservation equations. The energy equation for the liquid phase is also included to determine the temperature distribution in the liquid. The tank was assumed to be axisymmetrically cylindrical and vertical. A full statement of these governing equation together with the corresponding boundary conditions have been described elsewhere (Bunama and Karim, 1997b). The numerical procedure followed for their solution was also described. Throughout changes in the properties of the local mixture due to changes in temperature and concentration were accounted for.

Analytical Results and Discussion

Figure 2, for n-Pentane vaporization and spread into air, typically shows how the calculated lean limit boundary of the developed flammable zone progresses along the vertical cylindrical vessel, with unwetted side walls with time. This fuel lean boundary is always well ahead of the rich limit boundary that is on the side of the fuel surface. It can be seen that after a certain time from the commencement of the exposure of the liquid fuel surface to the air, the lean limit progression reaches the outlet of the tank. After the elapse of some further time, the rich flammability limit boundary arrives at the outlet. This

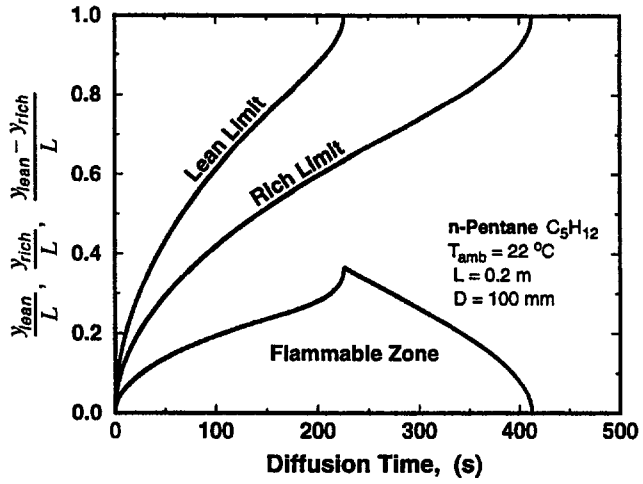

Fig. 2 Predicted lean and rich flammability limits boundary displacement with time and the resulting flammable zone

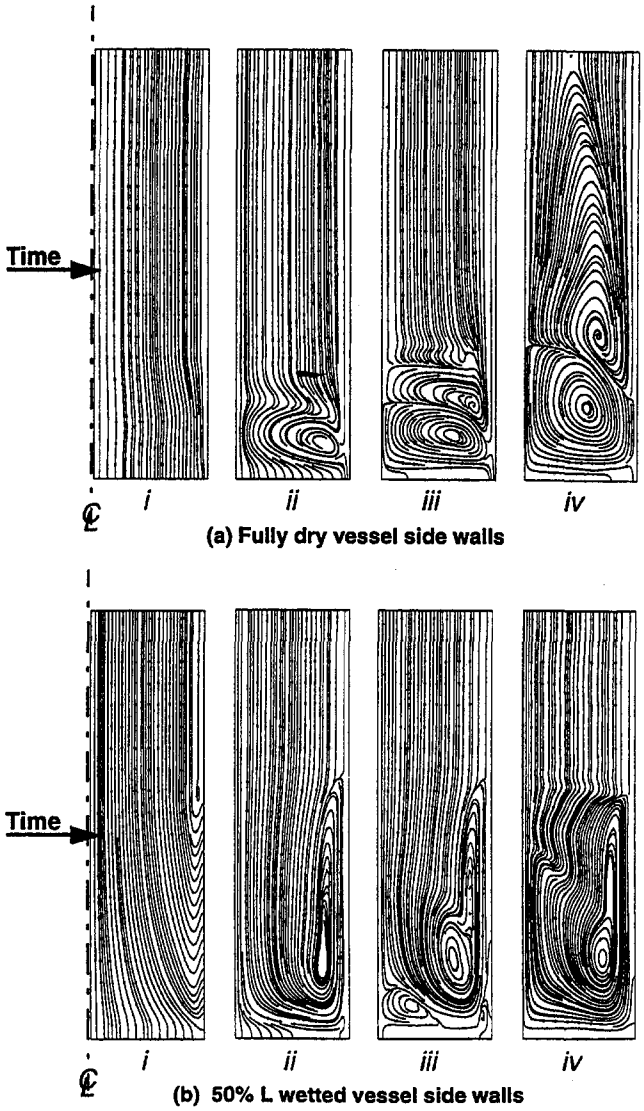

Fig. 3 Typical streamline distributions at different time intervals for two cases of side vessel walls wetting conditions, with *n*-pentane diffusing into air

will render the whole contents of the vessel too rich to support a flame initiated from an ignition source somewhere within the tank. Moreover, a flame anywhere just outside will be unable to lead to a flame flashing within the tank. The corresponding variation in the size of the flammable zone with time is also shown. It indicates a gradual growth in size throughout the time period when the lean limit concentration progresses upwards towards the open end of the tank. Beyond this period, the size of the flammable zone decreases somewhat more rapidly as the rich limit progresses upwards towards the open end. Beyond this time the flammable zone disappears altogether from the tank and remains usually so afterwards.

Accordingly, on this basis it can be seen that during the development of the flammable zone within the tank, there is a time when only an ignition source within the tank can lead to a flame flash. But, once the lean flammability limit concentration boundary reaches the outlet of the tank, then an ignition source just outside the tank outlet can also produce a flame flash within the tank contents.

The exposure of a liquid fuel surface within a vertical cylindrical container will involve in time the spread of fuel vapor upwards into the air due to the combined effects of diffusion and convection. Flammable mixtures will be formed and spread, while varying in size and location, at rates depending on the physical properties of the liquid, the initial concentration of fuel vapor in the air, geometrical configurations, and initial temperatures of the liquid, walls, and air. These flammable mixtures can be generated very rapidly, initially at locations immediately above the initial liquid fuel-air interface. Later on, as much fuel vapor diffusion takes place, the flammable region not only grows in size considerably, but also tends to move upwards bounded by a too fuel rich zone on the side of the liquid fuel surface and a too fuel lean region on the upper air side. Obviously, the phenomena involved will be modified at any location, not only by the changes in density and concentration, but also by the fact that the local temperature is likely to be changing as a result of the thermal requirements associated with evaporation and heat transfer. This will tend to cool the temperature of the liquid surface and the vapour-air layers above the liquid surface as well as setting a temperature gradient within the liquid. Accordingly, as indicated earlier, our modeling of these processes in full while accounting for these changes provide a much better agreement between calculated and measured fuel concentrations corresponding to the lean limit progression in the vessel with time. The corresponding predicted concentrations and their changes with time on the basis of constant temperature and property values displayed a significant deviation from those of the experiment (Bunama et al., 1995).

Figure 3(a, b) shows a typical development of the calculated streamline distribution with time both for a dry cylinder side wall and when wetted uniformly with a fuel to the extent of 50 percent of the cylinder height. It can be seen that a very diverse flow regime is developed with time controlled through the interaction of the solutal and thermal buoyancy forces. This multidimensional behavior of the flow field would result in a complex flammable region which justifies the need for the detailed model used to predict the flammable region development in space and time. The time required for the flammable region to sweep out of the vessel is very markedly reduced with the increased level of fuel wetting of the side walls. It would also represent an increased level of hazard and especially in case of an ignition source or a flame existing just outside that can lead to a flash fire within the vessel.

Changes in the initial temperature of the system fuel, air, and walls produce significant changes in the size of the flammable region and the times required for the lean and rich limits boundaries to reach the container outer rim. As can be seen in Fig. 4, reducing the temperature not only increases the size of the flammable zone but also prolongs the time needed to render the contents of the whole vessel nonflammable. Moreover, for cases

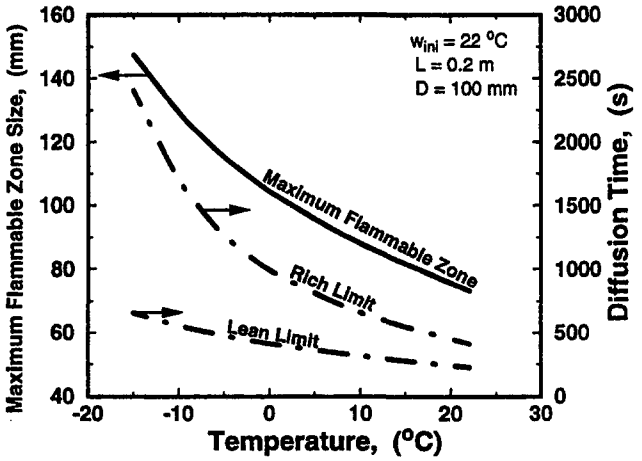

Fig. 4 Effects of the initial temperature of fuel, air, and vessel walls on the maximum flammable zone size and on the arrival times of the lean and rich flammability boundaries at the vessel outer rim

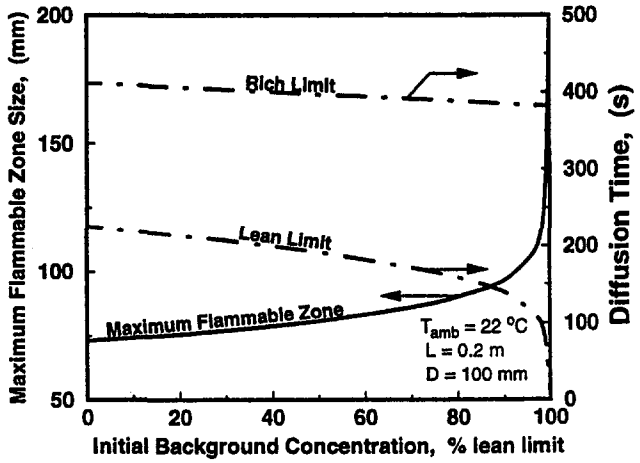

Fig. 5 Effects of the presence of initial fuel traces in the overlaying air on the maximum flammable zone size and on the arrival times of the lean and rich flammability boundaries at the vessel outer rim

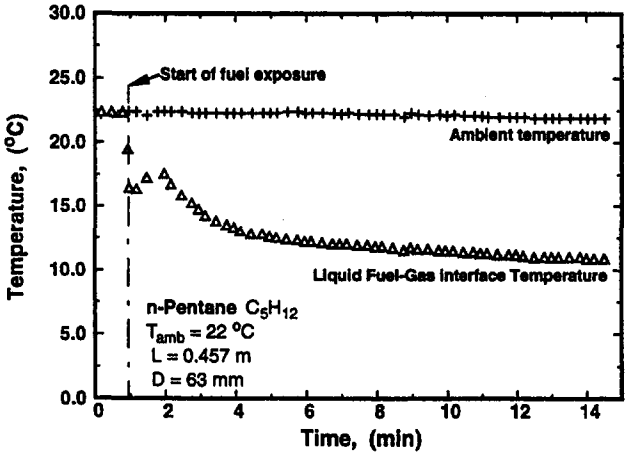

Fig. 6 Variations with time of the measured temperature of the liquid-gas interface

when the overlaying air initially contained some fuel vapour homogeneously mixed with it at concentrations represented as a percentage of the corresponding lean limit, it can be typically seen in Fig. 5 that although the time requirements to have the lean limit boundary arrive relatively quickly at the outlet of the vessel, the size of the flammable zone is extended very markedly while the total time required to render the contents of the vessel nonflammable is hardly affected. Thus, it can be seen from these calculated results that having full wetted walls, reduced ambient temperature, or the presence of pre-evaporated fuel with the air represent increased fire flash hazards in liquid fuel containers that are partially empty while they are exposed to the outside atmosphere.

The vaporization, convective diffusion, and flame spread phenomena were experimentally examined within smooth circular long vertical glass cylinders of varying lengths of up to 3.00 m and with different diameters varying from 25 mm to 100 mm. The typical tube arrangement is similar to that shown schematically in Fig. 1. These cylinders, which were either fully open to the atmosphere or partially closed with a circular central, aperture, initially contained only air. Some liquid fuel was promptly introduced at the base of the cylinder without contaminating the air with fuel vapor. The procedure employed to achieve this was through having to remove the base of the vessel while introducing the fuel in a shallow tray of a similar diameter so as to suddenly produce at the required time a vessel with a pool of liquid fuel at its base. This procedure was shown to be effective and produced repeatable results. The temperature of the liquid fuel could be made different from that of the overlaying atmosphere by external jacketing with ice or hot water. Of particular concern was the establishing at any specific location within the vessel the minimum time required to form a flammable region. This was determined through the mounting of horizontal ignition electrodes along a diameter within the tank at the location of interest and finding out through intermittent deliberate sparking whether a propagating flame can be initiated then or not. This approach could establish the minimum time requirements to produce a flammable mixture at any location. A similar procedure can be followed to determine whether after a certain time period the concentration of the diffusing fuel vapor in the space within the tank becomes sufficiently high at that location that no flame can propagate.

Much of the work carried out involved the use of the relatively volatile fuel n-pentane. The passage of an electric spark for this local flammability testing was ensured not to affect the diffusional processes. The period between the passage of consecutive sparks was typically varied between two to twenty seconds depending on the lapse of time from the commencement of the diffusion. Also, the characteristics and energy of these intermittent sparks used to monitor the first development of a propagating flame was strictly controlled since using highly energetic sparks could ignite mixtures and produce a localized flame flashes within mixtures that may not be wholly flammable. Prolonged application of the spark during the early stages of the diffusion was unnecessary and also avoided.

Experimental Results and Discussions

Figure 6 shows experimentally how the temperature around the base of the fuel tank changes with time when initially the whole liquid and apparatus were at the same temperature as that of the air. It can be seen for a typical case that a significant drop in temperature of the liquid fuel surface of around 10°C, is produced due to the effects of liquid fuel vaporization. Moreover, the walls of the base of the tank undergo similarly cooling as a result of heat transfer.

The progress of the lean limit concentration along the tube with time when, established experimentally on the basis of the time to the first successful flame flash at a specified location from a periodic electric spark as described earlier, is shown in Fig. 7 for two initial ambient temperatures of 22°C and 2.5°C. The slower progress of the lean flammability limit front at the lower temperature is evident. However, following a first flame flash while leaving the fuel vessel and the whole system undis-

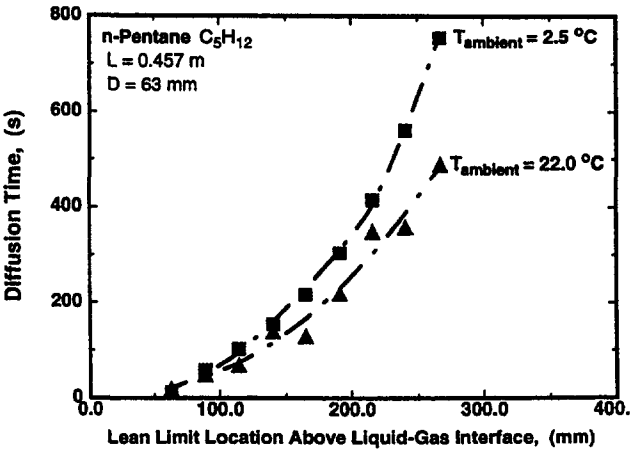

Fig. 7 Variation of the minimum time needed to achieve the required lean limit concentration at different heights above the liquid fuel-gas interface for two different temperatures

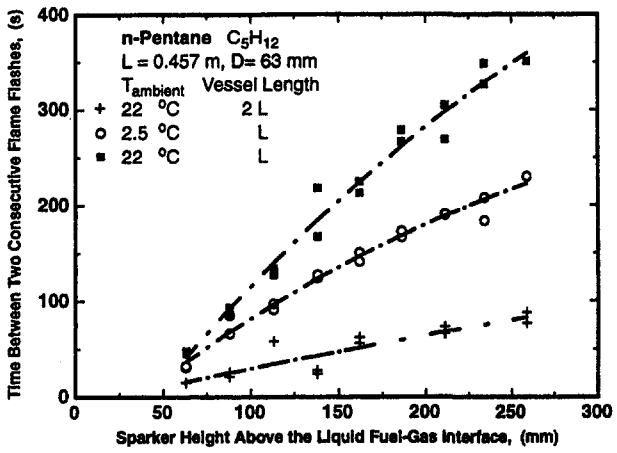

Fig. 8 The effect of changing ambient temperature and vessel length on the time interval between two consecutive flame flashes at different sparker heights above the liquid fuel-gas interface

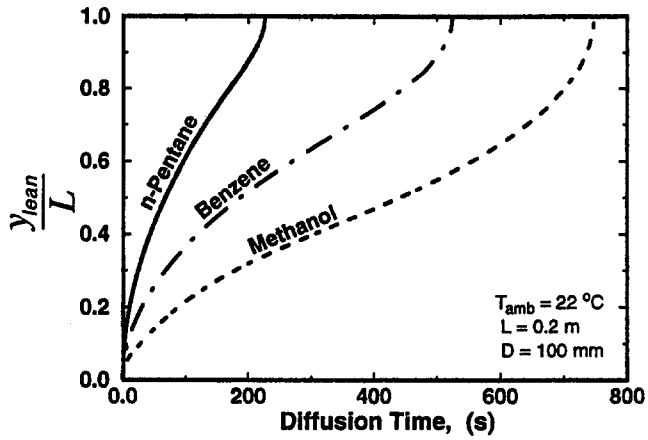

Fig. 10 Predicted lean flammability limits boundary displacement with time for *n*-Pentane, Methanol, and Benzene

turbed, the time needed to produce a second flame flash, as can be seen in Fig. 8 tends to increase approximately linearly with locations above the fuel surface. Moreover, this time period for any location along the vessel appears to be approximately of the same order as the time needed to form a flammable mixture the first time. Evidently the effects of vitiation with combustion products were counter-balanced by the heating due to energy release effects aiding both the fuel vaporization and the diffusional processes of fuel vapor and fresh air. It can also be seen that doubling the height of the vessel while keeping the diameter the same, reduced this time period between two consecutive flame flashes substantially. This is probably due to the reduced contribution of the dilution of the atmosphere within the larger capacity vessel and the greater availability of unconsumed air that can descend faster to replace the products of combustion and produce a flammable zone once more. Similarly, a colder ambient and fuel liquid temperature of 2.5°C generated more quickly a flammable mixture at any location. The faster convectional processes as a result of the much increased buoyancy forces speed up the scavenging of the products of combustion and their displacement by a heavier fresh air. The unconsumed fuel vapor adjacent to the surface of the liquid within the too rich region will provide some of the fuel vapour needed more readily as it becomes a little warmer and more agitated by the flashing flame propagation and subsequent diffusional processes. Moreover, the size of the flammable zone and consequently mixture requirements, are reduced significantly with the lowering of the temperature.

Figure 9 shows experimentally that changes in the diameter of the vessel with dry clean walls has only minor effects on the time needed to generate the first flame flashing. A small tendency to increase this time can be noted with larger diameter vessels, probably as a result of the reduced relative contribution of drag at the walls to the convective and diffusional processes. It was also evident that partially restricting the emergence of fuel vapour through having a partially open tank, speeds up the diffusional processes and permits a substantial reduction in the time between consecutive flame flashing, in comparison to the case of a fully open vessel. This is also reflected when a reduction in the diameter of the vessel is employed.

Much of the results shown were obtained at this stage for the relatively volatile fuel *n*-Pentane. However, it would be expected that changes in the type of the fuel though will show qualitatively similar trends, quantitatively a big difference can be observed. For example, Fig. 10 shows the variation of the predicted lean flammability limits relative displacement within the vessel with time for the three fuels benzene, *n*-pentane and methanol. It can be seen that as a result of the combined effects of the transfer processes involved the progress of the lean limit boundary for methanol is significantly slower than those for *n*-pentane and benzene. Fig. 11 shows the calculated variations of the rate of liquid fuel evaporation and subsequent rate of its emergence from the vessel with dimensionless time for the three

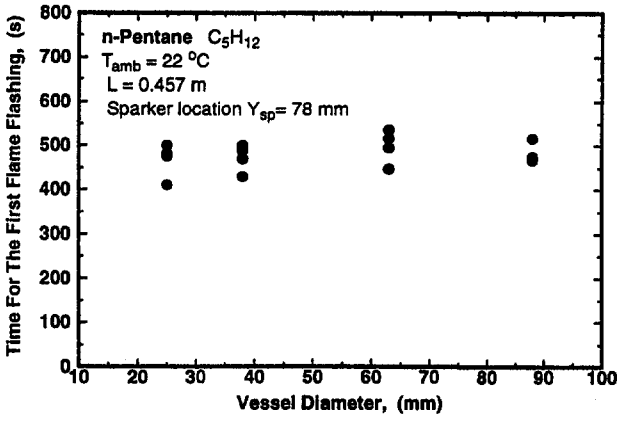

Fig. 9 Effects of changing the vessel diameter on the time of the first flame flashing at a fixed sparker location above the liquid fuel-gas interface

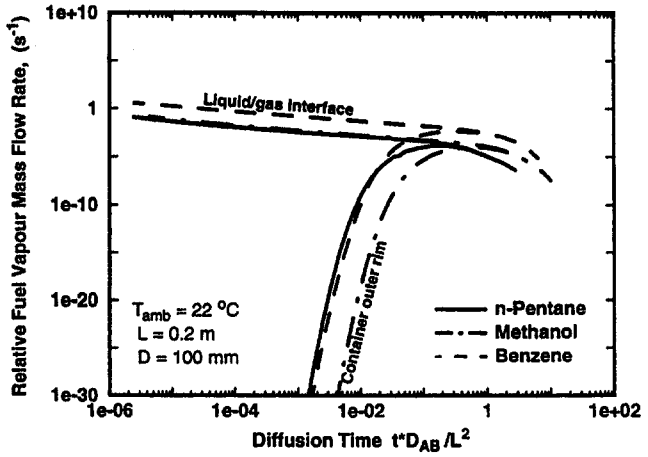

Fig. 11 Predicted relative evaporation rate of fuel from the liquid-gas interface and fuel vapour subsequent rate of emergence at the vessel outer rim for *n*-Pentane, Methanol and Benzene

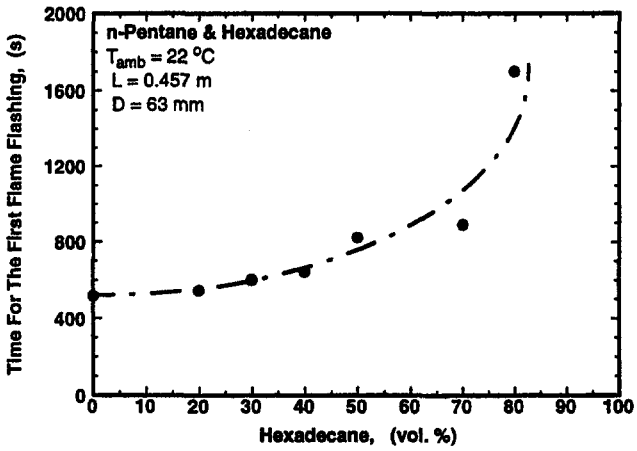

Fig. 12 Effects of adding hexadecane to *n*-pentane at different mixture ratios on the time for the first flame flashing

fuels when reckoned relative to the minimum amount of fuel needed to render the whole vessel volume at the lean limit. Similar trends are evident. However, as shown in Fig. 12 experimental results obtained for various binary mixtures of the volatile *n*-pentane, and the very much less volatile hexadecane, the minimum time requirements to produce a flammable mixture at a location around half way through the vessel increases very markedly as the volatility of the fuel mixture is reduced. This indicates that in fuel mixtures, such as commercial fuels that contain only small fractions of highly volatile components, the contents of the vessel will remain for a very substantially longer time than for *n*-pentane liable to fire spread and thus represents a greater fire hazard.

Conclusions

- The formation of flammable regions, their growth and decline within the confines of a vertical cylindrical tank containing initially air with unvaporized liquid fuel (*n*-Pentane) at the base can be established from the transient development of the local lean and rich flammability limits concentrations.
- Three time phases can be identified consecutively in this development. The first is associated with the flammable region located entirely within the vessel. The second begins after the lean limit boundary has reached the top while the rich limit boundary is still within. The third phase begins after both the lean and rich limit boundaries have arrived at the tank top rendering the whole contents too rich to support a flame.
- following some of the observations made experimentally: (1) the progress of the lean limit front upwards is slowed with lowering the system temperature; (2) in the presence of an ignition source, a flame flash may develop. This is followed after the lapse of some time by yet another flame; (3) the time interval between any reoccurring flame flashing increases approximately linearly with the height of the ignition source from the liquid fuel surface; (4) the evaporation of the liquid fuel at the liquid-gas interface resulted in a local temperature drop that significantly affected the mass transport processes involved; (5) changes in the diameter of the vessel, for the same height, has only a minor effect on the time needed to generate first flame flashing; (6) the diffusional processes in a partially open tank tend to be somewhat faster than those in fully open tanks; and (7) reducing the concentration of volatile components in liquid fuel mixtures will render the contents of a fuel tank more likely to undergo a flame flash for longer times than those rich in volatile components.

Acknowledgments

The financial support of the Imperial Oil Corporation of Canada (ESSO) and the Natural Sciences and Engineering Research Council of Canada (NSERC) is gratefully acknowledged.

References

Bunama, R., and Karim, G. A., 1997a, "Modeling the Transient Formation of Flammable Atmospheres Due to Convective Diffusion," *ASME Journal of Energy Resources Technology,* Vol. 119, pp 271–275.

Bunama, R., and Karim, G. A., 1997b, "Modeling the Transient Formation of Flammable Atmospheres Within Cylindrical Vessels Containing Some Fuel," *Proceedings, 5th Computational Fluid Dynamics Society of Canada Conference, CFD97,* pp. 12.9–12.15.

Bunama, R., Zhang, C., and Karim, G. A., 1995, "An Experimental and Analytical Examination of the Transient Formation of Flammable Atmospheres within Fuel Containers," *Proc. of Spring Technical Meeting,* The Combustion Institute, Canadian Section, pp. 197–200.

Cussler, E. L., 1992, *Diffusion Mass Transfer in Fluid Systems,* Cambridge, New York.

Karim, G. A., and Zhang, C. Y., 1992, "Flame Propagation Within Stratified Flame Mixtures Formed by Diffusion in a Vertical Tube," *Materials and Design Against Fire,* Proceedings of the Institution of Mechanical Engineers, London, U.K., pp. 75–81.

Markham, B. L., and Rosenberger, F., 1980, "Velocity and Concentration Distributions in a Stefan Diffusion Tube," *Chemical Engineering Communications,* Vol. 5, pp. 287–298.

The Effect of Time of Exposure to Elevated Temperatures on the Flammability Limits of Some Common Gaseous Fuels in Air

I. Wierzba

B. B. Ale

Department of Mechanical Engineering,
The University of Calgary,
Calgary, AB, T2N 1N3,
Canada

The flammability limits of methane, ethylene, propane, and hydrogen were experimentally determined at elevated initial mixture temperatures up to 350°C at atmospheric pressure for upward flame propagation in a steel test tube apparatus. The existence of preignition reactions at these levels of temperatures that may influence the value of the flammability limits was also investigated. The fuel-air mixtures were exposed to elevated temperatures over different periods of time before spark ignition (up to 2 h). It was shown that the flammability limits for methane widened approximately linearly with an increase in the initial mixture temperature over the entire range of temperatures tested and were not affected by the length of the exposure time to these temperatures before spark ignition. However, different behaviour was observed for the flammability limits of the other tested fuels—ethylene, propane, and hydrogen. At higher temperatures the flammability limits narrowed and were very significantly affected by the exposure time. The longer was the exposure time of fuel-air mixtures to the elevated temperatures, the narrower were their flammability limits.

Introduction

Alternative gaseous fuels are increasingly employed in industrial gas turbines installations in a variety of applications such as the production of power and for gas compression. This is prompted by their increased availability at attractive prices as well as by their potential for reduced emissions in comparison to liquid fuels. It is essential to ensure in such applications the safety against the risk of fire and explosion. The knowledge of the flammability limits is important in assessing these hazards. Although much research has been conducted in the field of flammability limits there are still many questions that cannot be answered adequately. For example, there are many industrial processes conducted at elevated temperatures and a knowledge of the corresponding flammability limits is needed for safety considerations. Reference to the literature indicates that at present only very limited such data are available (Coward and Jones, 1952; Zabetakis, 1965; Bunev, 1972; Hustad and Sonju, 1988). The apparatus used to determine the flammability limits as well as some operational conditions (e.g., temperature, pressure, direction of flame propagation, and ignition source) are usually described, while the time of exposure of fuel-air mixtures to elevated temperatures before spark ignition is usually not specified. However, there is the possibility that at elevated temperatures fuel-air mixtures will undergo substantial preignition reactions, especially when the test fuel-air mixture is allowed to stand at this temperature for a while before ignition. It was reported by Bunev (1972) that the time of exposure of hydrogen-air and methanol-air mixtures to elevated temperatures before ignition influenced significantly the rich flammability limit determined in a relatively small spherical stainless steel reactor with central ignition. The limit decreased when the exposure time increased, this was attributed to existence of unspecified preignition reactions. Moreover, for some fuel and temperature combinations there is the possibility of surface reactions taking place that effectively change the composition of the mixture (with time) before ignition is applied (Ale and Wierzba, 1997).

The purpose of the present work was to determine the flammability limits of some common gaseous fuels at elevated temperatures for upward flame propagation associated with the widest flammable range. Additionally, the extent to which time of exposure of fuel-air mixtures to the elevated temperatures before spark ignition influenced the limits was established. The existence of any preignition reaction activity under these conditions was also investigated.

Apparatus and Experimental Procedure

The apparatus (Fig. 1) was in general similar to that developed and used by the U.S. Bureau of Mines in their flammability limits work. The limits were established in a stainless steel smooth circular tube of 50.8 mm diameter and just over one metre in length. The tube was heated externally uniformly electrically. A set of unsheathed thermocouples (K-type) was used to monitor the wall and gas temperatures along the whole length of the flame tube. The test tube temperature was maintained at the required level for the desired residence time using a temperature controller. The pressure inside the test tube was monitored using a strain gage type pressure transducer located at the top of the tube. Ignition of the test mixture was initiated by an electric spark discharge between two horizontal conical tungsten electrodes. The electric power for ignition was supplied by a 10 kV, 23 mA centre-tapped transformer with its primary hooked to a 110 V, 60 Hz supply. The ignition system was optimized with respect to the electrode gap (6.4 mm), and the spark duration to give the widest flammability limits.

The homogeneous mixture of desired composition was prepared on the basis of partial pressures in the stainless steel mixing chamber at room temperature. It was introduced into the previously evacuated test tube when its temperature along the entire tube length was stabilized within ±3°C of the nominal test temperature. The gas mixture was permitted to flow from the mixing chamber to the test tube through inlet valves located at the top and bottom ends of the tube until the pressure within the tube was slightly above atmospheric. The valves between

Contributed by the International Gas Turbine Institute and presented at the International Gas Turbine and Aeroengine Congress and Exhibition, Stockholm, Sweden, June 2–5, 1998. Manuscript received by the ASME Headquarters April 1, 1998. Paper No. 98-GT-179. Associate Technical Editor: R. Kielb.

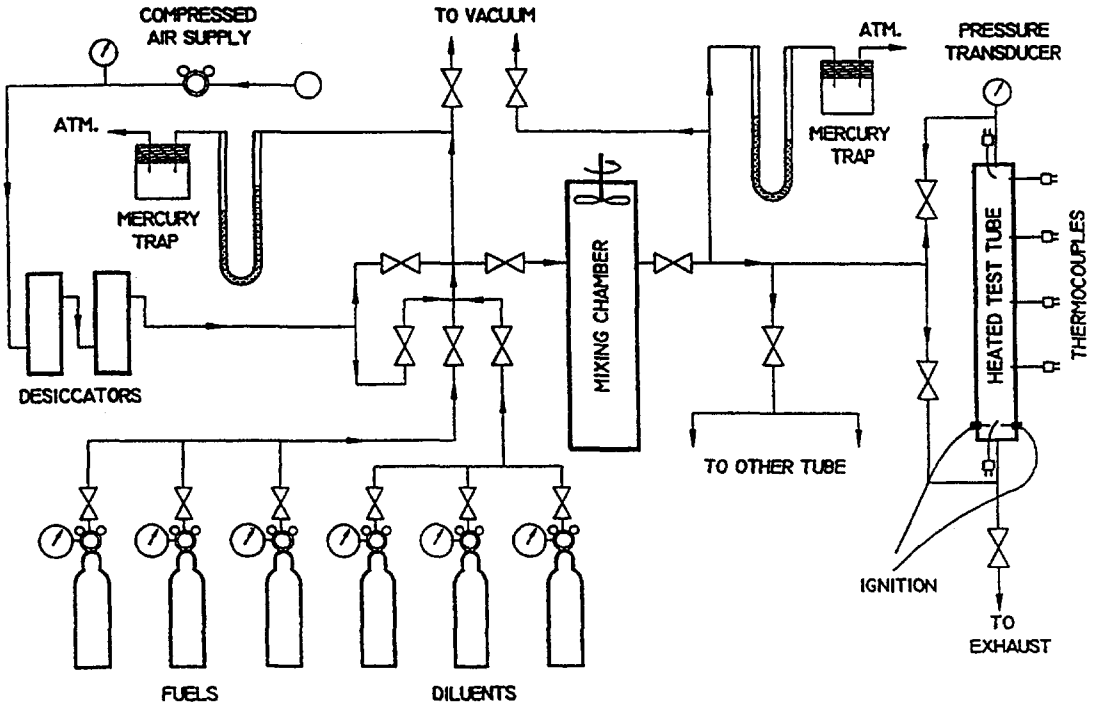

Fig. 1 Schematic diagram of the apparatus

the mixing chamber and the tube were then closed. The time for the gas mixture to reach thermal equilibrium with the tube wall usually did not exceed 30 s. The fuel-air mixture was then kept inside the test tube for the desired residence time. To allow the flame propagation at constant pressure, the valve at the bottom of the test tube was slowly opened to exhaust just prior to passing the spark. Ignition was initiated by activating the interval timer, while the top and bottom thermocouples readings were monitored. A sudden increase in the bottom thermocouple reading indicated the initiation of a flame kernel around the igniter, while a sudden rise in the top thermocouple reading marked arrival of the flame at the top of the tube. In the case of the flame arrival at the top of the tube, a new mixture with less fuel for lean mixtures or with more fuel for rich mixtures was prepared and tested again as described. In case when the flame did not arrive a new mixture with more fuel for lean mixtures or with less fuel for rich mixtures was prepared and tested. The entire procedure was repeated for various fuel-air mixture compositions until a mixture was found when the flame would not propagate the whole length of the tube, but propagation had been achieved in the mixture with a slightly modified composition.

A mixture was considered to be nonflammable if a flame kernel formed in the immediate vicinity of the spark at the bottom of the tube did not propagate the whole length of the tube in any of the repeated tests while using the same mixture composition. A number of experiments were also repeated to verify the repeatability of the results.

Using this procedure the flammability limits of hydrogen, ethylene, methane, and propane in air were determined for various initial temperatures of up to 350°C and various residence times of up to 2h.

Results

The flammability limits reported in this work relate to upward flame propagation at atmospheric pressure. The limits are quoted as the volumetric concentration of the fuel in the fuel air mixture.

The effect of the initial temperature on the flammability limits of methane, hydrogen, ethylene, and propane in air is shown in Fig. 2 for the residence time (i.e., time interval between the time of acquiring the desired initial temperature by the fuel-air mixture and initiation of spark ignition) of 10 min. It can be seen that the effect of the temperature depends on the type of the fuel.

Methane. The flammability limits of methane-air mixtures widen virtually linearly with an increase in the initial mixture temperature over the whole range of 21°C–350°C. No data are available in the literature for comparison for upward flame propagation. However, the observed trends for both lean and rich limits were similar with what has been reported by others in the literature (Coward and Jones, 1952; Zabetakis, 1965), for downward flame propagation.

Hydrogen. The flammable range of hydrogen-air mixtures also widens essentially linearly with increasing initial temperature but only at the initial temperatures lower than 200°C. The limits were somewhat narrowed when the initial temperature was higher than 200°C showing lower rich limits and approximately constant lean limits. This behavior of the lean limit was unexpected and inconsistent with trends reported for lean flammability limit of hydrogen-air mixtures at similar elevated temperatures by Hustad and Sonju (1988). No data are available for comparison of the rich limits of such mixtures for upward flame propagation.

Ethylene and Propane. For these fuels in air the flammable range widens with an increase in the initial temperature from 21°C to 300°C with a much stronger dependence for the rich limit. The only data available in the literature for comparison appears to be for downward flame propagation. However, our observed trends for upward flame propagation were similar with what has been reported in the literature for downward flame propagation (Coward and Jones, 1952; Zabetakis, 1965). When the initial temperature was higher than 300°C, the rich flammability limit for both of these fuels was sharply reduced. These limits were established in the absence of cool flames.

Effect of Residence Time. The effect of the residence time on the flammability limits depends on the type of fuel and the level of the mixture initial temperature.

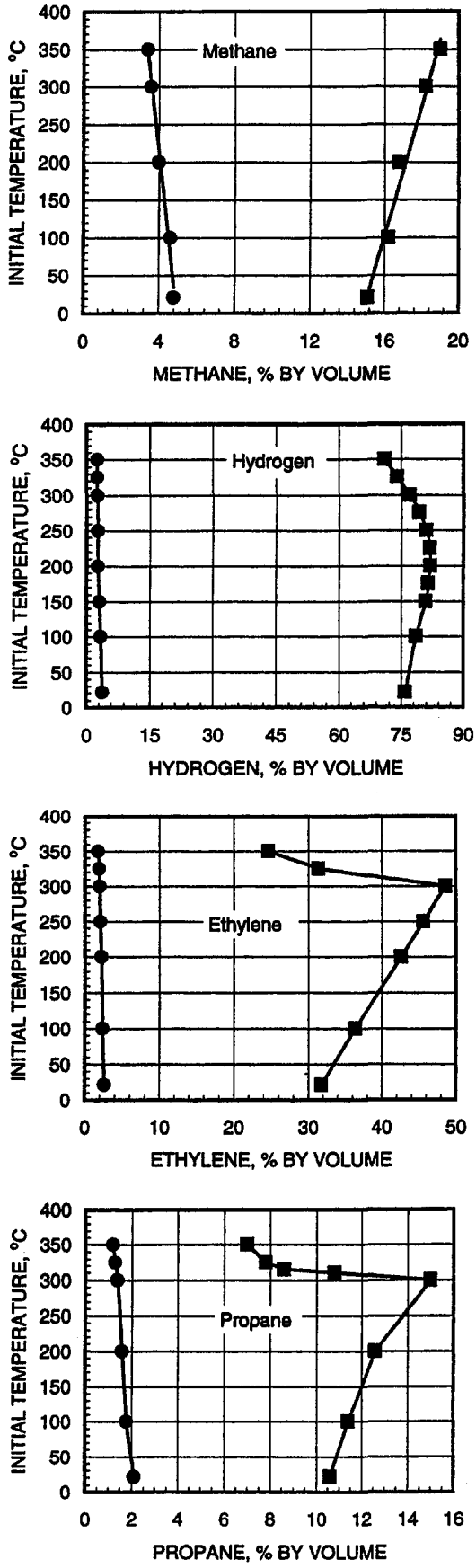

Fig. 2 Flammability limits of fuel-air mixtures as a function of initial temperature at residence time of 10 min

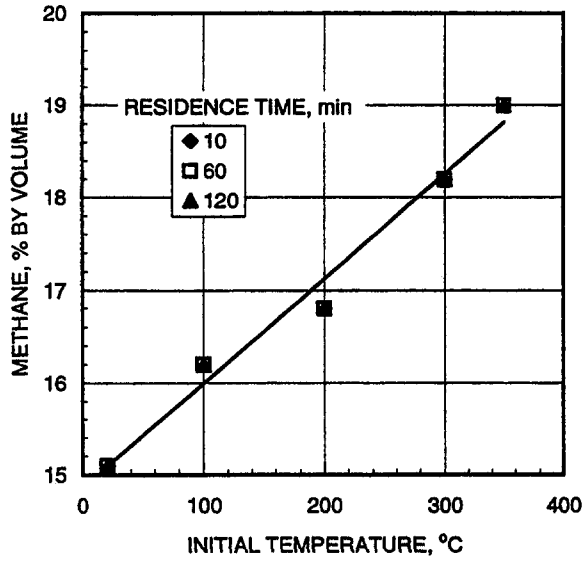

Fig. 3 Rich flammability limits of methane in air as a function of initial temperature at different residence times

The rich flammability limits of methane-air mixtures remained unchanged when the residence time was increased up to 2 h at all the different temperatures tested (Fig. 3). Different behavior was observed for the other fuels employed. The rich limits of ethylene and hydrogen were unaffected by the length of the residence time when the initial temperature was lower than about 200°C for hydrogen and 250°C for ethylene. When the temperature exceeded these values the rich flammability limits of both of these fuels were dependent of the duration of the residence time and the levels of the mixture temperature. The higher was the temperature and the longer was the time, the greater was the reduction in the limit (Figs. 4 and 5). Similar effect was also observed with propane-air rich mixtures as shown in Fig. 6 for the initial temperature of 350°C.

The lean limits of hydrogen, ethylene, and propane were also significantly affected by the duration of the residence

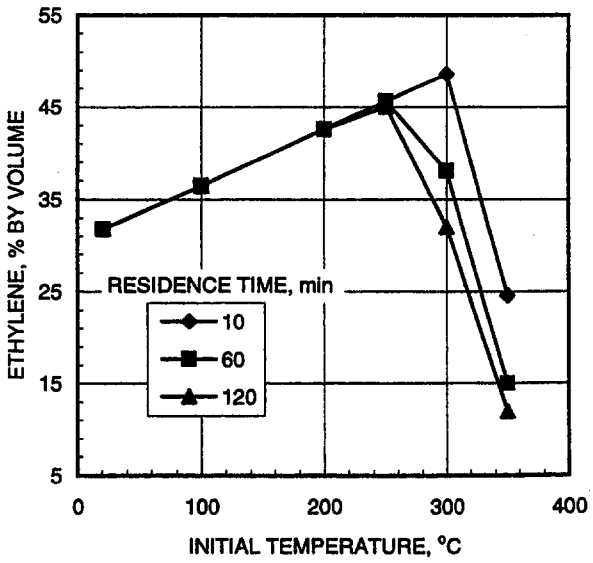

Fig. 4 Rich flammability limits of ethylene in air as a function of initial temperature at different residence times

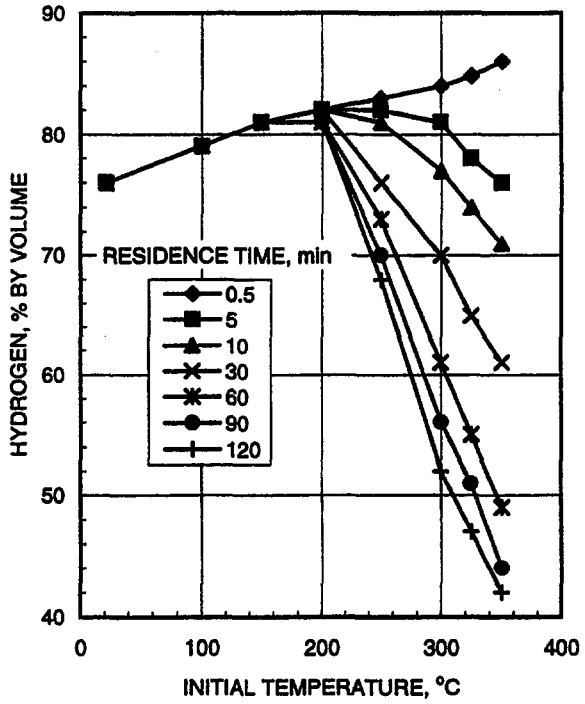

Fig. 5 Rich flammability limits of hydrogen in air as a function of initial temperature at different residence times

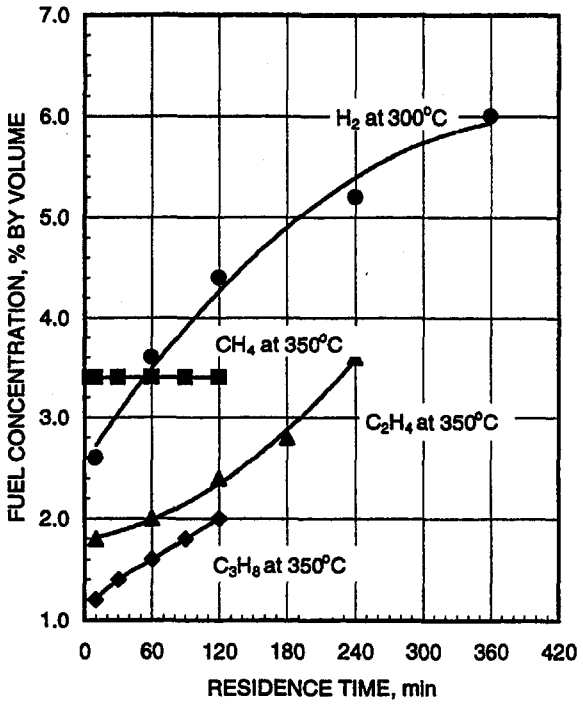

Fig. 7 Lean flammability limits of fuel in air as a function of the residence time at 300°C and 350°C

time as shown in Fig. 7 at the higher initial temperatures of 300°C and 350°C. The longer was the time, the higher was the lean limit.

Continuous measurements of the temperature of fuel-air mixtures within the test tube during the residence time showed that the temperature remained virtually constant during all experiments with all the fuels tested. However, the pressure within the test tube did not always remain constant during the residence time. The pressure remained constant for methane-air mixtures, decreased for hydrogen-air mixtures, increased for propane-air mixtures, and very slightly for ethylene-air mixtures. Examples of pressure variations within the different fuel-air mixtures at the initial temperature of 350°C are shown in Fig. 8.

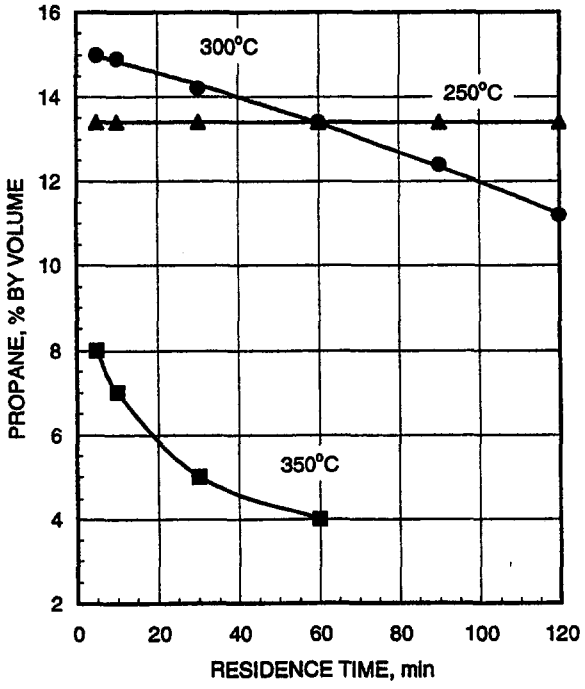

Fig. 6 Rich flammability limits of propane in air as a function of the residence time at different initial temperatures

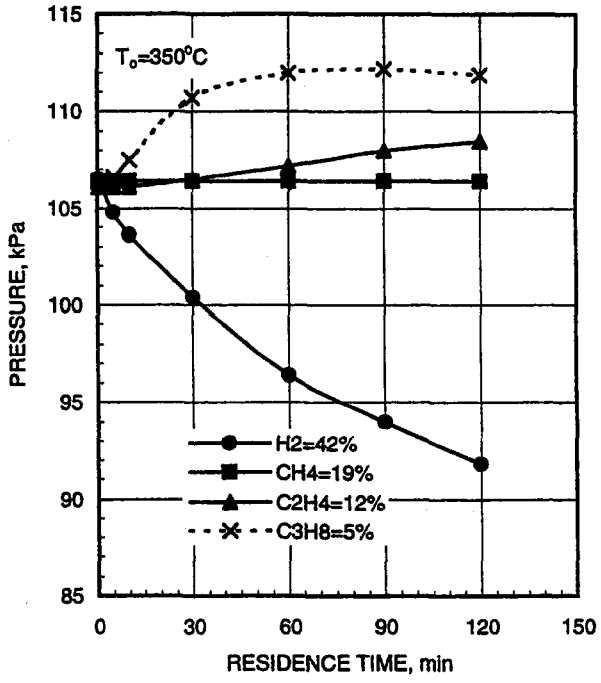

Fig. 8 Pressure variation within rich fuel-air mixtures as a function of the residence time at 350°C

Table 1

Test No.	Residence time, min	$L_{R,res}$ %	X %	Hydrogen depletion ($X/L_{R,res}$),%	Pressure, P_2 measured, kPa	Pressure, P_2 calculated, kPa	Remained oxygen, calculated,%	Remained oxygen, measured, %
1	5	81	1.3	1.60	104.2	104.3	3.34	3.4
2	10	77	3.0	3.90	103.4	103.4	3.53	3.6
3	30	70	5.9	8.43	101.3	101.9	3.35	3.8
4	60	61	9.7	15.90	98.9	99.9	3.44	3.8
5	90	56	11.8	21.07	96.7	98.8	3.34	3.8
6	120	52	13.5	25.96	94.6	97.9	3.33	3.6

Discussion

The independence of the flammability limits of methane-air mixtures of the residence time in the range of temperatures tested (up to 350°C) is indicative of the absence of significant preignition reaction activity whether due to gas-phase reactions or surface reactions. It was also confirmed by measuring the oxygen concentration within the mixture, which remained constant over the entire residence time.

On the other hand, the observed behavior of the flammability limits of the other fuels tested—hydrogen, ethylene, and propane—especially, at higher initial temperatures and longer residence times is not consistent with expectation in that it shows a reduction in the flammable range. This fact as well as the pressure variations within the fuel-air mixtures during the residence time is indicative of some chemical activity in the mixture taking place before spark ignition. The strong dependence of the rich limits of these fuels on the length of the residence time as well as the pressure variation within the tested mixtures supports this suggestion. The rich limits are associated with oxygen deficiency. A significant drop in the measured value of this observed limit would suggest the need for less fuel to consume the oxygen available or a more acute oxygen deficiency existing for the fuel available at the time of passing the spark for ignition. Some of the oxygen in the original mixture must have been consumed through oxidation of some fuel during the waiting period at higher temperature. Similarly, the lean limits are associated with fuel deficiency and an increase in the value of the limit could be indicative that some fuel could have also been oxidized before spark ignition. Measurements of oxygen concentration in the rich fuel-air mixtures at the end of the residence time confirm that some oxygen has been consumed. As an example, measured oxygen concentrations at the end of the residence time for different hydrogen-air mixtures (corresponding to different residence times) at the initial temperature of 300°C are shown in Table 1 together with the corresponding calculated oxygen concentrations (Eq. (2)).

Calculations involving detailed chemical kinetic simulation conducted for the oxidation of hydrogen (21 reactions, 8 species), ethylene (137 reactions, 32 species), and propane (137 reactions and 32 species) at initial temperature of 350°C showed an insignificant progress in the gas phase reactions of oxidation of these fuels at residence times up to 4.5 h (Fig. 9). However, a significant change in the value of their rich limit was observed experimentally at this temperature even for the short residence time of 10 min. Therefore, the observed changes in the flammability limits are most probably a result of the oxidation of these fuels over a period of time due to catalytic action on the stainless steel tube surface and not through gas phase oxidation. It is well-known that some metals (e.g., steel and iron are active catalysts for the oxidation of hydrogen and ethylene in air at elevated temperatures (Pangborn and Scott, 1979; Baker, 1974; Krishnankutty et al., 1996)).

Hydrogen Conversion. For hydrogen oxidation with the simplest product, water, the extent of hydrogen conversion during the residence time due to catalytic activity at the steel wall can be approximately estimated from the following considerations. It has been shown that the flammability limits are associated with a certain critical level of reaction temperature that is assumed to be proportional to the calculated adiabatic flame temperature, which has the same value under the same operating conditions (Zabetakis, 1965; Wierzba et al. 1996; Ale and Wierzba, 1997). If all the other operating conditions remain the same, this temperature should remain constant for limiting mixtures irrespective of the residence time length, i.e., any catalytic activity at the wall before ignition. Such temperature can be estimated on the basis of the known flammability, L_R, measured with very short residence time, i.e., before the onset of any catalytic activity. For the rich limiting hydrogen-air mixtures the following overall reaction applies:

$$L_R H_2 + (1 - L_R)(0.21O_2 + 0.79N_2) = \left.\begin{matrix}[L_R - 0.42\,(1 - L_R)]H_2 + \\ [0.42\,(1 - L_R)]H_2O + 0.79\,(1 - L_R)N_2\end{matrix}\right\} \quad (1)$$

At the surface of the stainless steel test tube some of the hydrogen is converted to water catalytically, and at the end of the residence time the overall reaction for the limiting mixture becomes the following:

$$\left.\begin{matrix}(L_{R,\mathrm{res}} - X)H_2 + XH_2O + 0.79\,(1 - L_{R,\mathrm{res}})N_2 + \\ \left[0.21\,(1 - L_{R,\mathrm{res}}) - \frac{X}{2}\right]O_2\end{matrix}\right\} = \left.\begin{matrix}0.79\,(1 - L_{R,\mathrm{res}})N_2 + [0.42\,(1 - L_{R,\mathrm{res}})]H_2O + \\ [L_{R,\mathrm{res}} - 0.42\,(1 - L_{R,\mathrm{res}})]H_2\end{matrix}\right\} \quad (2)$$

where $L_{R,\mathrm{res}}$ is the experimentally obtained rich limit at the corresponding residence time, and X is the amount of the hydrogen converted to water (volume percent in total mixture) during the residence time.

For an ideal gas constant volume and temperature conditions, changes in pressure are proportional to changes in the number of moles of the mixture or the pressure at the end of the residence time, P_2, is expected to be lower than the initial pressure at the commencement of the residence time, P_1, according to

$$P_2 = P_1\left(1 - \frac{X}{2}\right). \quad (3)$$

Oxygen concentration in the mixture at the end of the residence time can also be calculated from Eq. (2), and compared with those determined experimentally. As it can be seen from Table 1, the calculated values of the final pressure and oxygen concentration are in fair agreement with the experimental values. This supports the validity of the proposed approach.

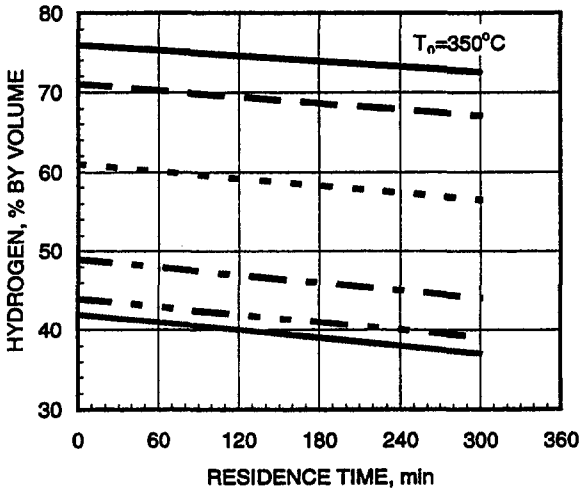

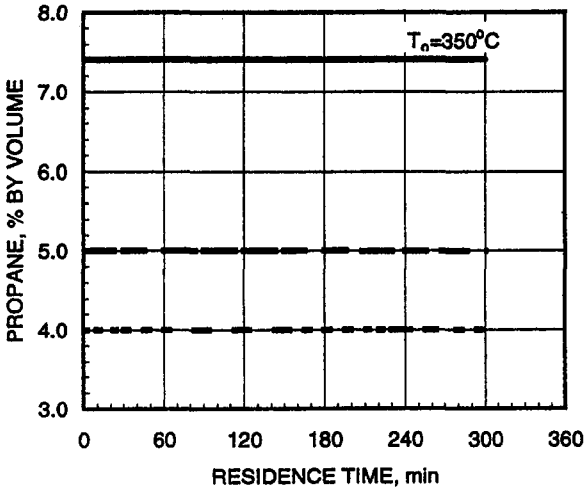

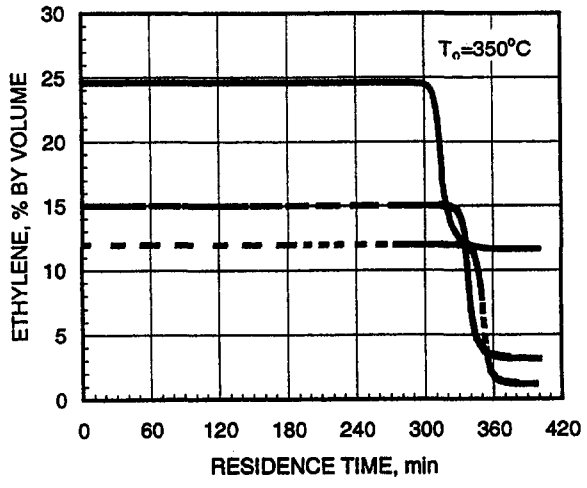

Fig. 9 Fuel concentration variation due to gas phase reaction activity at 350°C for different initial fuel-air mixtures

Similar approach can be used for ethylene and propane conversion on the steel surface if more information about products of their oxidation during the residence time is available.

Conclusions

- The residence time and the type of the test tube surface should be taken into consideration when determining the flammability limits at elevated temperatures.
- The flammability limits of methane in air widen with increasing the initial mixture temperature over the entire range of temperatures tested, i.e., from 21°C to 350°C. They are not affected by duration of the residence time and there is no chemical reaction activity during this time.
- The flammability limits of hydrogen, ethylene, and propane widen with increasing temperature up to a certain temperature level. With further increase in temperature the limits are narrowed with a significant drop in the rich limit value. At this temperature level the flammability limits depend on the duration of the residence time (before spark ignition). The higher initial temperature of the fuel-air mixture and the longer residence time, the smaller is the value of the rich limit.
- The narrowing of the limits is suggested to be mainly due to catalytic reactions on the stainless steel surface of the test tube.
- A simple method was proposed that allows estimate of the hydrogen conversion to water due to surface reactions within the steel test tube during the residence time fairly accurately.

Acknowledgments

The financial assistance of the Natural Sciences and Engineering Research Council of Canada (NSERC) and Canadian International Development Agency (CIDA) is gratefully acknowledged.

References

Ale, B. B., and Wierzba, I., 1997, "The Effect of Time Exposure of Ethylene-Air Mixtures to Elevated Temperatures on Their Flammability Limits," ASME 8th Annual International Energy Week Conference and Exhibition, Vol. IV, pp. 217–221.

Baker, N. R., 1974, "Oxides of Nitrogen Control Technologies for Appliance Conversion to Hydrogen Fuel," *Proceedings of the 9th Intersociety Energy Conversion Engineering Conference,* San Francisco, California, pp. 463–467.

Bunev, V. A., 1972, "Determination of the Concentration Limits of Flame Propagation at Elevated Temperatures," *Fizika Gareniya Vzryva,* Vol. 8, No. 1, pp. 82–86.

Coward, H. F., and Jones, G. W., 1952, "Limits of Flammability of Gases and Vapors," Bulletin 503, US Bureau of Mines, Pittsburgh, Pennsylvania.

Hustad, J. E., and Sonju, O. K., 1988, "Experimental Studies of Lower Flammability Limits of Gases and Mixtures of Gases at Elevated Temperatures," *Combustion and Flame,* Vol. 71, pp. 51–103.

Krishnankutty, N., Rodridnez, N. M., and Baker, R. T. K., 1996, "Effect of Copper on the Decomposition of Ethylene Over an Iron Catalyst," *Journal of Catalyst,* Vol. 158, pp. 217–227.

Pangborn, J., and Seott, M. L., 1979, *Hydrogen: Its Technology and Implications,* Volume IV, CRC Press, Inc., Boca Raton, Florida, USA, pp. 151–188.

Wierzba, I., Bade Shrestha, S. O., and Karim, G. A., 1996, "An Approach for Predicting the Flammability Limits of Fuel/Diluent Mixtures in Air," *Journal of the Institute of Energy,* Vol. LXIX, No. 480, pp. 122–130.

Zabetakis, M. G., 1965, "Flammability Characteristics of Combustible Gases and Vapors," Bulletin 627, Bureau of Mines, Washington, D.C.

The Development of a Computer Code for the Estimation of Combustor Exhaust Temperature Using Simple Gas Analysis Measurements

R. J. Bideau
Combustion Technology Center,
Aero and Industrial Technology Ltd.,
P.O. Box 46,
Burnley BB11 4BX, Lancashire,
United Kingdom

Advances in gas turbine technology have led to levels of turbine inlet temperature that preclude the use of thermocouple and simple gas analysis techniques for gas temperature determination. Simple gas analysis schemes rely on the measurement of a very limited range of species in the gas sample: typically, CO_2, CO, and hydrocarbons (UHC). A method of estimating the other important species is required. Simple gas analysis schemes that rely only on elemental mass balance equations to determine the concentration of species are inadequate where high temperature results in significant dissociation. A method has been developed to enable temperature determination at levels that render simple schemes inaccurate. The procedure is based on the measurement of CO_2, CO, UHC, and oxides of nitrogen in the exhaust gas. Other species concentrations are calculated using an assumption of partial thermodynamic equilibrium. This allows the calculation of many important combustion parameters. The method has been implemented as a computer code, with an object orientated design approach using the C++ language. The paper details the theory behind the approach and its implementation. The expected errors for practical applications are discussed and quantified. The method is illustrated by an exhaust temperature pattern factor investigation of an annular combustor. Temperatures determined by thermocouples are compared with those calculated from gas samples.

Introduction

The temperature distribution at the exhaust of a gas turbine combustor is not uniform, as there is insufficient time available for perfect mixing to take place. The distribution of temperature is a key parameter in the design of the cooling of the downstream stator and rotor elements, and, hence, knowledge of the temperature distribution is important in characterising the performance of a combustion chamber. Thermocouples have been used extensively to determine temperature profiles but are limited in their maximum temperature capability. Platinum/Rhodium thermocouples cannot be used above a temperature of approximately 2000 K and even at this temperature the life is short. The current trend towards combustors of higher mean exhaust temperature has resulted in the need for an alternative method.

A method has been developed to allow the gas temperature to be calculated from the measurement of exhaust gas species. The method, known as temperature by gas analysis (TBGA) allows measurements to be taken beyond the limitation imposed by thermocouples. The technique does introduce its own set of difficulties; the main problem is that, using currently available technology, it is impractical to measure all of the species in the exhaust in a time scale allowed by practical combustion tests. Instead, only a limited set of species can be measured; the rest must be calculated using a combination of assumptions and conservation requirements.

The method presented here has been developed specifically to bring together rigorous thermodynamics, numerical solution techniques and a modern object oriented programming technique. The emphasis has been on devising a method that is applicable to practical combustion testing; the intended application is the determination of combustion chamber exhaust temperature distribution.

Measurements

In general, combustion involves the reaction between a fuel and an oxidant to give combustion products. To allow calculations to be performed, measurements are required to determine the thermodynamic state and concentration of the reactants and products of the combustion process.

The product composition is determined by sampling a number of chemical species within the product gas. The methods developed in this paper are based on the measurement of the exhaust species CO_2, CO, UHC, and oxides of nitrogen. The accuracy of the method can be improved by measuring additional species. The emphasis here, however, is to present a practical method that can be used in routine combustion tests with commonly available equipment.

The fuel composition, temperature, calorific value, and in some cases specific heat capacity must be known. The composition and temperature of the oxidant must be measured. In the case of the most commonly used oxidant, air, the composition can be determined by measuring only the water content since the composition of dry air is known.

Development of the Algorithm

The reaction between a hydrocarbon fuel and an oxidant can be represented in general by Eq. (1).

Contributed by the International Gas Turbine Institute and presented at the International Gas Turbine and Aeroengine Congress and Exhibition, Stockholm, Sweden, June 2–5, 1998. Manuscript received by the ASME Headquarters April 1, 1998. Paper No. 98-GT-180. Associate Technical Editor: R. Kielb.

$$\text{Fuel} + \text{Oxidant} \rightarrow \text{Products} \quad (1)$$

Within a gas turbine combustor, combustion can be considered to be a steady flow process to which the steady flow energy equation can be applied (Rogers and Mayhew, 1980). Within the combustor, changes in kinetic energy and gravitational potential energy are dominated by the heat release due to chemical reaction. In addition, no work is done on the surroundings and the heat loss to the surroundings is small. Without significant error, only the enthalpy terms need be considered: there is merely a redistribution of energy from chemical to sensible.

Using the energy equation, provided that the enthalpy of the reactants and products can be evaluated, then the temperature of the products can be calculated. The problem, then, is that of determining the reactant and product compositions.

In general, the products consist of a very large number of species only a few of which are present in concentrations that make a significant contribution to the total enthalpy. The species list has been arrived at by considering a much larger set of species and then eliminating those that are found to have no significant bearing on the solution. This process has led to the same set of species as that used by other workers in the field of flame temperature (Ferguson, 1985a; Strehlow, 1984a).

With the restricted species list, the general combustion equation can be written as

$$\begin{aligned} &C_\alpha H_\beta O_\gamma N_\delta S_\varepsilon Ar_\theta + R(C_\kappa H_\lambda O_\tau N_\sigma S_\mu Ar_\upsilon) \rightarrow \\ &\quad n_1 CO_2 + n_2 CO + n_3 H_2O + n_4 H_2 + n_5 O_2 + n_6 N_2 \\ &\quad + n_7 O + n_8 H + n_9 OH + n_{10} N + n_{11} NO + n_{12} NO_2 \\ &\quad + n_{13} Ar + n_{14} SO_2 + n_{17}(C_\eta H_\omega O_\pi N_\rho S_\psi Ar_\phi) \end{aligned} \quad (2)$$

For each element, a species conservation equation can be written, as follows:

$$\alpha + R\kappa - n_1 - n_2 - \eta n_{17} = 0 \quad (3)$$

$$\beta + R\lambda - 2n_3 - 2n_4 - n_8 - n_9 - \omega n_{17} = 0 \quad (4)$$

$$\gamma + R\tau - 2n_1 - n_2 - n_3 - 2n_5 - n_7 - n_9 - n_{11} - 2n_{12} - 2n_{14} - \pi n_{17} = 0 \quad (5)$$

$$\delta + R\sigma - 2n_6 - n_{10} - n_{11} - n_{12} - \rho n_{17} = 0 \quad (6)$$

$$\varepsilon + R\mu - n_{14} - \psi n_{17} = 0 \quad (7)$$

$$\theta + R\upsilon - n_{13} - \phi n_{17} = 0 \quad (8)$$

In addition, an equation can be written for the total number of product moles; as follows:

$$\sum n_i - N = 0 \quad (9)$$

The exhaust concentrations of CO_2, CO, UHC, NO, and NO_2 will be measured on either a wet or a dry basis. Here it is taken that CO_2 and CO will be measured fully dry and the remaining species measured fully wet. Thus, the following constraints can be put on the solution:

$$n_1 = Ny_1\left(1 - \frac{n_3}{N}\right) \quad (10)$$

$$n_2 = Ny_2\left(1 - \frac{n_3}{N}\right) \quad (11)$$

$$n_{17} = Ny_{17} \quad (12)$$

$$n_{11} = Ny_{11} \quad (13)$$

$$n_{12} = Ny_{12} \quad (14)$$

The treatment of enthalpy, and in particular of heat release, can be simplified by considering the absolute enthalpy (Strehlow, 1984b) of all species. The absolute enthalpy of a species is defined as its enthalpy of formation at a standard reference state plus the sensible enthalpy above that reference state.

$$h_{abs}(T) = (\Delta h_f^\circ)_{298.15} + (h(T) - h_{298.15}) \quad (15)$$

By defining the enthalpy of all reactant and product species in this way, the overall enthalpy conservation requirement can be expressed simply as the reactant enthalpy being equal to the product enthalpy. The advantage of this approach is that the heat release due to combustion is automatically taken into account. The fuel enthalpy of formation can readily be calculated if the calorific value and composition are both known. For the generic fuel used, the enthalpy of formation can be determined from the calorific value and composition according to Eq. (16).

$$(\Delta h_f^\circ)_{\text{Fuel}} = (CV)_{\text{Fuel}} + \alpha(\Delta h_f^\circ)_{CO_2(g)} + \frac{\beta}{2}(\Delta h_f^\circ)_{H_2O(g)} + \varepsilon(\Delta h_f^\circ)_{SO_2(g)} \quad (16)$$

The enthalpy conservation requirement can be stated simply according to Eq. (17).

$$\sum (n_i h_i) - h_{\text{fuel}} - Rh_{\text{oxidant}} = 0 \quad (17)$$

The given equations are insufficient to define a unique solution; to proceed, simplifying assumptions must be made. For temperatures below about 2000 K (depending on the pressure and accuracy requirements) it is often permissible to assume that species 4, 7, 8, 9, and 10 have zero concentration. In this case, the measurements are sufficient to define a unique solution. At higher temperatures such an assumption leads to an over-prediction of temperature. A better assumption is that of partial chemical equilibrium at the flame temperature subject to the constraints imposed by the measured species.

The general requirement for a system at constant pressure and temperature to be in chemical equilibrium is that the Gibbs function for the system is a minimum (Zeleznik and Gordon, 1968). It is possible to construct equations based on this technique. The system Gibbs function can be minimized, subject to species conservation using the method of Lagrange (Grossman, 1988).

Such a method had been developed by the author for application to gas analysis. This approach shares some similarity to

Nomenclature

h = enthalpy
AFR = gravimetric air to fuel ratio.
UHC = unburnt hydrocarbon.
h_{abs} = absolute enthalpy
Δh = enthalpy change.
K = equilibrium constant.
CV = lower calorific value.
μ = chemical potential.
P_0 = standard state pressure.
P = reaction pressure.
R = molar air to fuel ratio.
N = total number of product moles.
n = moles of product.
y = measured species mole fraction.
T = temperature.
R_u = molar gas constant.
$C_\alpha H_\beta O_\gamma N_\delta S_\varepsilon Ar_\theta$ = fuel.
$C_\kappa H_\lambda O_\tau N_\sigma S_\mu Ar_\upsilon$ = oxidant.
$C_\eta H_\omega O_\pi N_\rho S_\varphi Ar_\phi$ = hydrocarbon.

Table 1 Definition of equilibrium constants

Reaction	Equilibrium Constant	Derived Expression
$\frac{1}{2}H_2 \leftrightarrow H$	$K_1 = P_H P_{H2}^{-\frac{1}{2}}$	$n_8 = K_1 n_4^{\frac{1}{2}} N^{\frac{1}{2}} P^{-\frac{1}{2}}$
$\frac{1}{2}O_2 \leftrightarrow O$	$K_2 = P_O P_{O2}^{-\frac{1}{2}}$	$n_7 = K_2 n_5^{\frac{1}{2}} N^{\frac{1}{2}} P^{-\frac{1}{2}}$
$\frac{1}{2}O_2 + \frac{1}{2}H_2 \leftrightarrow OH$	$K_3 = P_{OH} P_{O2}^{-\frac{1}{2}} P_{H2}^{-\frac{1}{2}}$	$n_9 = K_3 n_5^{\frac{1}{4}} n_4^{\frac{1}{2}}$
$\frac{1}{2}N_2 \leftrightarrow N$	$K_4 = P_N P_{N2}^{-\frac{1}{2}}$	$n_{10} = K_4 n_6^{\frac{1}{2}} N^{\frac{1}{2}} P^{-\frac{1}{2}}$
$H_2 + \frac{1}{2}O_2 \leftrightarrow H_2O$	$K_6 = P_{H2O} P_{H2}^{-1} P_{O2}^{-\frac{1}{2}}$	$n_3 = K_6 n_4 n_5^{\frac{1}{2}} P^{\frac{1}{2}} N^{-\frac{1}{2}}$
$H_2O + \frac{1}{2}O_2 \leftrightarrow 2OH$	$K_{20} = P_{OH}^2 P_{H2O}^{-1} P_{O2}^{-\frac{1}{2}}$	$n_9 = (K_{20} n_3 n_5^{\frac{1}{2}} N^{\frac{1}{2}} P^{-\frac{1}{2}})^{\frac{1}{2}}$
$H_2O \leftrightarrow 2H + \frac{1}{2}O_2$	$K_{21} = P_H^2 P_{O2}^{\frac{1}{2}} P_{H2O}^{-1}$	$n_8 = (K_{21} n_3 n_5^{-\frac{1}{2}} (N/P)^{1.5})^{\frac{1}{2}}$

that developed by other workers (Gordon and McBride, 1976; Zeleznik and Gordon, 1968) for calculating the equilibrium product composition for a given reactant composition. The major difference in this case is that the reactant composition is a function of the AFR which is itself an unknown. A solution can be obtained by adding the AFR as a dependant variable and reformulating the remaining equations accordingly.

The foregoing analysis includes the implicit assumption that the exhaust gas is spatially uniform in its composition and temperature. This, of course, is not the case and for practical applications there will always be concentration and temperature variation. For the method to be valid, it must be assumed that the transport of heat and species always occur at the same rate and by the same mechanism. If this assumption was violated then the temperature of a given gas sample would depend on heat transfer with neighbouring gas samples. It has been pointed out (Scott, 1991) that preferential diffusion of species of low molecular mass; principally, H_2 and H from high temperature regions to low temperature regions could be a serious source of error. The current justification for neglecting these effects is based on comparisons of gas temperatures from TBGA and from thermocouples an example of which is given later.

Gibbs Minimization Formulation. The Gibbs function can be minimized subject to the constraining equations by the method of Lagrange. A function F is defined according to Eq. (18).

$$F = \Sigma n_i \mu_i + \lambda_1[3] + \lambda_2[4] + \lambda_3[5] + \lambda_4[6] + \lambda_5[17] \quad (18)$$

The quantities denoted λ are Lagrangian multipliers and the terms appearing in square brackets are the species and enthalpy conservation equations that must be satisfied. The quantity μ_i is the chemical potential of the i^{th} species in the product list. The product mixture is assumed to behave as an ideal gas, hence, the chemical potential can be written as

$$\mu_i = \mu_i^0 + R_u T \ln\left(\frac{n_i P}{N P_0}\right) \quad (19)$$

The solution is obtained by taking partial derivatives of equation Eq. (18) with respect to the amounts of unknown product species (the n_i for unmeasured species), the molar AFR, R, the total moles of product N, the reaction temperature T, and the Lagrangian multipliers. For a minimum to exist, all of these partial derivatives must be simultaneously zero. The resulting system of nonlinear equations can be solved using a multidimensional Newton method, details are given later.

Equilibrium Constant Formulation. An alternative formulation has been used in addition to the Gibbs minimization approach. This possesses certain advantages in terms of the ease with which the resulting equations can be solved.

This method expresses relations between species in terms of equilibrium constants. This can be shown to be equivalent to the method of minimizing the Gibbs function (Zeleznik and Gordon, 1968).

Table 1 gives the equilibrium constants that are of use in formulating the solution. Not all of the relations given in the third column of table 1 are required; the set that is actually chosen depends on consideration of the stability of the solution technique.

The equations can be solved as a system of simultaneous nonlinear equations using the method of Newton (Press et al., 1992a). To do this, a set of independent variables must be chosen. A suitable set has been found to be the following:

1 The molar AFR
2 The temperature
3 The moles of H_2 in the product (n_4)
4 The moles of O_2 in the product (n_5)
5 The moles of N_2 in the product (n_6)
6 The total number of moles of product (N)

Using this set of variables, the equilibrium constants can be used to express the elemental conservation equations in terms of either measured quantities or the set of independent variables. To find the solution, six equations are required. These are the first four elemental conservation equations, Eq. (3) to Eq. (6), the fifth is Eq. (9), and the final equation is the enthalpy residual, Eq. (17).

Solution to both the Gibbs and equilibrium constant formulations is brought about using a multidimensional Newton method. A great deal of experimenting with different techniques and variations has been performed in order to select a method that is both fast and robust. The method of Broyden (Burden and Faires, 1889) was found to be fast but not robust with divergence frequently occurring if the starting approximation was not good. The disadvantage of the Newton method is that the Jacobian matrix is required for each iteration. Whilst this is not a major problem, the analytical expressions for the components of the Jacobian are tedious to derive. The current algorithms instead use a finite difference approximation to calculate the Jacobian. Whilst this increases the operations count, it still preserves the stability of the Newton method. Some form of guidance strategy has been found to be necessary to ensure convergence in some difficult cases. The Newton method can be embedded in a "globally convergent" strategy (Press et al., 1992b). Basically, if a Newton step would increase the residual, a scaled step is taken such that the function residuals are minimized along the Newton direction. This method can still fail if the solution temporarily wanders outside the domain of physical possibility for the independent variables; for example, a negative product concentration. A customized guidance strategy has been formulated that uses knowledge about the permitted and forbidden regions of the solution. The Newton direction is always followed, but, if it would take the solution into a forbidden region, the magnitude of the step is reduced by a small multiplicative factor. This strategy has been found to give an extremely robust algorithm.

It is necessary to obtain an approximate solution to start the main solution algorithms. This is easily accomplished by simplifying the species list in the combustion equation so that all products of dissociation are ignored. The resulting equations are close to being linear and can be solved from almost any physically possible starting point. The approximate solution thus obtained has been found to be suitable for starting the main algorithm. In the case of the Gibbs formulation, it has been found to be acceptable to start the solution procedure with all Lagrangian multipliers set to zero.

In both the Gibbs minimization and equilibrium techniques, the AFR and temperature are solved for simultaneously with the product composition. This ensures that the AFR is fully consistent with the solution unlike cases where the AFR is calculated from a simpler formula and imposed as a constraint on the partial equilibrium solution. Other workers have found it necessary to treat temperature as a special unknown; in the case of Hurley (1988) an outer temperature iteration is performed in which a composition solution is found at an imposed temperature. Solution is brought about in the outer

Table 2 Operating conditions for error analysis

Fuel		Aviation Kerosene
Gross calorific value	$MJkg^{-1}$	46.2
Net calorific value	$MJkg^{-1}$	43.2
Fuel carbon	$kgkg^{-1}$	0.8611
Fuel hydrogen	$kgkg^{-1}$	0.1389
Oxidant		Dry Air
Stoichiometric AFR		14.68
Fuel temperature	K	288
Oxidant temperature	K	800
Combustion pressure	kPa	700

iteration by the enthalpy conservation requirement. Whilst such an approach does work for the gas analysis calculation, the author has found that there is no need to treat the temperature as a special variable. Thus, temperature is an independent variable and solved for simultaneously with the AFR and species concentration. This has been found to have the additional advantage of reducing instability in the numerical solution technique and significantly reducing the overall operations count for the solution.

Implementation Details. The core algorithms have been implemented as machine independent C++ objects. Great emphasis has been placed on making the implementation modular so that algorithms can readily be modified, and new algorithms added without requiring changes to the whole of the code. As the code stands only a single line needs to be changed in order to select the solution technique. Thus, it is trivial to switch between the Gibbs minimization algorithms, the equilibrium constant algorithms and the undissociated algorithms. Other areas of the code, in particular, the sources of thermodynamic data can readily be substituted with no impact on other areas of the code.

This has been achieved using an object oriented programming approach. The chosen language, C++ was preferred over the more traditional scientific language, FORTRAN. In addition to the advantages of an object-oriented design, this allows the code to interface easily with modern operating environments such as Microsoft Windows and Unix. This aspect is vital, as, only by integration into control and data acquisition systems does TBGA realise its full potential.

Analysis of Errors and Uncertainty

The analysis of uncertainty is one of the most important, but at the same time, one of the more difficult tasks. This is particularly true at the higher temperatures where no comparison data from thermocouples are available. This section is not intended to give a definitive quantification of errors; instead indications are given of the magnitude of error that can be expected under typical scenarios. The discussion is relevant to a system using nondispersive infrared gas analyzers for CO_2 and CO with a flame ionization detector for UHC.

The errors in the predicted adiabatic flame temperature and AFR have been considered. The following are sources of error investigated:

1 Gas analyser readings
2 Oxidant inlet temperature
3 Fuel inlet temperature
4 Fuel calorific value
5 Fuel composition
6 Reaction pressure
7 The assumption of partial equilibrium

The errors are considered at the operating condition given in Table 2.

Errors in Measured Gas Concentration. The errors due to differences between the observed and actual species concentration are considered here. These differences arise due to a number of factors, principally, the errors due to the gas analyser and changes in gas composition introduced by the act of sampling the gas.

Errors due to sampling are not covered here; it is assumed that sufficient precautions will have been taken to ensure that the gas arriving at the analyzers has the same composition as that being sampled. However, it should be noted that the design of sampling probe and its operation are important parameters that affect the quality of the gas sample.

The measurement technique itself introduces a number of errors. CO_2 and CO are monitored using a nondispersive infra red (NDIR) technique, whilst UHC is measured using flame ionisation techniques (FID). There are errors inherent in the analysers themselves due to factors such as signal drift with ambient temperature, errors in the concentrations of calibration gases and errors due to interference from the presence of other species.

The interference from other species can be accounted for and this source of error is not considered further. The accuracy of the analysers is maintained by frequent calibration; it is limited by the uncertainty in the concentration of the calibration gases. The gases used to calibrate the analysers used in this study have a concentration uncertainty equal to ±1 percent of the stated value. In the subsequent analysis errors are considered to be a fixed percentage of the analyzer reading. Practical errors are in the region of ±1 percent to ±2 percent of reading.

The magnitude of the error has been quantified using simulated data. These have been generated by calculating the equilibrium composition and temperature at different AFRs, introducing perturbations to the composition, and processing it using the TBGA technique. The CO error presents some difficulty in that, due to the equilibrium technique, very little CO is predicted for AFRs a great deal leaner than stoichiometric. In practical systems, CO is present in super-equilibrium concentrations due to quenching for lean conditions. In such a case, the error due to CO is underestimated. Situations differ greatly from combustor to combustor in this respect, but provided that the CO level is small, the error in AFR and temperature will be small. Under the conditions given in Table 2, at an AFR of 150:1, the effect of introducing 500 ppm of CO is to change the calculated flame temperature by 4 K and the predicted AFR by 5. Hence, the temperature and AFR error in the lean region due to CO uncertainty is insignificant.

Figure 1 shows the effect of CO_2 uncertainty on predicted AFR. Apart from the behaviour about the stoichiometric point, the absolute uncertainty in AFR increases continuously with AFR. The relative uncertainty is approximately asymptotic to the assumed analyzer error as the error increases. Taking ±2 percent as a practical level of analyzer uncertainty, the error in AFR does not exceed ±3 AFR up to the maximum AFR of 150 plotted. In addition, the relative uncertainty in AFR only ex-

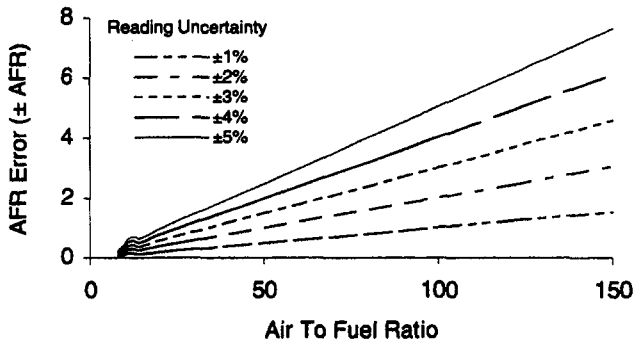

Fig. 1 The effect of CO_2 analyser error on AFR

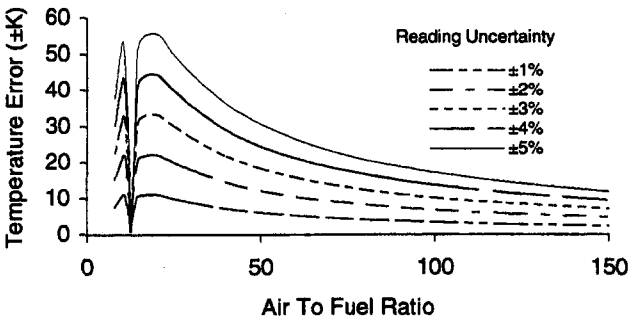

Fig. 2 The effect of CO_2 analyser error on temperature

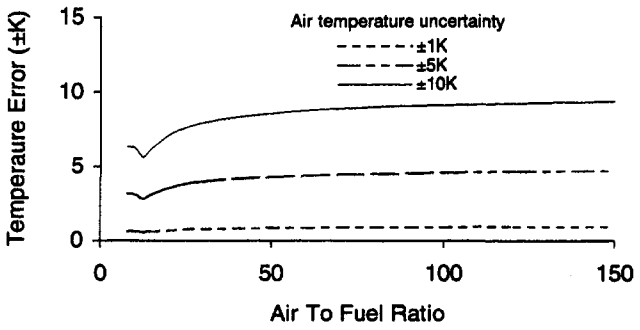

Fig. 3 The effect of air inlet temperature on flame temperature

ceeds ±2 percent in the near stoichiometric region, peaking at about ±2.5 percent.

The effect on temperature is shown in Fig. 2. The near stoichiometric region aside, this error decreases continually with increasing in AFR, for the ±2 percent analyser error, the maximum temperature error is about ±20 K just lean of stoichiometric.

The measured oxide of nitrogen concentration has only a tiny effect on flame temperature and AFR; at an AFR of 150:1, the introduction on 1000 ppm of NO only depresses the calculate flame temperature by 2.7 K. Thus, NO_x is not considered further as a source of error in temperature.

Hydrocarbon. The measurement of UHC is a problem because, instead of a single species, many are involved. These include unburnt fuel, partially oxidized fuel, pyrolyzed fuel, and new species formed in the flame. The commonly used technique of flame ionization detection (FID) for UHCs is not capable of resolving these individual species. The reading given is approximately proportional to the concentration of carbon chemically bound to hydrogen in the gas, however, the response of the analyzer is dependant on hydrocarbon molecular structure (Ferguson, 1985b). For practical calculation, it is necessary to approximate the properties of the UHC with those of known species. It is typical to assume that any hydrocarbon in the exhaust has the same composition as the fuel.

For the determination of combustor exhaust temperature under load conditions, where the UHC concentration is typically small, the temperature and AFR error are themselves small irrespective of the UHC composition assumed. For the conditions given in Table 2, the introduction of 100 ppm of UHC gives a relative AFR error of less than 0.7 percent and a temperature error of less than 0.6 K for the AFR range 8:1 to 150:1.

The situation can be different when combustion is very inefficient. In such a case the UHC reading can be very large and the error of assuming a simple UHC composition can give very significant temperature and AFR errors. The use of a technique that resolves individual hydrocarbon concentrations is required in this case. Gas chromatography is one such technique but is generally unsuitable for rapid determinations. Very large hydrocarbon concentrations are usually due to operating significantly rich of stoichiometric. Under such conditions the applicability of TBGA has to be questioned.

Oxidant Inlet Temperature. The effect of error in measured oxidant inlet temperature is shown in Fig. 3.

At high AFR, the absolute error in temperature is asymptotic to the absolute error in the inlet temperature. As the conditions become progressively richer, the error becomes less significant as the inlet air represents a reduced contribution to the reactant total enthalpy. Around stoichiometric there is a local dip in the magnitude of the error due to dissociation, here an increase in inlet temperature causes an increased amount of dissociation: the change in enthalpy is partially absorbed into a shift of composition rather than temperature.

The error in inlet temperature will be due to the inherent error of the transducer used, usually a thermocouple, together with errors due to heat loss from the thermocouple. For a typical thermocouple at an inlet temperature of 800 K, the error due to the thermocouple alone is likely to be ±3 K or ±0.4 percent of reading. The temperature error will be higher if due account is not taken of additional factors such as heat loss from the thermocouple.

Fuel Inlet Temperature. Liquid fuel temperatures are typically around 288 K, that is, the ambient temperature. Excellent thermal coupling can be achieved between the fuel and a measuring device such as a thermocouple. The inherent inaccuracy in the thermocouple, typically ±1.5 K, therefore governs the fuel temperature error. Figure 4 shows that the error in flame temperature decreases continuously with increasing AFR as the fuel makes progressively less contribution to the reactant enthalpy. For a practical uncertainty of ±1.5 K, the resulting temperature error is less than ±0.3 K in the range of AFR 8:1 to 150:1. In cases where the fuel temperature variation is known to be small, it could, therefore, be acceptable not to measure fuel temperature.

The contribution of fuel temperature to the overall error is small because of the small contribution to the total mass of the reactants made by a conventional liquid fuel or natural gas. This is no longer true when burning gases of low calorific value where the overall AFR may be as low as 2:1. In such cases, the contribution of the fuel sensible enthalpy to the reactant enthalpy can be significant and inlet temperature errors are correspondingly more significant.

The effect of fuel and oxidant inlet temperature on calculated AFR is insignificant.

Fuel Calorific Value. Fuel calorific value determined calorimetrically by the method of IP12 has an associated error of around ±1 percent of the stated calorific value. For the test fuel, of nominal gross calorific value 46.2 $MJkg^{-1}$, the method of IP12 states an error of ±0.85 percent. The effect on calculated

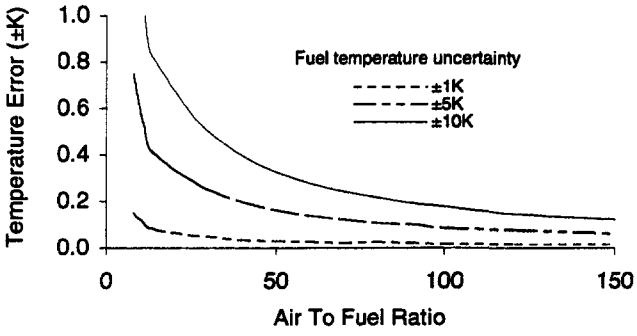

Fig. 4 The effect of fuel inlet temperature on flame temperature

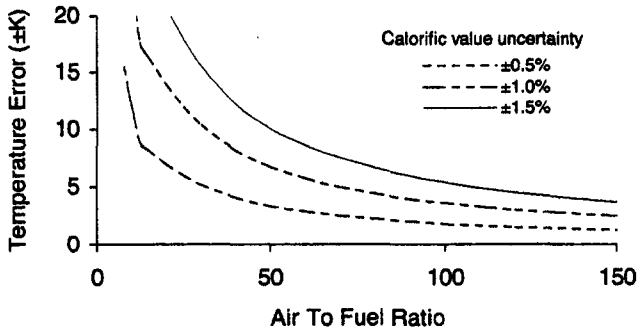

Fig. 5 The effect of fuel calorific value on flame temperature

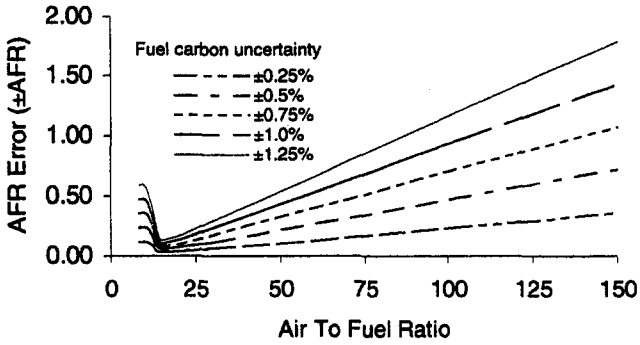

Fig. 8 The effect of fuel composition on AFR

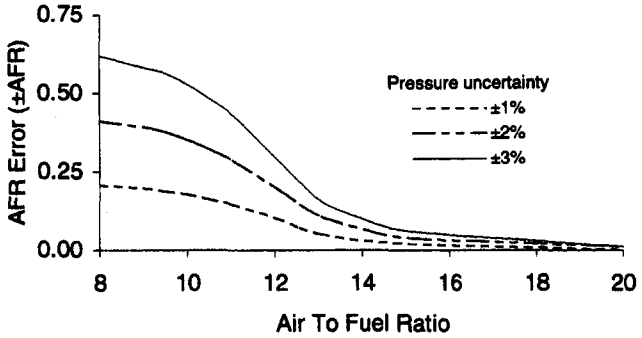

Fig. 6 The effect of combustion pressure on AFR

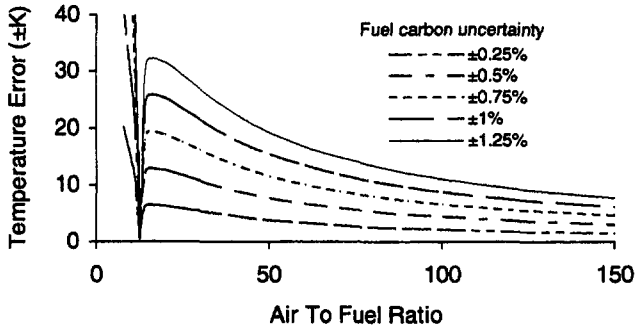

Fig. 9 The effect of fuel composition on flame temperature

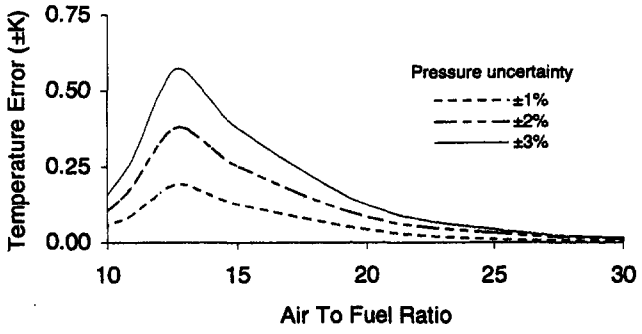

Fig. 7 The effect of combustion pressure on flame temperature

AFR is small. At the ±1 percent level it does not exceed ±0.2 percent of nominal for AFRs between 8 and 150.

The effect on temperature is shown in Fig. 5. The absolute error diminishes with increased AFR as the contribution to reactant enthalpy made by the fuel reduces. It remains significant at all conditions; for a uncertainty of ±1 percent it has a value of ±17 K at stoichiometric, increasing to ±30 K at the richest AFR investigated of 8:1.

Reaction Pressure. Reaction pressure affects flame temperature whenever dissociation is significant, in these cases, an increase in pressure moves the equilibrium composition towards the more exothermic products, thereby increasing the flame temperature. The calculated AFR is changed via the effect on the change in mole number from reactants to products.

Figures 6 and 7 illustrate the effect. In practice, it is possible to use a pressure measuring technique that will give an error of less than ±1 percent of reading thereby reducing the resulting errors to almost insignificant levels.

Fuel Composition. Uncertainty in fuel composition can have a significant effect on both calculated temperature and calculated AFR. The error has been estimated by considering a fuel containing hydrogen and carbon only. The values given in Fig. 8 and Fig. 9 are for errors in the percentage of the gravimetric carbon content, in each case the hydrogen is taken to be the remainder of the fuel. The nominal fuel composition is that given for aviation kerosene in Table 2. Ultimate analysis by the method of ASTM D5291-96 would give an uncertainty of ±1.2 in the gravimetric carbon percentage.

The absolute uncertainty in AFR increases continuously with AFR on the lean side of stoichiometric, reaching a maximum of ±2 AFR at 150:1 for the ±1.25 uncertainty level. With temperature the opposite trend can be seen in Fig. 9. Rich of stoichiometric the error falls to a minimum before rapidly increasing to very significant levels at still richer conditions. Below about 13:1 the temperature error is significant. On the lean side the error decreases continuously with increased AFR, but remains significant up to the maximum AFR investigated. At stoichiometric a temperature error of ±32 K can be expected for the ±1.25 uncertainty in fuel carbon percentage.

Oxidant Composition. Water content is the principle uncertainty in air, the most common oxidant. The error is given here for the case where the water content is determined from the dew point, and the air composition calculated from this and the known composition of dry air. There are two sources of error, the dew-point temperature and the dew-point pressure. In the case where the dew-point pressure is measured using a barometer, the error in the reading is very small and not significant. Figure 10 shows the errors in calculated temperature for different levels of dew-point error. In all cases, the absolute error in calculated temperature is less than the absolute error in dew-point temperature. The effect on calculated AFR is negligible for all AFRs for practical levels of dew-point temperature error.

Partial Equilibrium Assumption. Of all the errors, this is the most difficult to quantify; it is not possible to use simple arguments to get accurate error estimates.

Hydrogen is one species that can be dealt with as it can be measured by gas sampling. Data from a combustion test in

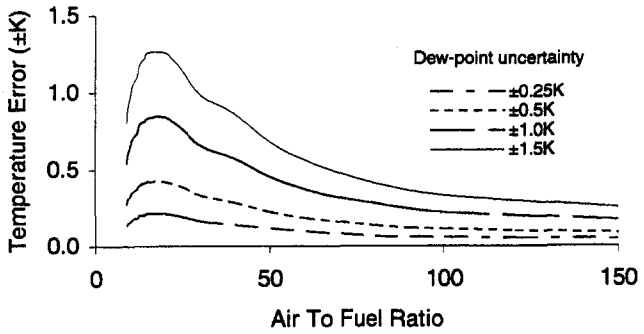

Fig. 10 The effect of air dew-point temperature on flame temperature

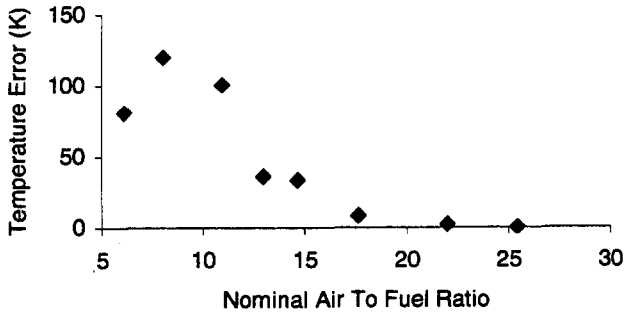

Fig. 11 The effect of hydrogen measurement on calculated flame temperature

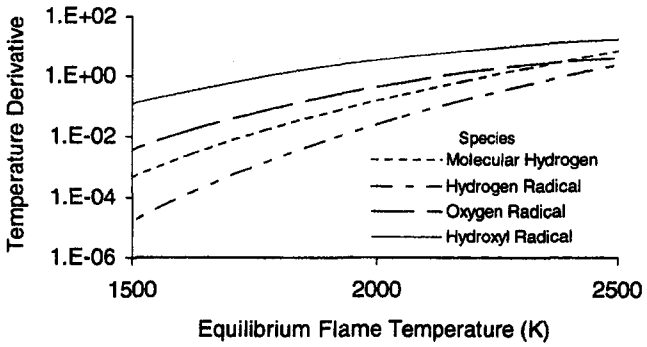

Fig. 12 Derivatives of flame temperature with respect to species concentration

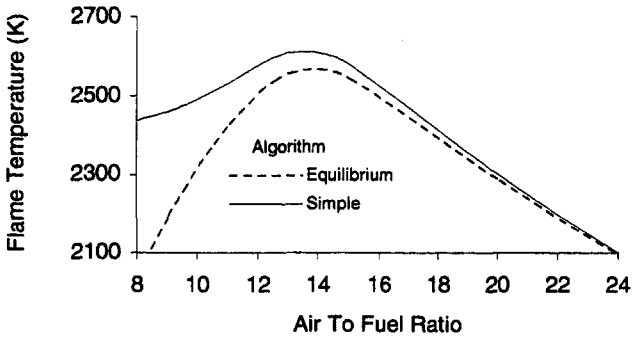

Fig. 13 Temperature predictions by equilibrium and simple calculation methods

Table 3 A comparison of thermocouple and TBGA temperatures

Test	Type	Method	Number of samples	Inlet Temp.	Inlet Pressure	Mean Exhaust Temp.
				K	kPa	K
1	A	T/C	450	693	697	1656
2	A	TBGA	450	680	695	1653
3	B	T/C	800	425	294	837
4	B	T/C	800	425	294	838

which hydrogen was measured have been used to show the effect of estimating hydrogen concentration. The gas samples used for the analysis were taken, in some cases, from the combustor primary zone as well as from the exhaust region. The combustor operating conditions were those given in Table 2. Two sets of analysis were performed on the data, one using the measured hydrogen concentration and the other ignoring it. Both the equilibrium constant and Gibbs minimization algorithms were used for this purpose and were found to give the same results. The results are shown in Fig. 11 plotted against the AFR calculated by including the hydrogen measurement. The temperature error is the difference between the temperature calculated using the hydrogen measurement and that calculated using partial equilibrium hydrogen. The partial equilibrium temperature is the greater in all the cases; the difference is significant for all AFRs richer than about 20:1.

The errors caused by a difference between the true radical concentrations and those at equilibrium cannot be generalized. However, the order of magnitude of the error and how it varies with operating conditions is illustrated in Fig. 12. For each species in turn, a scalar was defined that multiplied the nominal equilibrium concentration of the species. The partial derivative of the flame temperature with respect to this scalar was evaluated for the case of the scalar being unity. The resulting quantity shows the magnitude of the effect of perturbing the species concentration about its nominal value. This, in turn gives an indication of the relative sensitivity of the flame temperature to uncertainty in the radical concentration. Defining the threshold of significance as 1 K, none of the species has a significant effect below about 1850 K. Above this temperature, the effect of uncertainty in radical concentration becomes increasingly significant.

Figure 13 gives temperatures calculated using equilibrium assumptions compared with those calculated by assuming that radicals and molecular hydrogen are absent from the products. This clearly shows the divergence of temperature predictions that can occur by neglecting the radicals. It also illustrates that there is an AFR above which it is permissible to neglect the presence of radicals thereby simplifying the calculation.

Comparison of Thermocouple and Gas Analysis Results

Thermocouple measurements are not available for very high gas temperatures, so direct comparison is restricted to lower levels. The results from two different reverse flow annular combustors are presented as a means of comparison. The operating conditions are summarised in Table 3. In each case the exhaust temperature distribution was determined by use of a movable sampling rake with sample points at five different radial positions. For combustors A and B, respectively, 90 and 160 different circumferential positions were used. In the case of combustor A, the temperature distribution was determined at nominally the same operating condition using both heat shielded type-R thermocouples and by TBGA using a gas sampling probe. Tests 1 and 2 were performed using the same combustor and fuel injectors. Between the tests the combustor and injectors were removed from the test rig for inspection and cleaning. There are no repeat thermocouple measurements for combustor A so it is not possible to compare the variability of TBGA and thermocouples with the inherent variability of a single method. Tests 3 and 4 of combustor B were both done by type-R thermo-

Table 4 A comparison of thermocouple and TBGA temperatures

Comparison	Mean difference	RMS difference	RMS / mean Temp. rise
	K	K	%
1 and 2	3.0	54.0	5.6
3 and 4	-1.5	14.0	3.4

couples. In this case, the two tests were done simultaneously using a double-headed thermocouple instrument; in this case, therefore, there is not the additional variability introduced by removing the combustor and then reassembling it.

The data cannot be used for rigorous comparison, but can be used to give a general comparison of the two methods. Table 4 gives a summary of the differences. The RMS temperature difference is a misleading parameter since the uncertainty is not in the absolute temperature but in the temperature rise above the mean inlet temperature. Therefore, the RMS differences are also given as percentages of the mean temperature rise. This is the temperature increase above the inlet temperature rise. This is the temperature increase above the inlet temperature that would occur if the combustion products were perfectly mixed. The circumferential temperature variations at a fixed radial location are shown in Figs. 14 and 15. Figure 14 shows the temperatures determined by thermocouple and by TBGA for combustor A, tests 1 and 2, whilst Fig. 15 shows repeat thermocouple temperatures for combustor B, tests 3 and 4.

For the TBGA versus thermocouple comparison, the RMS difference is 5.6 percent of the mean temperature rise whilst for the repeat thermocouple case the corresponding value is 3.4 percent. Whilst it may seem that the TBGA versus thermocouple comparison is worse, the additional variability due to combustor rebuild must be considered. The graphical comparison in Fig. 19 does not reveal any systematic trends in the difference that could be symptomatic of a flaw in the TBGA method. Thus, the TBGA method does not consistently over or under predict the temperatures of the hot and cold extremes, instead, the variation is spread evenly throughout the temperature range. This is indicative of the differences being due to random effects rather than an underlying difference. The similar mean exhaust temperatures of 1656 K and 1653 K predicted by the two methods support this. Clearly more data is required, particularly at high temperatures, to perform a thorough comparison.

Concluding Remarks

A method of calculating gas temperatures from the measurement of a limited number of gaseous species in a combustor exhaust has been developed. The method combines rigorous thermodynamics and a robust numerical solution technique with an object oriented design in the C++ language. The uncertainties in the method have been illustrated using simulated and measured data from gas turbine combustion tests.

The main conclusions regarding errors are as follows:

1 The CO_2 analyser error gives significant temperature and AFR errors at all AFRs. For an error of ± 2 percent of CO_2 analyser reading, the maximum temperature error is ± 20 K.
2 The fuel CV uncertainty gives significant temperature errors for all but the leanest of conditions. At stoichiometric a ± 1 percent uncertainty in CV gives rise to a temperature uncertainty of ± 17 K, this falls to about ± 3 K at 150:1.
3 The fuel composition uncertainty gives significant errors for all but the leanest of conditions. At stoichiometric an uncertainty of ± 1 in the gravimetric fuel carbon percentage gives rise to a temperature uncertainty of ± 27 K, falling to ± 8 K at 150:1. Rich of stoichiometric, the error climbs to very high levels, exceeding ± 50 K at about 11:1.
4 Richer than about 25:1, depending on the pressure, failure to account for radicals and hydrogen in the products introduces a significant error.
5 Richer than stoichiometric, estimation of hydrogen from partial equilibrium, and CO analyser error become significant.
6 Hydrocarbon can be a significant source of error under very rich conditions.
7 Fuel and oxidant inlet temperature, NOx analyser and oxidant dew point are not significant sources of error.

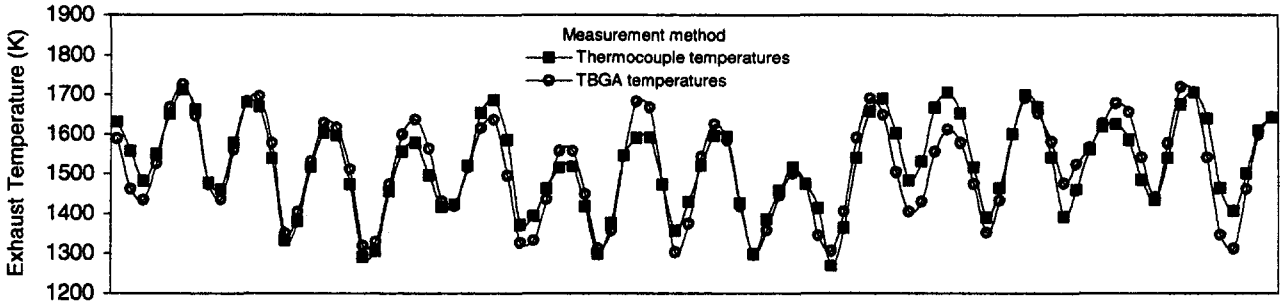

Fig. 14 The circumferential exhaust temperature profile of an annular combustor determined by thermocouples and TBGA

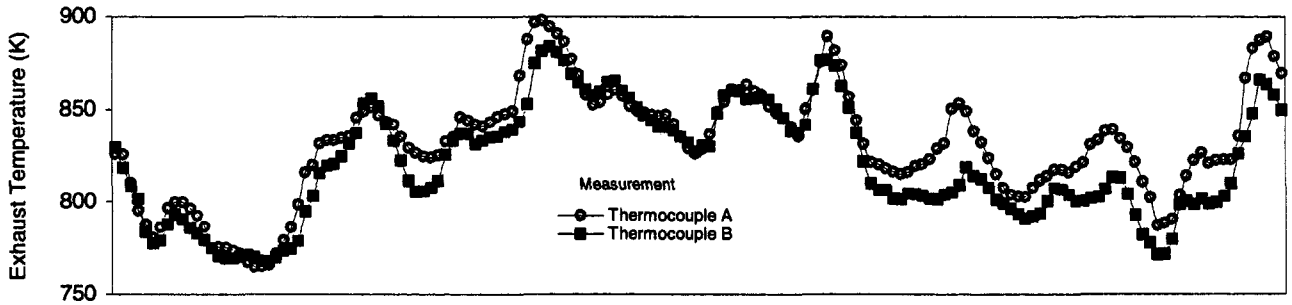

Fig. 15 The circumferential exhaust temperature profile of an annular combustor determined twice by thermocouples

The principle application of the technique is routine exhaust temperature pattern factor determination; as such, the technique presented in this paper extends the range of validity of simple gas analysis codes to the stoichiometric AFR. The technique can still give reasonably accurate results at richer AFRs provided that hydrogen is measured in the exhaust.

References

American Society For Testing and Materials, 1996, Standard Test Methods for Instrumental Determination of Carbon, Hydrogen, and Nitrogen in Petroleum Products and Lubricants, D5291-96.

Burden, R. L., and Faires, J. D., 1989, *Numerical Analysis,* 4th ed., PWS-Kent, Boston, pp. 544–551.

Ferguson, C. R., 1985a, *Internal Combustion Engines,* John Wiley & Sons, New York, pp. 121–122.

Ferguson, C. R., 1985b, *Internal Combustion Engines,* John Wiley & Sons, New York, p. 201.

Gordon, S., and McBride, B. J., 1971, "Computer Program for the Calculation of Complex Chemical Equilibrium Compositions, Rocket Performance, Incident and Reflected Shocks, and Chapman-Jouguet Detonations," NASA SP-273.

Grossman, S. I., 1988, *Calculus,* 4th ed., Harcourt Brace Jovanovich, New York, pp. 716–171.

Hurley, C. D., 1988, "The Calculation of Flame Gas Temperatures From Measurements of Chemical Composition," technical memo, Royal Aerospace Establishment, P1139.

Institute of Petroleum, 1984, "Methods For Analysis And Testing," Part 1, Vol. 1, Wiley, London, pp. 12.1–12.17.

Press, W. H., Vetterling, W. T., Teukolsky, S. A., and Flannery, 1992, *Numerical Recipes in C,* 2nd ed., Cambridge University Press, New York, pp. 379–383.

Press, W. H., Vetterling, W. T., Teukolsky, S. A., and Flannery, 1992, *Numerical Recipes in C,* 2nd ed., Cambridge University Press, New York, pp. 383–389.

Rogers, G. F. C., and Mayhew, Y. R., 1980, *Engineering Thermodynamics Work and Heat Transfer,* 3rd ed., Longman, Hong-Kong, p. 35.

Scott, C. J., 1991, "Gas Analysis Temperature Deductions. Uncertainties and Newly Identified Problems," internal report, Rolls-Royce, United Kingdom.

Strehlow, R. A., 1984a, *Combustion Fundamentals,* McGraw-Hill, Singapore, pp. 99–103.

Strehlow, R. A., 1984b, *Combustion Fundamentals,* McGraw-Hill, Singapore, p. 40.

Zeleznik, F. J., and Gordon, S., 1968, "Calculation of Complex Chemical Equilibria," *Applied Thermodynamics Symposium,* Vol. 60, No. 6.

CFD Modeling of a Gas Turbine Combustor From Compressor Exit to Turbine Inlet

D. S. Crocker

D. Nickolaus

C. E. Smith

CFD Research Corporation,
215 Wynn Drive,
Huntsville, AL 35805

Gas turbine combustor CFD modeling has become an important combustor design tool in the past few years, but CFD models are generally limited to the flow field inside the combustor liner or the diffuser/combustor annulus region. Although strongly coupled in reality, the two regions have rarely been coupled in CFD modeling. A CFD calculation for a full model combustor from compressor diffuser exit to turbine inlet is described. The coupled model accomplishes the following two main objectives: (1) implicit description of flow splits and flow conditions for openings into the combustor liner, and (2) prediction of liner wall temperatures. Conjugate heat transfer with nonluminous gas radiation (appropriate for lean, low emission combustors) is utilized to predict wall temperatures compared to the conventional approach of predicting only near wall gas temperatures. Remaining difficult issues such as generating the grid, modeling swirler vane passages, and modeling effusion cooling are also discussed.

Introduction

CFD modeling of combustors and fuel nozzles has progressed to the extent that CFD simulations are frequently included in the design process. Thus far, CFD models have generally been limited to isolated parts of the combustion system. Most models include only the reacting flow inside the combustor liner with assumed profiles and flow splits at the various liner inlets. Carefully executed models of this type can provide valuable insight into mixing performance, pattern factor, emissions and combustion efficiency. Some insight into liner wall temperatures can also be indirectly derived from the near wall gas temperatures. Perhaps the most important benefit of CFD modeling is the innovative ideas that CFD solutions sometime inspire.

There are numerous examples of combustor CFD solutions in the literature of which Lawson (1993), Fuller and Smith (1993), and Lai (1997) are a representative sample. Lawson was able to successfully match exit radial profile experimental data and then use the anchored CFD model to predict the radial profile that resulted from different cooling and dilution air patterns. Lawson used a one-dimensional code to predict flow splits and a two-dimensional CFD model to predict the flow profile at the exit plane of the swirl cup. This profile was then applied as a boundary condition in the three-dimensional model. Fuller and Smith were able to predict exit temperature profiles of an annular through-flow combustor that were in fairly good agreement with measurements. They also used a two-dimensional model to provide boundary conditions at the exit plane of the swirl nozzle. They did introduce the use of multi-block grids which are essential for modeling complex geometries. Lai was able to predict hot spots based on near wall gas temperatures that corresponded to locations in the combustor that had experienced deterioration. Lai included the swirler passages in his model which is an important step in reducing the uncertainty of prescribed boundary conditions. Although Lai modeled the swirler passages and the rest of the combustor with a single block grid, it is generally much easier and more efficient to use multi-block grids.

CFD models of the diffuser and annulus region have also been performed such as those of Srinivasan et al. (1990), Karki et al. (1992), and Little and Manners (1993). All three of these efforts at modeling the flow field outside of the combustor liner were reasonably successful in predicting velocity profiles with relatively coarse two-dimensional and three-dimensional models. However, Mongia (1994) points out that prediction of pressure losses is more difficult and the results are typically relatively poor.

A logical next step is to model the entire flow field from the compressor diffuser to the turbine inlet with the flow inside and outside the combustor liner fully coupled. There are at least two important reasons to attempt such an ambitious task: (1) flow splits and boundary conditions for the combustor liner inlets are modeled explicitly and no longer need to be approximated; and (2) liner wall temperatures can be predicted when the flow fields on both sides of the liner walls are modeled in a coupled fashion.

One-dimensional annulus codes have traditionally been utilized to provide a reasonable prediction of flow splits, but they cannot capture important two and three-dimensional flow features that can significantly affect total pressure losses. Nonuniform profiles of flow conditions, including velocities, jet angles and turbulence properties, at inlet boundaries can also have a significant influence on the flowfield in a combustor. Turbulence properties at inlets are particularly difficult to estimate. McGuirk and Spencer (1995) discuss the sensitivity of discharge coefficient and jet trajectory of dilution holes to small changes in the dilution hole geometry. They emphasize the need to provide realistic profiles at dilution hole inlets.

Another important issue is accurate definition of the flow through the dome/fuel injector air swirlers. Fuller and Smith (1993) demonstrated the sensitivity of the overall solution to the details of the swirler air flow. The aerodynamics of recent lean dome combustor designs are dominated by the large percentage of air that is admitted through the dome swirlers. Crocker et al. (1996) discusses the importance of detailed prescription of fuel nozzle/dome swirler boundary conditions and describes an approach for accurate prediction of flow splits and effective area. Fuller and Smith modeled the air swirler and combustor flow fields in a decoupled manner which may be appropriate in some cases. In general, though, it is necessary to couple the combustor solution and at least part of the swirler

Contributed by the International Gas Turbine Institute and presented at the International Gas Turbine and Aeroengine Congress and Exhibition, Stockholm, Sweden, June 2–5, 1998. Manuscript received by the ASME Headquarters April 1, 1998. Paper No. 98-GT-184. Associate Technical Editor: R. Kielb.

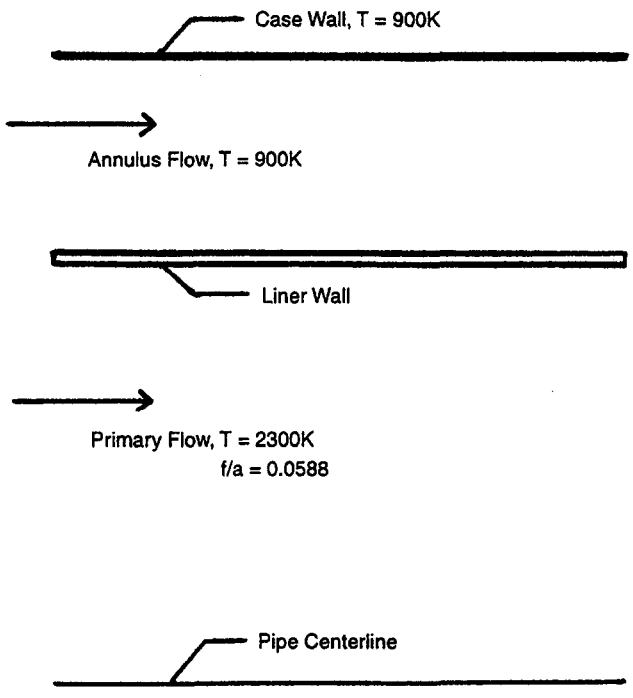

Fig. 1 Pipe and annulus test case geometry

passages because of strongly recirculating flow in the region of the swirler. Another important consideration is the effect of nonuniform feed pressure at the inlet of the dome swirlers. The advent of multi-block and many-to-one grid topology, discussed later in the paper, make it feasible to include a detailed model of the swirler passages in the overall combustor model.

The prediction of liner wall temperatures is becoming increasingly important as more aggressive cycles increase liner heat loads and low emissions designs reduce the available cooling air. Although conjugate heat transfer approaches that couple heat transfer in solid material with the fluid flow solution have been available for some time, the authors are not aware of any attempt (in the open literature) to directly model gas turbine combustor liner wall temperatures using CFD.

This paper describes CFD analyses of a model combustor from the deswirl vane exit of a centrifugal compressor to the turbine nozzle inlet. The combustor configuration is representative of a lean, low emission design. The model includes an airblast fuel nozzle, dome, and liner walls with dilution holes and cooling louvers. Since the combustor is a representative model and there are no experimental data, the emphasis is placed on the modeling methodology. The results of the analyses illustrate the influence of flow nonuniformities on the static pressure distribution around the liner and the resulting effect on flow splits and liner wall temperatures. The influence of nonluminous radiation and thermal barrier coating on wall temperatures is also examined.

Comparison of CFD and Empirical Heat Transfer Models

The simple geometry of a pipe flowing with hot combustion products surrounded by a concentric annulus flowing with cooling air is employed to examine the relative influence of radiation and convection in comparison with an empirical formulation for predicting wall temperature. The geometry is illustrated in Fig. 1. The empirical formula was originally derived by Lefebvre and Herbert (1960) and later restated by Lefebvre (1983). The equations, repeated below, utilize basic heat transfer principles and empirical data to account for radiation and convection on both sides of the liner.

$$\epsilon_g = 1 - \exp(-290\mathrm{PL}(ql_b))^{0.5} T_g^{-1.5} \tag{1}$$

$$R_1 = 0.5\sigma(1 + \epsilon_w)\epsilon_g T_g^{1.5}\,(T_g^{2.5} - T_{w_1}^{2.5}) \tag{2}$$

$$C_1 = K_{C1}\frac{k_g}{D_L^{0.2}}\left(\frac{\dot{m}_g}{A_L\mu_g}\right)^{0.8}(T_g - T_w) \tag{3}$$

$$R_2 = K_{R2}(T_{w_2}^4 - T_3^4) \tag{4}$$

$$C_2 = K_{C2}\frac{k_a}{D_{an}^{0.2}}\left(\frac{\dot{m}_{an}}{A_{an}\mu_a}\right)^{0.8}(T_{w_2} - T_3) \tag{5}$$

$$R_1 + C_1 = R_2 + C_2 = \frac{k_w}{t_w}(T_{w_1} - T_{w_2}) \tag{6}$$

A detailed description of the elements of Eqs. 1–5 is not repeated here since they are fully described in the widely available text by Lefebvre (1983). Each case discussed here had T_3 of 900K, a fuel/air ratio of 0.0588, and a hot product (gas) temperature T_g of 2300K. The luminosity factor was $L = 1.0$ and the beam length was 0.08 m. The emissivity of both sides of the liner and the case were assumed to be 0.7 and 0.4, respectively. The liner inner diameter was 0.132 m, the wall thickness was 1.2 mm and the case diameter was 0.192 m. The pressure and the inside and outside velocities were varied.

The commercially available CFD code CFD–ACE was used for all of the analyses. The CFD model used a modified k-e turbulence model based on the renormalization group (RNG) theory (Yakhot et al., 1992) and standard wall functions (Launder and Spalding, 1974) to predict the convective heat transfer. It is well known that wall functions are limited in their ability to predict convective heat transfer, especially for flow fields that are not parallel to the wall. Nevertheless, alternative low Reynolds number models require very fine grids near the walls and are currently not very practical for a full combustor model. The grid density near the wall was set for each case such that y^+ was approximately 25. Note that the near wall grid density varied considerably as a function of pressure and inlet velocity.

The turbulent Prandtl and Schmidt numbers were set to 0.25 for the CFD models. This relatively low value has consistently demonstrated better agreement with combustor fuel-air mixing results. However, the low value also results in increased heat transfer compared to the typical value of 0.9 (about 50 percent higher than with Prandtl number of 0.25 for a typical case with radiation). Since the convective heat transfer rate is increased on both sides of the liner, the effect on the wall temperature is relatively small. The temperature gradient through the wall, however, is overpredicted. An improved approach would be to use conventional turbulent Prandtl and Schmidt numbers in the wall functions. The convection terms (Eqs. 3 and 5) of the empirical model were calibrated so that the convective heat transfer for the empirical model and the CFD model was equal. The calibration was performed for primary and annulus velocities both set to 20 m/s. The constants K_{C1} and K_{C2} were set to 0.046 and 0.040, respectively. Both constants from Lefebvre (1983) are 0.020 based on fully developed pipe flow. Since the test case under consideration predicts heat transfer near the pipe entrance with an L/D less than 0.5, far from fully developed flow, the correction factors of 2.3 and 2.0 are reasonable.

Radiation heat transfer is calculated by solving the radiative transfer equation using a discrete-ordinate method. The discrete-ordinate method provides a reasonable balance between obtaining realistic results for complex geometries and computational cost. The approach, along with validation cases, is described by Giridharan et al. (1995). Only CO_2 and H_2O were assumed to contribute significantly to the nonluminous gas radiation. The local gas emittance was calculated as a function of species concentration, pressure and temperature based on the

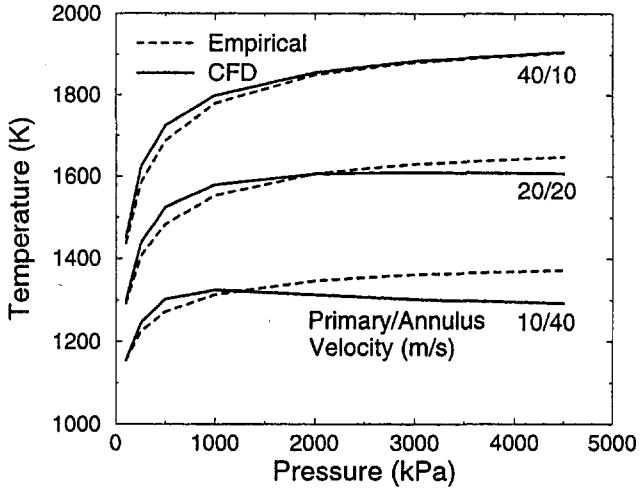

Fig. 2 Comparison of empirical and CFD wall temperature predictions for primary/annulus velocities of 10/40, 20/20, and 40/10 m/s

data of Hottel (1954). Luminous radiation was not considered for this effort since these cases only involved lean combustion.

Results of the empirical and CFD models are compared in Fig. 2 as a function of pressure and primary/annulus velocities. The agreement is remarkably good considering the uncertainties in both models. The most notable difference is that the CFD predicted wall temperature begins to drop below the empirical prediction as the pressure increases. This is caused by the lower rate of increase of the gas radiation to the wall for the CFD model. This is certainly an area of uncertainty since the data from Hottel (which both the empirical and CFD radiation models are based on) must be extrapolated beyond 5 atmospheres.

Combustor CFD Model Description

A single nozzle 24 deg periodic sector of the model combustor was analyzed. The combustor configuration included a centrifugal compressor diffuser section downstream of the deswirl vanes, a fuel nozzle and stem, typical cooling flow, and a single row of dilution holes on both the inner and outer liner. The fuel nozzle was an airblast design with about 65 percent of the combustor air admitted through the two axial air swirlers. An axial cross section of the 370,000 cell grid with 11 domains (blocks) is shown in Fig. 3.

Generation of a grid for such a complex geometry in a timely manner and with sufficient grid resolution is a challenging task. Mongia (1994), in his review of combustion modeling, estimated that as many as 12 million cells may be required to provide a near grid independent solution for a comprehensive one nozzle sector combustor model. Such a model would include detailed modeling of swirler vane passages. Second order numerical schemes can reduce that requirement to less than 5 million cells. (Second order upwind differencing was used for the current analyses.) Mongia's estimate is reasonable given the assumption of one-to-one grid cell interfaces between blocks. Many-to-one grid cell interfaces can dramatically reduce the total number of required cells. Many to one is illustrated by a close-up of the fuel nozzle grid interfaced with the primary zone grid shown in Figure 4. Detailed structures, such as swirler passages and even swirler vanes, can be modeled with a fine grid without transferring the high density grid into the rest of the combustor. (The grid quality could be improved by continuing the fine grid a short distance into the primary zone.) The swirler passages shown in Fig. 4 were modeled with 35,000 cells which does not include swirler vanes. Swirler vanes could be included with approximately 100,000 additional cells. The difficulties associated with constructing such a grid are considerable, but not insurmountable, and will be addressed in the last section of the paper.

The total airflow through the combustor was prescribed by the single boundary condition at the compressor diffuser. All of the remaining flow splits, except for the flow through the dome, were a product of the CFD model. In this analysis, the flow outside the dome feeding the fuel nozzle and the flow through the fuel nozzle were decoupled since detailed modeling of the swirler vanes was beyond the scope of this effort. Effusion cooling through the dome face was also modeled in a decoupled manner. (Conjugate heat transfer modeling of effusion cooling is briefly discussed in the last section of the paper.) The flow rates feeding the air swirlers and effusion cooled dome walls were modeled as exit boundaries and were matched to the inlet flow rates on the downstream side of the dome. The swirler inlet boundaries were modeled according to Crocker et al. (1996). Of course, the effect of variations in static pressure across the dome could not be captured. The liner walls with film cooling and dilution holes were modeled in a fully coupled manner. The holes feeding the film cooling slots were modeled by concentrated resistances since it was not practical to model the individual holes. A close-up of part of the outer liner grid is shown in Fig. 5. The walls containing the dilution holes were three cells thick and the upstream walls were two cells thick. The liner

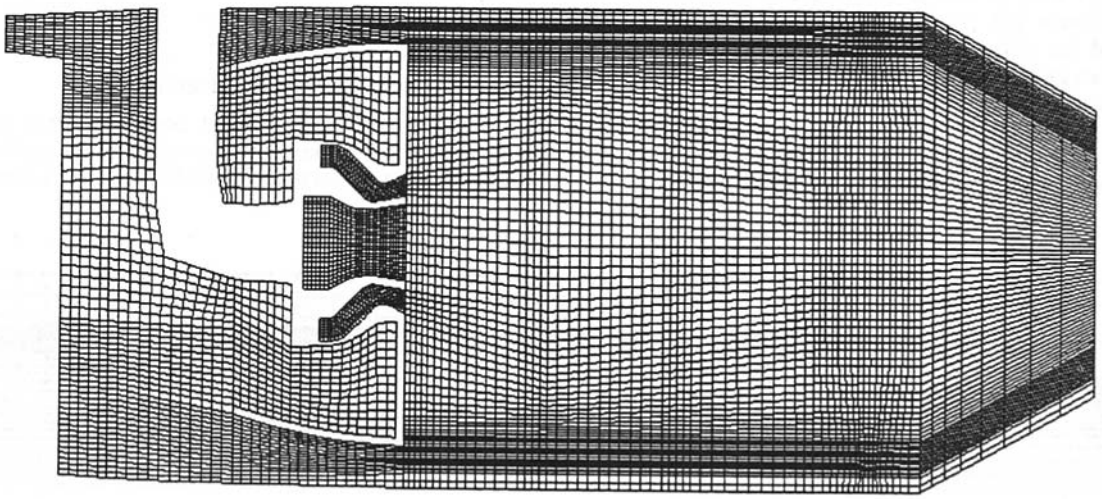

Fig. 3 Centerline axial plane of fine grid (370,000 cells)

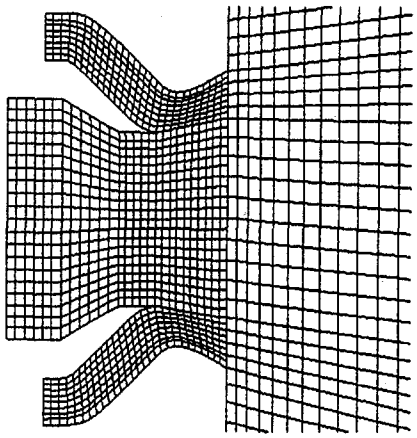

Fig. 4 Centerline axial plane of fuel nozzle portion of grid showing many-to-one interface

wall thermal conductivity was assumed to be 23 W/(m-K), typical of metallic liners. The case wall was assumed isothermal at the combustor inlet temperature. Other walls such as the atomizer stem and the dome cowl were assumed to be adiabatic.

The dilution holes were modeled as round holes (not castellated approximations) with 6 by 6 grid cells. This is a typical grid density for dilution holes in most current combustor models, however, it may not be enough to achieve grid independence. McGuirk and Spencer (1993) compared models of a dilution hole with the castellated approximation and with fitted round holes, both with about a 12 × 12 and 20 × 20 mesh in the hole. There were significant differences between the castellated and fitted solutions. The solutions for the coarse and fine grids with fitted round holes, based on the velocity profile across the hole, were quite similar. This indicates that a 12 × 12 mesh, and possibly less, is adequate for resolving dilution holes. Though not utilized for this analysis, many-to-one grid topology can again be used to keep the total number of grid cells to a manageable level.

Kinetics were modeled using a one-step finite rate reaction with equilibrium reaction products. This efficient model accounts for the significant effects of finite reaction time and provides a much better prediction of flame temperature compared to simple one-step models with only H_2O and CO_2 as products. The one-step kinetics is also amenable to the prescribed pdf model which was used to account for turbulent/chemistry interaction. The two-variable pdf was applied to the fuel mixture fraction and to the progress variable. The fuel mixture fraction pdf is of primary importance for diffusion flames and the progress pdf is most important for premixed flames. Lean direct injection, as employed in this case, is often a hybrid condition for which both are significant. The liquid fuel spray motion and evaporation was modeled as Lagrangian droplet packets that influence the Eulerian gas phase equations through mass, energy, and momentum source terms.

Results

Selected results of the CFD calculations are discussed below primarily for the purpose of illustrating the qualitative nature of the predictions of a full combustor model. The flow pattern in the primary zone is dominated by a strong centerline recirculation zone. Temperature contours in an axial plane along the nozzle centerline are shown in Fig. 6. Flame temperatures are relatively low as a consequence of the lean primary zone equivalence ratio. Relative static pressure contours (exit pressure is 3.0 MPa) for the same axial plane are shown in Fig. 7. Significant pressure variations of 1 to 2 percent of static pressure are evident around the liner. The most notable variation, typical of a centrifugal compressor configuration, is the approximately 1 percent higher pressure in the outer annulus. There are also significant circumferential variations of pressure, particularly around the fuel injector/dome region (not shown in any graphic). Hot side liner wall temperatures and velocity vectors are shown in Fig. 8. An increase in wall temperature with distance away from the cooling slots is predicted along with significant circumferential variation.

Gas temperatures as a function of radius at a location 2.54 cm downstream from the dome and in line with the nozzle centerline are shown in Fig. 9. Temperatures for a coarse grid and fine grid case with and without nonluminous gas radiation are compared. The coarse grid had just 80,000 cells compared with 370,000 cells for the fine grid. The coarse grid case had a slightly flatter profile as might be expected because of greater numerical diffusion. The effect of radiation on the gas temperatures was very small; a reduction of at most 5K near the combustor centerline was predicted. The effect of soot radiation, not modeled here, could potentially be more significant in many cases. In this case, however, soot should not play an important role because of the lean primary zone conditions.

Outer liner wall temperatures for the coarse and fine grid cases with and without radiation at a location 2.54 cm downstream of the dome are shown in Fig. 10. The metal wall temperature for a coarse grid case with a 1.25 mm thick thermal barrier coating (TBC) (k = 0.66 W/m-K) is also shown. The effect of the TBC was to reduce the hot side metal wall temperatures and to smooth out the variations considerably. The hot side of the TBC was considerably higher than the comparable metal wall case, so the heat transfer through the wall was reduced. Wall temperatures were consistently about 40 K higher for the radiation cases. There is considerable difference between the fine and coarse grid results. To further compare the fine and coarse grid cases, temperature contours for a transverse plane 2.54 cm downstream of the dome are compared in Fig. 11. The overall pattern is similar, but the variations near the wall are significant as reflected by the different wall temperature patterns.

Conclusions and Future Direction

CFD calculations of a model combustor from compressor diffuser exit to turbine inlet were successfully performed. The comprehensive model made it possible to predict flow splits for

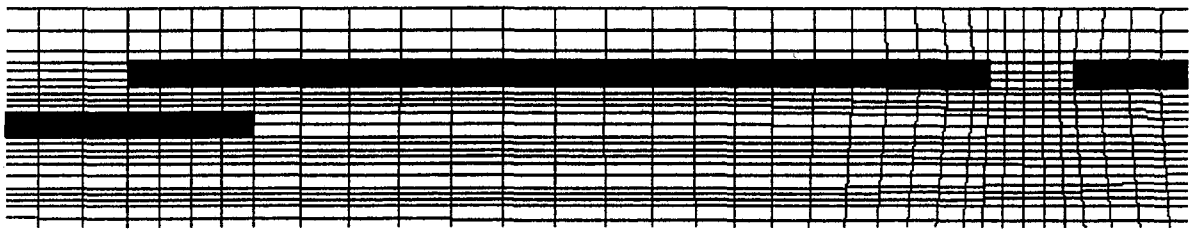

Fig. 5 Close-up of part of the outer liner grid with wall cells shaded

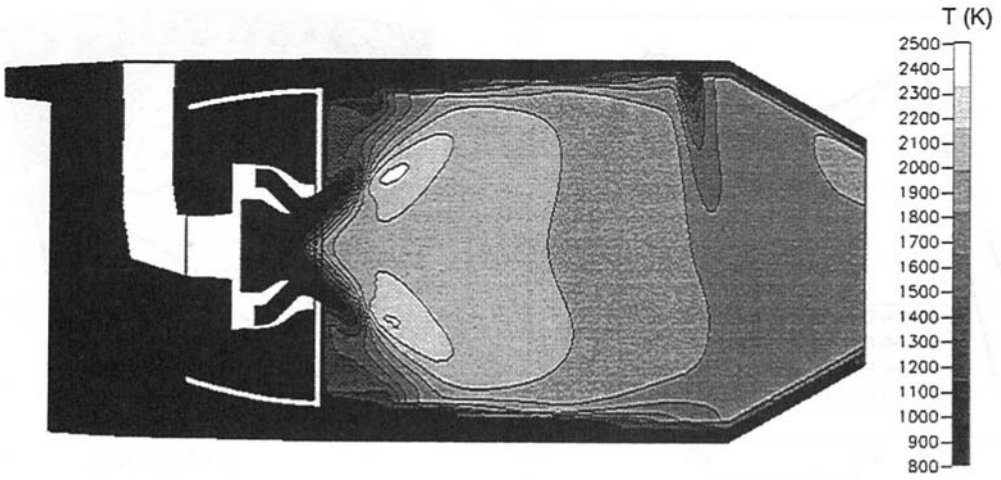

Fig. 6 Temperature contours for an axial plane along the nozzle centerline

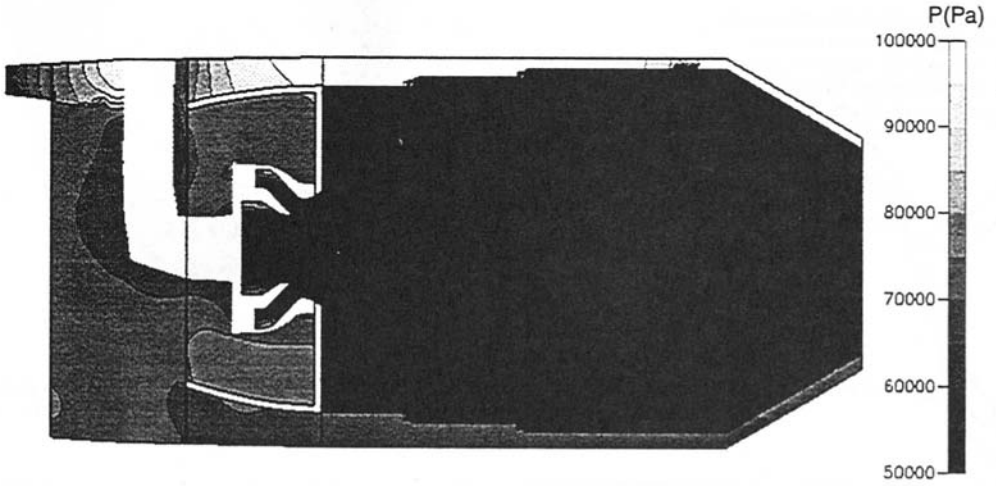

Fig. 7 Relative static pressure contours for an axial plane along the nozzle centerline (exit pressure = 3.0 MPa)

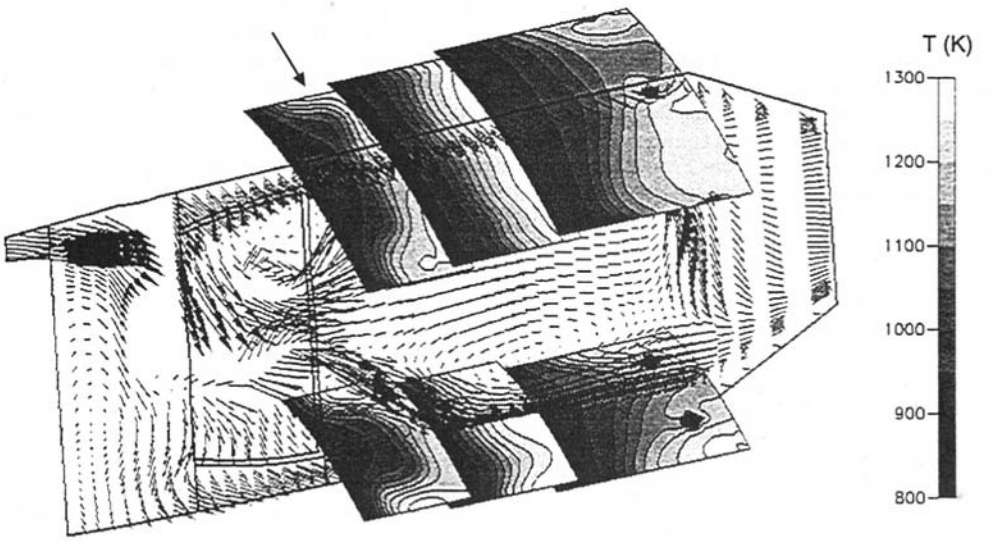

Fig. 8 Hot side liner wall temperature contours and velocity vectors for an axial plane along the nozzle centerline

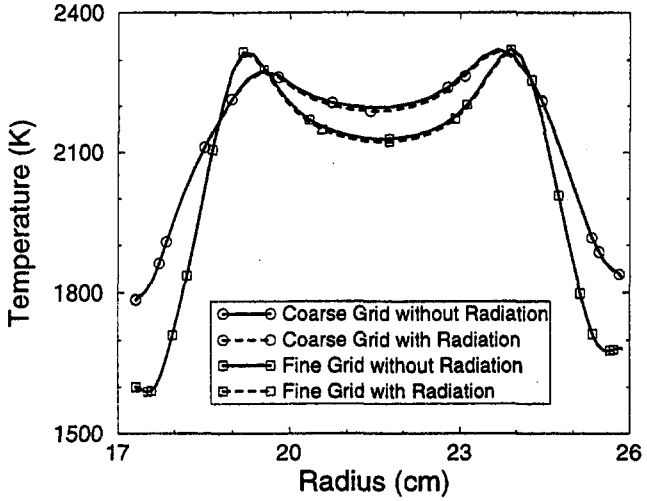

Fig. 9 Gas temperatures 2.54 cm downstream of the dome and in line with the nozzle centerline

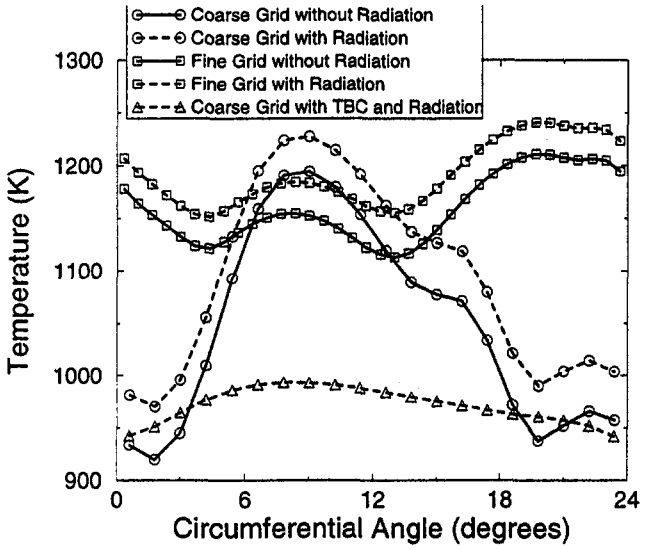

Fig. 10 Hot side wall temperatures on the outer liner 2.54 cm downstream of the dome (see arrow in Fig. 8 to identify location)

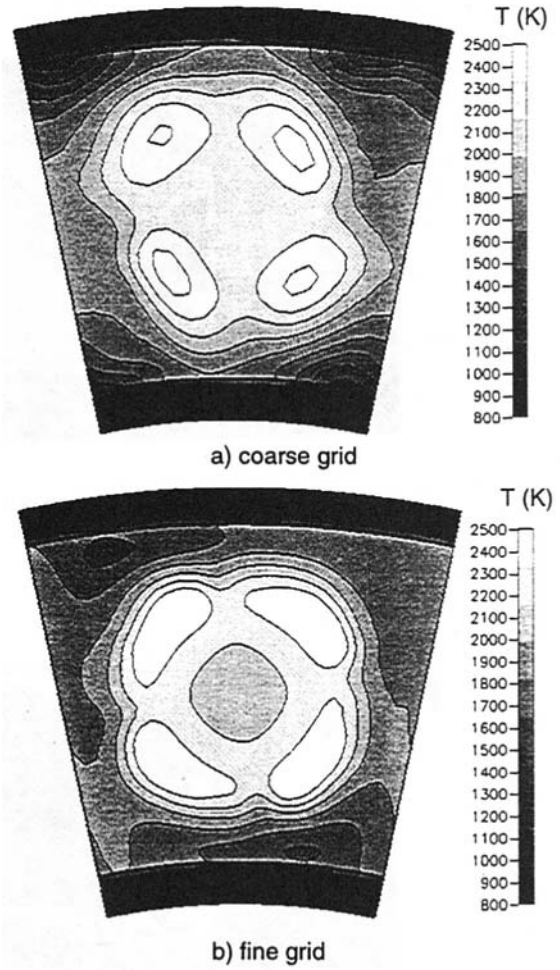

Fig. 11 Temperature contours for a transverse plane 2.54 cm downstream of the dome—comparison of coarse and fine grid cases

the various openings into the combustor liner and remove the guesswork required for prescribing accurate boundary conditions for those openings. The coupled modeling of the flow inside and outside the liner, combined with conjugate heat transfer analysis and participating gas radiation, provided a direct prediction of liner wall temperatures. Nonluminous gas radiation added approximately 40 K to the hot side metal wall temperature. TBC reduced peak metal wall temperatures by more than 200 K.

Several issues that were not addressed in this effort need to be resolved for a complete, comprehensive combustor model. Numerous physical models such as turbulence, kinetics, atomization, and soot need improvement and/or development. These issues are not considered here. The issues of interest here are those unresolved or incomplete capabilities required to fully couple the flow from the compressor diffuser exit to the turbine inlet. They include grid generation and modeling of effusion cooling.

The challenge in generating the grid is twofold: (1) it must be possible to generate a quality grid in a reasonable amount of time; and (2) the grid must have adequate resolution to capture the relevant physics but be small enough that 24 hour or less execution time can be maintained. Most CFD codes, including CFD–ACE, that have adequate physical models for solving reacting flow with spray, utilize a structured grid topology. It is possible to model virtually any geometry using a multiblock, many-to-one structured approach; however, the process is quite painful for complex geometries such as swirler vane passages. Unstructured grids are generally easier to generate for complex geometries and the potential for automation is greater. Automation of grid generation (e.g., swirler vanes, dilution holes, and cooling slots) is an important requirement for making comprehensive combustor modeling a practical design tool. Unstructured grids also usually require fewer grid cells since the grid packing can be isolated in the appropriate areas. (Many-to-one accomplishes the same thing to a lesser extent in structured grids.) The need for mixed element "brick" cells near walls is one of the primary difficulties. Physical models in unstructured grid solvers are generally less mature than for structured grid solvers, but should catch up in the relatively near future. One interesting approach is to use an unstructured solver for the nonreacting and generally more geometrically complex regions feeding the liner, and a more mature structured solver for the reacting region inside the liner in a fully coupled manner. An additional advantage to this approach is that the computational expense associated with reaction and radiation can be limited to the appropriate regions of the flow.

Effective modeling of effusion cooling, now used for liner wall cooling in many combustors, is essential for coupling the flow between the annulus and the combustor regions. The large number of very small holes associated with effusion cooling

make it impractical in the foreseeable future to directly model effusion cooled walls. One solution is to develop a submodel that calculates mass flow through the wall and heat transfer from the wall and provides the appropriate mass, momentum, and energy source terms for the gas phase cells adjacent to the wall and the appropriate energy source terms for the wall.

In the near to mid term future, it should be possible to perform fully coupled combustion system CFD calculations. Adequate grid resolution can be achieved with roughly 1 million cells using advanced grid generation techniques and second order discretization schemes. Execution time for the 370,000 cell case described in this paper was about 48 hours (with radiation and with little optimization) on a 500 MHz DEC Alpha 500. If one assumes 4 times more execution time for a 1 million cell case, a factor of 8 improvement is needed to achieve one day turnaround time. If history is a guide, such improvement may be realized for a single workstation within 5 years. Overnight execution can be achieved now with 10 to 15 workstations operating in parallel.

References

Crocker, D. S., Fuller, E. J., and Smith, C. E., 1996, "Fuel Nozzle Aerodynamic Design Using CFD Analysis," ASME Paper 96-GT-127.

Fuller, E. J., and Smith, C. E., 1993, "Integrated CFD Modeling of Gas Turbine Combustors," AIAA Paper 93-2196.

Giridharan, M. G., Lowry, S., and Krishnan, A., 1995, "Coupled Conductive-Convective-Radiative Conjugate Heat Transfer Model for Complex Applications," ASME Paper 95-WA/HT-5.

Hottel, H. C., 1954, "Radiant Heat Transmission," in W. H. McAdams, ed., *Heat Transmission,* 3rd ed., McGraw-Hill, New York.

Karki, K. C., Oeclsle, V. L., and Mongia, H. C., 1992, "A Computational Procedure for Diffuser-Combustor Flow Interaction Analysis," ASME JOURNAL OF ENGINEERING FOR GAS TURBINES AND POWER, Vol. 114, pp. 1–7.

Lai, M. K., 1997, "CFD Analysis of Liquid Spray Combustion in a Gas Turbine Combustor," ASME Paper 97-GT-309.

Launder, B. E., and Spalding, D. B., 1974, "The Numerical Computation of Turbulent Flow," *Comp. Methods Appl. Mech. Engr.,* Vol. 3, p. 269.

Lawson, R. J., 1993, "Computational Modeling of an Aircraft Engine Combustor to Achieve Target Exit Temperature Profiles," ASME Paper 93-GT-164.

Lefebvre, A. H., and Herbert, M. V., 1960, "Heat-Transfer Processes in Gas-Turbine Combustion Chambers," Proceedings, Inst. Mech. Engr., Vol. 174, No. 12, pp. 463–473.

Lefebvre, A. H., 1983, *Gas Turbine Combustion,* McGraw-Hill, New York.

Little, A. R., and Manners, A. P., 1993, "Predictions of the Pressure Losses in 2D and 3D Model Pump Diffusers," ASME Paper 93-GT-184.

McGuirk, J. J., and Spencer, A., 1993, "CFD Modeling of Annulus/Port Flows," ASME Paper 93-GT-185.

McGuirk, J. J., and Spencer, A., 1995, "Computational Methods for Modeling Port Flows in Gas-Turbine Combustors," ASME Paper 95-GT-414.

Mongia, H. C., 1994, "Combustion Modeling in Design Process: Applications and Future Direction," AIAA Paper 94-0466.

Srinivasan, R., Freeman, W. G., Mozumdar, S., and Grahmann, J. W., 1990, "Measurements in an Annular Combustor-Diffuser System," AIAA Paper 90-2162.

Yakhot, V., Orszag, S. A., Thangam, S., Gatski, T. B., and Speziale, C. G., 1992, "Development of Turbulent Models for Shear Flows by a Double-Expansion Technique," *Physics of Fluids,* Vol. 4, pp. 1510–1520.

Distributed Flight Control and Propulsion Control Implementation Issues and Lessons Learned

W. R. Schley
Parker Aerospace Group,
Control Systems Division-Military,
14300 Alton Parkway,
Irvine CA 92618-1814

This paper addresses the motivations for using a distributed control system architecture, technical challenges, typical functions which are off-loaded to remote terminals, sensor/effector interface issues, data bus selection, technology insertion issues, lessons learned, and objectives for future distributed control implementations. Typical design requirements, constraints, environmental conditions, and operational challenges will be described. Examples of various distributed control system implementations will be discussed, including both propulsion control and flight control examples.

Introduction

As aerospace control systems become progressively more sophisticated and capable, and budgets become tighter, designers are scrambling to find ways to control acquisition costs. Meanwhile in day-to-day operations, control system users and owners are under rising pressure to cut maintenance costs and to reduce flight delays caused by troubleshooting these complex systems. Currently, control systems are the dominant cause of unscheduled turbine engine maintenance [1]. Although the use of distributed architecture in flight control and propulsion control systems has excellent potential to offer relief in these areas, harsh environments have limited its implementation mainly to unmanned aircraft and one-of-a-kind flight control demonstrations. This is because much of the computational burden in a distributed control system is off-loaded to smart sensors and effectors; requiring small electronic packages to share the (often hostile) environments with the devices they control.

Now, however, high-temperature electronics technologies, particularly silicon-on-insulator (SOI), have advanced to the brink of enabling wide use of distributed architectures. The key criteria being monitored by control system designers include affordability, availability of viable components, resources to miniaturize complex electronic systems, and industry infrastructure. High-temperature components are beginning to become affordable: a competitive supplier base is taking shape, market demand continues to increase in down-hole oil drilling applications, and markets are emerging for industrial/manufacturing, automotive, and aerospace applications. In order for components to be viable they must have adequate performance and reliability. The infrastructure is necessary for systematic rapid development of new electronic controllers. It requires procedures and computer-based tools to exploit reuse and quick adaptation of previous designs.

Now that high-temperature electronics are poised to make distributed flight and propulsion control systems practical, the implementation considerations change, relative to centralized systems. Experience indicates that such architectures have some subtleties and pitfalls. *Failure to address these issues can quickly dilute the benefits of a distributed architecture.* The intent of this paper is to discuss the current industry status, the primary issues involved, and the lessons accumulated by the author, his co-workers, and others involved in implementing distributed control systems for aerospace applications.

Contributed by the International Gas Turbine Institute and presented at the International Gas Turbine and Aeroengine Congress and Exhibition, Stockholm, Sweden, June 2–5, 1998. Manuscript received by the ASME Headquarters April 1, 1998. Paper No. 98-GT-3. Associate Technical Editor: R. Kielb.

Advantages of a Distributed Architecture

The advantages of using a distributed control system architecture over a centralized one are made readily apparent by means of the following comparison.

Figure 1 shows an example of a conventional centralized architecture. The system consists of a variety of sensors and effectors interfaced to a centrally located computer. The sensors and effectors are supplied by a multiplicity of vendors. Since the interconnecting wiring is dedicated to each sensor or effector, the wire count is high. (The counts shown here are typical.) And due to the lengths of the runs, the wiring and its associated insulation, shielding, and tie-downs can contribute substantially to overall system weight. In fact, on the average, the overall propulsion control system weight accounts for approximately 15–20% of the engine weight [1]. Example sensors for propulsion control include devices to measure pressure, temperature, shaft speed, fluid flow, blade tip clearance, and flame-out.

Example effectors for propulsion control include devices to control stator vane angle, nozzle geometry, fuel flow, bypass air flow, and blade tip clearance. Many of the effectors themselves are servomechanisms, incorporating yet even more sensors which are not shown in Fig. 1. The simple fact that the effector needs feedback for its operation has some interesting consequences, since the feedback loop is implemented in the central computer: first, wires must run from the effector's internal sensors all the way to the central computer, and additional wires must run back to the effector in order to operate the various torque motors, electrohydraulic servovalves (EHSV), solenoid valves, etc. Second, at least two companies are involved in implementing the loop closure; the effector supplier, and the computer supplier. This means that even minor changes, such as a simple gain change, must be coordinated by both companies, each with its own separate configuration control procedures. Physical distance between these companies often creates a predisposition for overly simple effector designs in order to minimize risk and to facilitate efficient communication. This subtle group dynamic hampers incorporation of improved technologies into effector designs. In addition, when the time arrives to integrate the system and troubleshoot the effector, both companies have to be involved.

The typical central computer is relatively large (e.g., 75 × 60 × 12 cm), redundant, and quite complex. It performs control

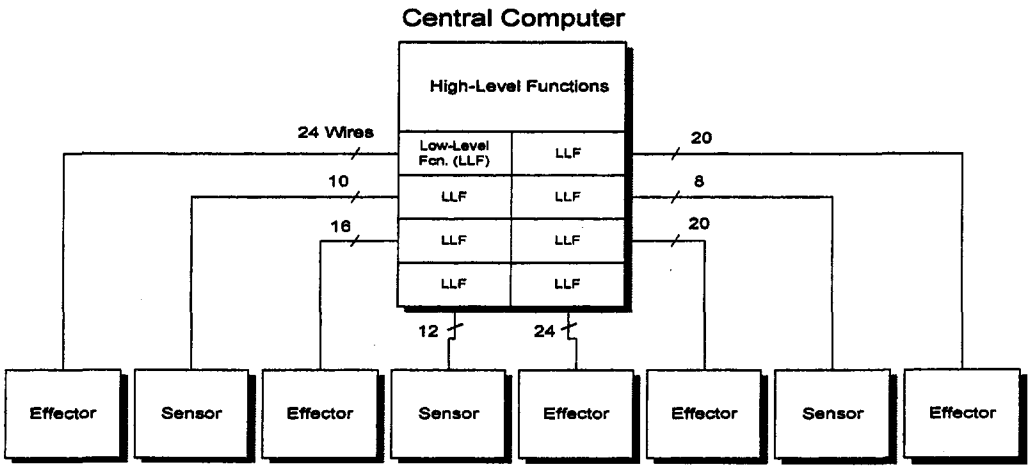

Fig. 1 Example of conventional centralized architecture

functions at all levels. The high-level control functions for propulsion typically include fan speed, core speed, engine pressure ratio (EPR), and temperatures at key locations. The general purpose of these functions is to regulate the engine thrust, optimize performance, and protect the engine from excessive temperatures, pressures, or speeds.

The central computer must also perform many low-level functions (LLF). Much of this computational burden consists of feedback algorithms for effectors, excitation/demodulation for sensors internal to effectors, excitation/demodulation for the other sensors, redundancy management for effectors and sensors, and built-in test (BIT). It is very important to note that the implementation of these low-level functions in central computer requires a multitude of dissimilar interface circuits and software elements because of dissimilarities among the sensors and among the effectors. Moreover, the redundancy management of the sensors and effectors is also device specific. The designers of both the computer hardware and software have only a few opportunities for multiple applications of their designs within a given computer. Their only cost savings comes from reusing and/or adapting designs from past computer development efforts, which are infrequent.

During the development of a control system, changes are inevitable. Let us return to the example of a gain change, and the impact it has on the central computer software. This simple change in one low-level software function requires some sort of proof that all other software functions, both low level and high level, have sustained no adverse effects. Because validation of this kind can be very expensive, the usual approach is to accumulate many changes between validations; an approach which complicates troubleshooting. Now consider a different example in which a sensor or effector has to be added to the control system. In a centralized architecture, such a change affects nearly every aspect of the central computer design.

These issues are confronted by control system designers on a daily basis. Although centralized architecture is viable for moderately complex control systems, the trend toward ever greater complexity seems irreversible. Development is becoming very difficult to manage. As the number and sophistication of functions increases, the costs of implementing all the functions in a single computer will soon outpace the mitigating factors, such as decreasing electronic component costs, increasing computing speeds, improving computer-aided design tools, and widening availability of standards.

In addition, the market for sensors and effectors continues to pull for greater performance. One trend trades increased complexity for various benefits such as lower weight, smaller envelope, lower input power, etc. For example, electronic filtering can be used to enhance stiffness in flight control servoactuators, enabling reduced structural weight.

In summary, centralized architectures have served the aerospace community well in the past, but the trend toward higher complexity has reached a point where distributed architecture is becoming preferable.

Figure 2 shows an example of a distributed architecture. Here, there is still a central computer, but it performs only high-level functions. This makes the computer considerably simpler, cheaper to develop, more compact, and requires far less connector real estate. All low-level functions are moved out to the sensors and effectors. Physically, small electronic packages (referred to as remote terminals or local controllers), which perform the low-level functions, are mounted on or near the devices they serve, making them "smart" subsystems. In variations of this architecture, a local controller serves a group of sensors and/or effectors simultaneously. This is referred to as a partly distributed architecture.

The central computer communicates with the smart sensors and effectors using a fault-tolerant data bus. Electrical power is distributed using a simple, redundant power bus. The difference in wiring topology combined with a greatly reduced wire count saves a great deal of harness weight. Also, wiring is less susceptible to damage which can cause hard-over effector failures. A reduction in connector count increases reliability.

An advantage of mounting a local controller directly on a sensor or effector is that it results in a logistically convenient package that can isolate its own faults and can be treated as a self-contained line replaceable unit (LRU). This offers a distinct improvement in maintainability over present day propulsion control systems: currently, faults are automatically detected and action is automatically taken to place the engine in a safe operating state. However, actual isolation of most faults requires time-consuming work by technicians. Quite often the entire control system has to be removed, and even then, a certain percentage of the faults cannot be duplicated.

In addition, other advantages can be exploited if the supplier of the smart sensor or effector is permitted to develop the local controller for his device: many suppliers have spent years developing their own local controllers. Substantial investments have been made in order to achieve a viable combination of reliability, size, weight, cost, etc. The advantage comes when the supplier is able to develop a new smart device by reusing or adapting a previous design. This is a cost savings opportunity that integrators of centralized control systems rarely get because their development cycle is so long. Whereas, the device supplier must evolve his product more quickly in order to stay competi-

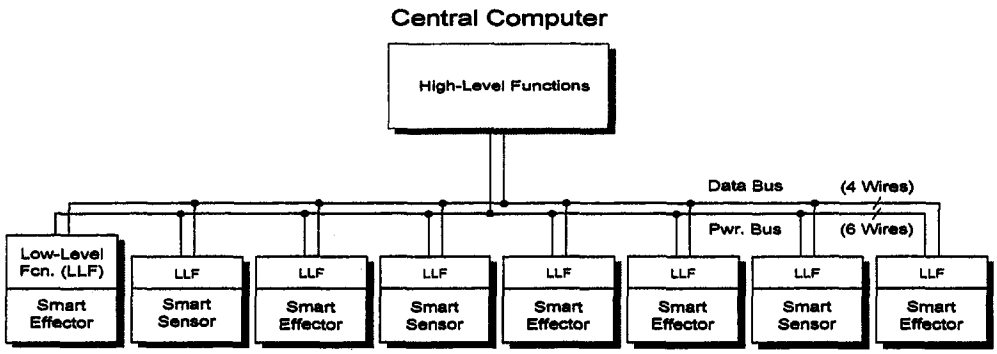

Fig. 2 Example of distributed architecture

tive. Since his design cycle is much shorter, the supplier is further down the learning curve and his costs are lower.

Yet another advantage of distributed architecture is that since its central computer performs only high-level functions, and since other control systems use similar high-level functions, the central computer is much more easily adapted to new systems. Distributed architecture has hierarchical structure in which the central computer has a general managerial function and the smart sensors and effectors have implementation-specific subordinate functions. The reuse and adaptation of existing central computers for new applications is anticipated to be one of the most powerful cost benefits of the concept. But in order to maximize this benefit, computer designers need to think very generally and exploit broad similarities in high-level functions shared by various control systems. Both existing and future systems should be considered.

In a distributed control system, changes tend to be minimally invasive and therefore, less expensive than changes in a centralized system. Consider the gain change example from before. Assuming the effector supplier also supplies its local controller, the change can be made and tested in minimal time by one company usually in one location, using only one set of configuration control procedures. For most simple changes, it is not necessary to formally validate that the other functions in the system are not adversely affected. This is because the system has been functionally decoupled.

Now consider the second example in which a sensor or effector has to be added to the control system. The smart device can be connected into the data and power buses with relative ease. There is little impact on the central computer hardware except that slightly more power is needed. The high-level software in the central computer must be modified, as before.

Advanced control algorithms and other new technologies can be introduced into sensors and effectors with less program risk when a distributed architecture is used. Here again, the single-company approach is more efficient. Many suppliers have their own inhouse model shops, electronic laboratories, circuit and software prototyping facilities, and qualification test laboratories. New ideas and components can be tried quickly. In many cases, the designer himself can run the tests and immediately modify the design as needed. Turnaround on tests can be very fast. Communication is greatly simplified. In addition, the directness of the competition stimulates new sensor/effector-related technologies and ideas to be developed by the suppliers on a frequent and continual basis.

Obsolescence of electronic hardware is an on-going problem in most avionics systems. But distributed architecture facilitates electronic hardware upgrades by allowing selected portions of the system to be upgraded at a time. This can save costs by upgrading only the portions which will benefit the most. Alternatively, upgrades can be retrofitted onto devices as a part of their routine maintenance.

Typical Partitioning of Functions

Low-level functions that are typically implemented in a smart effector include the following:

— feedback loop closure
— redundancy management
— operating mode control
— built-in-test (BIT)
— data bus interface

The function of the effector feedback loop is typically to control position, but other quantities can be controlled as well such as force (or torque), flow, etc. Input commands are received from the central computer via data bus at a fixed repetition rate. Considerable wire weight can be saved by performing the loop closure locally instead of at the central computer.

Fault-tolerant sensors and effectors need redundancy management algorithms for fault detection, isolation, and reconfiguration. These algorithms are highly device specific and usually account for 80–95 percent of the real time software (in terms of lines of code). This is an area where the sensor/effector supplier can really help to control costs by applying specialized experience, previously developed algorithms, and software.

The operating mode of the smart device is requested by the central computer but managed by the device. During control system start-up, the sequencing of power-up and operating mode changes of the individual smart devices is orchestrated by the central computer. Each device reports its operating mode back to the central computer periodically. In the event of a sensor/effector fault, action is taken locally by changing operating modes and reporting the event to the central computer.

A local controller provides a very convenient means to implement other functions as well. The input command signal can be scaled, shifted, transformed in order to linearize nonlinear effector motion, etc. The local controller can also log operating time and maintenance actions. For power-by-wire (PBW) effectors, motor drive functions are often included in the local controller.

Low-level functions which are typically implemented in a smart sensor include the following:

— excitation
— demodulation/decoding
— redundancy management
— data bus interface

By performing excitation and demodulation/decoding locally instead of in the central computer, more wire weight is eliminated. Signal conditioning such as filtering, time averaging, scaling, shifting, linearization, temperature correction, etc., can be performed by the local controller. As with effectors, sensor redundancy management functions are highly device specific. Performing this function locally removes computational burden

from the central computer. The smart sensor transmits the (possibly processed) signal of interest as well as health status to the central computer via the data bus at a fixed repetition rate.

Technical Challenges

In addition to the usual challenges of developing a control system, aerospace applications pose even more challenges: Continuous ambient temperatures for local controllers in engine applications are typically 200°C. This can drop to −40°C between periods of operation. For engine applications, the vibration levels are also severe. Mounting a controller onto a sensor or effector adds mass, making vibration requirements even more challenging. Faults must be isolatable to a specific LRU or data bus. Cost of the local controller must only be a fraction of that of the device it controls in order for the concept to be viable.

Similarly, the size of the controller must be small compared with that of the device it controls in order to fit into traditionally tight envelopes. Using current SOI technology, a single effector controller channel typically requires a volume of 600 cm^3 (roughly the size of a typical paperback novel). But for fault tolerance, at least two channels are usually used. The size which appears to be a commonly desired target for future controllers is 120 cm^3 for one channel (roughly the size of a cigarette pack). Thus, a size reduction by a factor of five is ultimately desired.

Interface Issues and Data Bus Selection

For aerospace control applications, analog sensors must maintain reasonable accuracy over a very wide range of temperatures. Currently available SOI components provide acceptable performance. For analog-to-digital (A/D) converters, a compromise must be struck between conversion time and resolution. Fortunately for most flight control and propulsion control effectors, a resolution of 10 or 11 bits can be achieved with a tolerable conversion time. SOI multiplexers that permit time sharing of A/D converters will soon be available.

Practical SOI current drivers have limited but useable current-sourcing capability. Practical drivers for use in proportional control are limited to about ±40 mA, and drivers for discrete loads, such as solenoids, are limited to about 225 mA.

The use of a low voltage, single-sided power supply is a very effective approach to reduce power supply size, but it has an obvious impact on sensor interfaces. The use of LVDT excitation circuits which supply pulses rather than a sine wave is one way to accommodate this approach.

The standard data bus protocols which are the current favorites for propulsion control include MIL-STD-1553, SP50 Fieldbus, and ARINC 429. Optical data buses are not yet viable because high-temperature diode laser technology has yet to mature.

Experience with 1553 transceivers indicates that devices available in SOI draw considerable power. However, power requirements can be greatly reduced by only requiring the transceiver to drive fewer remote terminals over shorter bus lengths. These limitations are judged to be inconsequential for most propulsion control applications.

Technology Insertion Issues

A few issues still impede the market insertion of distributed control technology for aerospace applications: since high temperature electronic components are not yet produced in large quantities, they are still expensive and difficult to obtain in prototyping quantities. However, relief is within sight as market demand for components continues to grow and as the array of available standard devices begins to fill out. Nearly all of the standard digital logic devices are already on the market in SOI form, along with a complete eight-bit microcontroller, the 80C51. The Defense Advanced Research Projects Agency (DARPA) is funding a multi-year technology reinvestment program (TRP) to help bring SOI components to marketable form and to demonstrate complete high-temperature controllers for aerospace and industrial applications. The program is named High Temperature Distributed Control Systems (HiTeC). As a result of this program, a full complement of SOI parts needed for real-time control is anticipated to be fully developed by mid 1998 and commercialized shortly thereafter:

Part:	Description:
HT8051	8-bit microcontroller
B320HT	32-bit floating point μP
SRAM	dual Port, 32k × 8 bit
ROM	64 k byte
A/D Converter	12 bit, 10 μs
Clock Chip	10 MHz
Databus Protocol	1553
Digital Sensor Interface	multiple input
Glue Logic Chip	watchdog, latch, RAM, ROM
LVDT Exciter	28V Excitation Generator
LVDT Demod	dual channel ratiometric
MUX	16 to 1
Op Amp	quad op amp
Power Supply Chip	28V switch mode power supply
Solenoid Driver	28V, PWM
Torque Motor Driver	15V, 50 mA
Transceiver	1553, 1 Mbit/sec
Voltage Reference	1.5% over temperature

A second market insertion issue is that high-temperature passive electronic components are considerably larger than their conventional counterparts. This has been somewhat of an impediment to miniaturization of local controllers because the passive components have tended to dominate the available space. Particular circuits in which passives become size drivers have included power supplies and EMI filters. Experience shows that it helps to use a shared, centralized power supply and to implement the minimum practical power conditioning in each local controller. Attention to innovative power bus design has already identified some very useful methods to mitigate this issue.

Definitive trade studies have been difficult to perform: in cost trade studies, for example, the cost breakdown of implementing low level versus high-level functions in a centralized architecture is uncertain. In reliability trade studies, reallocation of a reliability budget to a distributed system is challenging because it has different redundancy management and failure modes.

Perhaps the most critical and uncertain issue is that the companies which have traditionally developed centralized systems now want to have active roles in developing local controllers, potentially detracting from cost savings. It is hoped that this trend is only an interim risk-reduction measure while distributed systems become more prevalent. A key lesson learned after several implementations of distributed control is that the maximum cost benefit of this architecture comes when the systems integrator specifies functions and performance of the smart device, without specifying its implementation. Allowing the supplier of the smart device to implement the local controller invokes the most powerful cost-reduction methods:

— reuse/adaptation of existing designs
— use of established families of design features
— modularization
— use of a geographically-collocated design team
— rapid, iterative design/prototyping/testing

Example Implementations

A three-stage missile uses distributed control for all its flight control servoactuators (see Fig. 3) for both aerodynamic control surfaces and for thrust vector control (TVC). The missile has

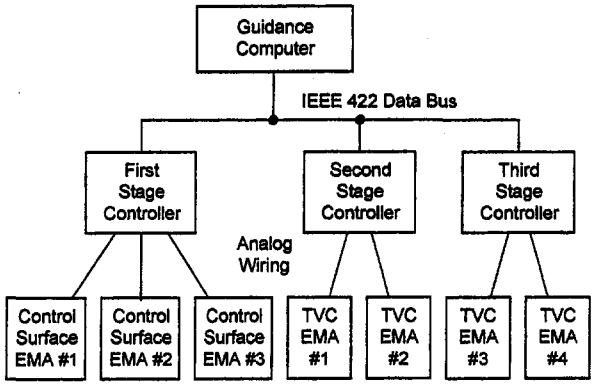

Fig. 3 Three-stage missile flight control system architecture

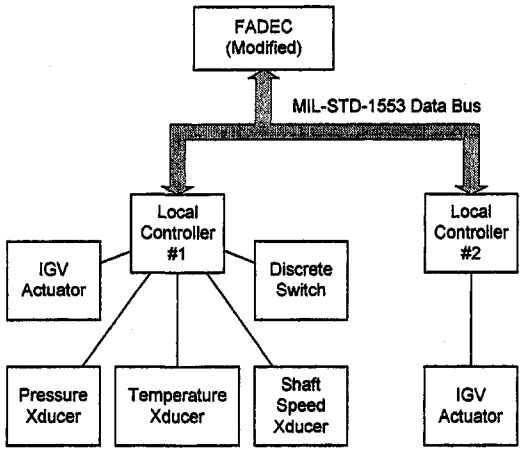

Fig. 5 HiTeC high temperature propulsion control demonstration

one controller located in each of its three stages. Each controller operates multiple electromechanical actuators (EMA). The first stage controller operates three independent aerodynamic control surface EMAs. The second stage controller operates two independent TVC EMAs. The third stage controller operates two more independent TVC EMAs. Position commands are provided to the local controllers via an IEEE422 data bus. The system is nonredundant.

The Joint Strike Fighter/Integrated Subsystem Technology (J/IST) program's AFTI-F16 demonstrator aircraft uses an unusual, retrofitted, distributed control architecture for its five primary flight control servoactuators (see Fig. 4). The program is particularly noteworthy because it involves a manned aircraft which is aerodynamically unstable in pitch. Stability is provided by a quad-redundant Digital Flight Control Computer (DFLCC) working in conjunction with inertial sensors, air data sensors, and the control surface servoactuators. Clearly, all of these items are safety critical. The original servoactuators are replaced by electrohydrostatic actuators (EHA) that comprise an electric motor driving a fixed-displacement hydraulic pump, which in turn drives a hydraulic actuator. Here, the DFLCC (playing the role of central computer) communicates with the triple-redundant control electronics unit (CE) via existing analog wiring. The CE performs position loop closure, redundancy management, operating mode control, and BIT for all five EHAs. Each individual EHA has its own dual redundant power drive electronics unit (PDE) which performs velocity loop closure and motor drive functions. The CE communicates velocity commands to the five PDEs via MIL-STD-1553 data buses. In this example, there is a hierarchical relationship between the flight control computer, the CE, and the five PDEs. Low-level DFLCC functions unique to the EHAs have been strategically redistributed among the CE and the PDEs. Those functions that can practically share one computer are implemented in the CE. The rest are implemented in the individual PDEs.

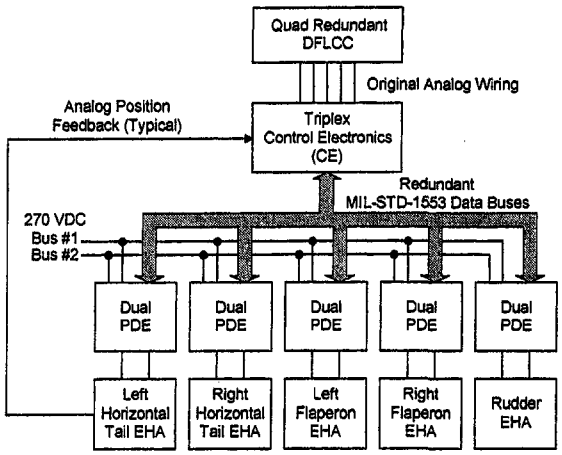

Fig. 4 J/IST flight control system architecture

One objective of the previously mentioned HiTeC program is to demonstrate a high temperature, actuator-mounted controller for a turbine engine inlet guide vane servoactuator. The dual-redundant controller will perform loop closure and redundancy management for the actuator. In addition, the controller will provide interfaces and redundancy management for nearby sensors unrelated to the servoactuator: pressure, temperature, shaft speed, and a discrete switch (see Fig. 5). Communication between the controller and the existing full authority digital engine controller (FADEC) will occur using a MIL-STD-1553 data bus. Modifications of the FADEC software permit relocation of these low-level functions to the smart servoactuator.

Additional Lessons Learned

In addition to the lessons already discussed, several more can be enumerated.

Place systems integration at the forefront of the design effort. Be clear and thorough in all interface definitions and requirement specifications. Preliminary versions of these should be written as early in the development program as possible.

Development of real time, fault-tolerant distributed controls requires specialized engineering talent. It is crucial to obtain and retain the necessary talent. Also, the project management must have a thorough understanding of electronic, mechanical, and functional details.

Distributed systems have subtleties. Ingenuity is needed in order to realize the full cost savings. An active effort is needed to control complexity; both by systems integrators and by the suppliers of the smart devices. Some functions in which complexity is usually hard to control are as follows: control algorithms, redundancy management, turn-on sequencing, operating mode control, and power interruption handling. Even moderate complexity in these functions can pose problems in verifying the safety of the control system.

Turn-on sequencing, BIT, and operating mode control of each smart device must harmonize with the rest of the distributed system. This requires early coordination between the systems integrator and suppliers of the smart devices.

In the event of failures or other unusual conditions, the distributed system must react predictably. Also, transients due to start-up, power interruptions, and failures must all be addressed in the context of the distributed system. For example, a start-up transient for a flight control surface effector should, by design, preclude any large sudden motions which might pose a hazard to ground personnel. As a second example involving flight control

effectors, preflight BIT must not be automatically initiated on power-up. If it were, a brief in-flight power interruption could cause loss of control of the aircraft while the effector is put through its paces.

For high temperature applications, power supply design can have a major impact on physical size of a local controller. It is not unusual for 60 percent of an effector controller's volume to be taken up by the power supply.

Design the local controller to accommodate internal and external changes. The need for changes during control system development is a given. Include spare memory, computation time, and data bus loading. Anticipate the effects of data latency. In effector controllers, include provisions for additional gains and compensation filters. Then, consider going one step further: the judicious addition of a few extra features can tremendously facilitate reuse/adaptation of the design in new applications. Of course, this entails some added weight, size, etc., but this approach can reap a big cost savings if the design can reapplied within the same control system, and/or in other control systems.

Integration testing for distributed systems requires considerable forethought. However, this architecture facilitates testing that progresses from the component level, to the subsystem level, to the system level. In addition, much of the testing can be done in parallel by using emulators.

EMI must be addressed in all of its forms. Consider both modes of transfer (radiation, conduction) and in both directions (emitted, incident).

Retrofitting a controller onto an existing effector can be challenging. The added mass changes the effector's structural dynamic mode shapes and natural frequencies, usually increasing stresses due to vibration. The original servoactuator design might barely meet its vibration requirements without the added mass. Unfortunately, design features which can mitigate this problem (i.e., vibration isolation) also tend to impede the transfer of heat from the controller into the servoactuator.

Suggested Objectives for Future Implementations

Perhaps the two things which can benefit a control system development the most are to keep the design as simple as possible, and to pursue the benefits of a distributed architecture to the fullest. This architecture provides an unusually effective framework in which to break the development effort down into tractable tasks. By carefully exploiting this important attribute, coupling between the tasks can be minimized. Doing this in turn minimizes the number of participants needed, makes communication more efficient, simplifies testing and troubleshooting, cuts costs, and reduces program risk.

It would also be useful to promote an infrastructure specifically intended to facilitate efficient reuse/adaptation of existing designs. Each system should be designed with future systems in mind. Infrastructure is an area rich with potential for reducing development costs.

The market insertion issues also deserve consideration in future implementations. Currently, SOI component prices are the result of a catch-22: prices are high not only because the technology is still relatively young, but also because markets are small. But demand is low because prices are high. The only logical approach to a solution is find ways to stimulate more purchases and in larger quantities. This means, at least for the time being, that local controllers for distributed control should be as generic and reusable as possible to promote component commonality. The size issue for passive electronic components is probably best addressed through more innovative power distribution and conditioning.

Acknowledgments

The author wishes to express his thanks to the following individuals for their valuable contributions of information spanning several years: Bill Nighan and George Foyt of UTRC who currently lead the HiTeC program Consortium, along with all of the Consortium members, Wally Al-Sherif of Lear Astronics, and Ed Stevens, Dick Kotalik, Dave Rumney, Arvind Ahluwalia, Nick Zamvakellis, and Shirl Carter all of Parker Control Systems Division-Military.

References

1 Lewis, T. J., "Distributed Architectures for Advanced Engine Control Systems," paper presented at the AGARD/Propulsion & Energetics Panel, 86th Symposium on Advanced Aero Engine Concepts and Controls, September, 1995.

Distributed Control System for Turbine Engines

P. L. Shaffer
General Electric Aircraft Engines,
1 Neumann Way, MD BBC5,
Cincinnati, OH 45215

A distributed control system (DCS) for a turbine engine has been demonstrated and tested, consisting of prototype electronic interface units (EIUs) connected to data and power busses. In the DCS, a central control computer communicated with smart sensors and smart actuators via a 2.5 megabit/sec digital data bus, using the Fieldbus protocol. Power was distributed to the smart devices as 100 kHz 100V peak AC, allowing light, simple power converters at each smart device. All smart sensors, smart actuators, and cables were dual redundant. The smart actuators received position demand from the central control computer, exchanged data between channels to provide local redundancy management, closed the position loop locally, and reported actuator position to the central controller. Smart sensors converted sensed signals to digital values in engineering units, and performed local built-in tests. Testing of the DCS was done in a closed-loop simulation with an engine model. Frequency response of the DCS was almost identical with the conventional system.

Introduction

A distributed control system (DCS) for turbine engines is a control system in which smart devices communicate via a digital data bus with the full-authority digital engine control (FADEC), as illustrated in Fig. 1. A smart device could be a smart sensor or a smart actuator, or could combine both sensing and actuation functions. Smart sensors convert analog sensor values to digital form, and provide outputs to the FADEC in engineering units, such as degrees F, Hertz, or PSIA. Smart actuators receive a position command from the FADEC, and perform closed-loop position control of the actuator. Smart sensors and actuators report their status to the FADEC, and can carry out functions such as compensation, built-in test, fault detection, and diagnosis. A smart device (sensor or actuator) consists of a baseline device plus an EIU. The EIU has a data bus and power bus interface to the FADEC. The smart device would be a line replaceable unit (LRU) on an engine, and EIUs would be serviced or repaired at a service center or by the manufacturer of the smart device. An engine area network (EAN) is a communications and power network that connects the FADEC and the smart devices. An EAN would probably have one or two separate cable assemblies per channel. Each EAN cable contains a shielded twisted pair of wires for transmission of digital data among FADEC and smart devices, and a shielded twisted pair of wires to carry power from the FADEC to the smart devices.

Design studies have indicated that the benefits of a DCS should include reduced weight for the control system, particularly in the cables; reduced development cycle time and design cost, due to common modules and standard interfaces; accommodating growth in sensors and actuators, making the FADEC design adaptable to new engine types, adaptability to changes in components, allowing the opportunity to introduce new technologies; improved reliability and reduced costs due to longer production runs based on standard components and designs; reduced maintenance costs, due to built-in test and diagnostics at each smart device; and enabling of off-engine FADEC for further weight saving, improved reliability and control system integration.

The distributed control system program defined a DCS architecture that should provide the benefits listed above. The program quantified the costs and benefits of the DCS, designed and fabricated elements of a DCS using low temperature parts, and tested and demonstrated a DCS in closed-loop operation with an engine simulation in a laboratory environment. Numerous design decisions relative to a DCS were examined, such as what functions should be carried out by smart devices, whether dual-redundant smart devices should have a local data link between the channels, and what the topology of the EAN should be. This paper will focus on only the following two issues: the characteristics of the power distribution bus and the protocol of the digital data bus. Alternatives will be examined, the rationale described for the choices made in this program, the results presented, and recommendations made for future distributed control systems for turbine engines.

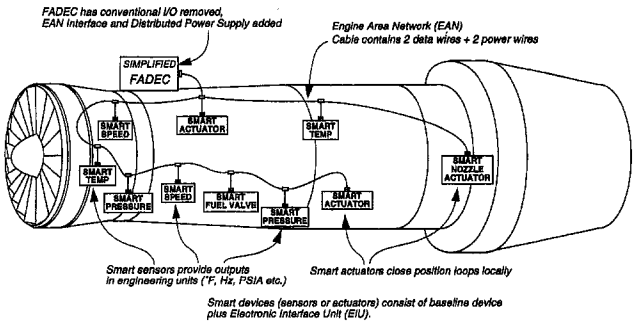

Fig. 1 Overview of a distributed control system on a turbine engine

DCS Design Issues

EAN Power Distribution. Three alternatives for power distribution from the FADEC or central power converter to the smart devices are (1) an AC bus with local AC/DC conversion, (2) a DC bus with local DC/DC conversion, and (3) a central DC/DC power converter generating all voltages, which are distributed to all smart devices. The third alternative can be eliminated immediately because this system would have heavier cables than the other alternatives, would limit EIU designs to use only the voltages produced centrally (or else add local DC/DC converters and thus have the worst aspects of both options 2 and 3), and would make it difficult to ensure good power quality without local regulation.

A DC bus would probably be either 28 VDC or 270 VDC, and an AC bus could be 115 VAC at 400 Hz. All three of these

Contributed by the International Gas Turbine Institute and presented at the International Gas Turbine and Aeroengine Congress and Exhibition, Stockholm, Sweden, June 2–5, 1998. Manuscript received by the ASME Headquarters April 1, 1998. Paper No. 98-GT-16. Associate Technical Editor: R. Kielb.

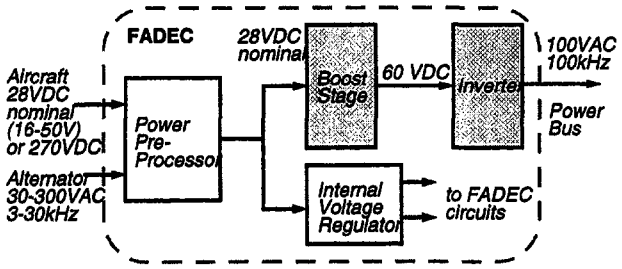

Fig. 2 Central power converter. Shaded portions are additions to existing FADEC power supply.

voltages are described by MIL-STD-704D and are used for power distribution in military aircraft. 270 VDC appears to be the power distribution choice for next-generation military aircraft. However, none of these voltages is very well regulated, or particularly well suited to the needs of a DCS. Instead, AC power distribution using high frequency (100 kHz) and fairly high voltage (100 Volt peak) was selected for this program because it has the following advantages:

— Smaller parts count than DC. Each EIU needs only a multiple-winding transformer with a secondary, rectifier diode, or bridge, and a series regulator for each required output voltage.
— Better stability than DC, because local supplies with series regulators provide a positive impedance to an AC bus while local DC/DC converters provide a negative impedance to a DC bus.
— Better reliability and lower weight than DC, because of the smaller parts count.
— Better high temperature capability than DC, because only simple semiconductors are needed at each EIU.
— High frequency results in smaller transformers, limited by losses in the bus cables and transformer inductance leakage, and by the potential for EMI emission.
— High voltage minimizes current losses in the cables, but is limited by concerns for insulation stress, corona, and personnel safety.

One negative feature of AC power distribution is that the overall power conversion efficiency is somewhat lower than in a DC distribution system, because the efficiency of series regulators in the AC/DC local converters is lower than the efficiency possible in DC/DC converters. The overall efficiency of the AC power system is expected to be about 68 percent, while DC/DC converters can achieve up to 86 percent efficiency (based on a survey of off the shelf, military-qualified DC/DC converters).

A trapezoidal (near-square) waveform was selected (versus a sine wave) because it reduces the peak current flow and low order harmonics (and thus EMI), and is easier to generate than a sine wave. This AC power would be generated within the FADEC or a central power conversion module, and distributed via shielded power distribution wires. A block diagram for the central power converter, which provides well-regulated power to the EAN bus, is given in Fig. 2.

DCS Bus Power Supplies. For evaluation of the prototype DCS, two 100 kHz 100 VAC power supplies were designed and built. Each power supply generated power for one channel of the prototype DCS. Each power supply utilized 60 Hz, 115 VAC power as its input, and generated 100 (±5) kHz, 100 (±5) Volts peak with a trapezoidal waveform. Each supply had a steady-state current output capability of over 2.0 A RMS, with a transient capability of 5.0 A RMS. Each of the supplies was constructed using two commercial off-the-shelf 115 VAC to 100 VDC power supplies as a front end. The outputs of the two DC supplies was switched using current-sensing MOSFET switches to produce the trapezoidal AC output. The bus power supplies were designed to be fully tolerant of any fault condition likely to be imposed on them, such as shorting of the outputs. The outputs were capacitor coupled, and the DC level of the outputs was monitored so that the outputs could be disabled if a fault occurred that resulted in a significant shift in DC level of the output.

EAN Data Bus Requirements. A protocol is a well-defined set of rules and conventions used by the nodes on a network to communicate with each other. A large number of different communication protocols are in use. These requirements for communication via the EAN data bus were defined as follows:

1 Reliability of message content. This requires at least an error-detection code, and preferably an error detection and correction (EDC) code within each message.
2 Assurance of delivery of data. For the FADEC to know that messages were delivered properly to the appropriate EIU, the EIU should always acknowledge the message and indicate whether the message was delivered without any apparent errors.
3 Adequate address range. The FADEC must be able to communicate with an adequate number of smart devices; 256 smart devices should be sufficient for the foreseeable future.
4 Minimum 16-bit data field. Data from sensors or to actuators on engines typically have 12 or 16 bits of resolution, so a 16-bit data field should accommodate system needs.
5 Status and data messages (or status field with data). The smart devices should regularly inform the FADEC of their health status; preferably, at least one status bit should be included with each message; detailed status could be transmitted in separate status messages.
6 Low overhead. Overhead includes bits in a message used for addressing, synchronization and error checking, as well as retransmissions due to collisions or other reasons. Messages in an EAN are expected to be short (one or two 16-bit words of data per message). Some protocols, designed to handle transmission of large messages, impose an excessive overhead on short messages, adding to data latency.
7 Minimum complexity. Because each EIU requires an interface circuit for the EAN, the complexity of the protocol should be kept as low as possible to reduce circuit complexity, cost, and component failure rate.
8 Command-response protocol. A protocol in which the smart devices only communicate in response to a command from the FADEC is preferred, because it is deterministic and less likely to allow failures in which one EIU disrupts the bus via uncontrolled transmissions.
9 Data rate. The minimum required data rate will depend on the amount of overhead in the protocol (and thus the effective data rate relative to the raw data rate), the maximum number of nodes (devices) permitted on the network, and the iteration time of the FADEC.
10 Synchronization. If transmission of data is synchronous with its production and use, then only the transport delay needs to be added to the delay from time of production to time of use. However, if transmission is asynchronous with either production or use of data, then additional delays are added based on the iteration times of production, transmission, and reception of the data.

In addition to these protocol requirements, the electronic devices used to implement the EIUs on engine sensors and actuators must be able to withstand the harsh conditions on engine cases. Most challenging of these conditions are the high temperatures found on engine cases. While temperatures vary among

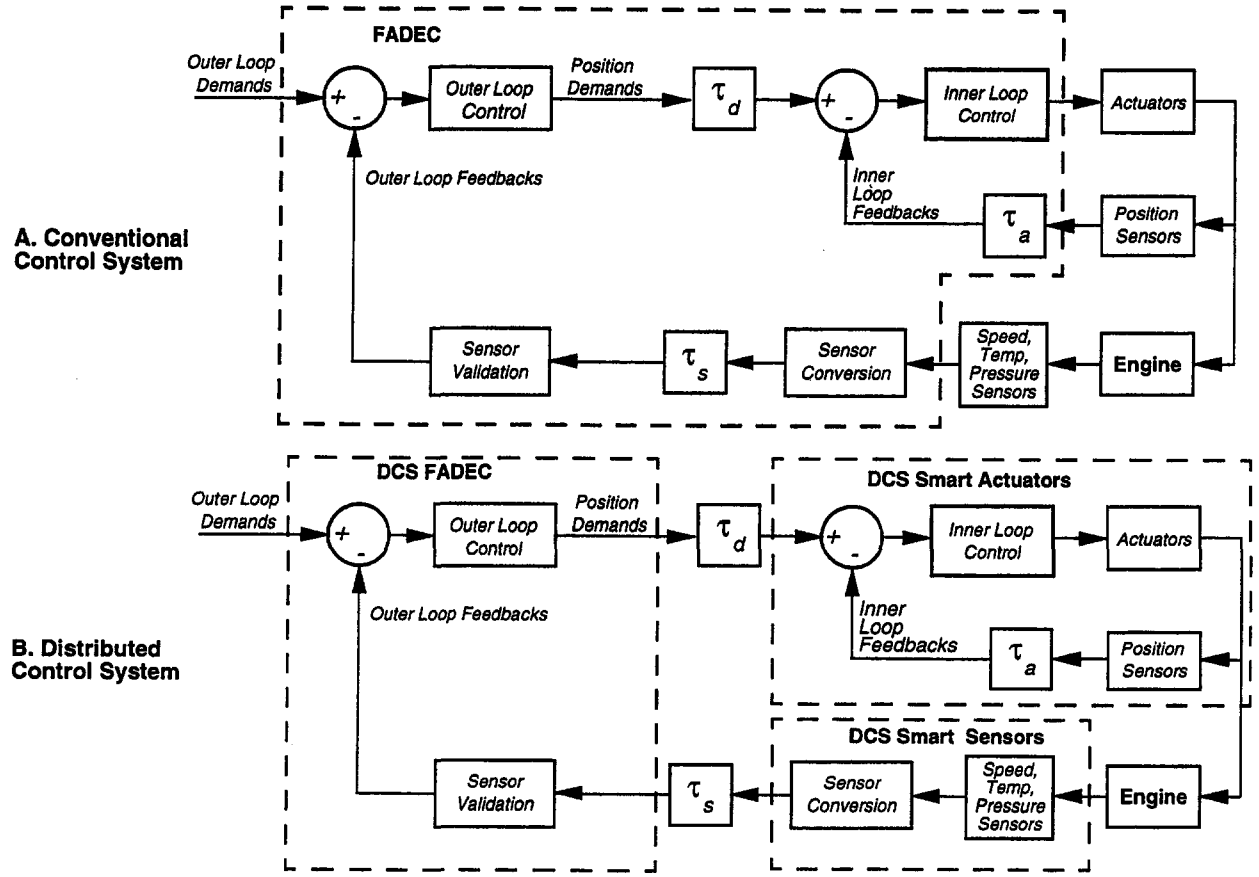

Fig. 3 Delays presented by (*A*) conventional and (*B*) distributed control systems. Areas in dashed boxes represent independent processing units.

engines and among locations on an engine, EIUs will have to operate at temperatures of at least 200°C to be usable over most regions of turbine engines.

Control System Delays. The net effect of data rate, overhead and synchronization can be summarized by the transaction time of the data bus, defined as the time for an interaction between the FADEC and a smart device, in which the FADEC sends a command or request to a smart device, and the smart device responds with an acknowledgment of the command or data fulfilling the request. The transaction time represents a communication delay between the FADEC and the smart device, and added time delays can have a negative impact on control system performance, particularly in reducing system stability.

Delays within a conventional control system and a DCS are illustrated in Fig. 3. Three delays are indicated in this figure: τ_s is the sensor acquisition delay, which includes all input signal processing, such as sensor conversion, validation and selection time; τ_d is the delay from production of a position demand until its use for inner loop position control; and τ_a is the iteration rate of an actuator inner loop control. It is assumed here that the fundamental iteration rate of the FADEC, typically 10 to 20 msec, is the same for the two systems.

Data bus communication delays in a DCS add to τ_s, where sensed engine values are passed to the outer loop control, and τ_d, where position demand values are passed from outer to inner loop control. However, in a DCS, sensor values can be acquired and processed in parallel by smart sensors and a reduced amount of input signal processing occurs sequentially in the FADEC, and inner loop closure computations and actuator output processing can be performed in parallel by the smart actuators. In a conventional control system, computations required for sensor input processing, actuator output processing, and inner loop closure must be done sequentially within the FADEC. Thus, τ_s will include delays due to the sequential processing of multiple sensor signals, and τ_d will include delays due to the sequential processing of multiple actuator signals. The actuator control loop is expected to run several times faster in smart actuators in a DCS than in a conventional control system, so τ_a would be smaller in a DCS (5 msec in this program) than in a conventional control system (typically, 15 msec). The actual impact of a DCS on control system delays will depend heavily on implementation details, but the net effect should be small. In an example control system analyzed, a DCS would have no adverse impact on control system stability relative to a conventional control system for a transaction time of up to 188 μsec.

Data Network Implementation. Existing computer communication protocols were surveyed. Some characteristics of a number of alternative data bus protocols are summarized in Table 1. Included in this table is a custom protocol optimized for engine control applications. This was a minimum overhead, command-response protocol with an EDC code for single-bit error correction. The protocol was designed to operate at 10 Mbps, and was implemented in a breadboard-quality prototype at 2.5 Mbps (due to a limitation in then-available Manchester encoder circuits).

Any of these protocols, except ARINC 429, would satisfy the typical 188 μsec requirement cited above. ARINC 629 can be eliminated from consideration because it is not a command-response protocol. MIL-STD-1773 can be eliminated because it uses an optical interconnect, and prospects for electro-optical interfaces operating at 200°C are poor for the foreseeable future. The protocols in Table 1 that are the most promising are the MIL-STD-1553 protocol, the GE custom protocol, and the

Table 1 Alternative candidate protocols for the EAN

Protocol	Speed (Mbps)	Number of ICs	Temp. Range	Time/ Transaction (μsec)[a]	Number of transmitters per bus
ARINC 429	0.1	2	125°C	674[b]	1
MIL-STD-1553	1.0	1 Hybrid + 1	125°C	72[c]	31
GE Custom	2.5	3 large + 16 small	125°C	28	256
ARINC 629	2.0	1 Hybrid + 3	125°C	83[d]	120
MIL-STD-1773	1.0	Not available	125°C	72[c]	31
Fieldbus	2.5	7	85°C	95[e]	65536

a. Transaction = 16-bit command to EIU from FADEC, plus 16-bit status / value response from EIU.
b. Plus delays introduced by hardware at each end.
c. Response time = 12 μsec (allowed range is 4 to 12 μsec).
d. Increases with number of EIUs; value given is based on 36 EIUs.
e. Delays due to lack of synchronization not included; smart device status is a separate transaction.

Fieldbus protocol. MIL-STD-1553 has the lowest data rate of the three, and has the lowest number of smart devices possible per data bus. But MIL-STD-1553 is widely used in military avionics systems, has low overhead in transmission compared to the Fieldbus, and may have adequate addressing for a turbine engine control system. The GE custom protocol is optimized for engine control, but exists only in a breadboard form, and has little prospect of being developed into a standard chip set. The Fieldbus protocol is an international standard (actually, competing standards), and may have support from manufacturers of smart sensors and actuators. There is some interest from semiconductor manufacturers in development of high temperature (200°C or more) versions of MIL-STD-1553 or Fieldbus chip sets.

The Fieldbus protocol was selected for use in this program and the FullFIP2 microcircuit (Cegelec, 1994) was used to implement the protocol. Table 1 reflects some knowledge gained since the selection of Fieldbus was made, and Fieldbus appeared more advantageous based on information available when the selection was made. Assessment of the success of this choice, and observations on the problems associated with the Fieldbus, are presented below.

The physical layer of the WorldFIP standard is described by ISA-S50.02 (ISA, 1992). Data are transmitted at 2.5 Mbps over shielded, twisted wire pairs. Peak-to-peak voltage of the signal is 5.5 to 9.0 Volts at a transmitter, and must be at least 0.7 Volt at a receiver. A transmission frame consists of a frame start sequence, data and check fields, and a frame end sequence. The frame start sequence consists of an 8-bit preamble, used for receiver synchronization, and a frame start delimiter that occupies 6-bit periods, signalling that a frame is starting. The frame end sequence consists of a frame end delimiter that occupies 7-bit periods, and signals the end of a frame.

The data-link layer of the WorldFIP protocol is described by C46-603 (UTE, 1990). At this layer of the communication protocol, the data and check fields of each frame are defined to consist of a Control byte, a data field of up to 128 bytes, and a 2-byte frame check sequence. The control byte identifies the type of frame. The frame check sequence consists of a cyclic redundancy check code, and is used to provide a data integrity check on the frame contents. The data-link layer provides two types of transmission service: cyclic exchanges of identified variables, and message transfer upon explicit request. Only cyclic exchanges of identified variables were used in the prototype DCS. With variables that are exchanged cyclically, the names and periods of all variables that are to be exchanged are defined at the time the system is configured. Each WorldFIP system has a fixed number of variables that are to be exchanged, and each variable has a unique 2-byte identifier. Each variable can consist of a single value, such as an integer or floating-point value, or can be a composite structure containing a number of values, with a size up to 128 bytes.

A WorldFIP network is composed of two functional types of nodes attached to the transmission medium: a bus arbitrator (BA), and producer/consumer functions. Any node on the bus can carry out producer/consumer functions, but only one node can carry out the BA function. Although the standard allows the BA function to move from one node to another, in an EAN the BA function should always be carried out by the FADEC. The BA controls access to the transmission medium, and is responsible for initiating each periodic variable exchange by broadcasting the identifier of the variable onto the bus in an identifier frame. The identifier frame contains a total of 61 bits, and so requires 24.4 μsec at 2.5 Mbps. One and only one node on the bus is a producer of each variable, and that node responds to the broadcast identifier of the variable by broadcasting the value of the variable in a data reply frame. Any node on the bus that uses ("consumes") that variable then receives the value, having been alerted that the value was imminent by the preceding identifier frame containing the variable's identifier. The BA maintains a list of variables that are to be exchanged cyclically, and scans that list over a fixed period. This ensures that all the variables are exchanged in a deterministic manner, and that real-time deadlines are always met.

The FADEC carries out both BA and producer/consumer functions; however, BA operation is asynchronous with the producer/consumer operations. Since the transmission of the position demand on the data bus is asynchronous with production of the value by the FADEC, and asynchronous with the reading of the demand value by the smart actuator, then the average delay associated with this transmission, illustrated as τ_d in Fig. 3, would be the transport time plus hardware delays, plus one half the periodic transmission interval, plus one half the smart actuator minor frame interval. With a 20 msec transmission interval and a 5 msec smart actuator iteration interval, the average τ_d would be about 12.5 msec. The worst case delay would be almost twice the average value.

Smart sensors and actuators only carry out producer/consumer functions. A smart device examines each identifier frame on the bus. If an identifier frame contains the identifier of a variable that the smart device produces, then the device broadcasts that variable on the bus. On a 2.5 Mbps WorldFIP network, the device should (according to the WorldFIP standard) respond with the data reply frame containing the value within 4 to 28 μsec; this is the turnaround time of the producer node. The turnaround time for the FullFIP2 device operating at 2.5 Mbps is 33 μsec (Cegelec, 1994), which exceeds the maximum allowed by the standard. If a smart device sees an identifier frame containing the identifier of a variable that it consumes, then it receives the following data reply frame, which contains the needed value. This interaction of a smart device with the bus is carried out by the Fieldbus communications processor and does not require intervention of the main processor in a smart device.

The response frame by the producer device includes a total of 61 bits of overhead in addition to the actual data sent by the producer. Efficiency of this protocol increases with the amount of data included in each data reply frame, and decreases with the turnaround time of the producer nodes. With 4-byte variables and a 33 μsec turnaround time by producer nodes, the

efficiency of data transfer is 10.7 percent, and 171 cyclic exchanges can take place in a 20 msec period.

The operation of the bus is determined by a configuration file that is processed by a configuration compiler program. This file specifies information about the Fieldbus such as data rate, and information about each of the nodes on the bus. Node information includes type of Fieldbus interface, turnaround time, whether it is the bus arbitrator, and what variables the node produces and consumes. Variable information includes an identifier, periodicity of the variable (in msec), and the data type of the variable. Optional characteristics that can be specified for variables exchanged on the bus are promptness and refreshment; these indicators of data freshness are supplied by the application layer of the Fieldbus protocol. Refreshment indicates whether the application process on the node which produces the variable actually has done so with the periodicity indicated in the configuration file. If for some reason the variable is not generated as frequently as required, the refreshment status will be false. Promptness indicates whether the messages containing a specified variable are received by a consumer with the periodicity indicated in the configuration file. If the bus arbitrator is not requesting the variable often enough, or the producer is not transmitting the message containing the variable with the indicated frequency, then the promptness status will be false. If either refreshment or promptness is false, then valid data have not been received at the desired frequency. In this program, promptness and refreshment were used for the critical variables.

The configuration compiler determines a schedule by which variables are to be transmitted on the data bus, and determines how much of the potential data rate of the data bus is used by the periodic variables. The schedule is compiled for use by the bus arbitrator, to control its sequence of operations. For the configuration file used in the prototype DCS, and representing a fully distributed control system, an average of 4.79 msec of a 20.0 msec frame was used in the transmission of data, or 23.6 percent of the frame. The maximum bus utilization was 24.5 percent of a frame. This indicates that, even with the substantial overhead of the Fieldbus protocol and the 33 μsec turnaround time of a FullFIP2 device, less than one quarter of the available bus data rate was used for data transmission.

Results

Power Bus Measurements. The power supply developed for this program was designed to provide nominal input voltage characteristics to the EIUs. Because these power settings were fixed, testing of the power bus was limited to characterization of its voltage signal. Measurements were taken to record power system characteristics during DCS operation.

Power bus voltage waveform characteristics were measured and compared to the specifications for the power supply. All specifications were met, with rise and fall times being 1 μsec, compared to the specified 3 μsec minimum rise time. No DC component, frequency modulation or amplitude modulation were observed in the power supply outputs.

Additionally, power bus performance was examined for interactions induced by the communication bus. No interaction was visible as distortion or modulation of the power bus waveform.

Communication Bus Measurements. Communication bus performance was examined for interactions induced by the 100 kHz power bus. In the absence of a power signal (i.e., with the power supply turned off), the data signal was a 3 V peak amplitude signal, with the data appearing as pulse-width modulations alternating with intervals of no signal. Minimum apparent pulse width was 200 nsec, corresponding to one half the period of a 2.5 Mbps Manchester-encoded signal. Durations of the pulse modulations, and the intervals between the modulations, varied with the usage of the data bus.

A noise signal at a frequency of 100 kHz was observed on the data bus when the power signal was applied to the power bus. The noise signal was a 100 kHz pulse train, where each pulse had an approximately triangular shape, with a peak voltage of about 1 V, and a pulse width of about 1 μsec. These noise pulses were best observed in the intervals between data transmissions on the data bus. When the noise pulses coincided with data transmissions, the distortion of the data waveform was evident. The pulse width corresponds to the observed rise time of the power signal. These pulses were clearly induced noise from the high frequency components of the power signal, despite the fact that both power bus and data bus were shielded cables. The only place where the two signals were unshielded were the backshells and contacts of the cable connectors, and inside the EIUs.

Smart Actuator Frequency Response. The frequency response of two smart actuator EIUs was evaluated by sinusoidal perturbation of the actuator position demand. This was done at a steady-state engine operating point with FADEC control laws disabled to prevent these control laws from counteracting the perturbations of position demand. The tests were performed on two EIUs with different position control algorithms: a proportional controller and a proportional plus integral (PI) controller. Frequency responses of the actuators were analyzed to produce Bode plots of gain and phase shift of the actuators versus frequency of the input perturbation. The bandwidth of the proportional control actuator decreased from 23 rad/sec for a reference model to 18 rad/sec for the DCS actuator. For the PI control actuator, which was underdamped, bandwidth increased from 25 to 30 rad/sec. For both actuators, the phase shift of the DCS actuator was larger than the reference model. At 10 rad/sec, the phase shift of the proportional control EIU increased from -5 to -7 degrees, while for the PI control, phase shift increased from -37 to -58 degrees. These changes in frequency response are ascribed to the communication delay, τ_d, which is primarily due to the lack of synchronization between production of the position demand and actual transmission under BA control.

System Frequency Response. The frequency response of the DCS system was evaluated by applying sinusoidal variations in power-lever angle command, and examining thrust of the engine simulation as a function of frequency of the input perturbation. Bandwidth of the DCS was about 9.6 rad/sec, versus 9.7 rad/sec for the conventional control system, and phase shift was unchanged between the conventional control system and the DCS. Thus, even with measurable changes in smart actuator frequency response, the response of the overall DCS did not change significantly.

Conclusions

Power Supply Issues. Using the 100 kHz power supplies, 100 kHz noise was visible on the data bus, although interference was not apparently a problem. The primary approach to alleviating this noise should be to improve the shielding of the EAN power bus from the EAN digital communication data bus. Efforts in this area should center around reducing the susceptibility of the communication bus to radiated noise generated by the power input, such as improved shielding in connector backshells, in the connector pins, and inside the EIUs. Lowering the frequency of the AC power source and changing the waveform of the AC power from a near-square wave to a sine wave would reduce the radiated emissions. However, use of a lower frequency would require larger transformers for comparable power supply efficiency, and both changes would require larger filter capacitors for comparable output voltage ripple. Thus, a change in frequency or waveform should be made only if power bus interference with the data bus cannot be resolved with shielding.

Power supplies in the EIUs for this program used half-wave rectification of the secondary outputs of the power transformer. The result was that all of the devices drew power from the same half cycle of power on the data bus, resulting in asymmetric loading of the two half cycles. Future designs should use full-wave rectification to balance power usage between the half cycles of the AC power.

Data Bus Issues. The most serious issue with the data protocol chosen, the WorldFIP Fieldbus, was the basic architecture of the bus in which a bus arbitrator schedules data transmissions on the bus, and runs asynchronously with sampling of the sensors and use or production of the data by the engine control. This results in a substantially larger transport delay than would be required with a synchronous data transmission. A protocol such as MIL-STD-1553, in which transmission occurs under processor control, would eliminate this issue.

Another issue with the Fieldbus is the overhead associated with the protocol. In the Fieldbus protocol, a command-response exchange between the FADEC and a smart device has a minimum of 122 bits of overhead. In contrast, the MIL-STD-1553 protocol has about 35 bits of overhead. As a result of the increased overhead, the Fieldbus at 2.5 Mbps actually takes longer for a transaction than the MIL-STD-1553 at 1.0 Mbps (see Table 1). When the selection of Fieldbus was made in this program, it was believed that 5.0 Mbps Fieldbus would be available, but the higher speed parts have not materialized.

The software drivers provided with the WorldFIP products were not optimized for performance, therefore requiring excessive overhead when used in a real-time embedded control application. Optimization of the embedded software drivers would be required if this protocol continued in use for DCS.

The complexity of the Fieldbus protocol requires a large and complex communications co-processor (the FullFIP2 microcircuit) with its own private memory. This also resulted in an unacceptably long initialization process (about 500 msec) in which the code was loaded onto the FullFIP2 processor. The method for shortening the initialization time would be to add a private read-only memory for the FullFIP2, which would increase the size, cost and weight of an EIU.

Finally, there were some unexplained behaviors related to the Fieldbus. There was a high level of errors reported from the bus interface (typically, several errors per second). Generally these were handled automatically by the application software, but in some cases they did interfere with system operation. At one point, when investigating the source of these errors, an oscilloscope connected to the data bus appeared to show instances when two transmissions occurred on the data bus at the same time (these apparent dual transmissions were coincident with reported errors). No assistance could be obtained from the vendors of the Fieldbus interface to determine the cause of this problem, and no solution was found. While this may have been a result of some unknown inadequacy of the system cabling or configuration, it was a serious concern that could not be resolved.

A future program should investigate standard protocols for potential adoption and use in aerospace distributed control applications. A standard protocol would allow a common data link layer within the engine communication network. MIL-STD-1553 is strong candidate for use as a standard data bus, despite its relatively low data rate. This data bus has the advantages of low protocol overhead, simple implementation (two ICs), and widespread use within the aerospace industry. With a standard data packet definition, sensors and control components from various manufacturers would operate on the network without requiring a change in communication software design.

Future Efforts. It must remain the goal of future programs to develop Distributed Control Systems to the state where they will be ready for use on production engines. The following are a number of issues that remain to be addressed:

- Development of reliable and affordable high temperature electronics and packaging.
- Development of compact and rugged, flight-weight, engine-mountable packaging for EIUs.
- Development and selection of industry-standard communication data bus and power bus standards that can be implemented with available high temperature electronics, and have the data rate and attributes needed for future distributed engine controls.
- Demonstration that the projected cost and weight savings can be achieved via a distributed control system.
- Demonstration that the projected life-cycle cost savings and maintainability improvements can be achieved via a distributed control system.

While the challenges remain substantial, we believe that the rewards of distributed control systems for turbine engines make the effort to meet these challenges worthwhile.

Acknowledgments

This program was carried out by a team under US Air Force contract F33615-92-C-2220. Kenneth J. Roth developed the specifications for the Electronic Interface Units and the 100 kHz power supply, and coordinated their design and fabrication. AlliedSignal Aerospace Equipment Systems performed the detailed design of the EIUs at their expense, and carried out fabrication and design assurance testing of the EIUs. Lockheed Martin Control Systems conducted a preliminary design trade study on a partially distributed system. Honeywell Solid State Electronics Center supplied data on high temperature electronics on a no-cost basis. The GE custom data bus protocol for engine control applications was developed by General Electric Corporate Research & Development under an internally funded program.

References

Cegelec, 1994, "FullFIP2 Component User Reference Manual," 1st Issue, DPS 50262 a-en, Clamart, France.

ISA, 1992, "Fieldbus Standard for Use in Industrial Control System—Part 2: Physical Layer Specification and Service Definition," Instrument Society of America ISA-S50.02-1992, Research Triangle Park, NC.

UTE, 1990, "FIP bus for exchange of information between transmitters, actuators and programmable controllers, Data Link Layer," Union Technique de l'Electricité NF-C46-603, Courbevoie, France.

N. Kizuka

K. Sagae

S. Anzai

S. Marushima

T. Ikeguchi

K. Kawaike

Power Industrial Systems,
R&D Division,
Hitachi Ltd.,
832-2 Horiguchi,
Hitachinaka-shi Ibaraki-ken,
312-0034, Japan

Conceptual Design of the Cooling System for 1700°C-Class, Hydrogen-Fueled Combustion Gas Turbines

The effects of three types of cooling systems on the calculated operating performances of a hydrogen-fueled thermal power plant with a 1,700°C-class gas turbine were studied with the goal of attaining a thermal efficiency of greater than 60 percent. The combination of a closed-circuit water cooling system for the nozzle blades and a steam cooling system for the rotor blades was found to be the most efficient, since it eliminated the penalties of a conventional open-circuit cooling system which ejects coolant into the main hot gas stream. Based on the results, the water cooled, first-stage nozzle blade and the steam cooled first-stage rotor blade were designed. The former features array of circular cooling holes close to the surface and uses a copper alloy taking advantage of recent coating technologies such as thermal barrier coatings (TBCs) and metal coatings to decrease the temperature and protect the blade core material. The later has cooling by serpentine cooling passages with V-shaped staggered turbulence promoter ribs which intensify the internal cooling.

Introduction

Energy consumption continues to rise with industrial growth, though it has been a long time since the conservation of natural energy resources was first advocated. Environmental pollution, caused by industrial development, has become serious worldwide. To mitigate these energy and environmental problems, the Japanese government has instituted the International Clean Energy Network Using Hydrogen Conversion (WE-NET) Program, a 28 year effort from 1993 to 2020. The studies have been administrated through the New Energy and Industrial Technology Development Organization (NEDO) as a part of the WE-NET program with funding from the Agency of Industrial Science and Technology (AIST) in Ministry of International Trade and Industry (MITI) of Japan. This research and development work in above-mentioned program has been directly entrusted by the Japan Power Engineering and Inspection Corporation (JAPEIC).

The final objective is to achieve an ecologically clean and an efficient hydrogen fueled, energy-conversion system. The combustion of pure hydrogen with pure oxygen produces only steam; it does not emit CO_2, NOx, or SOx. The goal is achieving a thermal plant with an efficiency of greater than 60 percent high heating value (HHV) or 71 percent low heating value (LHV) at a turbine inlet temperature of 1,700°C, to compensate energy losses that occur during production, transportation, and storage of valuable hydrogen. Hitachi is taking part in research and development program to develop an effective cooling system for hydrogen fueled, combustion gas turbines. The performance of such a high temperature turbine depends greatly on the coolant consumption; therefore, the keys to an effective cooling scheme for turbine blades includes a cooling system, the selection of coolant, and a cooling circuit.

It has been indicated that closed-circuit cooling systems for a current Brayton cycle gas turbine are effective to achieve higher thermal efficiencies by suppressing compressor work used to supply coolant to blades, dilution of the hot gas temperature with the coolant, aerodynamic mixing loss, and rotor blade pumping loss and by effective recovery of heat exchanged coolant (Kawaike et al., 1984; Alderson et al., 1987; Ikeguchi et al., 1994). Thus, the authors intended to apply the same methodology, the closed-circuit cooling systems, to a hydrogen-fueled thermal power plant.

In addition, water cooling was considered for the stationary nozzle blades, which is superior to steam cooling as a cooling medium. As for the moving rotor blades, closed-circuit internal steam cooling was chosen to avoid the expectable problems such as water leakage and difficulty in recovering water through the turbine rotor. The idea of water cooling was tried and tested for both nozzle and rotor blades featuring a composite material construction under high temperature turbine technology (HTTT) program (Geiling et al., 1983), though water cooled gas turbines have not been in practical use until now.

This paper will firstly discuss the studied effect of the cooling system on a plant performance based on the H_2/O_2 fired high temperature steam cycle (HTSC) (Jericha et al., 1991). Following the result that the closed-circuit cooling system was essential to achieve a targeted thermal efficiency of 60 percent HHV, the conceptually designed cooling circuit and the cooled first-stage nozzle and rotor blades will be presented. Attention is paid not only to enhance cooling but also to reduce large thermal gradients across the blade materials by taking advantage of recent coating technologies.

Effect of Cooling System

The HTSC, shown in Fig. 1, has two closed cycles: the topping and bottoming cycles. The former consists of a compressor, combustor, intermediate pressure (IP) turbine, steam cooler 1, and steam cooler 2. The later consists of low pressure (LP) turbine, condenser, preheater, high pressure (HP) turbine, combustor, and IP turbine. The combination of the compressor, combustor and twin-shaft IP turbine corresponds to a topping cycle gas turbine. The twin-shaft IP turbine has intermediate high pressure (IHP) and intermediate low pressure (ILP) turbines.

Contributed by the International Gas Turbine Institute and presented at the International Gas Turbine and Aeroengine Congress and Exhibition, Stockholm, Sweden, June 2–5, 1998. Manuscript received by the ASME Headquarters April 1, 1998. Paper No. 98-GT-345. Associate Technical Editor: R. Kielb.

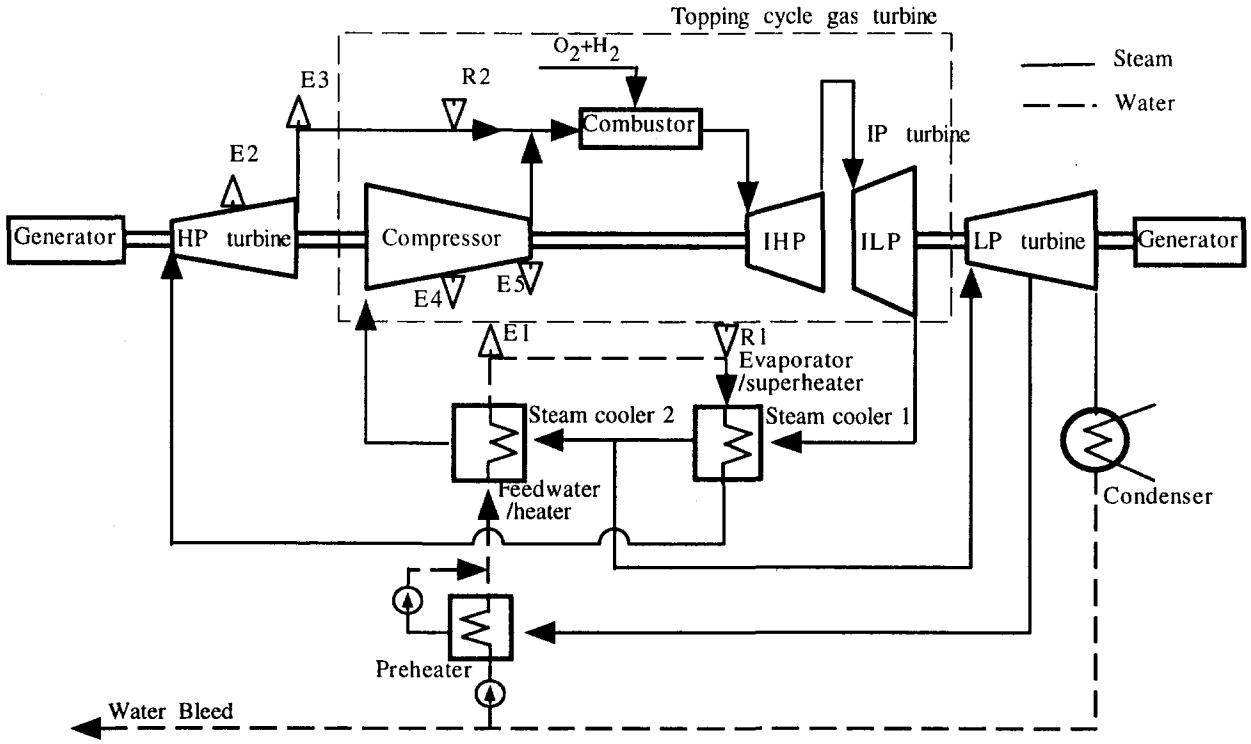

Fig. 1 Components of HTSC plant

The main component parameters used to analyze the cycle performance are shown in Table 1. The key points to achieve a high efficiency are to increase the outlet temperature of the IP turbine to generate more steam in the bottoming cycle and to increase the inlet temperature of the LP turbine to obtain more power. To meet them and cope with the high temperature of the IP turbine inlet, three types of cooling systems were selected and their effects were investigated. The three are as follows: (1) closed-circuit water cooling system for nozzle blades and steam cooling system for rotor blades (CCWCN-SCR); (2) closed-circuit steam cooling system for nozzle and rotor blades (CCSCN-R); and (3) open-circuit steam cooling system for nozzle and rotor blades (OCSCN-R).

In this analysis inlet gas flow of the IP turbine was fixed constant to achieve a plant power output of about 500 MW, and inlet and outlet pressures of HP and LP turbines were also kept constant. In each cooling system, coolants are supplied from and recovered at the points of the cycle as shown in Fig. 1 and Table 2.

Table 1 Main component parameters

IP Turbine (Topping Cycle Gas Turbine)		
Compressor		
Inlet pressure	(MPa)	0.14
Inlet temperature	(℃)	114
Outlet pressure	(MPa)	4.90
Rotational speed	(rpm)	6,500
Combustor		
Fuel		$H_2 + O_2$
Outlet temperature	(℃)	1,700
Turbine		
Stage		2(IHP)+6(ILP)
Rotational speed	(rpm)	6,500(IHP), 3,000(ILP)
Inlet gas flow	(kg/s)	222.3
Outlet pressure	(MPa)	0.16
Bottoming Cycle		
HP Turbine		
Inlet pressure	(MPa)	19.00
Outlet pressure	(MPa)	5.00
LP Turbine		
Inlet pressure	(MPa)	0.15
Outlet pressure	(MPa)	0.05

1 CCWCN-SCR System. Nozzle blades are cooled with 100°C water supplied from the feedwater heater (E1). After cooling, the heat exchanged water is returned to the evaporator/superheater (R1) and part of it is supplied to the attemperator to cool steam for cooling the rotor blades. Rotor blades are cooled with steam that is extracted from the middle stage of the HP turbine (E2) and cooled in the attemperator to 300°C. After cooling, the heat exchanged steam is returned to the combustor inlet (R2). The thermal energy gained by closed-circuit cooling is recovered at the evaporator and combustor. Interstage sealing steam for the IHP turbine is extracted from the compressor outlet (E5), while more interstage sealing steam for the ILP turbine is extracted from the middle stage of the compressor (E4). Interstage sealing steam for both the IHP and ILP turbines is finally ejected into the main stream gas.

2 CCSCN-R System. Nozzle and rotor blades are cooled with steam that is extracted from the middle stage of the HP turbine (E2) and cooled by the attemperator to 300°C. After cooling, the heat exchanged steam is returned to the combustor inlet (R2). The thermal energy gained by closed-circuit cooling is recovered at the combustor. Interstage sealing steam for the IP turbine is extracted as well as that of system (1) and finally ejected into the main stream gas.

3 CCSCN-R System. Nozzle and rotor blades are cooled with steam that is extracted from the middle stage of the HP turbine (E2) and cooled by the attemperator to 300°C. After

Table 2 Supply and recovery points of coolants

Cooling System	Blade	Supply		Recovery		System
(1) Closed-circuit water for nozzle blades and steam cooling system for rotor blades (CCWCN-SCR)	Nozzle	Feedwater /heater	E1	Evaporator /superheater	R1	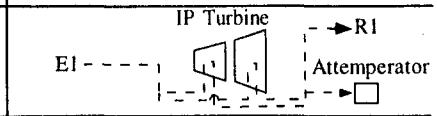
	Rotor	HP Turbine Middle Stage	E2	Combustor Inlet	R2	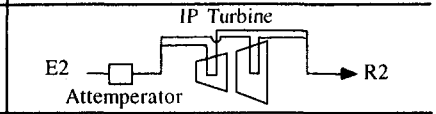
(2) Closed-circuit steam cooling system for nozzle and rotor blades (CCSCN-R)	Nozzle & Rotor	HP Turbine Middle Stage	E2	Combustor Inlet	R2	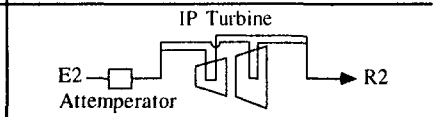
(3) Open-circuit steam cooling system for nozzle and rotor blades (OCSCN-R)	Nozzle	HP Turbine Outlet Compressor Middle Stage	E3 E4	———	—	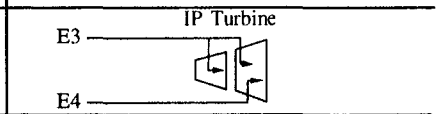
	Rotor	HP Turbine Outlet	E3	———	—	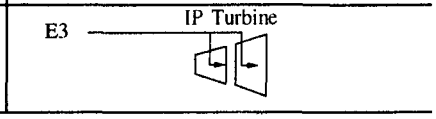

cooling, the heat exchanged steam is returned to the combustor inlet (R2). The thermal energy gained by closed-circuit cooling is recovered at the combustor. Interstage sealing steam for the IP turbine is extracted as well as that of system (1) and finally ejected into the main stream gas.

3 OCSCN-R System. Cooling and interstage sealing steam of 385°C is extracted from the HP turbine outlet (E3) for all blades of the IHP turbine, and the fore two stage nozzle and all rotor blades of the ILP turbine. More cooling and sealing steam of 362°C is extracted from the middle stage of the compressor for the rest of the nozzle blades of the ILP turbine. The spent steam is finally discharged into the main stream gas.

Evaluation. The analyzed cycle performance results based on cooling systems (1), (2), and (3) are shown in Table 3 in comparison with the performance of a no cooling system as an ideal case. System (1) was found to be the most efficient. The relative decreases in the plant efficiencies between the no cooling system and systems (1) and (2) were 2.0 percent and 4.2 percent. However the efficiency of system (3) decreased by 10.4 percent despite its total cooling steam flow ratio being almost the same as that of system (1) and two-thirds of that of system (2). This was because system (3) had an open-circuit cooling steam flow ratio of 27.9 percent, which was about five times as much as the values of systems (1) and (2), and this decreased the outlet temperature of the IP turbine to 673°C about 130°C lower than in systems (1) and (2), caused by dilution of main stream gas with the coolant. The decrease in the IP turbine outlet temperature reduced the amount of steam generated in the bottoming cycle, in other words the amount of steam returned to the LP turbine inlet decreased and the amount of steam returned to the compressor inlet increased instead, so that the compressor work increased and the efficiency decreased. However, the decrease in the IP turbine outlet temperatures of systems (1) and (2) were held within 70°C, so the high efficiencies were obtained. This means that open-circuit cooling system is not effective for the HTSC.

Comparison of systems (2) to (1) showed that system (2) required the amount of closed-circuit cooling steam which was twice as much as that of system (1) from the middle stage of the HP turbine and double the amount of spent steam was returned to the combustor inlet. That decreased the HP turbine output by 9.0 MW and increased the compressor work by 4.1 MW. However, in system (1) the cooling water was returned to the evaporator/superheater (R1) and supplied to the HP turbine inlet, so it could achieve performances closer to those of the ideal no cooling system. Therefore, system (1) had an efficiency of 60.1 percent, which were closer to 61.3 percent of the no cooling system, meeting the target.

Table 3 Performance results

Cooling System		No Cooling (base)	(1) CCWCN -SCR	(2) CCSC N-R	(3) OCSC N-R
Plant efficiency	(HHV%)	61.3	60.1	58.7	54.9
Plant output	(MW)	497	513	508	458
IP turbine output	(MW)	488	485	488	509
HP turbine output	(MW)	43.2	44.0	35.0	35.6
LP turbine output	(MW)	78.3	77.2	82.1	73.2
Compressor work	(MW)	99.0	78.9	83.0	147
Mechanical loss	(MW)	13.6	14.3	13.7	12.7
Open-circuit cooling steam flow ratio	(%)	-	5.5	5.7	27.9
Closed-circuit cooling steam flow ratio	(%)	-	19.7	40.8	-
Total cooling steam flow ratio	(%)	-	26.2	46.5	27.9
IP turbine outlet temperature	(℃)	866	798	806	673

Cooling Circuit of Gas Turbine

The gas path and cooling circuits of the compressor, combustor, and IP turbine based on cooling system (1) were conceptually designed as shown in Fig. 2. The HP turbine, compressor and IHP turbine are operated at the rotational speed of 6500 rpm and the ILP and LP turbines are operated at 3000 rpm. The compressor has 20 stages with a 4.90 to 0.14 pressure ratio and the axial length is approximately 1800 mm. The axial length of the IP turbine is approximately 3300 mm which includes the shaft bearing space from which cooling steam is supplied between the second and third stages.

Water for cooling the nozzle blades is externally supplied from the bottoming cycle through the outer casing and the heat exchanged water is returned to the bottoming cycle. Steam for cooling rotor blades of the IHP turbine is externally supplied from the bottoming cycle into the rotor shaft end through the

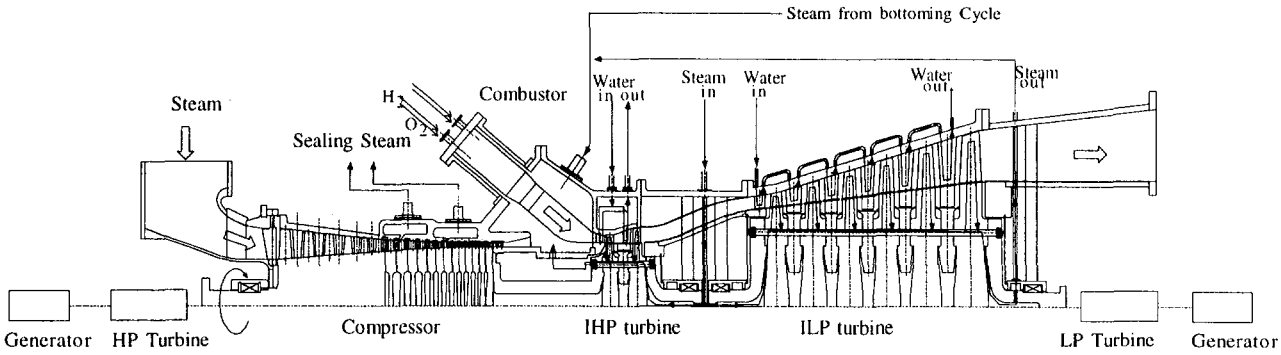

Fig. 2 Schematic view of gas path and cooling circuits of gas turbine

outer casing and it flows through the inner paths of the rotor disks to each rotor blade. After cooling the blades the heat exchanged steam returns to another inner paths of the rotor disks until it finally reaches the combustor inlet. More steam for cooling rotor blades of the ILP turbine is externally supplied into the rotor shaft end as well. After cooling the blades the heat exchanged steam is collected to the other rotor shaft end and returned to the casing outside. The steam is finally combined with discharged steam from the bottoming cycle in the combustor inlet.

Design of Cooled Blades

The cooling configuration of the water cooled first-stage nozzle and the steam cooled first-stage rotor blade needed to apply closed-circuit cooling system (1) were designed.

Nozzle Blade. The cooling design concepts for the first-stage nozzle blade (Fig. 3) were (1) having a blunt leading edge to reduce the thermal load at the leading edge region; (2) applying a copper alloy, whose thermal conductivity is about 15 times greater than that of conventional nickel base alloys, to reduce the metal temperature and thermal stress; (3) allocating many circular cooling holes as close to the blade surface as possible to keep the temperature below the allowable temperature of copper alloy of about 400°C; (4) having water cooling of outer and inner endwalls by drilled cooling passages; and (5) having a thermal barrier coating (TBC) to reduce the thermal load and protect the metal surface.

Before designing the cooled blade, the following three copper alloys were selected for the blade core material with respect to high allowable temperature and toughness: (1) copper alloy containing Cr and Zr (CZ-Cu); (2) copper alloy containing Ni, Si, and Zr (NSZ-Cu); and (3) oxide dispersion strengthened copper (ODS-Cu).

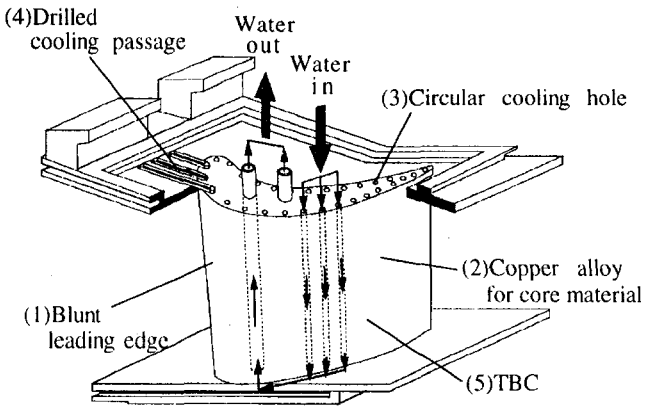

Fig. 3 The first-stage nozzle blade design concepts

The examined mechanical properties of CZ-Cu, NSZ-Cu, and ODS-Cu at 300°C are shown in Table 4. The thermal conductivity of NSZ-Cu was about 30 percent lower than that of CZ-Cu and ODS-Cu, while ODS-Cu was inferior to CZ-Cu and NSZ-Cu in 0.2 percent yield and tensile strength. Therefore, CZ-Cu was chosen for the water cooled first-stage nozzle blade.

The tensile and 0.2 percent yield strength of CZ-Cu are compared with those of a typical cobalt base alloy, which has been used for nozzle blades, in Fig. 4. It was found that CZ-Cu had the appropriate strength as well as the cobalt base alloy as long as it was used under 400°C. As regards low cycle fatigue, detailed research is necessary, because any cracks are not allowed for water cooled nozzle blades.

Thermal stresses of three combinations of copper alloy and coatings were compared by analyzing the two-dimensional heat conduction model (Fig. 5). The three were (a) the copper alloy with no coating, (b) the copper alloy coated with Inconel[1] 600 alloy (IN-600), and (c) the copper alloy coated with a TBC.

As regards case (b), IN-600 was applied mainly because of corrosion resistance and partly because of thermal barrier effect. As regards case (c), a TBC was used to decrease the temperature of the copper alloy because of its lower thermal conductivity compared with metal. The total thicknesses of the TBC including its bond layer of 0.1 mm and IN-600 were 0.3 mm.

Design conditions were determined taking the thermally hardest section of the blade into account. Two kinds of coolant heat transfer rates were assumed to keep the copper alloy below the allowable temperature of 400°C as shown in Fig. 5. As to cases (a) and (b), the heat transfer rate of 72 kW/m^{2}K was required by using the coolant velocity of 10 m/s above the usual maximum usage of 6 m/s, while as to case (c), the heat transfer rate of 48 kW/m^{2}K provided by the velocity of 6 m/s was sufficient. The allowable limit of thermal stress was assumed at 360 MPa, which was the tensile strength at 400°C. The model had a symmetrical shape, so only one side was solved. Thermal deformation along the Y-direction with boundaries A and B staying parallel to each other was assumed to be free. The temperature and thermal stress distributions along the X-direction are shown in Fig. 6. The maximum temperature of the copper alloy of cases (a), (b), and (c) were 393, 353, and

[1] Trademark of Inco Alloys International, Inc.

Table 4 Mechanical properties of copper alloys at 300°C

		CZ-Cu	NSZ-Cu	ODS-Cu
Thermal conductivity	(W/mK)	331	246	332
0.2% yield strength	(MPa)	375	379	255
Tensile strength	(MPa)	395	422	267
1000h creep rupture strength	(MPa)	333	127	69

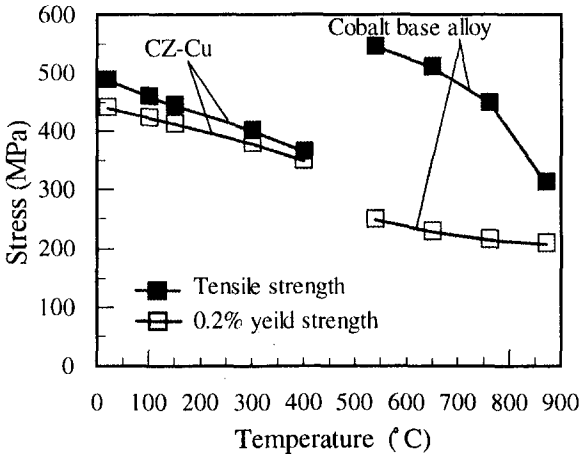

Fig. 4 Comparison of tensile and 0.2 percent yield strength

244°C, respectively. The maximum thermal stresses of the copper alloy of cases (a), (b), and (c) were 340, 250, and 124 MPa, respectively. Case (a) has no margin. Coatings are thought to be necessary not only to decrease the temperature and to reduce the thermal stress but also to protect surface of the copper alloy from corrosion. Comparison of cases (b) to (c) indicates that (b) requires the greater coolant velocity to achieve the greater coolant heat transfer to meet the design limit due to the weaker thermal barrier effect of the IN-600, while case (c) mostly depends on the thermal barrier effect of the TBC. Although both thermal gradients of the coating of cases (b) and (c) are greater than current level, it should be noted that the allowable strength of the TBC is much less than that of the IN-600. With respect to toughness and durability of the coating, case (b) is thought to be probable; however, the required coolant velocity is high. In this case water erosion problem is necessary to be examined, or use of another metal coating that has lower heat conductivity is conceivable to reduce the velocity. On the other hand, with respect to the thermal barrier effect, case (c) is thought to be probable; however, the reliability and durability of the coating are currently low. The verification tests are needed under such thermal load conditions and they are underway.

The design conditions for the nozzle blade are shown in Table 5. The peak temperature distribution factor at the inlet of the first-stage nozzle blade was assumed to be 10 percent. Since CZ-Cu has an allowable temperature of 400°C, the cooling effectiveness of 83 percent was required. The cooling effectiveness is defined as

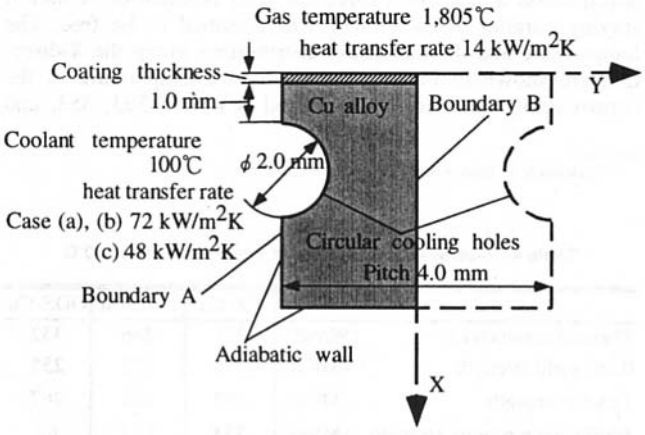

Fig. 5 Two-dimensional heat conduction model

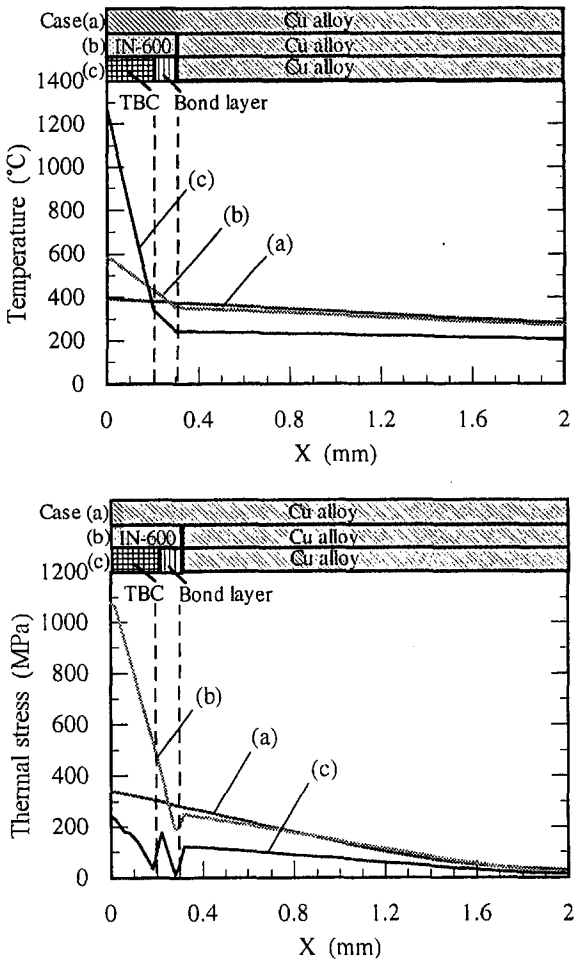

Fig. 6 Temperature and thermal stress distributions

$$\text{Cooling effectiveness} = \frac{\text{gas temp.} - \text{blade metal temp.}}{\text{gas temp.} - \text{coolant supply temp.}}$$

Figure 7 shows the calculated temperature distribution of the blade mean section. The water cooled nozzle blade designed here had a two layers TBC with a total thickness of 0.3 mm. It had a one circuit, 62-passage multihole cooling design. The diameter of the circular holes and the pitch were 2.0 and 4.0 mm, respectively.

Although the trailing edge section had to be cooled by only an array of cooling holes, the maximum temperature was 313°C, meeting the allowable limit. The surface average cooling effectiveness of 91 percent was obtained at the cooling flow ratio of 16.3 percent. The heat flux passing through the TBC was about 7.4 MW/m^2.

Table 5 Design conditions of nozzle blade

Blade inlet average total temperature	(°C)	1,700
inlet peak total temperature	(°C)	1,805
inlet total pressure	(MPa)	4.66
exit static pressure	(MPa)	3.65
Cooling water inlet temperature	(°C)	100
inlet pressure	(MPa)	9.81
outlet pressure	(MPa)	8.83

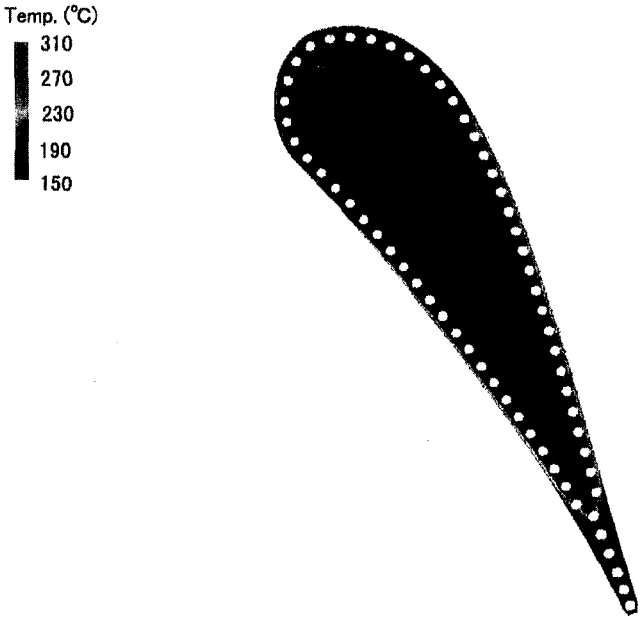

Fig. 7 Calculated temperature distribution

Rotor Blade. As mentioned, water cooling was thought to be difficult to be applied to the rotor blades which were moving parts, because of difficulties in recovering water, preventing leakage, and configuring complicated cooling paths in the rotor shaft, despite its superior thermal properties as a coolant. Thus, to achieve closed-circuit cooling with steam for the rotor blades, intensified internal cooling techniques were required.

The cooling design concepts for the first-stage rotor blade (Fig. 8) were (1) having a blunt leading edge to reduce thermal load at the leading edge region as well as the nozzle blade; (2) applying V-shaped staggered turbulence promoter ribs (Anzai et al., 1991; Kawaike et al., 1993) in the serpentine cooling passage to enhance internal heat transfer, (3) minimally allocating film cooling holes at only the leading edge region to achieve closed-circuit cooling as much as possible; and (4) having a TBC to reduce the thermal load and protect the metal surface.

As to turbulence promoter ribs, Table 6 summarizes some of the relevant studies on heat transfer enhancement. Among these studies, V-shaped staggered ribs have been the most efficient, though the experimental methods and conditions were different.

Figure 9 shows the comparison of heat transfer and pressure loss characteristics of typical turbulence promoter ribs conducted by the authors using the same experimental apparatus and measuring method. The heat transfer rate of V-shaped staggered ribs (angle = 20 deg, pitch/rib height = 5) improved 2.4 times greater than that of transverse ribs and 1.7 times greater than that of angled ribs without much increase of pressure loss.

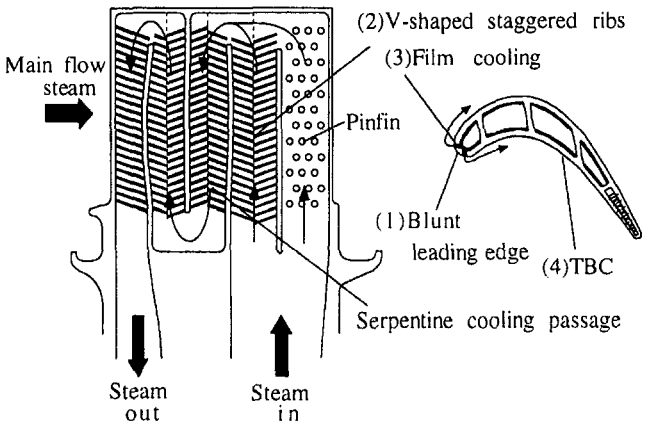

Fig. 8 The first-stage rotor blade design concepts

Table 6 Summary of relevant studies on heat transfer enhancement of turbulence promoter ribs

f : Pressure loss coefficient, Nu : Nusselt number
P/e : Pitch / Rib height, Re : Reynolds number
α : rib angle, suffix s : smooth duct

Rib configuration	Author(s)	Rib parameters Shape, α, P/e	Nu/Nus	f/fs	Nu/Nus / $(f/f_s)^{1/3}$
Transverse ribs	Han et al., 1985	, 90°, 10	2.1 - 2.5	5.8 - 6.8	1.2 - 1.3
	Kukreja et al., 1991		2.4 - 2.6	4.8 - 6.5	1.4
	Anzai et al. 1991		2.4 - 2.7	4.9 - 6.0	1.4 - 1.5
	Taslim et al., 1994		2.2 - 2.4	10 - 13	1.0
Angled rib	Han et al., 1985	, 75°, 10	3.3	5.3 - 9.5	1.6 - 1.9
		, 60°, 10	2.5 - 3.2	7.2 - 10	1.4 - 1.5
		, 45°, 10	2.9-3.0	4.3 - 6.4	1.6 - 1.7
	Anzai et al., 1991	, 70°, 10	3.2 - 3.5	6.5 - 8.5	1.7
	Taslim et al., 1994	, 45°, 10	3.1 - 3.8	11 - 14	1.4 - 1.6
V/Λ shaped ribs	Han et al., 1985	V, 60°, 10	2.8 - 3.6	8.0 - 11	1.4 - 1.6
		V, 45°, 10	2.5 - 3.3	8.0 - 10	1.3 - 1.5
		Λ, 60°, 10	2.4 - 3.3	8.5 - 13	1.2 - 1.4
		Λ, 45°, 10	2.3 - 3.0	8.0 - 11	1.2 - 1.4
	Anzai et al., 1991	V, 70°, 10	2.7 - 4.3	8.0 - 11	1.4 - 1.9
		Λ, 70°, 10	2.7 - 3.9	8.0 - 9.3	1.4 - 1.9
	Taslim et al., 1994	V, 45°, 10	2.9 - 3.3	13 - 17	1.7
Transverse staggered ribs	Kukreja et al., 1991	(a) 90°, 10	3.4 - 3.8	7.5 - 11	1.7
		90°, 20	2.6 - 2.8	4.0 - 6.5	1.5 - 1.6
		(b) 90°, 20	3.3 - 3.5	6.5 - 10	1.5 - 1.8
		90°, 20	1.3 - 1.6	4.0 - 6.0	1.3 - 1.5
		(c) 90°, 20	3.0 - 3.2	5.1 - 6.5	1.4 - 1.8
	Anzai et al., 1991	(a) 90°, 5	4.6 - 5.8	18 - 19	1.8 - 2.2
		90°, 10	3.2 - 3.9	6.5 - 10	1.7 - 1.8
V/Λ staggered ribs	Anzai et al., 1991	V, 70°, 5	5.9 - 6.6	10 - 13	2.7 - 2.8
		V, 70°, 10	3.0 - 5.0	10 - 11	1.4 - 2.2
		Λ, 70°, 5	3.5 - 4.1	7.4 - 8.0	1.8 - 2.1
		Λ, 70°, 10	2.5 - 3.1	5.0 - 6.0	1.5 - 1.7
	Taslim et al., 1994	Λ, 45°, 10	2.7 - 3.0	8.3 - 10	1.3 - 1.4

The design conditions for the rotor blade are shown in Table 7. The radial temperature distribution factor at the inlet of the first-stage rotor blade was assumed to be 6 percent. Single crystal (SC) alloy with an allowable temperature of 950°C was selected for the material and two layers TBC of the total thickness with 0.3 mm was applied. The cooling configurations (i.e., cooling passages) film cooling holes and turbulence promoter ribs were determined by using the integrated CAE system for a cooled turbine blade (Kawaike et al., 1992). The steam cooled rotor blade had a one circuit, five-passage serpentine cooling design.

The thermal conditions and calculated temperature distributions of the blade mean section are shown in Figs. 10 and 11. The main stream gas of steam increased the heat transfer rate up to 16.5 kW/m^{2}K at the leading edge section (Fig. 10) and that required film cooling. The metal surface temperature was almost entirely kept within 950°C because of the intensified internal cooling at the total cooling flow ratio of 5.0 percent (Fig. 11). The open-circuit cooling flow ratio for the film cooling and closed-circuit cooling flow ratio were 2.3 percent and 2.7 percent, respectively. The surface average cooling effectiveness of 58.5 percent was obtained. However, the maximum TBC surface temperature reached 1350°C and the TBC had a

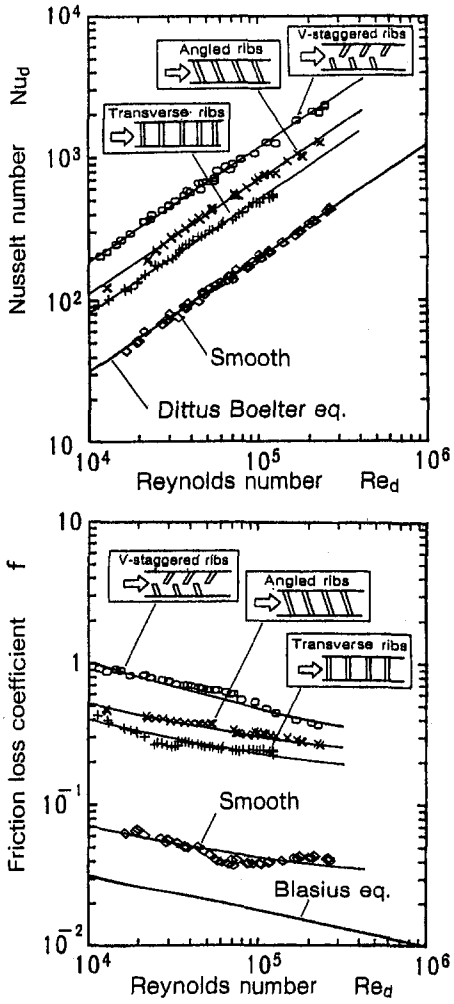

Fig. 9 Heat transfer and pressure loss characteristics

maximum thermal gradient of 400°C in 0.2 mm. The maximum heat flux passing through the TBC was 3.6 MW/m^2. These are about three times as much as current usage. Although this design entirely depends on the TBC severely requiring its reliability and durability and exceeds current level, the development of such coatings are thought to be within the scope in the near future.

Conclusion

The performances of a thermal plant having three different types of cooling systems for a 1,700°C-class, hydrogen-fueled combustion gas turbine were analyzed. The results indicated closed-circuit cooling systems were more effective for achieving high efficiencies than conventional open-circuit cooling systems. This was because the closed-circuit cooling systems can eliminate penalties of conventional open-circuit cooling systems

Table 7 Design conditions of rotor blade

Blade inlet average relative total temperature	(°C)	1,622
inlet peak relative total temperature	(°C)	1,699
inlet relative total pressure	(MPa)	3.69
exit static pressure	(MPa)	3.01
Cooling steam inlet temperature	(°C)	300
inlet pressure	(MPa)	5.88
outlet pressure	(MPa)	4.71

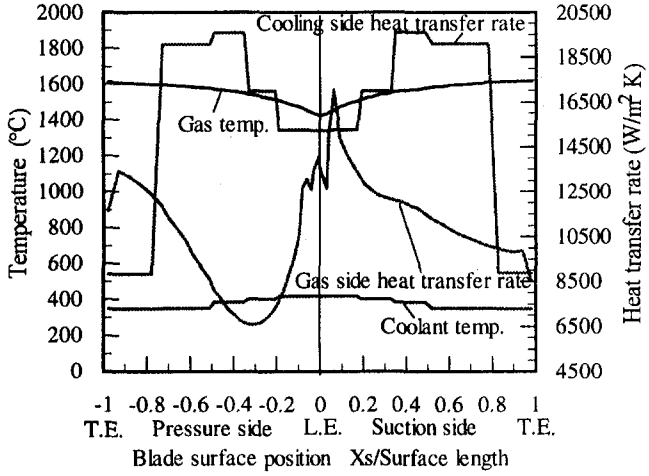

Fig. 10 Thermal conditions of rotor blade

such as dilution of main stream gas with the coolant, mixing loss, and pumping loss. Furthermore, it was found that the closed-circuit water cooling system for nozzle blades and steam cooling system for rotor blades (CCWCN-SCR) exceeded the closed-circuit steam cooling system for nozzle and rotor blades (CCSCN-R) in efficiency by reducing the consumption of cooling steam and an efficiency of 60 HHV percent was achievable.

The water cooled first-stage nozzle blade and the steam cooled first-stage rotor blade for the CCWCN-SCR were designed. The nozzle blade had a copper alloy for its core to reduce thermal stress and advanced coating technologies were used to protect its core material. The combination of CZ-Cu and a thermal barrier coating (TBC) was chosen with respect to its high thermal barrier effect. The multihole cooling design was found feasible for such high thermal-load conditions. However, as regards toughness and durability for other applications, combination of the copper alloy and a metal coating is also conceivable.

The rotor blade used a conventional nickel-base single crystal alloy with a TBC. The intensified internal serpentine cooling with V-shaped staggered turbulence promoter ribs also was found capable, only allowing film cooling at the leading edge part.

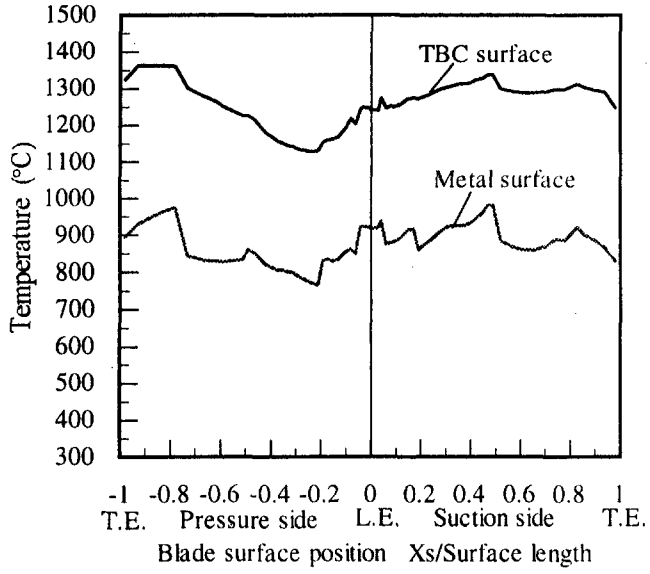

Fig. 11 Temperature distributions of rotor blade

Present blade cooling depends on coating technologies; therefore, reliable and durable coatings that can be operated under higher thermal load conditions are required.

Acknowledgments

The studies presented in this paper were administrated through the New Energy and Industrial Technology Development Organization (NEDO) as a part of the International Clean Energy Network Using Hydrogen Conversion (WE-NET) Program. The research and development work was directly entrusted by the Japan Power Engineering and Inspection Corporation (JAPEIC).

References

Alderson, E. D., Scheper, G. W., and Cohn, A., 1987, "Closed Circuit Steam Cooling in Gas Turbines," ASME Paper 87-JPGC-GT-1.

Anzai, S., Kawaike, K., Matsuzaki, H., and Takehara, I., 1991, "Effect of Turbulence Promoter Rib Shape on Heat Transfer and Pressure Loss Characteristics," *J. of the Gas Turbine Society of Japan,* Vol. 20, No. 75, pp. 65–73 (in Japanese).

Geiling, D. W., Klompas, N., and Zeman, K. P., 1983, "Water Cooled Gas Turbine Nozzle Technology Demonstration at Ultra-High Firing Temperature," ASME Paper 83-GT-15.

Han, J. C., Park, J. S., and Lei, C. K., 1985, "Heat Transfer Enhancement in Channels with Turbulence Promoters," ASME JOURNAL OF ENGINEERING FOR GAS TURBINE AND POWERS, Vol. 107, pp. 629–635.

Ikeguchi, T., and Kawaike, K., 1994, "Effect of Closed-Circuit Gas Turbine Cooling Systems on Combined Cycle Performance," ASME Paper 94-JPGC-GT-8.

Jericha, H., Starzer, O., and Theissing, M., 1991, "Towards a Solar-Hydrogen System," *ASME Cogen-Turbo,* IGTI-Vol. 6, pp. 435–442.

Kawaike, K., Kobayashi, N., and Ikeguchi, T., 1984, "Effects of New Blade Cooling System With Minimized Gas Temperature Dilution on Gas Turbine Performance," ASME JOURNAL OF ENGINEERING FOR GAS TURBINE AND POWER. Vol. 106, No. 4, pp. 756–764.

Kawaike, K., Anzai, S., and Sasada, T., 1992, "Integrated CAE System for Cooled Turbine Blade Design and Verification Tests of Analytical Codes," *Heat Transfer in Turbomachinery,* R. J. Goldstein, et al., Proceedings of International Symposium Heat Transfer in Turbomachinery, International Center for Heat and Mass Transfer, eds., Begell House, Inc., New York, pp. 73–84.

Kawaike, K., Anzai, S., Takehara, I., Sasada, T., and Matsuzaki, H., 1993, "Advanced Cooling Design of Turbine Blades With Serpentine Cooling Passages," CIMAC, G12.

Kukreja, R. T., Lau, S. C., and Mcmillin, R. D., 1991, "Effects of Length and Configuration of Transverse Discrete Ribs on Heat Transfer and Friction for Turbulent Flow in a Square Channel," *ASME/JSME Thermal Engineering Proceeding,* Vol. 3, pp. 213–218.

Taslim, M. E., Li, T., and Kercher, D. M., 1994, "Experimental Heat Transfer and Friction in Channels Roughened With Angled, V-Shaped and Discrete Ribs on Two Opposite Walls," ASME Paper 94-GT-163.

P. Mathieu
pmathieu@ulg.ac.be

R. Nihart

University of Liège,
Department of Nuclear Engineering
and Power Plants,
21, Rue Ernest Solvay,
B-4000, Liège,
Belgium

Zero-Emission MATIANT Cycle

In this paper, a novel technology based on the zero CO_2 emission MATIANT (contraction of the names of the two designers MAThieu and IANTovski) cycle is presented. This latter is basically a gas cycle and consists of a supercritical CO_2 Rankine-like cycle on top of regenerative CO_2 Brayton cycle. CO_2 is the working fluid and O_2 is the fuel oxidizer in the combustion chambers. The cycle uses the highest temperatures and pressures compatible with the most advanced materials in the steam and gas turbines. In addition, a reheat and a staged compression with intercooling are used. Therefore, the optimized cycle efficiency rises up to around 45 percent when operating on natural gas. A big asset of the system is its ability to remove the CO_2 produced in the combustion process in liquid state and at high pressure, making it ready for transportation, for reuse or for final storage. The assets of the cycle are mentioned. The technical issues for the predesign of a prototype plant are reviewed.

Introduction

Among many approaches to the CO_2 emissions mitigation extensively investigated in the scientific literature (Blok et al., 1992; Smith, 1993; Riemer et al., 1995) we propose here an original concept of zero-release of pollutants in the atmosphere as a competitor with systems using monoethanolamine scrubbing or membrane techniques and cutting the CO_2 releases by 80 to 90 percent. The removed CO_2 is then disposed of in proper sites, like in aquifers, in deep oceans or in depleted oil and gas fields. Of course, zero-emission is an ideal and desirable target and leakages are unavoidable. This is discussed here.

In this paper, the following two concepts are introduced:

1 The Stack Downwards. The common features to zero-emission cycles are the use of CO_2 as the working fluid and O_2 as the fuel oxidizer. In order not to release CO_2 in the atmosphere, we make a knot in the stack or better, we turn the power plant upside down (see Fig. 1) so the emissions are avoided and the combustion products are dealt with as effluents, possibly contaminated with NO_X, SO_X, particles, and toxics. The objective is to keep the effluents under total control. Such zero-emission cycles all require an air separation unit (ASU). (Iantovski et al., 1997a–c).

2 Grave-Into-The-Cradle. We take the fossil fuels from the bowels of the earth, we must send there back the products of their combustion. In the MATIANT concept, the removed CO_2 flow is liquid and at high pressure. We can consequently use it in separated from the extracted mixture CO_2/oil mixture, can be reinjected in the depleted well. Hence the waste (CO_2) in its final storage is replacing the fuel which produced it in the fuel site. So a closed fuel/CO_2 cycle is set up (see Fig. 1). This application is for where pressurized liquid CO_2 is required. It is, for example, the case in the oil extraction. CO_2 is used to increase the oil recovery efficiency. The higher the CO_2 injection pressure, the higher this efficiency. The oil well is then more depleted and the CO_2, has to be considered as a concept, the technical feasibility and the associated technical issue are the subject of a separate study.

Cycle Diagram and Layout of the Plant

The MATIANT gas cycle is shown on the T-S diagram in Fig. 2 and the layout of the corresponding plant is in Fig. 3 (Iantovski and Mathieu, 1996a, b; Iantovski et al., 1997a). It comprises a supercritical CO_2 Rankine-like cycle (2-3-4-5-6) combined with a regenerative CO_2 Brayton cycle with reheat (6-7-8-9-10-11-12-1-2).

The combustion takes place along the isobar 7-8. The fuel is injected at the proper pressure P_2 in the burners as well the mixture of the working fluid CO_2 and the O_2 at 7. At the exit, 8, of the combustion chamber (1300°C), the mixture CO_2/HO_2 is expanded along 8-9, and then reheated up to the temperature 10 in a second combustion chamber where other fractions of fuel and O_2 are injected at P_3. At 10, in stochiometric proportions, the fluid contains the combustion products, namely 8 percent CO_2 and 6 percent H_2O, in addition to the 100 percent CO_2 circulating along the total cycle. This fluid is expanded in 10-11. These two expanders produce electricity. The fluid is then cooled from 11 to 12 in a recuperator where it gives up its heat to CO_2 gas flows (2): first at the higher cycle pressure P_1, and then after expansion in 5-6 at the pressure P_2 of the combustion chamber. CO_2 is expanded along 5-6 in a steam-like turbine and generates electricity. As to O_2, its total throughput is 10 percent of the CO_2 mass flow rate whose around 7 percent is injected at 7 and another 3 percent is injected at 9 for the reheat process. It can be reheated from its temperature at the ASU outlet up to the temperature at the inlet of the burners 7 and 9 of the combustion chambers.

The gas generator is split into its two components: an expander with its associated turbogenerator, and the compressor driven by a motor.

At the recuperator outlet, the water is condensed in a cooler and extracted in a CO_2/H_2O separator. The remaining gas is then CO_2, and it is compressed in a three-stage compressor with intercooling along 1-2 up to the CO_2 saturation line in order to carry out a compression as close as possible to an isothermal process. Then CO_2 is condensed, and the liquid CO_2 at 3 (70.5 bar, 29°C) is easily compressed to a high pressure through a pump with a low energy consumption. At 4, the excess CO_2 (about 8 percent of the recirculated CO_2 mass flow rate) is removed in liquid state through a valve, without any energy consuming and costly system as it is the case in a CO_2 scrubber installed in the flue gas.

Basically, the effluents, possibly contaminated, remain under control. At this stage of the modeling, the cooling of the hot parts of the cycle is not included yet, but in this analysis, a cycle efficiency penalty of 2.5 percentage points to take it into account is adopted by similarity to an air GT (Bolland et al., 1992, 1993).

Of course, the fluid in the recuperator 11-12 contains small quantities of Ar and N_2 coming from the ASU and of O_2, not used in the combustion process because an excess of oxygen is necessary in practice to make the combustion complete. They

Contributed by the International Gas Turbine Institute and presented at the International Gas Turbine and Aeroengine Congress and Exhibition, Stockholm, Sweden, June 2–5, 1998. Manuscript received by the ASME Headquarters April 1, 1998. Paper No. 98-GT-383. Associate Technical Editor: R. Kielb.

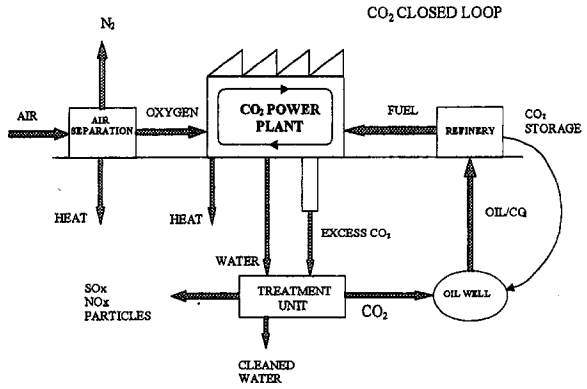

Fig. 1 Stack downwards and grave-into-the-cradle concepts

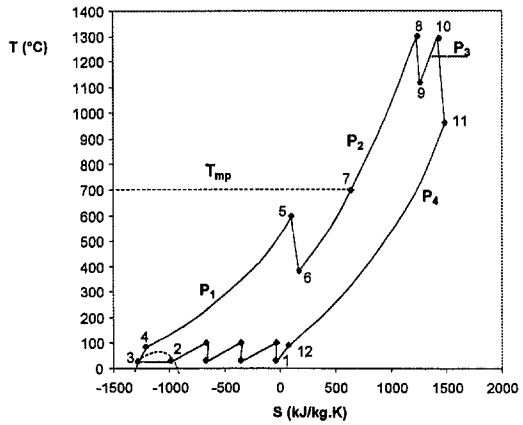

Fig. 2 Cycle representation in (T-S)

are present in the cycle and have an impact on the efficiency. However, the used ASU delivers O_2 at a purity of 99.5 percent with a specific electricity consumption of 0.28 kWh/Kg O_2 at 5 bar. Depending on the natural gas composition, the major part of the noncondensable gases are N_2 and argon. As their adiabatic exponent γ is much higher than that of CO_2, so is it for the resulting mixture. The compression asks then for more electricity than for pure CO_2, but more power is provided in the high temperature expanders 8-9 and 10-11. These gases are vented from the condenser at the lowest cycle pressure and temperature. Normally, they would take some CO_2 with them in the atmosphere. Also, with an oxygen purity of 99.5 percent, the amount of noncondensable gases should be very low (but of high commercial value, like argon). On the other hand, the pressure in the condenser could not be significantly affected by their presence. Figures about the effects of the inert gases will be given in a next step of this study. Another option to limit a possible CO_2 leakage is to avoid a condenser in the cycle and extract the noncondensable gases when the CO_2 is supercritical (point 4 in Fig. 2). Then, there is a small accumulation of noncondensable gases in the cycle, but, for instance, the accumulation of Ar in the cycle remains lower than about 1 percent of the total mass flow rate.

Design Point Calculation

Natural gas, not being pure methane, has its low heating value, in Europe anyway, around 42 MJ/kg. A mixture of about 84 percent of CH_4 and 16 percent of CO_2 (mass fractions) represents the LHV of this natural gas, and is used in the modelling.

In order to comply with the admissible mechanical stresses criteria for the advanced materials used here, the high pressure level is limited to 300 bar and the temperature of this high pressure gas flow at the recuperator outlet is limited to 600°C (point 5 in Fig. 2). The higher the pressure the lower this temperature limit.

Similarly, as the pressure P_2 is varied between 40 and 100 bar, the temperature T_{mp} at the recuperator outlet (point 7 in Fig. 2) has to be limited to 700°C, but should the materials withstand it, this latter could be further increased. Taking into account the thermal resistance of the materials and the limitation of the cooling techniques, the temperature inlet of the MP and LP expanders is limited to 1300°C as well.

Technical issues raised by the pressure and temperature levels are taken into account; the pressure P_2 is limited to 40 bar. The cycle efficiency is optimized with respect to the pressure P_3 and P_4. The calculations are carried out using the commercial ASPEN PLUS code.

Taking into account the previous constraints, the high pressure P_1 is equal to 300 bar, P_2 to 40 bar, and P_4 to 1 bar; the recuperator outlet and the LP and MP expanders inlet temperatures are 700 and 1300°C, respectively. The optimization process introduces a dependence of the maximization of the heat recovery in the system and of the temperature limitation at the recuperator outlet. The resulting P_3 is 9.3 bar, taking an isentropic effectiveness of 0.75 for the fuel compressors, the O_2 compressors and the CO_2 pump, 0.87 for the expanders, and 0.85 for the isentropic effectiveness of the CO_2 compressor (centrifugal compressor).

Typical values of the pressure losses in the heat exchangers are taken as 5 percent of the inlet pressure and 3 percent in the combustion chambers. Pressure losses in mixers, splitters, etc. are also taken into account. It is assumed that the cycle efficiency penalty due to the cooling of the hot parts of the system is equal to 2.5 percentage points in every case.

From the calculations it appears that the cycle efficiency can be increased by increasing P_2, but at the same time by adapting P_3 to comply with a limit of 700°C for T_{mp}. This is illustrated in Fig. 4.

For example, for P_2 = 70 bar, the efficiency is 43.3 percent; then, P_3 = 13.5 bar, namely, the value calculated to maximize the efficiency complying with the T_{mp} limit of 700°C. The results show that the cycle efficiency has a flat maximum with respect to P_3. Indeed, due to the fact that P_3 is limited by the T_{mp} constraint, the optimal efficiency is not very sensitive to P_3.

Here, we have to worry about the technical feasibility. When P_2 moves upwards, this means that the combustion takes place

Nomenclature

ASU = air separating unit
CC = combined cycle
GT = gas turbine
HP = high pressure (bar)
LHV = low heating value (MJ/kg)
LP = low pressure (bar)
MEA = monoethanol amine
MP = medium pressure (bar)
P_1 = high pressure cycle
P_2 = upper intermediate pressure (bar)
P_3 = lower intermediate pressure (bar)
P_4 = low pressure cycle
PC = pulverized coal
PFBC = pressurized fluidized bed combustor
TIT = turbine inlet temperature (°C)
T_{mp} = outlet recuperator temperature at upper intermediate pressure (°C)

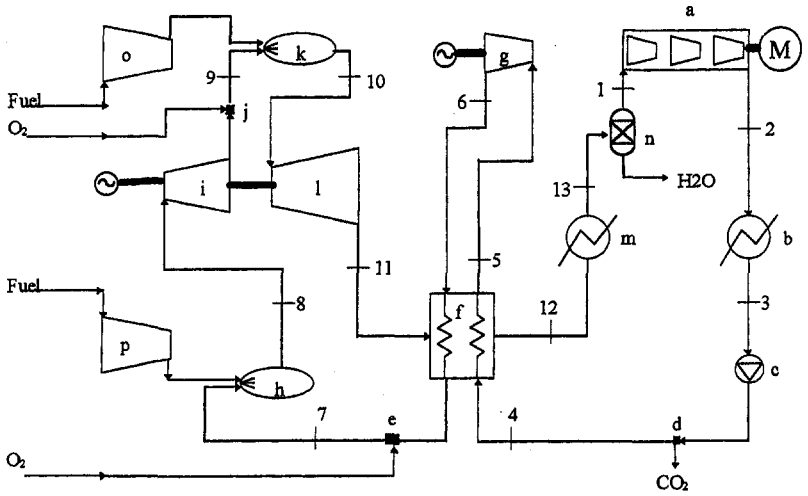

a : CO_2 compressor	b : condenser	c : CO_2 pump
d : splitter	e : mixer	f : recuperator
g : uncooled HP expander	h : combustion chamber 1	i : MP expander with internal cooling
j : mixer	k : combustion chamber 2	l : LP expander with internal cooling
m : cooler	n : water separator unit	o and p : fuel compressors

Fig. 3 Layout of the plant

at a high pressure and boilers operating at too high pressures could be unrealistic. On the other hand, due to the cooling requirements, P_2 is limited at the compressor outlet pressure (70 bar) if the cooling is made through CO_2 bleedings from the compressor.

In this modeling, the fuel is considered to feed the burners at ambient temperature (17°C) and at 3 bar. In reality, the delivery pressure of the natural gas depends on the network; in Europe in particular this pressure can be as high as 40 or 60 bar. Consequently, depending on P_2, the fuel compression can be low or even zero. If the combustion chamber is at a pressure lower than that of the network, a recovery in an expander can be considered. However, in this case a preheat of the fuel is required before its injection in the burners.

On the cold side, our calculations are made with a CO_2 condenser pressure of 70.5 bar—that is, a saturation temperature of 29°C. In very cold countries like Denmark, Norway, Sweden, and Finland, the heat sink (the ocean) is still more favorable.

For 1 kg/s of carbon dioxide recirculated, the fuel consumption is equal to 0.033 kg/s, the O_2 consumption is equal to 0.112 kg/s, and the mass flow rate of CO_2 removed from the cycle is 0.083 kg/s.

The net cycle efficiency is obtained by

$$\frac{W_{\text{production}} - W_{\text{consumption}}}{\dot{m}_{\text{fuel}} \cdot \text{LHV}_{\text{fuel}}} = 44.3 \text{ percent},$$

with $P_1 = 300$ bar, $P_2 = 40$ bar, $P_3 = 9.3$ bar, and $P_4 = 1$ bar when the cooling demand ($\Delta\eta$ cooling $= -2.5$ percentage points) and the ASU consumption are accounted for. This latter is taken from ASU manufacturers' data as 0.28 kWh/kg O_2 at a purity of 99.5 percent at 5 bar.

The compression of the gaseous O_2 at 5 bar up to the pressure of the second combustion chamber ($P_3 = 9.5$ bar) adds an electricity consumption of 0.03 kWh/kg O_2. So, taking into account the respective mass flows of oxygen at P_2 and P_3, the total consumption due to the production and the compression of the O_2 injected in the combustion chamber equals to 0.37 kWh/kg O_2.

The good value of the efficiency is not only due to high pressures and temperatures but also to the nonidealty of CO_2. This latter in the low temperature range (0–300°C) and at pressures around 60 bar near the CO_2 saturation line reduces the compressor consumption with respect to that of an ideal gas and nearly offsets the ASU consumption at the design point.

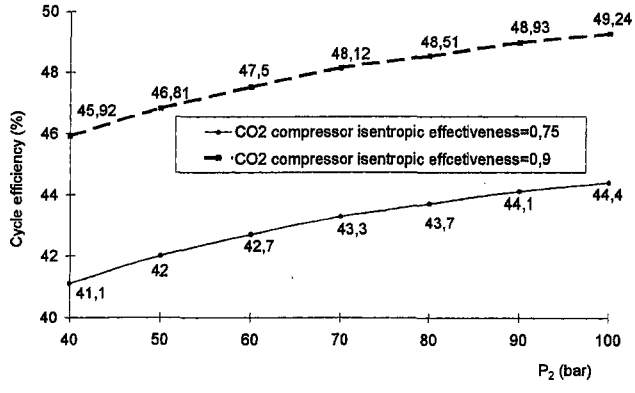

Fig. 4 Cycle efficiency versus upper intermediate pressure P_2 (P_3 is optimized at each point)

Technical Advantages

We have modeled CC plants (reference case) using CO_2 scrubbers for CO_2 removal from the flue gas without and with flue gas recirculation. CO_2 removal from the flue gas by an absorber/stripper system using MEA is considered currently as the state-of-the-art technology.

In addition to be very costly, this chemical plant installed at the exhaust of the plant leads to an efficiency penalty typically of the order of 6 to 8 percent points for a natural gas fuelled plant. As far as zero emission is concerned, we have studied CO_2 semiclosed CC cycles (Mathieu and Deruyck, 1993). We have shown that a CC with recirculation has better performance and lower cost for CO_2 scrubbing than a comparable semiclosed

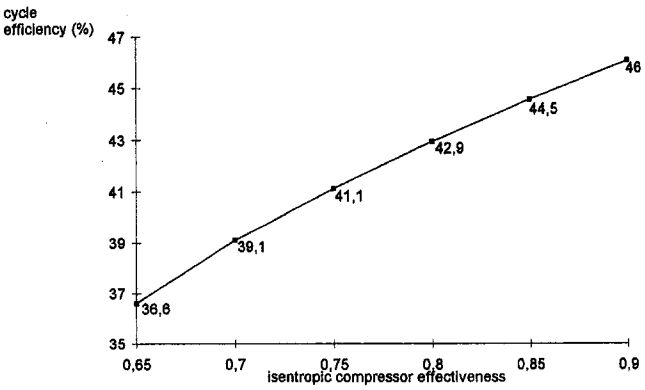

Fig. 5 Cycle efficiency according to three stages compressor effectiveness

CO_2 cycle of that type (Bolland and Mathieu, 1997). Here, we go a step further.

The assets of the MATIANT cycle: (1) good net cycle efficiency (between 40 and 45 percent when burning natural gas); (2) negligible release of pollutants in the atmosphere; (3) removal of a highly pressurized liquid CO_2 flow and possible reuse or final storage without further compression (it is the biggest asset); (4) no use of an industrial gas turbine as such—the compressor and expanders are separated from each others so there is no danger of surge of the compressor, especially when the LHV of the fuel is lower than that of natural gas, like that of a syngas; and (5) no need of expensive and energy consuming CO_2 scrubber.

Technical Issues and Predesign of a Prototype Plant

The ASU has to be integrated in the cycle and in particular the flow of N_2 or maybe the rejected heat.

A new design or a redesign of known industrial components is required when they operate on CO_2 instead of air or water.

Components Already Available or Needing Adaptations.

1 The compressor whose design is very important. Indeed, as shown on Fig. 4, the cycle efficiency is very sensitive to the compressor effectiveness. As an illustration, a decrease of this latter from 0.9 to 0.75 provokes an efficiency drop of around 5 percentage points.
2 A CO_2 expander without cooling at 600°C, 300 bar, similar to the high pressure section of an UltraSuperCritical Rankine cycle.
3 The gas/gas recuperator at high temperatures and pressures.
4 The supercritical pump.
5 A CO_2 condenser and intercoolers with water cooling circuits.
6 The water/CO_2 cooler and separator.

(Components requiring a new design.)

7 The combustion chamber using O_2/CO_2 instead of air.
8 The temperature expanders (1300°C) with internal cooling of the blades and vanes. The design of gas turbines has previously been investigated in Mathieu et al. (1994a and b) and Mathieu (1995).

Corrosion of the materials in presence of CO_2 at high pressures and temperatures must be addressed, as well as possible parasitic chemical reactions of CO_2 with other substances. We are currently integrating the cooling of the hot parts of the cycle in the model.

When natural gas will be replaced by a liquid or a solid fuel, an integration of a gasification unit and a clean-up system of the syngas in the MATIANT plant is required. This is the following development of the present study.

The following are other applications of the MATIANT cycle:

— electricity and heat cogeneration; for instance, district heating (Rasmussen 1997)
— use in a Pressurized Fluidized Bed Combustor (Jung, 1997)
— use in combination with a solar pond (Iantovski et al., 1997c)
— introduction of a MHD unit in the cycle in replacement of the low pressure expander (Iantovski et al., 1997b)
— use in a combination with a heat pump or with a refrigeration system
— coproduction of dry CO_2 ice (1 bar, −80°C; recommended for some storage options)
— use of the high pressure liquid CO_2 extracted flow for oil recovery enhancement
— use of chemical looping combustion using metal oxides cycles instead of the ASU
— use of chemical recuperation for efficiency increase
— hydrogen production

Conclusions

The MATIANT concept leads to a power plant design with high performance and no releases of pollutants in the atmosphere. Several applications are obtained by combination with other systems like a gasification unit, a MHD unit, heat pumps, chemical recuperators, and oil recovery installations. The concept is also used with technologies like cogeneration, district heating, a PFBC, as well as with solar energy (solar pond). This wide field of applications will, however, only be feasible when conventional components like compressors, expanders, pumps, heat exchangers, recuperators, and condensers, will be adapted or redesigned for the operation on CO_2 as the working fluid and in more severe thermal conditions.

As the power generation techniques using coal as the fuel are larger contributors to the greenhouse effect than those based on natural gas, the MATIANT cycle can be a possible alternative option when the time of an economic change of technology has come. The questions are as follows: is it technically feasible, and what is its attractiveness in terms of performance (in various regimes), cost, and environmental impact?

Therefore, it is time to design a pilot plant now, and this is an appeal towards the potential financial supporters.

References

Blok, K., Turkenburg, W. C., Hendriks, C. A., and Steinberg, M., editors, 1992, "Energy Conv. And Management," Proceedings, First Int. Conf. on CO_2 Removal, Pergamon Press New York, Vol. 33, No. 5–8, pp. 773–825.

Bolland, O., and Mathieu, P., 1997, "Comparison of Two CO_2 Removal Options in Combined Cycle Power Plants," Proceedings, FLOWERS '97, Florence, Italy, pp. 353–364.

Bolland, O., and Saether, S., 1993, "Option Evaluation Study. Gas Fired CC Modified for CO_2 Recovery," report, IEA Greenhouse Gas R&D Programme, CRE, Cheltenham, UK.

Iantovski, E., and Mathieu, P., 1996, "Highly Efficient Zero Emission CO_2-Based Power Plant," paper presented at the 3rd ICCDR, Cambridge, MA.

Iantovski, E., Mathieu, P., and Nihart, R., 1997a, "Incineration in High Efficiency Zero Emission CO_2-Based Power Plants," paper presented at the 4th European Conference INFUB, Porto, Portugal.

Iantovski, E., Lhomme, R., and Mathieu, P., 1997b, "Coal Fired MagnetoHydroDynamic Power Plant with Zero-CO_2 Atmospheric Emission," paper presented at ASME COGEN TURBO Conf., Singapore.

Iantovski, E., Greday, Y., and Mathieu, P., 1997c, "Biomass Fueled CO_2 with Zero Emission," paper presented at Power-Gen '97, Madrid, June 1997.

Jung, P., 1997, "Design of a Zero Emission Pressurized Fluidized Bed Combustor Plant," thesis (in French), University of Liège, Belgium.

Mathieu, P., and Deruyck, J., 1993, "CO_2 in Combined Cycle and IGCC Power Plants Using a CO_2 Gas Turbine," paper presented at ASME COGEN TURBO Conf., Bournemouth, U.K.

Mathieu, P., 1994a, "The Use of CO_2 Gas Turbines," Proceedings, Power Gen Europe '94, Cologne, Germany, pp. 7–28.

Mathieu, P., Dechamps, P. J., and Pirard, N., 1994b, "The Use of CO_2 in an Existing Industrial Gas Turbine," Proceedings, 49th ATI (Associazione Termotecnica Italiana) National Congress, Perugia, Italy, pp. 2309–2322.

Mathieu, P., 1995, "CO_2 Mitigation Through CO_2/Steam/Argon Gas Turbine Cycles and CO_2/Steam/Argon Gasification," final report of the Combined Cycle Project, European Joule II Programme, European Commission Publications, Bruxelles, Belgium.

Rasmussen, N., 1998, "Combined Heat and Power based on the MATIANT Concept," paper presented at the Second International Workshop on Zero Emission Power Plants, January 26, 1998, University of Liège, Belgium.

Riemer, P., Audus, H., and Smith, A., 1993, "Carbon Dioxide Capture From Power Stations," report, IEA Greenhouse Gas Programme, CRE, Cheltenham, U.K.

Riemer, P. W. F., 1995, "Greenhouse Gas Mitigation Technologies: An Overview of the CO_2 Capture, Storage and Future Activities of the IEA Greenhouse Gas R&D Programme," Proceedings, Int. Energy Agency Greenhouse Gases: Mitigation Options and Energy Conversion and Management, Vol. 37, No. 6–8, London, pp. 665–671.

Smith, I. M., 1993, "CO_2 and Climate Change: An Overview of the Science," Proceedings, International Energy Agency CO_2 Disposal Symposium, Pergamon Press, New York, IEA Greenhouse Gas R&D Programme, Oxford, UK, pp. 729–737.

A Numerical Investigation of the Cooling Effect of Compressed Natural Gas Throttling on Engine Delivery Ratio

Y. Yacoub

L. Marbun

R. Bata

Department of Mechanical and Aerospace Engineering, West Virginia University, Morgantown, WV 26506

A theoretical study was conducted to investigate the cooling effect of throttling compressed natural gas during the pressure regulation process. The concept of using this effect in cooling down the induction air was investigated. A thermodynamic model was developed for a typical fuel delivery system used on a vehicle fueled with compressed natural gas. The model was based on a set of integral conservation laws applied to each component of the fueling system. Several heat exchanging arrangements between the throttled gas and the inlet air were examined. The effect of the added heat exchanger on engine delivery ratio was examined for different engine sizes as well as for different operating conditions. An increase of 1 to 2.5% in engine delivery ratio was predicted due to the added heat exchanger.

Introduction

Compressed natural gas (CNG) is an attractive alternate fuel. Natural gas is already in use in a vast number of vehicles worldwide. Natural gas fueled engines generally have very low emissions of reactive hydrocarbons, carbon monoxide, and particulate matter. The principal constituent of natural gas is methane with the remainder being heavier hydrocarbons, nitrogen, and water (Maxwell and Jones, 1994).

Natural gas must be stored in high pressure tanks, up to 3600 psi, in order to store a large enough quantity of natural gas to provide sufficient vehicle driving range. A pressure regulator is required to reduce the natural gas pressure to an appropriate level (typically 100 to 200 psi) before the gas is passed to the fuel metering system. As the natural gas is expanded through the regulator, the throttling process will result in cooling the gas. This cooling effect is dependent on the Joule-Thomson coefficient of the throttled gas.

There are practical implications from cooling the fuel. One factor is that low fuel temperature may create water condensate inside the regulator or in the downstream tubing. Also, water vapor may condense externally on the highly cooled regulator and cause icing. These possible effects can be lessened using several approaches. One option is to use an initial step-down regulator near the storage tank and to use the fuel line from the tank to the engine compartment as a heat transfer surface. Another possible approach is to heat the regulator using the engine coolant (Liss and Thrasher, 1991).

The amount of natural gas cooling is a function of the CNG tank pressure and can cause fuel air ratio variations as the tank is being emptied. Meyer (Meyer et al., 1992) used an s-curved steel tube down stream of the high pressure regulator and traversed the intake manifold. Thus, at the metering point natural gas temperature was close to air temperature regardless of CNG tank pressure or ambient air temperature.

The objective of this study is to evaluate the potential of making use of the cooling effect due to the throttling of natural gas to cool down the induction air as a measure of enhancing the engine scavenging capability.

Contributed by the Internal Combustion Engine Division for publication in the JOURNAL OF ENGINEERING FOR GAS TURBINES AND POWER. Manuscript received on April 1, 1998; revision received on July 29, 1998. Associate Technical Editor: D. Assanis.

Theoretical Formulation

Figure 1 shows a diagram of the modeled system. Compressed natural gas (CNG) expands isentropically from total initial state (0) to state ($0s$) in the first nozzle (tank exit). As the gas flows through the fuel line to a high pressure regulator (HPR) in the engine compartment, it exchanges heat with ambient air surrounding the fuel line. At the HPR, the gas is throttled from state (1) to state ($1s$). CNG exchanges heat with the inducted air as it flows through a heat exchanger (HE), and reaches state (2) at the exit of the exchanger.

In the present study, two closed-loop fuel control systems are considered. For the first system, the LPR pressure setting is continuously adjusted, the second nozzle area ratio is set to unity and the gas is throttled from state (2) to state ($2s$). In the second system, the LPR is eliminated and the gas expands isentropically to state (3) through the second nozzle variable exit cross sectional area, where it is injected into the mixer.

The basic model assumptions are (1) real gas behavior occurs in the pressure regulation processes, and ideal gas behavior occurs for the other processes; (2) the flow is quasi-steady through ducts and nozzles; (3) constant rate of heat transfer across the boundaries of ducts; (4) no correction factor is considered for the HE configurations that are different from the ideal co-axial type; and (5) natural gas composition is 100 percent methane.

Conservation Equations

The normalized governing equations for one-dimensional steady flow with friction and heat transfer in a variable-area duct can be expressed as follows:

Mass.

$$\phi_T - \phi_P^2 \phi_M^2 \phi_A^2 = 0$$

Momentum.

$$1 - \phi_P \phi_A = \gamma M_m^2 \left(\left(1 + \frac{L}{D_{h,n}} f \cos\theta \right) \frac{\phi_T}{\phi_P \phi_A} - \left(1 - \frac{L}{D_{h,m}} f \cos\theta \right) \right)$$

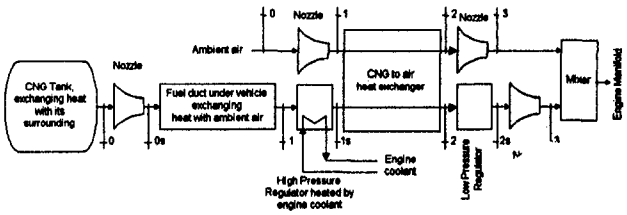

Fig. 1 Block diagram of a mixture delivery system

Energy.

$$\frac{1}{\gamma-1}\left((\phi_T-1)-\bar{\mu}_j\frac{\bar{P}_n}{\bar{T}_n}(\phi_P-1)\right)+\frac{1}{2}M_m^2\left(\frac{\phi_T^2}{\phi_P^2\phi_A^2}-1\right)=\frac{1}{\bar{T}_m}\frac{\bar{Q}}{\bar{m}}\frac{\bar{M}_w}{\bar{\gamma}},$$

where

$$\phi_T=\frac{\bar{T}_n}{\bar{T}_m}\quad \phi_P=\frac{\bar{P}_n}{\bar{P}_m}\quad \phi_M=\frac{M_n}{M_m}\quad \phi_A=\frac{\bar{A}_n}{\bar{A}_m}$$

and the subscripts m and n denote upstream and downstream states, respectively. The application of the above equations to each subsystem is detailed in the appendix section.

Numerical Solution

Define the solution vector of mach numbers X as

$$X^T=[M_{0s,\mathrm{cng}}M_{1,\mathrm{cng}}M_{1s,\mathrm{cng}}M_{2,\mathrm{cng}}M_{2s,\mathrm{cng}}M_{3,\mathrm{cng}}M_{1,\mathrm{air}}M_{2,\mathrm{air}}M_{3,\mathrm{air}}]$$

The energy equations are categorized as the main set of the governing equations, and the rest of the equations as the auxiliary set. The main set is used to calculate X simultaneously, meanwhile, the auxiliary set is used to update the other variables. The initial state of CNG in the tank is specified and the stagnation thermodynamic states of the air at exit of turbocharger (if any exist) and the air temperature under the hood are specified. If the gas chokes at the nozzle exit, the Mach number is set equal to unity, otherwise the exit pressure is set equal to the back pressure. The tank governing equations are integrated using the trapezoidal rule, and the state of the gas in the tank at the new time step is continuously updated using the most recent solution vector. Since the main set of governing equations are nonlinear, a numerical solution has to be sought.

Table 1 Default values of simulation parameters

Parameter	Set value	Parameter	Set value
D_{tnk} (in)	3.937	$P_{1s,cng}$ (psi)	250
L_{tnk} (ft)	3.281	$P_{2s,cng}/P_{back}$	1.0
D_{cng} (in)	0.125	$P_{back}/P_{0,air}$	0.95
$L_{0,cng}$ (ft)	16.4	$T_{0,cng}$ (°F)	80
L_{air} (ft)	3.281	$T_{0,air}$ (°F)	98
$A_{2,cng}/A_{2s,cng}$	0.10	$T_{uh,air}$ (°F))	125
$A_{2s,cng}/A_{3,cng}$	1.0	$T_{1s,pr}$ (°F)	206
$A_{2,air}/A_{3,air}$	1.0	$\dot{m}_{pr}$ (lbm/sec)	0.033
h_{tnk} (Btu/hr/ft²/R)	8.8	ε_{pr}	0.35
$P_{0,cng}$ (psi)	3000	φ	1.0
$P_{0,air}$ (psi)	14.7	η	0.35
Engine power (hp)	100	Fuel metering system	LPR setting

Define the residual vector R as the left hand side of the main set of equations and employing Newton-Raphson iterative technique, the solution vector X is updated each iteration r using $X^{r+1}=X^r-[\partial R/\partial X]^{-1}R^r$ where $[\partial R/\partial X]$ is the Jacobian matrix.

Results and Discussion

The simulation procedure is carried out in two steps. In the first step, the different parameters are adjusted for a given engine size with the HE removed. In the second step, the HE is added to the system and its effectiveness is maximized by increasing the number of CNG pipe windings around the air duct. The geometrical parameters are adjusted to prevent choking of the fuel flow, due to the increase in duct length. Table 1 shows the default values of the different simulation parameters.

The comparison between a system with an HE and a system without one is made in terms of its engine delivery ratio which is defined as the mass ratio of inducted to ideal air. The ideal air mass is the product of engine displacement and air density at ambient condition. The fractional increase in delivery ratio in an HE equipped engine compared to one without an HE is used as a measure of the comparative advantage. For both systems, engine displacement, speed, and air to fuel ratio are set equal. Using the above delivery ratio definition, it can be shown that the relative increase in delivery ratio is equal to the relative increase in the rate of air mass flow. Moreover, for equal values of engine speed and displacement, thermal efficiency, and fuel to air ratio, the relative increase in power is equal to the relative increase in delivery ratio.

Nomenclature

a = speed of sound
A = cross-sectional area, surface area
A_U = heat transfer area upon which the definition of the overall conductance coefficient is based
c_v = constant volume specific heat
c_p = constant pressure specific heat
D = duct diameter
D_h = hydraulic diameter
f = coefficient of friction
F^+ = nondimensional friction factor
FA = fuel to air ratio
h = convection heat transfer coefficient
L = duct length
m = mass
$\dot{m}$ = mass flow rate
M = mach number
M_w = molecular weight
NTU = heat exchanger maximum number of transfer units
P = pressure
$\dot{Q}$ = rate of heat transfer
r = iteration number
R = residual vector
Rc = heat exchanger capacity ratio
t = time
T = temperature
U = overall conductance coefficient
V = CNG storage tank volume
X = solution vector of mach numbers
ϵ = heat exchanger effectiveness
ϕ_P = pressure ratio
ϕ_T = temperature ratio
φ = equivalence ratio
γ = ratio of specific heats
η = engine thermal efficiency
μ_J = Joule Thomson coefficient
θ = angle between duct wall and axial direction
χ = ratio of gas temperatures at inlet to heat exchanger

Subscripts:

air = induction air
b = back
cng = compressed natural gas
i = gas state at station i where i is either (0, 1, 1s, 2, 3)
pr = pressure regulator heat exchanger fluid
ref = reference state
tnk = gas storage tank
uh = under the hood

Superscripts

z = nondimensional variable z

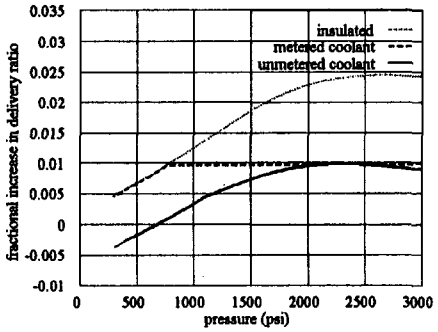

Fig. 2 Fractional increase in delivery ratio for different HPR heating arrangements

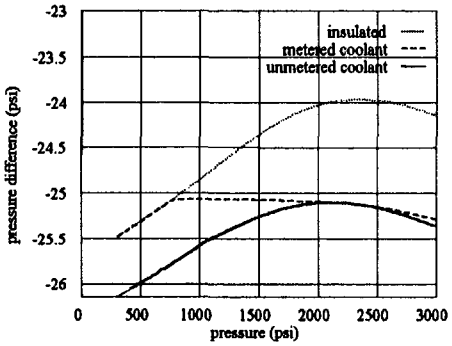

Fig. 5 Difference in pressure of CNG between the exit and inlet of the HE

The fractional increase in engine delivery ratio compared with the case of no HE is shown versus tank pressure in Fig. 2 for different cases of heating arrangements of the high pressure regulator (HPR). A maximum increase of ~2.5 percent is achieved for the case when the HPR is insulated and the temperature of the gas is allowed to drop below the water freezing point. The increase in delivery ratio reaches a slight peak, and then decreases to a value of ~0.5 percent at the end of the simulation. This is due to the fact that as the tank starts discharging, the temperature of the gas in the tank decreases, and the cooling due to throttling of the gas in the HPR is maximum. This results in more cooling of the induction air, and, thus, a larger increase in delivery ratio. As the pressure of the gas in the tank decreases, the cooling effect in the HPR decreases; therefore, the final increase in engine delivery ratio is only ~0.5 percent.

The increase in delivery ratio is ~1 percent for the case when the HPR is heated with engine coolant, the coolant is metered in order to maintain the gas temperature above 32°F at the exit of the HPR. The fractional increase in delivery ratio is constant over most of the discharge period which is a favorable behavior. Near the end of discharge, the cooling effect is minimal because the gas temperature is no longer below the water-freezing point. HPR heating is no longer needed and the coolant flow is stopped.

The case where the HPR is heated with an unmetered engine coolant is also shown in Fig. 2. A maximum increase in delivery ratio is ~1.0 percent, which drops as the tank pressure decreases to ~−0.25 percent. At the end of the simulation, the gas heats up the induction air rather than cooling it, which results in a loss of delivery ratio compared to the no HE case. Figures 3 through 7 show the relevant simulation results. The temperature drop of the gas, due to throttling in the HPR, is quite severe, reaching ~−130°F at the start of discharge, as shown in Fig. 3. Also, the temperature increase of CNG in the HE is significant as shown in Fig. 4. Figure 5 shows the CNG pressure drop across the HE. The decrease in the temperature of the induction air is shown in Fig. 6. The drop in temperature of the CNG across the LPR is almost constant (~11°F) over the simulated discharge period, as shown in Fig. 7.

In the next sections the effects of engine size, load, and other operating parameters on the estimated increase in delivery ratio are examined. Comparison charts are presented for the simulated discharge period with the tank pressure as the x-axis. Also, unless specified, the case of the HPR heated with metered engine coolant is considered.

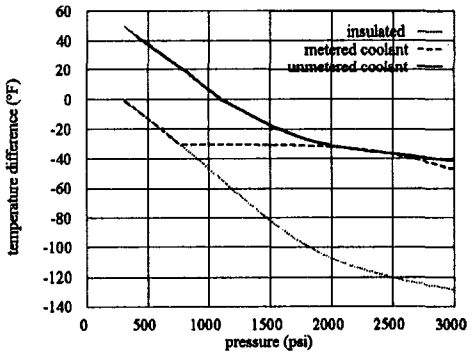

Fig. 3 Difference in temperature of CNG between the exit and inlet of the HPR

Engine Size. Figures 8 and 9 show the fractional increase in delivery ratio for different engine sizes for two different HPR heating arrangements. The fractional increase in delivery ratio is larger for larger engines. This is due to the fact that the larger the engine, the higher the CNG flow rate and the larger the drop in temperature due to throttling.

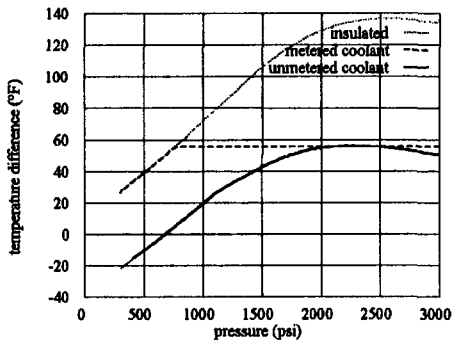

Fig. 4 Difference in temperature of CNG between the exit and inlet of the HE

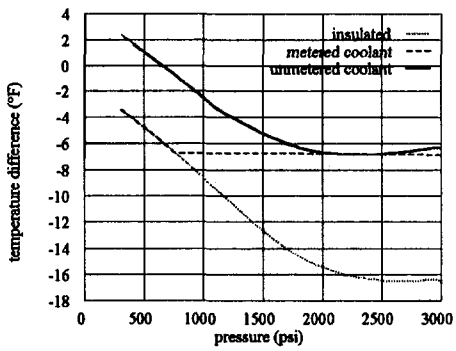

Fig. 6 Difference in temperature of air between the exit and inlet of the HE

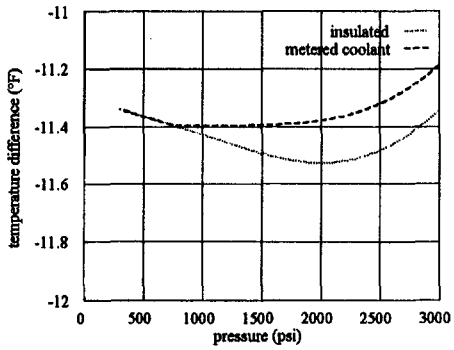

Fig. 7 Difference in CNG temperature between the exit and inlet of the LPR

Engine Load. In the previous section, the HE was optimized for maximum effectiveness for a given engine size operating at full load. It is of interest to evaluate the HE performance at part load. In order to simulate part load condition, the back pressure value at the mixer is increased. Figure 10 shows the fractional increase in delivery ratio for the different values of pressure ratio, $P_{back}/P_{0,air}$, for the case of a heated HPR with metered engine coolant. The fractional increase in delivery ratio is slightly larger at part load, and its value drops at an earlier stage when compared to full load.

Turbo-Charging. Case of turbocharging, the inlet air pressure is boosted to 1.25 and 1.5 atm in this simulation. The inlet air temperature is calculated assuming isentropic compression from the default value, and $P_{back}/P_{0,air}$ is set to its default value. The maximum fractional increase in delivery ratio is larger for a higher inlet air pressure, as shown in Fig. 11. In order to evaluate the effect of the HE on a turbocharged engine with an intercooler, the inlet pressure of air is set to 1.25 atm, and its inlet temperature is set to the default value. The fractional increase in delivery ratio is lower for the case where the turbocharger is equipped with an inter cooler, as shown in Fig. 12.

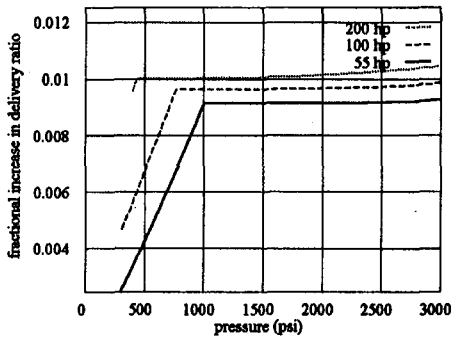

Fig. 8 Effect of engine size on the fractional increase in delivery ratio

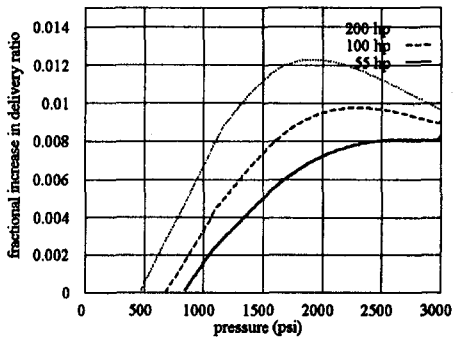

Fig. 9 Effect of engine size (HPR heated with unmetered coolant) on delivery ratio

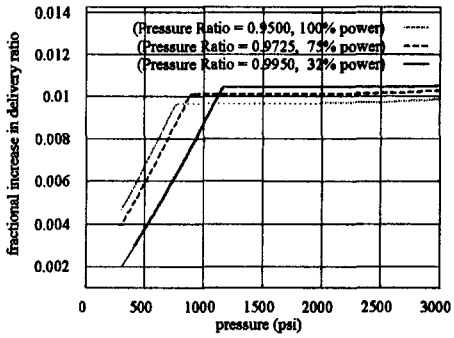

Fig. 10 Effect of engine load on the fractional increase in delivery ratio

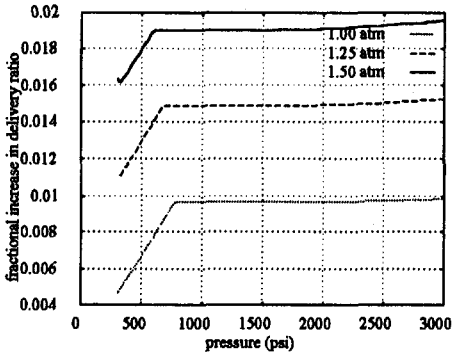

Fig. 11 Effect of turbocharging w/o intercooling on fractional increase in delivery ratio

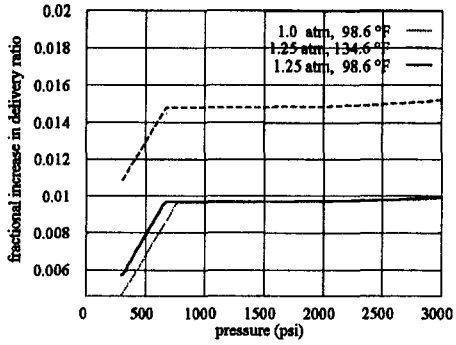

Fig. 12 Effect of turbo-charging w/ intercooling on fractional increase in delivery ratio

Initial Tank Pressure. Figure 13 shows the effect of initial tank pressure on fractional increase in delivery ratio. The fractional increase in delivery ratio is slightly higher for lower initial tank pressure, for the case of heated HPR. This is due to maintaining exit gas temperature to a value of ~32°F which limits the increase in delivery ratio.

Ambient Temperature. The effect of ambient temperature on the fractional increase in delivery ratio is shown in Fig. 14. The fractional increase in delivery ratio is significantly larger for a higher ambient temperature, in the case of heated HPR.

Equivalence Ratio. The richer the mixture, the higher the fractional increase in delivery ratio, as shown in Fig. 15.

Heat Exchanger Flow Arrangement. Figure 16 shows the effect the HE flow arrangements on the fractional increase in delivery ratio. As expected, higher increase in delivery ratio is

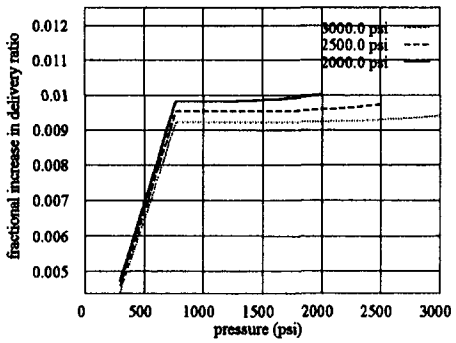

Fig. 13 Effect of initial tank pressure on the fractional increase in delivery ratio

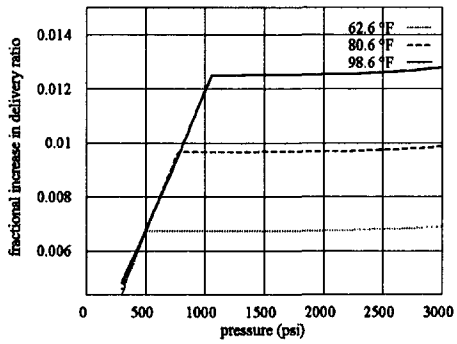

Fig. 14 Effect of ambient temperature on the fractional increase in delivery ratio

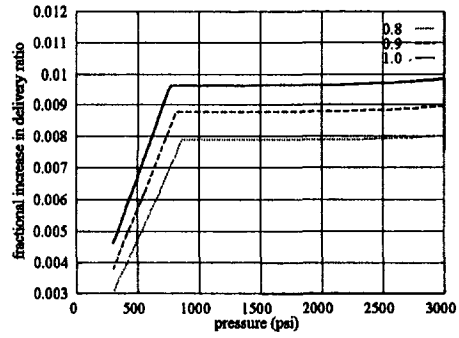

Fig. 15 Effect of equivalence ratio on the fractional increase in delivery ratio

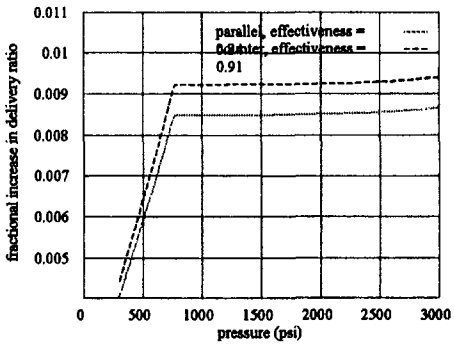

Fig. 16 Effect of the HE flow arrangement on the fractional increase in delivery ratio

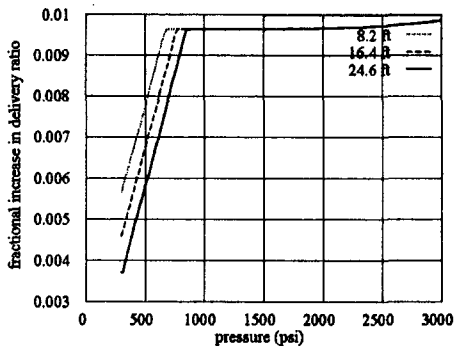

Fig. 17 Effect of CNG duct length on the fractional increase in delivery ratio

achieved for a counter flow arrangement, compared to the parallel flow arrangement.

CNG Duct Length. The effect of the length of the CNG duct from the tank to the HPR on the fractional increase in delivery ratio is shown in Fig. 17. The shorter the duct length, the later the drop in delivery ratio at low gas pressure in the tank.

High Pressure Regulator Setting. Figure 18 shows that low pressure at the exit of the HPR results in a slightly higher increase in delivery ratio.

Conclusions

1 The cooling effect of throttling natural gas during the pressure regulation process can be used to enhance engine delivery ratio. The current model estimates an increase in delivery ratio of approximately 2.5 percent for the case of an insulated high pressure regulator. The estimated increase in delivery ratio is approximately 1 percent, if the natural gas temperature is restricted to be above 32°F to avoid moisture content freezing.

2 Engines with large displacement which are also turbocharged, are estimated to acquire a higher increase in delivery ratio compared to engines which are smaller in size or nonturbocharged. The estimated fractional increase in delivery ratio is lower for turbocharged engines that are equipped with an inter cooler compared to engines which have no intercooler.

3 A heat exchanger which is designed to operate at full load would operate as effectively at part load condition. At part load, the fractional increase in delivery ratio is slightly higher for a heated high pressure regulator when compared to full load performance.

4 The higher the initial tank pressure, the lower the fractional increase in delivery ratio for the case where the high pressure

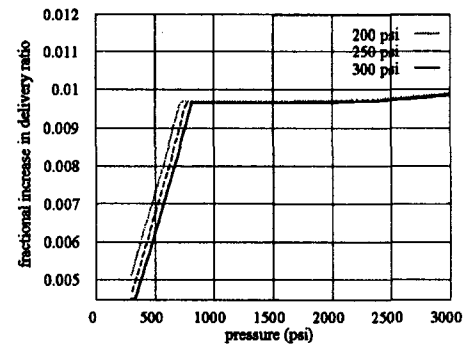

Fig. 18 Effect of HPR exit pressure setting on the fractional increase in delivery ratio

regulator is heated to maintain the gas temperature above water freezing temperature.

5 An increase in delivery ratio (~1.25 percent) is estimated for the case of high ambient temperature, when the high pressure regulator is heated.

6 The richer the fuel to air mixture, the higher the fractional increase in delivery ratio.

7 A shorter length of the gas duct from the tank to the high pressure regulator is recommended, to achieve a higher increase in delivery ratio.

8 A lower pressure regulation setting of the high pressure regulator is favorable in order to achieve delivery ratio enhancement. On the other hand, for large engines, a high pressure setting is required since the pressure drop across the exchanger is higher when compared to smaller engines.

Acknowledgment

The authors wish to thank the U.S. Department of Energy, the Office of Transportation Technologies. Special thanks are due to S. Goguen and J. Garbak for serving as program managers of the grant which made this study possible (Contract DE-FG02-90CH10451).

References

Bird, R. B., Stewart, W. E., and Lightfoot, E. N., 1960, *Transport Phenomena,* John Wiley & Sons, New York.

Kays, W. M., and Crawford, M. E., 1993, *Convective Heat and Mass Transfer,* 3rd ed., McGraw-Hill, New York.

Liss, W. E., and Thrasher, W. H., 1991, "Natural Gas as a Stationary Engine and Vehicular Fuel," SAE 912364, SAE Inc.,

Maxwell, T. T., and Jones, Jesse C., 1994, *Alternative Fuel, Emissions, Economics, and Performance,* SAE Inc.

Meyer, R., and Meyers, D., Shahed, S. M., and Duggal V. K., 1992, "Development of a heavy duty on-highway natural gas-fueled engine", SAE 922362.

Mills, A. F., 1995, Heat and mass transfer, Irwin.

Zeleznik, F. J., and Bonnie, J. M., 1985, "Modeling the internal combustion engine", NASA reference publication 1094.

APPENDIX

CNG and air undergo several processes. The governing equations given in a nondimensional form, as follows.

Discharge of CNG From Storage Tank.

The state of the gas in the tank is governed by the following differential equations:

Mass.

$$\frac{d\bar{m}_{\text{cng}}}{d\bar{t}} = -\bar{m}_{\text{cng}}$$

Energy.

$$\frac{d\bar{T}_{0,\text{cng}}}{d\bar{t}} = -(\gamma_{\text{cng}} - 1)\frac{\bar{m}_{\text{cng}}}{\bar{m}_{\text{cng}}}\bar{T}_{0,\text{cng}} + \left(h_{\text{tnk}}A_{\text{tnk}}\frac{t_{\text{ref}}}{m_{\text{ref}}c_v}\right)(1 - \bar{T}_{0,\text{cng}})\frac{1}{\bar{m}_{\text{cng}}}$$

State.

$$\frac{d\bar{P}_{0,\text{cng}}}{d\bar{t}} = \bar{T}_{0,\text{cng}}\frac{d\bar{m}_{\text{cng}}}{d\bar{t}} + \bar{m}_{\text{cng}}\frac{d\bar{T}_{0,\text{cng}}}{d\bar{t}}$$

Expansion Through Nozzle 1.

Isentropic Gas Relations.

$$\frac{\bar{T}_{0,\text{cng}}}{\bar{T}_{0s,\text{cng}}} = 1 + \frac{\gamma_{\text{cng}} - 1}{2}M^2_{0s,\text{cng}} \qquad \frac{\bar{T}_{0,\text{air}}}{\bar{T}_{1,\text{air}}} = 1 + \frac{\gamma_{\text{air}} - 1}{2}M^2_{1,\text{air}}$$

$$\frac{\bar{P}_{0,\text{cng}}}{\bar{P}_{0s,\text{cng}}} = \left(\frac{\bar{T}_{0,\text{cng}}}{\bar{T}_{0s,\text{cng}}}\right)^{\gamma_{\text{cng}}/\gamma^{-1}_{\text{cng}}} \qquad \frac{\bar{P}_{0,\text{air}}}{\bar{P}_{1,\text{air}}} = \left(\frac{\bar{T}_{0,\text{air}}}{\bar{T}_{1,\text{air}}}\right)^{\gamma_{\text{air}}/\gamma^{-1}_{\text{air}}}$$

Heat Exchange 1.

Define the following ratios:

$$\phi_{P0,\text{cng}} = \frac{\bar{P}_{1,\text{cng}}}{\bar{P}_{0s,\text{cng}}}, \quad \phi_{T0,\text{cng}} = \frac{\bar{T}_{1,\text{cng}}}{\bar{T}_{0s,\text{cng}}}$$

$$F^{\pm}_{0,\text{cng}} = 1 \pm \frac{L_{0,\text{cng}}}{D_{h0,\text{cng}}}f_{0,\text{cng}} \quad \phi_{T0,\text{air}} = \frac{\bar{T}_{wh,\text{air}}}{\bar{T}_{0,\text{air}}}$$

Mass.

$$\phi_{T0,\text{cng}} - \phi^2_{P0,\text{cng}}\left(\frac{M_{1,\text{cng}}}{M_{0s,\text{cng}}}\right)^2 = 0$$

Momentum.

$$\phi_{P0,\text{cng}} - \frac{1 + \gamma_{\text{cng}}F^-_{0,\text{cng}}M^2_{0s,\text{cng}}}{1 + \gamma_{\text{cng}}F^+_{0,\text{cng}}M^2_{1,\text{cng}}} = 0$$

Energy.

$$\frac{1}{\gamma_{\text{cng}} - 1}(\phi_{T0,\text{cng}} - 1) + \frac{1}{2}M^2_{0s,\text{cng}}\left(\frac{\phi^2_{T0,\text{cng}}}{\phi^2_{P0,\text{cng}}} - 1\right) - \frac{1}{\bar{m}_{\text{cng}}}\frac{\bar{Q}_{0s-1}}{\bar{T}_{0s,\text{cng}}}\frac{\bar{M}_{w,\text{cng}}}{\bar{\gamma}_{\text{cng}}} = 0$$

Define the following temperature ratio:

$$\chi_0 = \frac{\bar{T}_{0,\text{air}}}{\bar{T}_{0s,\text{cng}}}$$

The rate of heat transfer $\bar{Q}_{0s-1}$ is calculated from

$$\frac{\bar{Q}_{0s-1}}{\bar{T}_{0s,\text{cng}}} = (\overline{UA}_U)_{0s-1}\frac{\alpha_0 - \beta_0}{\ln(\alpha_0/\beta_0)}$$

$$(\overline{UA}_U)_{0s-1} = \frac{T_{\text{ref}}}{\dot{Q}_{\text{ref}}}\left(\frac{h_{0,\text{air}}h_{0,\text{cng}}}{h_{0,\text{air}} + h_{0,\text{cng}}}\right)(\pi D_{0,\text{cng}}L_{0,\text{cng}})$$

The values of α_0 and β_0 are given below for parallel and counter flow heat exchanger arrangements.

Case (1) Parallel Flow.

$$\alpha_0 = \chi_0\phi_{T0,\text{air}} - \phi_{T0,\text{cng}}, \; \beta_0 = \chi_0 - 1$$

Case (2) Counter Flow.

$$\alpha_0 = \chi_0\phi_{T0,\text{air}} - 1, \; \beta_0 = \chi_0 - \phi_{T0,\text{cng}}$$

CNG High Pressure Regulation.

Define:

$$\phi_{Ps1,\text{cng}} = \frac{\bar{P}_{1s,\text{cng}}}{\bar{P}_{1,\text{cng}}}, \; \phi_{Ts1,\text{cng}} = \frac{\bar{T}_{1s,\text{cng}}}{\bar{T}_{1,\text{cng}}}$$

Mass.

$$\phi_{Ts1,\text{cng}} - \left(\phi_{Ps1,\text{cng}}\frac{M_{1s,\text{cng}}}{M_{1,\text{cng}}}\frac{A_{1s,\text{cng}}}{A_{1,\text{cng}}}\right)^2 = 0$$

Energy.

$$\frac{1}{\gamma_{\text{cng}} - 1}\left((\phi_{Ts1,\text{cng}} - 1) - \bar{\mu}_{f1,\text{cng}}\frac{\bar{P}_{1,\text{cng}}}{\bar{T}_{1,\text{cng}}}(\phi_{P1s,\text{cng}} - 1)\right) + \frac{1}{2}M^2_{1,\text{cng}}\left(\frac{\phi^2_{Ts1,\text{cng}}}{\phi^2_{Ps1,\text{cng}}}\left(\frac{A_{1,\text{cng}}}{A_{1s,\text{cng}}}\right)^2 - 1\right) - \frac{1}{\bar{T}_{1,\text{cng}}}\frac{\bar{Q}_{1-1s}}{\bar{m}_{\text{cng}}}\frac{\bar{M}_{w,\text{cng}}}{\bar{\gamma}_{\text{cng}}} = 0$$

If the pressure regulator is equipped with a heat exchanger, $\bar{Q}_{1-1s}$ is calculated from

$$\bar{Q}_{1-1s} = \epsilon_{pr} \frac{1}{\gamma_{\text{ref}}} \min\left(\bar{m}_{pr}\bar{c}_{p,pr}, \bar{m}_{\text{cng}}\bar{c}_{p,\text{cng}}\right)$$

$$\times \max\left(\bar{T}_{1,\text{cng}}, \bar{T}_{1s,\text{cng}}, \bar{T}_{1pr}, \bar{T}_{1s,pr,}\right) - \min\left(\bar{T}_{1,\text{cng}}, \bar{T}_{1s,\text{cng}}, \bar{T}_{1,pr}, \bar{T}_{1s,pr,}\right).$$

The maximum number of transfer units NTU, is given for parallel and counter flow arrangements in terms of capacity ratio Rc, and effectiveness ϵ, as follows (Mills, 1995):

$$\text{NTU}_{\text{prll},pr} = \frac{1}{1 + Rc_{pr}} \ln\left(\frac{1}{1 - (1 + Rc_{pr})\epsilon_{pr}}\right)$$

$$\text{NTU}_{\text{prll},pr} = \frac{1}{1 - Rc_{pr}} \ln\left(\frac{1 - \epsilon_{pr}Rc_{pr}}{1 - \epsilon_{pr}}\right)$$

Heat Exchange 2.
Define:

$$\phi_{P1,\text{cng}} = \frac{\bar{P}_{2,\text{cng}}}{\bar{P}_{1s,\text{cng}}}, \quad \phi_{T1,\text{cng}} = \frac{\bar{T}_{2,\text{cng}}}{\bar{T}_{1s,\text{cng}}}, \quad F^{\pm}_{1,\text{cng}} = 1 \pm \frac{L_{1,\text{cng}}}{D_{h1,\text{cng}}} f_{1,\text{cng}}$$

$$\phi_{P1,\text{air}} = \frac{\bar{P}_{2,\text{air}}}{\bar{P}_{1,\text{air}}}, \quad \phi_{T1,\text{air}} = \frac{\bar{T}_{2,\text{air}}}{\bar{T}_{1,\text{air}}}, \quad F^{\pm}_{\text{air}} = 1 \pm \frac{L_{\text{air}}}{D_{h,\text{air}}} f_{\text{air}}$$

Mass.

$$\phi_{T1,\text{cng}} - \phi^2_{P1,\text{cng}}\left(\frac{M_{2,\text{cng}}}{M_{1s,\text{cng}}}\right)^2 = 0 \quad \phi_{T1,\text{air}} - \phi^2_{P1,\text{air}}\left(\frac{M_{2,\text{air}}}{M_{1,\text{air}}}\right)^2 = 0$$

Momentum.

$$\phi_{P1,\text{cng}} - \frac{1 + \gamma_{\text{cnv}}F^{-}_{1,\text{cng}}M^2_{1s,\text{cng}}}{1 + \gamma_{\text{cng}}F^{+}_{1,\text{cng}}M^2_{2,\text{cng}}} = 0$$

$$\phi_{P1,\text{air}} - \frac{1 + \gamma_{\text{air}}F^{-}_{\text{air}}M^2_{1,\text{air}}}{1 + \gamma_{\text{air}}F^{+}_{\text{air}}M^2_{2,\text{air}}} = 0$$

Energy Conservation.

$$\frac{1}{\gamma_{\text{cng}} - 1}(\phi_{T1,\text{cng}} - 1) + \frac{1}{2}M^2_{1s,\text{cng}}\left(\frac{\phi^2_{T1,\text{cng}}}{\phi^2_{P1,\text{cng}}} - 1\right) - \frac{1}{\bar{T}_{1s,\text{cng}}}\frac{\bar{Q}_{1s-2}}{\bar{m}_{\text{cng}}}\frac{\bar{M}_{w,\text{cng}}}{\bar{\gamma}_{\text{cng}}} = 0$$

$$\frac{1}{\gamma_{\text{air}} - 1}(\phi_{T1,\text{air}} - 1) + \frac{1}{2}M^2_{1,\text{air}}\left(\frac{\phi^2_{T1,\text{air}}}{\phi^2_{P1,\text{air}}} - 1\right) + \frac{1}{\bar{T}_{1,\text{air}}}\frac{\bar{Q}_{1s-2}}{\bar{m}_{\text{air}}}\frac{\bar{M}_{w,\text{air}}}{\bar{\gamma}_{\text{air}}} = 0$$

Define:

$$\chi_1 = \frac{\bar{T}_{1,\text{air}}}{\bar{T}_{1s,\text{cng}}}$$

The rate of heat transfer $\bar{Q}_{1-2}$ is calculated from:

$$\frac{\bar{Q}_{1s-2}}{\bar{T}_{1s}} = (\overline{UA}_U)_{1s-2}\frac{\alpha_1 - \beta_1}{\ln(\alpha_1/\beta_1)}(\overline{UA}_U)_{1s-2} = \frac{T_{\text{ref}}}{\dot{Q}_{\text{ref}}}\left(\frac{h_{1,\text{air}}h_{1,\text{cng}}}{h_{1,\text{air}} + h_{1,\text{cng}}}\right)(\pi D_{1,\text{cng}}L_{1,\text{cng}})$$

The values of α_1 and β_1 are given below for parallel and counter flow heat exchanger arrangements.
Case (1) Parallel Flow.

$$\alpha_1 = \chi_1\phi_{T1,\text{air}} - \phi_{T1,\text{cng}} \quad \beta_1 = \chi_1 - 1$$

Case (2) Counter Flow.

$$\alpha_1 = \chi_1\phi_{T1,\text{air}} - 1 \quad \beta_1 = \chi_1 - \phi_{T1,\text{cng}}$$

CNG Low Pressure Regulation.
Define:

$$\phi_{Ps2,\text{cng}} = \frac{\bar{P}_{2s,\text{cng}}}{\bar{P}_{2,\text{cng}}}, \quad \phi_{Ts2,\text{cng}} = \frac{\bar{T}_{2s,\text{cng}}}{\bar{T}_{2,\text{cng}}}$$

Mass.

$$\phi_{Ts2,\text{cng}} - \left(\phi_{Ps2,\text{cng}}\frac{M_{2s,\text{cng}}}{M_{2,\text{cng}}}\frac{A_{2s,\text{cng}}}{A_{2,\text{cng}}}\right)^2 = 0$$

Energy.

$$\frac{1}{\gamma_{\text{cng}} - 1}\left((\phi_{Ts2,\text{cng}} - 1) - \bar{\mu}_{j2,\text{cng}}\frac{\bar{P}_{2,\text{cng}}}{\bar{T}_{2,\text{cng}}}(\phi_{Ps2,\text{cng}} - 1)\right) + \frac{1}{2}M^2_{2,\text{cng}}\left(\frac{\phi^2_{Ts2,\text{cng}}}{\phi^2_{Ps2,\text{cng}}}\left(\frac{A_{2,\text{cng}}}{A_{2s,\text{cng}}}\right)^2 - 1\right) = 0$$

$$\frac{1}{2}M^2_{2s,\text{cng}}\left(\frac{\phi^2_{T2s,\text{cng}}}{\phi^2_{P2s,\text{cng}}}\left(\frac{A_2}{A_{2s}}\right)^2 - 1\right) - \frac{1}{\bar{T}_{2,\text{cng}}}\frac{\bar{Q}_{2-2s}}{\bar{m}_{\text{cng}}}\frac{\bar{M}_{w,\text{cng}}}{\bar{\gamma}_{\text{cng}}} = 0$$

Expansion Through Nozzle 2.
Define:

$$\phi_{Ps3,\text{cng}} = \frac{\bar{P}_{3,\text{cng}}}{\bar{P}_{2,\text{cng}}}, \quad \phi_{Ts3,\text{cng}} = \frac{\bar{T}_{3,\text{cng}}}{\bar{T}_{2,\text{cng}}}$$

$$\phi_{P3,\text{air}} = \frac{\bar{P}_{3,\text{air}}}{\bar{P}_{2,\text{air}}}, \quad \phi_{T3,\text{air}} = \frac{\bar{T}_{3,\text{air}}}{\bar{T}_{2,\text{air}}}$$

Isentropic Gas Relations.

$$\phi_{Ts3,\text{cng}} = \frac{1 + \frac{\gamma_{\text{cng}} - 1}{2}M^2_{2s,\text{cng}}}{1 + \frac{\gamma_{\text{cng}} - 1}{2}M^2_{3,\text{cng}}} \quad \phi_{T3,\text{air}} = \frac{1 + \frac{\gamma_{\text{air}} - 1}{2}M^2_{2,\text{air}}}{1 + \frac{\gamma_{\text{air}} - 1}{2}M^2_{3,\text{air}}}$$

$$\phi_{Ps3,\text{cng}} = (\phi_{Ts3,\text{cng}})^{\gamma_{\text{cng}}/\gamma^{-1}_{\text{cng}}} \quad \phi_{P3,\text{air}} = (\phi_{T3,\text{air}})^{\gamma_{\text{air}}/\gamma^{-1}_{\text{air}}}$$

Mass.

$$\phi_{Ts3,\text{cng}} - \phi^2_{Ps3,\text{cng}}\left(\frac{M_{3,\text{cng}}}{M_{2s,\text{cng}}}\right)^2\left(\frac{A_{3,\text{cng}}}{A_{2s,\text{cng}}}\right)^2 = 0$$

$$\phi_{T3,\text{air}} - \phi^2_{P3,\text{air}}\left(\frac{M_{3,\text{air}}}{M_{2,\text{air}}}\right)^2\left(\frac{A_{3,\text{air}}}{A_{2,\text{air}}}\right)^2 = 0$$

The mass flow rates of CNG and air are given by

$$\bar{m}_{\text{cng}} - \bar{P}_{0s,\text{cng}}\bar{T}^{-1/2}_{0s,\text{cng}}M_{0s,\text{cng}}\bar{\gamma}^{1/2}_{\text{cng}}\bar{M}_{w,\text{cng}} = 0$$

$$\bar{m}_{\text{air}} - \frac{A_{1,\text{air}}}{A_{1,\text{cng}}}\bar{P}_{1,\text{air}}\bar{T}^{-1/2}_{1,\text{air}}M_{1,\text{air}}\bar{\gamma}^{1/2}_{\text{air}}\bar{M}_{w,\text{air}} = 0.$$

The coefficient of friction (f) and the convection heat transfer coefficient (h) are computed for the case of a smooth duct, with constant heat transfer across its wall boundaries. Appropriate functional dependence on Reynolds and Prandtl numbers is considered for different flow regimes (Kays and Crawford, 1993). Thermal dependence for different gas transport and thermal properties is calculated by using polynomial fits provided by Zeleznik et al. (Zeleznik and Bonnie, 1985), and data by Bird et al. (Bird et al., 1960) for the tank gas temperature. The Van der Waal's equation of state is

used to account for real gas behavior in calculating the Joule-Thomson coefficient, μ_j.

The reference variables are given by

m_{ref} = initial mass of the gas in the tank

T_{ref} = initial temperature of CNG in the tank

$t_{ref} = \dfrac{V}{A_{1,cng} a_{ref}}$

$\gamma_{ref} = \gamma_{cng \text{ evaluated at } T_{ref}}$

$\dot{Q}_{ref} = (m_{ref}/t_{ref}) a_{ref}^2$

$M_{w,ref} = M_{w,cng}$

P_{ref} = initial pressure of CNG in the tank

a_{ref} = CNG speed of sound at T_{ref}

$U_{ref} A_{ref} = \dot{Q}_{ref}/T_{ref}$

$c_{p,ref}$ = CNG gas constant

Application of Stress Relaxation Testing in Metallurgical Life Assessment Evaluations of GTD111 Alloy Turbine Buckets

J. A. Daleo

K. A. Ellison

BWD Turbines Limited,
I-601 Tradewind Drive
Ancaster, Ontario, L9G 4V5,
Canada

D. A. Woodford
Materials Performance Analysis, Inc.,
Santa Barbara, CA 93101

Stress relaxation and constant displacement rate tensile tests were performed on polycrystalline GTD111 alloy material removed from General Electric MS6001B first stage combustion turbine buckets. Samples were examined in the standard heat treated condition, thermally exposed at 900°C for 5000 hours and from service run buckets. Creep rates of the material were measured and evaluated directly in terms of temperature capability at 850°C and 900°C. Stress relaxation tests done at 0.8 percent total strain indicated that the creep rate properties in the service exposed airfoil were an order of magnitude higher than the material properties in the standard heat treated condition measured in the root form. In terms of temperature capability, the creep rate properties of the service run airfoil material had decreased by the equivalent of almost 40°C. The stress relaxation test method was demonstrated to be a very useful tool in quantifying the degradation of creep properties in service run components. Creep data that would require years to gather using conventional creep tests was generated in a few days. This now makes realistic life assessment and repair/replace decisions possible during turbine overhauls. The test method's unique ability to measure changes in creep rate over a large stress range, enabled the technique to distinguish between changes in creep strength due to (normal) microstructural evolution from the combined effects of microstructural evolution and strain related creep damage. A method for estimating standard constant load creep rupture life from the stress relaxation creep rate data is also presented along with time-temperature parameter correlations. The data sets examined in this study indicate that creep rupture lives can be estimated within a factor of three from the stress relaxation data. The information and analysis techniques described in this paper are directly applicable to metallurgical life assessment evaluations and the requalification of repaired General Electric buckets in Frame 3, 5, 6, 7, and 9 engine models.

Introduction

The maintenance period of critical gas turbine components operating in advanced technology industrial turbines is often determined by the material's long term metallurgical stability at the actual operating conditions encountered in service. The progressively higher firing temperatures used in all of the advanced engine designs results not only in very high metal surface temperatures but also in very high temperature gradients and concomitant thermal stresses, induced in part by the complex cooling systems. Unexpected changes in alloy properties due to higher than expected operating temperatures or stress can result in poor structural performance of the component design and reduced life.

Operating conditions can dramatically affect the life of gas turbine hot section buckets. An understanding of the original design parameters and their affect on component life is essential to understanding degradation modes resulting from "off design" operation. Today's advanced alloy/coating systems are expected to withstand very high temperatures and stresses for periods up to 48,000 h. Steady-state centrifugal stresses range from a few MPa to 250 Mpa, however, the thermal stress in the airfoil due to temperature gradients can range from −350 MPa to 500 MPa. Typical steady-state metal temperatures range from 760°C to 985°C. It is very clear from the temperature and stress estimates that the base alloy and coating systems degrade with time and as longer hours of service are accumulated, maintenance considerations such as developing optimum component life strategies and repair processes become important.

Metallurgical life assessment of service-exposed buckets has proven to be the most effective means of identifying the important modes of material degradation affecting component life. Methods for performing comprehensive metallurgical life assessments and failure analysis of gas turbine components have been recently by described by Daleo and Boone (1996).

As part of the metallurgical analysis, the degradation of material properties is estimated, by performing mechanical tests on material taken from critical areas of representative components. The remaining creep strength is usually evaluated by conducting short-term, accelerated creep rupture tests at temperatures, and/or stresses that are higher than those actually encountered in service. These tests were originally developed as standard quality control tests for new materials to quickly screen out chemistry lots and heat treatment cycles that produced properties outside of the normal scatter band.

One objection to the use of short term creep tests to predict long term behavior arises from the fact that microstructural changes that occur during service reduce the creep rupture lives of test specimens tested at low to intermediate temperatures at high stress levels, but have a much smaller effect on long term rupture lives at stresses and temperatures which are more typical of those actually encountered in service (Koul and Castillo,

Contributed by the International Gas Turbine Institute and presented at the International Gas Turbine and Aeroengine Congress and Exhibition, Stockholm, Sweden, June 2–5, 1998. Manuscript received by the ASME Headquarters April 1, 1998. Paper No. 98-GT-370. Associate Technical Editor: R. Kielb.

Table 1

Serial Number	Heat Code	Sample Location	Condition
EIFM203939	VAF140	Root Form	Standard Heat Treatment
EIFM204757	VAF141	Root Form	Standard Heat Treatment + 5000 hours @ 900°C
EIFM142492	VAF108	50% Airfoil Height, Suction Side Between Holes 3 & 4.	23,000 Hours of Service
EIFM203939	VAF140	10% Airfoil Height, Pressure Side Between Holes 3 & 4.	19,150 Hours of Service

1993). This can, and often does, lead to very conservative recommendations being made to replace or HIP reheat treat buckets prematurely.

Experimental Program

The experimental program was designed to determine if the stress relaxation test method would be able to distinguish between the various material conditions that could be present in service exposed gas turbine components:

1 Reduction in creep properties due primarily to environmental and microstructural changes (e.g., vane segments, solid first, and second stage rotating blades or buckets operating at low stress and/or short times).
2 Reductions in properties induced by creep damage compounded by microstructural changes (e.g., cooled and/or shrouded first and second stage buckets operating at higher stress, or for very long times at lower stress).

The experimental program was conducted within the framework of a larger BWD Turbines project to develop improved analysis tools for gas turbine component failure analysis and life assessment.

The stress relaxation and constant displacement rate tensile tests in this investigation were performed by Materials Performance Analysis, Inc. in Santa Barbara, California using test specifications and procedures developed by Dr. David Woodford. The details of the test procedure and the equipment required to conduct accelerated stress relaxation tests are described in detail by Woodford et al. (1992).

The nickel base superalloy, GTD111, developed by General Electric (GE) was selected for use in these experiments because of the general absence of published metallurgical and mechanical properties data pertinent to the alloy and its wide usage. The material is used extensively for high temperature rotating buckets in land-based gas turbines in both the polycrystalline and directionally solidified forms in GE Frame 3, 5, 6, 7, and 9 engine models.

The GTD111 material was characterized in four conditions (Table 1). The material representing the standard heat treated condition was removed from the root form of bucket serial number EIFM203939. The metal temperature experienced in the root form during operation is relatively low (<540°C), thus the microstructural features and starting mechanical properties do not significantly change during service. This makes the root form material representative of the original chemistry and manufacturing process used to make the buckets and suitable material to base line the starting creep properties of the alloy.

Changes in creep strength due only to temperature based microstructural evolution (aging) were evaluated by testing sample material removed from the root form of bucket serial number EIFM204757 which was thermally exposed in a laboratory furnace at 900°C for 5000 h.

The samples tested from the airfoils of the two service run buckets were from two different base loaded turbines operated on natural gas. The samples were tested to characterize the effects of combined microstructural evolution and accumulated creep damage. The airfoil sample removed from bucket EIFM203939 was from a cooler region of the lower airfoil where minimum service damage was expected to occur while the airfoil sample removed from bucket EIFM142492 was from the hottest region of the component where severe coating degradation and microstructural aging had occurred.

These particular service run buckets were selected as worst case examples to make sure that the test technique could discriminate between the various conditions and to set some lower bounds for future interpretation of the test data. The material tested was removed from old style, 11 hole bucket designs that were operated beyond predicted design temperatures. These buckets in no way represent the superior performance obtained in the latest GE MS6001 bucket designs that are in use today.

The microstructure, tensile properties and constant load creep rupture properties of the material used in these experiments were examined and reported on in detail by Daleo and Wilson (1996) and the failure mechanisms of aluminized MCrAlY coating systems applied to this generation of buckets were recently reviewed by Daleo and Boone (1997).

Stress Relaxation Testing

The fundamental methodology and mathematics of stress relaxation testing was originally described by Soderberg (1936). Early examples of converting raw stress relaxation test data, stress versus time, to stress versus strain rate, and using it to compare creep properties of austenitic stainless steels were published by Oding (1959). As better strain gaging and high speed digital data recording technology became available, methods of accelerating the test method using tensile testing machines were developed and used (Lee and Hart, 1971).

Today, using the Woodford test method and state of the art equipment, very accurate and reproducible tests can be performed. Five decades of creep rate can be covered in a test that takes approximately 20 h to complete.

The use of stress relaxation test methods to help characterize creep properties of service run gas turbine components is a relatively new concept, first proposed by Woodford et al. (1992).

When Stress Relaxation Tests are performed under conditions of constant total strain, the total strain is defined by:

$$\epsilon_t = \epsilon_e + \epsilon_p, \tag{1}$$

where ϵ_t = total strain, ϵ_e = elastic strain, and ϵ_p = plastic (creep) strain. The elastic strain is further defined by

$$\epsilon_e = \sigma/E, \tag{2}$$

where σ = stress, and E = elastic modulus; therefore,

$$\epsilon_t = \sigma/E + \epsilon_p. \tag{3}$$

Under conditions where the total strain is held constant, plastic

(creep) strain (ϵ_p) can only occur if the elastic strain (ϵ_e) decreases. Differentiating Eq. (3) with time, remembering that the change in the total strain is zero, $d\epsilon_t/dt = 0$, results in the plastic (creep) strain rate ($d\epsilon_p/dt$), labeled $\dot{\epsilon}_p$, being defined as

$$\dot{\epsilon}_p = -1/E(d\sigma/dt.) \tag{4}$$

The stress relaxation test data generated by the Woodford technique is in the form of stress to maintain the desired total strain versus time. A plot of stress versus the natural logarithm of time produces a straight line approximation of the relaxation decay curve. A least squares regression model

$$\sigma = \beta_0 + \beta_1 \ln t + e$$

fitted to the curve describes the data in terms of stress versus in time. Differentiating the model with respect to ln (time) and multiplying it by $1/t$ produces an expression for the stress rate, $d\sigma/dt$.

The stress rate is then inserted into the creep rate formula $\dot{\epsilon}_p = -1/E(d\sigma/dt)$ to calculate the creep rate. The data is best presented as a plot of stress versus the log of creep rate.

An expression of the stress rate, $d\sigma/dt$ can also be obtained using a power law fit of the raw data, $\sigma = \beta_0 + t^n + e$. A plot of stress versus time^N produces a straight line approximation of the relaxation decay curve. A least squares regression model ($Y = \beta_0 + \beta_1 X + e$) fitted to the data results in a fit of the data in terms of stress versus time^N. Differentiating the model results in the stress rate being defined in terms of $d\sigma/d(t^N)$ which can be converted back to stress rate ($d\sigma/dt$) by multiplying

$$d\sigma/d(\ln t)$$

by $N*\text{time}^{(N-1)}$. (Values of N range from .01 to .001.)

Investigation

1 Microstructural Analysis. Knowledge of the alloy microstructure is fundamental to understanding the mechanical property behavior of the material. Superalloy microstructures continually change with time at the operating temperatures experienced in most gas turbine applications.

The starting microstructure of the GTD111 buckets is a product of the chemistry, the casting parameters, coating and heat treatment steps used to manufacture the component. The buckets used in this study were vacuum investment cast, hot isostatically pressed, machined and processed through the GE GT 29 IN PLUS coating process and the GE GTD111 alloy standard heat treatment.

The microstructural features generated by the processing were similar to other nickel based superalloy casting alloys previously described by Sims et al., 1987. In general, all of the bucket castings examined appeared to be of high quality. No excessively large grains, porosity, or areas of gross shrinkage were observed.

The microstructures of the material used in this study were examined and reported on in detail by Daleo and Wilson (1996). A brief overview is presented here to help in the interpretation of the stress relaxation data.

The GTD111 microstructure in the standard heat treated condition consisted of a duplex gamma prime (γ') (Ni_3(Al, Ti) precipitate evenly distributed in the face centered cubic (FCC) gamma (γ) matrix (Fig. 1). The average size of the primary γ' precipitates was 0.86 micron and the average size of the secondary γ' precipitates was 0.1 micron. The grain boundaries were decorated with a very thin, discontinuous $\gamma'/M_{23}C_6/M_6C$ carbide layer (Fig. 1). Scattered throughout the matrix and occasionally on the grain boundaries were eutectic γ' nodules and MC carbides (Ta, Ti, W). The grain boundaries were finely serrated and wavy on a macro scale. Eutectic γ' and MC carbides were present both along the grain boundaries and evenly distributed throughout the matrix.

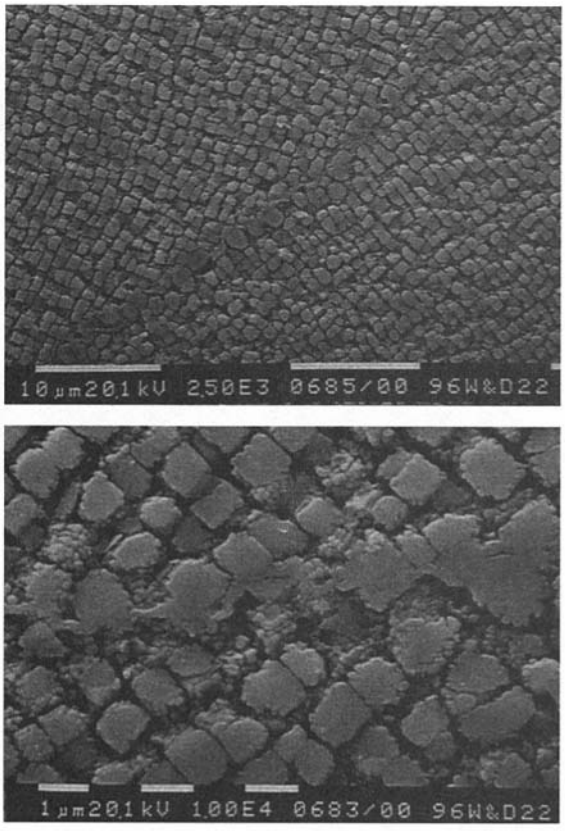

Fig. 1 Scanning electron micrographs of the GTD111 microstructure in the standard heat treated condition illustrating the duplex gamma prime precipitate structure and the grain boundary carbide morphology

The stability of the various microstructural phases at the operating temperatures experienced by gas turbine buckets is extremely important. In service the γ' phase increases in size with time and temperature, and complex carbide reactions occur. The most important of the carbide reactions is the continued growth of the $M_{23}C_6$ carbide phase along the grain boundaries. The migration of chromium to the boundary leaves the matrix locally enriched in the γ' forming elements nickel, aluminum, titanium etc. allowing a film of γ' to form along the boundary. Degeneration of MC carbides into $M_{23}C_6 + \gamma'$ in the matrix and along the grain boundaries accelerates the process. Examples of these phase changes were observed in the microstructure of the bucket thermally exposed at 900°C for 5000 hours as well as in service exposed material.

The microstructure of bucket EIFM204757 after the 5000 hour thermal exposure at 900°C is presented in Fig. 2. The primary γ' precipitates had transformed from cubic shaped particles to a rounded morphology. The size of the primary γ' precipitates had grown from an average size of 0.86 micron to 1.16 micron. The secondary γ' precipitates were consumed. The grain boundary carbides had coarsened and coalesced. Thick continuous $\gamma'/M_{23}C_6$ films had formed.

The microstructure of a GTD111 turbine bucket removed from service after 23,000 hours is presented in Fig. 3. Note that the matrix γ', the grain boundary carbides and the formation of γ' films along the boundaries have continued to coarsen. The formation of γ' along grain boundaries is normal and in most cases beneficial. However, when the films become too thick, the boundary is embrittled, becomes notch sensitive, and is prone to cracking. Continued growth of the γ' phase reduces the creep resistance of the material.

2 Stress Relaxation Tests

Stress relaxation tests were performed on each sample at four different combinations of temperature and total prestrain (850°C

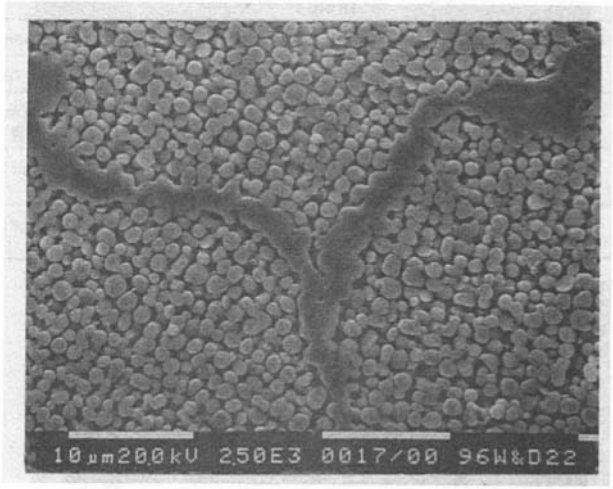

Fig. 2 A scanning electron micrograph illustrating the GTD111 microstructure after a 5000 h thermal exposure at 900°C (1650°F)

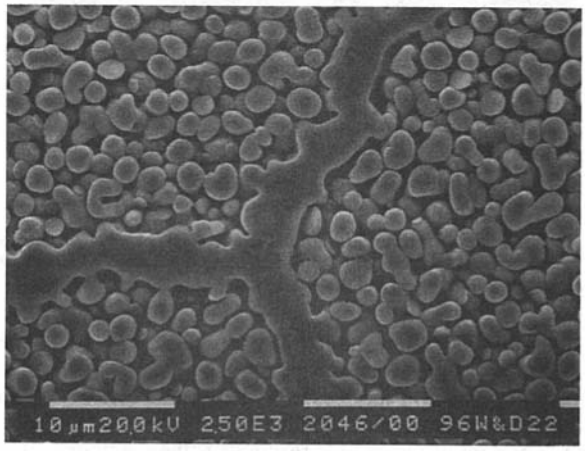

Fig. 3 A scanning electron micrograph illustrating the GTD111 microstructure observed at the 50 percent airfoil height location of the leading edge after 23,000 hours of service

and 900°C at 0.4 percent and 0.8 percent prestrain). A typical example of the test data, in the form stress versus log time, is illustrated in Fig. 4. Plots of the data expressed in terms of stress versus log creep rate are illustrated in Figs. 6–9.

2.1 Root Form, Standard Heat Treated Condition. The stress relaxation tests performed on the material in the standard heat treated condition were repeated on a second test bar two months after the first tests were made to determine the repeatability of the strain rate measurements and to provide an estimate of the variance. The test results at all test conditions were duplicated with extremely good precision. An example of the reproducibility of the test results is presented in Fig. 5.

2.2 Root Form, Furnace Exposed Condition. The stress relaxation tests done at 850°C at both 0.4 percent and 0.8 percent total strain conditions revealed that, compared to the material properties in the standard heat treated condition, the creep rate properties of GTD111 alloy were degraded by the 5000 hour thermal exposure at 900°C. In the test run done at 0.8 percent total strain, the strain rate curve at the lower stress levels fell back onto the new material curve (Fig. 7). This type of behavior is also observed in standard constant load creep rupture tests.

The stress relaxation tests done at 900°C at both 0.4 percent and 0.8 percent total strain did not detect the drop in properties in the thermally exposed material.

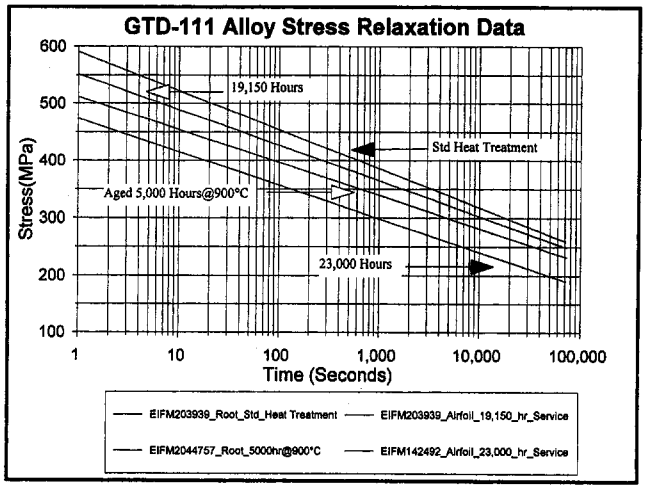

Fig. 4 A plot illustrating the GTD111 alloy stress relaxation test data at 850°C and 0.8 percent total strain

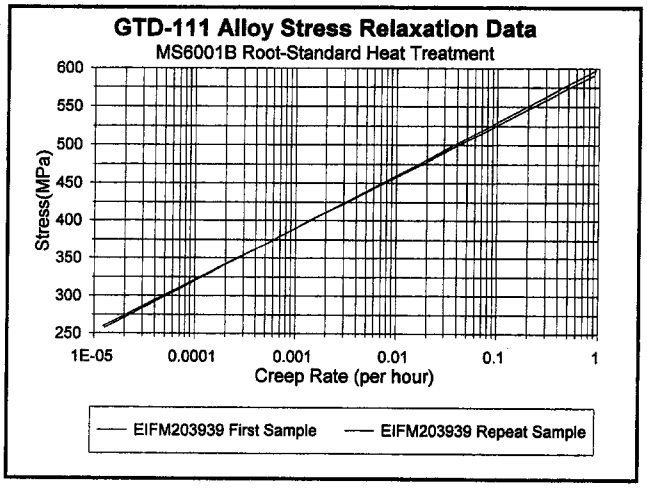

Fig. 5 A plot illustrating the repeatability of the strain rate measurements measured on a second test bar tested two months after the first test. Test parameters, 850°C and 0.8 percent total strain.

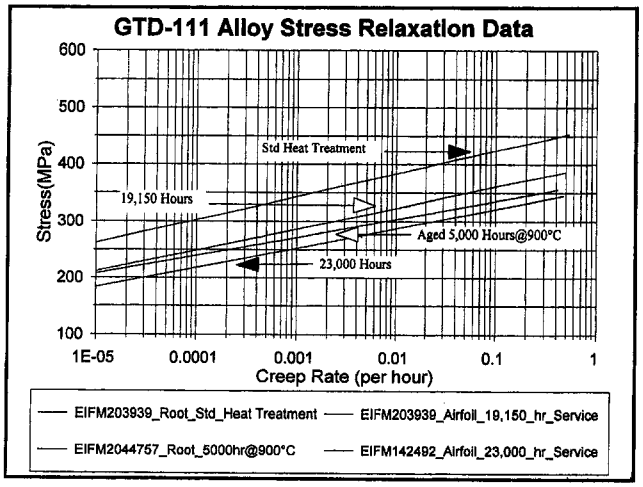

Fig. 6 A plot illustrating the strain rate data measured from the samples at 850°C and 0.4 percent total strain

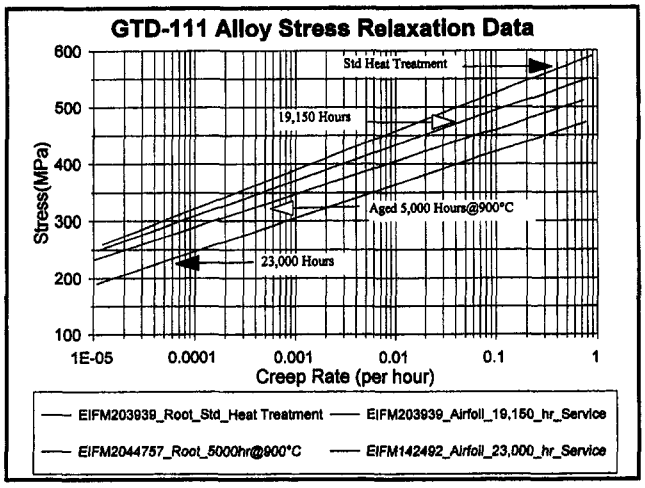

Fig. 7 A plot illustrating the strain rate data measured from the samples at 850°C and 0.8 percent total strain

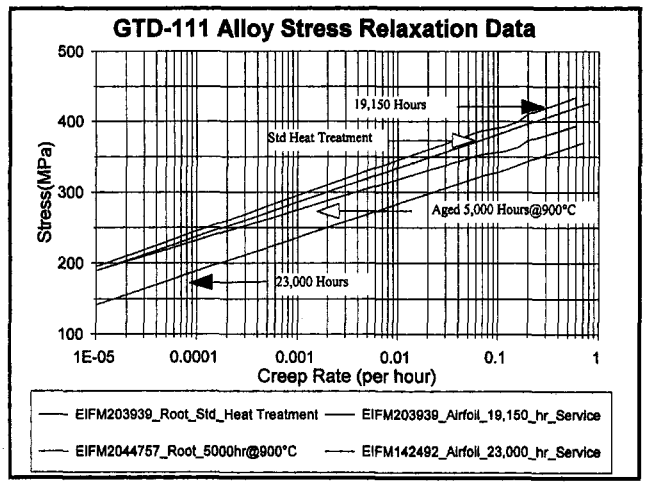

Fig. 8 A plot illustrating the strain rate data measured from the samples at 900°C and 0.4 percent total strain

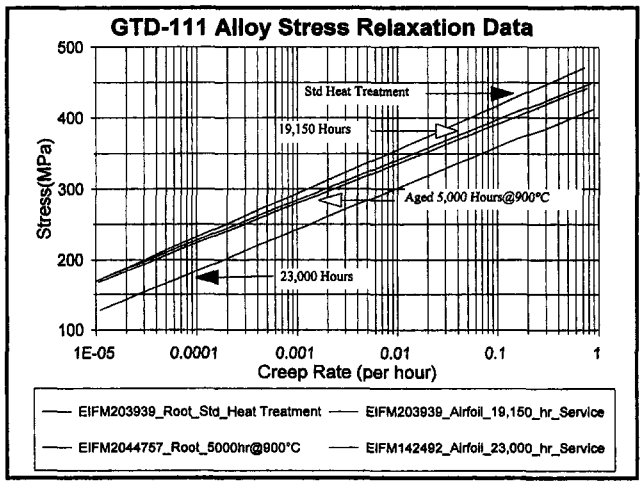

Fig. 9 A plot illustrating the strain rate data measured from the samples at 900°C and 0.8 percent total strain

2.3 Service Run Airfoils The stress relaxation tests completed at 850°C, indicated at both the 0.4 percent and 0.8 percent total prestrain conditions, that the material properties, expressed in terms of creep rate for a given stress, had increased by up to two orders of magnitude. The stress relaxation tests done at 900°C at both the 0.4 percent and 0.8 percent total strain also indicated an increase in creep rate, unlike the thermally aged material. However, the magnitude of the drop in properties measured at 900°C was not as large as in the tests performed at 850°C.

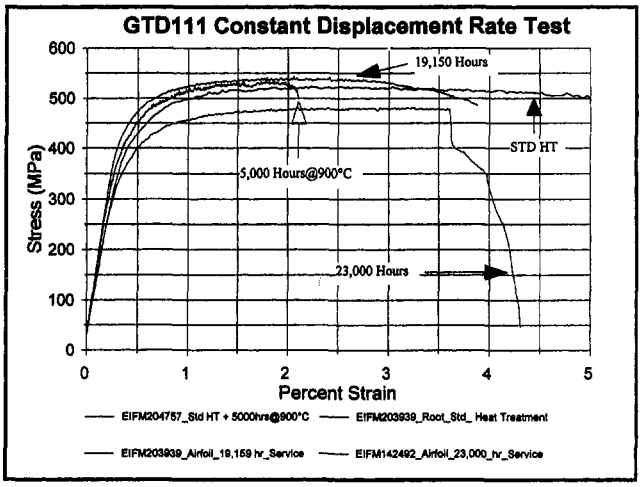

Fig. 10 A plot illustrating the constant displacement rate tensile data measured from the GTD111 alloy samples at 800°C and 1 percent strain per hour

3 Constant Displacement Rate Tensile Tests

Constant Displacement Rate tensile tests were performed after the stress relaxation test runs to provide a quantitative measure of the materials strain tolerance in each condition. The tests were performed at 800°C at a constant strain rate of 1 percent strain per hour. A plot of Stress versus Strain illustrating the test data is presented in Fig. 10.

The yield points of the tensile curves were approximately 30 percent lower than what would be typically measured in standard tensile tests of GTD111 alloy. This is normal and is a result of the creep component associated with the test.

The strain tolerance of the material thermally exposed for 5000 hours at 900°C was dramatically reduced compared to the material in the standard heat treated condition; however, the ultimate strength of the material had not deteriorated.

The service run buckets still possessed some creep ductility after operation. However, the ductility compared to the material in the standard heat treated condition was significantly reduced. The ultimate strength of the service run material removed from the hottest section of bucket EIFM142492 had deteriorated, while the ultimate strength of the material from the cooler section of bucket EIFM203939 had not deteriorated.

Discussion

1 Application of Stress Relaxation Testing in Metallurgical Life Assessment. When the stress relaxation data is expressed in terms of stress versus creep rate, the material creep properties in different conditions can be compared directly in terms of temperature capability of the new material in the fully heat treated condition (Fig. 11). In this plot, the stress relaxation tests performed at 850°C and 0.8 percent total prestrain conditions indicated that the material properties of the service run airfoil material had decreased by the equivalent of almost 40°C. Note that the GTD111 material properties in the standard heat treated condition are presented as the mean regression line of the two data sets together with the 95 percent confidence inter-

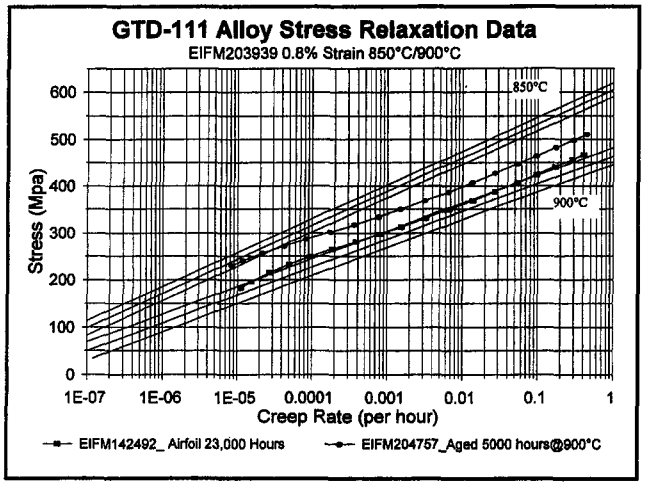

Fig. 11 A plot illustrating the drop in creep rate properties measured in the bucket airfoil in terms of temperature capability of "new" material in the standard heat treated condition

vals for individual readings and that the data sets were extrapolated to lower strain rates by two orders of magnitude.

To use this approach in life assessment applications, an estimate of the starting material properties generated by the original processing would be obtained by measuring the material properties in the root form at three temperatures that bracket the service temperature range of interest. The service run airfoil samples would then be measured at the two most relevant temperatures of interest. Plotting the data all together on one plot provides a direct estimate of the drop in creep rate properties in terms of temperature. Once the drop in temperature capability is known, the extrapolation procedure of choice can be used to analyze the data. The creep rates of different materials tested in this manner can also be compared directly. This provides the materials engineer with a very powerful tool for new alloy development and for alloy selection in critical applications.

The differences observed between the fully heat treated GTD111 alloy and the degraded materials were found to be sensitive to the testing parameters (stress, temperature, and prestrain). In the test run done at 850°C and 0.8 percent total prestrain, the stress versus strain rate curve for the microstructurally aged condition fell below the new material curve by almost an order of magnitude at the highest stress levels (Fig. 7). However, the two curves ultimately converged at the lower stress levels, which are more typical of those actually encountered by rotating turbine buckets. As noted earlier, this type of behavior is also observed in standard constant load creep rupture tests. However, creep rupture tests conducted at the lower stress levels would require thousands of hours to reach completion, which is clearly impractical for the purposes of conducting a life analysis.

If the same result had been obtained on airfoil material taken from a service-exposed component, it might be concluded that the higher creep rates (corresponding to reduced stress rupture lives) determined at higher stresses were simply indicative of the normal change in the microstructure of the material which is brought about by service exposure. However, the similarity in creep rates at the lower stress levels would be an indication that the material has not experienced a significant degree of (unexpected) creep damage which could otherwise make it incapable of reaching its intended design life.

In contrast, the sample removed from the hottest area of bucket serial number EIFM142492 showed even greater reductions in creep strength as compared to the "new" material. At 850°C and 0.8 percent total prestrain, the creep rates of the service-degraded airfoil material remained almost an order of magnitude higher than those of the new and furnace exposed samples, even at the lowest stress levels. In addition, the curve for the airfoil material did not show any indication of convergence with the two other samples. Based on the history of creep failures in this bucket design, it seems reasonable to conclude that these differences in measured properties can be attributed to the combined effects of microstructural aging and creep damage.

The differences in creep behavior at 900°C were not as pronounced as those observed at 850°C (Fig. 9). This is probably an indication of the influence of the test parameters on the alloy microstructure and the predominant creep mechanism that is controlling the creep rate of the material in the standard heat treated condition. The rate of dissolution of the secondary gamma prime particles are significantly higher at 900°C, and subtle changes occur in the grain boundary precipitate morphology. It has also been suggested that there may be a significant change in the activation energy for creep at temperatures close to those used in this investigation (Koul and Castillo, 1993). It is beyond the scope of this paper to discuss these effects in greater detail. We merely point out that, by specifying the appropriate test parameters, the stress relaxation test is a powerful tool, capable of distinguishing between different forms of material degradation that could be encountered by highly stressed gas turbine components.

Based on the observed differences in creep behavior, the stress relaxation test technique appears to be capable of distinguishing between the two limiting forms of material damage selected for this investigation. This is a very important and useful result since it indicates that the test could help to sort out the changes in creep strength as a result of (normal) microstructural evolution from the combined effects of microstructural evolution and strain related creep damage. This has historically been one of the uncertainties arising from the use of conventional creep rupture tests which are routinely performed as part of an overall metallurgical life assessment.

2 Estimates of Rupture Life Based on Stress Relaxation Data. The mechanism resulting in fracture in the shortest time or after the lowest strain determines the failure characteristics of the material. In terms of creep mechanisms, time to failure is a function or a measure of the material's creep strength (i.e., creep rate) while strain tolerance at failure is primarily a function of the microstructure.

Creep strength can be best thought of in terms of changes in the steady state or average creep rate ($\dot{\epsilon}$) with respect to time, stress, and temperature.

$$\dot{\epsilon} = f(t, \sigma, T) \tag{5}$$

The most widely accepted (used) expression for $\dot{\epsilon}$ is

$$\dot{\epsilon} = B\sigma^n e^{(-Qc/RT)}, \tag{6}$$

where B and n are constants, σ = stress, Q_c is the activation energy for creep (KJ/mole), R is the universal gas constant (8.314 KJ/mole), and T = temperature in °K.

Recognizing that the time for rupture, t_f, is also a function of the creep rate (Monkman Grant ($t_f \propto 1/\dot{\epsilon}$) and many more sophisticated models to follow), the rupture life can then be expressed as

$$1/t_f \propto \dot{\epsilon} = B\sigma^n e^{(-Qc/RT)} \tag{7}$$

The stress relaxation test can be thought of as taking a cross section through a series of constant load creep rupture curves at a set total strain and temperature. At 0.8 percent total strain, in most constant load creep rupture curves, the steady state creep rate has been reached. Thus in a single stress relaxation test an estimate of the steady-state creep rate is obtained over a large range of stress conditions.

The time to failure at any given stress and temperature combination can therefore be estimated directly from the creep rates measured in the stress relaxation test runs.

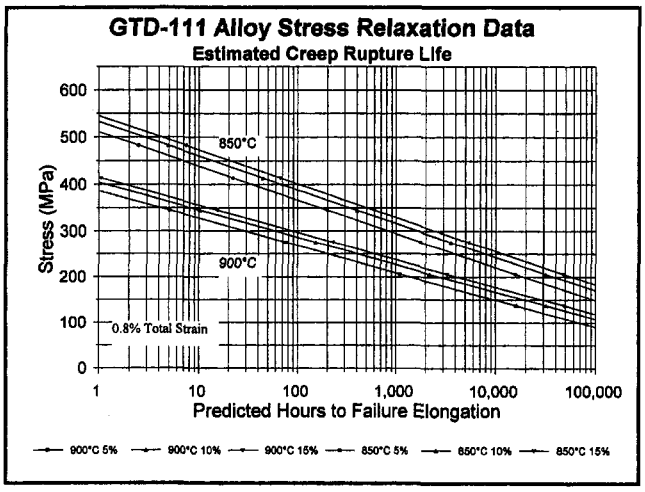

Fig. 12 A plot of stress versus estimated creep rupture life of the root form material in the standard heat treated condition based on 5 percent, 10 percent, and 15 percent failure elongations

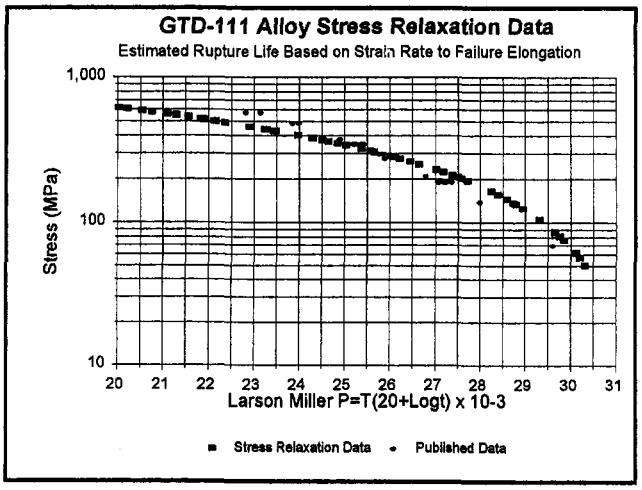

Fig. 14 A plot comparing a Larson–Miller curve created from estimated creep rupture life based on strain rate to failure elongation, to published GTD111 creep rupture data

The Monkman–Grant method of relating rupture lives to minimum creep rates is not really applicable here, since it is based on a simple correlation between minimum creep rates and rupture lives, as measured in constant load creep rupture tests. However, at the optimum total strain parameter of each alloy, the stress relaxation test provides a measure of the average steady state creep rate. This allows a more precise estimate of creep rupture life to be extracted from the data by dividing the expected or the minimum acceptable fracture elongation directly by the measured creep rate.

The polycrystalline GTD111 superalloy system examined in this study exhibit creep ductilities that range from a low of about 5 percent to approximately 15 percent when measured in standard constant load creep rupture tests. Thus a plot of stress versus calculated life based on 5 percent, 10 percent, and 15 percent elongation at any particular temperature would provide not only a measure of the expected life but also an indication of the possible scatter to be expected (Fig. 12). In fact, a universal plot of life versus strain rate can be produced and used (Fig. 13).

One could argue that the accuracy of the estimate of the time to rupture will be slightly nonconservative because no account has been made for the creep rates during primary and tertiary creep. However, because the creep rate measured by the stress relaxation technique is an average instantaneous value, the errors are minimized.

The data sets examined in this study indicate that rupture lives can be estimated to within a factor of three, which is quite remarkable since the data needed to estimate rupture properties can be generated and analyzed within a few weeks.

3 Correlation of Stress Relaxation Test Data With Time-Temperature Parameter Approaches. A Larson–Miller curve was produced by converting the rupture time estimates generated by this method into Larson–Miller format (Larson and Miller, 1952) and fitting the data into a best fit curve using a least squares regression model ($Y = \beta_0 + \beta_1 X + e$). Comparing the plot made using the estimated data with published Larson–Miller plots in the open literature (Schilke, 1992; Daleo, 1996) indicates that this technique can rapidly produce these plots with reasonably good accuracy, Fig. 14. This technique was also used to produce Larson Miller plots for two other widely used gas turbine blading alloys, IN-738LC and IN-939, Figs. 15 and 16, for which stress relaxation data had been previously obtained (Woodford et al., 1996).

Note that the plotted points in Fig. 14 below about 175 MPa, or strain rates below about $1 \times 10^{-5}\ \mathrm{h}^{-1}$ are based on extrapola-

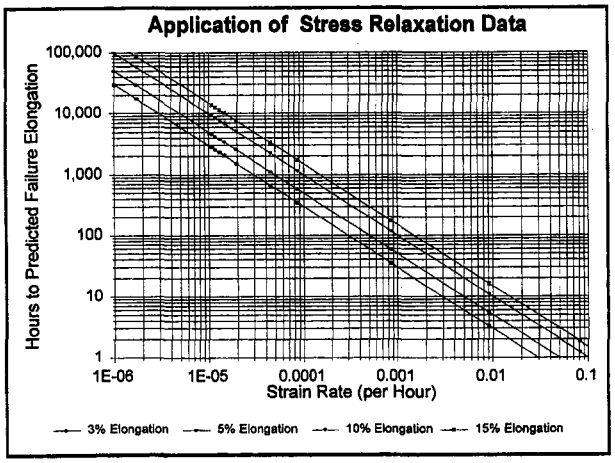

Fig. 13 A master plot of stress versus estimated creep rupture life based on 3 percent, 5 percent, 10 percent, and 15 percent failure elongations

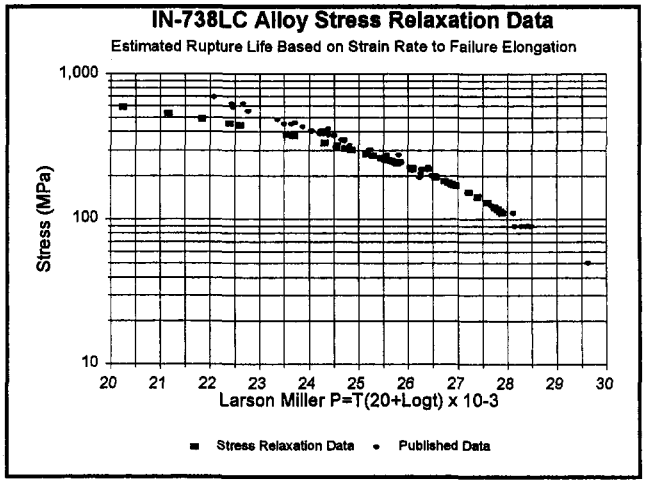

Fig. 15 A plot comparing an IN-738LC Larson–Miller curve created from estimated creep rupture life based on strain rate to failure elongation, to published IN-738LC creep rupture data

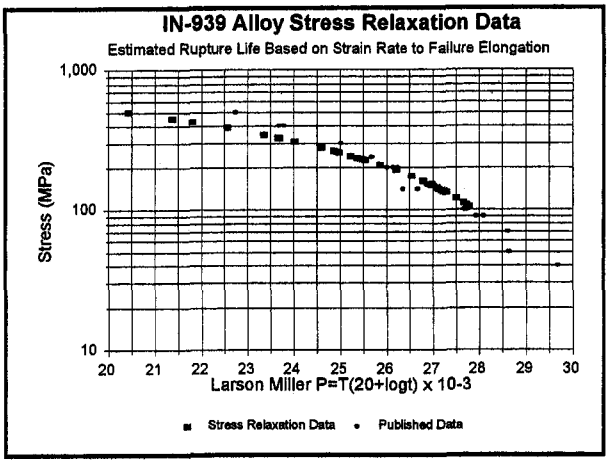

Fig. 16 A plot comparing an IN-939 Larson–Miller curve created from estimated creep rupture life based on strain rate to failure elongation, to published IN-939 creep rupture data

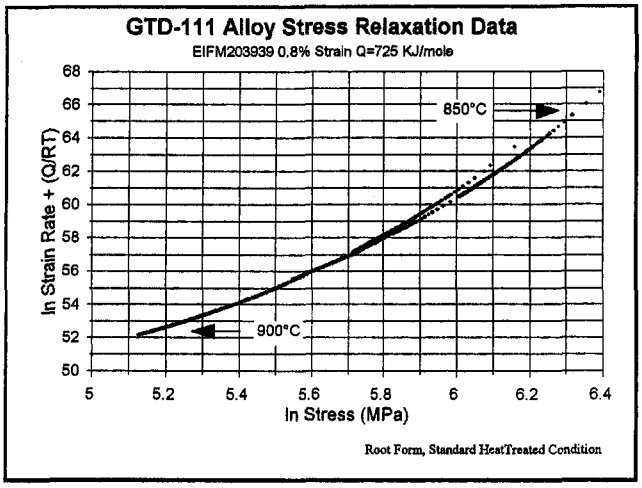

Fig. 18 A plot illustrating the GTD111 strain rate data at 850°C and 900°C for the standard heat treated condition with the temperature dependence of creep rate represented in terms of the activation energy for creep

tions of the linear fits to the experimental data shown in Figs. 7 and 9.

The creep rates measured at the various temperatures for any given total strain can be directly parameterized using common prediction algorithms such as the Larson Miller Parameter,

$$P = T(C - \log_{10}\dot{\epsilon})$$

described by Conway (1965) and illustrated in Fig. 17.

Alternatively, the creep rate plots can be parameterized using Eq. (6) ($\dot{\epsilon} = B\sigma^n e^{(-Qc/RT)}$). By converting the equation into logarithmic form, an estimate of the activation energy for creep can be obtained by systematically varying the activation energy for creep until a plot of $\ln \dot{\epsilon} + Q_c/RT$ versus $\ln \sigma$ aligns the creep rate curves at the various test temperatures into one line. The slope of this line provides an estimate of n directly while the intercept provides an estimate of B in the form of $\ln B$.

$$\ln \dot{\epsilon} = \ln B + n \ln \sigma - Q_c/RT \qquad (8)$$

The data from the sample in the standard heat treated condition tested at 850°C and 900°C at 0.08 percent total strain was parameterized in this form and is presented in Fig. 18. The activation energy for creep was estimated at 725 KJ/mole and from the plot, the constants B and N were estimated at 3.9512 and 10.2, respectively. Inserting the estimation of the activation energy and the constants back into Eq. (6), the creep rates were then calculated and compared to the measured creep rates from the stress relaxation tests Fig. 19. A reasonable approximation of the original test data was obtained indicating that with a little more effort a better creep model could be established to use the creep relaxation data.

Summary and Conclusion

When combined with our comprehensive metallurgical evaluation methods for gas turbine failure analysis and life assessment, the stress relaxation test methodology can be a very powerful tool in helping to quantify degradation of creep properties in service run components. The speed at which the testing and analysis can be performed now makes realistic life assessment and repair replace decisions possible during turbine overhauls.

The unique ability to measure changes in creep rate over a large stress range, enabled the technique to distinguish changes in creep strength due to (normal) microstructural evolution from the combined effects of microstructural evolution and strain related creep damage.

The creep rate data measured in the stress relaxation tests can be used in its direct form, where the creep rates of the

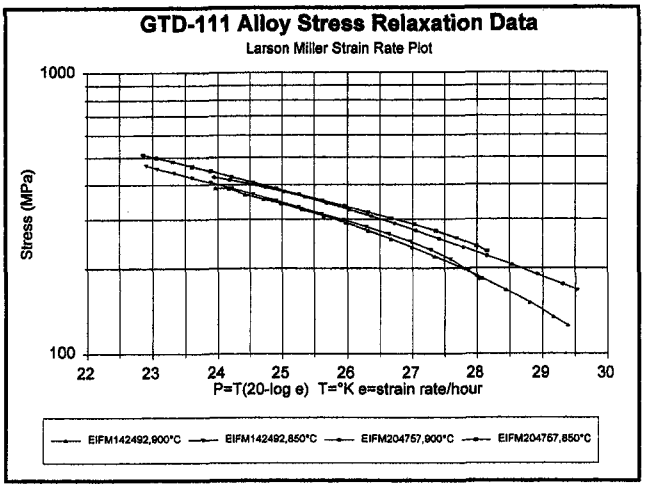

Fig. 17 A Larson–Miller strain rate plot illustrating the GTD111 strain rate data for the service run condition and the test sample exposed for 5000 hours at 900°C

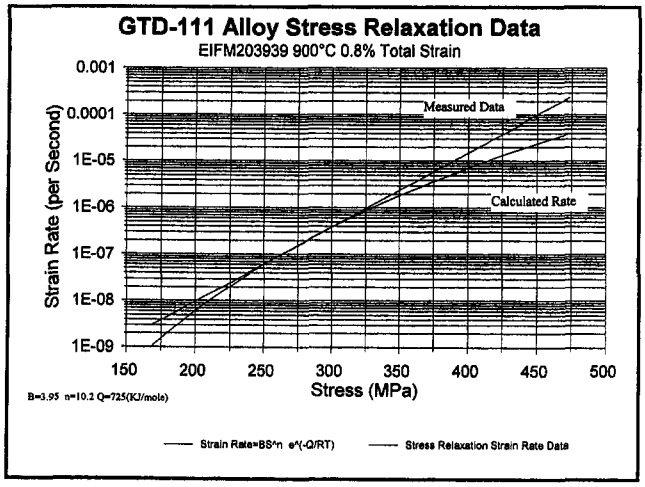

Fig. 19 A plot illustrating the calculated strain rate ($\dot{\epsilon} = B\sigma^n e^{(-Qc/RT)}$) versus the strain rate measured in the stress relaxation test for the standard heat treated condition at 900°C/0.8 percent strain

material in different conditions are compared directly in terms of temperature capability or by estimating the time to failure at any given stress and temperature combination. The data sets examined in this study indicate that rupture lives can be estimated within a factor of 3.

The stress relaxation tests performed on the GTD111 material removed from the old style 11 hole bucket designs revealed that, compared to the material properties in the standard heat treated condition, the creep rate properties in the bucket airfoil were deteriorating in service. The stress relaxation tests done at 850°C at 0.8 percent total strain indicated that the material properties had decreased by an order of magnitude or approximately 40°C.

The direct measurement of the creep strength using the stress relaxation test method described in this paper provides the component designer with a very efficient way of comparing creep strengths of different materials and also accurately predicting failure times. The analysis techniques can be used to examine a wide range of components (blades, vanes, discs, etc.) from all makes of turbines, as well as in numerous other areas of endeavor where creep problems exist. For example, the test methodology can be used to assess the quality and the amount of material rejuvenation that actually occurs during component repairs involving regenerative HIP and reheat treatment cycles or to examine the strength of welded or brazed, joints and thermal spray powder build ups.

Acknowledgments

This work was partially funded by the National Research Council of Canada's Industrial Research Assistance Program.

References

1 Conway, J. B., 1969, *Stress-Rupture Parameters: Origin, Calculation and Use,* Gordon and Breach, Science Publishers, New York.

2 Daleo, J. A., and Boone, D. H., 1996, "Metallurgical Evaluation Techniques In Gas Turbine Failure Analysis and Life Assessment," *Failures 96, Risk, Economy and Safety, Failure Minimization and Analysis,* R. K. Penny, ed., ISBN 90 5410 8231.

3 Daleo, J. A., and Wilson, J. R., 1996, "GTD111 Alloy Material Study," ASME Paper 96-GT-520.

4 Daleo, J. A., and Boone, D. H., 1997, "Failure Mechanisms of Coating Systems Applied to Advanced Turbine Components," ASME Paper 97-GT-486.

5 Koul, A. K., and Castillo, R., 1993, "Creep Behavior of Industrial Turbine Blade Materials," *Advanced Materials and Coatings for Combustion Turbines*" ASM International, ISBN 0-87170-487-0.

6 Larson, F. R., and Miller, J., 1952, *Trans. ASME,* Vol. 74, p. 765.

7 Lee, D., and Hart, E. W., 1971, "Stress Relaxation and Mechanical Behavior of Metals," *Metallurgical Transactions,* Vol. 2, pp. 1245–1248.

8 Monkman, F. C., Grant, N. J., 1956, "An Empirical Relationship Between Rupture Life and Minimum Creep Rate in Creep Rupture Tests," *Proc. ASTM,* Vol. 56, pp. 593.

9 Oding, I. A., et al., 1959, *Creep and Stress Relaxation in Metals,* (English translation by A. J. Kennedy) Oliver and Boyd Limited, London.

10 Schilke, P. W., Foster, A. D., Pepe, J. J., and Beltran, A. M., 1992, "Advance Materials Propel Progress in Land-Base Gas Turbines," *Advanced Materials And Processes,* ASM International, Vol. 4, No. 92, pp. 22–30.

11 Sims, C. T., Stoloff, N. S., Hagel, W. C., eds., 1987, *Superalloys II,* Wiley-Interscience, New York.

12 Soderberg, C. R., 1936, "The Interpretation of Creep Tests for Machine Design," *Trans. ASME,* Vol. 58, p. 733.

13 Woodford, D. R., Van Steele, K., Amberg, K., and Stiles, D., 1992, "Creep Strength Evaluation for IN 738 Based on Stress Relaxation," *Superalloys 1992,* Antolovich S. D. et al., eds., The Minerals, Metals and Materials Society, Warrendale, PA.

14 Woodford, D. R., Daleo, J. A., and Wilson, J. R., 1996, "Analysis of Service Run Ruston TB5000 Components," 96 Mpa/W&D 01, internal report, Materials Performance Analysis Inc., Santa Barbara, CA.

Improved Performance Rhenium Containing Single Crystal Alloy Turbine Blades Utilizing PPM Levels of the Highly Reactive Elements Lanthanum and Yttrium

D. A. Ford

K. P. L. Fullagar

H. K. Bhangu

Rolls-Royce plc,
CRDF, Postal Code GP1-6,
P.O. Box 3,
Gypsy Patch Lane,
Filton, Bristol, BS12 7QE,
United Kingdom

M. C. Thomas

P. S. Burkholder

P. S. Korinko

Allison Engine Company,
Rolls-Royce plc,
Indianapolis, IN

K. Harris

J. B. Wahl

Cannon-Muskegon Corporation,
SPS Technologies, Inc.,
Muskegon, MI

Turbine inlet temperatures have now approached 1650°C (3000°F) at maximum power for the latest large commercial turbofan engines, resulting in high fuel efficiency and thrust levels approaching or exceeding 445 kN (100,000 lbs.). High reliability and durability must be intrinsically designed into these turbine engines to meet operating economic targets and ETOPS certification requirements. This level of performance has been brought about by a combination of advances in air cooling for turbine blades and vanes, computerized design technology for stresses and airflow, and the development and application of rhenium (Re) containing, high γ' volume fraction nickel-base single crystal superalloys, with advanced coatings, including prime-reliant ceramic thermal barrier coatings (TBCs). Re additions to cast airfoil superalloys not only improve creep and thermomechanical fatigue strength but also environmental properties, including coating performance. Re slows down diffusion in these alloys at high operating temperatures [1]. At high gas temperatures, several issues are critical to turbine engine performance retention, blade life, and integrity. These are tip oxidation in particular for shroudless blades, internal oxidation for lightly cooled turbine blades, and TBC adherence to both the airfoil and tip seal liner. It is now known that sulfur (S) at levels <10 ppm but >0.2 ppm in these alloys reduces the adherence of α alumina protective scales on these materials or their coatings by weakening the Van der Waal's bond between the scale and the alloy substrate. A team approach has been used to develop an improvement to CMSX-4[1] alloy which contains 3 percent Re, by reducing S and phosphorus (P) levels in the alloy to <2 ppm, combined with residual additions of lanthanum (La) + yttrium (Y) in the range 10–30 ppm. Results from cyclic, burner rig dynamic oxidation testing at 1093°C (2000°F) show thirteen times the number of cycles to initial alumina scale spallation for CMSX-4 [La + Y] compared to standard CMSX-4. A key factor for application acceptance is of course manufacturing cost. The development of improved low reactivity prime coats for the blade shell molds along with a viable, tight dimensional control yttrium oxide core body are discussed. The target is to attain grain yields of single crystal CMSX-4 (ULS) (La + Y) turbine blades and casting cleanliness approaching standard CMSX-4. The low residual levels of La + Y along with a sophisticated homogenisation/solutioning heat treatment procedure result in full solutioning with essentially no residual γ/γ' eutectic phase, Ni (La, Y) low melting point eutectics, and associated incipient melting pores. Thus, full CMSX-4 mechanical properties are attained. The La assists with ppm chemistry control of the Y throughout the single crystal turbine blade castings through the formation of a continuous lanthanum oxide film between the molten and solidifying alloy and the ceramic core and prime coat of the shell mold. Y and La tie up the <2 ppm but >0.2 ppm residual S in the alloy as very stable Y and La sulfides and oxysulfides, thus preventing diffusion of the S atoms to the alumina scale layer under high temperature, cyclic oxidising conditions. La also forms a stable phosphide. CMSX-4 (ULS) (La + Y) HP shroudless turbine blades will commence engine testing in May 1998.

Introduction

The assumption that S is the dominant element in degrading the protective aluminum oxide scale is supported by a number of researchers [1–3, 5–11]. The beneficial effect of Y additions has been identified by Aimone and McCormick [5] and is considered to be due to the combination of this element with S, forming Y oxysulphide ($Y_2O_2S_2$). The available data for the Gibbs standard free energy of formation at 1100°K gives the following values. (12)

$$\Delta G \quad Y_2O_2S = -354 \text{ k cal/g mol} \quad (4)$$

$$\Delta G \quad YS = -97.4 \text{ k cal/g mol} \quad (5)$$

Contributed by the International Gas Turbine Institute and presented at the International Gas Turbine and Aeroengine Congress and Exhibition, Stockholm, Sweden, June 2–5, 1998. Manuscript received by the ASME Headquarters April 1, 1998. Paper No. 98-GT-371. Associate Technical Editor: R. Kielb.

[1] CMSX-4® is a registered trademark of Cannon-Muskegon Corporation.

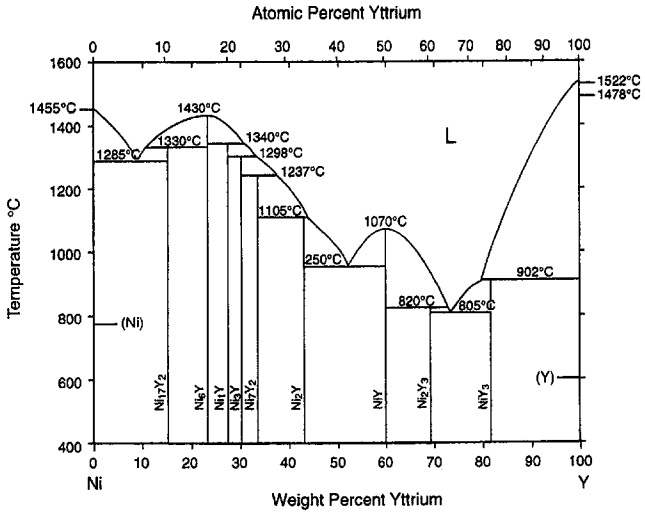

Fig. 1 Equilibrium diagram of Ni–Y

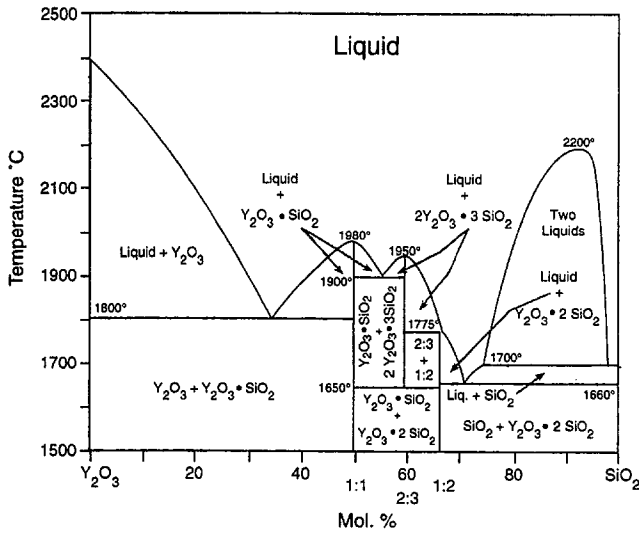

Fig. 2 Equilibrium diagram of Y_2O_3–SiO_2

The suppression of the detrimental effect of S will therefore require the addition of Y to a level at least 6 times the S content based stoichiometrically on the ratio of atomic weights viz. S 32, Y 89. For superalloys containing a nominal 5 ppm of S, an addition of at least 30 ppm of Y is required. At this level, which exceeds the solubility limit in CMSX-4 alloy, there is a significant risk of internal incipient melting since Y forms a series of eutectics with nickel from 1285°C to 805°C (Fig. 1).

Manufacturing Technology

The manufacturing difficulties associated with Y additions are well known [4] and it is necessary to make significant Y additions to the alloy charge to give sufficient residual Y in the SX casting. Work reported by Aimone (5) suggest that only 10 percent at best is retained in round test bars. Turbine blades with high surface area/volume ratios and containing cores will be expected to retain significantly less than round bars.

The reason for this loss of Y includes evaporation from the melt, reaction with the mold, and reaction with the core material. Considering loss by evaporation, the equilibrium vapor pressure of Y at 1475°C is 7.4×10^{-4} m bar and 1.6×10^{-3} m bar at 1525°C [15]. Since a typical casting vacuum is around 5×10^{-4} m bar there is a possibility of evaporation, particularly if the vacuum pressure is dynamic.

Turning to Y loss through shell and core reaction, both materials contain silica and from thermodynamic considerations [11] it is clear that Y will reduce silica to yttria, which in turn will form Y_2O_3 $2SiO_2$ (Fig. 2).

$$\Delta G\ SiO_2 = -538\ \text{kj/g mol}\ (1727°C)$$

$$\Delta G\ Y_2O_3 = -1348\ \text{kj/g mol}\ (1727°C)$$

and

$$3SiO_2 + 4Y \rightarrow 2Y_2O_3 + 3Si$$

A practical solution is to vacuum induction melt and refine the SX alloy using high quality, low S and P virgin raw materials, and ultra-low S and P containing refractories. The evaluation and development work at RR to establish a low cost manufacturing method for Y additions used CMSX-4 (nominal composition shown in Table 1) melted by CM with a nominal S level of approximately 1.5 ppm. To achieve the required combination with Y, 7–10 ppm of this element is needed to be retained in the single crystal (SX) castings.

Evaluation work has been carried out by the RR research foundry to investigate the extent of Y loss in the manufacture of SX turbine blades. The work involved the casting of turbine

Table 1 Density 8.70 kg/dm³ CMSX-4 Alloy Nominal Composition Wt %

Ni	Base
Cr	6.5
Co	9
Mo	.6
Ta	6
W	6
Re	3
Al	5.6
Ti	1.0
Hf	.1

Nomenclature

Ce = cerium
ETOPS = extended over water, twin engine certification requirements
k cal/g mol = kilo calories/per gram mol
kj/g mol = kilo joules/per gram mol
kN = kilo Newton
La = lanthanum
LCF = low cycle fatigue
m bar = milli bars
mg = milligram
mm = millimeter
Ni = nickel
O = oxygen
P = phosphorus
ppm = part per million
Re = rhenium
RE = reactive elements
S = sulfur
SFC = specific fuel consumption
SX = single crystal
TBC = thermal barrier coating
ULS = ultra low sulfur
Y = yttrium
Zr = Zirconium
α = alpha
μm = micro meters
γ = gamma phase
γ' = gamma prime phase
ΔG = free energy of formation

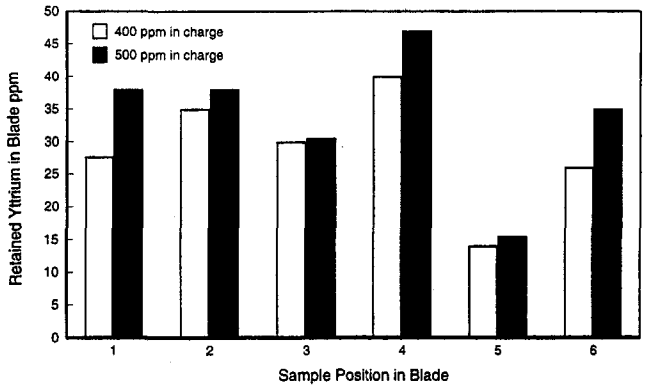

Fig. 3 Retained yttrium in solid blades

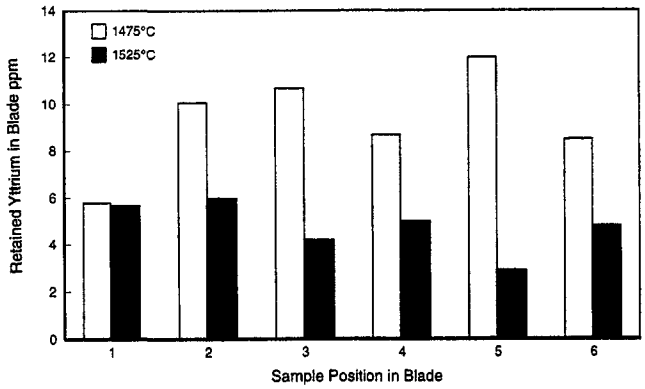

Fig. 4 Retained yttrium in cored blades

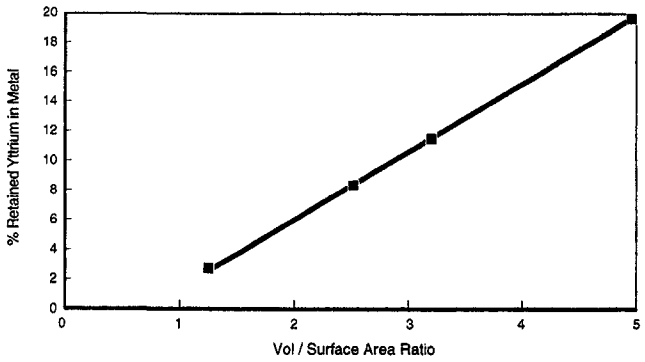

Fig. 5 Effect of surface area on level of retained yttrium

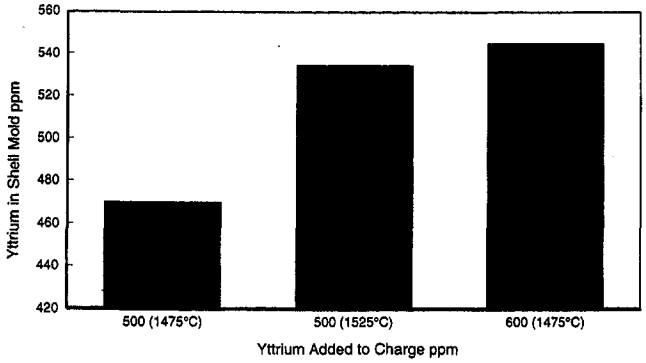

Fig. 6 Yttrium in shell molds cast a different temperatures

Test Piece (25 mm dia)	Residual Quantity ppm	
	Yttrium	Lanthanum
CMSX-4 + Y (400 ppm)	30	–
CMSX-4 + La (500 ppm)		70
CMSX-4 + La (180 ppm)		26
CMSX-4 + La (100 ppm) + Y (75 ppm)	5	9

Fig. 7 Comparitive Retention of Y, La, and La + Y in round SX test bars

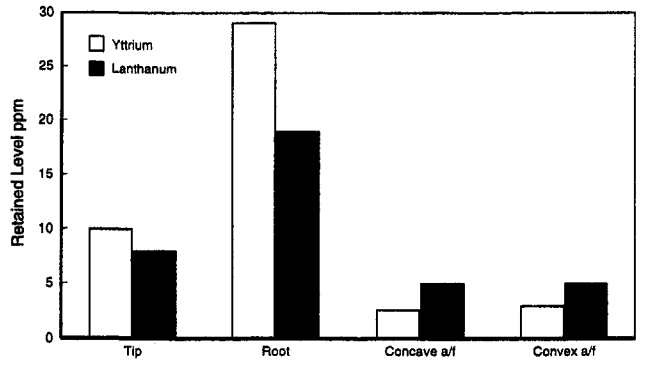

Fig. 8 Retained yttrium and lanthanum in turbine blades

blades with and without ceramic cores under different casting conditions and analyzing the residual Y in the casting and the ceramic mold. The following variables were investigated, using constant conventional molding materials based on silica, zircon, and alumina: (i) Y charge additions of 400 ppm and 500 ppm; and (ii) mold/cast temperatures of 1475°C and 1525°C.

The results are shown in Figures 3, 4, 5 and 6 and the relationship between the amount of retained Y and the volume to surface area relationship shown in Fig. 5. These results clearly show that the loss of Y is due to reaction with ceramics used in the casting process. However, provided the casting temperature can be kept to a minimum, it is possible to retain sufficient Y in low S alloys without resorting to special ceramics such as yttria molds.

Additions of La were carried out to establish if this element could be retained in SX castings at a higher level than an equivalent amount of Y. The results of analysis from round test bars showed a retention level of approximately twice that of Y. Further trials with additions of both Y and La gave similar results. The amount of La added was the same atomic percentage of Y. The results from these trials are summarised in Fig. 7.

To establish if the results from the test bars could be applied to actual turbine blades, a number of the same design as used for the Y trials were SX cast. The aim was to produce the same levels of Y and La in the blades. To achieve this, 200 ppm of Y and 160 ppm of La were added to the remelt bar charge. Typical results from the analysis of the castings are shown in Fig. 8.

The results from both the CMSX-4 + Y and CMSX-4 + Y + La trials show that it is possible to retain these elements at a level sufficient to reduce the detrimental effect of S using conventional foundry materials and practice. However, the effect of cores is significant as this material appears to be responsible for most of the dilution of Y and La (Figs. 3 and 4). This problem has been addressed through the development of core materials and cores have been manufactured in both alumina and yttria. Of these two materials, yttria offers the most advan-

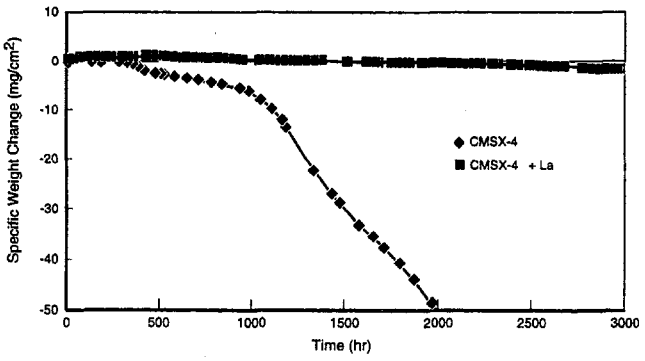

Fig. 9 1038°C (1900°F) dynamic oxidation test results for Bare CMSX-4 with La addition and without

Table 2 Life of oxidation tested CMSX-4 with and without reactive element additions. Life is based on the time to lose approximately 10 mg/cm², which corresponds to roughly 25 μm based on density considerations.

CMSX-4 and reactive element addition	Time (hours) to reach 10 mg/cm² (25μm)
1038°C (1900°F)	
None	1100
La	>3000
1093°C (2000°F)	
None	100
La	950
Y + La	1100
Ce	>300
Y	600
1149°C (2100°F)	
None	30
La	~520
La + Y	350
Ce	410

tage due to its chemical inertness and ease of removal (15) by core leaching. Work to further investigate this material with respect to Y and La ppm chemistry control and minimisation of grain defects in the SX cored airfoil castings is continuing.

Burner Rig Oxidation Testing

Test Procedure. To initially evaluate the potential benefits for oxidation performance of CMSX-4 with highly reactive element (RE) additions, cyclic dynamic oxidation tests were conducted. Samples of 5.5 mm diameter by 115 mm long were machined from SX test bars. The CMSX-4 alloy used to produce the test bars with and without RE additions contained <2 ppm S. The samples were lightly grit blasted prior to testing. The samples were tested in a Becon burner rig which is comprised of a modular combustor in which the JP-5 fuel is injected into the primary region, mixed with air, and ignited. Secondary air is used to dilute the combustion products to control the burner outlet temperature. The total pressure of the air used in the primary was fixed, yielding approximately the same gas Mach number. During the test, the pins were removed from the flame and blasted with room temperature air for five minutes following every hour of flame testing.

The oxidation progression was monitored visually and gravimetrically. The samples were photographed after intervals during which significant amounts of oxidation had occurred. The samples were also weighed to the nearest 0.01 mg. The mass change from the initial mass was determined and divided by the areas which were exposed to the hottest portion of the flame, a length of approximately 25 mm. The specific mass change was plotted with a microscopic examination of the test articles occurring after the final exposure. Tests with La doped CMSX-4 were conducted at 1038°C, 1093°C, and 1149°C (1900°F, 2000°F, and 2100°F), while the other reactive element additions were tested at 1093°C and 1149°C.

Oxidation Results. CMSX-4 + La tested at 1038°C (1900°F) exhibits approximately a 15 times increase in life to zero crossover of specific weight change compared to conventional CMSX-4; no comparison can be made regarding the life to a fixed mass loss since the RE doped sample was not tested for a sufficiently long enough time to reach sizable mass losses. These results are shown in Fig. 9. The doped sample did not exhibit significant amounts of surface roughening after 3000 hours of exposure compared to the localized attack which occurred on the standard CMSX-4 alloy surface after only 1000 h.

The trend of increased life of the RE doped alloys over the conventional chemistry alloy can further be seen in Fig. 10, which shows the plot of the gravimetric results for the 1093°C (2000°F) test. All of the reactive element doped samples are included on this plot. These samples include CMSX-4 + Y, La, (La + Y), and Ce in addition to the conventional CMSX-4 alloy. The data clearly reveal increased oxidation resistance with the addition of the RE. The lives relative to a sample loss of approximately 25 μm of metal, calculated based on the density of the alloy, are presented in Table 2. The benefit of reactive elements also depends on the type of RE that is added. At 1093°C the Y or La additions alone are not as potent as the Y + La dopants combined. The effect of the Ce addition cannot be ascertained due to the short time the sample was exposed (<400 h.).

Oxidation of the samples at 1149°C (2100°F) reveals a slightly different result regarding the benefits of RE dopants, as shown in Figure 11. Conventional CMSX-4 clearly does not have adequate oxidation resistance at this temperature in this test as evidenced by its loss of approximately 25 μm in less than 30 hours. Samples with RE additions exhibit lives at least ten times greater than conventional CMSX-4. As indicated in the graphs and Table II. The ranking of the additions from worst to best is as follows: (La + Y), Ce and La at 1149°C.

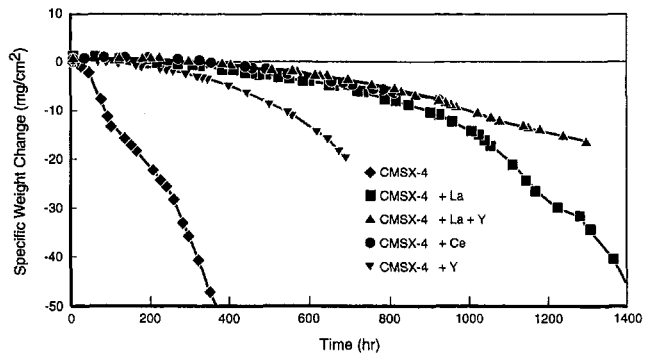

Fig. 10 1093°C (2000°F) dynamic oxidation test results for Bare CMSX-4 with RE additions and without

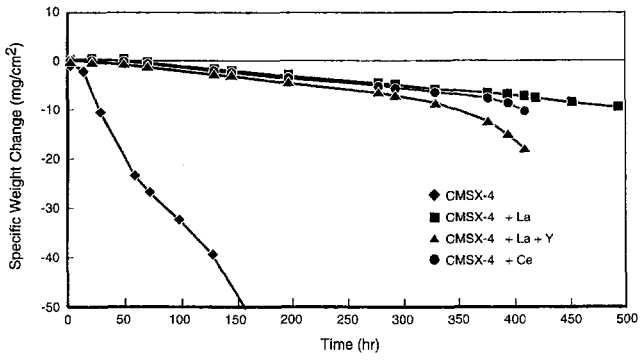

Fig. 11 1149°C (2100°F) dynamic oxidation test results for Bare CMSX-4 with RE additions and without

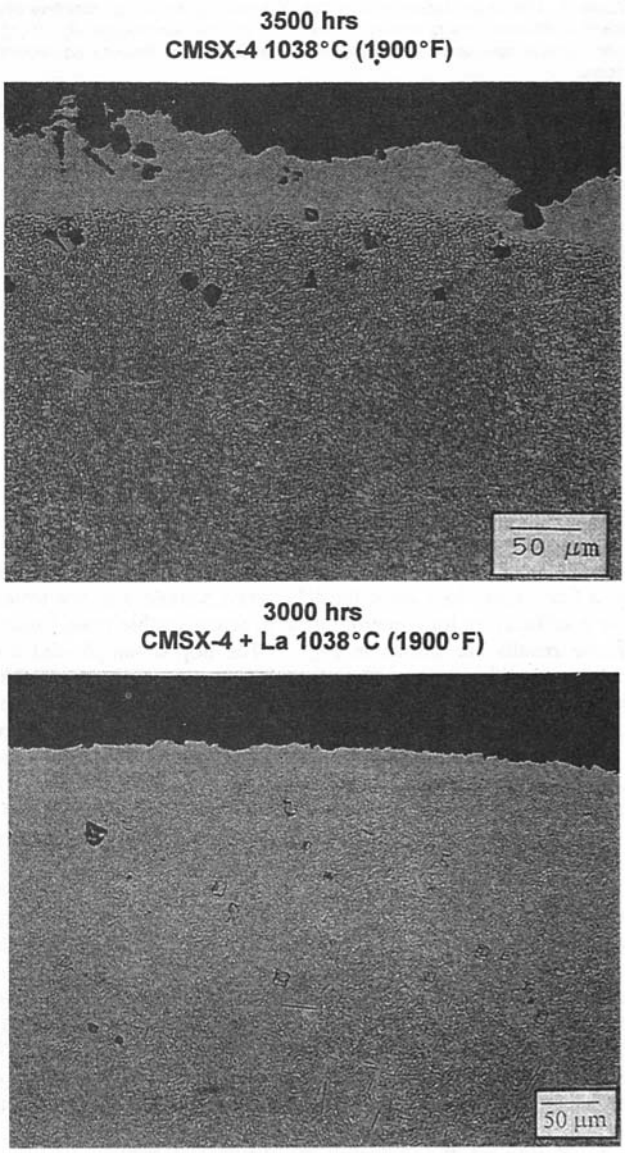

Fig. 12 Burner rig post-test microstructures

Summary. The oxidation behavior of bare CMSX-4 can be dramatically improved by the addition of highly reactive elements (REs). The factor of improvement varies from in excess of 3 to approximately 13 depending on the elemental addition and exposure temperature. There is some variability of the effect of the RE. This could be due to minor variations in the actual RE content in the test pieces. Only one sample from each mold was analyzed for chemistry.

Figure 12 shows the change in sample surface morphology of CMSX-4 and CMSX-4 + La following burner rig cyclic oxidation testing at 1038°C (1900°F) for 3000–3500 h. These micrographs clearly demonstrate that fewer voids and pores are present in the La doped sample. In addition, the amount of surface region alloy depletion is appreciably less.

Turbine Engine Application and Testing

The design of commercial turbofan engines continues to improve in response to the needs of the extremely competitive airline market. Designs that weigh less and have higher fuel efficiencies are required to keep a competitive advantage, and, thus, during recent years both the compressor delivery and turbine rotor inlet temperatures have continued to rise. While improved cooling schemes are employed, the demand for higher fuel efficiencies quickly dictates the minimum required cooling air for the turbine blades and as a result blade metal temperatures have been pushed to new levels.

In addition to fuel efficient, light weight engines, the military and commercial aero turbine engine markets also need engines that will remain on wing for extended overhaul intervals and drive down operating cost. As a result the design must carefully consider durability and specific fuel consumption (SFC) (temperature margin) deterioration rates. One of the single most dominating factors in turbine performance is high pressure turbine blade tip clearance and this clearance can easily be impacted by the oxidation of the blade tip [16] in case of the shroudless blades and of tip seal liners for both shrouded and shroudless blades. Tip coatings are often used to provide environmental protection but they can present bonding and durability problems particularly if the blade and the tip seal liners touch. The optimum cost effective solution is to develop a method of improving the oxidation characteristics of the bare blade alloy itself, thus providing full oxidation protection for the entire tip configuration. The addition of La + Y to CMSX-4 shows intriguing promise of accomplishing this goal by reducing base metal oxidation rates by an order of magnitude combined with improved SX castability and product casting yield compared to the use of Y alone. Additionally, the application of CMSX-4 to the tip seal liners has enabled the plastic deformation of the component to be minimized, resulting in small tip clearances and resultant improved engine efficiency.

Internal oxidation of air-cooled turbine airfoils also represents a technical challenge in modern gas turbine engines. The cooling air temperatures have risen with increased pressure ratio engines and the second generation single crystal alloys are allowing higher metal temperatures before being limited by creep or stress rupture strength. This can lead to internal oxidation, since many turbine blades operate with protective coatings only on the external surfaces of the airfoil. Coating internal passages is possible; however, there are several unique challenges: (1) blocking and plugging of small passageways, (2) embrittlement due to the coating leading to low cycle fatigue (LCF) failures, and (3) verification of coating coverage and consistency inside the component. A more robust, lower cost and consistent design can be accomplished if the base material has high inherent oxidation protection, as shown with CMSX-4 with La + Y.

Further advances are being made today in commercial turbofan engines by the addition of thermal barrier coatings. A recent design modification to an existing Allison turbofan engine realized 125°C (225°F) temperature reduction to the airfoil metal temperature without any increase in the cooling air. In another Rolls-Royce application, the prime-reliant use of TBC has enabled both a reduction in the cooling air flow and effective metal temperature. However, chipping and spallation of the ceramic coating can become critical failure modes if the airfoil cooling levels have been determined relying on the TBC. This concern has forced several engines to use TBCs as a non-prime-reliant system. While this can offer significant durability enhancements it does not allow the engine cycle temperature to be raised and thus the full benefits of the TBC are not realized. CMSX-4 with La + Y has demonstrated improved adherence with coatings, and, therefore, may be instrumental in allowing thermal barrier coatings to be used on CMSX-4 as prime reliant with greater confidence.

Finally, in either prime or non-prime-reliant application, there is always the possibility of local loss of TBC due to foreign object damage. The local heat transfer to the damaged area is enhanced due to surface roughness and out-of-wind step. In this event it is essential that the substrate possesses excellent high temperature oxidation properties to enable the engine to stay on-wing for an interval to suit the airline or military operator and yet be repairable.

Single crystal HP turbine blades in CMSX-4 with La + Y will commence engine testing in May 1998.

Conclusions

The RE combination ppm addition of La + Y to CMSX-4 alloy has shown the best combination of manufacturability, RE ppm chemistry control throughout the SX turbine blade and burner rig cyclic oxidation results where the life of bare CMSX-4 can be improved by a factor as large as approximately 10.

Turbine engine testing in several different applications scheduled for 1998 and 1999 will determine the value of this technology to turbine engine performance and life cycle costs.

References

1 Broomfield, R. W., Thomas MC, and Harris, K., 1997, "Development and Turbine Engine Performance of Three Advanced Rhenium Containing Superalloys for Single Crystal and Directionally Solidified Blades and Vanes," paper presented at the ASME Turbo Expo '97, 2–5 June 1997 Orlando, Fl.

2 Smeggil, J. G., et al., 1985, "Reactive Element—Sulphur Interaction and Oxide Scale Adherence," *Met. Trans.*, Vol. 16A, pp. 1164–1166.

3 McVay, R. T., Williams, P., Meier, G. H., Pettit, F. S., and Smialek, J. L., (NASA Lewis), "Oxidation of Low Sulfur Single Crystal Nickle-Base Superalloys," *Superalloys,* TMS Proc. Seven Springs, PA. pp. 807–816.

4 Smialek, J. L., Pettit, F. S., et al., 1996, "The Control of Sulfur Content in Nickel-Base Single Crystal Superalloys and Its Effects on Cyclic Oxidation Resistance," paper presented at the 8th International Symposium on Superalloys sponsored by the Minerals, Metals, and Materials Society, Seven Springs, PA, September 22–26, 1996.

5 Aimone, P. R., McCormick, R. L., "The Effects of Yttrium and Sulphur on the Oxidation of an Advanced Nickel Base Superalloys," paper presented at the 8th International Symposium on Superalloys.

6 Mickle, T.-H., 1994, "Environmental Resistance of Desulfurized Nickel-Based Alloys," paper presented at the AeroMat '94 ASM Int., June, 6–9, 1994.

7 Smeggil, J. G., Funkenbusch, A. W., Bornestein, N. S., 1986, "A Relationship Between Indigenous Impurity Elements and Protective Oxide Scale Adherence Characteristics," *Met. Trans.*, Vol. 17a, pp. 923–932.

8 Goldschmidt, D., Marchionni, M., and Maldini, M., 1992, "High Temperature Mechanical Properties of CMSX-4 + Yttrium Single-Crystal Nickel-Base Superalloy," *Superalloys,* TMS Proc., Seven Springs, PA., pp. 775–784.

9 Hondros, F. D., 1989, "The Magic of Active Elements in the Oxidation Behavior of High Temperature Metals and Alloys," P. Lang, ed., Vol. XI.

10 Thomas, M. C., et al., Harris, K., et al., 1994, "Allison Manufacturing, Property, and Turbine Engine Performance of CMSX-4® Single Crystal Airfoils," paper presented at the COST 501 Conference, Materials for Advanced Engineering, Liege, October 3–6, 1994.

11 Korinko, P. S., et. al., 1996, "Coating Characterization and Evaluation of Directionally Solidified CM 186 LC® and Single Crystal CMSX-4®," paper presented at the ASME Turbo Expo '96, NEC, Birmingham UK, June 10–13, 1996.

12 Gschneider, K. A., et al., 1992, "Thermochemistry of the Rare Earth Carbides, Nitrides and Sulphides," Rare Earth Information Centre, Ames, Iowa.

13 Gschneider, K. A., et al., 1973, "Thermochemistry of the Rare Earths," Rare Earth Information Centre, Ames, Iowa.

14 *Smithells Metal Reference Book,* 1972, 7th ed., Butterworth-Heinmann Ltd., Oxford.

15 British Patent Application number 9714135.2.

16 Brentnall, W. D. et. al., "Extensive Industrial Gas Turbine Experience With Second Generation Single Crystal Alloy Turbine Blades," ASME Paper 97-GT-427.

A Quasi-Two-Dimensional Method for the Rotordynamic Analysis of Centered Labyrinth Liquid Seals

M. Arghir

J. Frêne

Laboratoire de Mécanique des Solides
(UMR 6610 CNRS),
Université de Poitiers,
France

The work presents a method for analyzing the dynamic regime of labyrinth liquid seals. By using the traditional simplifying assumptions for the centered seal (sinusoidal, harmonically varying, first order dynamic perturbation), the approach can be addressed as "quasi" two-dimensional. A numerical coordinate transformation capable to treat displacement perturbations is introduced. The first order mathematical model is then deduced following the same steps as in a previously published work (Arghir and Frêne, 1997b). From this standpoint, the present method can be regarded as an extension of the above mentioned approach which was able to deal only with stator-grooved seals. The method is validated by comparisons with Nordmann and Dietzen's (1988) theoretical results for a seal with grooves on both stator and rotor and with the experimental results of Staubli's (1993) test case concerning a general seal.

Introduction

During the last decade, theoretical methods for annular seals analysis became quite mature and elaborate. According to the involved mathematical model, one can distinguish between bulk flow based approaches (the thin film model is the foundation of the lubrication theory when inertia forces are important) and methods based on the full, time averaged Navier-Stokes equations. Methods of the first category are accurate in predicting the characteristics of a large category of bearings and straight annular seals, and they are more or less successfully applied to the analysis of stator grooved annular seals. Methods of the second category are used only when moving beyond the validity of the thin film hypothesis is imperiously necessary. Due to the inertia dominated turbulent flow with important recirculation zones, the labyrinth seal analysis is such a problem.

The analysis introduced in the present work belongs to the approaches based on the time averaged Navier-Stokes equations and only methods of this class will be briefly discussed. In all approaches, the vibration is modeled as a constant precession of the rotor on a circular or conical orbit. The alternate way would be a nonlinear time integration of the whole system (rotor, bearings, seals, etc.) but it seems that forces and moments deduced by using this simplified model are accurate enough for rotordynamic simulation purposes (San Andres, 1997). At this stage, the problem could be described as the solution of an unsteady (but harmonically varying), turbulent, three-dimensional flow field. Computational fluid dynamics codes are mature enough to enable such solutions and it is indeed the analysis adopted by some authors (Tam et al., 1988; Nordmann and Dietzen, 1988; Rhode et al., 1992; Athavale et al., 1994). These approaches have no a priori limitations (moreover, moving grid algorithms could enable any rotor movement), but the computational effort is expected to be quite important.

A way to reduce the CPU time is to assume that the vibration amplitude is small compared to the film thickness. Following this traditional hypothesis, the flow variables and the geometric characteristics of the seal are expressed in terms of small perturbations around the operating position. The resulting first order equations are linear and still strongly coupled. Forces and moments obtained for several precession frequencies serve to obtain the dynamic coefficients used in rotordynamic analysis. Such three-dimensional first order models were presented by Nordmann and Dietzen (1988), Baskharone and Hensel (1991), and Athavale and Hendricks (1994). The numerical solution requires less effort as for the unperturbed approach but the computational effort is still important due to the specific geometry of labyrinth seals. Generally, the axial flow in labyrinth seals consists of zones characterized by a single length scale (chamber or groove) alternating with two lengths scales zones (film). The presence of two different length scales renders the governing equations parabolic, and enables the introduction of film thickness averaged variables used in simplified models. Single length scale zones are due to discontinuities in the film thickness that provoke more or less intense flow recirculations. The equations are then elliptic and it is difficult to define film thickness averaged quantities. While parabolic equations require fine grid spacing in the direction where diffusion effects are present and accept coarse grids in the marching direction(s), no favored direction can be distinguished in the case of elliptic equations. So, structured grids have difficulties in imposing the optimal grid size for each flow zone. The most favorable situation is when a good resolution of a zone can lead only to an unnecessary refined solution in another zone. When taking into account that these problems are encountered in each circumferential section, it results that the three-dimensional analysis of general labyrinth seals might be a CPU consuming task. Nevertheless, it is the only one which can deal with eccentric operating positions of the seal.

If the annular seal works in centered position, the computational effort can be drastically reduced by considering that the perturbed flow variables have only a sinusoidal variation in the circumferential direction. The zeroth order problem becomes axisymmetric (two-dimensional) and by analytically expressing $\partial/\partial\theta$, the first order equations have a similar form. Due to the presence of all three velocity components in the first order continuity equation, these models can be addressed as "quasi" two-dimensional and they obviously require less computational effort than the preceding ones. The main drawback is that all

Contributed by the International Gas Turbine Institute and presented at the International Gas Turbine and Aeroengine Congress and Exhibition, Stockholm, Sweden, June 2–5, 1998. Manuscript received at ASME Headquarters April 1, 1998. Paper No. 98-GT-5. Associate Technical Editor: R. Kielb.

of the proposed approaches (Dietzen and Nordmann, 1987; Feng and Nordmann 1992; Arghir and Frêne, 1997a, b) are based on an analytic coordinate transformation that limit their application to grooved-stator/smooth-rotor seals. For an industrial practitioner, this inconvenience might be quite severe if one takes into account that he can dispose of three volume bulk flow methods (Florjancic, 1990; Marquette and Childs, 1996). These simplified approaches have other problems (a strong dependence on user-defined parameters) but the analysis of grooved-stator/smooth-rotor seals can be done with a negligible computational effort.

The purpose of the present paper is to introduce a quasi-two-dimensional method for the analysis of general labyrinth liquid seals, a niche that seems to be empty. The method can be regarded as an extension of a previously presented approach (Arghir and Frêne, 1997b), which is included as a particular case. It was originally developed for taking into account either cylindrical or conical vibrations in a unified approach (Arghir, 1997), but it seems that misalignement vibrations were never a problem for general labyrinth seals and the necessary validation data are completely absent in the literature. So, in the following we will limit ourselves to the presentation of the first part of the method, dealing with displacement vibrations and to its validation.

The Mathematical Model

The mathematical foundation is given by the incompressible, isothermal, three-dimensional, time averaged Navier-Stokes equations expressed in cylindrical coordinates (Schlichting, 1978), in conjunction with the k-epsilon turbulence model (Launder and Spalding, 1974). Apart from the no slip wall boundary conditions, a rough law at the wall (Koh, 1992) is used to compute the wall shear stress on coarse computational grids. The interaction of the seal with the main flow is described by imposing either the (leakage) flow rate or the pressure difference between the upstream and the downstream chambers, the circumferential velocity and the turbulence level in the inlet section. In the exit section, one imposes zero axial diffusion, which means the flow is not completely developed but streamlines are smooth without recirculation zones. The model is well known and was previously detailed (Arghir and Frêne, 1997b).

The Coordinate Transformation Expression. The labyrinth seal is described as a succession of "elementary" rectangles. For example, the geometry of the seal presented in Fig. 1 can be decomposed in three such rectangles, $R_1R_2S_2S_1R_1$, $R_2R_3R_4R_5S_5S_4S_3S_2R_2$, and $R_5R_6S_6S_5R_5$. For nominal operating conditions (Fig. 1(a)), the rotor is centered and the domain between the rotor and the stator is axisymmetric. A Cartesian, variable step grid is then generated in the $\xi\eta$ plane. Due to the dynamic regime, the whirling rotor is displaced (Fig. 2) and rectangles describing the geometry of the labyrinth seal become modified (Fig. 1(b)). The approach will be to transform the physical space $xr\theta$ (Fig. 1(b)) into the computational space $\xi\eta\zeta$ (Fig. 1(a)), both coordinate systems being cylindrical ones.

The physical grid is defined as a transformation of the Cartesian computational grid. For each rectangle representing a single block, we need to define a 1:1 mapping from the computational space to the physical one. In the following, an algebraic grid generation method known as the transport-projection approach is used (George, 1991). The basic idea is to interpolate the grid the from the physical boundaries by using the topology of the computational mesh.

First, the boundaries of the computational space must map into the boundaries of the physical space. The displacement (or eccentricity) perturbed position of a point P located on the

Nomenclature

$\tilde{a}, \tilde{b}, \tilde{f}, \tilde{g}$ = functions depending on the numerical coordinate transformation
C = gap or film thickness (m)
D, d = direct and cross-coupling damping coefficients (Ns/m)
e = excentricity (m)
F_X, F_r = radial force (N)
F_Y, F_t = tangential force (N)
in, jn = number of control volumes in the axial and in the radial direction
K, k = direct and cross-coupling stiffness coefficients (N/m)
k = turbulent kinetic energy (m^2/s^2)
L = seal length (m)
l_m = mixing length (m)
M, m = direct and cross-coupling mass coefficients (kg)
n = exponent of the "$\frac{1}{7}$" turbulent velocity profile in the inlet section
$OXYZ$ = fixed reference system
p = pressure (Pa)
Re = Reynolds number, $\rho U2C_0/\mu$
$r_{\hat{Z}}$ = correction factor
S_Φ = source term
T = turbulence level
t, τ = time (s)
u, v, w = velocity components in cylindrical coordinates (m/s)
U, W, P = film thickness averaged variables
x, r, θ = cylindrical coordinates
y = normal distance to the wall (m)
$\hat{Z}$ = terms containing the perturbed turbulent viscosity
ϵ = small perturbation parameter
γ = angle on Fig. 2
$\mu_{lam}, \mu_t, \mu_{(eff)}$ = laminar, turbulent and effective dynamic viscosity (Pa·s)
ρ = density (kg/m^3)
σ = prerotation coefficient, $W/\omega r_R$
τ = shear stress (N/m^2)
Ω = precession frequency (rad/sec)
ω = angular velocity (rad/sec)
$|\tilde{\omega}|$ = vorticity modulus (1/s)
ξ, η, ζ = transformed coordinate system
ξ_{in}, ξ_{ex} = inlet pressure drop and exit pressure recovery coefficients
$\mathcal{R}$ = real part

Subscripts

ax/c = axial/circumferential direction
in/ex = inlet/exit section
$P, E, W, N, S, NE, NW, SE, SW, e, w, n, s, FE, FW$ = grid points
$R/S, Rot/Stat$ = rotor/stator
t = turbulent
Φ = dependent variable, ($\Phi = u, v, w, p, \mu$)
$0/1$ = zeroth/first order variable
ref = reference value
w = wall

Superscripts

$\hat{}, \sim$ = complex value
$*$ = values on the boundary of the elementary rectangle
0 = total values in upstream/downstream chambers

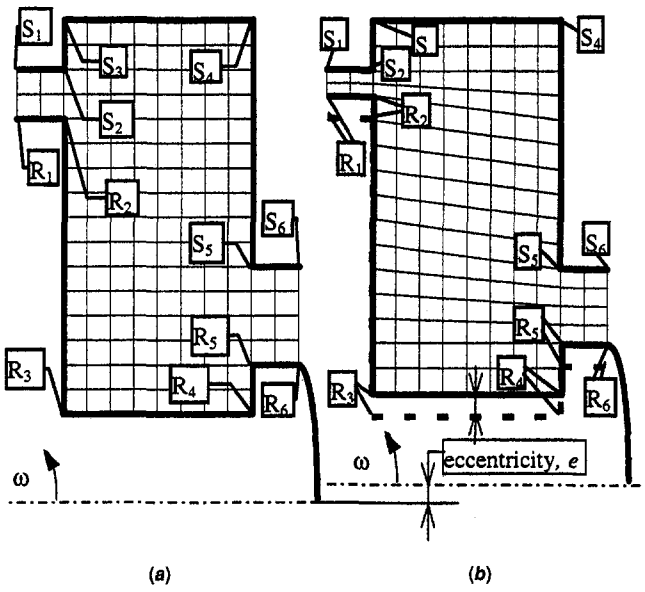

Fig. 1 Effect of the coordinate transformation: (*a*) axi symmetric domain; and (*b*) displacement perturbation

border of an "elementary" rectangle can be expressed as (Fig. 1(*b*)) follows:

$$x(\xi, \eta, \zeta, \tau) = \xi$$

$$r(\xi, \eta, \zeta, \tau) = \begin{cases} \eta + e\hat{h}(\zeta, \tau), & P \in \text{Rotor} \\ \eta + \dfrac{r_{\text{Stat}} - \eta}{C_0} e\hat{h}(\zeta, \tau), & \text{Rotor} < P < \text{Stator} \\ \eta, & P \in \text{Stator} \end{cases}$$

$$\theta(\xi, \eta, \zeta, \tau) = \zeta, \quad t(\xi, \eta, \zeta, \tau) = \tau, \tag{1}$$

where r_{Stat} and C_0 are taken on upstream (left) and downstream (right) faces of each rectangle. In this way, the above defined transformation represents an exact maping relation which preserves the continuity on the interface between two successive rectangles in the physical space.

Two of the traditional simplifying hypothesis employed in the analysis of the dynamic regime were directly introduced via the complex function $\hat{h}(\zeta, \tau) = \exp(-i\zeta)\exp(i\Omega\tau)$. The first exponential expresses that the height of the elementary rectangle has only a sinusoidal variation in the circumferential direction, which means that only the first Fourier component was considered. The second exponential is introduced to take into account the rotor whirl when the coordinate system is fixed on the stator. The circumferential angle is measured as on Fig. 2. This model is somewhat traditional and is largely described in the literature (e.g., Childs, 1993).

The whirl amplitude is supposed to be small compared to the film thickness. The perturbation parameter is defined with respect to the maximum physically allowable perturbation that avoids the contact between rotor and stator. For displacement vibrations

$$C_{\text{ref}} = e_{\max \text{ allow}} = \min\{C_0(x), 0 \le x \le L\} \tag{2}$$

$$e = \frac{e}{C_{\text{ref}}} C_{\text{ref}} = \epsilon \cdot C_{\text{ref}} \quad \epsilon = \frac{e}{C_{\text{ref}}}. \tag{3}$$

After the introduction of the perturbation parameter, the transformation maping the boundary of the "elementary" rectangle from the computational space into the physical one can be expressed as

$$x(\xi, \eta, \zeta, \tau) = \xi, \quad r(\xi, \eta, \zeta, \tau) = \eta + \epsilon\tilde{f}^*(\xi, \eta, \zeta, \tau),$$
$$\theta(\xi, \eta, \zeta, \tau) = \zeta, \quad t(\xi, \eta, \zeta, \tau) = \tau \tag{4}$$

$$\tilde{f}^*(\xi, \eta, \zeta, \tau) = \begin{cases} C_{\text{ref}}\hat{h}(\zeta, \tau), & P \in \text{Rotor} \\ \dfrac{r_{\text{Stat}} - \eta}{C_0} C_{\text{ref}}\hat{h}(\zeta, \tau), & \text{Rotor} < P < \text{Stator} \\ 0, & P \in \text{Stator}, \end{cases} \tag{5}$$

where the superscript $\sim$ denotes a variable containing a real part multiplied by $\hat{h}(\zeta, \tau)$. The function $\tilde{f}^*$ is defined on the border of the "elementary" rectangles.

The second step for obtaining the coordinate transformation is the projection of the computational grid points into the physical domain. The mapping function for inside nodes is deduced by using a linear interpolation between points lying on the right border and the corresponding points on the left border of each rectangle. The correspondence is straightforward on a structured grid when one takes points situated at the same radial distance.

$$\tilde{f}(\xi, \eta, \zeta, \tau) = (\tilde{f}^*)_{\text{upstr.}} + \frac{(\tilde{f}^*)_{\text{downstr.}} - (\tilde{f}^*)_{\text{upstr.}}}{\xi_{\text{downstr.}} - \xi_{\text{upstr.}}}(\xi - \xi_{\text{upstr.}}). \tag{6}$$

For example, in rectangle $R_2R_3R_4R_5S_5S_4S_3S_2R_2$, one can identify $(\tilde{f}^*)_{\text{upstr.}} \equiv (\tilde{f}^*)_{R_3R_2S_2S_3}$ and $(\tilde{f}^*)_{\text{downstr.}} \equiv (\tilde{f}^*)_{R_4R_5S_5S_4}$. The linear interpolation is the most simple projector. If necessary, other functions could be used in order to match normal derivatives at interfaces between rectangles or in order to control the grid density.

The Jacobian Matrix. The introduced coordinate transformation enables to express the inverse of the Jacobian matrix needed for writing the transformed equations.

$$\begin{bmatrix} \partial/\partial\xi \\ \partial/\partial\eta \\ \partial/\partial\zeta \\ \partial/\partial\tau \end{bmatrix} = \begin{bmatrix} 1 & \epsilon\cdot\tilde{a} & 0 & 0 \\ 0 & 1+\epsilon\cdot\tilde{b} & 0 & 0 \\ 0 & \epsilon\cdot(-i\tilde{f}) & 1 & 0 \\ 0 & \epsilon\cdot i\Omega\tilde{f} & 0 & 1 \end{bmatrix} \cdot \begin{bmatrix} \partial/\partial x \\ \partial/\partial r \\ \partial/\partial\theta \\ \partial/\partial t \end{bmatrix} \tag{7}$$

$$\tilde{a}(\xi, \eta, \zeta, \tau) = \frac{\partial\tilde{f}}{\partial\xi}, \quad \tilde{b}(\xi, \eta, \zeta, \tau) = \frac{\partial\tilde{f}}{\partial\eta},$$

$$\tilde{g}(\xi, \eta, \zeta, \tau) = \frac{\tilde{f}}{\eta} \tag{8}$$

Taking into account the effect of the linearisations introduced

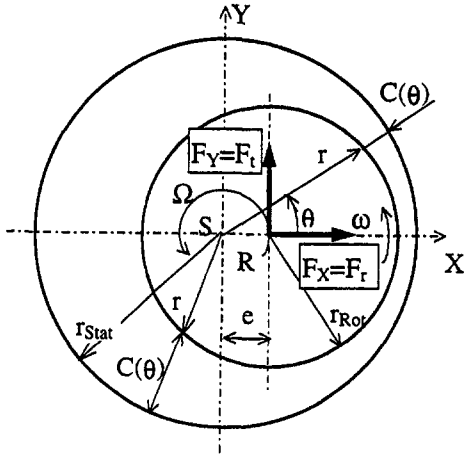

Fig. 2 Forces on the whirling rotor

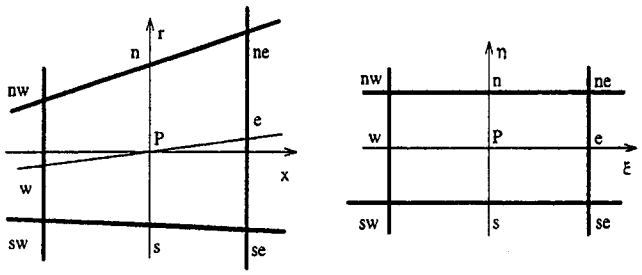

Fig. 3 The transformed control volume

by the perturbation parameter, the Jacobian matrix can be analytically derived.

$$\begin{bmatrix} \partial/\partial x \\ \partial/\partial r \\ \partial/\partial\theta \\ \partial/\partial t \end{bmatrix} = \begin{bmatrix} 1 & -\epsilon\cdot\tilde{a} & 0 & 0 \\ 0 & 1-\epsilon\cdot\tilde{b} & 0 & 0 \\ 0 & \epsilon\cdot i\tilde{f} & 1 & 0 \\ 0 & \epsilon\cdot(-i\Omega\tilde{f}) & 0 & 1 \end{bmatrix} \cdot \begin{bmatrix} \partial/\partial\xi \\ \partial/\partial\eta \\ \partial/\partial\zeta \\ \partial/\partial\tau \end{bmatrix}, \quad (9)$$

where its determinant is $1 - \epsilon\tilde{b}$. The transformed radius is written as

$$r = \eta(1 + \epsilon\cdot\tilde{g}), \quad \frac{1}{r} = \frac{1}{\eta}(1 - \epsilon\cdot\tilde{g}). \quad (10)$$

The functions $\tilde{a}$, $\tilde{b}$, and $\tilde{g}$ were introduced in order to simplify notations. Derivatives $\partial/\partial\zeta$ and $\partial/\partial\tau$ can be analytically expressed as

$$\frac{\partial\tilde{\Psi}}{\partial\zeta} = -i\tilde{\Psi}, \quad \frac{\partial\tilde{\Psi}}{\partial\tau} = i\Omega\tilde{\Psi}, \quad \tilde{\psi} \in \{\tilde{f}, \tilde{a}, \tilde{b}, \tilde{g}\}, \quad (11)$$

but grid node values and derivatives $\partial/\partial\xi$ and $\partial/\partial\eta$ are numerically estimated using centered finite differences. For example (Fig. 3), the functions $\tilde{f}$ being defined in the vertexes of the control volumes, one can write

$$\tilde{a}_P(\xi, \eta, \zeta, \tau) = \frac{\tilde{f}_e - \tilde{f}_w}{\xi_e - \xi_w} = \frac{(\tilde{f}_{ne} - \tilde{f}_{nw})(\eta_N - \eta_P) + (\tilde{f}_{se} - \tilde{f}_{sw})(\eta_P - \eta_S)}{(\xi_e - \xi_w)(\eta_N - \eta_S)}. \quad (12)$$

The First Order Equations. To obtain the first order mathematical model, the flow variables are expressed using the traditional simplifying assumptions (sinusoidal, harmonical variation, first order dynamic perturbations).

$$\Phi(\xi, \eta, \zeta, \tau) = \Phi_0(\xi, \eta) + \epsilon\Phi_1(\xi, \eta, \zeta, \tau) + \epsilon^2 \ldots, \Phi \in \{u, v, w, p, \mu\}$$

$$\Phi_1(\xi, \eta, \zeta, \tau) = \mathcal{R}[\hat{\Phi}_1(\xi, \eta)\hat{h}(\zeta, \tau)],$$

$$\hat{\Phi}_1 = \Phi_{1\cos} + i\Phi_{1\sin} \quad (13)$$

These relations and the coordinate transformation (9) are systematically introduced in the three-dimensional equations and in the corresponding boundary conditions. The steps in obtaining the first order mathematical model were pointed out in previous works (Arghir and Frêne, 1997a, b) when an analytical coordinate transformation was used. The present approach follows the same steps so the results will be directly introduced.

The resulting zeroth order equations govern the axisymmetric flow in centered position. The first order ones are three-dimensional, but the sinusoidal circumferential variation with only the first Fourier component taken into account enables one to write them in the same form as the zeroth order equations. In order to facilitate the numerical integration they are expressed as general two-dimensional transport equations.

$$\frac{\partial}{\partial\xi}(\rho u_0\hat{\Phi}_1) + \frac{1}{\eta}\frac{\partial}{\partial\eta}(\eta\rho v_0\hat{\Phi}_1) = \frac{\partial}{\partial\xi}\left(\mu_0\frac{\partial\hat{\Phi}_1}{\partial\xi}\right) + \frac{1}{\eta}\frac{\partial}{\partial\eta}\left(\eta\mu_0\frac{\partial\hat{\Phi}_1}{\partial\eta}\right) + \hat{S}_\Phi \quad (14)$$

The source terms $\hat{S}_\phi$ are presented in Table 1. The first order continuity equation is written as

$$\frac{\partial}{\partial\xi}(\rho\hat{u}_1) + \frac{1}{\eta}\frac{\partial}{\partial\eta}(\eta\rho\hat{v}_1) = i\frac{\rho}{\eta}\hat{w}_1 + \left[\tilde{a}\frac{\partial(\rho u_0)}{\partial\eta} + \tilde{b}\frac{\partial(\rho v_0)}{\partial\eta} + \tilde{g}\frac{\rho v_0}{\eta} - i\tilde{g}\frac{\partial(\rho w_0)}{\partial\eta}\right]. \quad (15)$$

As found in the previous first order models (Arghir and Frêne, 1997a, b), the present one includes the perturbation of the turbulent viscosity field in terms $\hat{Z}_i$. The perturbed turbulent viscosity is obtained using an algebraic relation borrowed from the turbulence model of Baldwin and Lomax (1978) for the inner layer.

$$\mu_t = \rho l_m^2|\vec{\omega}| = (\mu_t)_0 + \epsilon(\hat{\mu}_t)_1, \quad l_m = 0.4y \quad (16)$$

$$(\hat{\mu}_t)_1 = (\mu_t)_0\left(\frac{|\vec{\omega}|_1}{|\vec{\omega}|_0} + 2\frac{\hat{y}_1}{y_0}\right), \quad (17)$$

where $(\mu_t)_0$ is calculated with the k-epsilon turbulence model. The above relation, which is certainly limited to cases when rotor and stator solid surfaces are close enough, was preferred in order to avoid the perturbation of the transport equations of the differential turbulence model. Details are given in the Appendix.

Boundary Conditions. No-slip boundary conditions are

$$\text{Stator: } \hat{u}_1 = (0, 0), \quad \hat{v}_1 = (0, 0), \quad \hat{w}_1 = (0, 0) \quad (18)$$

$$\text{Rotor: } \hat{u}_1 = (0, 0), \quad \hat{v}_1 = [0, (\Omega - \omega)C_{\text{ref}}], \quad \hat{w}_1 = [\Omega C_{\text{ref}}, 0] \quad (19)$$

For turbulent flow, first order gradient boundary conditions are formulated by perturbing the universal velocity profile. As for the zeroth order flow, these gradient boundary conditions enable the employment of a coarse grid close to walls.

The rest of the boundary conditions write

$$\text{Inlet: } (\hat{U}_{in})_1 = -\frac{(\hat{P}_{in})_1}{\rho(U_{in})_0(1 + \xi_{in})}, \quad (20)$$

$$(\hat{v}_{in})_1 = (\hat{w}_{in})_1 = 0$$

$$\text{Exit: } (\hat{P}_{ex})_1 = (\xi_{ex} - 1)\rho(U_{ex})_0(\hat{U}_{ex})_1 \quad (21)$$

$$\frac{\partial^2\hat{\Phi}_1}{\partial\xi^2} = 0, \quad \hat{\Phi}_1 = \{\hat{u}_1, \hat{v}_1, \hat{w}_1\}$$

The gradient type boundary conditions, the special treatment of $\hat{v}_1$ imposed by the presence of the source terms in the first order continuity equation and the treatment of the pressure recovery effect in the exit section are important parts of the mathematical model but they are similar to those presented for the analytic coordinate transformation (Arghir and Frêne, 1997a, b), and can be easily deduced.

Numerical Solution

The same solver was used for both the zeroth and the first order problems. The equations are discretized using the finite

Table 1 Source terms of the first order transport equations

$\hat{\Phi}_1$	$\hat{S}_\Phi$
$\hat{u}_1$	$-\frac{\partial \hat{p}_1}{\partial \xi}+\frac{\partial}{\partial \xi}\left(\mu_0\frac{\partial \hat{u}_1}{\partial \xi}\right)+\frac{1}{\eta}\frac{\partial}{\partial \eta}\left(\eta\mu_0\frac{\partial \hat{v}_1}{\partial \xi}\right)-\frac{\mu_0\hat{u}_1}{\eta^2}-i\frac{\mu_0}{\eta}\frac{\partial \hat{w}_1}{\partial \xi}-\frac{\partial}{\partial \xi}(\rho u_0\hat{u}_1)-\frac{1}{\eta}\frac{\partial}{\partial \eta}(\eta\rho u_0\hat{v}_1)-i\rho\Omega\hat{u}_1+i\frac{\rho w_0 u_1}{\eta}+i\frac{\rho u_0\hat{w}_1}{\eta}-\tilde{a}\frac{\partial p_0}{\partial \eta}$ $-\frac{\partial}{\partial \xi}\left(\tilde{a}2\mu_0\frac{\partial u_0}{\partial \eta}\right)-\tilde{a}\frac{\partial}{\partial \eta}\left(2\mu_0\frac{\partial u_0}{\partial \xi}-\frac{2}{3}\rho k\right)-\frac{1}{\eta}\frac{\partial}{\partial \eta}\left[\eta\mu_0\left(\tilde{a}\frac{\partial v_0}{\partial \eta}+\tilde{b}\frac{\partial u_0}{\partial \eta}\right)\right]-\tilde{b}\frac{\partial}{\partial \eta}\left[\mu_0\left(\frac{\partial v_0}{\partial \xi}+\frac{\partial u_0}{\partial \eta}\right)\right]-\tilde{g}\frac{\mu_0}{\eta}\left(\frac{\partial v_0}{\partial \xi}+\frac{\partial u_0}{\partial \eta}\right)$ $+\frac{\mu_0}{\eta}\tilde{g}\frac{\partial u_0}{\partial \eta}+i\frac{\mu_0}{\eta}\tilde{a}\frac{\partial w_0}{\partial \eta}+i\tilde{g}\frac{\partial}{\partial \eta}\left(\mu_0\frac{\partial w_0}{\partial \xi}\right)+i\Omega\eta\tilde{g}\rho\frac{\partial u_0}{\partial \eta}+\tilde{a}\frac{\partial}{\partial \eta}\left(\rho u_0^2\right)+\tilde{g}\frac{\rho v_0 u_0}{\eta}+\tilde{b}\frac{\partial}{\partial \eta}(\rho v_0 u_0)-i\tilde{g}\frac{\partial}{\partial \eta}(\rho w_0 u_0)+r_z\hat{Z}_1$ $\hat{Z}_1=\frac{\partial}{\partial \xi}\left(2\hat{\mu}_1\frac{\partial u_0}{\partial \xi}\right)+\frac{1}{\eta}\frac{\partial}{\partial \eta}\left[\eta\hat{\mu}_1\left(\frac{\partial v_0}{\partial \xi}+\frac{\partial u_0}{\partial \eta}\right)\right]-i\frac{\hat{\mu}_1}{\eta}\frac{\partial w_0}{\partial \xi}$
$\hat{v}_1$	$-\frac{\partial \hat{p}_1}{\partial \eta}+\frac{\partial}{\partial \xi}\left(\mu_0\frac{\partial \hat{u}_1}{\partial \eta}\right)+\frac{1}{\eta}\frac{\partial}{\partial \eta}\left(\eta\mu_0\frac{\partial \hat{v}_1}{\partial \eta}\right)-\frac{\partial}{\partial \xi}(\rho v_0\hat{u}_1)-\frac{1}{\eta}\frac{\partial}{\partial \eta}(\eta\rho v_0\hat{v}_1)-i\mu_0\frac{\partial}{\partial \eta}\left(\frac{\hat{w}_1}{\eta}\right)-3\frac{\mu_0}{\eta^2}\hat{v}_1+i\rho\left(\frac{w_0}{\eta}-\Omega\right)\hat{v}_1$ $+\left(2\frac{\rho w_0}{\eta}+i2\frac{\mu_0}{\eta^2}+i\frac{\rho v_0}{\eta}\right)\hat{w}_1-\tilde{g}\frac{\rho w_0^2}{\eta}+\tilde{g}\frac{\rho v_0^2}{\eta}+\tilde{g}\frac{2\mu_0 v_0}{\eta^2}-\tilde{g}\frac{2\mu_0}{\eta}\frac{\partial v_0}{\partial \eta}+\tilde{b}\frac{\partial}{\partial \eta}\left(\rho v_0^2\right)+\tilde{b}\frac{\partial p_0}{\partial \eta}-\tilde{b}\frac{\partial}{\partial \eta}\left(2\mu_0\frac{\partial v_0}{\partial \eta}-\frac{2}{3}\rho k\right)$ $+i\tilde{g}\frac{\partial}{\partial \eta}\left[\mu_0\eta\frac{\partial}{\partial \eta}\left(\frac{w_0}{\eta}\right)\right]-i\tilde{g}\frac{\partial}{\partial \eta}(\rho w_0 v_0)+i\Omega\eta\tilde{g}\frac{\partial(\rho v_0)}{\partial \eta}-\frac{\partial}{\partial \xi}\left[\mu_0\left(\tilde{a}\frac{\partial v_0}{\partial \eta}+\tilde{b}\frac{\partial u_0}{\partial \eta}\right)\right]-\tilde{a}\frac{\partial}{\partial \eta}\left(\mu_0\left(\frac{\partial v_0}{\partial \xi}+\frac{\partial u_0}{\partial \eta}\right)\right)-\frac{1}{\eta}\frac{\partial}{\partial \eta}\left(2\eta\mu_0\tilde{b}\frac{\partial v_0}{\partial \eta}\right)$ $+\frac{\mu_0}{\eta}\tilde{g}\frac{\partial v_0}{\partial \eta}+2\frac{\mu_0}{\eta}\tilde{g}\frac{v_0}{\eta}-i\frac{\mu_0}{\eta}\left(\tilde{g}\frac{w_0}{\eta}-\tilde{b}\frac{\partial w_0}{\partial \eta}\right)-i2\frac{\mu_0}{\eta}\tilde{g}\frac{\partial w_0}{\partial \eta}+\tilde{a}\frac{\partial}{\partial \eta}(\rho u_0 v_0)+r_z\hat{Z}_2$ $\hat{Z}_2=\frac{\partial}{\partial x}\left[\hat{\mu}_1\left(\frac{\partial v_0}{\partial x}+\frac{\partial u_0}{\partial \eta}\right)\right]+\frac{1}{\eta}\frac{\partial}{\partial \eta}\left[\eta\left(2\hat{\mu}_1\frac{\partial v_0}{\partial \eta}\right)\right]-i\hat{\mu}_1\frac{\partial}{\partial \eta}\left(\frac{w_0}{\eta}\right)-\frac{2\hat{\mu}_1}{\eta}\frac{v_0}{\eta}$
$\hat{w}_1$	$i\frac{\hat{p}_1}{\eta}-i\frac{\partial}{\partial \xi}\left(\frac{\mu_0}{\eta}\hat{u}_1\right)-i\frac{1}{\eta}\frac{\partial}{\partial \eta}(\mu_0\hat{v}_1)-\frac{\partial}{\partial \xi}(\rho w_0\hat{u}_1)-\frac{1}{\eta}\frac{\partial}{\partial \eta}(\eta\rho w_0\hat{v}_1)-\frac{\rho\hat{v}_1 w_0}{\eta}-2\frac{\mu_0}{\eta^2}\hat{w}_1-i3\frac{\mu_0}{\eta^2}\hat{v}_1+i2\frac{\rho}{\eta}w_0\hat{w}_1-\frac{\rho v_0\hat{w}_1}{\eta}-i\rho\Omega\hat{w}_1$ $-\frac{1}{\eta}\frac{\partial}{\partial \eta}(\mu_0\hat{w}_1)+\mu_0\frac{\partial}{\partial \eta}\left(\frac{\hat{w}_1}{\eta}\right)-\tilde{b}\frac{1}{\eta}\frac{\partial}{\partial \eta}\left(\mu_0\eta\frac{\partial w_0}{\partial \eta}\right)+\tilde{b}\frac{1}{\eta}\frac{\partial}{\partial \eta}(\mu_0 w_0)+\left(\tilde{b}-2\tilde{g}\right)\mu_0\frac{\partial}{\partial \eta}\left(\frac{w_0}{\eta}\right)+\tilde{b}\frac{\partial}{\partial \eta}(\rho v_0 w_0)+i\Omega\eta\tilde{g}\frac{\partial}{\partial \eta}(\rho w_0)$ $-i\tilde{g}\left[\frac{\partial p_0}{\partial \eta}-\frac{\partial}{\partial \eta}\left(2\mu_0\frac{v_0}{\eta}-\frac{2}{3}\rho k\right)+\frac{\partial}{\partial \eta}\left(\rho w_0^2\right)\right]+2\tilde{g}\frac{\rho v_0 w_0}{\eta}-\frac{1}{\eta}\frac{\partial}{\partial \eta}\left(\tilde{b}\mu_0\eta\frac{\partial w_0}{\partial \eta}\right)+\frac{1}{\eta}\frac{\partial}{\partial \eta}(\mu_0\tilde{g}w_0)+\frac{\mu_0}{\eta}\left(-\tilde{b}\frac{\partial w_0}{\partial \eta}+\tilde{g}\frac{w_0}{\eta}\right)+i\tilde{g}\frac{2\mu_0 v_0}{\eta^2}$ $+2\frac{\mu_0}{\eta}\tilde{g}\frac{\partial w_0}{\partial \eta}+i\frac{\partial}{\partial \xi}\left(\tilde{g}\mu_0\frac{\partial u_0}{\partial \eta}\right)+i\frac{1}{\eta}\frac{\partial}{\partial \eta}\left(\tilde{g}\frac{\partial v_0}{\partial \eta}\right)+i\tilde{g}\frac{\mu_0}{\eta}\frac{\partial v_0}{\partial \eta}-\frac{\partial}{\partial \xi}\left(\tilde{a}\mu_0\frac{\partial w_0}{\partial \eta}\right)-\tilde{a}\frac{\partial}{\partial \eta}\left(\mu_0\frac{\partial w_0}{\partial \xi}\right)+\tilde{a}\frac{\partial}{\partial \eta}(\rho u_0 w_0)+r_z\hat{Z}_3$ $\hat{Z}_3=\frac{\partial}{\partial x}\left(\hat{\mu}_1\frac{\partial w_0}{\partial x}\right)+\frac{1}{\eta}\frac{\partial}{\partial \eta}\left[\hat{\mu}_1\eta^2\frac{\partial}{\partial \eta}\left(\frac{w_0}{\eta}\right)\right]-i\frac{2\hat{\mu}_1}{\eta}\frac{v_0}{\eta}+\hat{\mu}_1\frac{\partial}{\partial \eta}\left(\frac{w_0}{\eta}\right)$

volume method on a structured grid. Staggered control volumes are used for the axial and radial velocity component and collocated ones for the rest of the transport equations. The SIMPLEC algorithm (Van Doormal and Raithby, 1984) was used to solve the coupling between the velocity and the pressure fields. The convective terms are discretized using the second order scheme of Zhu and Rodi (1991) and implemented using Khosla and Rubin's (1974) deferred correction algorithm. The rest of the derivatives are discretized using centered differences. The convergence of the iterative process is controlled by the 10^{-5} value of the nondimensional mass conservation error. When convergence is attained, the nondimensional residuals in the rest of the transport equations are well under that limit.

Results and Discussions

There are very few theoretical or experimental data enabling the validation of general form labyrinth liquid seals.

For stator-grooved/smooth-rotor seals (and straight annular ones as a particular case), the numerical coordinate transformation is written as

$$f = r_{\text{Stat}} - \eta, \quad a = 0, \quad b = -1, \quad g = \frac{r_{\text{Stat}}}{\eta} - 1 \tag{22}$$

that is exactly the form of the analytic coordinate transformation used in previous works. By replacing these expressions in the transport and mass conservation equations one obtains the previously introduced first order mathematical model (Arghir and Frêne, 1997b). It follows that results obtained for this particular category of seals are not characteristic for the present method and serve merely to debug the computer programs.

Two general labyrinth seals are presented in the following text. Results are presented either in terms of the first order pressure, or in terms of dynamic coefficients defined below.

$$-\frac{F_r}{e} = -\frac{\pi}{C_{\text{ref}}}\int_0^L \eta_{\text{Rot}}(\xi)p_{1\cos}(\xi, \eta_{\text{Rot}})d\xi = K + d\Omega - M\Omega^2 \tag{23a}$$

$$-\frac{F_t}{e} = -\frac{\pi}{C_{\text{ref}}}\int_0^L \eta_{\text{Rot}}(\xi)p_{1\sin}(\xi, \eta_{\text{Rot}})d\xi = -k + D\Omega + m\Omega^2 \tag{23b}$$

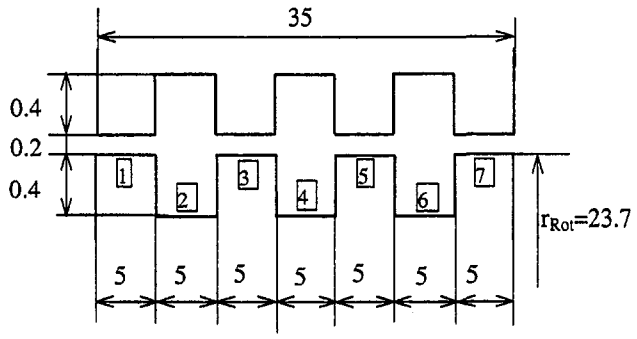

Fig. 4 Geometry of Nordmann and Dietzen's (1988) labyrinth seal (all lengths are in mm)

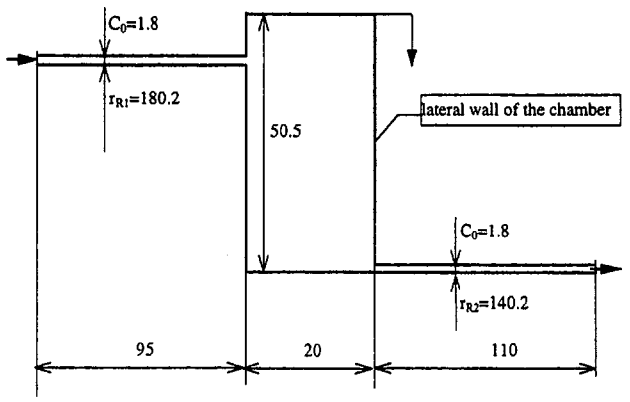

Fig. 6 Geometry of Staubli's (1993) test case (all lengths are in mm)

One of the first results was obtained by Nordmann and Dietzen (1988) for the seal in Fig. 4. They performed a full three-dimensional calculation for an $e = C_0/40$ rotor displacement and zero whirl. The following data were used in calculations: $\rho = 996$ kg/m^3, $\mu = 0.7 \cdot 10^{-3}$ Pa·s, $\Delta P^0 = 0.8$ MPa (imposed pressure difference), $\xi_{in} = 0.5$, $\xi_{ex} = 1$, $\omega = 418.88$ rad/s, $\sigma = 0.5$, and hydraulically smooth walls. The present calculations were performed considering $n = 3$, $T = 10$ percent and a computational grid containing 2656 control volumes (234 in the axial direction with a ratio of 1.1, and 22 equally spaced in the radial direction). The contribution of each land and groove zone to the direct and cross coupling stiffness is presented in Fig. 5. The total value of the direct stiffness is well predicted but the contribution of each zone is somewhat different. In Dietzen's results, the direct stiffness contribution of land zones is progressively decreasing and that of groove zones is increasing, whereas the present calculations show an almost constant contribution of land and groove zones. Differences in cross coupled stiffness are more important but the contribution of each zone shows the same trends as Dietzen's results. The last bar chart presents the direct damping. Its values were estimated by dropping the effect of m in relation (23b) and by calculating the difference of the first order pressures (imaginary part) obtained for $\Omega = 0$ and $\Omega = \omega$ divided by ω. The whirl-frequency ratio of the seal results $k/D\omega = 0.47$. Finally, in the absence of any measurements or of a third theoretical result, it is difficult to appreciate the accuracy of one set of results versus the other. Not at least, it should be underlined that the computational effort of the two-dimensional approach for this test case lays within very reasonable limits (3474 CPU sec, for the zeroth order problem and 1383 CPU s for the first order one, on a DEC ALPHA 4000).

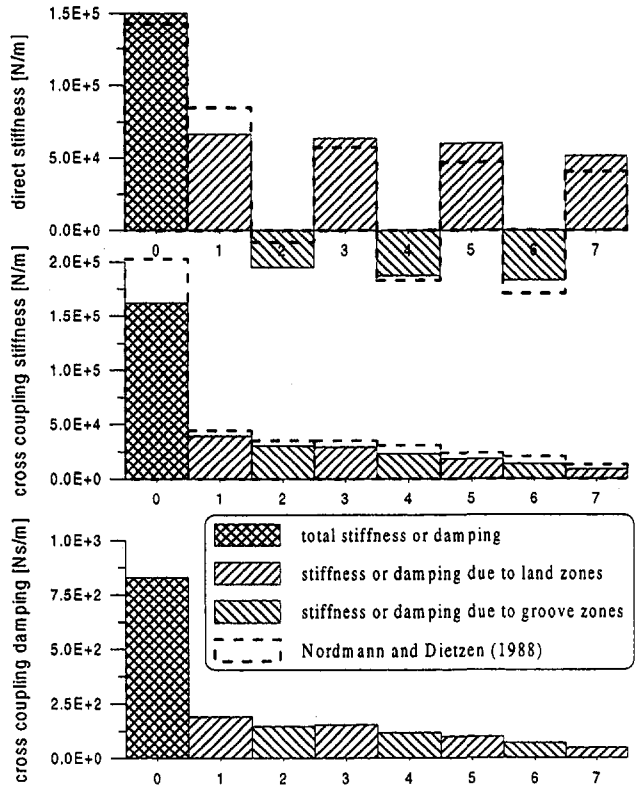

Fig. 5 Stiffness and damping; total value and contribution of each land and groove zone

A test case for labyrinth seals based on experimental data was proposed by Staubli (1993). Full details can be found in Amoser's work from 1995. The geometry of the test case is presented in Fig. 6 and it consists of two straight seals separated by a large chamber. Stator pressures were measured both for centered operating conditions and for zero whirl, 40 percent eccentricity. Data used in calculations were $\rho = 998.5$ kg/m^3, $\mu = 10^{-3}$ Pa·s, $\mathrm{Re}_{axl}/2 = 14838$ (imposed flow rate), $\xi_{in} = 0.5$, $\xi_{ex} = 1$, $\omega = 104.72$ rad/s, $\sigma = 0.16$ (3 m/s), $n = 7$ (estimated), $T = 2$ percent, and hydraulically smooth walls. Calculations were performed using two unequally spaced grids. Both grids use the same number of control volumes in the straight seals ($in = 16$, $jn = 8$ in the first seal and $in = 64$, $jn = 8$ in the second one) but different number of control volumes in the chamber ($in = 24$, $jn = 48$ for the first grid and $in = 40$, $jn = 72$ in the second one).

Zeroth order stator pressures (centered operating conditions) in the axial direction are presented in Fig. 7. The nondimensional distance $y^+ = \rho y \sqrt{\tau_w/\rho}/\mu_{lam}$ of cells next to the walls for the second grid is presented in Fig. 8. Pressures on the lateral wall of the chamber are superposed after being rotated (the origin and the direction of the plot are indicated by arrows in Fig. 6 and 7).

It can be seen that the stator pressure is well predicted in the second seal. The slope is well predicted in the first seal too, but absolute pressures are shifted to greater values and the same difference is observed on the lateral wall of the chamber. One can conclude that the flow in the chamber acts as an "enhanced" hydraulic resistance. This overestimation cannot be eliminated by reasonable grid refinements, so the responsibility is carried by the employed turbulence model. As underlined by Launder (1991), the standard k-epsilon model uses an isotropic turbulent viscosity which prevents the correct prediction of the anisotropic normal stresses. The model overestimates the turbulent kinetic energy and also μ_t in zones with important normal stresses such as in the vicinity of the impact (stagnation) point on the stator lateral wall. The time averaged flow is not very affected in this region that is dominated by pressure gradient

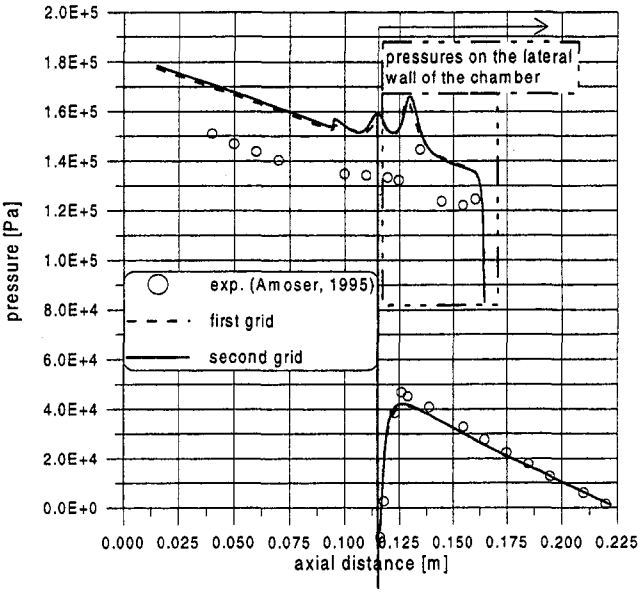

Fig. 7 Zeroth order stator pressure

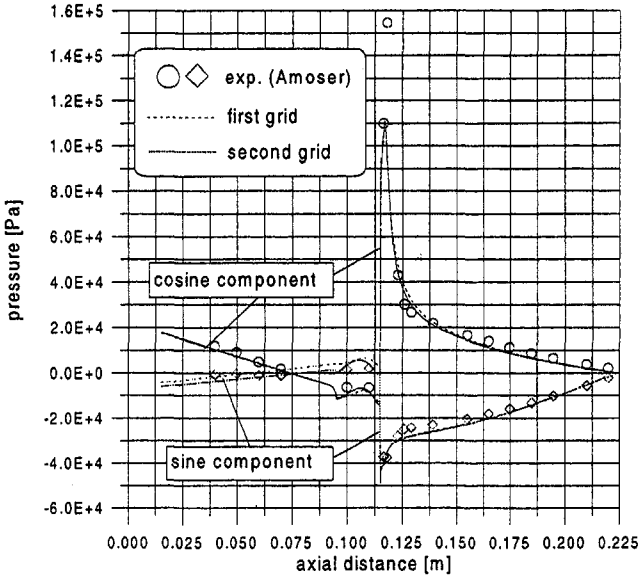

Fig. 9 First order stator pressure (walls normal to the radial direction)

effects, but due to transport phenomena in the recirculation zones, the overestimation of μ_t will influence the upstream flow. It is expected that turbulence models enabling a more accurate prediction of normal stresses would give a better answer but were not employed for this test case.

Experimental first order pressures were extracted from measured ones. They are compared with calculated results in Figs. 9 and 10, separately for $p_{1\cos}$ and $p_{1\sin}$. For zero whirl the cosine and the sine components give the direct and the cross coupling stiffness, respectively. It was appreciated that this comparison characterizes better the first order pressure field than the comparison with the eccentric pressure field which was actually measured. The results show a good agreement with experiments especially in the inlet zone of the second seal where all the details are well reproduced. It should be underlined that for the

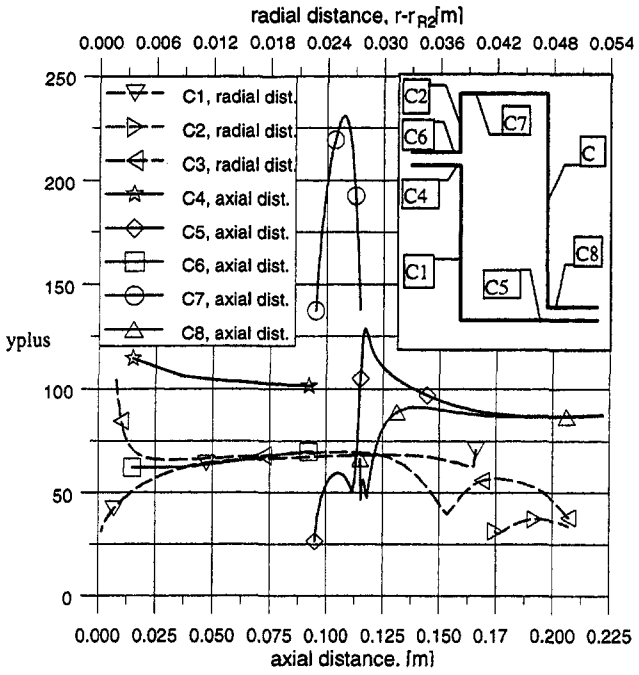

Fig. 8 Nondimensional position of grid points next to the walls for the second grid

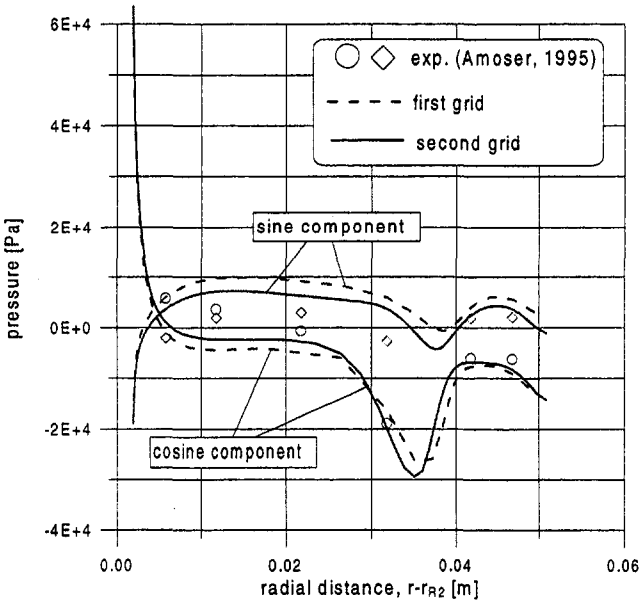

Fig. 10 First order stator pressure (lateral wall of the chamber)

refined grid the convergence was extremely difficult with $r_{\hat{z}} = 1$ so calculations on both grids were made using $r_{\hat{z}} = 0.5$. Values less than 1 of this coefficient correspond to an incomplete inclusion of the perturbed turbulent viscosity effect. Perturbed Navier-Stokes methods presented in the literature usually neglect this effect and its inclusion is a unique feature of the present approach. By testing the present mathematical model and its former variants (Arghir and Frêne, 1997b) it was found that, neglecting the perturbed turbulent viscosity contained in $\hat{Z}_i$ terms, entrained an overestimation of the direct stiffness. The relative errors are presented in Table 2. The trend is also

Table 2 Influence of the perturbed viscosity terms

$\Phi_{r_{\hat{z}}=1}/\left(\Phi_{r_{\hat{z}}=1}-\Phi_{r_{\hat{z}}=0.5}\right)\cdot 100$	K	k	D
Complete geometry analysis	-11.1	4.7	0.5
Second straight seal (isolated)	-8	1.1	1

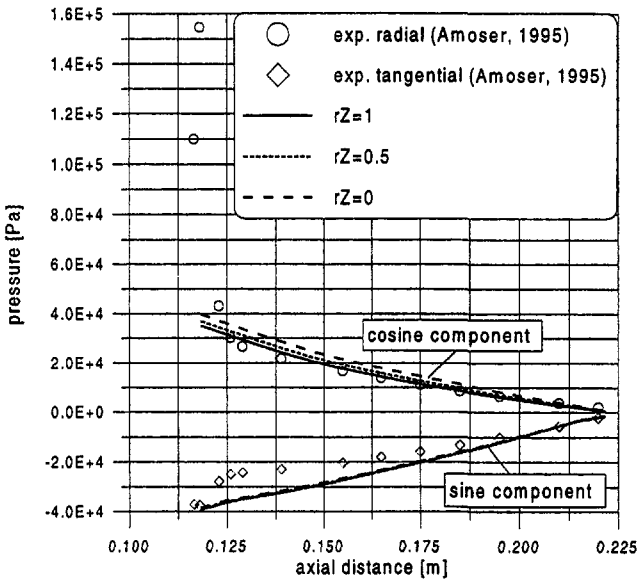

Fig. 11 Influence of the perturbed viscosity terms on the first order pressure in the second (straight) seal calculated as an isolated one

clear for straight annular seals operating at high Re_{ax}. Figure 11 presents the axial distribution of the first order pressures for the second straight seal calculated as an isolated one ($Re_{ax}/2 = 19071$, $\xi_{in} = 0.6$, $\sigma = 0.48$, $n = 7$, $T = 15$ percent, equally spaced grid with $in = 16$, $jn = 8$). It can be seen that, at least for straight seals, the best agreement with either experimental or theoretical values is obtained when completely taking into account the perturbed turbulent viscosity ($r_2 = 1$). The good agreement obtained when analyzing the complete geometry of Staubli's test case with $r_2 = 0.5$ can be explained by the fact that inertia effects that occur in the inlet section and are swept in the second seal are more important than the viscous ones. The small value of L/C_0 (usually greater than 100 but only 61 for the second straight seal) sustains this explanation. The convergence problems encountered due to the large chamber show that the algebraic relation (17) used for estimating $(\hat{\mu}_t)_1$ is not best suited when recirculation zones dominate the flow. Fortunately the chamber effect is not so important by itself but merely by modifying the inlet conditions in the straight seal which are correctly predicted.

Conclusions

The present paper introduces a numerical method for the dynamic analysis of general labyrinth liquid seals operating in centered position. The method is based on the time averaged Navier-Stokes equations and a numerical coordinate transformation. Traditional simplifying assumptions (dynamic perturbations, sinusoidal, harmonical variation) render the analysis quasi-two-dimensional and less time consuming than three-dimensional methods. From a literature survey, it seems that a two-dimensional analysis method for general form labyrinth seals was not available up to now. Former methods of this class enabled the analysis of stator grooved seals only and they are now included in the present approach.

Results for two general seals are presented. Comparisons with Dietzen's (1988) full three-dimensional results show a good to moderate agreement but it is not possible to appreciate the accuracy of one set of results versus the other. A good agreement was obtained with the experimental results of Staubli's (1993) test case. It was shown that the inertia effects that occur at the passage from the chamber in the straight seal are particularly well predicted. The algebraic relation used for estimating the first order turbulent viscosity has only a limited validity and caused some convergence problems when large recirculation zones dominate the flow.

One must underline that the present methodology can treat general form labyrinth seals as long as the lateral walls are in planes perpendicular to the seal axis. The coordinate transformation used for treating the first order problem can handle labyrinths with tapered walls but the limitation comes from the zeroth order solver which employs a Cartesian grid. Inclined walls are then poorly approximated and flows with important wall shear stresses are inaccurately predicted. Boundary fitted coordinates would be more appropriate for labyrinths with tapered walls. The methodology can be extended by decomposing the labyrinths in blocks formed by generalized rectangles or polygons, but the coordinate transformation should include a modification of the axial coordinate.

As it was explained in the Introduction paragraph, flow in general labyrinth seals can be very complex, so, in order to profit from CFD's latest achievements, future efforts should be concentrated toward the improvement of the numerical resolution scheme.

Acknowledgments

This work was performed with the financial support of Electricité de France.

References

Amoser, M., 1995, "Strömungsfelder und Radialkräfte in Labyrinthdichtungen hydraulischer Strömungmashinen," Dissertation ETH Zürich Nr. 11150.

Arghir, M., 1996, "Modélisation du comportement dynamique des joints annulaires rainurés à fluide incompressible," Thèse de docteur de l'Université de Poitiers.

Arghir, M., and Frêne, J., 1997a, "Forces and Moments Due to Misalignement Vibrations in Annular Liquid Seals Using the Averaged Navier-Stokes Equations," *ASME Journal of Tribology,* Vol. 119, pp. 279–290.

Arghir, M., and Frêne, J., 1997b, "Rotordynamic Coefficients of Circumferentially Grooved Liquid Seals Using the Averaged Navier-Stokes Equations," *ASME Journal of Tribology,* Vol. 119, pp. 556–567.

Arghir, M., 1997, "Logiciel LABYR—Dossier Mathématique," Rapport P41/6A1149.

Athavale, M. M., and Hendricks, R. C., 1994, "A Small Perturbation CFD Method for Calculation of Seal Rotordynamic Coefficients," paper presented at the ISROMAC-5, Maui, Hawaii, May.

Athavale, M. M., Przekwas, A. J., Hendricks, R. C., and Liang, A., 1994, "SCISEAL: A 3D CFD Code for Accurate Analysis of Fluid Flow and Forces in Seals," paper presented at the Advanced ETO Propulsion Conference, May.

Baldwin, B. S., and Lomax, H., 1978, "Thin-Layer Approximation and Algebraic Model for Separated Turbulent Flows," AIAA Paper, 78-257, Huntsville, AL.

Baskharone, E. A., and Hensel, S. J., 1991, "A Finite-Element Perturbation Approach to Fluid/Rotor Interaction in Turbomachinery Elements: Part 1—Theory," *ASME Journal of Fluids Engineering,* Vol. 113, September, pp. 353–361.

Childs, D. W., 1993, *Turbomachinery Rotordynamics: Phenomena, Modeling and Analysis,* John Wiley & Sons, New York.

Dietzen, F. J., and Nordmann, R., 1987, "Calculating Rotordynamic Coefficients of Seals by Finite-Difference Techniques," *ASME Journal of Tribology,* Vol. 109, pp. 388–394.

Feng, T., and Nordmann, R., 1992, "Identification of Fluid/Structure Interactionsin Centrifugal Pumps (Part 1: Computational Procedure)," *ISROMAC-4,* Vol. A, Hawaii, USA, pp. 34–43.

Florjancic, S., 1990, "Annular Seals of High Energy Centrifugal Pumps: A New Theory and Full Scale Measurement of Rotordynamic Coefficients and Hydraulic Friction Factors," Diss ETH Nr. 9087, Swiss Federal Institute of Technology, Zurich, Switzerland.

George, P. L., 1991, *Automatic Mesh Generation. Application to Finite Element Methods,* John Wiley & Sons, New York.

Khosla, P. K., and Rubin, S. G., 1974, "A Diagonally Dominant Second-Order Accurate Implicit Scheme," *Comput. & Fluids,* No. 2, pp. 207–209.

Koh, Y.-M., 1992, "Turbulent Flow Near a Rough Wall," *ASME Journal of Fluids Engineering,* Vol. 114, pp. 537–542.

Launder, B. E., and Spalding, D. B., 1974, "The Numerical Computation of Turbulent Flows," *Computer Methods in Applied Mechanics and Engineering,* Vol. 3, pp. 269–289.

Launder, B. E., 1991, "Current Capabilities for Modelling Turbulence in Industrial Flow," *Applied Scientific Research,* Vol. 48, pp. 247–269.

Marquette, O. R., and Childs, D. W., 1995, "An Extended Three-Control-Volume Theory for Circumferentially Grooved Liquid Seals," Paper no. 95-TRIB-15, ASME/STLE Tribology Conference, October 8–11, Orlando, FL.

Nordmann, R., and Dietzen, F. J., 1988, "Finite Difference Analysis of Rotordynamic Seal Coefficients for an Eccentric Shaft Position," paper presented at the Rotordynamics Instability Problems in High Performance Turbomachinery, Texas A&M University, College Station, TX.

Rhode, D. L., Hensel, S. J., and Guidry, M. J., 1992, "Labyrinth Seal Rotordynamic Forces Using a Three-Dimensional Navier-Stokes Code," *ASME Journal of Tribology,* Vol. 114, pp. 683–689.

San Andres, L., 1997, "Transient Response of Externally Pressurized Fluid Film Bearings," *Tribology Transactions,* Vol. 40, pp. 147–155.

Schlichting, H., 1978, *Boundary Layer Theory,* Seventh ed., McGraw-Hill, Inc, New York.

Staubli, T., 1993, "A Labyrinth Seal—ETHZ Test Case," presented at Société Hydrotechnique de France, October, Paris.

Tam, L. T., Przekwas, A. J., Muzsynska, A., Hendricks, R. C., Braun, M. J., and Mullen, R. L., 1988, "Numerical and Analytical Study of Fluid Dynamic Forces in Seals and Bearings," *ASME Journal of Vibration, Acoustics, Stress and Reliability in Design,* Vol. 110, pp. 315–325.

Van Doormal, J. P., and Raithby, G. D., 1984, "Enhancements of the SIMPLE Method for Predicting Incompressible Fluid Flow," *Numerical Heat Transfer,* Vol. 7, pp. 147–163.

Zhu, J., and Rodi, W., 1991, "A Low Dispersion and Bounded Convection Scheme," *Computer Methods in Applied Mechanics and Engineering,* Vol. 92, pp. 87–96.

APPENDIX

Relations used to calculate the first order turbulent viscosity (16):

$$|\vec{\omega}|_0 = \sqrt{\left(\frac{\partial v_0}{\partial \xi} - \frac{\partial u_0}{\partial \eta}\right)^2 + \left(\frac{\partial w_0}{\partial \eta} + \frac{w_0}{\eta}\right)^2 + \left(\frac{\partial w_0}{\partial \xi}\right)^2} \quad \text{(A.1)}$$

$$|\vec{\omega}|_1 = \frac{1}{|\vec{\omega}|_0}\left\{\left(\frac{\partial v_0}{\partial \xi} - \frac{\partial u_0}{\partial \eta}\right)\left[\left(\frac{\partial v}{\partial x}\right)_1 - \left(\frac{\partial u}{\partial r}\right)_1\right] + \left(\frac{\partial w_0}{\partial \eta} + \frac{w_0}{\eta}\right)\cdot\left[\left(\frac{\partial w}{\partial r}\right)_1 + \left(\frac{w}{r}\right)_1 - \left(\frac{\partial v}{r\partial \theta}\right)_1\right] - \left(\frac{\partial w_0}{\partial \xi}\right)\left[\left(\frac{\partial u}{r\partial \theta}\right)_1 - \left(\frac{\partial w}{\partial x}\right)_1\right]\right\} \quad \text{(A.2)}$$

$$\left(\frac{\partial v}{\partial x}\right)_1 = \frac{\partial \hat{v}_1}{\partial \xi} - \tilde{a}\frac{\partial v_0}{\partial \eta}, \quad \left(\frac{\partial u}{\partial r}\right)_1 = \frac{\partial \hat{u}_1}{\partial \eta} - \tilde{b}\frac{\partial u_0}{\partial \eta}, \quad \text{(A.3a)}$$

$$\left(\frac{\partial w}{\partial r}\right)_1 = \frac{\partial \hat{w}_1}{\partial \eta} - \tilde{b}\frac{\partial w_0}{\partial \eta}, \quad \left(\frac{w}{r}\right)_1 = \frac{\hat{w}_1}{\eta} - \tilde{g}\frac{w_0}{\eta}, \quad \text{(A.3b)}$$

$$\left(\frac{\partial v}{r\partial \theta}\right)_1 = -i\frac{\hat{v}_1}{\eta} + i\tilde{g}\frac{\partial v_0}{\partial \eta}, \quad \text{(A.3c)}$$

$$\left(\frac{\partial u}{r\partial \theta}\right)_1 = -i\frac{\hat{u}_1}{\eta} + i\tilde{g}\frac{\partial u_0}{\partial \eta}, \quad \left(\frac{\partial w}{\partial x}\right)_1 = \frac{\partial \hat{w}_1}{\partial \xi} - \tilde{a}\frac{\partial w_0}{\partial \eta} \quad \text{(A.3d)}$$

Derivatives in wall-neighboring cells were estimated from the simplified momentum equations. For walls aligned to the axial direction, $\Phi \in \{u, w\}$,

$$\frac{\partial \hat{\Phi}_1}{\partial \eta} = \frac{\mu_{lam}}{\mu_0}\left[\left(\frac{\partial \hat{\Phi}_1}{\partial \eta}\right)_w - \left(\tilde{b}_w + \frac{\hat{\mu}_1}{\mu_0}\right)\left(\frac{\partial \Phi_0}{\partial \eta}\right)_w\right] + \tilde{b}\frac{\partial \Phi_0}{\partial \eta}, \quad \text{(A.4)}$$

and for walls aligned to the radial direction, $\Phi \in \{v, w\}$,

$$\frac{\partial \hat{\Phi}_1}{\partial \xi} = \frac{\mu_{lam}}{\mu_0}\left[\left(\frac{\partial \hat{\Phi}_1}{\partial \xi}\right)_w - \frac{\hat{\mu}_1}{\mu_0}\left(\frac{\partial \Phi_0}{\partial \xi}\right)_w - \tilde{a}_w\left(\frac{\partial \Phi_0}{\partial \eta}\right)_w\right] + \tilde{a}\frac{\partial \Phi_0}{\partial \eta}. \quad \text{(A.5)}$$

The wall distance $y = y_0 + \epsilon \cdot \tilde{y}_1$ is

$$\frac{\tilde{y}_1}{y_0} = -\frac{\eta \tilde{g}}{(r_{\text{Stat}} - \eta)}. \quad \text{(A.6)}$$

Experimental Rotordynamic Coefficient Results for (a) a Labyrinth Seal With and Without Shunt Injection and (b) a Honeycomb Seal

E. A. Soto
Conjunto Gran Sabana,
Edif. Auyantepuy,
Apartamento PH-A,
Calle Chile

D. W. Childs
Turbomachinery Laboratory,
Texas A&M University,
College Station, TX 77843

Centrifugal compressors are increasingly required to operate at higher pressures, speeds, and fluid density. In these conditions, compressors are susceptible to rotordynamic instabilities. To remedy this situation, labyrinth seals have sometimes been modified by using shunt injection. In shunt injection, the gas is taken from the diffuser or discharge volute and injected into an upstream chamber of the balance-piston labyrinth seal. The injection direction can be radial or against rotation. This study contains the first measured rotordynamic data for labyrinth seals with shunt injection. A comparison has been made between conventional labyrinth seals, labyrinth seals with shunt injection (radial and against rotation), and a honeycomb seal. Labyrinth seals with injection against rotation are better able to control rotordynamic instabilities than labyrinth seals with radial injection; however, the leakage is slightly higher. The leakage comparison for all seals demonstrates that the honeycomb seal has the best flow control. Test data are presented for a top rotor surface velocity of 110 m/sec, a supply pressure of 13.7 bars, and IPr = 0.95 (injection pressure is 1.05 = 1/0.95 times the seal inlet pressure). For these conditions, and considering effective damping, the labyrinth seal with injection against rotation is better than the honeycomb seal when the pressure ratio across the seal PR < 0.45. On the other hand, the honeycomb seal is better when PR > 0.45. The effectiveness of the shunt-injection against rotation in developing effective damping is reduced with increasing rotor surface velocity.

Introduction

Labyrinth seals have been used extensively in compressors and have a good capacity to control leakage. Field experience, experimental tests, and analysis of labyrinth seals have shown that they can generate rotordynamic instabilities. Honeycomb seals have shown better rotordynamic characteristics than labyrinth seals (for length $L \geq 50.8$ mm). Childs et al. (1989) presented the first published data of stiffness and damping for smooth-rotor/honeycomb-stator (honeycomb) gas annular seals. They concluded the following: for prerotated flows entering the seal in the direction of rotation, honeycomb seals provided the best rotordynamic stability, followed in order by the labyrinth seal, and smooth-stator seals. Childs et al. (1990, 1992) also measured rotordynamic coefficients for honeycomb seals, and showed (for a variety of geometries) that honeycomb seals have good rotordynamic stability characteristics and are insensitive to inlet preswirl.

Shunt injection is one approach to improve the rotordynamic characteristics of labyrinth seals. High pressure gas, usually from compressor discharge, is injected into an intermediate labyrinth cavity at several circumferential locations. The injection can be radial or against rotation[1]. Shunt injection against rotation or negative swirl is shown in Fig. 1. In this approach, the flow injection is sufficient to reverse the flow direction in the seal. The principal advantage of shunt injection is a reduction of the circumferential velocity, which leads to a reduction in the cross-coupled stiffness, k. One disadvantage of shunt injection is the performance penalty involved in diverting flow from compressor discharge and recirculating it through the machine.

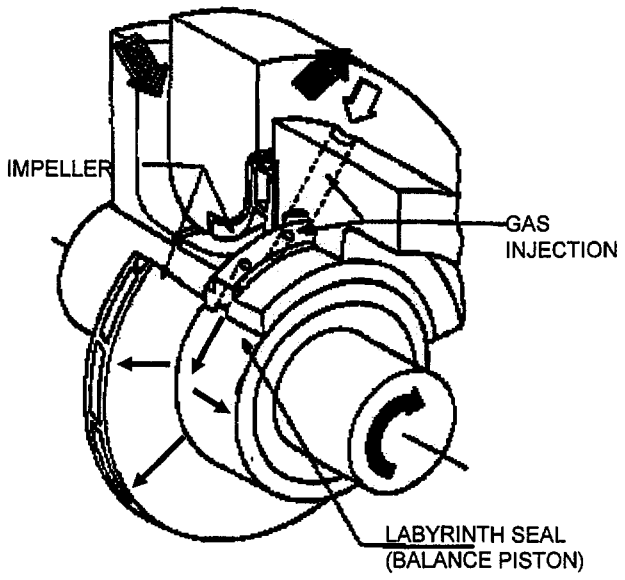

Fig. 1 Labyrinth seal with shunt injection, adapted from Kanki et al. (1988)

Contributed by the International Gas Turbine Institute and presented at the International Gas Turbine and Aeroengine Congress and Exhibition, Stockholm, Sweden, June 2–5, 1998. Manuscript received by the ASME Headquarters April 1, 1998. Paper No. 98-GT-8. Associate Technical Editor: R. Kielb.

[1] Tondl (1967) initially proposed injection against rotation for gas bearings to improve stability.

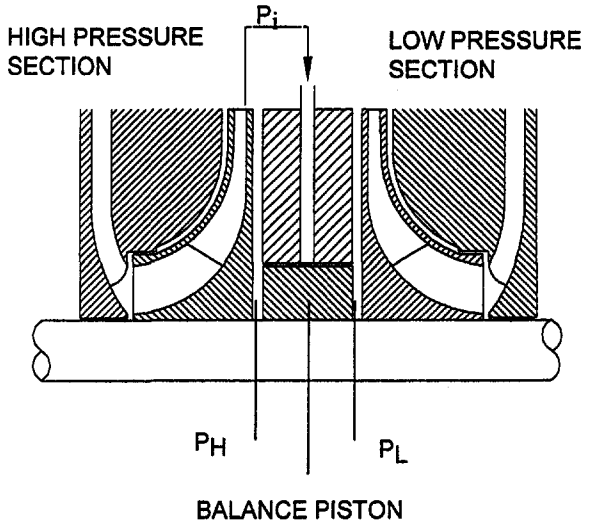

Fig. 2 Shunt injection application

Labyrinth seals with shunt injection have been used in centrifugal compressors since the early 1970s, Memmott (1990, 1992). Shunt injection was adopted to solve instability problems and subsynchonous vibrations, especially in back-to-back centrifugal compressors in high-speed and high-pressure applications (Memmott, 1990; Fozi, 1986). Back-to-back centrifugal compressors are susceptible to rotordynamic instabilities due to the destabilizing effects of long (mid-rotor) labyrinth seals (Kirk and Donald, 1983).

There are case histories that support the application of shunt injection seals. Kirk (1986) discussed a subsynchronous vibration problem with a centrifugal compressor that was solved using shunt injection against rotation on a labyrinth seal. Kanki et al. (1988) presented a rotordynamic analysis for a back-to-back centrifugal compressor. They implemented shunt injection against rotation in the balance-piston labyrinth seal to achieve stable operation. The compressor's test results showed high rotordynamic stability and low vibration levels.

Test Apparatus and Experimental Set-Up

Shunt-injection Geometries. Two different shunt injection seals were tested, radial and against rotation injection. The principal dimensions are shown in Fig. 3. To avoid choking in the shunt injection feed holes, the diameter of the injection holes was calculated, requiring that the exit Mach number be smaller than 0.33. This condition was checked with test data, and the Mach number ranged between 0.22 and 0.32. The standard labyrinth seal without injection has 20 teeth with a pitch of 3.18 mm and tooth height of 3.17 mm. The fourth tooth is removed for shunt injection.

Test Apparatus. All tests and experimentation were done in the air rig facility developed as part of a joint NASA-USAF funded program. The rig was designed in 1982 by J. B. Dressman of the University of Louisville. A full description is provided by Childs et al. (1986). The rig can measure axial pressure distribution, air flow rate, temperature, vibration amplitudes, and seal reaction forces. The rotordynamic coefficients are calculated from transient measured reaction force and motion data.

The working fluid of the rig is air. The basic configuration of the test apparatus includes a rotor coupled to an electric motor. The test apparatus can control the static eccentricity position of the seal. The rotor is suspended in a pendulum fashion from an upper, rigidly mounted, pivot shaft. This arrangement allows horizontal motion control of the rotor. A cam within the pivot shaft is used to control the vertical position.

The test rig was originally designed to test annular seals with axial flow; i.e., the flow goes from high pressure to low pressure side. In shunt injection application, gas is supplied to an intermediate cavity of the labyrinth seal, and the flow goes to both sides of the seal. Consequently, modifications were introduced to adapt the test apparatus for intermediate injection.

Test Parameters. The test rig can be used to study the effects of the following independent test parameters on the rotordynamic and leakage characteristics of annular gas seals: rotor speed, pressure ratio across the seal, injection pressure ratio, inlet fluid prerotation[2], seal clearance, seal supply pressure, and seal geometry. Test points are measured by varying the first three parameter over the values specified in Table 1.

Seal pressure ratio across the seal (PR), is the ratio between the low pressure side and the high pressure side of the seal, $PR = P_L/P_S$ for the normal labyrinth and honeycomb seals, and $PR = P_H/P_L$ for the shunt injection seals; see Fig. 2. In real applications, this fraction represents the pressure ratio across the balance piston of the compressor.

In compressors, the injection pressure of shunt injection seals depends on where the gas is taken from the stage's volute, as well as pressure losses in the channel. The injection pressure ratio (IPr), is the ratio of the high pressure side of seal to the shunt-injection pressure, $IPr = P_H/P_i$. Three injection pressure ratios IPr were tested for each pressure ratio across the seal; specifically, 95 percent, 90 percent, and 85 percent ratio were used. This parameter only applies to the shunt injection seals.

[2] Inlet prerotation is provided by guide vanes. Inlet swirl parameters are provided in Appendix A.

Nomenclature

C, c = direct and cross-coupled damping coefficients (N-s/m)
$C_{\text{eff}} = C(1 - k/C\omega)$, effective damping (N-s/m)
C_r = seal clearance (mm)
D = shaft diameter (mm)
$f_w = k/C\omega$, whirl frequency ratio
f_{SX}, f_{SY} = seal reaction forces on the stator housing (N)
$IPr = P_H/P_i$ injection pressure ratio for shunt injection seals
K, k = direct and cross-coupled stiffness (N/m)
L = seal length (mm)
M_S = stator housing mass (Kg)
P_H = supply high pressure for seals with shunt injection (bar)
P_i = injection pressure (bars), for shunt injection seals
P_L = exit low pressure for seals with shunt injection (bar)
P_s = supply pressure (bars), for labyrinth without injection and honeycomb seals
$PR = P_L/P_H$ pressure ratio across the seal
R = shaft radius (mm)
r = whirl amplitude (mm)
$u_0 = U_0/R\omega$, inlet circumferential velocity ratio
U_0 = inlet circumferential velocity component (m/s)
X, Y = displacement of the rotor relative to the stator
$\dot{X}, \dot{Y}$ = velocity of the rotor relative to the stator (m/s)
$\ddot{X}, \ddot{Y}$ = acceleration of the stator relative to ground (m/s^2)
ω = rotor angular velocity (rpm)

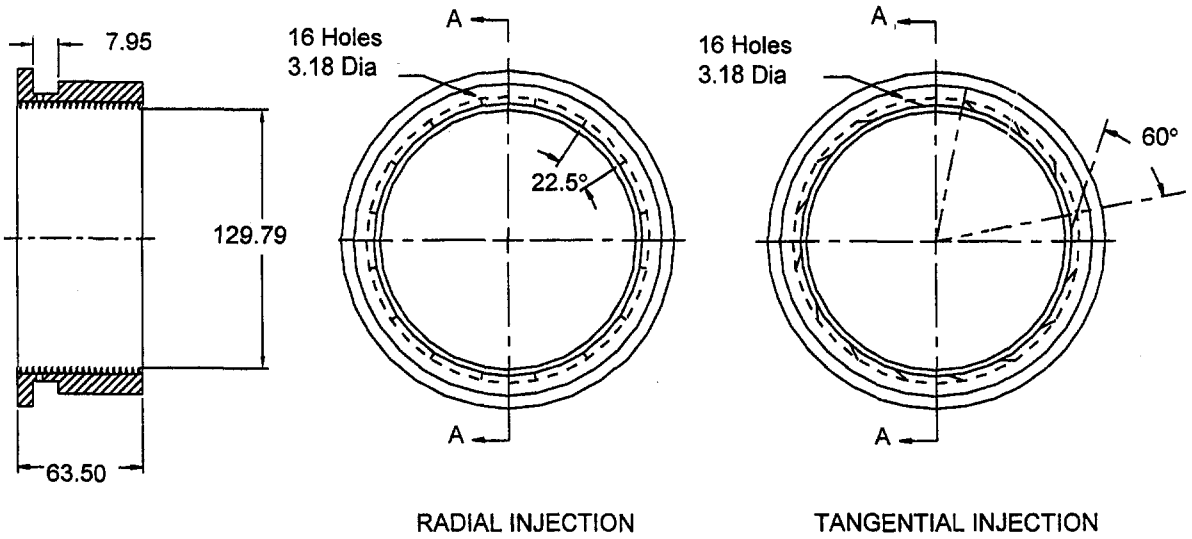

Fig. 3 Labyrinth seal with shunt injection, dimensions in mm

Table 1 Test points at an injection pressure of 13.77 bars

Rotor Speed ω (cpm)	Pressure Ratio PR
4680	0.65
	0.45
	0.30
8640	0.65
	0.45
	0.30
16500	0.65
	0.45
	0.30

Table 2 Seal geometries

Seal Number	Seal Type	
1	Labyrinth*	Full Pre-Swirl
2	Labyrinth (Shunt Injection)	Radial Injection
3	Labyrinth (Shunt Injection)	Injection Against Rotation
4	Honeycomb**	Full Pre-Swirl

Internal Dia. (mm) = 129.79, L/D = 0.5, Cr (mm) =0.22
* Tooth height = 3.17 mm; Tooth pitch = 3.18 mm; Tooth taper angle = 12 degrees.
** Cell width = 1.58 mm, Cell depth =2.29 mm

The seal injection pressure of 13.77 bars is the same as the pressure supply for the labyrinth seal and honeycomb seal.

Rotordynamic Coefficient Identification. The equation of motion for the seal stator housing is:

$$\begin{Bmatrix} f_{SX} - M_S\ddot{X}_S \\ f_{SY} - M_S\ddot{Y}_S \end{Bmatrix} = \begin{bmatrix} K & k \\ -k & K \end{bmatrix} \begin{Bmatrix} X \\ Y \end{Bmatrix} + \begin{bmatrix} C & c \\ -c & C \end{bmatrix} \begin{Bmatrix} \dot{X} \\ \dot{Y} \end{Bmatrix}, \quad (1)$$

where M_S is the stator housing mass, f_{SX} and f_{SY} are the measured forces on the stator housing, K and k are the direct and cross-coupled stiffness, and C and c are the direct and cross-coupled damping. The acceleration components of the housing, measured by the accelerometers, are denoted by $\ddot{X}_S$ and $\ddot{Y}_S$. The rotordynamic coefficients are identified in the frequency domain by a method that was previously defined by Childs et al. (1986). A swept sine-wave excitation is used over the 40 ~ 70 Hz frequency range.

Seal Geometries. This study was carried out to make comparisons of rotordynamic performance and leakage flow control between labyrinth seals (with preswirl), labyrinth seals with shunt injection (radial and against rotation), and a honeycomb seal. Table 2 summarizes the test configurations. Preswirl flow in the direction of rotation is the normal inlet seal flow condition in centrifugal compressors. Consequently, the labyrinth seal with full preswirl simulates a normal situation in compressors. The honeycomb seal is tested in only one swirl condition because preswirl has a minimal influence with honeycomb seals that are longer than 50.8 mm, Childs et al. (1989, 1990, 1992).

Table 3 Shunt injection seals representation in graphs

Symbol	Seal
■	Shunt Radial Injection, IPr=.85
⊟	Shunt Against Rotation, IPr=.85
◆	Shunt Radial Injection, IPr=.90
◇	Shunt Against Rotation, IPr=.90
●	Shunt Radial Injection, IPr=.95
○	Shunt Against Rotation, IPr=.95

Test Results and Comparison (Shunt Injection Seals)

Table 3 shows the different symbols used to identify the labyrinth seals with shunt-injection test results. The dark squares, diamonds, and circles represent the radial shunt injection with injection pressure ratio of 0.85, 0.90 and 0.95, respectively. The light squares, diamonds, and circles represent injection-against-rotation data points for the same injection pressure ratios.

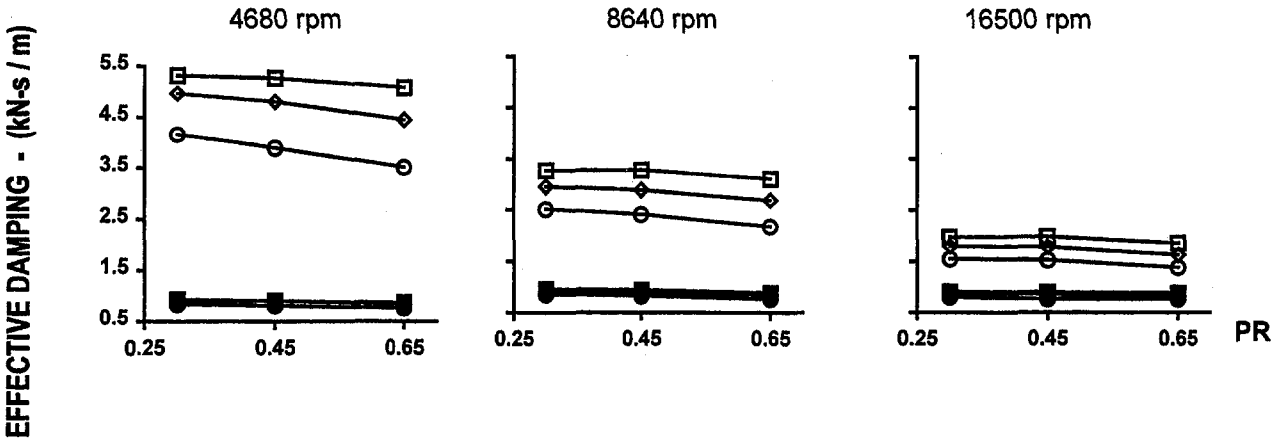

Fig. 4 Effective damping versus pressure ratio (Shunt injection)

In all figures, the independent parameter is the pressure ratio across the seal (PR). Inlet circumferential velocity of the fluid entering the seal is not used for comparison because it is not an appropriate parameter for the shunt-injection seals.

The rotor surface speeds for the three cases tested are 31.1, 57.5, and 110 m/sec, respectively, versus a normal operating range for compressors of 100 to 170 m/sec. Hence, the highest speed tested is close to the bottom "real" speed in compressors, and this velocity condition (110 m/sec) is an adequate point for comparison with compressors. In compressor applications, the pressure ratio across the balance piston varies between 0.5 to 0.6 for back-to-back and 0.4 to 0.5 for straight-through machines.

An uncertainty analysis was carried out for the rotordynamic coefficients using the approach of Holman (1989). The maximum calculated uncertainty values for K, k, and C were 100. N/m, 56. N/m, and .13 N-s/m, respectively. Over the frequency range of excitation (30–70 Hz.), the rotordynamic coefficients are frequency independent. The results were entirely repeatable.

Effective Damping. Effective damping, $C_{\text{eff}} = C(1 - k/C\omega)$, is used here to evaluate the overall seal stability performance. This is an important parameter in comparing annular seals for rotordynamic stability. It combines the effect of direct damping and cross-coupled stiffness, which are both associated with rotor stability.

The effective damping for injection against rotation is three or four times larger than for radial injection, Fig. 4. The effective damping for radial injection is largely independent of speed, pressure ratio across the seal, and seal inlet pressure ratio. For injection against rotation, the higher the injection pressure, the larger the effective damping. Furthermore, C_{eff} is reduced with increasing running speed and is not very sensitive to changes in Pr.

Cross-Coupled Stiffness. Cross-coupled stiffness k can cause rotordynamic instability in turbomachinery. Consequently, k should have a low or negative value. Measured values for cross-coupled stiffness are illustrated in Fig. 5 for shunt injection at the highest running speed. The injection against rotation gives the greatest negative values. The higher the injection pressure in the seal, the larger the (negative) cross-coupled stiffness. The cross-coupled stiffness for the radial shunt injection seal is constant in all cases; hence, the data points fall on top of each other.

Direct Damping. A positive and large magnitude of direct damping in the annular seal improves rotordynamic response. Direct damping counteracts the destabilizing effects of cross coupled stiffness in the rotors. Figure 6 shows the direct damping for the shunt injection seals. The higher the injection pressure in the seal, the greater the damping. For both shunt injection seals at the same injection pressure ratio IPr, the direct damping values are just about the same. When the pressure ratio across the seal (PR) increases, the direct damping decreases slightly. This effect could be related to the higher density of the fluid.

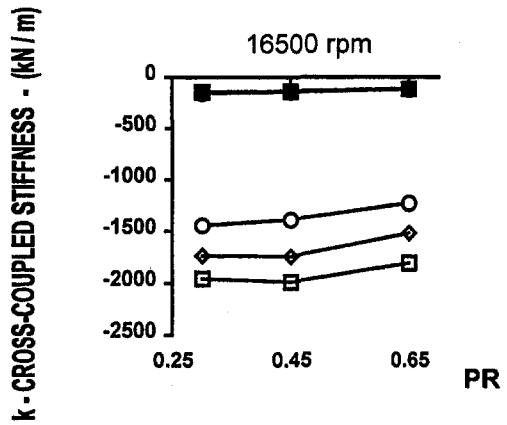

Fig. 5 Cross-coupled stiffness versus pressure ratio (shunt injection seals)

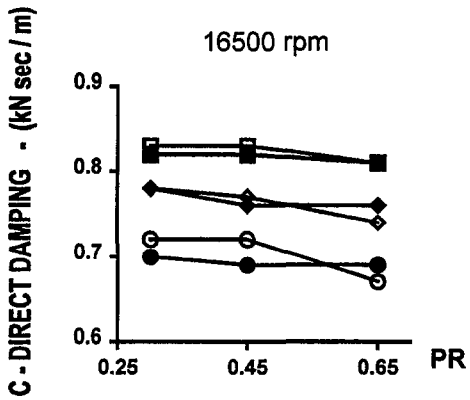

Fig. 6 Direct damping versus pressure ratio (shunt injection seals)

Whirl Frequency Ratio. In an annular seal, the tangential force on a synchronous precessing seal (forward whirl) is $f_\theta = (k - C\omega)A$, where A is the radius of precession. Hence, the

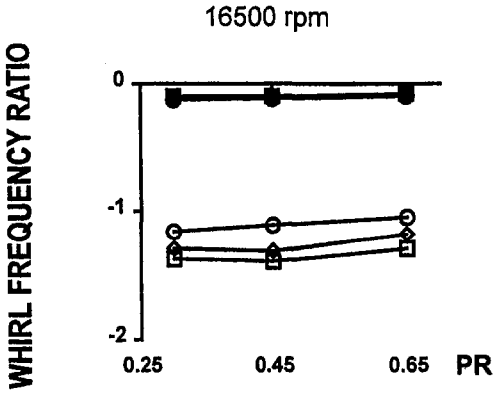

Fig. 7 Whirl frequency ratio versus pressure ratio (shunt injection seals)

Table 4 Seals representation in graphs

Symbol	Seal
—□—	Labyrinth - Full Pre-Swirl
—▲—	Shunt Radial Injection, IPr=.95
—●—	Shunt Against Rotation, IPr=.95
—✱—	Honeycomb

whirl frequency ratio, $f_w = k/(\omega C)$, is the ratio of the destabilizing force contribution due to k, and the stabilizing force contribution due to C.

The whirl frequency ratio of the shunt injection seals are compared in Fig. 7. The whirl frequency for radial injection is constant (negative and close to zero). A negative value of the whirl frequency ratio means that the seal could destabilize the rotor for backward whirl. Unstable backward whirl is a rarely reported condition in turbomachinery (normally associated with rubbing) versus the prevalent forward-whirl instability conditions. Hence, negative values for f_w are considered as beneficial in their potential to resist forward whirl.

Test Results and Comparison (all seals)

Table 4 shows the symbols used to identify the seals test results. The square, triangle, circle, and asterisk represent the labyrinth seal, the labyrinth seal with radial injection, the labyrinth seal with injection against rotation, and the honeycomb seal, respectively.

Effective Damping. Figure 8 shows the magnitude of effective damping for the labyrinth and honeycomb seals. For low and medium running speed, the effective damping of the labyrinth seal with injection against rotation is usually larger; however, in one case it was lower than the honeycomb seal (PR = 0.65 and rpm = 8640). For the highest speed and $PR > 0.45$, the honeycomb seal has better effective damping than the labyrinth seal with injection against rotation. In all cases, the effective damping of the shunt injection configuration is at least twice the magnitude of the labyrinth seal without injection. For honeycomb seals, C_{eff} is insensitive to running speed and increases with increasing PR.

Cross-Coupled Stiffness. Figure 9 shows the measured values of cross coupled stiffness for both the labyrinth and honeycomb seals. The lower magnitudes are for the labyrinth seal with shunt injection, radial, and against rotation (largest negative values), while the highest positive (destabilizing) values are for the honeycomb seal.

Direct Damping. Figure 10 compares direct damping for both the labyrinth and honeycomb seals. Direct damping is generally larger for the honeycomb seal than the labyrinth seals and increases with increasing pressure ratio (increasing density of the flow). In all cases, the direct damping of the shunt injection configurations is at least twice the magnitude of the labyrinth seal without shunt injection.

Whirl Frequency Ratio. Figure 11 shows the whirl frequency for the labyrinth and honeycomb seals. In all cases, the whirl frequency ratio of the labyrinth seals with shunt injection is less than zero (i.e., negative magnitude). This result is caused by the negative cross-coupled stiffness. f_w of the labyrinth seals without injection is insensitive to change in PR.

Mass Flow Rate. Figure 12 shows the mass flow rate for the labyrinth and honeycomb seals. The mass flow rates of the labyrinth seals with shunt injection are the largest; while the honeycomb seal has the lowest flow rate.

Summary, Conclusion, and Discussion

Labyrinth seals with shunt-injection against rotation are better able to control rotordynamic instabilities than seals with radial injection.

Leakage comparison for all seals demonstrates the superiority of honeycomb seals, followed by labyrinth without injection, radial shunt injection, and finally, against-rotation shunt-injection.

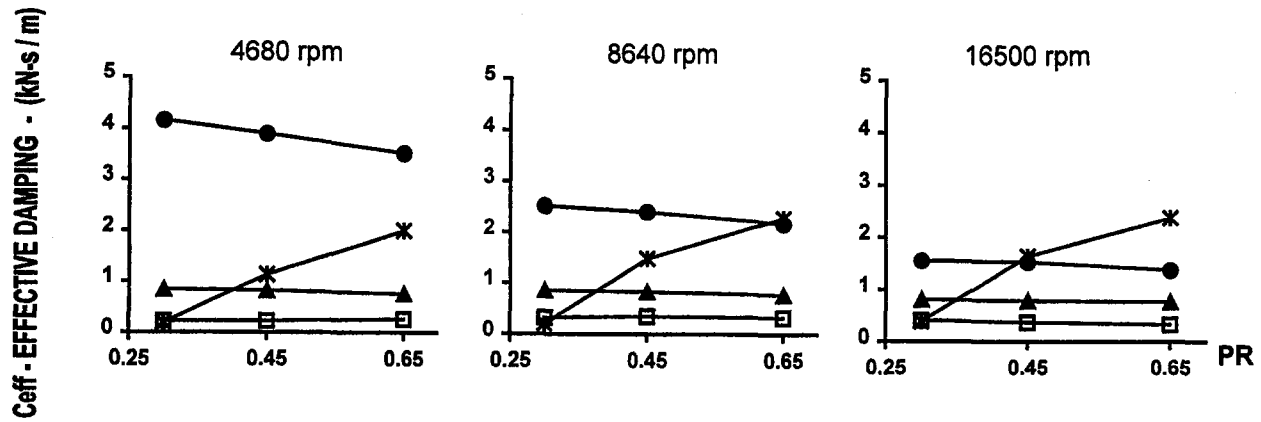

Fig. 8 Effective damping versus pressure ratio (all seals)

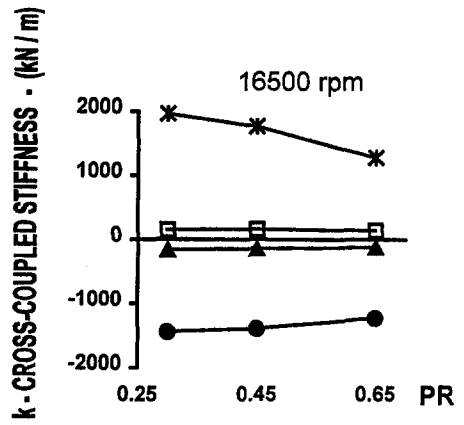

Fig. 9 Cross-coupled stiffness versus pressure ratio (all seals)

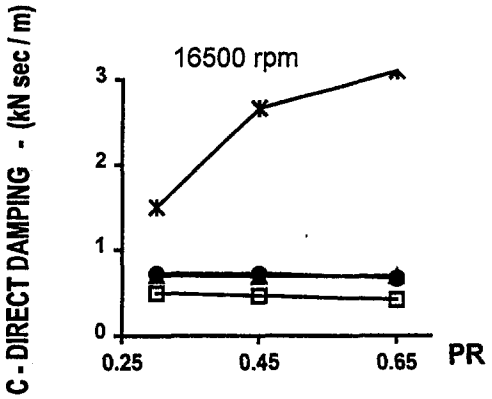

Fig. 10 Direct damping versus pressure ratio (all seals)

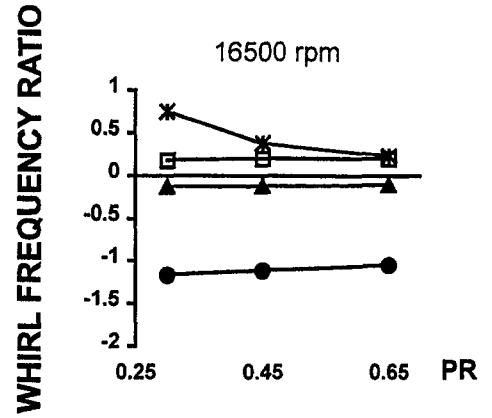

Fig. 11 Whirl frequency ratio versus pressure ratio (all seals)

For a surface velocity of 110 m/sec, intermediate pressure of 13.77 bars, and $IPr = 0.95$, the against-rotation shunt-injection seal had the highest effective damping for $PR < 0.45$; for $PR > 0.45$, the honeycomb seal was better. Note that these results apply only for the relatively low supply pressure conditions achievable in the present test apparatus. Calculations at pressure conditions that are more representative of compressor conditions predict that honeycomb seals will have significantly higher values for effective damping.

The relative advantages of honeycomb and against-rotation shunt-injection seals in an actual compressor application depend on many factors including surface velocity, gas density, injection velocity, and on factors other than rotordynamics. Hence, the decision on which approach to use should be based on a full rotordynamic calculation of the seal coefficients and the rotor response and stability characteristics.

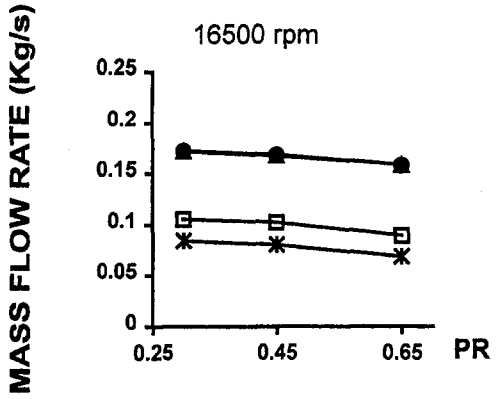

Fig. 12 Mass flow rate versus pressure ratio (all seals)

Zeidan et al. (1993) described a rotordynamically unstable centrifugal compressor. The instability continued after the central labyrinth seal was replaced with a labyrinth seal with shunt injection against rotation. Finally, a honeycomb seal was installed to solve the problem. This is the only case (known to the authors) when against-rotation injection failed, and honeycomb worked. Unfortunately, the material presented by Zeidan et al. are not adequate to evaluate the shunt-injection design in term of a comparison to the results presented here.

References

Childs, D. W., Nelson, C. E., Nicks, C., Sharrer, J., Elrod, D., and Hale, K., 1986, "Theory Versus Experiments for the Rotordynamics Coefficients of Annular Gas Seals: Part 1—Test Facility and Apparatus," *ASME Journal of Tribology,* Vol. 108, pp. 426–432.

Childs, D. W., Elrod, D., and Hale, K., 1989, "Annular Honeycomb Seals: Test Results for Leakage and Rotordynamic Coefficients; Comparisons to Labyrinth and Smooth Configurations," *ASME Journal of Tribology,* Vol. 111, pp. 293–301.

Childs, D., Elrod, D., and Ramsey, C., 1990 "Annular Honeycomb Seals: Additional Test Results for Leakage and Rotordynamic Coefficients," Proceedings, IFToMM Third International Conference on Rotordynamics, Lyon, France.

Childs, D., and Kleynhans, G., 1992, "Experimental Rotordynamic and Leakage Results for Short (L/D = 1/6) Honeycomb and Smooth Annular Pressure Seals," Proceedings, IMECHE Fifth International Conference on Vibrations in Rotating Machinery."

Fozi, A. A., 1986, "An Examination of Gas Compressor Stability and Rotating Stall," Rotordynamic Instability Problems in High Performance Turbomachinery, NASA CP 2443, Proceedings of a Workshop held at Texas A&M University, pp. 19–33.

Holman, J. P., (1989), *Experimental Methods for Engineers,* McGraw-Hill, New York, NY, pp. 41–42.

Kanki, H., Katayama, K., Morii, S., Mouri, Y., Umemura, S., Ozawa, U., and Oda, T., 1988, "High Stability Design for New Centrifugal Compressor," Rotordynamic Instability Problems in High Performance Turbomachinery, NASA CP 3026, Proceedings of a Workshop held at Texas A&M University, pp. 445–459.

Kirk, R. G., and Donald, G. H., 1983, "Design Criteria for Improved Stability of Centrifugal Compressors," *Rotor Dynamical Instability,* Proceedings, Applied Mechanics, Bioengineering, and Fluids Engineering Conference, Vol. 55, ASME, New York, pp. 59–71.

Kirk, R. G., 1986, "Labyrinth Seal Analysis for Centrifugal Compressor Design—Theory and Practice," Proceedings, Second IFToMM International Conference, Tokyo, Japan, pp. 589–596.

Memmott, E. A., 1990, "Tilt Pad Seal and Damper Bearing Applications to High Speed and High Density Centrifugal Compressor," Proceedings, Third IFToMM International Conference, Lyon, France, pp. 585–590.

Memmott, E. A., 1992, "Stability of Centrifugal Compressor by Application of Tilt Pad Seals, Damper Bearings and Shunt Holes," Proceedings, Fifth International Conference on Vibrations in Rotating Machinery IMechE, Bath, England, pp. 99–108.

Tondl, A., "Bearings with a Tangential Gas Supply," Proceedings, Gas Bearing Symposium, Paper No. 4, University of Southhampton.

Zeidan, F., Perez, R., and Stephenson, E., 1993, "The Use of Honeycomb Seals in Stabilizing Two Centrifugal Compressors," Proceedings, Twenty-Second

Turbomachinery Symposium, The Turbomachinery Laboratory, Texas A&M University System, College Station, Texas, pp. 3–15.

APPENDIX

Preswirl Conditions for Labyrinth and Honeycomb Seals

Table 2.1 provides data for $u_0(0) = U_0(0)/R\omega$, the circumferential-velocity preswirl ratio for the labyrinth and honeycomb seals with full preswirl inlet conditions. The prerotation values achieved in the test rig are small compared to values existing in real compressors.

Table 2.1 $u_0(0)$ for labyrinth and honeycomb seals

RPM	Pr	Labyrinth	Honeycomb
4680	0.65	0.6081	0.4686
	0.45	0.7099	0.5473
	0.30	0.7312	0.5723
8640	0.65	0.3522	0.2530
	0.45	0.3750	0.2891
	0.30	0.3848	0.3058
16500	0.65	0.1526	0.1168
	0.45	0.1760	0.1372
	0.30	0.1813	0.1448

A Test Facility for the Measurement of Torques at the Shaft to Seal Interface in Brush Seals

P. E. Wood

T. V. Jones

Department of Engineering Science,
Osnex Laboratory,
University of Oxford,
Parks Road, Oxford,
United Kingdom

An important factor in the performance of brush seals for a wide range of gas turbine applications is the rate of wear at the seal to shaft interface, which is dependant on the contact pressure that exists between the bristles and rubbing surface. This is dependent on a variety of effects. Principally, these are the aerodynamic forces bending the bristles onto the rubbing surface, frictional effects within the bristle pack and at the backing ring that arise with the application of pressure differential, geometrical changes due to centrifugal and thermal growths, and transient differential movements of the rotor that develop in flight manoeuvres. In order to investigate the effect of these phenomena on contact pressure, a test facility has been devised in which the torque exerted by a brush seal on a rotating shaft is used as an indirect measurement of contact pressure. This has necessitated the design of a test facility in which all system torques can be fully calibrated. Consequently, a pressure balanced design has been adopted in which applied seal differential and pressure levels have a minimal effect on axial loads at the rotor bearing assembly. The primary method of torque measurement is the instantaneous deceleration of the rotor. Thus, measurements over a wide speed range are acquired with high frequency instrumentation. The means whereby small parasitic torques are evaluated and corrected is given. Results demonstrating the dependence of contact pressure on seal differential and pressure levels are presented.

Introduction

The life of brush seals (Fig. 1.) for gas turbine sealing applications is limited by the rate of wear at the bristle to shaft interface. The wear is dependant on the contact pressure that exists between bristle tips and the rubbing surface. This contact pressure is in itself dependent on a number of operational factors.

The force field that is generated with the application of differential pressure across a brush seal is responsible for two phenomena that influence the bristle tip contact load. A tendency for the bristles to move radially inward under applied pressure is first mentioned by Ferguson (1988), and has subsequently been termed "blow down". Bayley and Long (1992) made pressure measurements at the backing ring of a brush seal. They observed a radial pressure gradient with decreasing magnitude toward the bristle tip. This gradient develops as a consequence of the flow within the seal converging, in order to pass between the backing ring and shaft surface. Since the bristles are inclined to the shaft surface, a radial pressure differential within the bristle matrix will produce a gross radial resultant force on the bristles that may be responsible for the "blow down" phenomena.

The axial pressure drop across a brush seal intensifies both frictional and interfacial contact forces between neighboring bristles and at the backing ring. Several effects have, in some part, been attributed to the consequent "stiffening" of the bristle matrix. Measurements of bristle tip contact pressure (Long and Marras, 1995; Basu et al., 1993) obtained by measuring load and displacement when a static rotor is deflected into a pressurised seal have shown that bristle stiffness increases almost linearly with pressure differential. "Hysteresis" has been observed in pressure drop versus mass flow characteristics (e.g., Chupp and Dowler, 1991) and in flow versus speed characteristics (Basu et al., 1993).

Brush seals offer a significant advantage over labyrinth seals in their ability to recover from excursions of the rubbing surface that occur in the flight cycle (Ferguson, 1988). "Blow down" is, therefore, to some extent, desirable as a recovery mechanism. It is particularly significant when clearance exists between the steady-state unpressurised bristle position and the rubbing surface (i.e., one which can not be closed by mechanical bending of the bristle alone). However, the magnitude of blow down should be limited so that wearing of the bristle tip does not result.

Bristle "stiffening" considerably increases the contact pressure at the bristle tips in the presence of excursions. Additionally, subsequent to transient differential movements (i.e., hysteresis) prevents full recovery of the bristles, and a degradation in sealing performance may result (Basu et al., 1993). A possible desirable effect is that an increase in the effective stiffness of the bristle mechanism may increase its resilience to excitations induced by unsteady upstream flow conditions.

The purpose of the current paper is to describe an apparatus and experimental technique that allows an indirect measurement of bristle tip contact pressure to be obtained under dynamic rotor conditions. This is achieved via the torque inferred from observation of rotor deceleration when drive power is removed. In order to isolate the torques produced by the brush seal, a semianalytical technique, based on published theory and observation, has been developed to calibrate the parasitic aerodynamic torques acting on the rotor—this is described. Results demonstrating the interaction of "blow down" and "stiffening" effects are presented for seals of both an initial build

Contributed by the International Gas Turbine Institute and presented at the International Gas Turbine & Aeroengine Congress & Exhibition, Orlando, FL, June 2–5, 1997. Manuscript received by the ASME Headquarters July 1997. Paper No. 97-GT-184. Associate Technical Editor: H. A. Kidd.

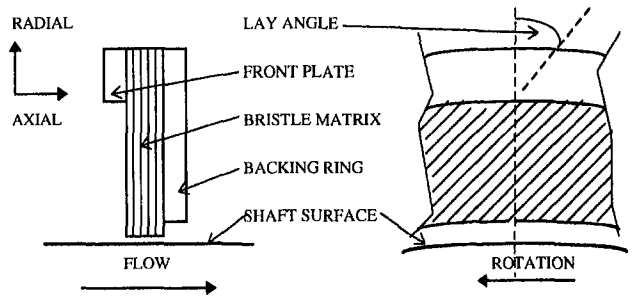

Fig. 1 Schematic of conventional brush seal

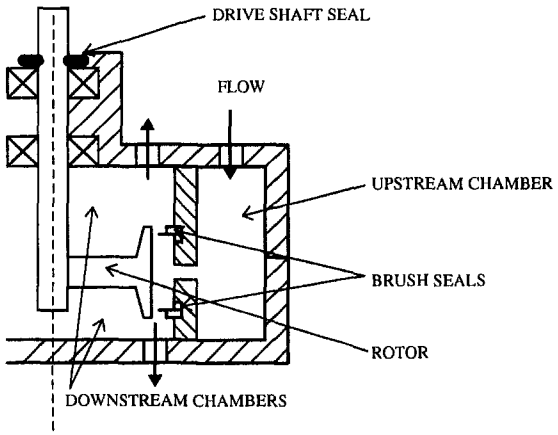

Fig. 2 General arrangement of working section

clearance and interference, over a range of engine representative conditions. Thus, the effect of operational parameters (pressure, speed, rotor displacements, and geometries) on seal performance characteristics (mass flow and contact loads) were investigated. The paper also includes results of a static flow test, demonstrating hysteresis in seal behavior, and an unpressurized dynamic test that is indicative of a hydrodynamic lift effect at the bristle tips.

Apparatus

A general arrangement of the working section of the brush seal test facility is shown in Fig. 2. Approximate geometries for the apparatus and seals are given in Table 1. In order to provide good experimental conditioning, all parasitic torques are minimized and, where possible, eliminated.

Two test seals of equivalent geometry but opposite lay angle were employed in a back-to-back configuration. Consequently, when pressurized via the interseal cavity, both faces of the rotor experienced the same downstream pressure, and axial loading

Table 1 Approximate geometries for apparatus and seals

Rotor Diameter / Seal Bore	300 mm
Bristle length	15 mm
Bristle Diameter	0.1 mm
Lay angle	30 degrees

of the rotor bearing was minimized. Additionally, the requirement for auxiliary seals, with their associated and undesirable torque, was removed. Aerodynamic torques were minimized with a small and geometrically simple rotor.

The rotor shaft was supported by two self-lubricating and mechanically preloaded angular contact ball races. Bearing temperatures were measured and used as to assess changes in operating conditions that may lead to variation in bearing torques. Precise location of the rotor was achieved by means of an eccentric arrangement. The position of the seals in the radial plane can also be adjusted. The shaft is driven by a 100 kW air turbine.

Air enters an annular plenum through four equally spaced holes that are circumferentially positioned in the face of the upper housing. Flow was then evenly distributed to the upstream face of each seal by being ducted through a narrow slot and then through an annular passage between the rotor and seal carriers. The outlets from both seals were connected to a single collector that was vented to the atmosphere via an orifice plate measuring section (British Standard institution, 1981).

Pressures were measured by a ZOC 14 Scanivalve. An accurate measurement of shaft speed was confirmed by comparison of data from three digital encoders operating at different frequencies. Deceleration was obtained from the discrete differential of the speed measurements. Centrifugal changes in rotor diameter and eccentricities were measured using two capacitance probes. Data acquisition to a PC was via a CIL interface.

Calibration

For a test facility configuration without brush seals, the total torque is comprised of the torques at the rotor and air motor bearings and aerodynamic drag on the rotor and at the air motor turbine. The bearing torques are considered to be constant with speed, being a function of the bearing load and the coefficient of sliding friction at the bearing interface. The differential pressure across the drive shaft seal gives rise to a small bearing load, and, consequently, a torque that will have linear dependence on the differential pressure between the downstream rotor cavities and atmosphere. The total bearing torque can therefore be described as

$$t_B = t_b + C_b \Delta P. \tag{1}$$

To estimate the aerodynamic torques, the torques generated by a disk and cylinder rotating in fluid are first considered independently. The integral momentum equations for a thin disk

Nomenclature

c_f = resistance coefficient for cylinder
C = linear coefficient pertaining to torque
D = diameter
$F = \dot{m}\sqrt{RT}/D_o^2 P_u$ = dimensionless flow rate term
I = moment of inertia
l = axial length of rotor
$\dot{m}$ = mass flow rate
P = absolute pressure
r = radius
R = gas constant
$\mathrm{Re}_\theta = \rho \omega r_o^2/\mu$ = rotational Reynolds number
t = torque
T = absolute temperature (static)
μ = dynamic viscosity
ρ = density
τ_θ = shear stress
ω = angular velocity
$\dot{\omega}$ = angular acceleration

Subscripts

A = aerodynamic
b = bearing component
B = total bearing
S = system
i/o = inner/outer
u/d = upstream/downstream

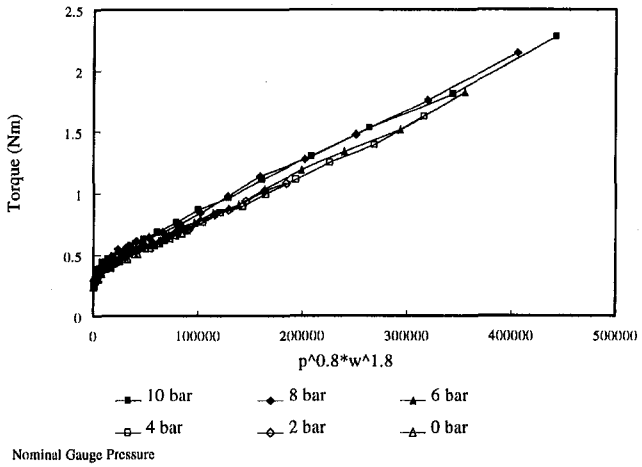

Fig. 3 Results for the torque calibration tests

rotating in an infinite quiescent environment were first derived and solved by von Karman (1921), in which the tangential shear stress on the disc (assuming constant fluid properties) is given by

$$\frac{\tau_\theta}{\rho\omega^2 r^2} = 0.0267\left(\mathrm{Re}_\theta\left(\frac{r}{r_o}\right)^2\right)^{-0.2}. \quad (2)$$

Torque is obtained by integrating the shear stress over the area and radius of the disc as follows:

$$t = \int_0^{r_o} r\tau_o 2\pi r dr = \int_0^{r_o} 0.168\rho\omega^2 r^4\left(\frac{\rho\omega r^4}{\mu r_o^2}\right)^{-0.2} dr. \quad (3)$$

Hence,

$$t = 0.04\mu^{1/5}\rho^{4/5}\omega^{9/5}r^{23/5}. \quad (4)$$

The experimental correlation of Theodorson and Regier (1944) for a cylinder rotating in fluid is

$$c_f = 0.0437\ \mathrm{Re}_\theta^{-0.2}, \quad (5)$$

where the shear stress coefficient is of the form

$$c_f = \frac{2\tau_\theta}{\rho\omega^2 r_o^2}. \quad (6)$$

Torque at the cylinder surface is expressed as the product of shear stress (from Eq. 6), surface area, and radius:

$$t = 0.137\mu^{1/5}\rho^{4/5}\omega^{9/5}r^{18/5}l \quad (7)$$

The functional form of Eqs. (4) and (7) is similar. Therefore, for a fixed geometry in a fluid of constant viscosity, the total aerodynamic torque acting on a body of circular cross section can be described by a function, such that,

$$t_A = C_A(\rho^{4/5}\omega^{9/5}). \quad (8)$$

Also from Eqs. (4) and (7), it can be seen that the aerodynamic torque is a strong function of radius. Consequently, The torque generated by the air motor turbine, which is of small radius and only operates in a low-density environment, is neglected in the presence of the dominant rotor torque. Combining Eqs. (1) and (8), the total system torque can be expressed by the following linear equation:

$$t_S = t_b + C_b\Delta P + C_A(\rho^{4/5}\omega^{9/5}). \quad (9)$$

Thus, the calibration constants for Eq. (9) can be derived from the results of rig tests without brush seals. The total system torque is determined from deceleration data using Eq. (10).

$$t_S = I\dot{\omega} \quad (10)$$

Experimental results for torque are plotted against the aerodynamic parameter of Eq. (9), results for six tests at different chamber pressures are presented in Fig. 3. The linearity of the data for different pressures gives confidence in the calibration. The low speed deviation from linearity can be attributed to the transition from turbulent to laminar flow, where the dependence no longer fits the form derived in Eqs. (4) and (7). For each run, these lower Reynolds numbers points are ignored; a line of best fit is extrapolated through the torque axis intercept. Hence, the coefficients of Eq. (9) are determined: the aerodynamic torque calibration constant from the gradient and the differential pressure effect on bearing torques from the variation in torque axis intercept with pressure and the unpressurized bearing torque term from the torque axis intercept for the zero differential pressure line.

For a test facility configuration incorporating brush seals, the outer cylindrical face of the rotor is subjected to the upstream seal pressure, and the remainder of the rotor is subjected to the downstream pressure. Hence, Eq. (9) is used to calculate torque for the total system at downstream pressure, and Eq. (7) is used to correct this value to account for the higher pressure at the outer cylindrical face.

Accuracy Considerations. Measured and derived quantities, along with their fractional uncertainties, are given in Table 2. Uncertainties for derived quantities ρ, μ, C_A, C_b, t_S, t_b, and t_A are established from typical arguments for independent and random errors (e.g., Taylor, 1982, p. 53). The error in speed measurement is due to digitization. Since deceleration is obtained from the discrete differential of successive speed measurements, its fractional uncertainty is inversely proportional to the deceleration and a typical uncertainty is quoted.

The errors incurred in the derivation of the seal torque from the sum of the system and parasitic torques are judged to be cumulative. Consequently, the degree of error in the derived seal torque, is dependant upon its magnitude in relation to the total system torque. In the present study, the seal torque typically accounts for between 30 percent and 50 percent of the total system torque. In the worst case, for a seal torque which is 30 percent of the total system torque, the maximum error in seal torque is ±7.5 percent.

Results

Prior to testing, the rotor was dynamically balanced to a quality consistent with that of the engine shaft. Capacitance probes were used to measure the centrifugal increase in rotor diameter. The radial growth of the outer cylindrical face was 40 microns at 10,000 rpm.

Clearance Seal Run Down Tests. Regulators were used to adjust the upstream pressure, and the pressure ratio across the seal was set with the manual outlet valve. The pressure supply was then isolated so that the pressure throughout the system was atmospheric. The rotor was accelerated to approximately 9500 rpm, at which point the seals were pressurized,

Table 2 Uncertainties in measured and derived quantities

Quantity	Instrumentation	Uncertainty
P	ZOC 14	+/- 0.08%
ω	Encoder	+/- 0.1%
$\dot{\omega}$	N.A.	+/- 1%
T	K- thermocouple	+/- 0.04%
ρ	N.A.	+/- 0.09%
μ	N.A.	+/- 0.04%
C_A	N.A.	+/- 1.01%
$C_b\Delta P$	N.A.	+/- 1.01%
t_S	N.A.	+/- 1.02%
t_b	N.A.	+/- 1.02%
t_A	N.A.	+/- 1.02%
$\dot{m}$	N.A.	+/- 1.5%

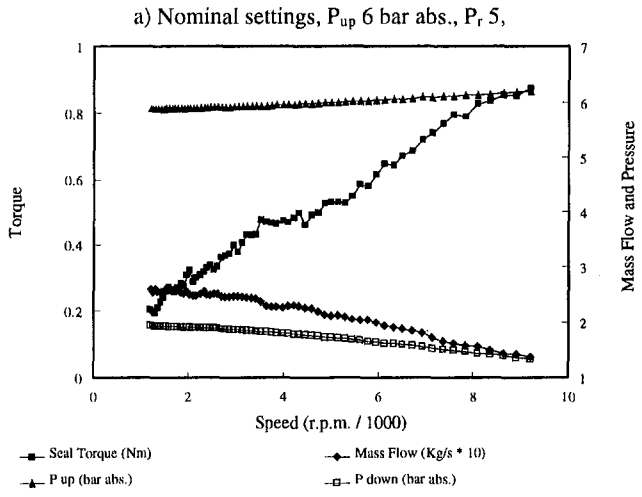

Fig. 4 Clearance seal run down tests

and the drive power was removed. Rotor speed, leakage flow, and seal cavity pressures were monitored as the rotor decelerated. Results are discussed for a series of tests conducted at different pressure ratios, all at a nominal upstream chamber pressure of 6 bar absolute.

Figures 4(a), 4(b), and 4(c) present test results for the seal pair conducted at pressure ratios of 5, 2, and 1.3, respectively. At high pressure ratio (Fig. 4(a)), seal torque is observed to decrease with decreasing rotor speed; mass flow and downstream pressure are observed to increase. There is a slight decrease in upstream pressure as the rotor decelerates; this can

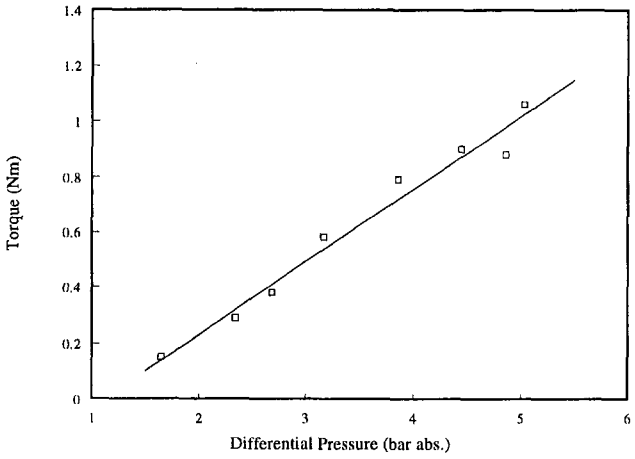

Fig. 5 Effect of differential pressure on maximum seal torques for a series of tests conducted at an upstream pressure of 6 bar abs

probably be attributed to the increasing mass flow. These phenomena are also apparent in the test with a pressure ratio of 2 (Fig. 4(b)). However, the magnitude of the torque generated when pressure is initially applied has decreased. The change in both seal torque and mass flow in the course of the test is less pronounced at the lower pressure ratio.

The phenomena of decreasing seal torque with decreasing rotor speed is characteristic of all tests conducted at a pressure ratio in excess of 1.3. For the test conducted at a pressure ratio of 1.3 (Fig. 4(c)), the seal torque remains nominally constant as the rotor decelerates. Mass flow and downstream pressure are both observed to increase. These phenomena are characteristic of all tests that were conducted at pressure ratios of 1.3 and below.

Given that the seals are of an initial build clearance, the measured seal torque is attributed to bristle "blow down". For the complete series of the present tests, the peak torque developed when pressure is initially applied to the seal is plotted against the differential pressure that existed between the seal cavities when the torque measurement was made (Fig. 5). These results demonstrate an apparently linear dependence in "blow down" generated bristle tip contact loads with differential pressure. These "blow down" related loads are developed when pressure is initially applied to the seal. It is reasonable to assume that bristle deflections propagate when frictional effects are reduced—due to transient and excited nature of the bristle matrix that results from a step change in pressure. The pressure axis intercept of Fig. 5 is indicative of a minimum differential pressure requirement to close the clearance between bristle tips and shaft surface.

For the present tests conducted at pressure ratios in excess of 1.2, the observed reduction in seal torque as the rotor decelerates is indicative of a frictional effect. It is reasoned that as the rotor centrifugally contracts; "blow down", responsible for radial deflection of the bristle tip, is restricted by the presence of frictional forces within the bristle matrix that arise as a result of the differential pressure across the seal. Consequently, as the bristle tip to shaft contact forces reduce, seal torque is reduced. Mass flow increases as a radial clearance develops between the shaft surface and some of the bristle tips and as a consequence of an overall increase in flow area. The fact that a measurable torque is always evident indicates that radial displacement of some of the bristle tips is always able to occur. The fact that changes in torque and mass flow become less pronounced as pressure ratio is reduced suggests that the magnitude of the frictional effect is dependant on the differential pressure across the seal.

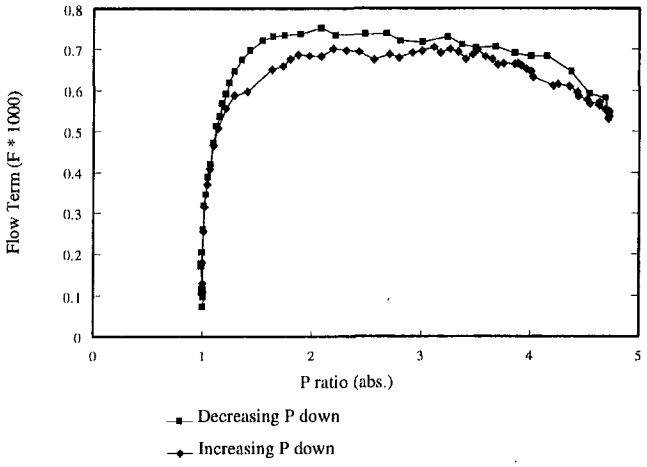

Fig. 6 Clearance seal static flow test at a nominal upstream pressure of 6 bar abs

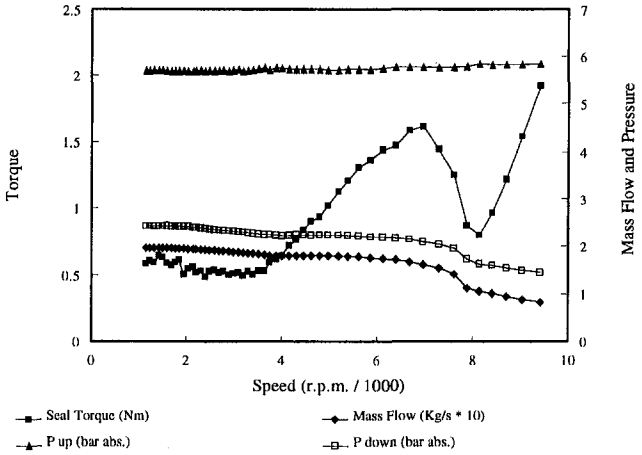

Fig. 7 Interference seal run down test

Clearance Seal Static Flow Test. The downstream outlet valve was closed, and the entire working section pressurised to 6 bar absolute. The outlet valve was then manually cycled from closed to open to closed. Cavity pressures and mass flow are monitored. Results are presented in the form of a dimensionless flow term "F", which is defined as

$$F = \frac{\dot{m}\sqrt{RT}}{D_o^2 P_u} \tag{11}$$

In Fig. 6, as downstream pressure is decreased, the reduction in the magnitude of the flow term at pressure ratios in excess of 2 is indicative of physical change in the seals geometry that is responsible for an improvement in sealing performance. Two mechanisms that could implement this change are bristle "blow down" and improved packing of the bristle matrix with an increase in differential pressure.

Frictional effects are evident from the hysteresis that is produced as pressure ratio is decreased from the maximum. It would appear that the changes in seal geometry that result from "blow down" and compacting of the bristle matrix are maintained by frictional forces as the pressure ratio is reduced, and improved sealing results. Below a pressure ratio of 1.2, hysteresis, and, consequently, frictional effects are no longer evident. This is entirely consistent with the dynamic tests conducted at the same nominal upstream pressure, where, at pressure ratios of 1.2 and below, constant seal torque throughout the speed range implies that frictional effects are no longer a factor inhibiting blowdown.

Interference Seal Dynamic Tests. The seal pair were of an initial build interference with greater lay angle (bristles more tangential to the shaft surface) than the previously discussed clearance seals. Figure 7 presents the result of a run down test that was conducted at a nominal upstream pressure of 6 bar absolute. The experimental procedure was identical to the previously discussed clearance seal tests.

Below 7000 rpm, the interference seals exhibit similar operational characteristics to the clearance seals. Decreasing torque and increasing mass flow, as the rotor decelerates, are both indicative of frictional effects. The local minimum in torque at 8000 rpm is accompanied by a sharp increase in mass flow and downstream pressure. An increase in seal torque implies a geometrical change that increases the magnitude of contact loads between bristle tips and shaft surface. A possible explanation for the observed inflection in the torque line is that vibration of the bristles temporarily allows them to overcome frictional restraint and blow down freely onto the shaft. Since upstream pressure is nominally constant in the course of the test, it seems likely that vibration is not flow induced. Additionally, during commissioning of the test facility, a small rotor resonance was measured at 6000 rpm, and stable behavior was noted in the rest of the speed range. Consequently, vibration of the bristles probably occurs as a result of resonance to excitation at their own natural frequency or an appropriate harmonic. A small eccentricity in the rotor could impose a suitable forcing function.

Figure 8 demonstrates the results of a test conducted with the same experimental procedure of the test of Fig. 7, with the exception that the upstream pressure was manually pulsed as the rotor decelerated. At speeds in excess of 3000 rpm, the initial application of pressure yields a torque and mass flow that is consistent with that obtained with initial application of pressure in the conventional rundown test. The present test also indicates frictional restraint of the bristles from the decrease in torque and increase in mass flow, once a steady upstream supply has been established. At 3500 rpm, shortly after the application of pressure at 4000 rpm, the seal torque is observed to decay rapidly despite the presence of full upstream pressure, such behaviour could be indicative of a vibratory effect. The application of pressure at approximately 3000 rpm yields a seal torque that is almost twice the magnitude of those produced at higher rotor speeds. Mass flow is also significantly reduced from that of the higher-speed applications of pressure.

Results of an acceleration/deceleration test are presented in Fig. 9. Seal pressure was applied whilst the rotor was stationary. The rotor was then accelerated to approximately 10000 rpm, at

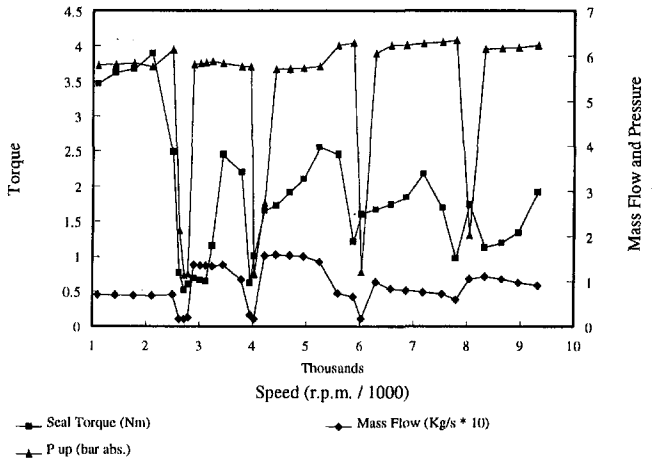

Fig. 8 Interference seal pulsed run down test

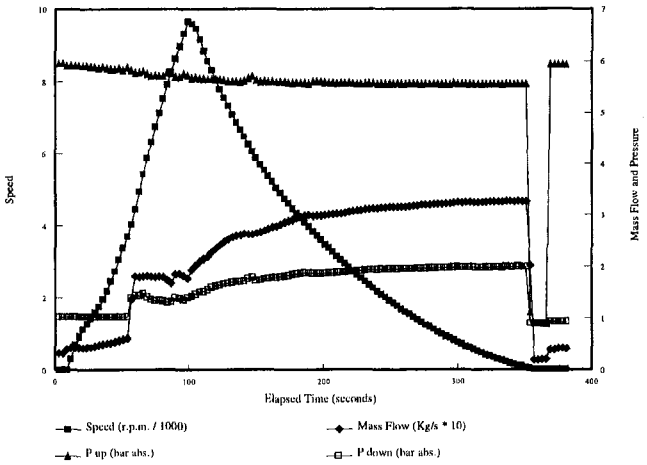

Fig. 9 Interference seal acceleration/deceleration test

which point drive power was removed. On the rotor coming to rest, the upstream pressure was cut, permitted to vent to upstream conditions, and then reapplied.

In the acceleration phase of the test (Fig. 9), at just before 4000 rpm, large increases in both mass flow and downstream pressure are observed. This is consistent with the pulsed run down test (Fig. 8), where improved seal performance is observed when pressure is applied at below 3500 rpm. As rotor speed is further increased, the downstream pressure and mass flow remain nominally constant. In the deceleration phase, an increase in downstream pressure and mass flow are observed, and this is consistent with the rundown tests.

The dynamic response of a viscously damped system is such that a system is typically capable of tracking an excitation that occurs at below its natural frequency. However, as the excitation frequency approaches and exceeds the systems natural frequency, the amplitude ratio and phase of the response become such that the system can no longer track the input (Rao, 1986). In the context of the current test (Fig. 9), if the bristles can no longer track the inherent orbiting eccentricity of the rotor, it is conceivable that the bristle tips are radially displaced and held in position by the differential pressure and frictional effects. The sudden decrease in seal performance could therefore be explained. The increase in torque and decrease in mass flow measured at low speeds in the pulsed rundown test (Fig. 8), could be attributed to a similar effect, where at low speed the bristles can track eccentricity in the orbiting rotor.

In Fig. 10, the results of an unpressurized, interference seal rundown test are presented. In order to obtain a figure for the coefficient of dynamic friction at the bristle to rotor interface (for the known bristle to rotor interference), an equation for bristle bending is applied to the low speed data, where centrifugal and hydrodynamic effects are not considered to be influential. The curve marked Model A, is obtained by applying the known centrifugal increase in rotor diameter to the bending equation. Model A is corrected with an estimate for the mean hydrodynamic pressure generated under the bristle tips; thus, the curve marked Model B is obtained. The estimate of hydrodynamic pressure is derived from the Reynolds equation; the bristles are assumed to be in contact with the high points of the rotor surface profile, and it is assumed that hydrodynamic pressure is generated in the clearance between bristle tips and the remainder of the rotor surface.

Model B does not exactly replicate the experimental data; it does, however, predict the same general trend, and, therefore, supports the theory of a hydrodynamic phenomena at the bristle tip.

Conclusions

Accurate calibration of the aerodynamic torques acting on the rotating system allows the effect of small changes in seal operating conditions on bristle-tip-to-shaft contact pressure to be measured. The centrifugal growth of the rotor provides a useful means of assessing the degree to which frictional effects prevail.

Frictional effects have been observed in the form of bristle locking in the rundown tests and hysteresis in static flow tests. Friction, therefore, prevents the seal being truly compliant and excursion of the rotor surface away from the bristle tips produces an undesirable reduction in sealing performance. A further implication is that friction considerably increases the stiffness of the seal-to-radial excursions of the rotor, and, therefore, it increases the potential for the bristle tips to wear.

The magnitude of contact forces generated by bristle blow down has been observed to have a linear relation with the differential pressure across the seal. Blow down is observed to develop in the presence of pressure transients, and thereafter becomes arrested by frictional effects. Consequently, seal designs that attempt to alleviate friction may permit blow down to be prevalent. Seal compliance would therefore be improved, however, it is conceivable that wear could result in the presence of sustained blow down loads.

Rotation of the rubbing surfaces induces hydrodynamic lift at the bristle tip. The associated reduction in contact pressure is small in comparison to the overall contact loads. However, if frictional and blow down forces can be reduced, this hydrodynamic effect could possibly be utilized as a wear-reducing mechanism.

Mass flow is observed to increases with decreasing rotor speed. At least some of the increase in leakage can be attributed to the centrifugal decrease in rotor diameter, and, consequently, increase in the flow area. A more compliant seal, in which frictional effects are reduced, is likely to have leakage characteristics that are less sensitive to displacements of the rubbing surface. It is conceivable that rotation might induce phenomena in the incoming flow (e.g., swirl) that may also have effect on leakage. No attempt to isolate these from centrifugal effects has been made in the present study.

In the interference seal tests, the observed changes in seal performance at approximately 4000 rpm and 8000 rpm provide strong evidence that changes in seal performance can result from vibrations of the bristle matrix that are induced at rotor frequencies that are close to the bristles natural frequency or at appropriate harmonics.

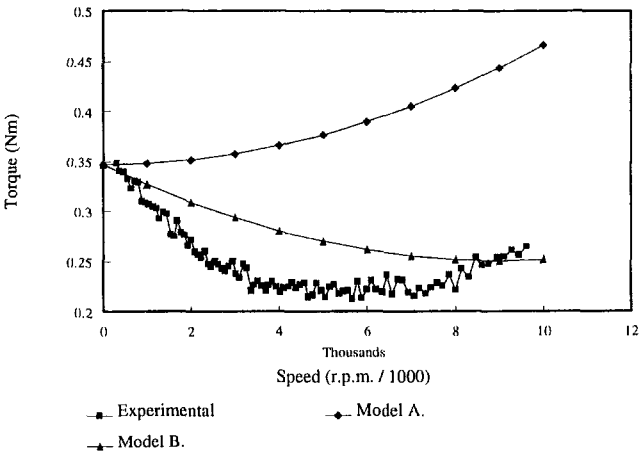

Fig. 10 Interference seal unpressurised run down test

Acknowledgments

Financial support for the work described in this paper was provided by Rolls-Royce plc. The authors would like to thank Dr. J. Chew and Mr. P. A. Withers, of Rolls-Royce, for their technical support and the directors of Rolls-Royce for their permission to publish.

References

Basu, P., Datta, A., Johnson, R., Loewenthal, R., and Short, J., 1993, "Hysteresis and Stiffening Effects of Conventional Brush Seals," AIAA Paper No. 93-1996.

Bayley, F. J., and Long, C. A., 1992, "A Combined Experimental and Theoretical Study of Flow and Pressure Distributions in a Brush Seal," ASME Paper No. 92-GT-355.

British Standard Institution, 1981, "Methods of Measurement of Fluid Flow in Closed Conduits," BS1042, section 1.1.

Chupp, E., and Dowler, A., 1991, "Performance Characteristics of Brush Seals for Limited-Life Engines," ASME Paper No. 91-GT-281.

Ferguson, J. G., 1988, "Brushes as High Performance Gas Turbine Seals," ASME Paper No. 88-GT-182.

Long, C. A., and Marras, Y., 1995, "Contact Force Measurement Under a Brush Seal," ASME Paper No. 95-GT-211.

Theodorsen, T., and Regier, A., 1944, "Experiments on Drag of Revolving Discs, Cylinders and Streamline Rods at High Speeds," NACA Report 793.

von Karman, T., 1921, *Über Laminare und Turbulente Reibung,* Z. Angew. Math. Mech (ZAMM), Vol. 1, pp. 233–252; Also, NACA TM 1092, 1946.

Rao, S., 1986, *Mechanical Vibrations,* 2nd ed., Addison-Wesley Publishing Co., Reading, MA.

Taylor, J. R., 1982, *An Introduction to Error Analysis, The Study of Uncertainties in Physical Measurements,* University Science Books, Mill Valley, CA.

High Temperature Proximity Measurement in Aero and Industrial Turbomachinery

A. G. Sheard
Broadbridge and Company,
Bedford, England

S. G. O'Donnell

J. F. Stringfellow

Fylde Electronic Laboratories Ltd.
Preston, England

The measurement of disc and shaft displacement has been performed for many years as part of the development, commissioning and monitoring of all classes of turbomachinery. This measurement has traditionally been performed using sensors that cannot operate above the curie point of rare earth magnets. In this paper a programme of work is described that was undertaken to develop a measurement system that could make a measurement of target proximity in a high temperature environment. The specific objectives were to make possible the measurement of turbine disc axial movement and shaft motion in the engine core, close to the combustion chamber or turbine; and secondly to make possible the measurement of tip clearance over shrouded turbine rotors.

1.0 Introduction

The measurement of proximity from a sensor to target is a routine measurement within all classes of turbomachinery. The most common measurement principle is the eddy current sensor, described by Sutcliffe (1977). These sensors classically operate only to the curie point of rare earth magnets, typically 200°C, and calibrations are effected by target material property variations.

Improvements to the basic concept have been reported by Hastings and Jensen (1996), which largely eliminate the susceptibility to target material property variations but do not address the issue of limited temperature capability.

There are many possible operating principles for a high temperature blade tip clearance measurement or proximity measurement system, Table 1. The use of lasers was studied by Barranger and Ford (1981), but found to be bulky and expensive in practice. Microwave sensors have been studied, Grzybowski et al. (1996), and show potential; however, practical implementations of the sensors are as yet unavailable. Electromechanical techniques have been successfully employed by Sheard and Turner (1992), but again are bulky and expensive so are not favored.

The use of capacitive-type sensors is common within the gas turbine industry (Muller et al., 1997), where they are classically used to measure the gap between an engine casing and rotor blades. Capacitive-type sensors are routinely used in the automotive industry (Hughes, 1995; Grice et al., 1990) to measure proximity to solid surfaces. The small size and low cost made the capacitance measurement sensor a logical operating principle to apply to high temperature proximity measurement. This technique is not fundamentally susceptible to errors induced by change in temperature (Chivers, 1989). The technique is also insensitive to target material properties.

This paper reports a program of work undertaken to develop a high temperature proximity measurement system that is based on the principle of measuring the capacitance between sensor and target. The design and performance of proximity measurement signal conditioning is described. The design and laboratory testing of a sensor suitable for use with the proximity measurement signal conditioning and blade tip clearance signal conditioning is also presented.

Contributed by the International Gas Turbine Institute and presented at the International Gas Turbine and Aeroengine Congress and Exhibition, Orlando, FL, June 2–5, 1997. Manuscript received by the ASME Headquarters September 16, 1998. Paper No. 97-GT-198. Associate Technical Editor: H. A. Kidd.

2.0 Principle of Operation

The proximity measurement system comprises three components. The first is a sensor, Fig. 1, described in detail by Sheard and Lawrence (1996). The second is an engine mounted oscillator, amplifier, and filter, refered to as the capacitive displacement transducer (CDT) amplifier. The third is a rack mounted receiver that is linked to the CDT amplifier via standard test bed 50 Ohm coaxial cables, Fig. 2. The CDT Amplifier and receiver constitute the proximity measurement system electronics, described in detail by Stringfellow (1996).

The sensor is a triaxial device, with the center wire being connected to the sensor tip. A guard surrounds the center wire and sensor tip, and an outer screen surrounds the guard. The three system components are described in sections 2.1 to 2.3.

2.1 Sensor. The sensor differed from the typical capacitance proximity sensor, described by Grice et al. (1990), in that it is a triaxial, not a coaxial, device.

Classical coaxial proximity sensors measuring sensor tip to target capacitance are isolated from their surroundings using high temperature plastic. This plastic is limited to approximately the same working temperature as the rare earth magnets within an eddy current sensor. The coaxial capacitance sensor, therefore, offers no better high temperature capability than an eddy current sensor.

In order to produce a higher temperature proximity sensor, it was necessary to eliminate all plastic components, replacing them with materials resistant to higher temperatures. The approach adopted was to isolate the coaxial sensor of Grice et al. from its environment by encapsulating it in a third layer. The sensor, therefore, becomes a triaxial device. The same approach is taken with the cable.

The triaxial sensor construction is employed only to provide a high temperature electrical isolation of the center wire and guard from the environment. Once the environmental temperature falls below 200°C the cable between sensor and oscillator can change to a low noise PTFE coated coaxial cable (Fig. 2) as described in section 4.4.

2.2 Engine Mounted CDT Amplifier. The engine mounted CDT amplifier drives the guard at 16 kHz at constant amplitude, Fig. 3. It is insensitive to low speed thermal changes in cable capacitance, keeping amplitude constant irrespective of cable capacitance. This induces an identical sinusoidal oscillation in the center wire that is immune from changes in cable capacitance. As soon as a target comes into range of the sensor

Table 1 Clearance sensor comparison of capability in gas turbine applications

Sensor	Resolution	Temperature Limit (Current State of the Art)	Target Geometry Dependent	Size Comparison	Cost Per Sensor
Electro-Mechanical	0.05mm	1,200C*	No	Large	High
Optical	0.05mm	1,550C*	No	Large	Very High
Capacitive	5% of Range	1,100C	Yes	Very Small	Low
Eddy Current	5% of Range	650C	Yes	Small	Low
Microwave	0.10mm	1,200C	No	Medium	Medium
Fluidic	0.25mm	1,400C	Yes	Small	Low

*Purged.
Additional Factors. Optical & Capacitive most mature. Capacitive least complex. Capacitive and microwave most durable.
Compiled from data contained in Burr (1994).

tip, the additional capacitive couple between sensor tip and target results in a change in the induced voltage on the center wire. This manifests itself as a reduced center wire voltage relative to that on the guard.

The CDT Amplifier contains a very high gain/bandwidth product differential amplifier, with both the reference guard voltage and the induced center wire voltage being fed into it. The differential amplifier output is a 16 kHz sine wave, the amplitude of which is proportional to the difference between reference and induced inputs.

2.3 Signal Conditioning. The engine mounted CDT Amplifier output is fed through a 50 Ohm drive stage to enable it to be linked to a distant receiver module using standard test bed 50 Ohm coaxial cable, Fig. 4. Cable lengths of 150 meters have been used in practical engine installations.

Within the receiver module the 16 kHz sine wave is synchronously rectified to eliminate quadrature errors. The signal is then passed through a 3 pole low pass filter with a 3 db point at 5 kHz. The DC voltage output is then scaled to give 0–10 Volts output proportional to sensor tip to target capacitance over the sensor working range. Drive electronic specification is summarized in Table 2.

3.0 Sensor Development

Sensor design objectives are summarized in Table 3. These targets were set as representative of turbine environments found

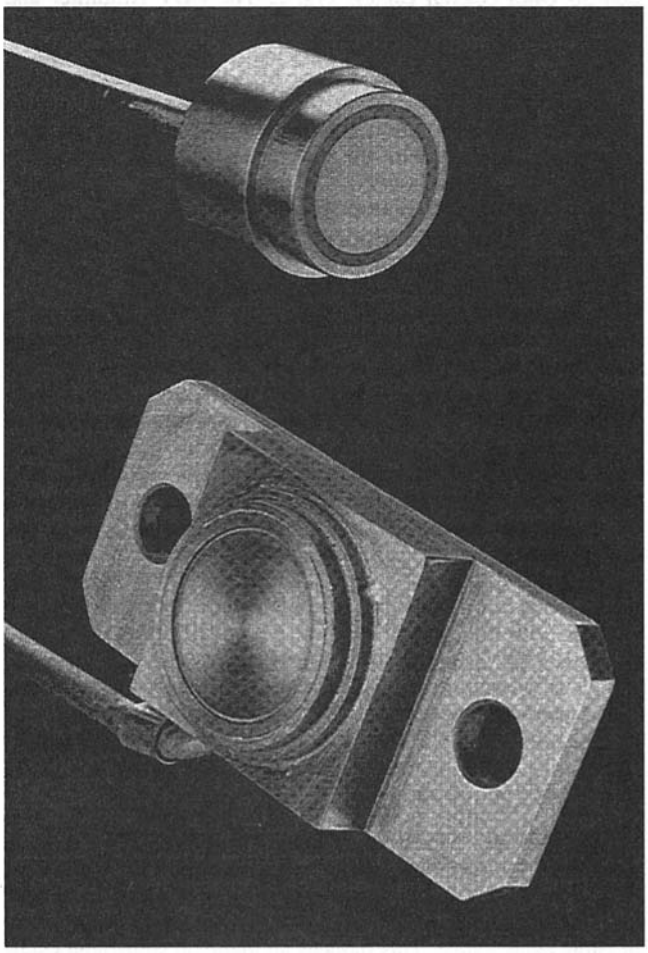

Fig. 1 Traditional (top) and prototype NT (bottom) triaxial capacitive sensors

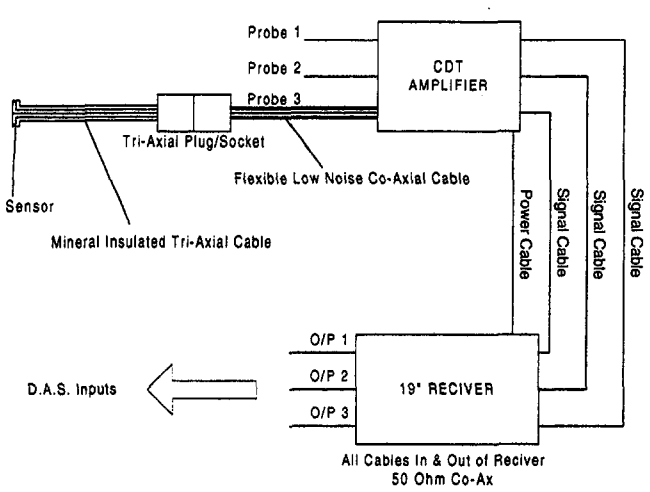

Fig. 2 Proximity measurement system component parts and cable configuration

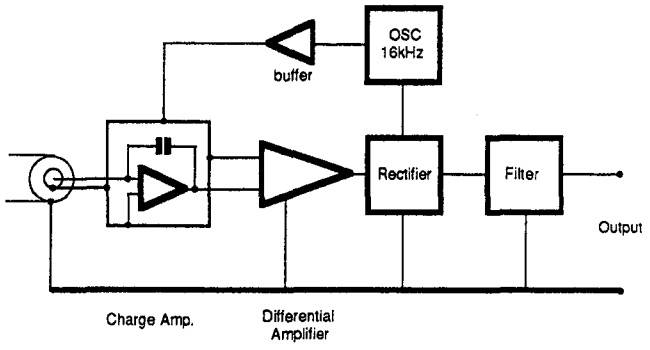

Fig. 3 Schematic diagram of the engine mounted capacitive displacement transducer (CDT) amplifier

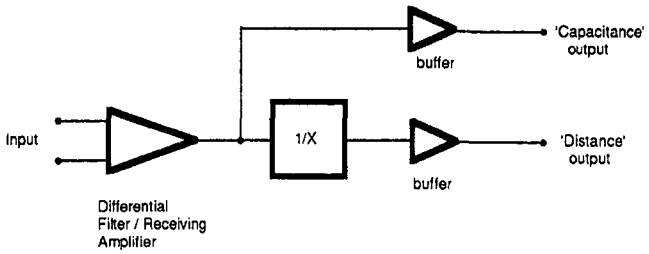

Fig. 4 Schematic diagram of the rack mount receiver

in current generation gas turbines. The next generation of gas turbines was considered by Atkinson (1994) with predicted combustor flame temperatures of 1,773°C, and a requirement for instrumentation capable of operating at 1,500°C. This design objective was considered, and rejected. A future program of work will address next generation requirements. In the following sections, the program of work undertaken to achieve the specification in Table 3 is described.

3.1 Traditional Triaxial Sensor Configuration. Triaxial capacitance sensors are classically complex assemblies of metal and ceramic components, Fig. 5. These sensors have been utilized by Chivers (1989), Killeen et al. (1991), Muller et al. (1997) and Gill et al. (1997) in turbine applications for tip clearance measurement. This sensor will not operate with the proximity electronics of Stringfellow (1996), as the guard ring does not extend to the sensor tip. This introduces typically a 4.5 pF "stray" linkage between electrode and outer screen, which is indistinguishable from the signal to the proximity electronics, and takes the system out of its operating range, Table 2.

A fully guarded sensor would typically have less than 0.1pF stray capacitance, attributable to air linkage from electrode across the guard ring to earth. A fully guarded sensor could be utilized with the electronics of Stringfellow (1996) to a solid target, or over unshrouded blades with the electronics of Muller et al. (1997).

3.2 New Technology Sensor. A New Technology (NT) sensor design, Fig. 6, was developed by Sheard and Lawrence (1996). The concept eliminates all ceramic components, maintaining electrical isolation by alumina coating the electrode and guard. The elimination of machined ceramic components enables extension of the guard to sensor tip, which makes the design suitable for use with proximity and tip clearance electronics.

The electrode, guard, and body comprise a set of inverted cones, which are preloaded into one another. The use of inverted cones produces an intrinsically safe, fully captive design. By preloading the cones into one another during sensor assembly,

Table 2 Drive electronic specification

Oscillator	
Frequency	16 kHz
Level	Preset 10V pk-pk
Distortion	<0.5% harmonic Distortion
Amplitude Stability	<100ppm/C
Amplifier	
Target Capacitance	(1) 1.500pf to 0.150pf
	(2) 0.750pf to 0.075pf
	(3) 0.375pf to 0.0375pf
Rectifier	Synchronous
Filter Type	3 Pole Butterworth
Cut off Frequency	1kHz Typ., 5kHz Max.
Output	+/-10 Volts @ 2mA
Stability	<0.1%/C

Table 3 Sensor specification

Front face peak operating temperature	1,100 C
Sensor body temperature	800 C
Mineral Insulated (MI) cable temperature	600 C
MI cable length	6 Meters
MI to Flexible joint temperature	200C
Flexible cable length	5 Meters
Flexible cable temperature	200C
Drift with temperature over operating range	>+/-2% FS

all components remain positively located at all times. This reduces susceptibility to high cycle fatigue—the design criterion used being the ability to withstand 500G acceleration loads at peak operating temperature.

It is unlikely that any triaxial sensor will compete on cost with coaxial, or multicore sensors, described by Monich and Bailleul (1993) and Bailleul and Albijat (1996) for use with the electronics of Dooley (1989) or Foster (1989). The primary consideration, however, must be a sensor design that is fully captured that will not fail mechanically.

3.3 Sensor Geometry. The objective of good sensor design is to give the maximum operating range for a given sensor diameter. A large guard ring improves linearity by reducing stray capacitive linkage to the sensor body. The total range however is reduced, as for a fixed overall sensor diameter, a large guard results in a smaller electrode.

A small guard ring results in increased capacitive linkage through the air from electrode to sensor body. This stray capacitance reduces sensor linearity, and ultimately dominates, limiting sensor range. The use of a small guard, however, for a fixed overall sensor diameter results in a larger electrode, which increases sensor range.

The trade-off between guard and active sensor diameter was assessed empirically. A ratio between electrode and guard diameter of 1.4 was found to give greatest sensor range.

A finite element analysis of the electrical field between sensor face and target was performed for the optimized tip geometry. The predicted lines of constant voltage, Fig. 7, across the sensor face indicate slight distortion of the field across the electrode guard interface. Clearly, the guard is not perfect; however, it is working well enough to prevent the field in front of the electrode being badly distorted, therefore enabling maximum linkage between electrode and target.

3.4 Sensor Range. The NT sensor range was evaluated when attached to Stringfellow's proximity electronics, Fig. 8. A range of approximately 75 percent overall sensor diameter was achieved. The sensors of Grice et al. (1990) typically have a guard to electrode diameter ratio of 2, which gives good linearity over a short range of approximately 50 percent overall sensor diameter. The NT sensor increases overall sensor range by about 50 percent from 50 percent to 75 percent of overall sensor diameter.

Performance of the electronics of Muller et al. when fitted with NT sensors, was being studied at the time of writing, and will be reported in a future publication. For the sake of completeness, though not the subject of this publication, NT sensor range, when attached to an enhanced version of the tip clearance electronics of Muller et al. is included, Fig. 8. As with the electronics of Stringfellow, range was demonstrated to be 75 percent of overall sensor diameter.

The same enhanced version of the electronics of Muller et al. was utilized by Gill et al. (1997) when attached to a traditional triaxial sensor. The range was found to be 45 percent of overall sensor diameter, Fig. 8. The range reported by Muller et al. was 35 percent of overall sensor diameter.

Tip clearance systems with similar principles of operation by Chivers (1989) and Killeen et al. (1991) were found to have

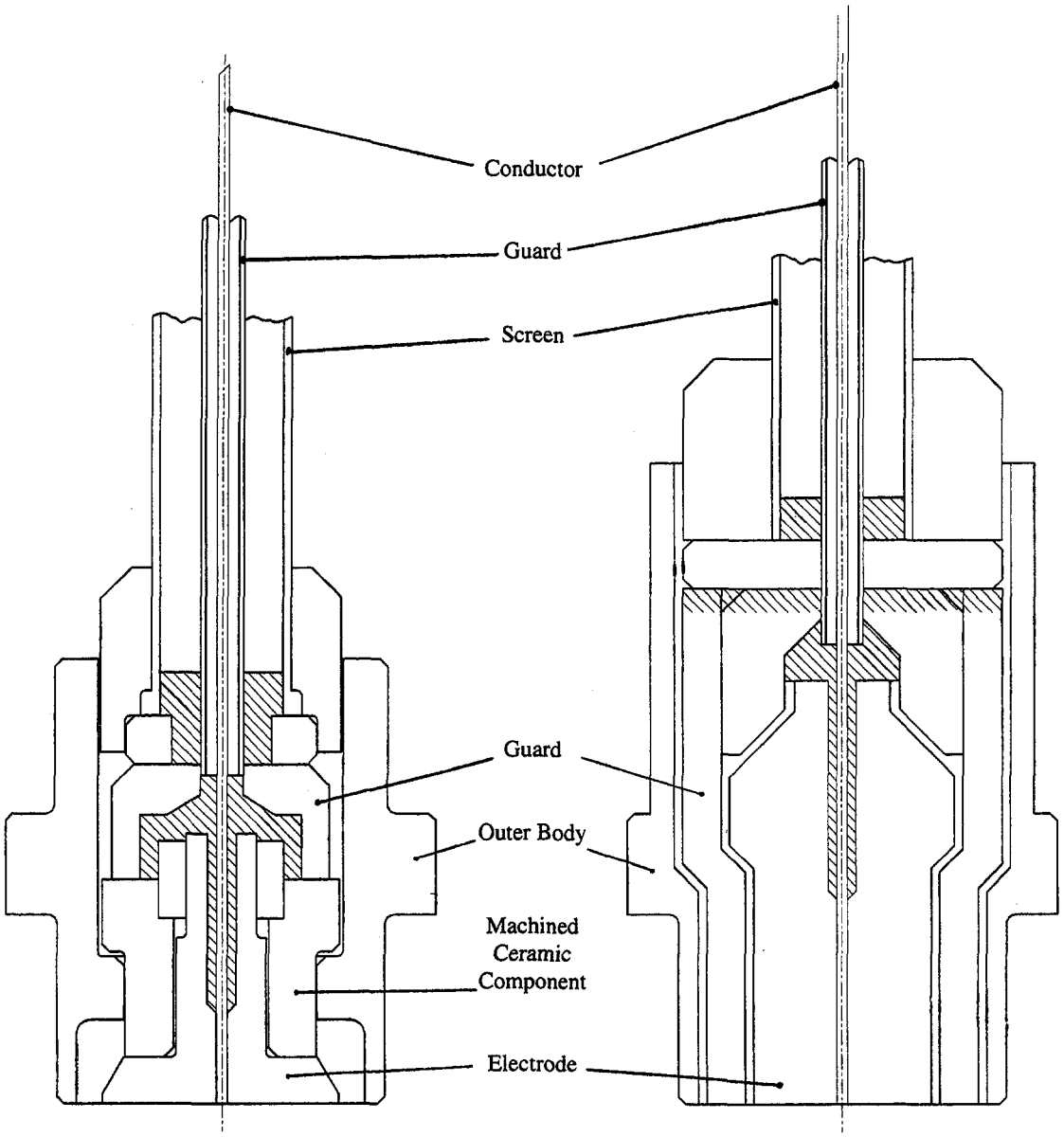

Fig. 5 Traditional tri-axial capacitive sensor

Fig. 6 New technology (NT) capacitive sensor

ranges of 25 percent and 35 percent of overall sensor diameter, respectively.

4.0 Cable Development

The sensor and CDT Amplifier must be linked using a cabling system, Fig. 2. For high temperature installations the only viable cable type is mineral insulated (MI).

4.1 Mineral Insulated Cable. MI cables are signal transmission cables consisting of an impervious sheath, an oxide insulator, and a conductor. In the case of triaxial sensors, the conductor is separated from the sheath by a guard sheath and second oxide layer. The sheath material must suffer low oxidation at elevated temperature, with stainless steel or inconel favored.

The insulator is a compressed metal oxide powder. The CDT amplifier is insensitive to cable capacitance, therefore, Magnesium Oxide (MgO or Magnesia) is favored as the insulator.

4.2 MgO Filled Cable. At the target cable operating temperature, 600°C, Table 3, the relative permittivity of Magnesia changes by 7 percent from 6.3 to 6.7, Table 4, which will result in a corresponding change in cable capacitance of 7 percent. For a typical cable configuration with approximately 2,000 pF capacitance between conductor and guard and guard and sheath, a 100 percent change in cable capacitance affects system output by less than 2 percent; therefore, the performance of Magnesia is considered adequate for the NT sensor application.

4.3 SiO_2 Filled Cable. The principal advantage of Silica over Magnesia is its low relative permittivity, Table 4. Below approximately 500°C, the relative permittivity of Silica is half that of Magnesia, giving a cable of half the capacitance per meter. This enables cables to be twice the length for the same overall capacitance as a Magnesia-filled cable. Above 500°C, the relative permittivity of Silica increases rapidly, Table 4, therefore making Silica-filled cable unsuitable for use. Silica is not the only low dielectric insulating material; however, it is the only readily available low cost material.

The cable configuration is given in Table 5, and is described in detail by Stringfellow (1996). The choice of stainless steel for the center wire and outer screen was made for mechanical strength at high temperature. A low electrical resistance metal was chosen for the guard, as low electrical resistance of the

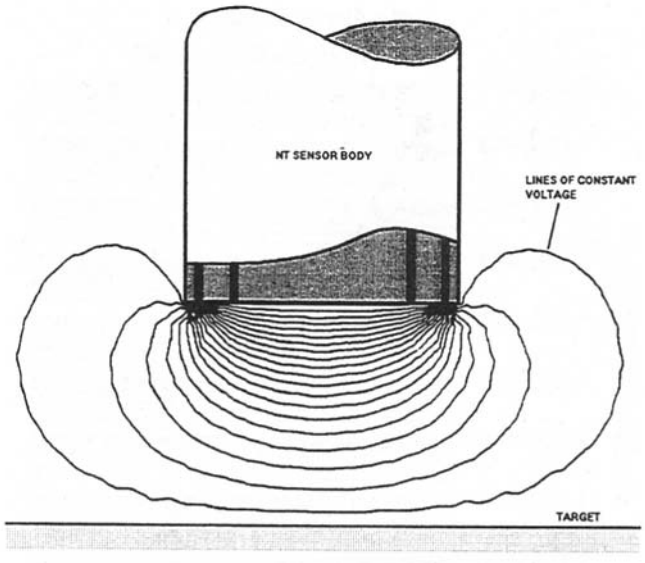

Fig. 7 Finite element analysis of optimized sensor tip. Predicted lines of constant voltage to target at one sensor diameter from the sensor tip.

guard improves CDT amplifier performance, as described in section 5.5.

4.4 Flexible Cable. The CDT amplifier does not require the NT sensor earth returning. For this reason, a coaxial PTFE cable can be used to connect the guard and conductor to the NT sensor, Fig. 2. The outer screen of the triaxial cable performs the same function as the PTFE wrap around a coaxial cable, simply insulating the guard from earth.

5.0 System Performance

Laboratory testing of the NT sensor is summarized in the following section, and the most significant data presented.

5.1 High Temperature Sensor Performance. As the cable and sensor are intimately connected, it is impossible to study sensor performance independently of the cable to which it is connected. To overcome this, probe components were mounted in a jig with no MI attached to allow them to be studied independently.

The critical parameter at elevated temperature is isolation resistance between components. To ascertain change in isolation resistance with temperature of the jig-mounted components, they were oven tested.

Results from the oven testing, Fig. 9, were encouraging, with measured isolation matching theoretical resistivity for pure Alumina well. With an isolation of 10 kOhms within the sensor, CDT amplifier performance is unaffected; however, by 1 kOhm the system had collapsed, as described in section 5.5. Oven tests indicate that at 1,100°C parts maintain over 10 kOhms isolation, making them fit for purpose.

5.2 High Temperature Cable Performance. Cable samples were studied to verify performance at high temperature. The cable samples started to exhibit a thermoelectric effect above 700°C. The dissimilar metals used in the construction of the cable began to generate a voltage between screen and guard and guard and conductor, which was up to 50 mV at 1,100°C. This effect was decoupled in the CDT amplifier, and, therefore, did not affect system performance; however, it proved impossible to make an accurate measurement of isolation resistance above 700°C.

Below 700°C, change in isolation with temperature was consistent with the theoretical resistivity for pure Magnesia and Silica. An isolation resistance of 10 kOhms was predicted at 800°C within Silica filled cable and 1,200°C within Magnesia-filled cable. This was considered consistent with the NT sensor specification, Table 3.

5.3 Sensor and Cable Coupled Performance. The assumption that sensor and cable could be decoupled and studied separately was evaluated. An NT sensor was attached to a Sil-

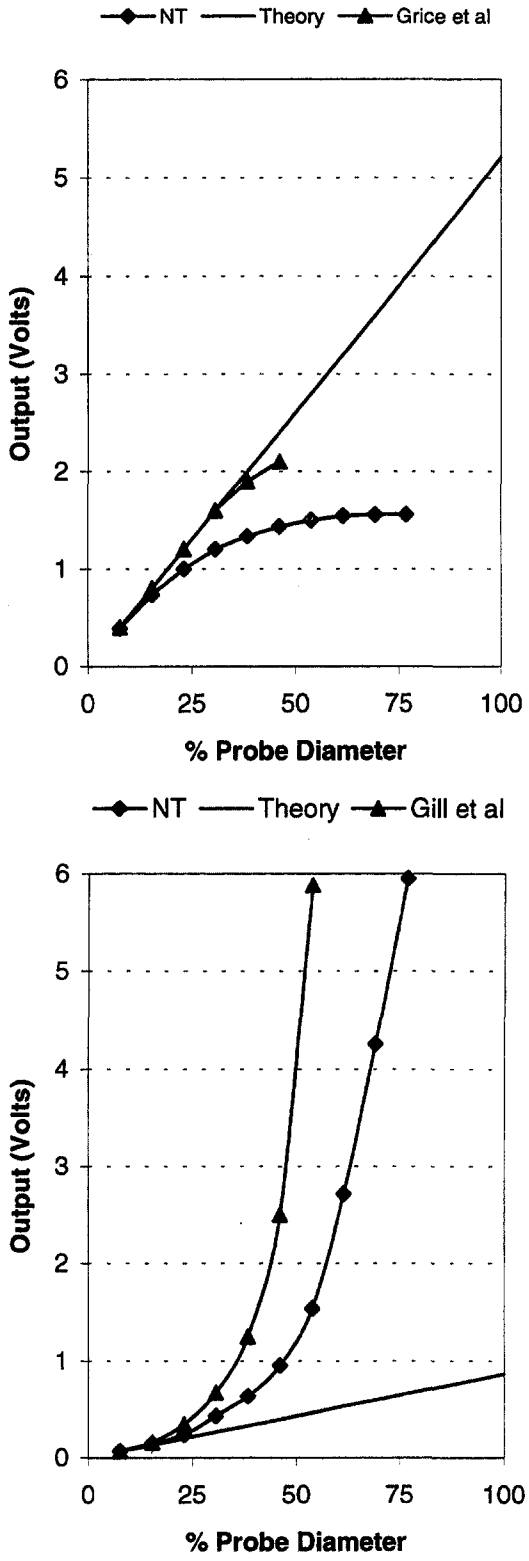

Fig. 8 NT sensor range (top) when coupled with proximity electronics of Stringfellow (1996) and (bottom) tip clearance electronics of Muller et al. (1997)

Table 4 Relative permitivity of silica and magnesia

Temperature (C)	Silica	Magnesia
20	3.0	6.3
100	3.0	6.3
200	3.0	6.4
250	3.1	6.4
300	3.1	6.4
350	3.1	6.5
400	3.2	6.5
450	3.5	6.5
500	3.9	6.5
550	4.7	6.6
600	6.2	6.7
650	11.9	6.9
700	21.0	7.3
750	26.7	7.8
800	29.2	8.6

ica-filled cable and oven tested. The isolation resistance with temperature was within the measurement uncertainty of a repeat-cable-only trial. From this it was concluded that there were no close coupled interactions between sensor and cable, and that their study in isolation was valid.

5.4 Electronic System Performance. The engine mounted CDT amplifier operates by oscillating a voltage at 16 kHz on the guard, which induces an in phase voltage on the center wire. It was noted that with Silica-filled cable above 800°C, phase of the induced voltage on the center wire shifted. By 950°C the return signal was flooded with quadrature and the system collapsed, Fig. 10.

At a temperature of 800°C, the relative permittivity of Silica has increased by an order of magnitude, Table 4. This will increase cable capacitance by an order of magnitude. The CDT amplifier may be set up to function with almost any cable capacitance required in practical applications. Very large changes in cable capacitance, however, do result in system collapse, as discussed in section 5.5. The dramatic increase in the relative permittivity of Silica is, therefore, believed to be the primary cause of system collapse at 950°C.

To confirm that the sensor itself was not responsible for system collapse, a sensor tip (attached to Silica-filled cable) was heated with a blow torch to approximately 1,100°C. System sensitivity was checked, and found to remain stable to within 1 percent.

Measured system sensitivity with Magnesia-filled cable remained virtually unchanged from ambient to 1,100°C, Fig. 10. System output was observed during the oven test. Phase of the induced voltage on the centre wire remained virtually unchanged, with no evidence of quadrature.

5.5 Accuracy Considerations. The effect of guard resistance and its relationship to the measurement must be considered. Conventional stainless steel cable with its inherent low conductivity can lead to measurement errors in the capacitance measurement system of Stringfellow (1996). The guard resistance when combined with guard to outer cable capacitance

Table 5 Cable specification

Conductor material	Stainless Steel
Guard material	Cl
Outer screen material	Stainless Steel
Insulating material	MgO or SiO2, plus additives
Conductor/Guard capacitance	130 pF/M (SiO2)
Guard/Outer capacitance	130 pF/M (SiO2)
Guard resistance	0.2 Ohms per meter
Overall cable diameter	3.00 mm

Cl = BICC Thermoheat Ltd. classified data.

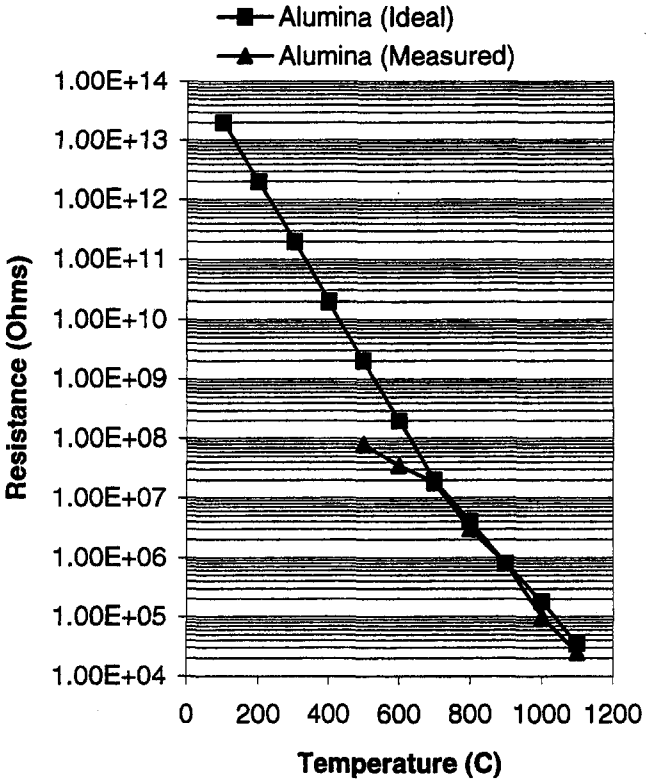

Fig. 9 Measured and theoretical isolation resistance for alumina coated sensor components

develops a quadrature interference signal which can become significant.

The specific conditions needed for the quadrature to become significant occur at high cable temperature, when the cable

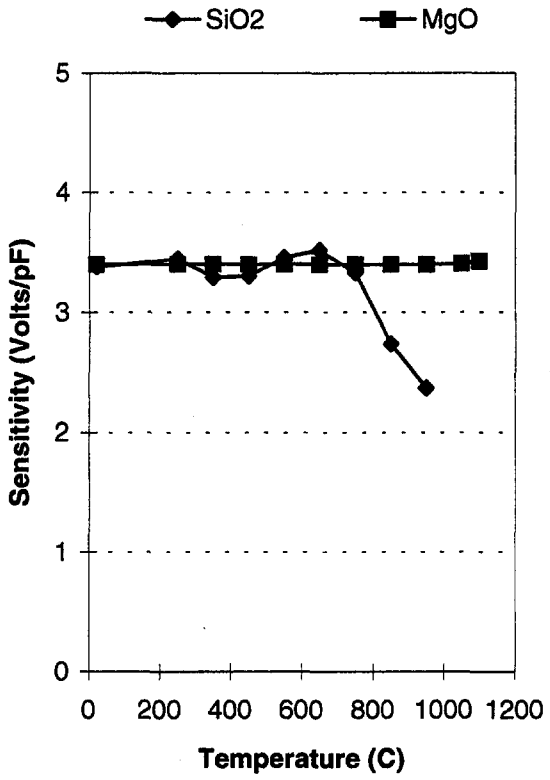

Fig. 10 Measured system sensitivity

guard to inner resistance is reduced, and leakage between the two becomes significant. The combined effects of guard resistance, guard to outer capacitance, and guard to inner leakage are responsible for the error in system output.

A second effect is associated with low isolation between cable guard and screen at high cable temperatures. As guard to screen leakage becomes significant, resistive leakage produces an interference signal that is "in phase". This error signal is indistinguishable from sensor tip to target signal capacitance.

The two effects described above have been found to become dominant with cable guard resistances above 10 Ohms and isolation resistances below 10 kOhms. With cable guard resistances below 1 Ohm and isolation resistances above 10 kOhms, they have been found to induce errors in system output of less than 1 percent, and, therefore, may be regarded as negligible.

The approach to minimizing the two effects was considered by Stringfellow (1996) who used a triaxial cable with low guard resistance, Table 5. In practical applications of the measurement system it is envisaged that the provision of engine mounted electronics should facilitate the use of sensors with MI cable lengths short enough to keep guard resistance close to 1 Ohm. Flexible cables use a low resistance copper guard, with a resistance per meter that is negligible.

6.0 Conclusions

1 A new proximity measurement system has been developed, with an extended operating temperature range making its installation in back end compressor and turbine applications possible.
2 A novel electronic concept has been developed which enables triaxial sensors to be driven in a manner that is not susceptible to low frequency changes in cable and sensor properties induced by changes in their operating temperature.
3 A novel sensor had been developed that eliminates ceramic components, thus avoiding thermal cycle fatigue due to mismatched component coefficients of expansion.
4 The sensor has a fully captive design, and is, therefore, intrinsically safer than conventional sensors.
5 The sensor range was found in practice to be at least 50 percent greater than previous designs in both proximity and tip clearance applications.
6 Triaxial cables have been produced that successfully incorporate the requirement for low capacitance, low guard resistance, and high working temperature.
7 The NT sensor can operate with either the proximity electronics of Stringfellow (1996) or the blade tip clearance electronics of Muller et al. (1996).
8 The NT sensor is considered to be the first sensor concept that is suitable for routine uncooled turbine application at 1,100°C.

Acknowledgments

The authors would like to thank Les Wayman and Brian Knocks of BICC Thermoheat for their assistance in the production of cable prototypes. The assistance of Paul Wilson of Fylde Electronic Laboratories who developed the electronic components is also gratefully acknowledged.

Lastly, the authors would like to thank Mr. N. M. Morton, General Manager, BICC Thermoheat Ltd. for permission to publish the data contained within Table 5 of this publication.

References

Atkinson, W., 1994, *Sensor Requirements*, P&W internal unpublished report.

Bailleul, G. D., and Albijat, S., 1996, "Review of Progress in the Development of Capacitive Sensors for Blade Tip Clearance Measurement," ASME 96-TA-001.

Barranger, J. P., and Ford, M. J., 1981, "Laser Optical Blade Tip Clearance Measurement System," *ASME Journal of Engineering for Power*, Vol. 103, No. 2, pp. 457–460.

Burr, R., 1994, *Sensor Comparison*, P&W internal unpublished report.

Chivers, J. W. H., 1989, "A Technique For the Measurement of Blade Tip Clearance in a Gas Turbine," Ph.D. thesis, University of London.

Chivers, J. W. H., 1989, "A Technique For the Measurement of Blade Tip Clearance in a Gas Turbine," AIAA 89-2916.

Dooley, K., 1989, Capacitive Signal Conditioning, patent application for Pratt & Whitney No. 4795/965 and 4818/948.

Foster, R. L., 1989, "Linear Capacitive Reactance Sensors for Industrial Applications," SAE 890974.

Grice, N., Sherrington, I., Smith, E. H., O'Donnell, S. G., and Stringfellow, J. F., 1990, "A Capacitance Based System For High Resolution Measurement of Lubricant Film Thickness," *Proc. of Nordtrib '90*, 4th Nordic Symposium on Tribology, Lubrication, Friction, and Wear, Hirtshals, Denmark 10–13 June, 1990 (ISBN: 8798353802).

Gill, S. J., Ingallinera, M. D., and Sheard, A. G., 1997, *Industrial Gas Turbine Clearance Measurement System Evaluation*, ASME Paper No. 97-GT-466.

Grzybowski, R., Foyt, G., Atkinson, W., Knoell, H., and Wenger, J., 1996, "Microwave Blade Tip Clearance Measurement System," ASME 96-GT-002.

Hastings, M. M., and Jensen, H. B., 1996, "A Novel Proximity Probe Unaffected by Shaft Electromagnetic Properties," ASME 96-GT-004.

Hughes, S. T., 1995, "Sensors for Road Vehicles Based Upon Capacitance Variation," I. Mech. E. C498/21/214.

Killeen, B., Sheard, A. G., and Westerman, G. C., 1991, *Blade by Blade Tip Clearance Measurement in Aero and Industrial Turbomachinery*, Proc. of the 37th ISA Int. Instrumentation Symp., p. 429–447 (ISBN: 1-55617-312-1).

Monich, M., and Bailleul, G., 1993, *New Digital Capacitive Measurement System for Blade Clearances*, Procs. of the 39th ISA Int. Instrumentation Symp., pp. 419–430 (ISBN: 1-55617-458-6).

Muller, D., Sheard, A. G., Mozumdar, S., and Johann, E., 1997, *Capacitive Measurement of Compressor and Turbine Blade Tip to Casing Running Clearance*, ASME JOURNAL OF ENGINEERING FOR GAS TURBINES AND POWER, Vol. 119, pp. 877–884.

Sheard, A. G., and Turner, S. R., 1992, "Electromechanical Measurement of Turbomachinery Blade Tip-to-Casing Running Clearance," ASME 92-GT-50.

Sheard, A. G., and Lawrence, D. C., 1996, "Gap Measurement Device," patent application for BICC plc No. 9608111.2 & 08/615,372.

Stringfellow, J. F., 1996, "Capacitance Transducer Apparatus and Cables," patent application for Fylde Electronic Laboratories Ltd. No. 9602134.0.

Sutcliffe, H., 1977, "Principles of Eddy Current Distance Gauging," IEE 7816C.